Metal Organic Framework and their Derived Composites for Catalytic Applications

A Thesis Submitted

To

Sikkim University

In Partial Fulfilment of the Requirement for the

Degree of Doctor of Philosophy

By

Sagarmani Rasaily

Roll No.: 18PDCH03

Ph.D. Regn. No.: 18/PhD/CMS/01

Department of Chemistry

School of Physical Sciences

Sikkim University

Supervisor:

Dr. Anand Pariyar

Assistant Professor

Department of Chemistry

Sikkim University

May 2023

Dedicated to…

Grandfather (Late Harka Bahadur Rasaily),

Father (Late Raju Rasaily),

Mother (Smt. Bimala Baraily),

and

The martyrs of Gorkhaland Agitation.

"The dream is real*"*

6 माइल, सामदुर, तादोंग -737102
गंगटोक, सिक्किम, भारत
फोन-03592-251212, 251415, 251656
टेलीफैक्स -251067
वेबसाइट - www.cus.ac.in

6th Mile, Samdur,Tadong -737102
Gangtok, Sikkim, India
Ph. 03592-251212, 251415, 251656
Telefax: 251067
Website: www.cus.ac.in

सिक्किम विश्वविद्यालय
SIKKIM UNIVERSITY

(भारत के संसद के अधिनियम द्वारा वर्ष 2007 में स्थापित और नैक (एनएएसी) द्वारा वर्ष 2015 में प्रत्यायित केंद्रीय विश्वविद्यालय)
(A central university established by an Act of Parliament of India in 2007 and accredited by NAAC in 2015)

DECLARATION

The Ph.D. Thesis entitled "***Metal Organic Framework and their Derived Composites for Catalytic Applications***" has been solely prepared by me under the supervision of Dr. Anand Pariyar, Assistant Professor, Department of Chemistry, Sikkim University.

No part of this work has been submitted previously for fulfilment of any other degree, diploma, associate or fellowship.

Sagarmani Rasaily
Roll no: 18PDCH03
Reg no: 18/Ph.D/CMS/01
Department of Chemistry,
School of Physical Sciences,
Sikkim University.

Place: Sikkim University, Gangtok
Date: 23rd May 2023

We recommend that this thesis be placed before examiners for evaluation

Supervisor
(Dr. Anand Pariyar)

Head of the Department
(Prof. Sanjay Dahal)

6 माइल, सामदुर, तादोंग -737102
गंगटोक, सिक्किम, भारत
फोन-03592-251212, 251415, 251656
टेलीफैक्स -251067
वेबसाइट - www.cus.ac.in

6th Mile, Samdur,Tadong -737102
Gangtok, Sikkim, India
Ph. 03592-251212, 251415, 251656
Telefax: 251067
Website: www.cus.ac.in

सिक्किम विश्वविद्यालय
SIKKIM UNIVERSITY

(भारत के संसद के अधिनियम द्वारा वर्ष 2007 में स्थापित और नैक (एनएएसी) द्वारा वर्ष 2015 में प्रत्यायित केंद्रीय विश्वविद्यालय)
(A central university established by an Act of Parliament of India in 2007 and accredited by NAAC in 2015)

CERTIFICATE

This is to certify that the thesis entitled "***Metal Organic Framework and their Derived Composites for Catalytic Applications***" submitted to **Sikkim University** for the award of **Doctor of Philosophy, Ph.D. in Chemistry** is a result of *bonafide* research work carried out by **Mr. Sagarmani Rasaily** under my supervision in the **Department of Chemistry, Sikkim University**. No part of this dissertation has been previously submitted for any degree, diploma, associate ship, or fellowship.

Anand Pariyar 23/05/23

Dr. Anand Pariyar
Assistant Professor,
Department of Chemistry,
School of Physical Sciences
Sikkim University
Sikkim, India - 737102

Place: Sikkim University, Gangtok
Date: 23rd May, 2023

6 माइल, सामदुर, तादोंग -737102
गंगटोक, सिक्किम, भारत
फोन-03592-251212, 251415, 251656
टेलीफैक्स -251067
वेबसाइट - www.cus.ac.in

6th Mile, Samdur,Tadong -737102
Gangtok, Sikkim, India
Ph. 03592-251212, 251415, 251656
Telefax: 251067
Website: www.cus.ac.in

सिक्किम विश्वविद्यालय
SIKKIM UNIVERSITY

(भारत के संसद के अधिनियम द्वारा वर्ष 2007 में स्थापित और नैक (एनएएसी) द्वारा वर्ष 2015 में प्रत्यायित केंद्रीय विश्वविद्यालय)
(A central university established by an Act of Parliament of India in 2007 and accredited by NAAC in 2015)

Date: 19th May 2023

PLAGIARISM CHECK REPORT

This is to certify that plagiarism check has been carried out for the following Ph.D. Thesis with the help of **URKUND Software** and the result is 0%, which is within the permissible limit (below 10% tolerance rate) as per the norms of Sikkim University.

"Metal Organic Framework and their Derived Composites for Catalytic Applications"

Submitted by, **Sagarmani Rasaily** under the supervision of **Dr. Anand Pariyar, Assistant Professor, Department of Chemistry, School of Physical Sciences,** Sikkim University, Gangtok.

.....

(Sagarmani Rasaily)
Signature of Research Scholar

.....

(Dr. Anand Pariyar)
Signature of Supervisor

.....19/5/2023

Vetted by Librarian

पुस्तकालयाध्यक्ष
LIBRARIAN
केन्द्रीय पुस्तकालय Central Library
सिक्किम विश्वविद्यालय
SIKKIM UNIVERSITY

Acknowledgement

My journey towards completing this thesis was not solely accomplished by my own efforts, but rather with the support and encouragement of numerous unsung heroes. They believed in me more than I could have ever anticipated. In this section, I would like to seize the opportunity to express my heartfelt gratitude to all those remarkable individuals who played a vital role in completing this thesis.

I would like to begin by expressing my utmost respect and love for my parents, **Late Raju Rasaily** and **Smt. Bimala Baraily**. The challenges I faced during my Ph.D. journey were not only mine to bear, as they wholeheartedly embraced them as their own. I will forever remain indebted to their unwavering love and unwavering support. I am immensely grateful for their belief in me. Also, I consider myself lucky to have had the presence of my grandparents, **Late Harka Bahadur Rasaily** and **Smt. Panchu Rasaily**, with me. It is only due to their blessings that I am able to write this thesis.

I wish to express my deepest gratitude to **Dr. Anand Pariyar,** Assistant Professor, Department of Chemistry Sikkim University, for his exceptional guidance, mentorship, and unwavering support throughout my Ph.D. journey. His passion for science, an astute understanding of research, and remarkable team management skills, even in challenging circumstances, are truly commendable. Dr. Pariyar's methodical and well-organized approach has been invaluable throughout my Ph.D., and I have learned a great deal from his guidance. Working in his team has been an enriching experience, and I am grateful for the opportunity to learn and grow under his tutelage. In addition to Chemistry, he has also played a significant role in helping me grasp the philosophy of life, for which I am profoundly indebted. His guidance and teachings have broadened my perspective and enriched my understanding of the world. I am incredibly grateful for his invaluable contributions to my personal and intellectual growth.

I express my heartfelt gratitude to **Dr. Sudarsan Tamang**, Assistant Professor, Department of Chemistry Sikkim University, for his invaluable suggestions and guidance. He has been an exceptional mentor, patiently providing clear explanations whenever I encountered challenges, and always making me feel supported. Despite not having had direct contact with him, I grew up hearing success stories about him in the field of science from my high school teachers and has always motivated me. He has been a role model not just in science, but also in literature and music.

I am immensely appreciative of the seamless research facilities provided to me by **Sikkim University**. My sincere thanks to **Prof. Sanjay Dahal,** the Head of the Department of Chemistry, Sikkim University, for his unwavering guidance throughout my journey. I owe a tremendous debt of gratitude to all the other esteemed faculty members of the Department of Chemistry, namely **Dr. Somendra Nath Chakraborty, Dr. Souvik Chatterjee**, **Dr. Biswajit Gopal Roy**, and **Dr. Akhilesh Kumar Gupta**, for their valuable comments, suggestions, and feedback that significantly contributed to the refinement of my work. I would also like to extend my acknowledgment to **Shri. Binod Chettri**, Laboratory Assistant in the Department of Chemistry at Sikkim University. I am grateful for his assistance and dedication in ensuring a smooth laboratory experience and administrative processes. Additionally, I would like to thank entire **non-teaching staff** of **Sikkim university** for their cooperation regarding administrative work.

I extend my heartfelt thanks to **Dr. Achintesh Narayan Biswas**, Associate Professor at NIT-Sikkim, Ravangla, **Prof. Bhasker Biswas**, Professor at the University of North Bengal, Darjeeling, and **Dr. Anup Gurung**, Assistant Professor, SRM University, Sikkim for sharing expertise and guidance that has helped me to overcome various scientific challenges. I would like to express my profound gratitude towards **Dr. Sajan**

Pradhan, Post-Doctoral fellow, Ewha Women's University South Korea and **Dr. Sachidulal Biswas** for sharing their vast knowledge and experience in the field.

I extend my sincerest thanks to **Mr. Debesh Sharma**, **Mr. Siddhant Basel**, **Mr. Karan Chhetri**, **Mr. Shivanand Chettri**, **Mr. Bikram Gurung**, **Mrs. Surakcha Thapa**, **Mr. Deshaj Bhujel**, **Dr. Samuzal Bhuyan**, **Dr. Susanta Mandal**, and **Mrs. Karishma Bhardwaj** from the Department of Chemistry at Sikkim University. Furthermore, I would like to express my gratitude to **Mr. Subas Chandra Mohanta**, **Dr. Pranish Bomzon, Mr. Khanindram Baruah, Miss Sunu Hangma Subba, Mr. Nilankar Diyali, Mr. Panjo Lepcha**, and **Dr. Ranjan Kaushal Tirwa** for their invaluable laboratory support. All of them have been a constant source of inspiration and support, and their assistance have been invaluable to me. I will always cherish their contributions to my journey.

I express my sincere gratitude to the **Department of Science and Technology**, Government of India, for providing financial support through the DST-Inspire project (DST/INSPIRE/04/2015/002674).

I would also like to express my sincere gratitude to all the teachers of my learning institutions: **Dibya Jyoti Academy Mungpoo**, **Saraswati Higher Secondary School Mungpoo**, **Saint Alphonsus School Kurseong**, and **University of North Bengal, Darjeeling.** They have played a significant role in shaping my academic journey and have been instrumental in my growth and development.

In addition, I would like to express my heartfelt gratitude to my dear friends, **Dr. Rajshree Rai**, **Smt. Deepmala Khadka**, **Shri. Nawin Rai**, **Shri. Pravakar Rai**, and **Shri. Siddarth Thapa**, for their initial encouragement and motivation in embarking on the journey of pursuing a Ph.D. Their support and belief in my abilities have been invaluable, providing me with the necessary inspiration to pursue this academic path.

I am filled with profound gratitude for the unwavering support and love I have received from my brother, **Mr. Saugat Mani Rasaily**. I could fly this high only because he has been my wing to date. I wholeheartedly would also like to be great full towards my uncle **Shri Binod Rasaily**, **Shri Santa Kumar Baraily** and **Shri Kamal Rasaily** who has been a fatherly figure and utmost support in my life. I am thankful to my brothers, **Shri Roshan Ruchal**, **Shri Rupen Baraily**, **Shri Yogen Baraily**, and all family members for their constant love and support.

I would like to express my deepest gratitude to my fiancé, **Miss. Rojina Gazmer**, for her unwavering love and support during the most challenging moments. Her presence has been my rock, providing me with strength and stability when I needed it the most. Without her by my side, the path would have been overwhelmingly difficult. I am truly grateful for her countless contributions, too numerous to list, but above all, for her boundless love and unwavering support that has been constant in my life.

Lastly, I would like to take this opportunity to acknowledge staffs and express my gratitude to SAIF-CDRI, Lucknow, University of North Bengal, Darjeeling, and SAIF-NEHU, Shillong for providing paid instrumental facilities.

Sagarmani Rasaily

Research Scholar
Department of Chemistry
Sikkim University
Tadong, Gangtok – 737102

Abstract

Metal-organic frameworks (MOFs) are a type of coordination polymer consisting of highly ordered crystalline structures. These structures are composed of inorganic secondary building units and organic ligands that can extend indefinitely, forming rigid frameworks in one, two, or three dimensions. The remarkable characteristics of MOFs, such as, high surface area, permanent porosity, and well-defined framework, have generated significant interest in their applications for gas storage and separation. Recently, catalysis has emerged as a rapidly growing field in MOF. The current state of MOFs in catalysis is a transitional phase, as efforts are being made to establish them as robust catalysts for industrial applications and viable alternatives to conventional heterogeneous catalysts. In this thesis the catalytic application of MOF and its derived composites has been broadly studied towards molecular and electrocatalytic reaction. For molecular catalysis, application of MOFs in coupling reactions has been focused where emphasis was given for the formation of C-N, C-O, C-S, and C=C bonds through Ullmann coupling, cross-dehydrogenative coupling (CDC) *via* C-H activation, and Knoevenagel condensation reactions. Additionally, the thesis demonstrates the use of MOFs as a beneficial template for deriving metal composites and their subsequent application in electrocatalytic oxygen processes. The overall study of the thesis is divided into five comprehensive chapters, providing detailed discussions on the various aspects of the research work conducted.

In **Chapter I**, the discussion revolves around the latest breakthroughs in utilizing MOFs towards heterogeneous catalysis. The subsequent section focuses on the recent progress in catalytic applications of MOFs for coupling reactions, specifically involving the formation of C-N, C-O, C-S, and C-C bonds. Furthermore, this chapter extensively

explores the diverse aspects of MOFs as templates for deriving metal-composites. A detailed account of the current trends and developments concerning MOF-derived metal oxides and metal composites in relation to the oxygen reduction reaction and oxygen evolution reaction is also presented. Additionally, this chapter encompasses an understanding of the thesis's origin of research along with the aims and objective.

Chapter II provides an in-depth exploration of the synthetic methods employed for MOFs. This chapter offers a comprehensive overview of the synthetic process used for various well-known and novel MOFs studied in this work. The discussion includes detailed accounts of the synthesis and characterization procedures for established MOFs such as HKUST-1, Cu-BDC, ZIF, MIL, MOF-74, Mn-SKU-1, Mn-SKU-2, Cu-SKU-3 and Cu-1D. Additionally, the chapter provided more information into the synthesis of novel MOFs, including Cu-SKU-4, and Ni-SKU-5 (SKU=Sikkim University). The characterisation and analysis of synthesized MOFs using SCXRD, PXRD, FTIR, BET surface area analysis, elemental analysis, TGA, and SEM techniques has been discussed in details.

Chapter III explores the utilization of Cu-1D MOF in coupling reactions, highlighting the crucial significance of coordinatively unsaturated sites (CUS) in metal-centered catalysis. The Cu-1D MOF possesses inherent CUS upon synthesis, eliminating the need for additional activation processes to render its catalytical potential. The Cu-1D MOF, was found efficient towards the intermolecular C-heteroatom cross-coupling of diverse *N*-heterocycles, aliphatic, aromatic, and alicyclic amines & amides (C-N), phenols (C-O), and thiols (C-S) with aryl halides (halide = I, Br), yielding impressive yields ranging from 70% to 95%. Notably, these results surpassed the performance of the current state-of-the-art Cu-based homogeneous system. The mechanistic pathway was thoroughly investigated through a combination of experimental and computational

methods that revealed *in-situ* reduction of Cu(II) to Cu(I) species using KOH/DMSO. The Cu(I) species formed undergoes oxidative addition followed by reductive elimination. Furthermore, Cu-1D MOF was also explored towards intramolecular reactions forming tetrahydro quinoxalines and high stereoselectivity with an enantiomeric excess (*ee*) of more than 98.5%.was found for desired product.

Following the, results from the previous chapter, **Chapter IV** discusses the role of CUS in MOF towards cross-dehydrogenative reaction (CDC) reaction forming C-O bond *via* C-H activation and Knoevenagel reaction forming C=C bond. The catalyst shows high efficiency towards CDC reaction yielding 2-((1,4-dioxan-2-yl)oxy)benzaldehyde as the desired product in 95% yield within 0.5 h. The same catalyst is also used to form different carbamate molecules by reacting the 2-hydroxybenzaldehyde derivative with DMF, resulting in yields ranging from 87-92%. Comparisons with other Cu-based MOFs such as HKUST-1, CU-BDC(DMF), Cu-SKU-5, and Cu-SKU-4 highlight the importance of available coordinating sites in catalysing the CDC reaction. Cu-1D MOF, with its Lewis acid and Bronsted basic sites, is further explored for Knoevenagel condensation reactions, where more than 99% yield of 2-benzylidenemalononitrile was obtained within 0.5 h for the reaction between benzaldehyde and malononitrile. The catalyst is tested for its recyclability and was found to be heterogeneous, where it can be recovered and reused for up to four cycles, maintaining 82% and 98% product yields for CDC and Knoevenagel reactions, respectively.

Next, in **Chapter V**, the Mn & Ni based MOFs were used as an altruistic template to derive metal/metal oxide composites for electrocatalytic oxygen process. Two novel Mn-MOFs (Mn-SKU-1 and Mn-SKU-2) were pyrolyzed under N_2 at 600 °C, and porous α-Mn2O3 composites (PSKU-1 and PSKU-2). These mesoporous MOF-derived α-Mn_2O_3 when applied towards electrocatalytic reduction of oxygen in 0.1 M KOH

solution, shows onset potential of 0.90 V for PSKU-1 and 0.93 V for PSKU-2 vs RHE, with the current density of 4.8 and 6.0 mA cm^{-2}, respectively at 1600 rpm. Similarly, Ni/NiO-composites was derived from Ni-SKU-5 MOF at 450 °C for 4 h. The derived nickel composites were applied as a bifunctional electrocatalyst for both ORR and OER with an overpotential of 290 mV and 350 mV vs RHE respectively.

Lastly, **Chapter VI** provides a comprehensive summary of the thesis and the future prospects of the study.

Table of Content

List of Figures

List of Tables

List of Schemes

List of Abbreviations, Symbols and Acronyms

• 1D	One Dimension
• 2D	Two Dimension
• 3D	Three Dimension
• nm	Nanometer
• Å	Angstrom
• dec	decade
• h	Hour
• s	Second
• min	Minutes
• cm	Centimeter
• mm	Millimeter
• V	Volt
• mL	Milliliter
• µL	Microliter
• g	Grams
• mg	Milligram
• µg	microgram
• mmol	Millimoles
• mA	Milliampere
• i.e.	That is
• *viz.*	Namely
• UV	Ultraviolet
• NP	Nanoparticle
• NCs	Nanocrystals
• MHz	Megahertz
• TEA	triethylamine
• Hz	hertz
• rGO	graphene oxide
• E_{onset}	Onset potential
• MeIM	2-methylimidazole
• SKU	Sikkim University
• *J*	Coupling constant
• CNTs	carbon nanotubes
• bpy	2,2′-bipyridine
• HINA	isonicotinic acid
• DCM	Dichloromethane
• Mim	*N*-methylimidazole
• SA	Surface Area

• MOF	Metal-organic Framework
• IRMOF	isoreticular MOF
• PBU	Primary Building Unit
• SBU	Secondary Building Unit
• PSM	Post-synthetic modification
• CUS	coordinatively unsaturated sites
• OMS	open metal sites
• BET	Brunauer–Emmett–Teller
• TON	Turn-over number
• TOF	Turn over frequency
• SHAB	soft-hard acid-base
• TMO	transition metal oxide
• $E_{1/2}$	Half wave potential
• PXRD	Powder X-ray Diffraction
• SCXRD	Single Crystal X-ray Diffraction
• FTIR	Fourier Transform Infrared
• NMR	Nuclear Magnetic Resonance
• kV	Kilo Volt
• EDX	Energy- Dispersive X-ray
• NGPC	N-doped porous carbon
• *ee*	enantiomeric excess
• DFT	density functional theory
• ORR	oxygen reduction reaction
• OER	Oxygen Evolution reaction
• LDH	layered double hydroxides
• CV	cyclic voltammetry
• FWHM	Full Width at Half Maximum
• K-L Plot	Koutecky-Levich Plot
• RDE	Rotating Disc Electrode
• RRDE	Rotating Ring Disc Electrode
• GCE	Glassy carbon electrode
• RHE	Reversible Hydrogen electrode
• LSV	Linear sweep voltammetry
• CPE	Control Potential Electrolysis
• SACs	single-atom catalysts
• TMU	Tarbiat Modares University
• MIL	Matériaux de l'Institut Lavoisier
• UiO	Universitetet i Oslo

• PEMFCs	polymer electrolyte membrane fuel cells
• HKUST	Hong Kong University of Science and technology
• DUT	Dresden University of Technology
• VNU	Vietnam National University
• ZIF	Zeolitic imidazolate frameworks
• BDC	benzene dicarboxylic acid
• BTC	1,3,5-benzentricarboxylate
• NDC	2,6-naphthalene dicarboxylate
• DABCO	1,4-diazabicyclo[2.2.2]octane
• PyDC	Pyridine-3,5-dicarboxylate
• DMF	*N, N*-dimethylformamide
• CDC	cross dehydrogenative coupling
• J_k	kinetic current density
• dd	Doublet of doublet
• LIBs	lithium-ion batteries
• EPR	Electron Paramagnetic Resonance
• HPLC	High- Performance Liquid Chromatography
• TEM	Transmission Electron Microscope
• TLC	Thin-Layer Chromatography

Chapter I:

Recent Trends in Metal-Organic Framework Towards Catalysis

I.1. Catalysis and its background:

Catalysis is at the forefront of the modern world with numerous applications in various fields including chemistry, energy, medicine, and materials science. Catalysts are substances that can accelerate chemical reactions without being consumed in the process. It lowers the activation energy required for the reaction to occur, allowing the reaction to proceed faster or at a lower temperature than it would otherwise. The impact of catalysis on the modern world is immeasurable as it is used in numerous industries, ranging from the production of fuels and chemicals to pharmaceuticals and food processing. The origins of catalysis can be traced back to ancient times when people discovered that certain materials could accelerate the rate of reactions. For example, the ancient Egyptians used yeast to produce bread and beer, and the Greeks used vinegar to produce wine. However, it was not until the 19th century that the concept of catalysis was formally introduced by the Swedish chemist Jöns Jacob Berzelius.[1a-b] He observed that the reaction rate of the esterification of alcohol and acetic acid was increased in the presence of sulfuric acid, which he concluded to act as a catalyst. In the 20th century, catalysis became a major field of research, and World War I & II had a significant role in escalating the advancement of catalysis. During the war, there was a high demand for chemicals such as explosives, fertilizers, and synthetic materials.[2a-b] This demand led to an increased interest in catalysis, which is the process of accelerating chemical reactions by using a catalyst. One of the most important developments in catalysis during World War I was the Haber-Bosch process developed by Fritz Haber and Carl Bosch.[2,3] In this process iron is used as a catalyst for the large-scale production of ammonia from nitrogen and hydrogen gases. Ammonia was a key component in the production of explosives and fertilizers, which were essential for the war effort. Furthermore, this process revolutionized the

production of fertilizer and led to the well- known Green Revolution in agriculture.[4] Similarly, during World War II, various technologies, including the production of synthetic rubber, aviation fuel, and explosives were advanced. One significant example of catalysis during World War II was the development of the Fischer-Tropsch process,[5] which allowed for the synthesis of liquid fuels from coal and natural gas. Also, catalysts, such as cobalt and nickel, were used to accelerate the polymerization reaction and improve the yield and quality of the rubber. In the current era, catalysts are extensively utilized worldwide in producing more than 10,000 products that hold a value of over $10 trillion annually, contributing to 15% of the global GDP. Catalytic processes are responsible for manufacturing over 95% of chemical products in volume, making the industrial catalyst manufacturing market worth nearly $16 billion.[6] These data are therefore easy to comprehend why research in catalysis is forefront in the fields of chemistry, materials science, and chemical engineering. Today, there are several emerging trends and future directions in the field of catalysis. These include the development of new catalysts for renewable energy conversion, drug design, sustainable reactions, etc and the use of artificial intelligence, machine learning for catalyst discovery, design, and the development of catalytic materials has begun.

Catalytic materials can be classified into three broad categories: heterogeneous, homogeneous, and biocatalysis. Heterogeneous catalysis involves the use of a solid catalyst that is in a different phase than the reactants, while homogeneous catalysis involves the use of a catalyst that is in the same phase as the reactants. Biocatalysis involves the use of enzymes or other biological catalysts to facilitate a reaction. Over the years, there have been significant advancements in the field of catalysis, including the development of new catalysts, improved characterization techniques, and novel

applications. Amongst all, heterogeneous or solid catalysts are one of the most preferred owing to their sustainable properties such as easy separation, highly stable, recyclability, tolerance over wide reaction conditions, etc.[7] Despite these advantages, heterogeneous catalysts also have some limitations, compared to homogeneous counterparts. Heterogeneous catalysts often suffer from mass transfer limitations, as the reactants must diffuse through the bulk of the reaction mixture to reach the catalyst surface, eventually, the rate of the reaction decreases. Heterogeneous catalysts are often limited in their reactivity, as only the surface of the catalyst is involved in the reaction. This can reduce the efficiency of the reaction and require a larger amount of catalyst to achieve the desired conversion. Heterogeneous catalysts can be more difficult to synthesis than homogeneous, as they often require specific surface properties and can be sensitive to the synthesis conditions. However, most of these limitations of heterogeneous catalysts could be addressed with the use of porous material with sufficient pore diameter and surface area for a substrate to access the active sites.

Various porous material has been reported in past years that has catalytic activity. Some classic examples of porous materials are carbon materials,[8] metal oxides,[9] porous aromatic frameworks,[10] mesoporous silica,[11] polymers,[12,13] zeolites[14], etc. However, these materials are either fully organic or inorganic in nature and the majority of these substances lack a defined structure, have irregular pores, and are classified as amorphous porous solids, which makes it difficult to establish clear relationships between their structure and catalytic properties. Zeolites are a class of naturally occurring or synthetic crystalline porous solids composed of silicon, aluminium, and oxygen atoms in a three-dimensional framework.[15] With superior stability, inherent acidity, and regular arrangement of pores and channels of molecular

dimension makes them ideal for use in various industrial applications such as adsorption, separation, and catalysis. However, the precise regulation of the distribution of acidic sites within zeolites is difficult to achieve, and the inadequate variety of pore structures are its serious limiting factor. As a result, the pursuit of highly developed porous materials that possess distinct, abundant, and easily customizable structures for a wide range of applications remains a highly active field of scientific inquiry. Recently a material known as metal organic framework have been established as a new class of porous material that has diverse functionality, high porosity and flexibility compared to the previous porous material (figure I.1).

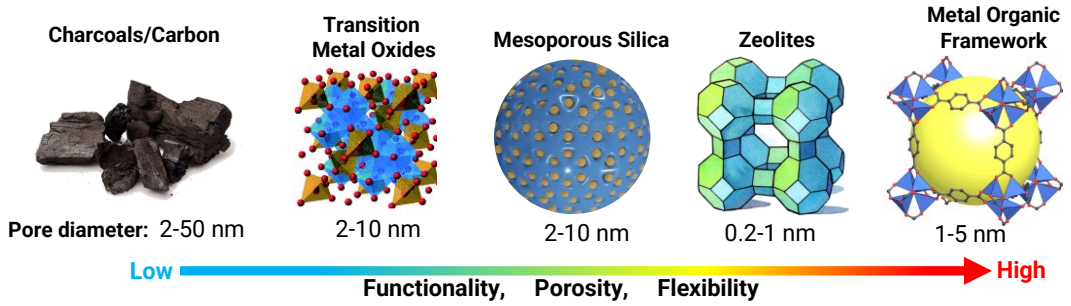

Figure I.1: Evolution of porous material in terms of functionality, porosity, and flexibility.

I.2. Metal-Organic Framework (MOFs):

Metal-organic frameworks (MOFs) are a new class of porous hybrid material that combines organic and inorganic components into a crystalline and porous structure of one, two, or three dimensions (Figure I.2). The basic structural unit of MOF is formed by connecting metal nodes with co-ordinating atoms of organic ligands and referred as secondary building unit (SBU). These building blocks or SBU are also used to describe the repeating unit of a MOF. Various SBU is linked by an organic ligand thereby giving rise to a three-dimensional framework generating a potential void as represented by a yellow sphere in figure I.2. Therefore, with a meticulous selection of

favourable metal ions and organic linkers MOFs structures, pore environment and functionality can be precisely tuned.

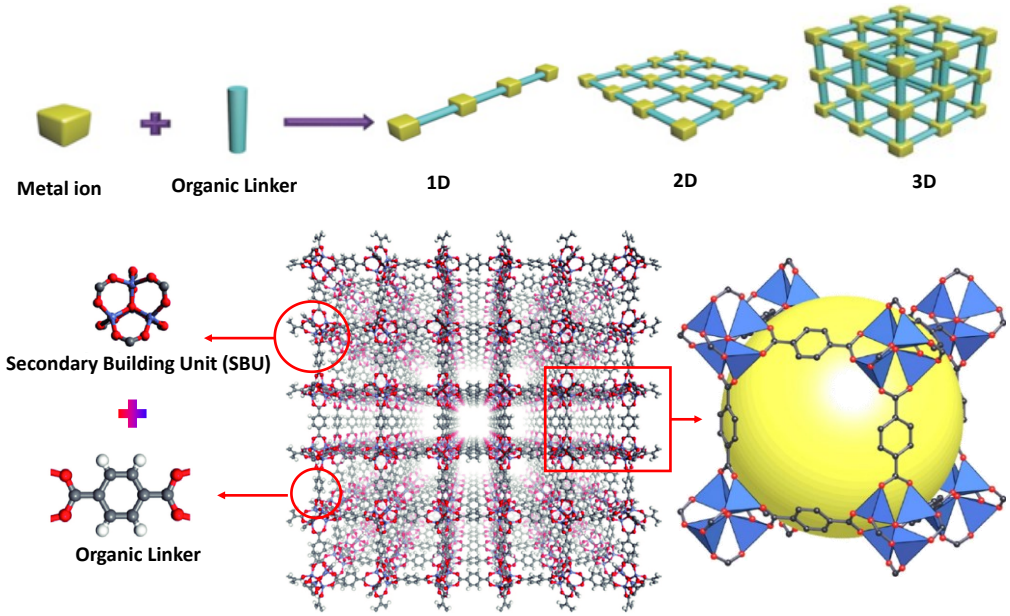

Figure I.2: Schematic illustration for the synthesis of MOF along with visualization of different units of MOF.

Furthermore, the use of metal ions and organic ligand allows infinite possible combinations for MOFs structural diversity and functionality. Hence, in contrast to conventional porous materials, MOFs possess numerous advantages such as follows;

(1) The crystalline and precisely defined structures allows MOFs in comprehending the fundamental mechanism and structural-reactivity correlations.[16]

(2) The hybrid structures of organic-inorganic compounds not only blend the advantageous qualities of their organic and inorganic constituents but also bestow unique properties that surpass those of a mere blend of their individual components.[17]

(3) The substantial surface area and porosity of these materials guarantee an abundance of accessible functional sites that promote the adsorption and enrichment of substrate molecules around the active sites. Till today the surface area of 7800 m^2 g^{-1} is the highest reported for Zr-based MOF well known as DUT-60[18] (DUT=

Dresden University of Technology) and theoretically the surface area of MOF can go beyond 14000 m^2 g^{-1}.[19] Furthermore, uniform size and shape of pores, facilitates the entry and exit of reaction substrates and products that match their specific size and shape. As a result, MOFs exhibit a permeability that selectively filters substances based on their size.

(4) The ability to adjust the pore wall environment at the molecular level, either through *de novo* construction or post-synthetic modifications has made MOFs a versatile and compatible material of choice for many applications.[20]

(5) Due to their large pore volume and compatibility with a variety of materials such as metal nanoparticles, biomolecules, polymers, etc, MOFs offer an inherent environment for the integration of functional species, resulting in the creation of MOF composites that serve a multitude of purposes. The permanent pore space within MOFs provides the ideal conditions for these incorporations to take place.[21]

(6) MOFs are exceptional precursors/templates for a wide range of porous carbons, metal-based compounds, and their composites. Further, the derived composites can inherit the structural properties of its parent MOF thereby resulting in a metal composite of high surface area, unique morphology, improved conductivity, etc.[22,23]

With all the intriguing properties discussed above, MOF as a functional material has been a burning topic for two decades and it can be well understood from the publications that is being reported in recent years. Since their discovery in the late 1990s,[24–26] MOFs have been used to create a variety of aesthetically fascinating structures, with nearly 90,000 different MOFs reported to date as per the web of science database. Over the past 15 years, there has been a gradual increase in the

number of publications on the topic of "Metal-Organic Framework," as shown in figure I.3.

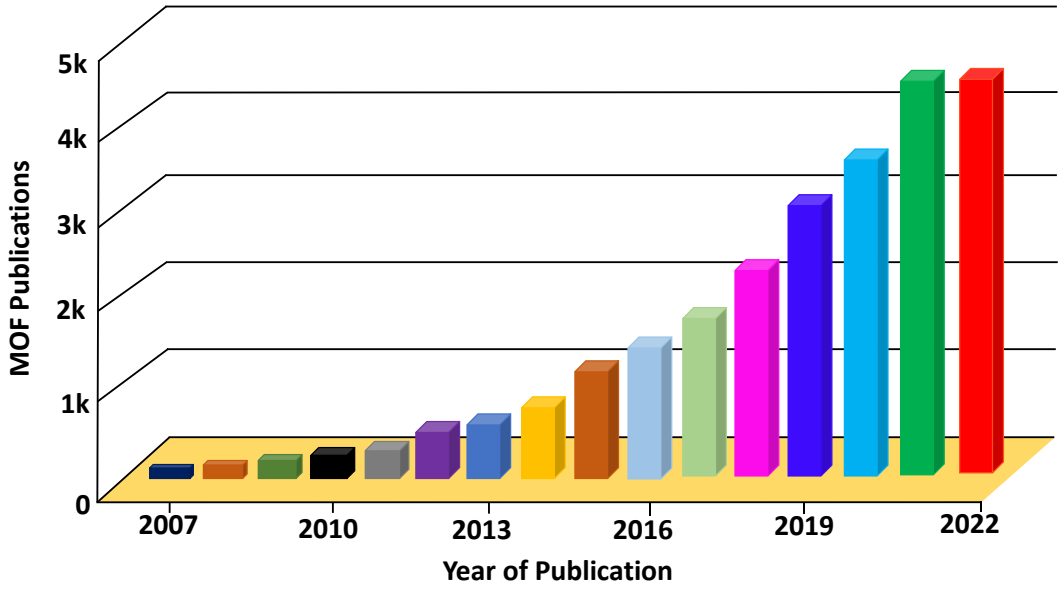

Figure I.3: A graphical representation of MOF-based publications per year. Source: the web of science, database. Keywords: Metal-organic framework, MOFs.

I.3 MOF as a heterogeneous catalyst:

In 1959, there have been reports on the type of material that combines organometallic and pore-selectivity functionalities by means of coordination polymers. In the same year, Kinoshita *et al.*[27] described the crystal structure of bis(adiponitrile)copper(I) nitrate, which is now could be considered a coordination polymer or MOF material. Despite early reports on coordination polymers in 1960[28,29] the subject did not receive much attention until it was rediscovered and revived in the late 1990s, particularly through the works of Robson *et al.*[30,31] and Yaghi *et al.*[32] The discovery of the well-known MOF-5 (Zn-BDC MOF, BDC= benzene dicarboxylic acid) material in 1999[25] further fuelled interest in the field. Initially, much efforts were focused on synthesizing new materials, and in the latter half of the decade, there has been significant interest in exploring potential applications of these coordination polymers. In the preliminary years, the application of MOF has been extensively explored

towards gas storage and separation.[33,34] Recently, MOFs have also been identified as highly promising contenders for various potential applications such as catalysis,[35] photocatalysis,[36] sense,[37] drug delivery,[38] bio application,[39] optical applications,[40,41] energy applications,[42–44] heat transformation,[45], etc.

Recently, more focus is devoted towards the study and design of MOFs toward potential application in catalysis. The structural diversity, inherent hybrid organic-inorganic behaviour, possibility of deliberate design, and well-defined porosity, are some of the most intriguing properties of MOFs that makes them efficient material as heterogeneous catalyst. The various structural attribute of MOF as a heterogenous catalyst can be characterized into various cases, these include (i) the generation of co-coordinatively unsaturated sites (CUS) in SBU of MOF, where removal of the liable ligand from the metal node is carried out thereby generating a catalytically active site. (ii) Post synthetic modification (PSM) on MOF to anchor the catalytically active site, where either organic ligand is used to hook the organocatalytic site. (iii) Using MOFs as hosts to encapsulate various catalytic sites, such as nanoparticles, enzymes, homogenous complexes, or other catalytically active moieties. (iv)And using MOFs as precursors for the formation of nanoparticles or metal composites *via* controlled decomposition. The detailed discussion on these points has been highlighted below as an independent subtopic.

I.3.1. Coordinatively unsaturated sites in MOFs as catalytic sites:

The use of polar solvents such as DMF, H_2O, etc during the synthesis of MOF results in labile coordination of these solvents to metal nodes or SBU. The labially coordinated solvents can be removed from metal nodes following various post-

synthetic methods thereby generating CUS or open metal sites (OMS) in MOF. A figure representation of generating CUS in metal nodes in given in figure I.4.

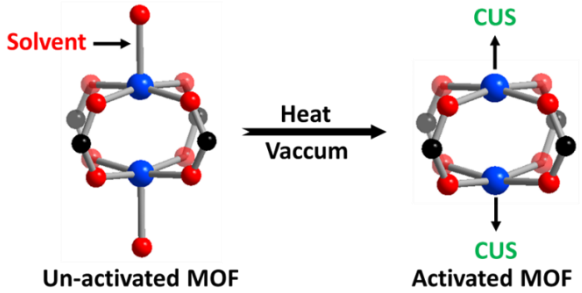

Figure I.4: Illustration for the generation of CUS for activation of MOF.

As the generation of CUS creates the catalytic sites within the framework the process is also known as activation of MOF and the MOF with CUS can be referred to as activated MOF. The metal nodes with CUS or OMS can act as a catalytic site due to the availability of vacant *d*-orbitals which in turn increase the Lewis acid character of metal nodes. Therefore, the metal with a high oxidation state can behave active site compared to the metal with a low oxidation number. The various method to generate CUS in MOF has been discussed below.

(1) **Thermal treatment or convectional method**: In this method, the MOF sample is treated at a high temperature (>100 °C) under a high vacuum for a longer time (10-24 h). The activation of MOF can be well understood by taking an example of the generation of open Cu^{2+} sites on HKUST-1, which is composed of $Cu_3(BTC)_2(H_2O)_2$. The framework is formed by linking di-copper paddle-wheel SBUs through trigonal BTC (BTC = 1,3,5-benzentricarboxylate) linkers.[26] The Cu metal is coordinated by four carboxylate groups in a square planar arrangement with a coordination number of 4. The Cu-Cu has an internuclear separation of 2.628 Å and each Cu-metal obtains a pseudooctahedral coordination geometry.[26] The two H_2O

molecules coordinated axially to Cu-metal remains as weakly-bounded due to the Jahn-Teller effect of d^9-Cu^{2+} ion. These water molecules can be removed easily upon thermal activation under vacuum. Pariyar *et al.*[46] recently studied the catalytic properties of activated HKUST-1 for aziridination reaction and its ring-opening reactions forming C-N, C-S, C-O, and C-C bonds. The generation of CUS in the Cu^{2+} site is provided by strong evidence and is supported by several lines of evidences such as, (i) the turquoise colour of HKUST-1 changes to navy blue after activation and the colour reverts on exposing the activated MOF on air (Figure I.5a). The experimental Brunauer−Emmett−Teller (BET) surface area increased from 836 m^2 g^{-1} in as-synthesized HKUST-1 to 1667 m^2 g^{-1} in activated HKUST-1, suggesting that the material has become more porous as a result of the activation process. (ii) The powder X-ray diffraction (PXRD) patterns of Pristine HKUST-1 and activated HKUST-1 are identical with no new peaks, indicating that the material's structural integrity has not been compromised despite the loss of water molecules and the creation of CUS (Figure I.5.b). Despite being the convenient method to activated MOF, the thermal activation method has a few drawbacks. Simply heating under vacuum in an attempt to remove solvent/guest molecules from the pores and the loosely coordinated solvents can often lead to degradation or complete decomposition of the framework. The reason for this is that some solvent/ligands, such as DMF, have low volatility and require either high temperatures or prolonged evacuation times for its effective removal. Additionally, certain solvent/ligands such as H_2O, are more strongly coordinated to the network, through stronger metal coordination or hydrogen bonding to the ligand donor atoms. These ligands may also have a high surface tension in their liquid state, leading to cavitation effects, which can cause the network to collapse upon their removal.

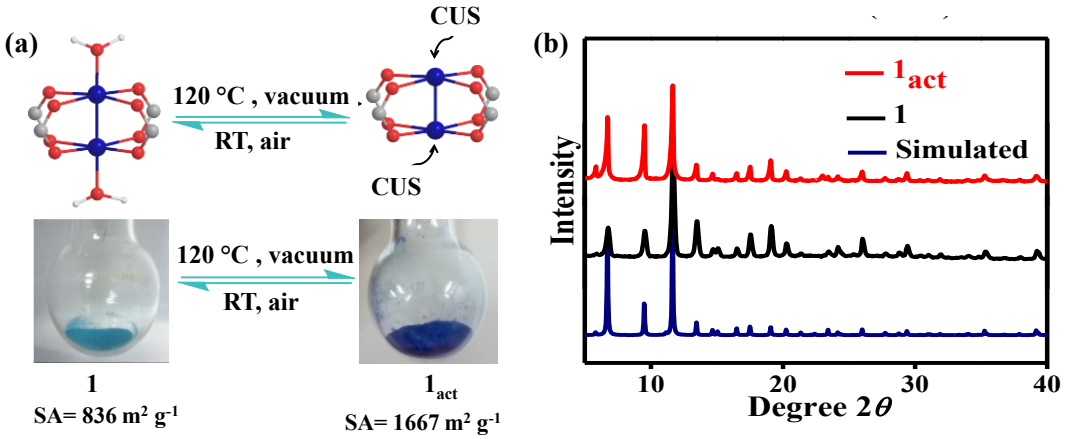

Figure I.5: Activation process of HKUST-1 and its characterization. (a) Generation of CUS indicated by a colour change from turquoise to navy blue on activation. (b) PXRD pattern of simulated from SCXRD, Activated, and non-activated HKUST-1.

(2) Solvent-exchange method: In the solvent-exchange method the high boiling point solvent such as DMF is exchanged by a low boiling point solvent such as CH_3CN, CH_3Cl, acetone, ethanol, etc. As the solvents with lower boiling points have weak intermolecular interactions, that leads to reduction in surface tension and capillary forces therefore with mild heat and vaccum, activation of MOF can be achieved (Figure I.6).

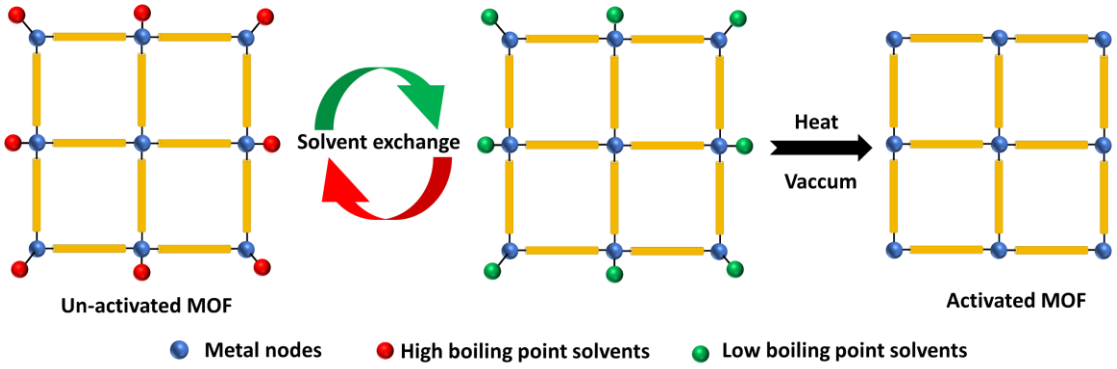

Figure I.6: Illustration of solvent exchange method for activation of MOF.

Yaghi *et al.*[47] reported the activation of MOF-505, a copper-based with an isoreticular structure to HKUST-1, employing the H_4bptc ligand (3,3',5,5'-biphenyl

tetracarboxylic acid) ligand. The synthesized MOF-505 was subjected to activation by first immersing it in fresh acetone thrice for 24 h each (total of 72 h) to replace the DMF molecules present in the pores with acetone. Secondly, the material in the acetone was meticulously evacuated to eradicate the coordinated water molecules at a pressure of less than 1 x 10^{-6} bar.

(3) Photothermal activation*:* Compared to the methods mentioned earlier that involve using solvents and heat energy for solvent exchange and removal as well as chemical activation, photothermal activation (PA) achieves the same results by solely irradiating the solid MOF sample with light. For kinetically stable metal ions, such as Cr^{3+}, traditional methods of solvent ligand exchange and thermal ligand exchange are very sluggish. Instead, irradiation with (UV-vis) light can induce a rapid ligand exchange or removal by populating a photoactive excited state. Maspoch *et al*.[48] introduced this one-step activation approach in 2018, utilizing UV-vis irradiation ranging from 300 to 650 nm. The authors suggested that light-to-heat conversion is a promising technique for evaporation processes due to localized heat generation, leading to reduced heat diffusion and energy loss. Upon direct irradiation, the MOFs experience a significant temperature rise (120-220 °C) within a few minutes (approximately 30 min) at atmospheric pressure, enabling the removal of solvent molecules and the creation of open metal sites. The MOFs display absorption bands within the range of 300-650 nm (Figure I.7). To confirm the success of the activation, the authors employed various verification techniques, including PXRD, N_2 sorption, and UV-vis spectroscopy.[48]

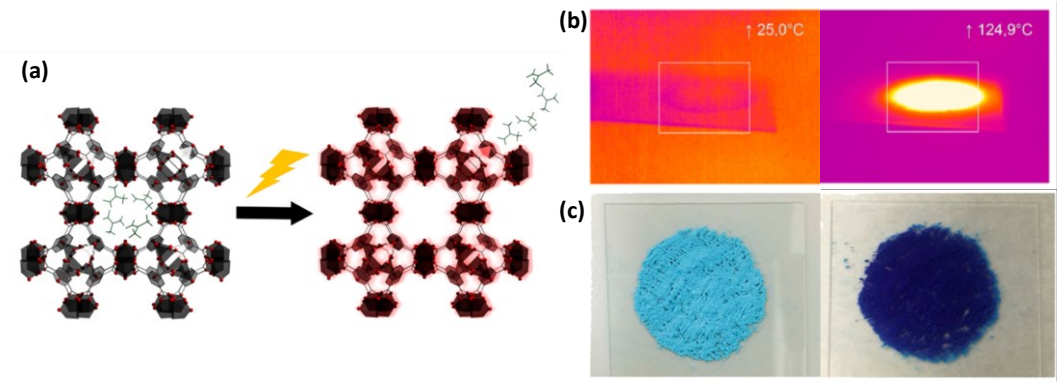

Figure I.7: (a) Schematic representation of the photothermal activation of MOFs. (b) IR camera pictures (top) of HKUST-1 before (left) and during UV−vis irradiation (right). Photographs of HKUST-1 powder (bottom) before (left) and after (right) irradiation. Reprinted with permission from ref.48 Copyright 2018 American Chemical Society.

(4) Freeze drying: It is a newly developed technique for the activation process where the solvent/guest molecules in MOF is first exchanged with benzene and is left in benzene solution to freeze. After freezing the sample at 0 ℃ and bringing it back to room temperature repeatedly, the sample is subjected to a final freeze cycle (Figure I.8). During this cycle, the sample is placed under reduced pressure and at a temperature and pressure lower than the solvent's triple point. Upon warming the sample under these conditions, the benzene undergoes sublimation, which is a direct transition from the solid to the gas phase.

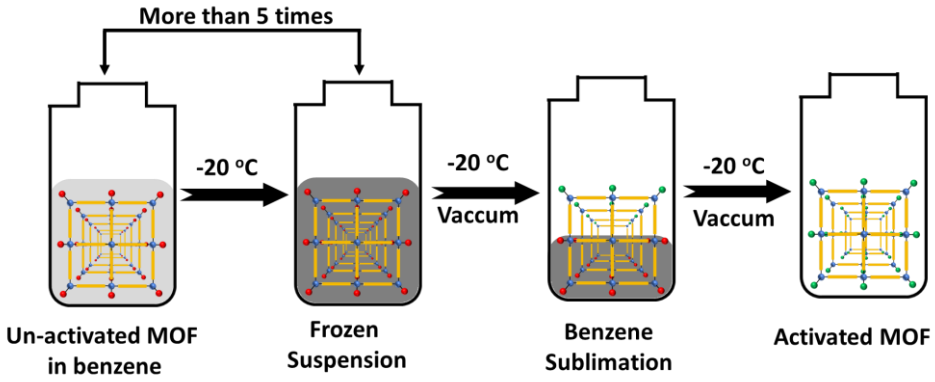

Figure I.8: Illustration of the freeze-drying method for activation of MOF.

Besides the activation of MOF, the creation of defects within the framework can also generate CUS in MOF. Defects in MOF[49] can be generated by using polytopic organic ligands functionalized with electron-withdrawing or donating groups, which often lead to catalytically advantageous high efficiency.[50–52]. The catalytically active defects within MOF can also be produced by adjusting the synthetic parameters, as depicted in figure I.9. Additionally, defect engineering can generate mixed-valence metal sites within MOF. Fischer *et al.*[53] reported the substitution of BTC ligand with truncated pyridine-3,5-dicarboxylate (PyDC) to prepare Cu-BTC type MOF, leading to the formation of mixed-valence Cu(I)–Cu(II) paddlewheels, as shown in Figure I.9.

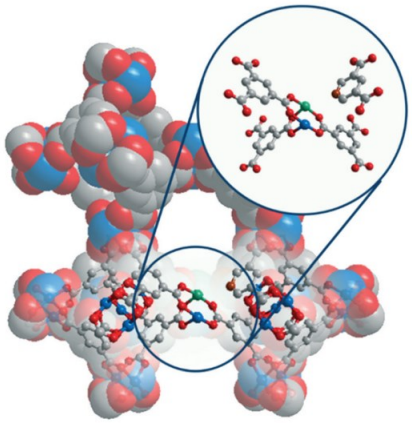

Figure I.9: Schematic illustration of the reduced Cu(I)–Cu(II) in Cu-BTC framework. Reprinted with permission from ref.53. Copyright 2021 Royal Society of Chemistry

I.3.2. MOF decorated with active sites via post-synthetic modification:

Post-synthetic modification (PSM) of MOF is a powerful strategy to tailor the catalytic properties of MOFs. PSM involves modifying the structure and/or functionality of MOFs after their synthesis, often using mild reaction conditions. This allows for the introduction of new functional groups or moieties onto the framework, or the modification of existing ones, without altering the fundamental MOF There

have been several reviews that discuss the progress and development of post-synthetic modification (PSM) strategies for MOFs. In many cases, the incorporation of other metals or active metals within the MOF framework has been achieved by using an amino functional group containing organic molecules as the linker during MOF synthesis. For instance, Yaghi *et al.*[54] recently reported the successful installation of three biologically relevant imidazole moieties, including L-histidine (His), 4-imidazole acrylic acid (Iza), and 5-benzimidazolecarboxylic acid (Bzz), followed by subsequent metallation of CuI within Zr-based MOF-808 (Figure I.10). By post-synthetically modifying MOFs in this way, they can serve as a scaffold to activate Cu-O sites and exhibit functional activities similar to methane monooxygenase enzymes. These modified MOFs have shown selective conversion of methane to methanol under isothermal conditions.

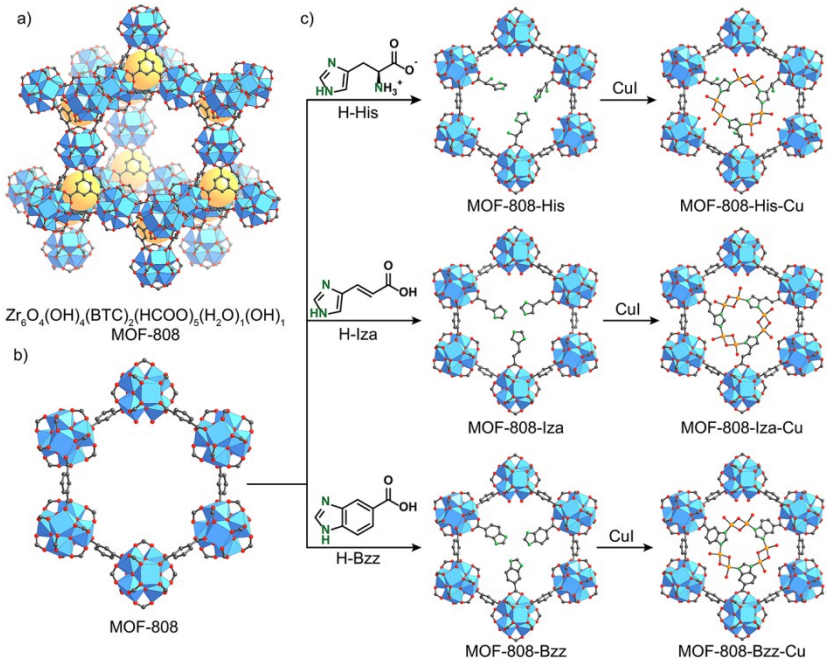

Figure I.10: Design and synthesis of the catalysts bearing copper-oxygen complexes in MOF-808 for methane oxidation to methanol. (a) Structure of MOF-808. (b) Pseudohexagonal pore opening of MOF-808. (c) Synthesis of the catalysts comprising the replacement of formate with imidazole-containing ligands and metalation with Cu(I). Reprinted with permission from ref.54 Copyright 2018 American Chemical Society.

Cao *et al.*[55] presented an explanatory demonstration of the multivariate functionalities incorporated in a MOF (Figure I.11). Typically, a multivariate MOF is a structure that consists of two or more different functionalities that can be achieved *via* mixed linker one-pot synthesis or post-synthetic modification. In their study, LIFM-80 was involved in the dynamic installation and removal of functional secondary and ternary ligands in the primitive LIFM-28, as well as in metal-chelation and covalent post-modification processes. The researchers obtained several active catalytic systems for various reactions such as oxidation, Knoevenagel condensation, click chemistry, and more. Zhou *et al.*[56] also reported a fascinating example of an isoreticular family of catalysts based on the multicomponent MOF, MUF-77.

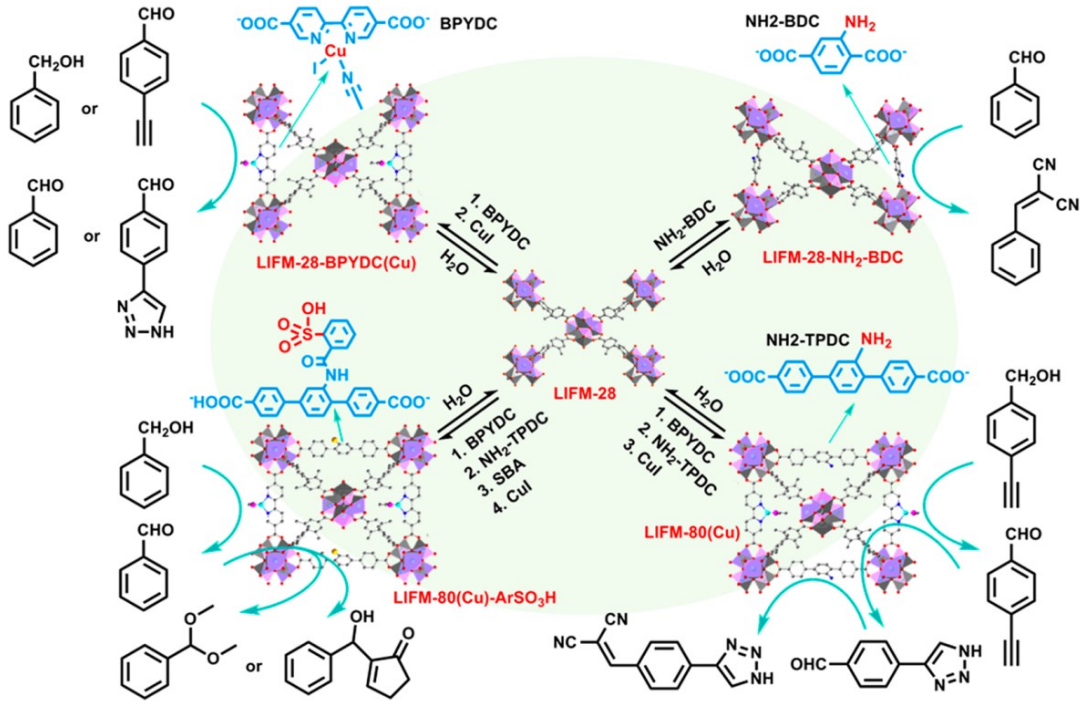

Figure I.11: Generation of multivariate MOF catalysts *via* the dynamic spacer installation approach using proto-LIFM-28 and the resultant interconversions for different catalytic purposes. The molecular structures of the inserted functional spacers are illustrated for the crystal structures, in which the −ArSO3H group is simplified as an orange ball and Zr6-clusters are shown as purple polyhedrons. H and F are omitted for clarity. Reprinted with permission from ref.55 Copyright 2019 American Chemical Society.

They adjusted the microenvironment around an active site by introducing functional groups (modulators) to the organic linkers at locations away from the catalytic unit. These catalysts displayed distinct features, including simultaneous enhancements in both reactivity and stereochemical selectivity for aldol reactions, the ability to catalyse Henry reactions that cannot be accomplished by homogeneous analogues, and discrimination between different reaction pathways (Henry *vs* aldol) that compete for a common substrate.

I.3.3. MOFs as hosts to encapsulate various catalytic sites:

Another alternative for MOF to show active participation in organic reactions is by applying it as a host to encapsulate various active materials, especially nanoparticles (NPs). MOFs offer several advantages as hosts for encapsulating various materials. Especially MOFs with high surface area and permanent porosity make them ideal for trapping gases and volatile organic compounds. Additionally, MOFs can be synthesized with specific functional groups or surface properties, which allows for the tailoring of their properties to target specific guest molecules. MOFs have been successfully used to encapsulate a wide range of materials, including small molecules, drugs, proteins, and even other solid materials such as nanoparticles. The encapsulation of these materials can lead to improved stability, protection from degradation or external stimuli, and controlled release.

In general, there are three main methods for encapsulating active materials within MOF, which can be categorized as shown in figure I.12. Firstly, the "ship-in-a-bottle" approach involves confining active NPs within the cavities or channels of the MOF matrix (Figure I.12a). Secondly, the "bottle-around-ship" approach entails

surrounding active NPs with MOFs (Figure I.12b). Finally, the "one-pot" synthesis method involves embedding active NPs inside MOFs (Figure I.12c).

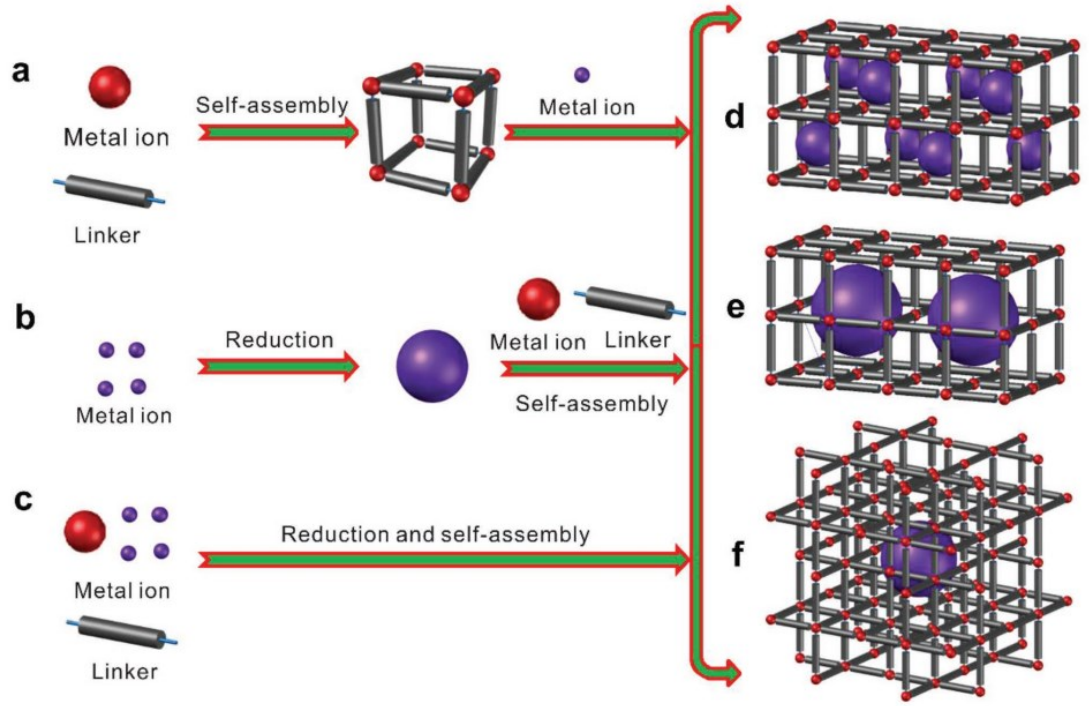

Figure I.12: Schematic illustration of a) "ship-in-a-bottle" approach, b) "bottle-around-ship" approach, and c) "one-pot" synthesis approach for active NPs encapsulated by porous MOFs. Reprinted with permission from ref.21 Copyright 2018, Wiley.

The ship-in-a-bottle approach involves synthesizing MOFs around pre-formed nanomaterials to create a hybrid material with improved properties. This approach allows for the precise control of the location and distribution of the nanomaterials within the MOF framework. The process typically involves several steps. First, the nanomaterials are synthesized or obtained from a commercial source. Next, the MOF precursor components are mixed in a solution with the nanomaterials. The solution is then heated to initiate MOF formation around the nanomaterials, creating a hybrid material. The resulting hybrid material can then be further characterized and tested for its properties and applications. The ship-in-a-bottle approach for encapsulating nanomaterials into MOFs has several advantages. It allows for the creation of hybrid

materials with enhanced properties, such as increased stability and reactivity. It also enables the precise control of the size and location of the nanomaterials within the MOF framework, which can impact the material's overall performance.

The term "bottle-around-ship" refers to the fact that the MOF acts like a bottle that surrounds and protects the active NPs (the "ship") from the external environment. In this approach, the active NPs are first coated with a stabilizing agent to prevent aggregation and facilitate their encapsulation within the MOF. The MOF is then grown around the coated NPs to form a composite material. This approach is particularly useful for applications in which the active NPs are sensitive to their surroundings, such as in catalysis, sensing, and drug delivery. The encapsulation of active NPs within MOFs can provide several advantages over other types of materials. For example, the MOF can provide a protective environment for the NPs, preventing their degradation and increasing their stability. Additionally, the MOF can act as a scaffold for the NPs, enhancing their activity and selectivity. Finally, the MOF can also facilitate the separation and recycling of the active NPs from the reaction mixture, which can be important for industrial applications.

In the one-pot synthesis method, all the necessary components for the synthesis of the MOF and the encapsulation of the active NPs are combined in a single reaction vessel. This simplifies the process and reduces the need for multiple purification steps. The one-pot synthesis approach typically involves the use of metal precursors, organic ligands, and a reducing agent. The metal precursors and organic ligands are first mixed in a solvent to form a coordination complex. The reducing agent is then added to the mixture, which initiates the formation of the NPs. During the synthesis process, the NPs become encapsulated by the MOF framework, resulting in a highly porous material with active NPs embedded within. The porosity of the MOF allows

for the efficient transport of reactants and products to and from the active NPs, enhancing their catalytic properties. One advantage of the one-pot synthesis approach is that it can be easily scaled up for industrial production. It also offers greater control over the size, shape, and distribution of the NPs within the MOF, which can be optimized for specific applications.

I.3.4 MOFs as precursors for the formation of metal composites:

Another fascinating aspect of MOFs is that they can serve as sacrificial templates to produce a range of porous nanomaterials through the application of distinct thermal and/or chemical treatments, aside from their primary application. As an example, subjecting MOFs to heat treatment in an inert atmosphere and subsequently removing the surface metal ions through chemical etching can result in the production of highly porous carbons with a significantly high specific surface area. In comparison to carbonaceous materials made using conventional precursors, carbons derived from MOFs often showcase controllable porous architectures, pore volumes, and surface areas. The production of porous carbons from MOFs through carbonization can typically be achieved through two methods: direct carbonization, which involves the carbonization process without the use of secondary precursors, or indirect carbonization, which involves the use of secondary precursors such as ethylenediamine[57] or furfuryl alcohol.[58] The direct carbonization method is considered more advantageous as it is simpler and involves only one calcination step. So far, a wide range of porous carbon materials with controlled morphologies, ranging from 0-D to 3-D, have been successfully derived from MOFs through carbonization. These examples showcase the versatility of MOFs as precursors for the production of various types of porous carbon materials. In addition, MOF-derived carbons can be

doped with elements such as nitrogen (N), phosphorus (P), and/or sulphur (S) to further enhance their functional performance.

Conversely, subjecting MOFs to direct heat treatment in an air environment can result in their breakdown into the corresponding metal composites, especially metal oxide (Figure I.13). Due to the coordination of metal ion centers with organic linkers, MOFs can be transformed into porous transition metal oxide (TMO) nanomaterials by controlled heating in air or N_2 atmosphere. This process involves the oxidation of metal ions and the release of gaseous CO_2 and NO_2 which originate from the decomposition of organic linkers during the heat treatment.[59] The nano-porous oxide materials obtained through this process generally maintain the shape and porosity of the original MOFs, making them suitable for achieving a large surface area. Further, by controlling the annealing temperature and time one can tune the composition, structural activity, surface area, and pore size distribution of MOF-derived oxides.[60]

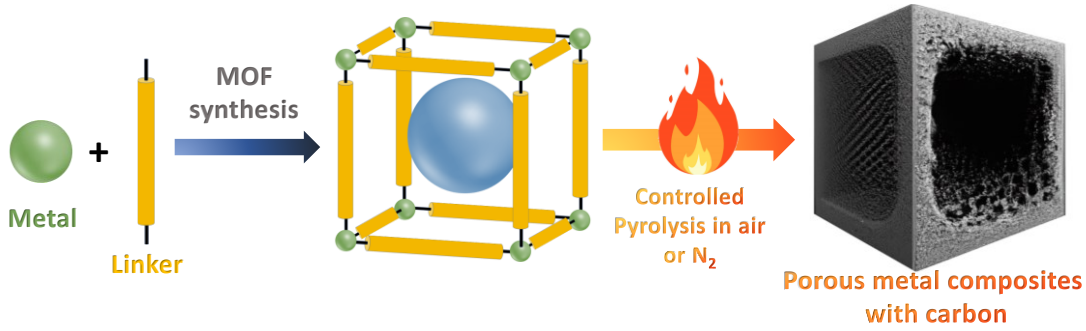

Figure I.13: Schematic illustration showing the fabrication of MOF-derived porous metal composite.

In addition to producing pure metal oxide nanostructures, it is also possible to create porous metal oxide nanocomposites by subjecting bimetallic MOFs or core-shell MOF composites to high-temperature heat treatments in the air or through a two-step annealing process involving nitrogen and air. The second method mentioned, involving the two-step annealing process with nitrogen and air, is especially

advantageous in terms of maintaining the structure of the original MOFs and consequently achieving greater surface area and porosity in the resulting metal oxide nanocomposites. Furthermore, MOF-derived oxides can also be combined with a range of carbon-based materials, including reduced graphene oxide (rGO), carbon nanotubes (CNTs), and 3-D graphene networks, to serve as conductive matrices and improve their electrochemical performance.[61] Numerous types of porous TMO nanomaterials with enhanced properties have been produced using MOF precursors. These materials include cupric oxide (CuO), cuprous oxide (Cu_2O),[62] cobalt oxide (Co_3O_4),[63,64] iron oxide (Fe_2O_3),[65] magnesium oxide (MgO),[66,67] manganese oxide (Mn_2O_3),[68,69] nickel oxide (NiO),[70] titanium dioxide (TiO_2),[71,72] zinc oxide (ZnO),[73,74] cerium oxide (CeO_2),[75,76] as well as mixed TMOs like ferrites ($CoFe_2O_4$ and $Mn_{1.8}Fe_{1.2}O_4$)[77,78] and cobaltites ($CuCo_2O_4$, $ZnCo_2O_4$, $Zn_xCo_{3-x}O_4$, and $ZnMn_2O_4$).[79–82] The highly adjustable properties of metal oxides derived from MOFs, in combination with the potential to incorporate them with highly conductive carbon supports, render them highly appealing candidates for the development of next-generation electrocatalysts and have been utilized for various applications such as lithium-ion batteries (LIBs),[83] supercapacitors,[68,84] gas sensors, catalysis,[85] fuel cell cathode materials,[35,44,86,87] and water splitting.[88–90] MOFs have been recognized as a significant category of heterogeneous catalysts towards a wide range of organic transformations such as Claisen–Schmidt reaction,[92] epoxidation[93,94] ring-opening of epoxides,[95–98] Friedel-Craft alkylation,[25] cyanosilylation,[100] acetalization,[104] C─H activation,[105–107] cyclopropanation,[36] CO_2 fixation,[48] Biginelli reactions,[37] Aldol condensation reaction,[39] Henry reaction,[112] biomass valorisation[45,46] cyclization reaction,[47] polymerization,[49] and Diels Alder reaction,[50] etc. In this chapter, we have broadly highlighted the use of MOF and MOF-derived material in various catalytic

reactions. The comprehensive discussion was categorized into two topics viz., (i) MOF towards molecular catalysis that precisely involves coupling reaction to form C-N, C-O, C-C, and C-S bonds formation, and (ii) MOF towards electrocatalysis that involves the use of MOF as a template to derive metal composites for electrocatalytic oxygen process.

I.4. MOF towards molecular catalysis:

Amongst the various organic transformation, the cross-coupling reaction is a versatile method to introduce heteroatom in organic molecules through C–X (X= N, O, S, C) bond formation. It has expanded the wide scope as these bonds are the backbone of many value-added organic molecules and their direct synthesis, shortens the synthetic procedures of retrosynthesis. It is widely employed in both laboratory and industrial processes to synthesize a wide variety of molecules, being compatible with many organic functional groups, including carboxyl, hydroxyl, nitro, cyano, multiple bonds, and others. Traditionally, the production of C-X bonds involved various methods such as nitration, nucleophilic aromatic substitution, and copper-mediated Ullmann coupling. However, these methods had several limitations such as poor atom economy, the need for strong activating groups on the substrate, multi-step procedures, high amounts of catalysts, generation of hazardous waste, low yields, and poor selectivity. Metal-catalyzed cross-coupling reactions have been introduced as a promising alternative that overcomes some of these limitations. Other methods successfully employed towards cross-coupling reactions are Chan Lam coupling, Buchwald and Hartwig coupling, and C-H amination for C-N bond formation. Similarly, cross dehydrogenative coupling, for C-O, C-S bond formation and Suzuki-Mayuri, Sonagashira, Heck-coupling, Knoevenagel condensation, etc for C-C bond formation. Specifically, Buchwald and Hartwig are one of the most famous cross-

coupling reactions. They proposed a palladium-catalyzed coupling method between aryl halides and amines as a replacement for traditional Ullmann coupling. However, palladium-catalyzed reactions have limitations such as high cost, low abundance, moisture sensitivity, low stability, and difficulty in separating residual palladium from the reaction mixture. To improve the recyclability issue and overcome the limitations of homogenous coupling/cross-coupling reactions, MOFs have emerged as promising option. The various cross-coupling reactions involving the formation of C-N, C-O, C-S, and C-C bonds have been discussed below highlighting the recent progress and literatures.

I.4.1. MOF catalyzed reactions for C–N bond formation

I.4.1.1 MOF catalyzed C–N bond formation: Ullmann coupling

Long et al. conducted separate studies on the effectiveness of Cu-TDPAT (TDPAT = 2,4,6-tris(3,5-dicarboxylphenylamino)-1,3,5-triazine),[110] in catalyzing Ullmann-type C-N coupling reactions between an aryl halide and *N*-heterocycles using pristine MOF. The Cu-TDPAT MOF was found to efficiently facilitate C-N bond formation between imidazole and iodobenzene at 120 °C in the presence of K_2CO_3 base and DMSO polar solvent. The reaction was found to achieve a maximum yield of 91% within 8 h, and the substrate scope was established to include primary and secondary amines. Cu-TDPAT's catalytic efficiency was attributed to its numerous open copper sites within the framework, its high surface area of 1855 m^2g^{-1}, and large pore volume. Similarly, Truong *et al.* have reported the Ullmann-type C-N coupling reaction with solvothermally synthesized $[Cu(INA)_2]$ (INA=isonicotinic acid) MOF.[111] The single crystal structural refinement of $[Cu(INA)_2]$ MOF shows square-pyramidal geometry of centra Cu(II) metal coordinated to five isonicotinate ligands

and Cu(II) metal node has one CUS as a catalytic site. The $[Cu(INA)_2]$ catalytic system produced 94% of desired C-N coupled product between aryl halide and pyrazole at 100 °C and 6 h in the presence of dimethylacetamide (DMA), ^tBuOLi, and K_2CO_3 as a solvent, oxidant and base (Scheme I.1). The $[Cu(INA)_2]$ catalytic system was also found efficient with aryl bromides and aryl chlorides producing 87% and 61% of desired product respectively. The justification for this excellent catalytic activity is attributed to three factors: (i) the coordinating rigid linkers working in synergy, (ii) the presence of dicopper active sites, and (iii) the strong ligation mode of NH-amines with copper centers in the framework.

Scheme I.1. General scheme for $[Cu(INA)_2]$ catalyzed Ullmann type C–N coupling reaction.

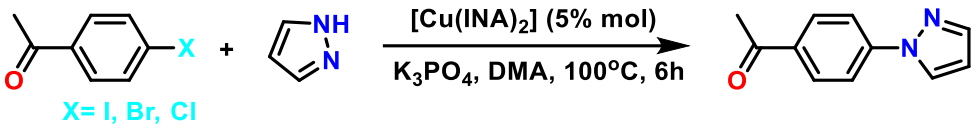

In another study, Dai *et al.* investigated the efficacy of copper-based MOF-199,[112] and amorphous Cu-MOF-74 (aCu-MOF-74)[113] as recyclable and efficient heterogeneous catalysts for direct *N*-arylation of heterocycles with aryl halides. MOF-199, which is identical to HKUST-1 MOF, has an exposed copper site. The reaction was conducted using 10 mol% of MOF-199 and NaOH as a base in DMSO at 120 °C. At the optimized reaction conditions, a maximum yield of 97% was obtained for the formation of C–N bonds between *p*-methoxyiodobenzene and pyrrole in 12 h. The heterogeneity of MOF-199 in the reaction system was confirmed through leaching tests and atomic absorption spectroscopy (AAS) analysis, which revealed that only a small amount (0.18%) of metallic copper was present in the supernatant after the removal of MOF-199. Additionally, the catalytic system was effective for the formation of C–N bonds between various N-heterocycles (e.g., indole, triazole,

imidazole) and aryl iodide. Further to evaluate the industrial application of MOF, the optimized reaction condition was enabled towards large-scale synthesis of the coupling product, as depicted in scheme I.2 where MOF-199 formed C–N cross-coupled products on a large scale with a good yield, indicating its potential industrial use as a catalyst.

Scheme I.2. Gram-scale reactions of N-arylation of heterocycles with 4-iodotoluene catalyzed by MOF-199.[112]

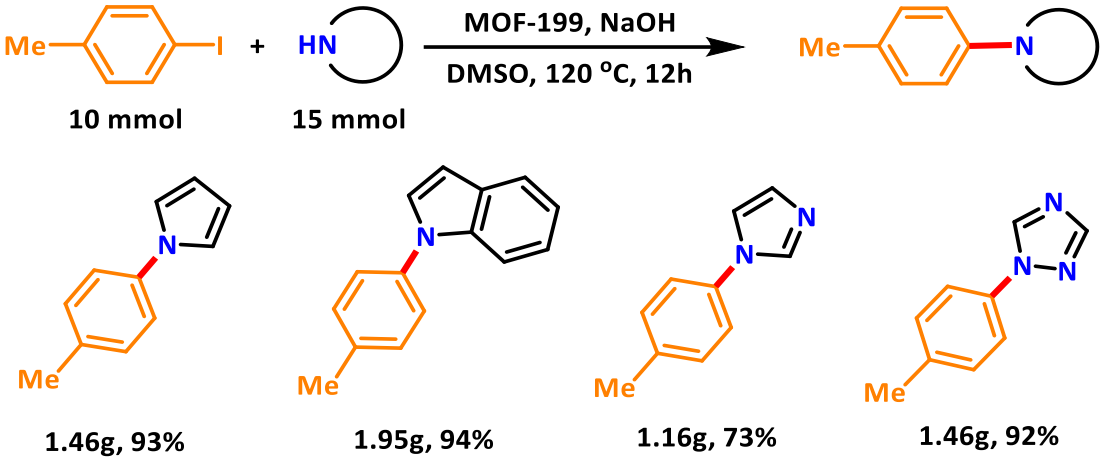

In contrast to the homogeneous palladium catalyst, MOF-199 showed a noticeable decrease in reaction yield when bromo- and chloro-benzene were used as coupling partners. On the other hand, aCu-MOF-74 was able to produce 90% of the expected product with a reaction between *N*-heterocycles and aryl halide, and counter to MOF-199 it can also produce an appreciable product with chlorobenzene.[113] The crystallinity of Cu-MOF-74 MOF was disrupted in the presence of NaOH at 120 °C, after the first catalytic cycle however no leaching of Cu-metal was found in the reaction system and the amorphous MOF was reported to be reusable for up to six cycles, resulting in an 83% yield of the product (Figure I.14a-b).

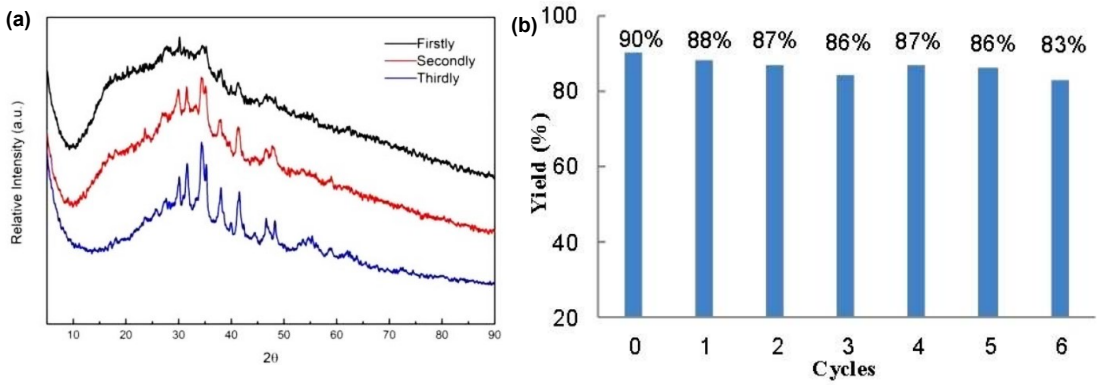

Figure I.14: (a) PXRD of Cu-MOF-74 after the first and second cycle (b) The recyclability histogram of Cu-MOF-upto six cycles. Reprinted with permission from ref.113 Copyright 2018, Wiley.

Zhang *et al*[114] reported the synthesis of 2D Cu-MOF using 2,2',5,5'-tetramethoxy-[1,1'-biphenyl]-4,4'-dicarboxylic acid as an organic linker. The Cu-MOF was activated at 100 ℃ for 24 h to obtain a five coordination of Cu(II) metal sites. The activated Cu-MOF was applied to various organic transformations that include dehydrogenative oxidation of alcohol and *N*-arylation of azole compounds. The catalytic system produced 99%, 97%, and 26% of desired N-arylated azole products with aryl iodide, aryl bromide, and ary chloride respectively. Apart from using pristine MOF towards Ullmann coupling C-N coupling reaction Maity *et al*.[115] report the use of zinc-based porous IRMOF-3 (IRMOF=isoreticular MOF) as a host to encapsulate Cu(II) ion. The post-synthetic treatment of Zn metal containing IRMOF-3 with pyridine-2-aldehyde formed a Schiff base moiety within the IRMOF-3 framework. Treatment with Cu(II) ion resulted in the formation of Cu(II)-Schiff base anchored to the IRMOF-3 framework thereby forming IRMOF-PI-Cu (Figure I.15a). The PSM IRMOF-PI-Cu catalyst forms 95% of desired product for the Ullmann coupling reaction under the optimized condition. The substrate scope was extended to different substituted *N*-containing heterocycles that include imidazole, benzimidazole, 1,2,4-triazole, and 1,2,3-triazole with substituted aryl bromide. Except benzimidazole,

all reactions produced high yields of the desired product. Convincing DFT analysis shows that the larger size of benzimidazole barred it from entering the catalyst's pores showing pore-controlled reactivity. The catalyst remained structurally stable even after the fifth cycle, as demonstrated by several characterization techniques, including PXRD, FI-IR, and gas adsorption, all of which indicated that the catalyst retained the same characteristics as it did when it was freshly prepared. Sobhani *et al.*[116] reported Fe-MIL-101-NH_2 MOF functionalized with a cobalt-complex by PSM, the introduction of isatin-Schiff-base followed by metalation with Co complex (Figure I.15b).

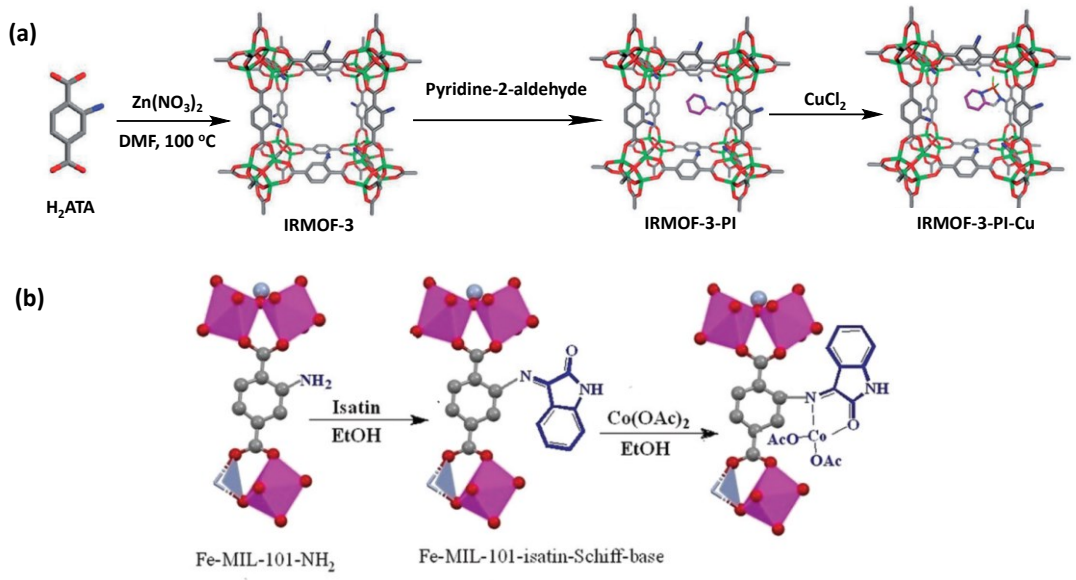

Figure I.15: (a) General process followed for PSM of IRMOF-3 for synthesis of IRMOF-3-PI-Cu. Reproduced with permission from ref.[115] Copyright 2014 Wiley. (b) Generic scheme for the post-synthetic modification of Fe-MIL-101-NH_2 MOF for preparation of MOF containing the Fe-MIL-101-NH_2-isatin-Schiff base-Co(II) moiety. Reprinted with permission from ref.116 Copyright 2021 Royal Society of Chemistry.

The modified Fe-MIL-101-NH_2-isatin-Co MOF is capable of catalyzing Ullmann, Buchwald-Hartwig, Hirao, Hiyama, and Mizoroki-Heck cross-coupling reactions involving a variety of aryl halides/phenylboronic acid/phenyl-tosylate with phenols, anilines/heterocyclic amines, triethyl phosphite, triethoxyphenylsilane, and alkenes.

Furthermore, the reaction is heterogeneous and can be recycled, resulting in good to excellent yields of the intended coupling products. Similarly, Rabiei *et al.*[117] reports the anchoring of Pd metal on Cu-(BDC-NH_2) MOF for C-N coupling reaction. Following similar chemistry Veisi *et al.*[118] report the anchoring of Cu NPs on Zr-UiO-66 (UiO= Universitetet i Oslo) MOFs that can be efficiently used in Buchwald–Hartwig and Ullmann-type coupling reactions. Cho *et al.*[119] report the use of Fe_3O_4@SiO_2@MOF-199 for the synthesis of imidazo[1,2-f]phenanthridines and cyclization followed by aromatization of 2-(2- Bromoaryl)imidazoles with Cyclohexane-1,3-diones forming C-C and C-N bond. The use of metal composites derived from MOF has also been reported for the Ullmann-type C-N coupling reaction. Retailleau *et al.*[120] reported the synthesis of bimetallic (Co and Cu) TMU-81 MOF (TMU= Tarbiat Modares University) and its derived cobalt-/copper-doped carbon nanohybrids. The pyrolysis of MOF was conducted at 800 °C under an argon atmosphere for 10h. The authors also found an increase in surface area as TMU-81 has a BET surface area of 420 m^2g^{-1} and on pyrolysis, it increased to 835 m^2g^{-1} for derived composites. The derived composites were applied directly to the C-N bond between aniline and aryl iodide that produces a yield of 85% for the desired product. Similarly, Cu-BTC MOF was employed by Kar *et al.*[121] as a sacrificial template for the creation of porous metal/metal oxide nanomaterials. In their study, the Cu-BTC MOF was subjected to pyrolysis under an N_2 atmosphere at various temperatures (450, 550, and 650 °C), yielding porous Cu-Cu_2O/C_x (where x denotes the temperature). The Cu–Cu_2O/C_{550} material was discovered to be the most effective catalyst for the Ullmann-type C-N coupling reaction, with a 96.2% yield of the desired product. When compared to traditional Cu and Cu_2O nanoparticles, the catalyst demonstrated superior performance.

I.4.1.2 MOF catalyzed C–N bond formation: Chan Lam Coupling

Chan-Lam Coupling is a cross-coupling reaction in organic chemistry that involves the coupling of arylboronic acids and aryl triflates to form biaryl compounds.[122–124] The reaction is catalyzed by a copper complex and an amine ligand and typically proceeds under mild reaction conditions. The Chan-Lam Coupling is a useful tool for the synthesis of complex organic molecules and is widely used in the pharmaceutical and agrochemical industries.[125] The article by Wang *et al.* describes the application of Cu-based MOF, specifically $Cu(4\text{-tba})_2$ (tba=4-(1*H*-1,2,4-triazol-1-yl)benzoic acid), in the Chan-Lam coupling reaction involving the reaction of phenylboronic acid with imidazole, aryl halide, and styrene to form C-N, $C(sp^3)$- $C(sp^3)$ and $C(sp^2)$- $C(sp^2)$ bond as shown in figure I.16.[126] The product yield was found to be excellent (94%) even after the sixth cycle and the authors attribute the impressive catalytic activity of $Cu(4\text{-tba})_2$ MOF to its porous open framework of pore sizes ca. 3.0 × 6.0 $Å^2$.

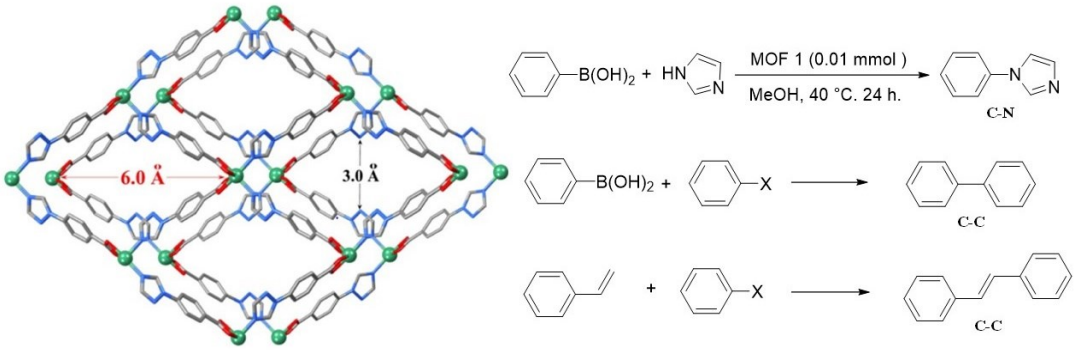

Figure I.16: A 2-fold interpenetrating framework of $Cu(4\text{-tba})_2$ and scheme for the different catalytic systems. Reprinted with permission from ref.126 Copyright 2015 Elsevier.

Zhao *et al.*[127] reported a study on the use of a two-dimensional MOF $[Cu(ima)_2]_n$ (ima =imidazole) towards Chan-Lam-type reactions. The coordination environment of the Cu(II)ion was found to consist of two monodentate carboxylate groups and two imidazole nitrogen atoms, resulting in a square-planar geometry with uncoordinated

axial positions. The imidazole ligands bridged two Cu(II)ions using both carboxylate oxygen and imidazole nitrogen atoms, creating a (4, 4) 2D wavelike rhombic layer (Figure I.17). $[Cu(ima)_2]_n$.

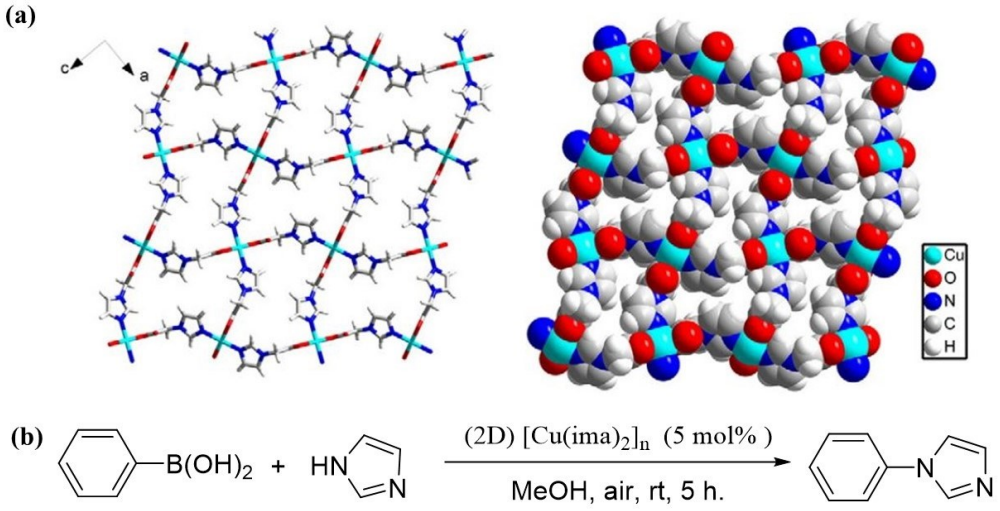

Figure I.17: (a) Structure of (2D)$[Cu(ima)_2]_n$ and (b) General scheme for the $[Cu(ima)_2]_n$ catalyzed Chan-Lam type coupling. Reprinted with permission from ref.127 Copyright 2013 Elsevier.

Under ambient conditions and utilizing a 5 mol% of $[Cu(ima)_2]_n$ as a catalyst, the *N*-arylation reaction of imidazole and phenylboronic acid can be carried out in the presence of air. The reaction occurs in a short period of 5 h using methanol as a solvent and produced a yield of 90%. The high catalytic efficiency of the Cu-MOF was attributed to the distorted square planar geometry of Cu(II) centers and the vacant axial positions, which made the Cu^{2+} centers readily accessible for chemical reactions. Panahi *et al.* introduced a noteworthy green strategy for the Chan-Lam reaction by utilizing $Cu_2(BDC)_2(BPY)$ as a catalyst, which was synthesized at room temperature using a solvent-free ball milling technique.[128] The MOF created from $Cu(OAc)_2.H_2O$, terephthalic acid, and *4,4'*-bipyridine exhibited an impressive BET surface area of 305.5 m^2g^{-1} and a total specific pore volume of 0.462 cm^3g^{-1}. The ideal conditions were achieved by utilizing aniline and phenylboronic as a coupling partner in a 1:1

H_2O/MeOH mixture at room temperature, with 20 mg of catalyst and K_2CO_3 as a base. The reaction was completed in just one hour, and the extension of substrate scope demonstrated high selectivity for monoarylation products, with no formation of diarylation. Moreover, the reaction worked well with 2-aminopyrimidine and 1-naphthylamine, giving yields of 82% and 84%, respectively. A heterogeneous catalyst with high recyclability URJC-1-MOF (URJC=Rey Juan Carlos University) towards C-heteroatom coupling under mild reaction conditions was developed by Calleja *et al.*.[129] The URJC-1-MOF was created formed by bonding of Cu(II) with a 1*H*-imidazole-4,5-tetrazole ligand. This resulted in a one-dimensional microporous channel that forms part of a three-dimensional structure and includes an available Cu(II) metal site. The catalyst showed significant catalytic activity for the formation of C-N and C-O bonds *via* cross-coupling, without the need for extra additives or ligands, under "open flask" conditions. The URJC-1-MOF was easily recoverable through simple filtration and demonstrated the potential to be used repeatedly without any noticeable loss of activity or stability. Li *et al.*[130] reported three novel Cu MOFs such as three novel polyoxovanadates-based copper frameworks (POVCFs), i.e., $[Cu0.5(1\text{-}i\text{pIM})_2]_2[V4O11]$ (POVCFs **1**) and $[Cu(1\text{-}i\text{pIM})_2](VO_3)_2$ (POVCFs **2**) and $[Cu(1\text{-pIM})_4](HpIM)_4[V_{10}O_{28}]$ for formation of C-N bonds *via* Chan Lam coupling and a yield upto 89% was reported. The Cu(I)-MOF $[Cu_4I_4(DABCO)_2]$ (DABCO= 1,4-diazabicyclo (2,2,2) octane) can also facilitate the Chan-Lam type coupling reaction as reported by Srivastava *et al.*[131] The Cu central metal ion has +1 oxidation state and structure is composed of four cubane clusters linked by DABCO ligands to form a flat, four-membered ring in the *ab* plane. Each four-membered ring is then connected to eight neighbouring four-membered rings. The MOF's catalytic performance was evaluated by reacting cyclohexylamine and phenylboronic acid with

0.05 mmol of the catalyst in methanol at 27 °C for 5 h, resulting in a constant product yield of 99% even after the third cycle. The Cu(I)-MOF exhibited greater activity due to its highly ordered structure, which isolated the Cu-sites more effectively than the Cu-clusters, allowing for greater access to the reactant sites. Palaniswamy *et al.* reported the ligand free C-N coupling reaction between arylboronic acids and imidazole was catalyzed by [Cu(tpa)-MOF] (tpa=terepthalic acid) (Figure I.18).[132]

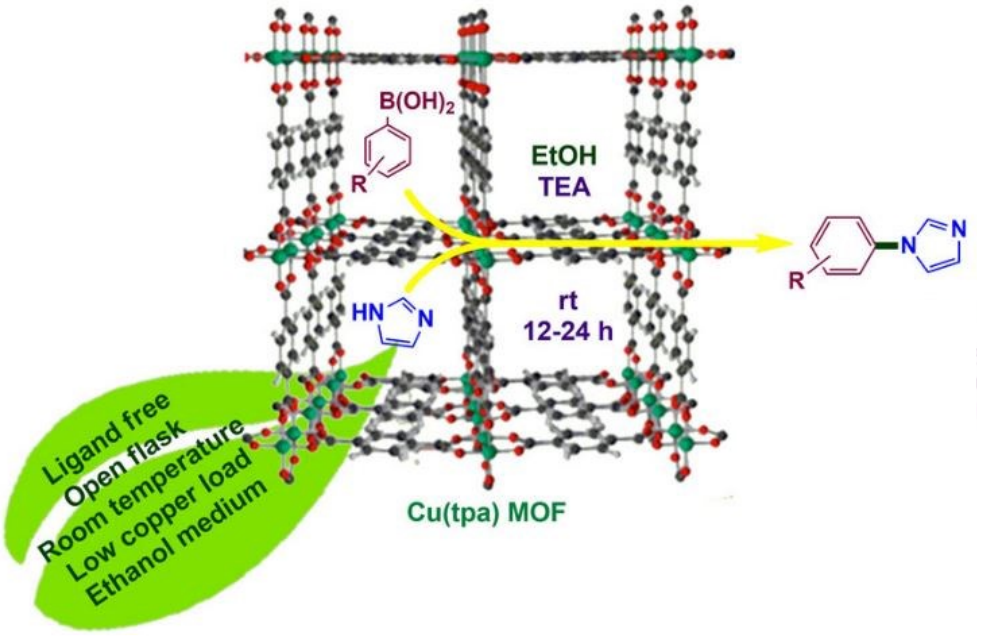

Figure I.18: Structure and general scheme for Cu(tpa)MOF catalyzed Chan–Lam C–N coupling reaction. Reprinted with permission from ref.132 Copyright 2015 Wiley.

However, when using disubstituted arylboronic acids that have both electron-donating and electron-withdrawing substituents, the yield decreased due to electronic reinforcement. The authors report no homo-coupling product and the reaction was not affected by steric factors. Even ortho-substituted arylboronic acids and fused-ring moieties produced consistent yields. Furthermore, functional groups such as formyl, nitrile, and amino groups were compatible with the reaction and did not undergo oxidation or hydrolysis. The catalytic system is also found to be efficient for, non-polar ethers and polar substituents, such as aryl and alkyl amides and sulfones.

Additionally, imidazole could be selectively arylated in the presence of amide *N*-atoms. The reaction was also successful on a large scale. The catalyst was effective and could be used with other electron-rich nitrogen heterocycles like pyrrole, pyrazole, and benzimidazole. Isatin and primary aromatic amine formed arylated products only when coupled with phenylboronic acid. However, heterocycles reacted slowly and required long reaction times and the catalyst system was ineffective for indoles and aliphatic amines. When compared the catalyst system outperformed various other catalysts, including homogeneous Cu-salt such as $Cu(NO_3)_2 \cdot 3H_2O$, $Cu(OAc)_2 \cdot H_2O$, $CuSO_4 \cdot 5H_2O$, $Cu(BF_4)_2 \cdot H_2O$, CuCl, $CuCl_2 \cdot 2H_2O$, and heterogeneous $[Cu(bpy)(H_2O)_2(BF_4)_2](bpy)$ (bpy= 2,2′-bipyridine),[133] Cu(BTC),[134] MIL-53(Fe),[135] Fe(BTC),[136] and IRMOF-3.[137] MOF catalyst. Dhakshinamoorthy *et al*. also reported the use of $Cu_3(BTC)_2$ MOF for Chan-Lam coupling.[138] They used benzimidazoles and phenylboronic acid as a coupling partner with 25mg catalyst, and Et_3N as a base in ethanol at 60 °C for 12h to produce 99% of the desired product. When the catalytic activity of $Cu_2(BTC)_3$ MOF was compared with Cu(I)-MOF,[131] $Cu(4\text{-tba})_2$,[126] $[Cu(ima)_2]_n$,[127] and Cu(tpa)[132] MOFs, all the catalysts except $[Cu(ima)_2]_n$ afforded higher conversion than $Cu_3(BTC)_2$. However, $Cu_3(BTC)_2$ with its large pore diameter could efficiently be applied to a couple of substrates like benzimidazoles with phenylboronic acid which is not reported for other Cu-based MOF catalyst.

I.4.1.3 MOF catalyzed C–N bond formation via C–H activation

The direct activation of inert C-H bonds to introduce a C-N bond in organic molecules is an intriguing process. [105] Over the past two decades, MOFs have been utilized as efficient catalysts for a broad range of C-H activation reactions, by introducing

catalytically active materials through *in situ* synthesis or PSM. MOF-based catalysts have been reported to successfully perform challenging C-H activation reactions, such as benzene hydroxylation,[139] CH_4 oxidation,[53] oxidative dehydrogenations of propane to propylene, [141], benzene to phenol, etc. Arai *et al.* has reported on the coupling of phenylacetylene with 2-oxazolidone through C–H activation in the formation of a C–N bond using Cu-carboxylate MOF.[142] The Cu-carboxylate MOF was prepared from $Cu(NO_3)_2.3H_2O$ and biphenyl-4,4′-dicarboxylic acid following Uozumi's synthetic method,[143] and was found to be stable for one month under ambient conditions. For the catalytic investigation, 20 mol% of the catalyst was utilized in an O_2 environment with Na_2CO_3 as a base in toluene for 4 h (Scheme I.3).

Scheme I.3: General scheme for Cu-carboxylate MOF catalyzed C–N bond formation through C–H bond activation.

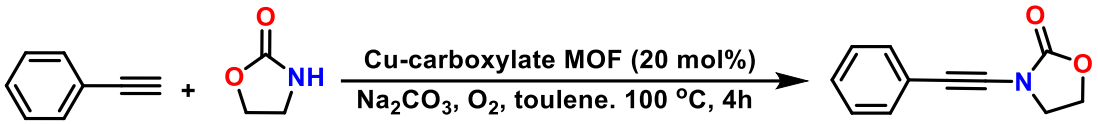

The coupling reaction occurred at 70 °C, resulting in a 49% yield of amide product and a 35% yield of phenylacetylene dimer as a side product. The dimer yield was reduced by increasing the temperature to 100 °C. The Cu-carboxylate MOF was successfully recycled, but the high reaction temperature resulted in a reduction in its catalytic efficiency. Phan *et al.* discovered that a particular MOF ($Co_2(BDC)_2(DABCO)$) formed using Co-salt, BDC and DABCO demonstrated catalytic activity towards amination reactions based on its topology.[144] By introducing CH_3COOH and HCl into the reaction mixture, a new isomer of the MOF was formed, called VNU-10, which had a pillar-type kgm topology, different than the original

MOF's sql topology (Figure I.19). VNU-10 (VNU = Vietnam National University) showed activity towards direct amination of azoles *via* C-H activation, while the original MOF was inactive towards the same reaction. The authors optimized the reaction conditions using piperidine where 5% of the catalyst, 2 equivalent acetic acids and TBHP in acetonitrile solvent at room temperature was reacted for 60 minutes. The optimized condition yielded excellent results for piperidines (82%-89%), but only moderate yields (<57%) for morpholine, *N*-methyl benzylamine, and 4-methyl piperazine. The authors observed that the reaction likely took place within the cavities of the Co-MOFs, as indicated by the decrease in conversion rate for larger

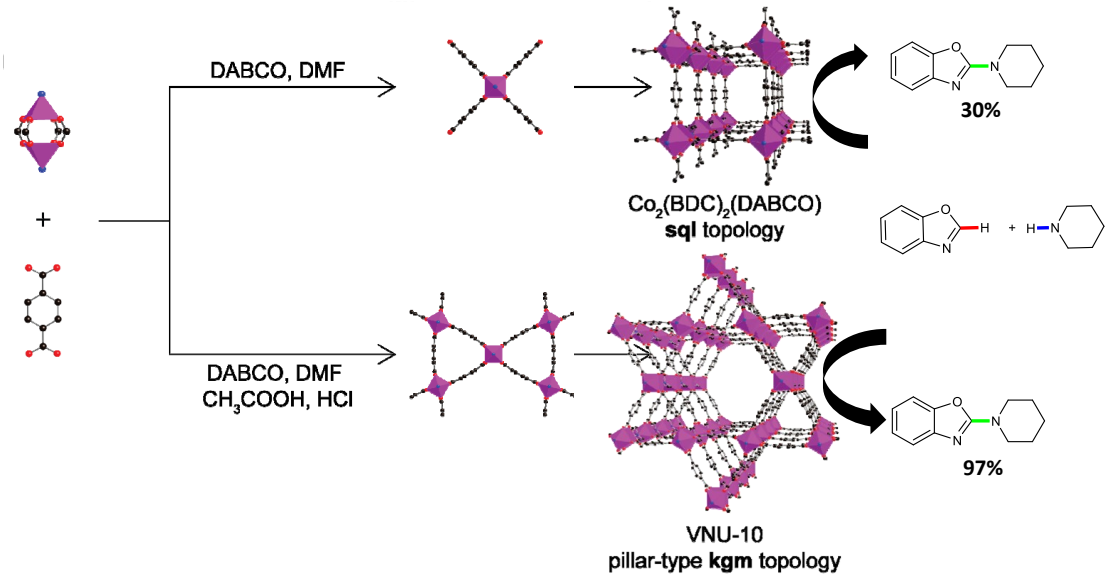

Figure I.19: Schematic diagram for the formation of sql and kgm topology and scheme for VNU-10 catalyzed direct amination of azoles by N–H bonds. Reprinted with permission from ref.144 Copyright 2016 Royal Society of Chemistry.

particles (70 µm) to 84%, compared to the high yield of 98% obtained for smaller particles (8 µm). The performance of VNU-10 was superior to other MOFs, such as Co(BDC)(DMF) (Co-MOF-71), $Co_2(BDC)_2(DABCO)_{sql}$, Co-ZIF-67, Co-Zeolite-X $CoFe_2O_4$, $Ni_2(BDC)_2(DABCO)_{kgm}$, $Cu_2(BDC)_2(DABCO)_{kgm}$, as well as homogeneous

catalysts like $CoCl_2$, $Co(OAc)_2$ and $Co(NO_3)_2$. The catalyst proved to be both recoverable and reusable for at least the tenth cycle while still maintaining an 80% yield of the product for the tenth cycle. Additionally, the ICP-MS analysis of the reaction filtrate indicated that the reaction mixture contained less than 20 ppm of leached Co in the supernatant. Phan *et al.* also reported the C-N bond formation of through C-H activation by other MOF such as $Fe_3O(BPDC)_3$,[145] and $Cu_2(BPDC)_2(DABCO)$.[146] Truong *et al.* has utilized the Cu-based VNU-18 ($Cu_5O_2(PDC)_5Cu(OH)_2$) MOF to facilitate the formation of a C-N bond between amines and ketones through C-H activation.[147] The VNU-18 MOF is constructed from a 3D framework consisting of 3,5-pyridine dicarboxylate linker units and copper building blocks where each pyridine dicarboxylate links to three distinctly different Cu polyhedra (Figure I.20a). The MOF was activated *via* solvent exchange method, followed by thermal treatment. First, DMF was replaced with methanol, and then subsequently with DCM, resulting in the removal of guest molecules from the pores and creating five coordinated Cu(II) metal sites. The optimized conditions employed in the study used ethyl phenyl ketone and morpholine as coupling partners with 5 mol% catalysts, KBr, and morpholine in DMF solvent at atmospheric temperature for 12 h. The cross-coupling between morpholine and aromatic/aliphatic ketone resulted in a good product yield. Additionally, the optimized conditions were used to synthesize high-profile medicinal agents, such as amfepramone, clopidogrel, and α-pyrrolidinovalerophenone, with yields of 75%, 61%, and 82%, respectively (Figure I.20b). The authors reports VNU-18 catalyst system to be more efficient in terms of activity and stability when compared with other MOFs such as $Cu_3(BTC)_2$, Cu(BDC), $Cu_2(BDC)_2(BPY)$, $Cu_2(BDC)_2(DABCO)$, and $Cu_2(BPDC)_2$ (BPY), Cu/Zeolite X, Cu/ZSM-5, $CuFe_2O_4$, $Cu(NO_3)_2$, PDC, $FeBr_3$, $CoBr_2$, and $NiBr_2$.

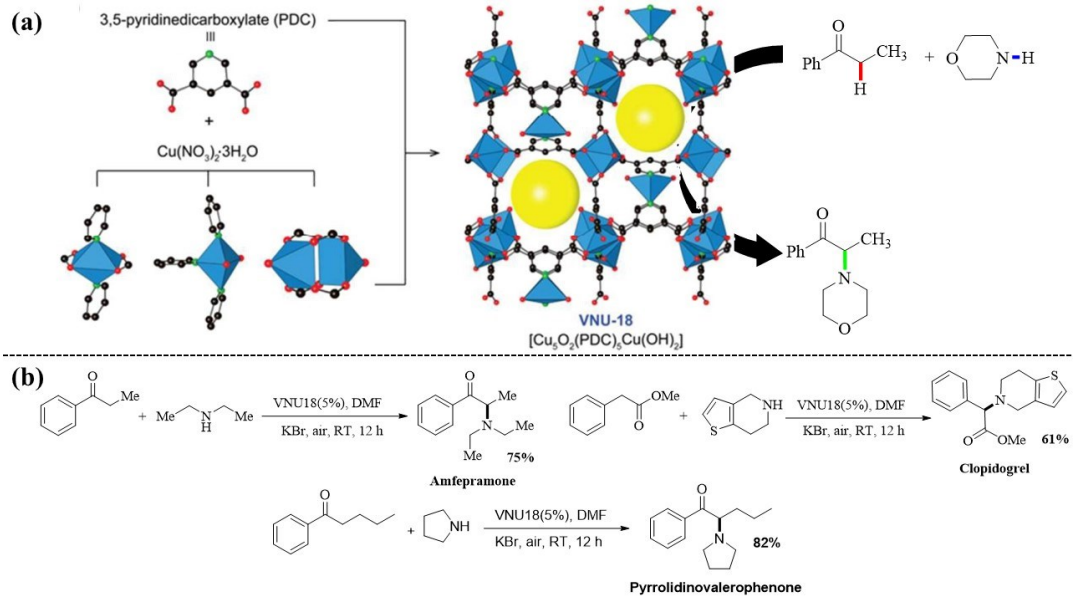

Figure I.20: (a) Synthetic scheme for the formation of VNU-18 with three different types of Cu-clusters. (b) Synthetic scheme of medical agents conducted under the optimized conditions using VNU-18 catalyst. Reprinted with permission from ref.147 Copyright 2017 Royal Society of Chemistry.

I.4.1.4 MOF catalyzed aziridination reaction via C–N bond formation

Aziridines, which are nitrogen-based analogues of epoxides, are commonly used as a fundamental building block for synthesizing complex heterocyclic compounds. [148–150] In comparison to conventional organic approaches, transition metal-catalyzed synthesis of aziridine *via* nitrene transfer reaction is gaining importance due to its varied substrate tolerance and improved enantioselectivity.[151] Initially reported by Mansuy *et al.,* using Mn and Fe porphyrin complexes, the transition metal-catalyzed aziridination of alkenes using hypervalent iodinane has been widely studied and many transition metal salts and complexes have been identified to facilitate the reaction. [152–158] However, the use of heterogeneous catalysts in aziridination reactions has been

less explored. Hutching *et al.* achieved a high yield of 85% (91% ee) using a heterogeneous copper exchanged zeolite (CuHY) for catalytic aziridination of olefins.[159] MOFs have been widely used as catalysts, but their use as a heterogeneous catalysts for aziridination reactions is limited. Chi *et al.* reported the use of chiral Cd-salen MOFs where the struts were modified through Cu-complexation for aziridine synthesis (Figure I.21).

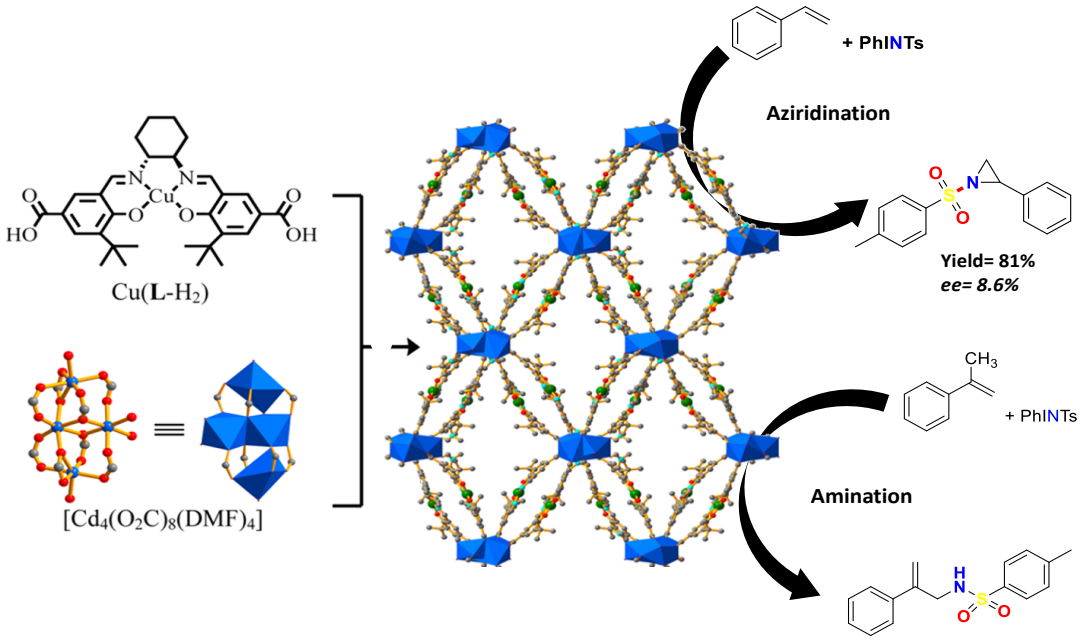

Figure I.21: General scheme for the synthesis of Cu-modified 3D homochiral Cd-salen and reaction scheme for aziridination and amination reaction. Reproduced with permission from ref. [160] Copyright 2016 American Chemical Society.

The catalyst yielded a competitive amination product using α-methyl styrene as the substrate and a product yield of 76% was observed for the 5th cycle in the recyclability of the catalyst.[160] Pariyar *et al.* reported the HKUST-1 catalyzed aziridination reaction, and the coordinatively unsaturated sites in MOFs were found to be crucial for such group transfer reactions.[46] They also demonstrated the feasibility of ring-opening of aziridine with a non-activated catalyst, without the generation of CUS, and designed a one-pot method for synthesizing β-aryl-substituted sulfonamide derivatives possessing new C-N, C-C, C-S, and C-O bonds (Scheme I.4).

Scheme I.4. General scheme for HKUST-1 MOF catalyzed aziridination reaction and the one-pot ring-opening reaction of aziridine with the various nucleophile.

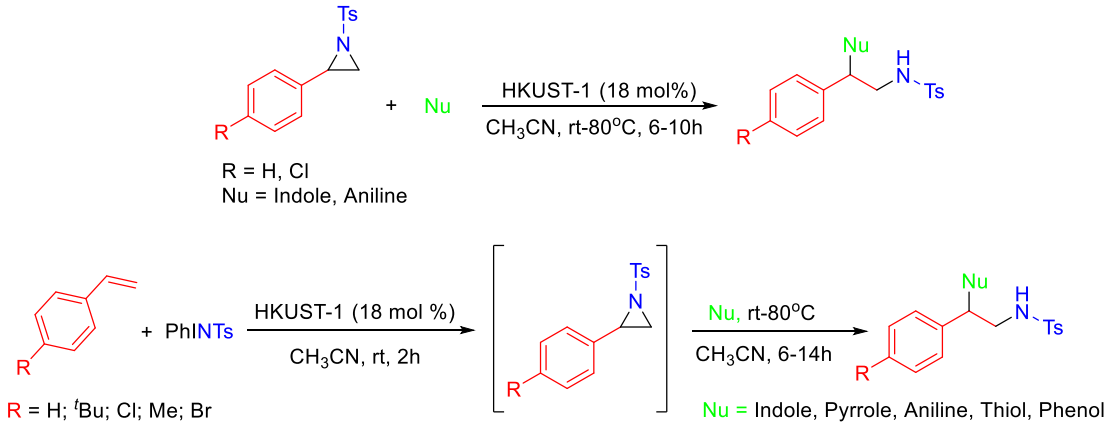

I.3.2. MOF Catalyzed C-O bond formation

I.3.2.1 MOF catalyzed C–O bond formation: Ullmann and Chan-Lam Coupling

Previously discussed for C-N coupling reactions, the URJC1-MOF based on Cu(II) has also been found effective for C-O bond formation, as reported by Calleja *et al.*[129] The researchers observed the formation of C-O bond between various phenols, alcohols, and phenyl boronic acid through Chan-Lam-Evans-type reactions. The resulting O-arylated products were obtained in yields ranging from 23% to 75%. In a recent publication by Tavangar *et al.,*[161] they demonstrated the utilization of a one-dimensional $[Cu(BT).2H_2O]_n$ (BT=5,5'-bistetrazole) MOF as a catalyst for the Ullmann-type reaction, leading to the formation of C-O bonds (Figure I.22). The authors observed a maximum yield of 95% of the O-arylated product in the presence of $[Cu(BT).2H_2O]_n$ (5mg), K_2CO_3, and DMSO at 70 °C within 1 hour. Moreover, the $[Cu(BT).2H_2O]_n$ catalyst was found to be easily retrievable and reusable. The authors successfully recycled the catalyst for up to six cycles, with an 87% product yield reported after the sixth cycle.

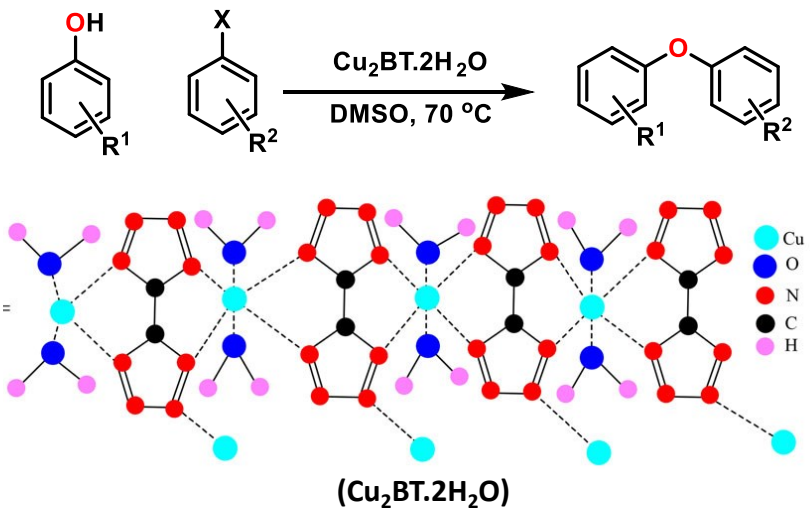

Figure I.22: Ullmann coupling reaction with $[Cu_2BT.2H_2O]_n$ as a recyclable Catalyst and its one-dimensional framework. Reprinted with permission from ref.161 Copyright 2021 Taylor & Francis.

In 2012, Li et al.[162] utilized MOF-253, an aluminium-based metal-organic framework Al(OH)(bpydc) (bpydc = bipyridinedicarboxylate), to support CuI that catalyzed Ullmann reaction with favorable yields. The 0.5 eq. of CuI was immobilized on each MOF-253 unit *via* non-coordinated bipyridine moieties, and its catalytic activity was assessed in the *O*-arylation of phenols and alcohols with aryl halides without the need for additional ligands. When 20 mol% MOF-253 containing 0.5 eq. CuI was added to a reaction mixture containing 4-methoxyiodobenzene and p-cresol in the presence of DMSO and Cs_2CO_3 as a base, the C-O coupling product was obtained with a 96% yield. Conversely, independent CuI and MOF-253 catalysts produced only 3% and 0% yields of the coupling product, respectively. These results indicate that MOF-253 significantly promotes the activity of CuI due to the formation of the metal bipyridyl complex. However, when attempting to use aryl chlorides as substrates, the desired products were not obtained, indicating that further development of a more efficient MOF-253 catalyst is necessary to promote this coupling reaction with aryl chlorides. 0.5 eq. CuI anchored MOF-253 also displayed very high activity towards the coupling of methanol with iodobenzene, producing a 98% yield of the coupling product.

Additionally, alcohols with an aromatic or cyclic ring underwent O-arylation smoothly under the same reaction conditions. The amount of Cu leaching was less than 0.1% of the initial Cu content, and XRD analysis of the catalyst performed after three cycles did not reveal significant changes compared to the fresh one, suggesting that MOF-253's structural integrity remained intact during catalysis. Following a similar method, Sadeghi *et al.* incorporate melamine within UiO-66-NH_2 MOFs *via* a post-synthesis approach.[163] They then doped copper oxide onto the MOF's surface using the available amine groups and stabilized by π-electron interaction of melamine(Mlm) and ligand that resulted in the formation of UiO-66-NH_2-Mlm/CuO NPs composite (Figure I.23).

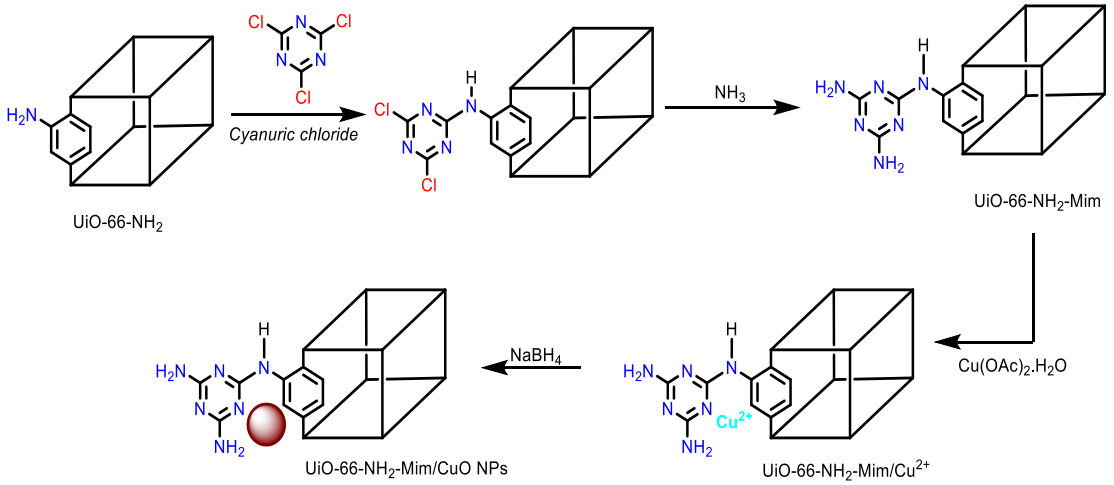

Figure I.23: Synthetic route for the preparation of UiO-66-NH_2-Mlm/CuO NPs. Reproduced with permission from ref.163 Copyright 2017 Taylor & Francis

The UiO-66-NH_2-Mlm/CuO NPs was characterized by SEM and used it as a heterogeneous catalyst in the Ullmann etherification reaction. The UiO-66-NH_2-Mlm/CuO NPs efficiently promoted C-O bond formation between aryl halide (halide=I, Br, Cl) and phenol with just 5 mol% catalysts, which produced 93% yield of the desired *O*-arylated product. Interestingly, a catalytic system for C-O bond

formation using Ag co-catalyst along with Cu-BTC-MOF was developed by Leila *et al.*[164] The Ag-CuBTC-MOF was found to exhibit unexpectedly high catalytic activity for coupling chloro arenes with phenols, without the presence of any additional ligands (Figure I.24).[164] Ag-CuBTC-MOF demonstrated an exceptionally high TON value (>15,000), surpassing all its previous counterparts, including Pd catalysts. This achievement represents the highest TON value observed to date for this type of reaction.

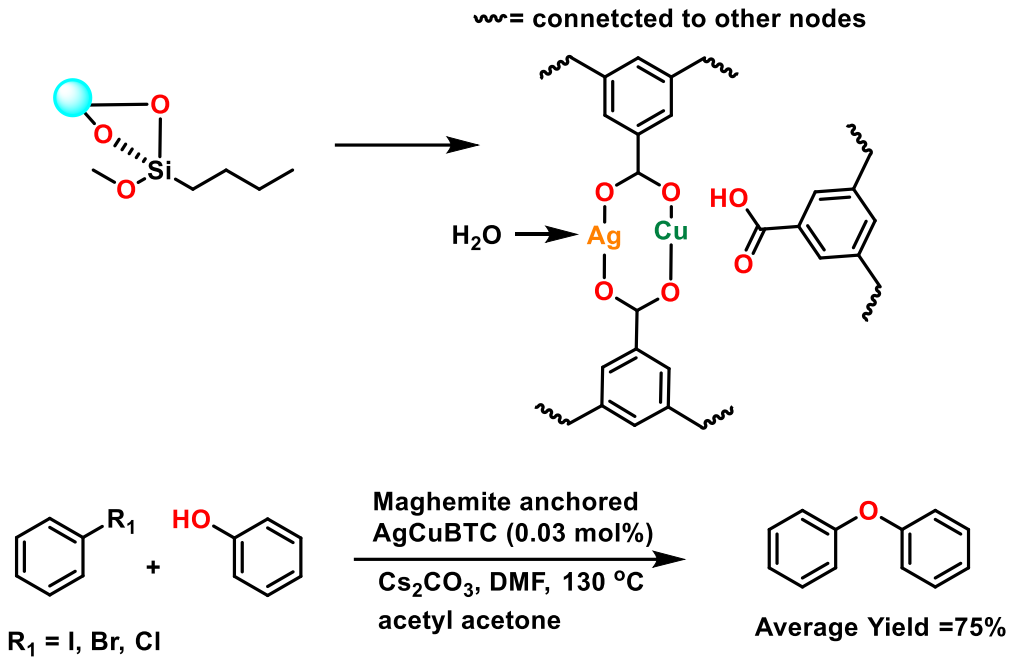

Figure I.24: (a) Structure of AgCuBTC-MOF. (b) The synthesis of various type of biphenyl ether by Ag-CuBTC-MOF. Reproduced with permission from ref.164 Copyright 2021 Taylor & Francis.

Later on, Truong *et al.*[165] reported the photocatalytic application of $Cu_2(BDC)_2(DABCO)$ towards C-O bond formation. The arylation of phenol with iodobenzene was caried out and 81% of desired arylated product was obtained in presence of *t*-BuOLi as a base and acetylacetone as a ligand under 365 nm light at room temperature.

I.4.2.2 MOF catalyzed C–O bond formation via C-H Bond activation

The process of C–O bond formation through the activation of C–H bonds using transition metal catalysts presents a significant challenge in organic synthesis. Therefore, there is a need to explore alternative approaches that offer a more direct route to the desired products while adhering to green protocols. One such strategy is to employ reusable heterogeneous catalysts like MOF, which allow for a simple workup and the use of mild reaction conditions.[166] Phan *et al.* studied the use of $Cu_2(BPDC)_2(BPY)$ as a highly effective heterogeneous catalyst towards cross dehydrogenative coupling (CDC) reaction.[167] These reactions were achieved through direct C-H functionalization of ethers with 2-hydroxybenzaldehyde at 80 °C, using TBHP as an oxidant (Scheme I.5). The authors reported the excellent yield of desired products in the presence of the catalytic amount of $Cu_2(BPDC)_2(BPY)$ MOF and the catalytic activity is superior compared to other Cu-based MOF such as $Cu_3(BTC)_2$, Cu(BDC), Cu(bpdc) and other copper salts, like $CuCl_2$, CuCl, CuI, $Cu(NO_3)_2$, and $Cu(OAc)_2$. The authors also achieved easy recyclability and re-used the catalyst for up to the 8th cycle with 88% yield.

Scheme I.5: $Cu_2(BPDC)_2(BPY)$ MOF catalyzed cross dehydrogenative coupling reaction *via* C-H functionalization

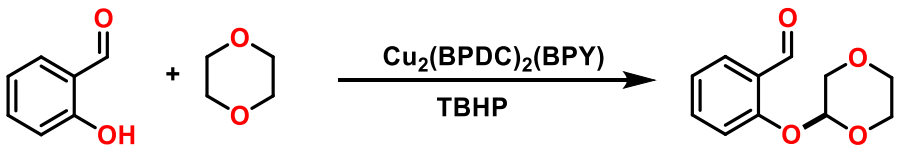

The use of Cu based MOF catalysts for C–O cross-dehydrogenative coupling reaction were utilized more broadly by Corma and Xamena (Scheme I.6).[168] They studied copper-MOFs ([$Cu(im)_2$] and [$Cu(2\text{-pymo})_2$]), which contain CuN_4 centers with either imidazolate (im) or 2-hydroxypyrimidinolate (pymo) hydroxypyrimidinolate ligands

and found to be active towards cross dehydrogenative coupling reaction forming C-O bond *via* C-H activation.[168] These reactions were achieved through direct C-H functionalization of formamides, benzaldehydes, and ethers with 2-hydroxyacetophenone or β-ketoesters, in DMF at 80 °C, and using TBHP as an oxidant.

Scheme I.6: Oxidative C–O bond coupling reactions through direct activation of the *sp2* C–H bond of formamides or aldehydes or the C–H bond of ethers in the presence of Cu-MOFs.[168]

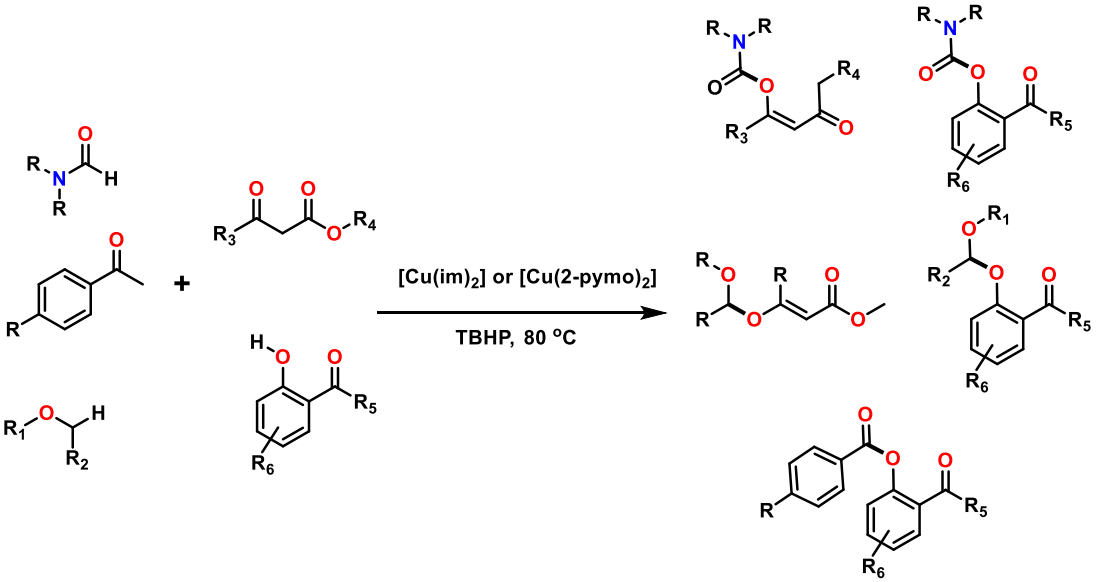

The CDC reaction is also studied by Bharadwaj *et al.* designing a multifunctional Cu-MOF ($[Cu_6(L)_3(H_2O)_6](14DMF)(9H_2O)_n$) (L=5′-amino-1,1′:4′,1″-terphenyl-3,3″,5,5″-tetracarboxylic acid) under solvothermal conditions, using $Cu(NO_3)_2$ and a bent amino-functionalized tetracarboxylate ligand (Figure I.25a-b).[169] The synthesized Cu-MOF was reported to contain unsaturated Cu(II) after activation. The CDC reaction through direct C-H activation between 1,4-dioxane and 2-hydroxybenzaldehydes was explored in a solvent-free environment and a yield of 96% was reported for desired product in 1 h at 100 °C (Figure I.25c). Superior catalytic activity of synthesized Cu-MOF catalyst compared to $Cu_3(BTC)_2$, $Cu_2(BPDC)_2(BPY)$, and Cu-(BDC) were noted.

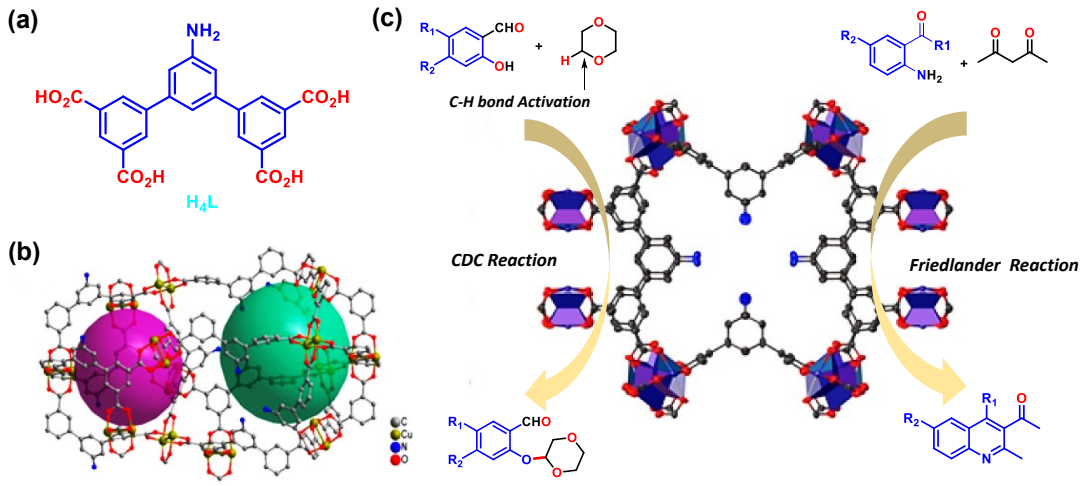

Figure I.25: Structure of ligand H4L. (b) Nanospherical cages of synthesized Cu-MOF highlighting potential void. (c) open metal sites (polyhedra) of Cu-MOF with reaction scheme for CDC and Friedländer reactions. Reproduced with permission from ref.169 Copyright 2018, American Chemical Society.

A highly effective method was developed for the alkoxylation and phenoxylation of sp^2 C–H bonds in 8-aminoquinoline under heterogeneous catalysis with the use of Cu-MOF-74 as catalyst.[170] The ideal conditions for this process involve using Cu-MOF-74 (20%) as the catalyst, K_2CO_3 as the base, and either pyridine or dimethyl formamide as the solvent, along with O_2 as the oxidant, at a temperature of 80 °C or 100 °C for 24 h with 48–86% yield of the desired product (Scheme I.7). Cu-MOF-74 shows significantly greater activity when compared to other frequently used Cu based MOFs in cross-coupling reactions, copper supported catalyst and homogeneous copper salts. It is noteworthy that the developed conditions can be extrapolated to produce biologically relevant molecule such as ethanzamide. The leaching test has confirmed the heterogeneity of the reaction, and the catalyst can be reused and recycled at least 8 times with only slight degradation in activity.

Scheme I.7: 8-Aminoquinoline assisted selective etherification of sp^2 C–H bonds over Cu-MOF-74.

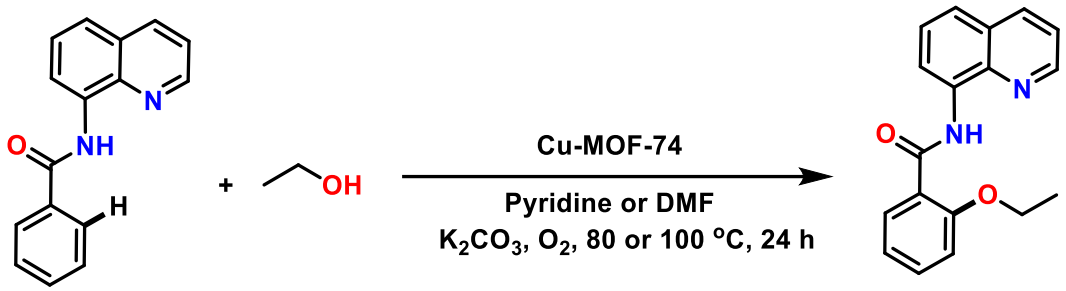

Mokhtari *et al.* presented a straightforward and effective method for transforming benzaldehyde into symmetric carboxylic anhydrides through Csp^2-H bond activation (Scheme I.8).[171] This reaction is achieved by utilizing $Cu_2(BDC)_2(DABCO)$ as a, and TBHP as the oxidant and CH_3CN for 2 h under reflux. The product yields for this process were observed to be between 67-82%. Pandey *et al.*[171] showed that MOFs can be used to access benzoic anhydride *via* sp^2 C–H bond activation of benzaldehyde. They formed three one-dimensional coordination polymers (CPs) with the formulas [M(pdca)-$(H_2O)_2$]n (M = Zn, Cd, and Co, and named as **1**, **2**, and **3**, respectively) and a three-dimensional coordination framework with the formula $[(CH_3)_2NH_2][CuK(2,3\text{-}pdca)(pa)(NO_3)_2])_n$ (named as **4**) (pdca=pyridine-2,3-dicarboxylate and pa = picolinic acid). The synthesized metal MOFs has both Lewis acid and basic sites (such as carboxylate and free pyridyl groups). Their potential as catalysts with dual functionality was investigated for the formation of C-O bonds through the activation of C-H bonds in the presence of TBHP, using benzaldehyde The production of benzoic anhydride yielded outstanding results, with the catalytic effectiveness exhibiting a descending trend of **3** < **1** < **4** < **2**, which corresponded with the anticipated increase in coordination number (7-, 9-, and 10-fold coordination) and

larger size of Cd(II) across these compounds. Moreover, the materials were identified as highly effective and capable of being reused.

Scheme I.8: $Cu_2(BDC)_2(DABCO)$ catalyzed synthesis of anhydrides from sp^2 C–H bond activation of benzaldehyde.[171]

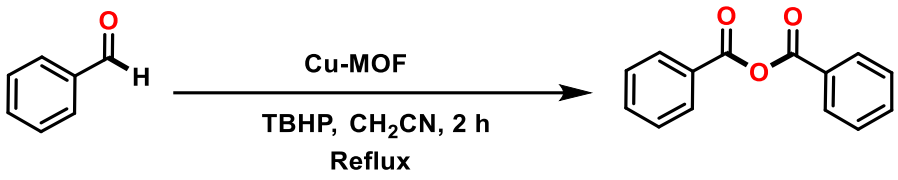

I.4.3. MOF Catalyzed C-S bond formation

Unlike the C-N and C-O coupling reactions, only a handful of MOFs have been reported for the C-S coupling reaction. The study done by Dhakshinamoorthy *et al.* shows that the framework of $Cu_3(BTC)_2$ MOF (HKUST-1) collapsed during a reaction with thiol and bromobenzene under mild conditions and the formation of copper nanoparticles was observed.[172] However, when they studied the reaction with Fe(BTC) MOF (MIL-101) they observed the formation of diphenyldisulfide as a desired product from thiophenol.[173] Currently, C-S bond formation has been reported by a few other MOFs. Wang *et al.* reported $Cu_2(TPTC)$ MOF (TPTC=terphenyl-3,3′,5,5′-tetracarboxylic acid) with binuclear Cu(II) paddlewheel nodes to facilitate a new and efficient cascade reaction strategy for disulfide-directed C_{sp2}–H hydroxylation.[174] This strategy involves coupling disulfide with arylboronic acid, catalyzed effectively by $Cu_2(TPTC)$ MOF, to yield the desired hydroxylation reaction (Figure I.26). It is noteworthy that this reaction can be carried out with good yields under the $Cu_2(TPTC)$ MOF catalyst, providing an effective method for synthesizing functional organic molecules such as 2-(Phenylthio)phenol derivatives. Lin *et al.*[175] reported the synthesis of photocatalyst Zr_{12}-Ir-Ni by incorporating Ir^{III} photoredox and Ni^{II} cross-coupling catalysts into a stable Zr_{12} MOF. The photocatalytic activity of the

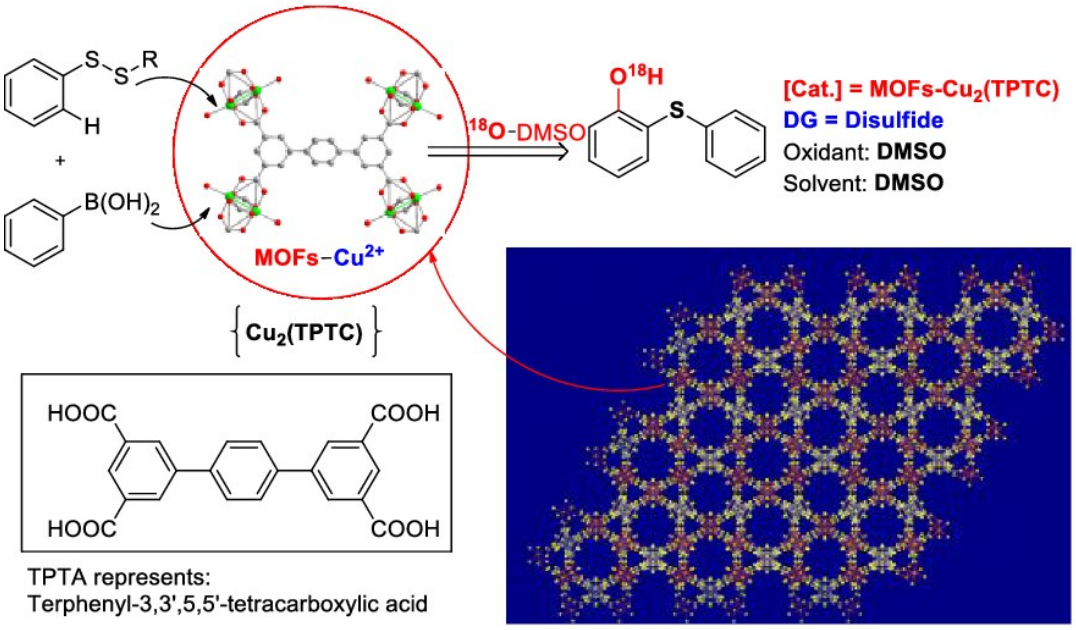

Figure I.26: Representation of Cu_2(TPTC) MOF and its reaction for disulfide-directed C–S coupling/C–H hydroxylation reaction. Reprinted with permission from ref.174 Copyright 2020 Springer Nature.

synthesized catalyst was validated by performing C-S bond forming between various thiols and aryl iodides and conversion of 91% with turn-over number (TON) of 4550 was reported. The PSM approach of MOF to encapsulate NPs has also been reported for the C-S bond formation. In particular, Alinezhad *et al* reported the synthesis of UiO-66-NH_2-Fu@Ni catalyst by anchoring nickel furfural (Fu) moieties into a Zr-based MOF, UiO-66-NH_2.[176] The catalyst shows the activity towards C-S bond formation. The reaction between iodobenzene and 4-chlorothiophenol, in presence of K2CO3, DMF and UiO-66-NH_2-Fu@Ni produced 85% of desired product in 8 h under 110 °C. The catalyst was recycled for three consecutive times and the PXRD performed after third cycle confirms the structural intregrity of the MOF framework. Similarly, Fe_3O_4@AMCA-MIL53(Al)-NH_2-Co^{II} NPs has been synthesized by Akhlaghinia *et al.* using Al-based MOF and its reactivity was explored towards C-N and C-S coupling reaction under solvent free condition.[177] A yield of 95% was

reported for a produced formed by reacting iodobenzene and thiophenol at 70 ℃ for 4.5 h in presence of K_2PO_4. The heterogeneity of reaction was confirmed by executing the hot filtration test. The ICP-OES analysis performed for the supernatant shows the presence oof 4.9×10-6 and 4.8×10-6 mol% of active-species for C-N and C-S reaction system indicating negligible leaching of the metal ion into the reaction system. Despite few reports an effort to established a more versatile and efficient catalytic system based on MOFs for C-S coupling is much needed.

I.4.4. MOF catalyzed C-C bond formation

I.4.4.1. MOF catalyzed C–C bond formation: Suzuki-Miyaura cross-coupling reaction

The Suzuki-Miyaura cross-coupling reaction is a versatile method for synthesizing biaryl compounds, including those with heterocyclic moieties.[178,179] This reaction involves coupling an aryl halide with an arylboronic acid, and the reactivity of the aryl halide generally follows the order of iodides > bromides > chlorides. The presence of electron-withdrawing substituents increases the reactivity of the aryl halide, while the presence of ortho substituents decreases reactivity due to steric hindrance. Bases such as carbonates, phosphates, or amines are required for the reaction, which typically occurs in polar solvents. Numerous solid catalysts containing Pd, including Pd/hydrotalcite,[180] Pd-oxides,[181] metal oxide/ aluminosilicates,[182] and silica-supported Pd, have been documented to be used in the Suzuki-Miyaura cross-coupling reaction. The catalytic performance of Pd supported on inorganic materials can be limited concerning the variety of reactions it can catalyze, and in certain circumstances, it may display poor stability as a catalyst. Corma *et al*. made a significant contribution to the field of Suzuki–Miyaura cross-

coupling reaction by synthesizing a Pd-MOF, denoted by the formula [Pd(2-pymo)$_2$]$_n$3H$_2$O.[183] This Pd-MOF successfully formed a C-C bond *via* Suzuki–Miyaura cross-coupling reaction between phenylboronic acid and 4-bromoanisole (Scheme I.9). The conversion of 85% and a selectivity of 99% was obtained for 4-methoxybiphenyl after 5 h at 150 °C. Using the turnover frequency (TOF) measurement, the researchers calculated that the Pd-MOF catalyst (0.25 mol% Pd) had a turn-over frequency (TOF) value of 1230 h^{-1}.

Scheme I.9: Pd-MOF catalyzed Suzuki-Miyaura cross-coupling reaction.

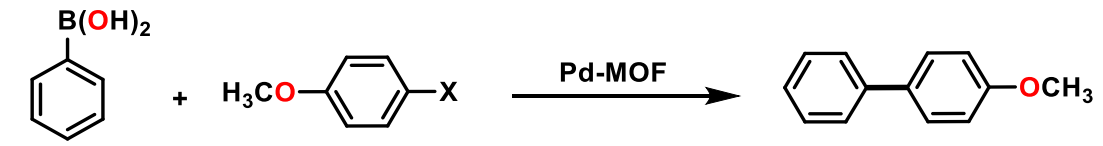

Pd-MOF: [Pd(2-pymo)$_2$]$_n$3H$_2$O, Pd/MIL-101

Espallargas *et al.*[184] recently published a study on incorporating Pd(II) into an iron-based MOF known as MUV-22 through a solvent-assisted reaction (Figure I.27a). This MOF, which features a stable square-octahedron (*soc*) topology and a porosity of 710 m^2g^{-1}, exhibits high activity, selectivity, and recyclability for the Suzuki–Miyaura allylation of aryl and alkyl boronates, as demonstrated by the coupling of cinnamyl bromide and Me-Bpin (Figure I.27b). The authors reported product yields ranging from 58-76% using a variety of substrates. Encapsulation of palladium on MOFs for Suzuki–Miyaura reactions is a well-established technique, and there are a few examples of such catalysts available. Catalysts' such as Pd@MOF-808,[185] Pd@NH$_2$-UiO-66(Zr),[186] PdCl$_2$/UiO-67-bpydc (bpydc=2,2'-bipyridine-5,5'-dicarboxylic acid),[187] Cu-BTC@Fe$_3$O$_4$,[188] Pd@HKUST-1,[189] Ni@UiO-66NH$_2$,[190] has also been reported recently towards Suzuki-Miyaura cross-coupling reaction.

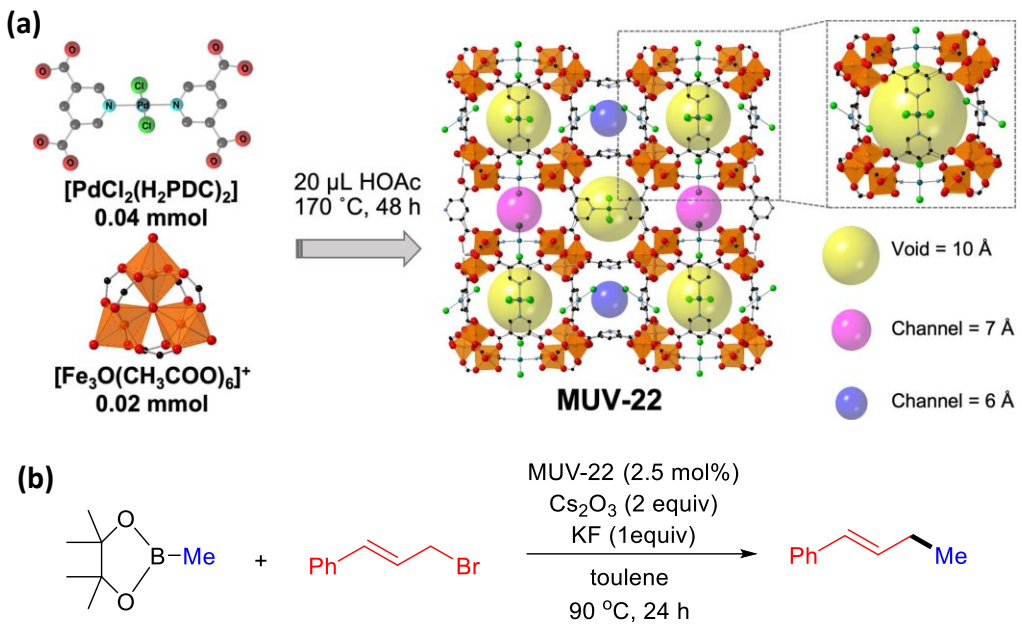

Figure I.27: (a) Scheme of the chemical reaction between the metalloligand $PdCl_2(H_2PDC)_2$ and $[Fe_3(m_3O)(CH_3COO)_6]^+$ to produce MUV-22. (b) Reaction scheme for MUV-22 catalyzed Suzuki-Miyaura cross-coupling reaction. Reprinted with permission from ref.184 Copyright 2023 Royal Society of Chemistry.

I.4.4.2 MOF catalyzed C–C bond formation: Sonogashira-coupling reaction.

Sonogashira coupling involves C–C coupling reaction between an aryl halide and a terminal alkyne. This reaction leads to the formation of aryl-substituted alkynes, which serve as intermediates in the synthesis of various pharmaceutically relevant compounds. Shu *et al.* utilized a chemical deposition method to embed palladium nanoparticles (Pd-NPs) onto MOF-5.[191] They then tested the catalytic activity of Pd/MOF-5 in the Sonogashira coupling reaction between iodobenzene and phenylacetylene using 1.5 equivalents of $K_3PO_4.3H_2O$, which resulted in a 98% yield of diphenylacetylene (Scheme I.10).

Scheme I.10: Scheme for Pd/MOF catalyzed Sonogashira coupling reaction

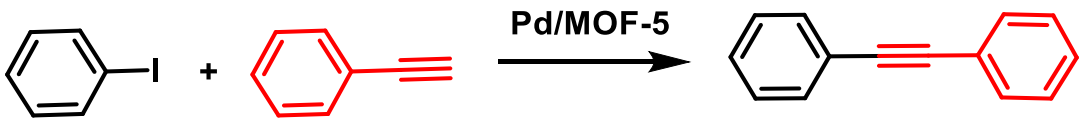

Pd/MOF-5 also demonstrated good catalytic activity for many derivatives with various substituents of iodobenzene and phenylacetylene, leading to the formation of corresponding diarylethynes in good yields (90%). Moreover, Pd/MOF-5 exhibited high activity for aliphatic alkynes and aryl iodide. Shifting the focus to Cu, Konar *et. al.* synthesized a 2D pillared-bilayer flexible open MOF {[Cu(tdc)(bpe)]$_{n2}$n(H_2O)$_n$(MeOH)} [H_2tdc = 2,5 thiophene di carboxylic acid; bpe = 1,2-bis(4-pyridyl)ethane] and tested its catalytic activity in the homocoupling of phenylacetylene.[192] The reaction mixture, which consisted of phenylacetylene, K_2CO_3, and 5 mol% of a catalyst in toluene, was heated to 110 °C under an O_2 atmosphere, resulting in an 82% yield. In contrast, the blank control using $Cu(NO_3)_2$2.5H_2O under identical conditions yielded only 9%, suggesting that the presence of electron-rich ligands tdc and bpe may have facilitated the *in situ* reduction of Cu(II) to the Cu(I) state, which is presumed to be the responsible species for the coupling reaction. Vaezi *et al.* have developed an efficient and reusable catalyst using a step-by-step PSM approach to incorporate nitrogen-rich organic ligands into UiO-66-NH_2 MOF.[193] Specifically, they introduced cyanuric chloride and 2-aminopyrimidine into the MOF, followed by the addition of Pd nanoparticles, as shown in Figure I.28. The resulting composite structure, facilitated by the PSM with nitrogen-rich organic ligands, proved conducive for C-C coupling reactions. The produced catalyst was found to promote three different cross-coupling reactions, including Suzuki, Heck, and Sonogashira coupling reactions.

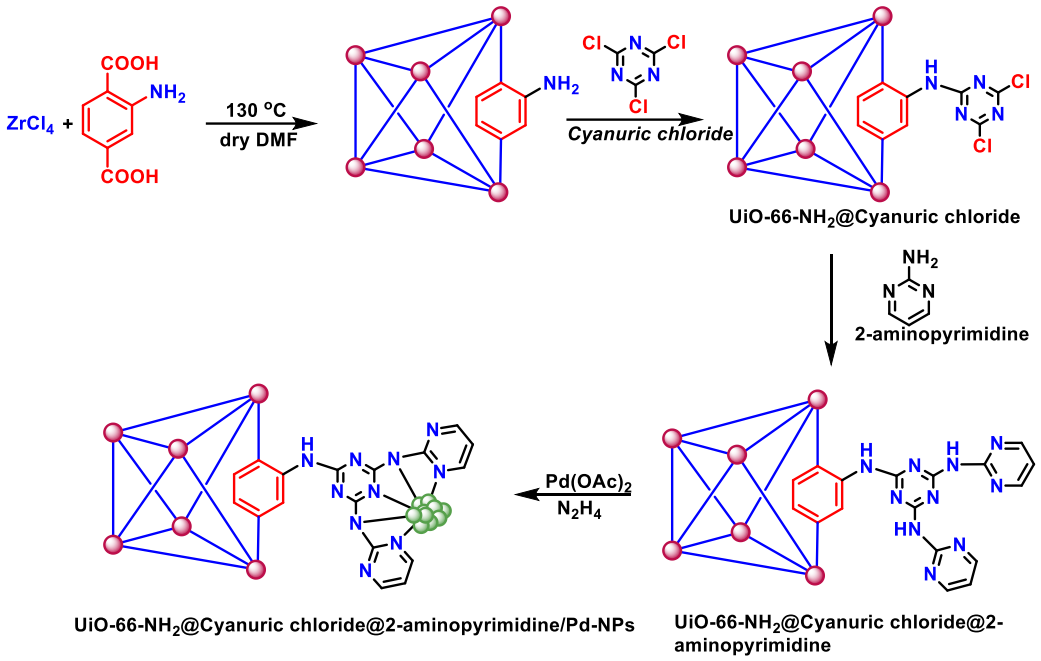

Figure I.28: Synthesis of Pd NPs immobilized on UiO-66-NH_2@Cyanuric Chloride@2-Aminopyrimidine. Reproduced with permission from ref.193 Copyright 2023 American Chemical Society.

I.4.4.3 MOF catalyzed C–C bond formation: Mizoroki-Heck Coupling reaction

The Mizoroki–Heck coupling is well known to form β-substituted styrene with the reaction between aryl halides and alkenes generally catalyzed by Pd-based complexes. Cao and colleagues utilized the ion-exchange method to support Pd NPs (3.2 nm) on amine-functionalized mixed-linker MOFs based on MIL-53(Al). The Pd/MIL-53(Al)-NH_2 catalyst was tested for its activity in the Mizoroki-Heck reaction of bromobenzene and styrene (Scheme I.11).[194] Using Et_3N as a base, a maximum yield of 81% (TOF 270 h^{-1}) was achieved with only 0.05 mol% of the Pd/MIL53(Al)-NH_2 catalyst in DMF. The reaction also proceeded with a low catalyst loading of 0.001 mol%, resulting in a maximum TOF value of 983 h^{-1}. In comparison, Pd/C exhibited only a 49% yield with a TOF value of 164 h^{-1}, highlighting the superior activity of Pd/MIL-53(Al)-NH_2.

Scheme I.11: Reaction scheme MOF catalyzed for Mizoroki-Heck Coupling reaction

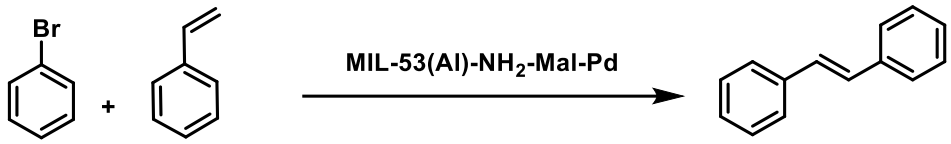

A novel Pd-MOF framework was created by Konar *et al.* by replacing metal nodes in Cu-MOF with Pd(II) ions.[195] The unit formula of the new framework (Pd-MOF) was estimated as $[Pd_2(pypz)_4(Cl)_2]_nCl_2 \cdot 2n(DEF)$ based on the results of the experiment. This framework demonstrated remarkable catalytic activity in C-C bond formation by cleaving the C-N bond of arylhydrazines. Additionally, the catalyst exhibited selectivity for substituent size and shape and retained its activity for at least four catalytic cycles while remaining recyclable. Some other notable MOF-based catalysts reported for the Mizoroki-Heck Coupling reaction are UMCM-1-NH_2-F_2C-Pd,[196] UiO-66-NH_2@Cyanuric Chloride@2-Aminopyrimidine,[193] Pd NPs@NHC@ZIF-8.[197]

I.5. MOF as a template to derive metal composites by pyrolysis.

On control pyrolysis, MOFs are capable of retaining the original MOF's structure, morphology, and size efficiently on control pyrolysis. Additionally, a wide range of MOFs is available, and multiple derived materials can be synthesized. The considerable potential has driven the exploration of various carbon-based electrocatalysts derived from MOF by utilizing diverse metal ions/clusters, organic ligands, and synthesis strategies, resulting in varying morphologies, compositions, and structures. Over the past decade, significant progress has been made in the synthesis strategies and electrocatalytic activity of carbon-based electrocatalysts derived from MOF. Many reviews today highlights the application of MOF-derived electrocatalyst towards energy applications.[23,88,198–202] The pyrolysis of MOF derived

carbon-based electrocatalysts has been extensively demonstrated to enhance the conductivity of metal oxides or nanoparticles consequently enhancing the efficiency of electrocatalytic oxygen processes. The numerous benefits of MOF as precursors have made it a highly promising approach for developing carbon-based oxygen reduction reaction (ORR) catalysts. In contrast to conventional porous materials, MOF-derived materials possess distinct advantages. In 2011, Liu *et al.*[203] successfully synthesized the first carbon-based ORR electrocatalyst using MOF.

I.5.1 MOF-derived metal composites for oxygen reduction reaction (ORR):

Oxygen Reduction reaction or ORR is a fundamental electrochemical process that involves the reduction of oxygen molecules to form water with an equilibrium potential of 1.23 V (*vs* reversible hydrogen electrode, RHE). It is an important reaction that takes place in various energy conversion and storage technologies, such as fuel cells, metal-air batteries, and solar cells. In ORR, oxygen molecules are typically reduced at the cathode of an electrochemical cell, where they react with electrons and protons to form water. The reaction can occur *via* several pathways, with the most commonly observed mechanism involving a four-electron transfer process that yields water as the final product. ORR is a complex process that involves multiple steps and intermediates, and its efficiency can be influenced by various factors, such as the nature of the electrode material, the pH of the electrolyte, and the presence of catalysts. As such, the study of ORR is of great interest to researchers in the fields of materials science, electrochemistry, and energy technology. Extensive research has been dedicated to creating non-precious metal catalysts in the past few decades.[204–206] Recently, there has been a significant focus on investigating MOF-based materials as ORR electrocatalysts. These materials are attractive due to their

ability to modify chemical composition at the molecular level and their highly porous framework that can enhance the speed of mass and charge transfer. An overview of the exploration history of MOF-derived carbon-based electrocatalysts for ORR has been recently documented by Zhang *et. al*.[202] Briefly, in 2008, MOF-derived nanoporous carbon was reported for the first time.[58] Subsequently, in 2011, Liu *et al.* presented their findings on utilizing MOF-derived composites for ORR.[203] Similarly, in 2013, an efficient metal-free electrocatalyst for ORR was reported as nitrogen-doped porous carbon derived from ZIF.[207] In 2014, Hong *et. al.* prepared highly graphitized N-doped porous carbon (NGPC) derived from ZIF-8 for ORR.[208] The following year, in 2015, Jiang *et al.* prepared bimetallic MOF-derived porous carbon for excellent electrocatalysis.[209] In 2016, Li *et al.* were the first to prepare MOF-derived single cobalt atoms catalysts (Co-SAs/N-C) for ORR.[210] Recently, in 2019, the ultrathin graphene nano-mesh (GM) derived from ZIF nano-leaves displayed unprecedented ORR activity.[211] In 2020, MOF-derived porous carbon (S-Cu-ISA/SNC) exhibited high ORR activity.[212] While in 2021, Pt-Fe dual metal single atoms catalyst (PtFeNC) were prepared for ORR.[213]

While discussing the recent progress on MOF-derived metal oxide for ORR, Zhan *et al.* reported the synthesis of an N-doped carbon matrix (Co_3O_4@N/C) catalyst by hydrothermal reaction between the carbonized 2D cobalt-based MOF product and graphitic carbon nitride.[214] Typically, 2D cobalt MOF was hydrothermally synthesized and carbonized at 500-800 °C under an N_2 atmosphere (Figure I.29a). Subsequently, the carbonized MOF was mixed once more with C_3N_4 under solvothermal conditions at 150 °C for 48 h to produce the Co_3O_4@N/C nanocomposite. This nanocomposite capitalizes on the benefits of N-doped carbon nanomaterials such as high nitrogen content, good conductivity, high stability, etc,

and Co_3O_4 nanoparticles (known for their high electrocatalytic activity), resulting in outstanding catalytic performance ORR (Figure I.29 b-c). The authors report the onset potential, half-wave potential, and diffusion-limited current density of the derived catalyst to be 0.90 V, 0.80 V, and 5.36 mA cm^{-2} which is almost the same as that of 20% Pt/C (0.91 V, 0.80 V, and 5.14 mA cm^{-2}). The electron transfer number of 3.73 for Co_3O_4@N/C was reported that is close to the four-electron process of oxygen reduction. The derived catalyst also has high durability and better methanol tolerance. The authors claim the excellent ORR performance of Co_3O_4@N/C due to the synergistic interaction between N-doped carbon and Co_3O_4.

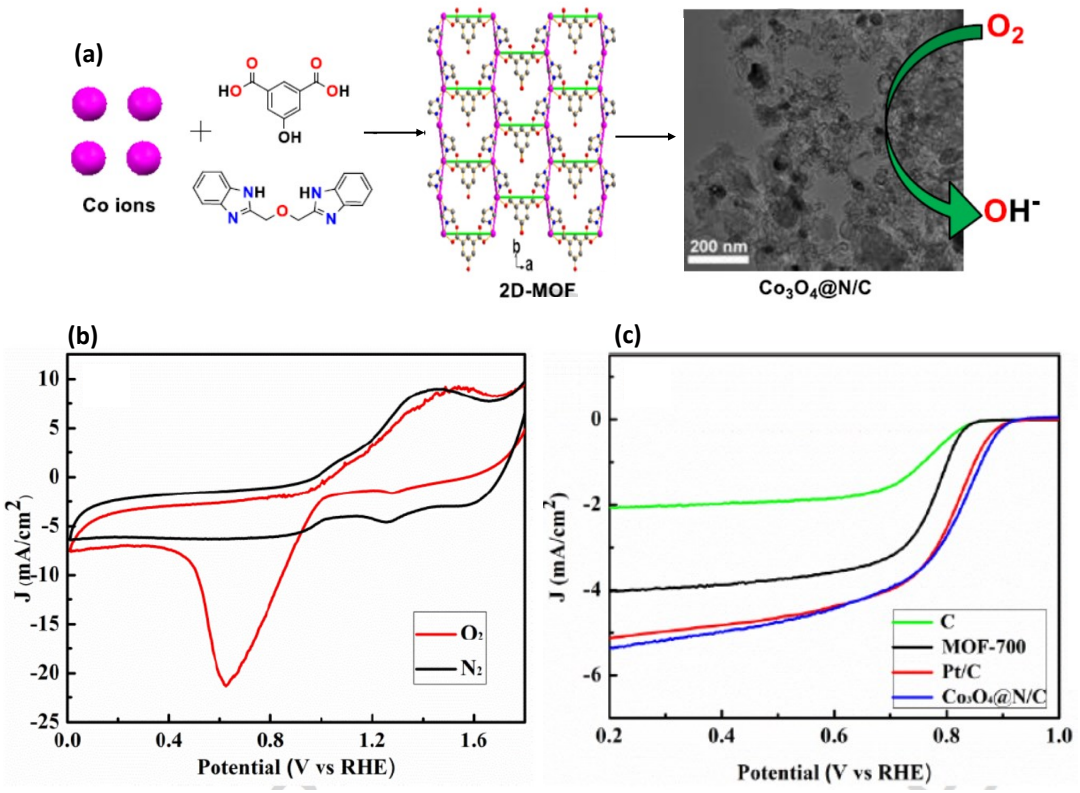

Figure I.29: (a) The synthetic process of Co_3O_4@N/C electrocatalyst. (b) CV of Co_3O_4@N/C in 0.1 M KOH (c) Comparative LSV plot of Co_3O_4@N/C. Reprinted with permission from ref.214 Copyright 2018 Elsevier.

Guo *et al.*[215] also reported the MOF-derived cobalt oxide for ORR. Two cobalt-based MOF [$Co_2(INA)_4$•DMF] (HINA=isonicotinic acid) and [$Co_2(TPI)(H_2O)_2(OH)$• DMF]

[H_3TPI = 5-(4-(tetrazol-5-yl)phenyl)isophthalicacid] were synthesized and pyrolyzed at 800 ℃ for 10 h under N_2 atmosphere to deliver Cal-MOF-1/CC and Cal-MOF-2/CC, as a derived composite respectively. The authors characterized the derived material with PXRD, FT-IR, SEM, elemental mapping, and XPS, which confirmed the materials as N-doped Co_3O_4/CoO/Co composite. The authors explored the electrocatalytic activity of derived composites towards ORR and half-wave potential, diffusion limit current was reported to be 5.64 mA/cm^2, 0.80 V, and 6.04 mA/cm^2, 0.82 V for Cal-MOF-1/CC and Cal-MOF-2/CC respectively. Efficient four-electron oxygen reduction pathway was found for Co_3O_4/CoO/Co composites. Due to increased nitrogen (doped) content, the Cal-MOF-1/CC derived from [Co_2(TPI)($H_2O)_2$(OH)]DMF has enhanced ORR activity compared to Cal-MOF-2/CC. Khomami *et al.* has reported the synthesis of bimetallic nanoparticles PtCo@C–Co_3O_4 *via* laser ablation techniques.[216] Precisely, the fabrication process involved the systematic pyrolysis of ZIF-67 MOF scaffolds that contained Pt-Co alloyed nanoparticles. Comprehensive analyses of the structure, morphology, and composition demonstrate the creation of a carbon-based framework adorned with tiny Co_3O_4 crystals and dispersed Pt-Co alloy nanoparticles, which are partially coated with a highly graphitized carbon layer. The catalyst outperforms for ORR with an onset potential of 0.95 V *vs* RHE which was found to be 60 mV positive than the C state-of-the-art Pt catalyst. The exceptional results are attributed to the electrocatalytic improvements stemming from the nano-alloyed Pt-Co structures, as well as the co-catalytic collaborations that arise due to the distinctive synergistic spill-over effects facilitated by the Co_3O_4 crystallites within the carbon matrix support. Yamauchi *et al.* reported the synthesis of hybrid polymeric fibers containing ZIF-MOF using a dual-phase electrospinning technique.[217] These fibers were then subjected to multi-step

annealing treatment to create Co_3O_4-nanoparticle-decorated with porous N-doped carbon fibers (ZIF-Co_3O_4/NCF). The derived catalyst can function as a bi-functional catalyst for catalysing oxygen reduction in both aqueous and non-aqueous electrolytes. The ZIF-Co_3O_4/NCF catalyst displays a high catalytic activity for oxygen reduction, as demonstrated by electrochemical tests, with an $E_{1/2}$ of 0.81 V (*vs* RHE) and a favourable four-electron reduction pathway in an alkaline medium. The ZIF-Co_3O_4/NCF catalyst exhibits excellent stability, showing only a 4.0 mV negative shift of $E_{1/2}$ even after undergoing 5000 continuous CV (cyclic voltammetry) cycles.

The ORR activity of MOF-derived carbon composites with atomically dispersed metal sites or single-atom catalysts (SACs) was studied by Li *et al.* in 2016. The development of Co-SACs, with Co single-atom catalysts (4.0 wt% loading) embedded in nitrogen-doped carbon (CoSAs/N-C) was achieved by pyrolysis of Zn/Co-bimetallic MOF.[210] As shown in figure I.30 the CoSAs/N-C catalysts showcase exceptional ORR performance in 0.1 M KOH, achieving a half-wave potential ($E_{1/2}$)

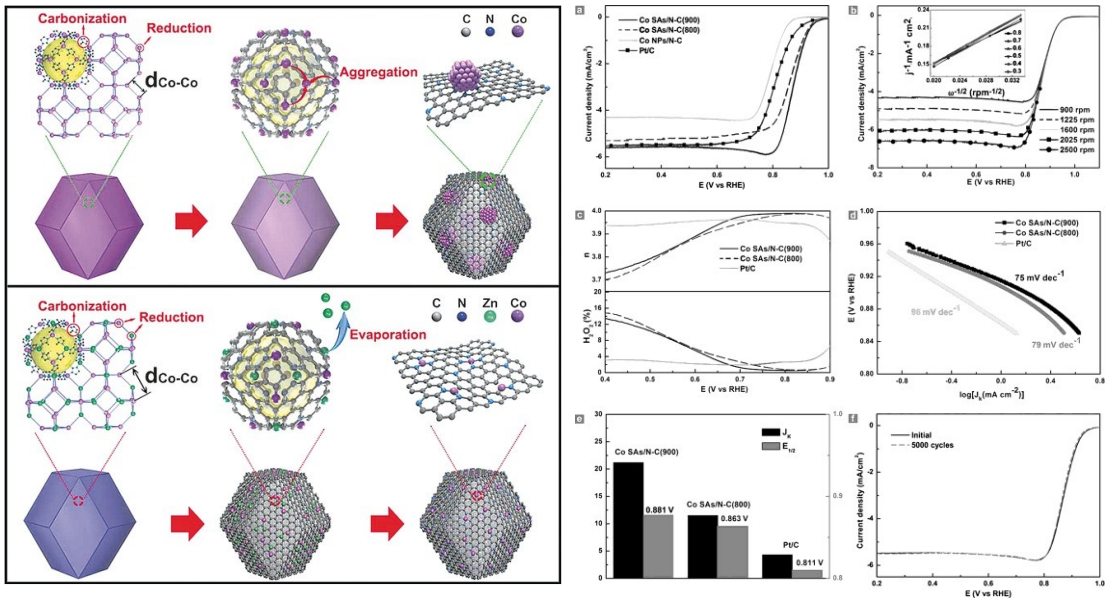

Figure I.30: The formation of Co NPs-N/C (top) and Co SAs/N-C (bottom). Results for Co SAs/N-C catalyzed electrocatalytic ORR. Reprinted with permission from ref.210 Copyright 2016, Wiley.

of 0.881 V (*vs* RHE), which surpasses the 0.811 V (*vs* RHE) for commercial Pt/C, studied under the same electrocatalytic condition. The ORR activity was found to be superior in the CoSAs/N-C sample containing CoN_2 active centers compared to those with CoN_4 environment. RRDE testing shows a nearly four-electron ORR pathway over the Co-N_2 active sites which is also confirmed through DFT calculations where a stronger interaction of Co-N_2 species was found with hydrogen peroxide compared to Co-N_4. These strong interactions of Co-N_2 species from CoSAs/N-C further boost the oxidation of H_2O_2, leading to a four-electron oxygen reduction to H_2O.

Wu *et al.* developed the surfactant-assisted MOF approach, that Co-doped ZIF-8 on pyrolysis at 900-1100 ℃ formed Co-N-C SAC with Co-N_4 moieties embedded in porous carbon.[218] Among various surfactants such as SDS, CTAB, Pluronic F127 and PVP the use of Pluronic F127 surfactant was found to be optimum. The cohesive interactions between the optimized surfactant and the Co-doped ZIF-8 nanocrystals lead to a unique confinement effect. The derived Co-N-C SAC was studied towards ORR and found to be efficient even in acidic electrolytes (0.5 M H_2SO_4). The E_{onset} of 0.93 V and $E_{1/2}$ 0.80 V (*vs* RHE), was reported for the derived catalyst. Furthermore, the authors also verified the practical application of derived catalyst in polymer electrolyte membrane fuel cells (PEMFCs) where a power density of 0.56 W cm^{-2} was reported with long time stability of 100 h.

Next, Li *et al.* reported an electrocatalyst ORR in which cobalt nanoparticles were decorated on a honeycomb-like carbon framework using a ZIF-67 MOF precursor.[219] The ZIF-67 MOF grown on 2D, Co-Al layered double hydroxides (LDH) was carbonized at 800 ℃ to produce LDH@ZIF-67-800. The SEM and TEM characterization showed the retention of 2D morphology while the collapse of the ZIF-67 framework was observed. The ORR performed in 0.1 M KOH with the

derived catalyst has an E_{onset} and $E_{1/2}$ of 0.94 and 0.83 V *vs* RHE respectively which is superior to the Pt/C catalyst. The high efficiency of the derived catalyst was ascribed to the well-distributed Co nanoparticles of the active material. Furthermore, the data obtained from the RRDE suggested that LDH@ZIF-67-800 undergoes a nearly four-electron process and produces H_2O_2 in low yield.

MOF-derived cobalt sulphides and phosphates have also been investigated as active materials for ORR.[220] In particular, Zhou *et al.*[221] reported an ORR electrocatalyst, $Co_3(PO_4)_2$C-N/rGOA, which was derived from a Co-based MOF with phosphonate-based ligand (N-(phosphonomethyl)proline). The cobalt phosphate nanoparticles embedded uniformly in a carbon sheet. The coordination of cobalt phosphate with nitrogen atoms from MOF ligands was found to enhance the ORR activity of the electrocatalyst. The $E_{1/2}$ of $Co_3(PO_4)_2$C-N/rGOA was slightly more negative than that of Pt/C, as revealed by LSV tests conducted in O_2-saturated 0.1 M KOH electrolyte. From the LSV data of 1600 rpm the electron transfer number was calculated using the K-L equation, and was found to be nearly 4.0 at 0.60-0.75 V. Further the various cobalt-based MOF-derived material towards ORR has been found on various published reports.[222–226]

Apart from cobalt, the atomically dispersed Fe sites are widely recognized as efficient electrocatalysts for the ORR. Studies have revealed that in both acid and alkaline electrolytes, the electrocatalytic activity of M-Nx-C catalysts based on transition metals follows the order of Fe > Co > Mn > Cu > Ni. Given its exceptional performance, Fe seems to be the most viable transition metal to substitute noble metal catalysts in the ORR. Favourable, ORR activity has also been observed in Fe-based metallic nanoparticles. [209,227–229] Also MOF-derived carbon-supported metallic iron, iron oxides, and iron carbides have been studied as potential ORR

electrocatalysts.[230,231] Chen *et al.* developed MOF-derived nitrogen-doped core-shell-structured porous Fe/Fe_3C@ C nanoboxes supported on graphene sheets and have found half-wave potential of 0.83 V and an electron transfer number of 3.08 at 0.7 V in O_2-saturated 0.1 M KOH electrolyte.[232] Gao *et al.* synthesized N-doped-carbon-coated Fe_3O_4 electrocatalyst by the carbonization of polyaniline (PANI) coated MIL-101-Fe MOF. The electrocatalyst exhibited a very positive ORR E_{onset} close to that of Pt/C, a quasi-4e reduction pathway and high long-term electrocatalytic stability in alkaline solution.[233] In the production of electrocatalysts for ORR activation, Fe-MOFs were also identified as components, alongside the Fe-Nx-C and N-doped Fe/Fe_3C@C/RGO materials.[234] Chen *et al.* utilized a successful host-guest chemistry technique to develop the FeSA-N/C electrocatalyst for ORR from MOFs.[235] In electrochemical evaluations, the 5% FeSA-N/C catalyst, featuring abundant five-coordinated N-Fe-N4 sites, demonstrated a current density of 5.12 mA cm^{-2} at 0.4 V *vs* RHE for the ORR, equivalent to that of the 30% Pt/C catalyst in 0.5 M H_2SO_4 media. To gain a deeper understanding of the correlation between Fe-N_x active sites and electrocatalytic performance, DFT calculations were conducted. These calculations indicated that specific N-Fe-N_4 sites with a coordination number of 5 act as the active centers, initiating the four-electron ORR pathway by reducing the reaction energy barrier in the rate-determining step for the FeSA-N/C. Li *et al.* employed a cage-encapsulated-MOF pyrolysis strategy to develop a highly stable Fe-based SAC.[236] The resulting FeSAs/NC catalyst comprised of isolated Fe single atoms anchored in N-doped carbon, which exhibited remarkable performance with a kinetic current density (J_k) of 37.85 mA cm^{-2} at 0.85 V and $E_{1/2}$ of 0.9 V (*vs* RHE) in 0.1 MKOH. This performance was 58 mV more positive than that of commercial Pt/C. Furthermore, the FeSAs/NC catalyst also demonstrated excellent methanol tolerance

and long-term stability. Specifically, there was a negligible change in current density in the presence of 1.0M methanol and only minimal degradation of the ORR polarization curve was observed after 5000 cycles. Similarly, Wang and Chen carried out edge-site engineering of Fe-N_4 atoms, which were dispersed atomically and embedded within micro-mesoporous carbon through the pyrolysis of iron phthalocyanine (FePc) encapsulated ZIF-8 precursor.[237] The resulting 3D hierarchically porous carbon material contains 0.2 wt% of Fe atoms and anchored by Fe-N_4 sites (FeSAs-N/C-20), demonstrated exceptional ORR performance with an $E_{1/2}$ value of 0.909 V (*vs* RHE) in 0.1 M KOH, surpassing that of commercial Pt/C ($E_{1/2}$ = 0.85 V) and other reported M-Nx-C catalysts, as illustrated in figure I.31.

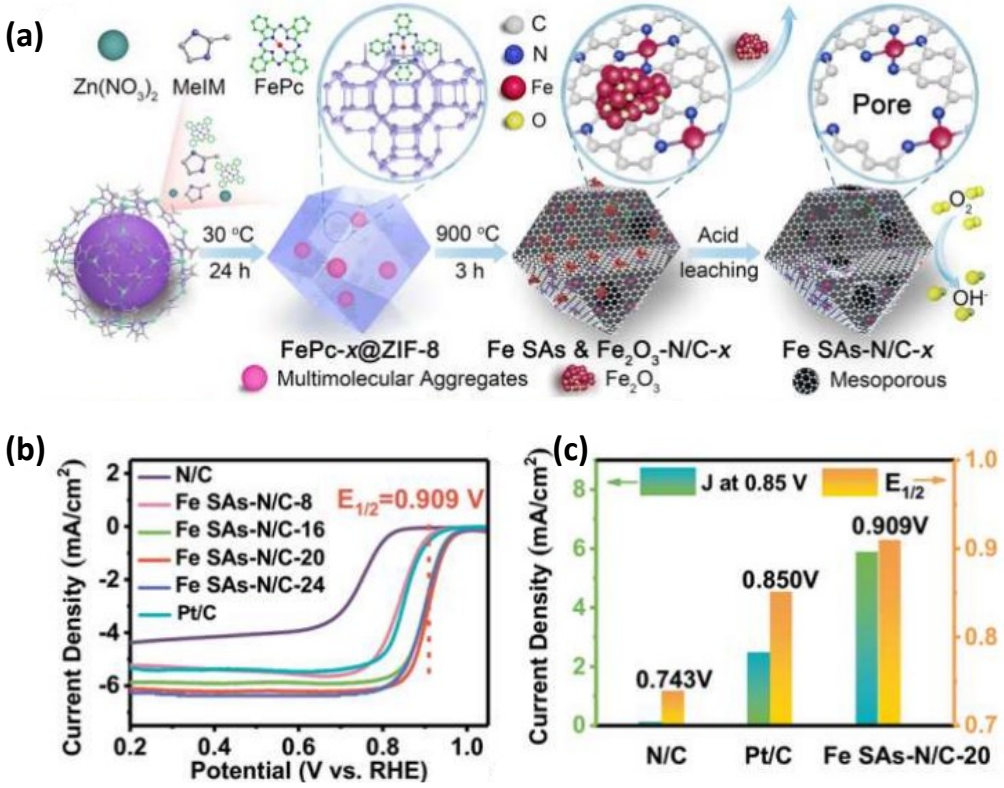

Figure I.31: (a) Schematic illustration of FeSAs-N/C-x synthesis; (b) LSV curves, (c) comparison of J and $E_{1/2}$, LSV curves before Reprinted with permission from ref.237 Copyright 2018, American Chemical Society.

Experimental and DFT calculations revealed that porosity engineering facilitated the selective cleavage of C-N bonds adjacent to Fe centers, generating edge-hosted Fe-N4 sites that decrease the overall ORR free energy change, thus enhancing the catalytic activity and long-term durability. It is widely accepted that doping heteroatoms into the carbon matrix skeleton can adjust the electronic features and electrical conductivity of SACs, and modifying the Fe-Nx active centers through doping extra elements is one approach to tuning the catalytic performance of SACs. Wang *et al.* have devised a technique that involves, which contains isolated Fe single atoms supported on a hollow carbon polyhedron that is doped with nitrogen, phosphorus, and sulfur (FeSAs/NPS-HC).[238] Thanks to its distinctive physical and electronic properties, the FeSAs/NPS-HC catalyst enhances the kinetics of the ORR and delivers superior performance, displaying a favourable half-wave potential of 0.912 V in O_2-sat 0.1M KOH, which is better than that of Pt/C (0.984 V vs RHE).

The J_k achieved by FeSAs/NPS-HC was 71.9 mA cm^{-2} at 0.85 V, which was 15 times higher than that of Pt/C (4.78 $mAcm^{-2}$), thus indicating the excellent catalytic activity of FeSAs/NPS-HC towards ORR. Fe-N-C and Co-N-C SACs show promising ORR activity. However, these catalysts still face challenges of limited durability in harsh acidic conditions and practical voltage ranges, which affects their long-term operation in energy conversion devices. This instability issue is partly caused by the H_2O_2 oxidative Fenton attack that induces instability and dissolution of active metal centers during the ORR process. DFT calculations indicate that Mn-based SACs with Mn-N4-C centers possess comparable electrocatalytic activity to Fe-N_4-C moieties. To this end, Wu *et al.* synthesized an atomically dispersed Mn_{SA}-N-C catalyst using ZIF-8 precursors *via* two-step doping and adsorption synthesis(Figure I.32a).[239] The Mn_{SA}-N-C catalyst showed $E_{1/2}$ of 0.80 V (*vs* RHE) for ORR in 0.1 M $HClO_4$, which was

comparable to Fe_{SA}-N-C and Co_{SA}-N-C SACs (Figure I.32b). The catalyst also demonstrated highly efficient four-electron ORR pathway with H_2O_2 yield less than 2.0% and has long-term stability (Figure I.32c). The Mn_{SA}-N-C catalyst was employed as cathode catalyst for PEMFC application and achieved a high open circuit voltage of 0.95 V in H_2-O_2 PEMFC, indicating its high intrinsic ORR activity. The Mn_{SA}-N-C-based PEMFC showed a maximum power density of 0.46 W cm^{-2} and generated the current density of 0.35 A cm^{-2} at 0.6 V, surpassing the reported performance of Fe-N-C catalysts. Copper based few MOF derived composites also have been reported for efficient ORR. In 2018, a straightforward and convenient method for synthesizing Cu- based CuSAs/N-C SACs (Cu with a weight percentage of 0.54%) on a large scale was reported by Wu and Li.[240] The method involves

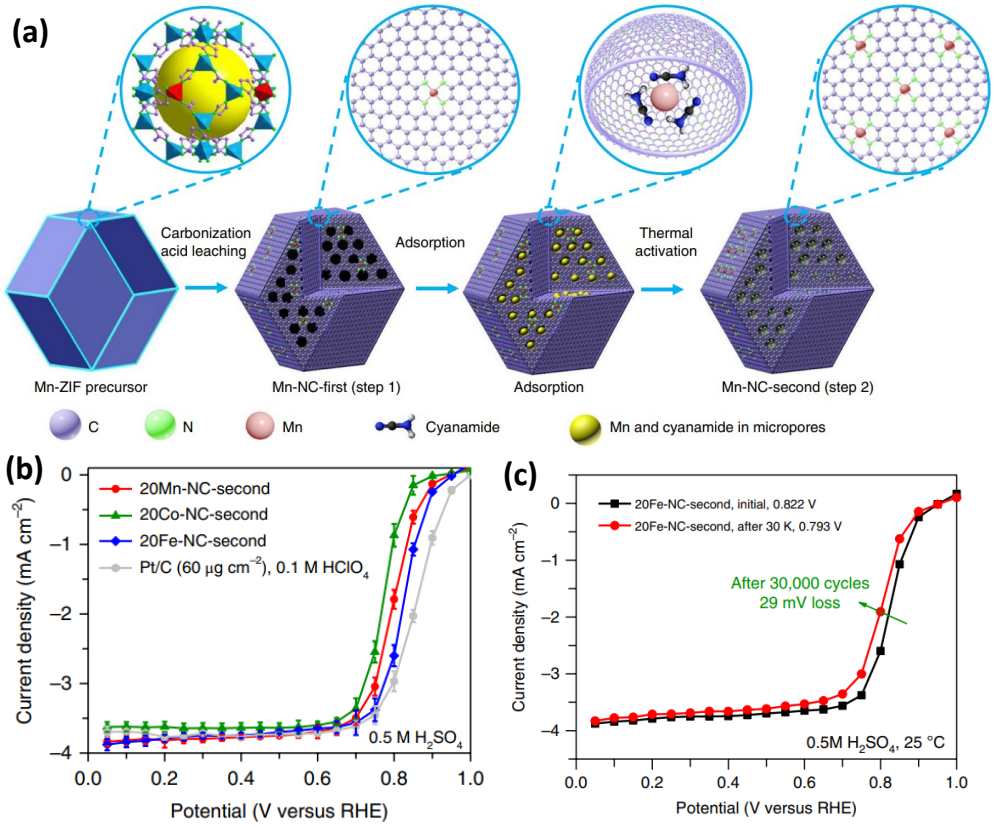

Figure I.32: (a) Schematic of atomically dispersed MnN_4 site catalyst synthesis. (b) ORR activity and (c) stability of MnN_4 site catalyst studied by using RRDE. Reprinted with permission from ref.239 Copyright 2018, Nature Publications.

synthesis of CuSAs/N-C by pyrolysis of ZIF-8 under an argon atmosphere in the presence of copper foam. Based on electrochemical activity, CuSAs/N-C showed superior ORR activity compared to Pt/C catalysts in 1.0 M KOH, for instance, the $E_{1/2}$ of CuSAs/N-C was 0.895 V (*vs* RHE), which is more positive than that of Pt/C (0.87 V) and CuNPs/N-C (0.77 V).

The nearly parallel K-L plot and RRDE results demonstrated that CuSAs/N-C has a four-electron pathway and high selectivity for the ORR. The excellent activity of the CuSAs/N-C catalyst was further confirmed by its advanced kinetic current density and a lower Tafel slope of 63 mV dec^{-1}. In a similar way, Lai *et al.* also produced N-doped carbon polyhedra containing both trapped Cu ions and Cu nanoparticles by subjecting Cu-doped ZIF-8 to pyrolysis.[241] When tested in an O_2-saturated 0.1 M KOH electrolyte, this electrocatalyst demonstrated a half-wave potential for ORR of 0.813 V *vs* RHE. Tang *et al.* reported Cu-MOF-derived Cu/Cu_2O nanoparticles and non-crystalline CuNxCy species on Ketjenblack carbon (KB).[242] The modified KB carbon demonstrated significantly improved catalytic activity towards the ORR, which was likely due to the synergistic effect of the two types of particles. In comparison to commercial 20 wt% Pt/C, this hybrid catalyst displayed similar half-wave potential (0.82 V *vs*, RHE), as well as superior limiting-current density and durability. Similarly, Kim *et al*. synthesized the Cu_xO-C/PANI composite through *in-situ* polymerization of aniline on multi-layered mesoporous Cu_xO-C obtained from Cu-MOF.[243] This integrated hybrid offers a promising pathway for electron transfer and enhances the kinetics of redox reactions. As a proficient catalyst for oxygen reduction, Cu_xO-C/PANI displays exceptional onset potential (0.94 V) and $E_{1/2}$ (0.76 V) when compared to the reversible hydrogen electrode, while also exhibiting good

stability. The summary of MOF-derived metal oxide towards electrocatalytic ORR has been given in Table I.1.

Table I.1: Summary of the MOF-derived metal oxide as electrocatalyst for ORR.

Sl. No	Catalyst	Electrolyte	Onset potential (V *vs* RHE)	$E_{1/2}$ (V *vs* RHE)	Ref
1.	MOF(Co)/C(3:1)-500	0.1 M KOH	0.92	0.82	244
2.	ZIF-67/CNs(1)-600	0.1 M KOH	0.93	0.85	245
3.	Co3O4@N/C	0.1 M KOH	0.90	0.80	214
4.	Cal-MOF-1/CC	0.1 M KOH	-	0.80	215
5.	Cal-MOF-2/CC	0.1 M KOH	-	0.82	215
6.	PtCo@C–Co_3O_4	1.0 M KOH	0.95	-	216
7.	ZIF-Co_3O_4/NCF	0.1 M KOH	-	0.81	217
8.	CoSAs/N-C	0.1 M KOH	0.98	0.88	210
9.	Co-N-C SAC	0.5 M H_2SO_4	0.93	0.80	218
10.	LDH@ZIF-67-800	0.1 M KOH	0.94	0.83	219
11.	$Co_3(PO_4)_2$C-N/rGOA	0.1 M KOH	0.962	0.837	221
12.	Fe/Fe_3C	0.1 M KOH	0.91	0.83	232
13.	FeSA-N/C	0.5 M H_2SO_4	0.861	0.735	235
14.	FeSAs-N/C-20	0.1 M KOH	-	0.909	237
15.	FeSAs/NPS-HC	0.1 M KOH	-	0.912	238
16.	CuSAs/N-C SACs	0.1 M KOH 0.1 M $HClO_4$	0.99 0.83	0.895 -	240
17.	Cu-doped ZIF-8	0.1 M KOH	0.914	0.813	241
18.	Cu/Cu_2O	0.1 M KOH	-	0.82	242
19.	Cu_xO-C/PANI	3.0 M KOH	0.94	0.76	243

I.5.2 MOF-derived metal composites for oxygen evolution reaction (OER):

Oxygen Evolution reaction (OER) is a chemical process that involves the electrochemical oxidation of water to generate oxygen gas, protons, and electrons. This process is a crucial component of several renewable energy technologies, such as water electrolysis and photoelectrochemical cells, that aim to produce hydrogen gas or other chemicals through the utilization of renewable energy sources. In an electrochemical cell, the OER occurs at the anode, which is typically composed of a transition metal oxide catalyst that facilitates the reaction. During the reaction, water molecules are oxidized, resulting in the generation of oxygen gas, which is released into the surrounding environment, and protons (H^+), which are released into the electrolyte solution. Meanwhile, electrons are transferred to the catalyst, where they participate in further chemical reactions to facilitate the overall process. The reactions involving OER in alkaline/ acidic solutions are as follows:

Alkaline conditions: $4OH^- \rightarrow O_2 + 2H_2O + 4e^-$

Acidic conditions: $2H_2O \rightarrow O_2 + 4H^+ + 4e^-$

The OER is a complex process that involves several steps, including the formation of reactive intermediates, the transfer of electrons and protons, and the formation and release of oxygen gas. These intermediate steps are often rate-limiting and require the use of efficient and stable catalysts to achieve high reaction rates and minimize the energy required for the process. The assessment criteria used for evaluating OER include various parameters such as onset potential, Tafel slope, and the over potential to achieve 10 mA cm^{-2} current density (E_{10}) at ambient temperature and 1 atm O_2. Since a 10% efficient solar water-splitting device under 1 sun illumination is expected

to generate a current density of 10 mA cm^{-2} at the anode, the E_{10} is used as a benchmark for evaluating OER activity.[246] Again, a lower Tafel slope indicates better OER kinetics. Research efforts have focused on the development of efficient and stable catalysts for the OER, such as iridium oxides, ruthenium oxides, etc.[247–249] However, their high cost, less stability, and less durability hinder their practical application. In this section, we will introduce MOF-derived metal composites that have been found efficient and favourable for OER.

Modifying single metal-based MOFs with heteroatoms such as B,[250] C,[251] N[87] O,[252] S,[253] P,[254,255] and Se,[256] are commonly used to enhance the catalysis efficiency of OER with MOFs-derived catalysts. The pyrolysis treatment of MOFs is a conventional strategy generally made in use to produce transition metal catalysts by subjecting them to different atmospheres. Calcination of MOFs in air yields MOFs-derived metal oxides, with the organic ligands being converted into carbonaceous gases.[90] In contrast, the pyrolysis process of the MOFs in inert gases such as Ar and N_2 results in the carbonization of organic ligands, and transition metal-based nanoparticles can be synthesized from metal nodes. Electrocatalysts generated from this method display numerous well-dispersed metal nanoparticles, encapsulated by graphitic and amorphous carbon or CNTs. The pyrolysis environment is highly customizable to modify MOFs-derived products. The precursors, such as PH_3, H_2S, and NH_3, or heat-induced degradable precursors of elements like solid S and metal Se can be utilized to produce metal phosphides, sulfides, nitrides, and selenide composites from MOFs. The addition of varied elements can increase the electrocatalytic activity of MOFs, which may have previously exhibited moderate performance, by altering the valence state of their electroactive metal sites.[22,88,200]

Cobalt oxides are considered good materials for producing high-performance OER electrocatalysts as they are easy to synthesize and can exhibit good stability.[257] However, cobalt oxides typically have insufficient catalytic ability, and therefore significant advancements are necessary to achieve high performance. To enhance their catalytic activity, researchers have synthesized various cobalt oxide hybrids. For instance, Liu *et al.*[258] synthesized a RuO_2/Co_3O_4 composite material with a well-ordered distribution of RuO_2 nanoparticles on linear Co_3O_4, which was derived from Co-BTC. This composite material showed high performance for OER catalysis when noble-metal was added, exhibiting an overpotential of 305 mV at a current density of 10 mA cm^{-2}. The study is noteworthy for its successful combination of noble-metal and cobalt oxide, demonstrating that cobalt oxide can function not only as an electrocatalyst but also as a supporting material. Zhou *et al.*[259] published a study where 1D, 2D and 3D MOFs of various metals (Ni, Co, and Cu) were used as templates to derive metal oxide embedded in carbon (MO_x/C, M = Co, Ni, and Cu) (Figure I.33a). The study revealed that MO_x/C composites derived from MOFs demonstrated high activity in electrocatalytic OER. Additionally, 2D MO_x/C arrays exhibited enhanced electrocatalytic activity and durability when compared to their corresponding 1D or 3D MOF-derived MO_x/C composites. Specifically, the 2D Co_3O_4/C_{BDC}, NiO/C_{BDC}, and Cu_2O/S-C_{TDC} composites demonstrated overpotentials of 208, 285, and 313 mV, respectively, at a current density of 10 mA cm^{-2}, surpassing the performance of previously reported TMO-based catalysts with similar compositions (Figure I.33b-d). This study is noteworthy for its successful integration of the advantageous structure and intrinsic properties of cobalt oxide, which synergistically served OER catalysis. However, the synthesis process is relatively complicated compared to other cobalt oxide materials.

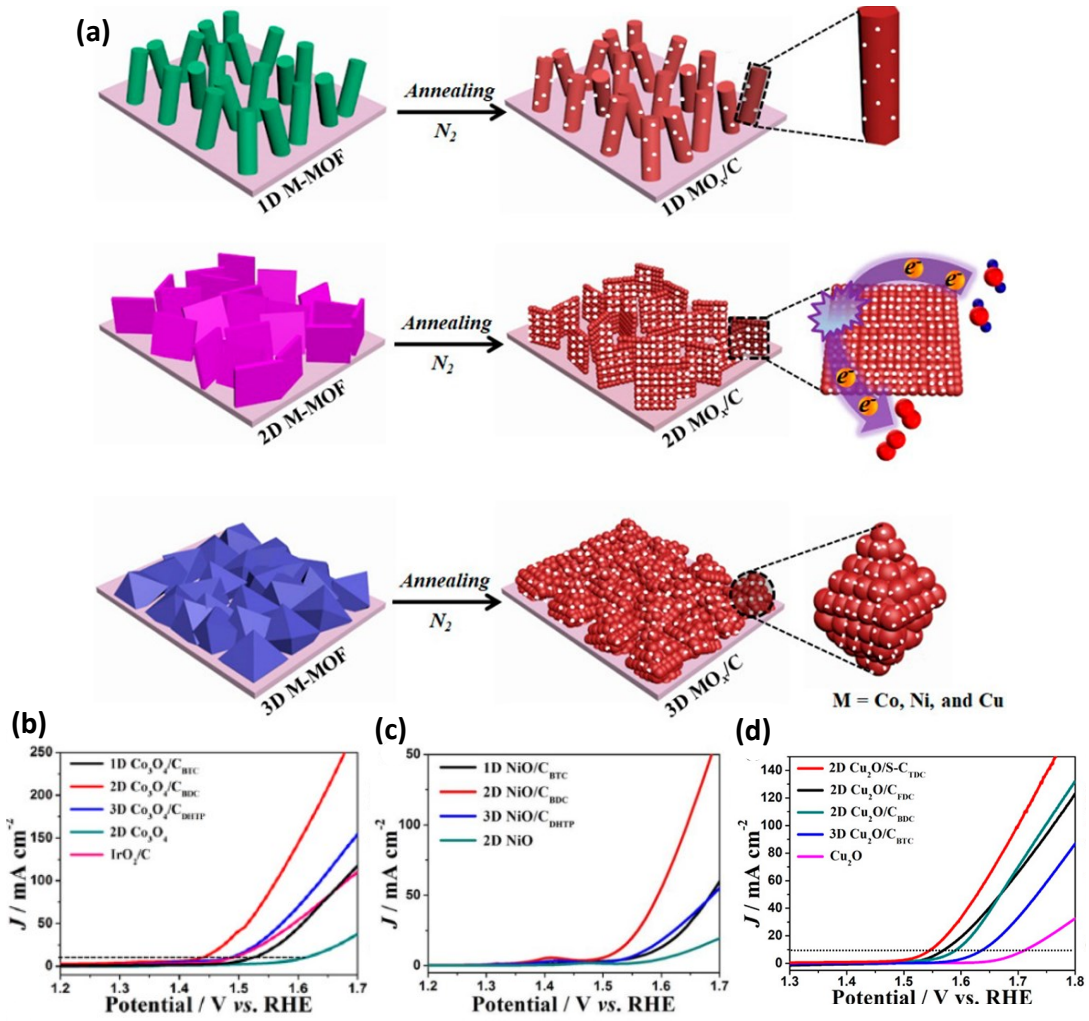

Figure I.33: Scheme for deriving MOx/C (M = Co, Ni, and Cu) from 1D, 2D, and 3D MOFs (b) OER LSV of different Co_3O_4/C derived composites (c) OER LSV of different NiO/C derived composites (d) OER LSV of different Cu_2O/C derived composites. Reprinted with permission from ref.259 Copyright 2018, Royal Society of Chemistry.

Gong *et al.*[260] developed a simple and straightforward approach for synthesizing porous Co_3O_4 composites (Co_3O_4-350 ℃) from MOF precursor, which showed promising performance for OER catalysis. The Co_3O_4-350 ℃ composite was obtained by calcining the MOF-derived Co complex. This study is notable for its attempt to produce a high-performance OER catalyst using a very simplified synthetic route. The Co_3O_4-350 ℃ composite demonstrated an overpotential of 420 mV at a current density of 10 mA cm^{-2} and a Tafel slope of 55 mV dec^{-1}. 4rCoO-Co_3O_4/NC

composite, combined with carbon black, demonstrated excellent electrocatalytic performance, achieving an overpotential of 400 mV at a current density of 10 mA cm^{-2} and a Tafel slope of 59 mV dec^{-1}. Additionally, the calculated mass activity of Co-CoO-Co_3O_4/NC was 204.17 A g^{-1}cat, which is higher than the benchmark IrO_2 at 135.23 A g^{-1}cat, indicating a good turnover frequency. This study is noteworthy for its attempt to reduce the preparation steps, which could potentially lower the development cost and facilitate practical uses. Zheng *et al.*[261] synthesized a hybrid material of cobalt oxides by *in situ* growing Co_3O_4 nanocubes on a Co-based metal-organic framework (Co_3O_4@Co-MOF) surface for electrochemical OER. The well-distributed elements of carbon, oxygen, and cobalt were observed in the hybrid material through energy-dispersive X-ray spectrometry (EDS) mapping. The electrochemical measurements of the Co_3O_4@Co-MOF hybrid material showed remarkable performance, requiring an overpotential of 277 mV, a Tafel slope of 79 mV dec^{-1}, and maintaining electrochemical performance over 2000 cycles without severe degradation. This study is significant for its approach in combining cobalt oxides and a metal-organic framework to create a hybrid material with enhanced OER performance.

Cobalt phosphides have recently gained recognition as one of the most promising materials for OER electrocatalysts. This is due to their exceptional properties such as high conductivity, optimized crystallinity, and excellent chemical stability, which make them ideal candidates for replacing noble metals in the production of electrocatalysts. Consequently, there is ongoing research focused on investigating MOF-derived cobalt phosphides as a viable alternative. Huang *et al.*[262] synthesized a mesoporous ultrathin nanosheet of C- and N-doped Co-based phosphate, denoted as Co-Pi-900, from a phosphonate-based MOF precursor. This was achieved by

subjecting the 2D-layered structure of the Co-based phosphate MOF to pyrolysis. Co-Pi-900 exhibited exceptional OER activity, with a low overpotential of 291 mV, a Tafel slope of 57 mV/dec in a 1.0 M KOH electrolyte, and sustained performance for 2000 cycles with negligible degradation. Despite the potential of cobalt phosphides as efficient OER catalysts, the challenging preparation process involving the use of phosphine (PH_3) remains a hindrance. Cobalt sulfides[263] also has gained significant interest as promising materials for the development of efficient and stable electrocatalysts for the OER.[264,265] They are known to exhibit excellent electrochemical performance and stability, making them attractive candidates for OER electrocatalysis. Recently, Li *et al.*[266] have developed a highly efficient electrocatalyst for the OER called P-anion decorated cobalt disulphide (P-CoS_2 HNA/CC). This electrocatalyst exhibits superior catalytic activity, owing to its optimized electronic structure, vast exposure of active sites, and 3D hollow conductive structure. P-CoS_2 HNA/CC requires a low overpotential of only 250 mV to achieve a current density of 10 mA cm^{-2} for OER. Overall, cobalt composites have shown promising performance for OER electrocatalysis and are known for their relatively simple preparation steps. Not only in OER, Co-based composites have also been applied in designing bifunctional catalysts for ORR & OER process.[244,245,267–271]

Apart from cobalt, Cu-based materials can also serve as catalysts for OER, however, there are only on Cu-based OER electrocatalysts are rare. Nevertheless, some investigations have indicated that through post-treatments and modifications, Cu-based materials can be employed as OER catalysts. The creation of copper oxides and phosphides may result in efficient and beneficial Cu-based OER catalysts. For instance, Wang *et al.*[272] investigated the use of graphene-wrapped MOF-derived CuO nanoflowers (CuO NF@G/CF) produced through normal pulse-voltage-assisted

synthesis and chemical vapor deposition, resulting in high-quality CuONP@G/CF requiring only a small overpotential of 320 mV to reach a current density of 10 $mAcm^{-2}$ and gave a low Tafel slope of 63.1 $mVdec^{-1}$ (Figure I.34a). Similarly, Wu *et al.*[273] synthesized an ultrathin CuO-decorated Cu-C hybrid (Cu@CuO-C) from $[Cu_2(OH)(BTC)(H_2O)]\bullet 2H_2O$ MOF *via* pyrolysis for OER electrocatalysis. The synthesis involves growing Cu-MOF nanorod arrays (ZnO as template) on a conductive carbon fibre cloth (CFC), which on pyrolysis and oxidation treatment resulted in core–shell Cu@CuO nanoparticle- embedded carbon nanorods. The Cu@CuO-C was found to exhibit excellent OER catalysis, with an overpotential of 340 mV at a current density of 10 mA cm^{-2}(Figure I.34b).

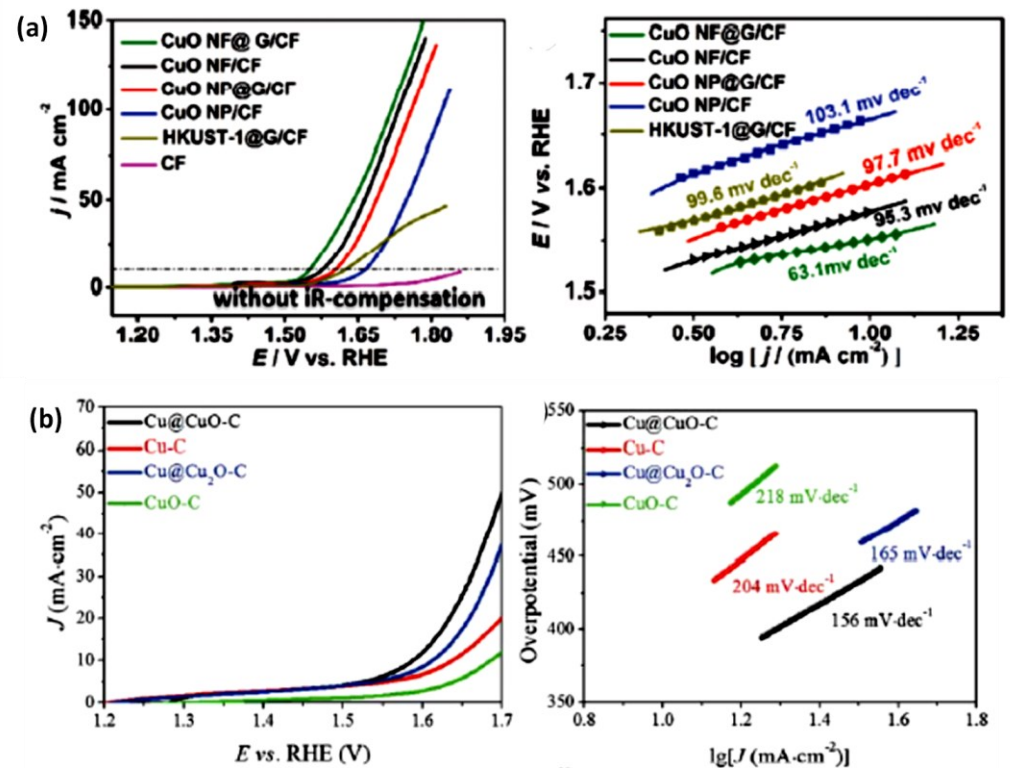

Figure I.34: OER activity of (a) CuO NF@G/CF. Reprinted with permission from ref. [272] Copyright 2020, Royal Society of Chemistry and (b) Cu@CuO-C. Reprinted with permission from ref.274 Copyright 2018, Royal Society of Chemistry.

These results indicate that both the ultrathin CuO layer and the nanorod morphology are essential for enhancing the electrocatalytic activity. This method provides a way to use low-cost and environmentally friendly Cu-based materials for energy conversion. Cu-based MOFs such as MOF-199,[275] Cu(II)- TDPAT,[276] have also been reported to derive OER active Cu-based composite with noticeable activity. Similarly, Cu-BDC was reported to form a copper phosphides catalyst that is active towards OER.[277,278]

Next, the fabrication process of Ni-based OER electrocatalysts shares many similarities with that of Co-based electrocatalysts, as evidenced by numerous reports and case studies. Nickel oxides have emerged as highly effective OER catalysts due to their straightforward production process. As a result, many nickel oxide-based OER catalysts are either produced in composite form or subjected to substantial modifications in terms of their intrinsic properties and shape. Luo *et al.*[279] reported the synthesis of efficient OER electrocatalysts in the form of Ni@NiO/N-C nanowires with a core-shell structure of Ni-based MOF. This was achieved through a combination of pyrolysis and oxidation processes. The resulting electrocatalysts demonstrated excellent stability and negligible reduction of activity, as evidenced by an overpotential of 390 mV and a Tafel slope of 100 mV dec^{-1}. In addition, Song *et al.*[280] synthesized an efficient OER catalyst in the form of core-shell-structured CNH@PDA@NiMOF (CNHs=carbon nanohorns and PDA=polydopamine) (Figure I.35a). The resulting CNH-PDA-NiMOF catalyst demonstrated impressive OER performance, with current densities of 20 and 100 mA cm^{-2} achieved at overpotentials of 270 and 340 mV, respectively. He *et al.*[281] also developed an electrochemical OER catalyst by synthesizing defect-rich NiO within ultrathin MOF nanosheets (Figure I.35b).The resulting 2D Ni-MOF-250 catalyst displayed excellent OER performance,

with an overpotential of only 250 mV at a current density of 50 mA cm^{-2} in 1.0 M KOH (Figure I.34c).

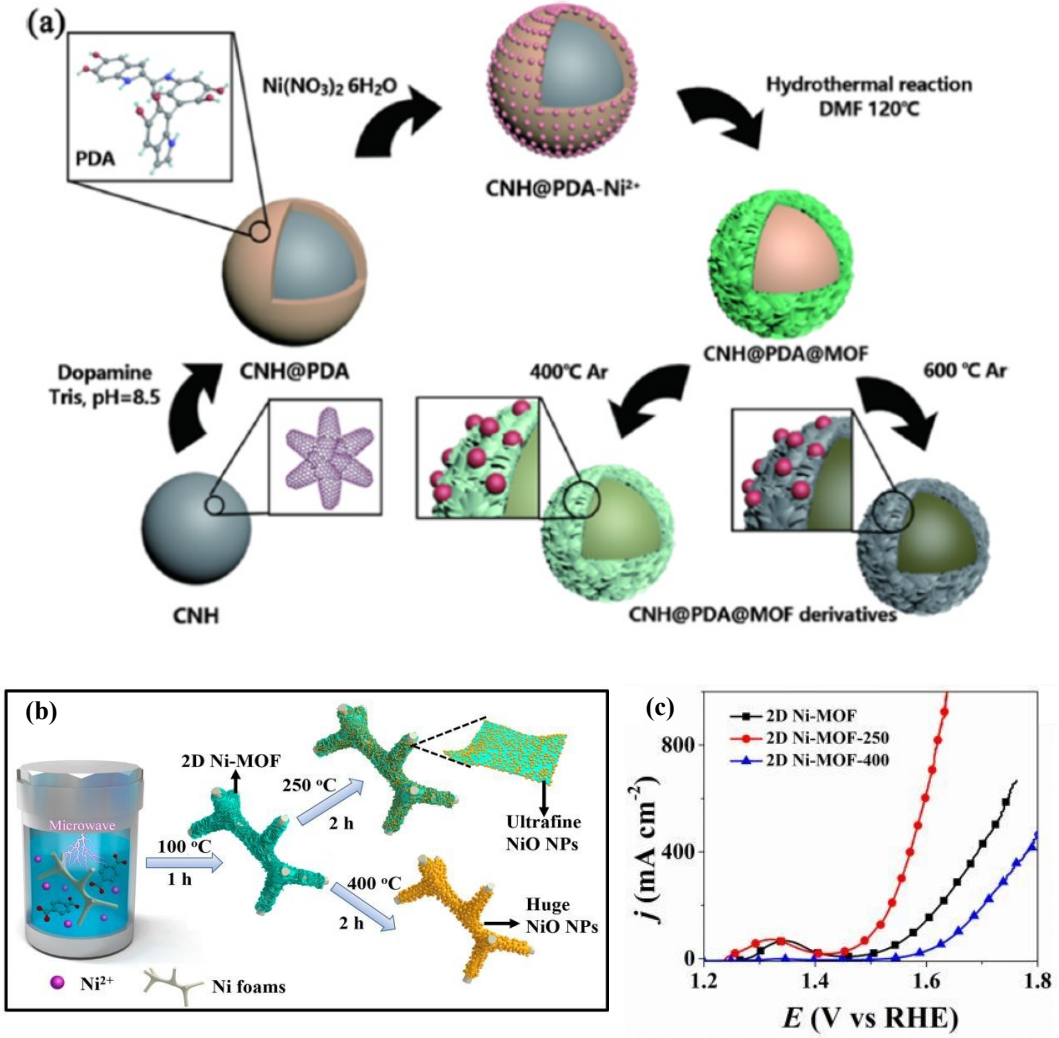

Figure I.35: (a) Scheme for the synthesis of CNH−D−Ni-MOF and its Derivatives Reprinted with permission from ref [280] Copyright 2020, American Chemical Society. (b) Schematic illustration for in-situ growth of ultrathin 2D Ni-MOF nanosheet arrays on the Ni foams and (c) Catalytic activity of derived Ni-composites towards OER. Reprinted with permission from ref.281 Copyright 2020, Royal Society of Chemistry.

Ma *et al.*[282] reported on the development of a new OER electrocatalyst, Ni_9S_8@graphite from Ni(NDC)MOF (NDC= naphthalene-dicarboxylate) and sulphur powder, which has a unique structure and simpler preparation process (Figure I.36a).

This catalyst consists of well-distributed NiS on graphite, and exhibited impressive electrochemical performance, with an overpotential of only 278 mV needed to reach 10 mA cm^{-2} and a Tafel slope of 87 mV dec^{-1}. In addition, the electrochemical examination revealed that Ni_9S_8@graphite has an excellent capability as a rechargeable lithium battery anode material. Wan *et al.*[89] took a different approach to increase the surface area of nickel sulfides for efficient OER catalysis by developing hierarchical porous Ni_3S_4 (NM50-Ni_3S_4) with high-valence Ni sites (Figure I.36b). The meso-macro hierarchical porous structure of NM50-Ni_3S_4 with Ni^{3+} enriched design exhibited excellent electrocatalytic activity for OER, achieving a low overpotential of 257 mV at 10 mA cm^{-2} and 300 mV at 50 mA cm^{-2}, respectively. This work is noteworthy the enhanced surface area leads to improved electrocatalytic characteristics. The various MOF-derived metal oxide electrocatalyst for OER have been summarized in table I.2.

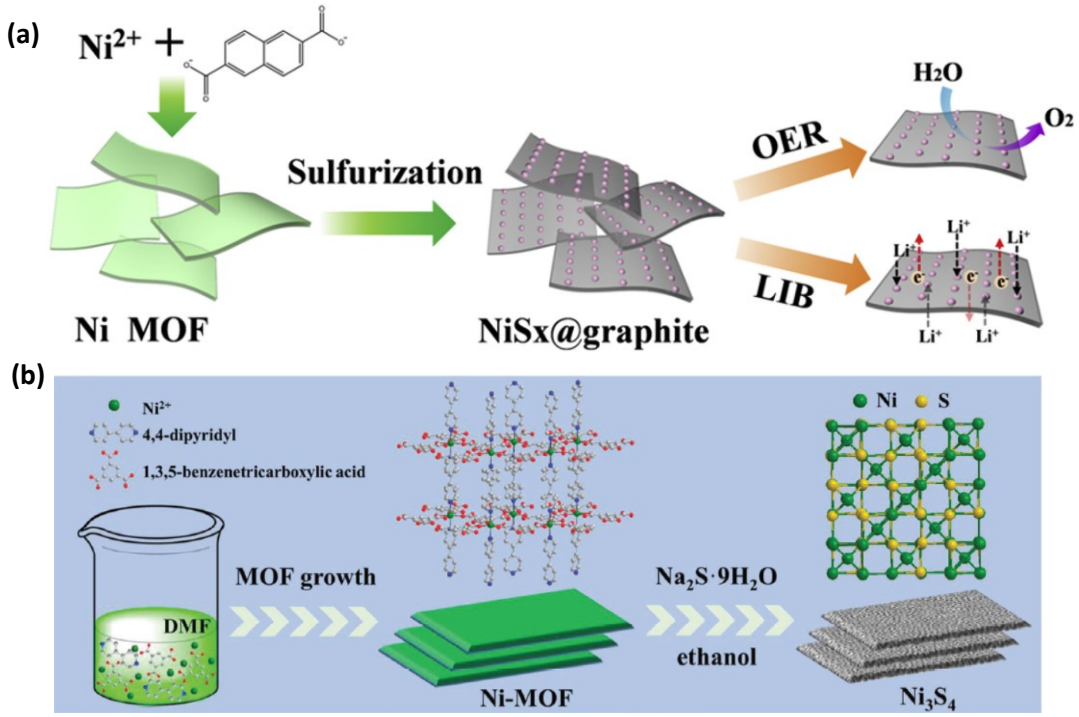

Figure I.36: Synthetic procedure of (a) Ni_9S_8@graphite, reproduced with permission from ref. [282] Copyright 2019, Elsevier and (b) Ni_3S_4. Reprinted with permission from ref. 89 Copyright 2019, Wiley.

Table I.2: Summary of the MOF-derived metal oxide as electrocatalyst for OER.

Sl No	Catalyst	Electrolyte	Overpotential (mV) at 10 mA cm^{-2}	Tafel ($mV\ dec^{-1}$)	Ref.
1.	RuO_2/Co_3O_4	1.0 M KOH	305	69	258
2.	Co_3O_4/C_{BDC}	1.0 M KOH	208	50.1	259
3.	NiO/C_{BDC}	1.0 M KOH	285	61.9	259
4.	$Cu_2O/S\text{-}C_{TDC}$	1.0 M KOH	313	65.6	259
5.	Co_3O_4-350 °C	1.0 M KOH	420	55	260
6.	MOF(Co)/C(3:1)-500	0.1 M KOH	400	59	244
7.	Co_3O_4@Co-MOF	0.1 M KOH	277	79	261
8.	Co-Pi-900	1.0 M KOH	291	57	262
9.	P-CoS_2 HNA/CC	1.0 M KOH	250	90	266
10	ZIF-67/CNs(1)-600 (Co-Co_3O_4)	0.1 M KOH	350	94.3	245
11.	Ni@NiO/N-C	1.0 M KOH	390	100	279
12.	CNH@PDA@NiMOF	1.0 M KOH	270	85.3	280
13.	Ni_9S_8@graphite	1.0 M NaOH	278	87	282
14.	NM50-Ni_3S_4	1.0 M KOH	257	67	89
15.	CuO NF@G/CF	1.0 M KOH	320	63.1	272
16.	Cu@CuO-C	1.0 M KOH	340	156	273
17.	CuO/CN C_3N_4/ Ni-f	0.5 M KOH	310	59.4	276
18.	Cu_3P@C-120	1.0 M KOH	300	24	277
19.	$(Cu_3(PO_4)_2$/Cu-BDC-150-6 foam	1.0 M KOH	241	76	278

I.6. Origin of the problem:

The challenges related to limited energy resources, sustainable environment, and health are of utmost importance and require aggressive catalytic solutions. Several homogeneous and heterogeneous catalyst have been advancing towards development of new catalytic system for renewable energy conversion, drug design, sustainable reactions, fine chemicals etc. However, owing to high stability, reusability, easy separation, recyclability and reproducibility, heterogeneous catalysts are more preferred over homogeneous catalyst. As the surface of the catalyst plays key role in heterogeneous catalysis, the amount of catalytic surface (*i.e.* surface area) becomes a critical in defining the number and availability of catalytic sites. Furthermore, accessibility of catalytic sites increases its ability to approach, bind and reacts with substrate and holds a key for better performance of the catalytic sites/surfaces. Overall, the main aspect in heterogeneous catalysis is to maximize the surface-to-volume ratio of the catalyst in order to increase the catalytic performance. In that regard MOF have been establishing as an efficient heterogeneous catalyst with its unique properties such as, high surface area, accessible pores, well defined catalytic sites, high crystallinity, simple preparation methods, multiple design possibilities etc.

Since its initial reports, MOFs have been extensively explored in the field of gas separation and storage purposes. Recently, researchers are reconnoitring the catalytic activity of MOFs and the research field is increasing exponentially. As shown in figure I.37 where almost every MOFs reported in recent publication have been applied towards catalysis. Also, from the perspective of the global market, MOFs can be a profitable future material, and companies such as Strem Chemicals, novoMOF AG, ProfMOF, MOFWORX, etc have already been established that dedicatedly produces MOFs for various applications. However, most of the global market is

concentrated to use MOF for gas storage/separation applications. Nevertheless, with well-exposed catalytic sites, accessible pores, and large surface area, the infinite possibility of deliberate design MOF have been established as an efficient heterogeneous catalyst. Only a small part (<10%) of MOF application towards catalysis is considered to contribute to the future global market. This is because of the limited industrial application of MOF as a heterogeneous catalyst. All of these data indicate the requirement of rigorous research to establish MOFs as an efficient material for heterogeneous catalysis. The progress in MOFs catalytic system brings us closer to the practical implementation of using them as solid catalysts in various industrial applications.

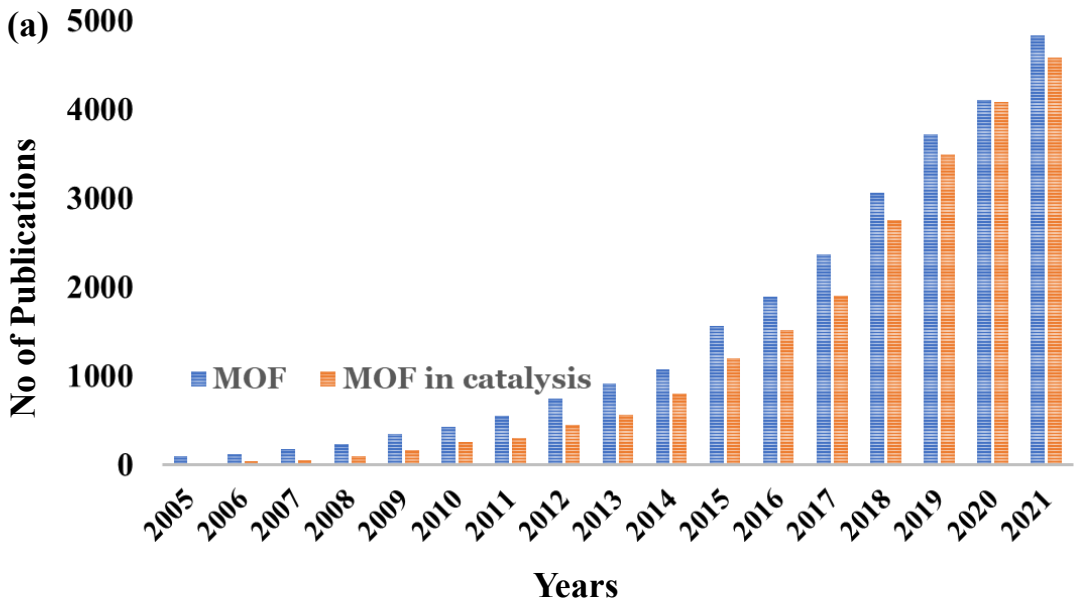

Figure I.37: Histogram of research publication for MOFs and MOFs in catalysis. Derived cumulatively from Sci-finder and web of science.

The advancement of C–C and C–heteroatom (C–N, C–O, C–S, and C–P) bond formation has garnered significant interest in the field of catalysis. These bonds play a crucial role in the construction of foundational organic molecules with enhanced value and diverse functionalities through the incorporation of heteroatoms.

Furthermore, the utmost consumption of non-renewable source has provoked the global energy crisis, focused on future unavailability and greenhouse gas emission. A practice to use sustainable and renewable feedstocks as an energy source can benignly deliver future energy demands where advancement on electrocatalytic oxygen process plays vital role. The noble metal catalyst such as Pt, Pd, Ir, Ru are still the state-of the art catalyst for coupling reactions and electrocatalytic oxygen process. However, this noble metal catalyst has an undeniable limitation such as, less abundant, high cost, toxicity, corrosive nature, low stability, etc. Therefore, despite the tremendous progress made so far developing an affordable cost-effective and sustainable catalyst for these reactions is an urgent task.

I.7. Scopes and objectives of this thesis:

Owing to the above-discussed challenges, the aims and objectives purposed for the thesis are as follows:

i. 1-D, 2-D, and 3-D MOFs would be synthesized using transition metals and polytopic ligands. Various reported MOFs would also be synthesized. Special emphasis would be made on designing MOFs containing co-ordinately unsaturated sites that can be applied towards various catalytic processes without an activation process.

ii. The synthesized materials would be structurally and physically characterized using a conventional spectroscopic and analytic tool such as SCXRD, PXRD, BET surface area analyzer, FT-IR, TGA, EPR, TEM, SEM, EDX, and elemental analysis.

iii. Heterogeneous catalytic properties of MOFs would be explored with an aim to develop efficient catalytic methods for the formation of new C-X (X= O, N, S, etc.) bonds.

iv. Post-synthetic modification of MOFs would be done to produce porous composites and their electrochemical studies would be performed.

v. The post-synthetically derived composites will be modified as electrodes to develop an efficient electrocatalytic system for ORR (oxygen reduction reaction) and OER (oxygen evolution reaction) process.

vi. The plausible catalytic pathway for the catalytic processes would be proposed with support from experimental, computational, and literature studies.

I.8 References:

(1) (a) Wisniak, J. The History of Catalysis. From the Beginning to Nobel Prizes. *Educ. Quim.* **2010**, *21*, 60–69. (b) J. J. Berzelius, *Jahres-Bericht,* 1835, **14**, 237.

(2) (a) Humphreys, J.; Lan, R.; Tao, S. Development and Recent Progress on Ammonia Synthesis Catalysts for Haber–Bosch Process. *Adv. Energy Sustain. Res.* **2021**, *2*, 2000043. (b) J. Hagen, in Industrial Catalysis: A Practical Approach, Third Edit., Chapter 17 Economic Importance of Catalysts, **2015**, 459–462.

(3) Smith, C.; Hill, A. K.; Torrente-Murciano, L. Current and Future Role of Haber-Bosch Ammonia in a Carbon-Free Energy Landscape. *Energy Environ. Sci.* **2020**, *13*, 331–344.

(4) Perkins, J. H. Geopolitics and the Green Revolution: Wheat, Genes, and the Cold War. Oxford University Press January 22, **1998**.

(5) Höök, M.; Fantazzini, D.; Angelantoni, A.; Snowden, S. Hydrocarbon Liquefaction : Viability as a Peak Oil Mitigation Strategy. *Phil.Trans.R.Soc.A* **2014**, *372*, 20120319.

(6) Hagen, J. *Chapter 17, Industrial Catalysis: A Practical Approach*, Third Edit.; 2015.

(7) Hutchings, G. J. Promotion in Heterogeneous Catalysis: A Topic Requiring a New Approach? *Catal. Letters* **2001**, *75*, 1–12.

(8) Rodriguez-reinoso, F. The Role of Carbon Materials in Heterogeneous Catalysis. *Carbon N. Y.* **1998**, *36*, 159–175.

(9) Jacques, C. V. Ø. Metal Oxides in Heterogeneous Oxidation Catalysis : State of the Art and Challenges for a More Sustainable World. *ChemCatChem* **2019**, *12*, 577–588.

(10) Tian, Y.; Zhu, G. Porous Aromatic Frameworks (PAFs). *Chem. Rev.* **2020**, *16*, 8934–8986.

(11) Sun, L. B.; Liu, X. Q.; Zhou, H. C. Design and Fabrication of Mesoporous Heterogeneous Basic Catalysts. *Chem. Soc. Rev.* **2015**, *44*, 5092–5147.

(12) Jiang, Y. N.; Li, D. C.; Yang, Y.; Zhan, Z. P. Porous Organic Polymers as Heterogeneous Ligands for Highly Selective Hydroacylation. *Org. Chem. Front.* **2019**, *6*, 2964–2967.

(13) Zhang, Z.; Shen, X.; Li, Z.; Ma, S.; Xia, H.; Liu, X. Multifunctional Chiral Cationic Porous Organic Polymers: Gas Uptake and Heterogeneous Asymmetric Organocatalysis. *Polym. Chem.* **2021**, *12*, 3367–3374.

(14) Chen, L. H.; Sun, M. H.; Wang, Z.; Yang, W.; Xie, Z.; Su, B. L. Hierarchically Structured Zeolites: From Design to Application. *Chem. Rev.* **2020**, *120*, 11194–11294.

(15) Liang, J.; Liang, Z.; Zou, R.; Zhao, Y. Heterogeneous Catalysis in Zeolites,

Mesoporous Silica, and Metal–Organic Frameworks. *Adv. Mater.* **2017**, *29*, 1701139.

(16) Kim, D.; Liu, X.; Lah, M. S. Topology Analysis of Metal-Organic Frameworks Based on Metal-Organic Polyhedra as Secondary or Tertiary Building Units. *Inorg. Chem. Front.* **2015**, *2*, 336–360.

(17) Baumann, A. E. .; Burns, D. A. .; Bingqian, L. .; Thoi, V. S. Metal-Organic Framework Functionalization and Design Strategies for Advanced Electrochemical Energy Storage Devices. *Commun Chem* **2019**, *2*, 1–14.

(18) Hönicke, A. I.; Senkovska, I.; Bon, V.; Baburin, I.; Boenisch, N.; Raschke, S.; Evans, J. D.; Kaskel, S. Balancing Mechanical Stability and Ultrahigh Porosity in Crystalline Framework Materials. *Angew. Chemie Int. Ed. English* **2018**, *57*, 13780.

(19) Farha, O. K.; Eryazici, I.; Jeong, N. C.; Hauser, B. G.; Wilmer, C. E.; Sarjeant, A. A.; Snurr, R. Q.; Nguyen, S. T.; Yazaydin, A. Ö.; Hupp, J. T. Metal-Organic Framework Materials with Ultrahigh Surface Areas: Is the Sky the Limit? *J. Am. Chem. Soc.* **2012**, *134*, 15016–15021.

(20) Eryazici, I.; Malliakas, C. D.; Hauser, B. G.; Farha, O. K.; Kanatzidis, M. G.; Nguyen, S. T.; Snurr, R. Q.; Hupp, J. T. De Novo Synthesis of a Metal–Organic Framework Material Featuring Ultrahigh Surface Area and Gas Storage Capacities. *Nat. Chem.* **2010**, *2*, 944–948.

(21) Li, G.; Zhao, S.; Zhang, Y.; Tang, Z. Metal–Organic Frameworks Encapsulating Active Nanoparticles as Emerging Composites for Catalysis: Recent Progress and Perspectives. *Adv. Mater.* **2018**, *30*, 1–43.

(22) Lu, X. F.; Fang, Y.; Luan, D.; Lou, X. W. D. Metal−organic Frameworks Derived Functional Materials for Electrochemical Energy Storage and Conversion: A Mini Review. *Nano Lett.* **2021**, *21*, 1555–1565.

(23) Xiao, W.; Cheng, M.; Liu, Y.; Wang, J.; Zhang, G.; Wei, Z.; Li, L.; Du, L.; Wang, G.; Liu, H. Functional Metal/Carbon Composites Derived from Metal-Organic Frameworks: Insight into Structures, Properties, Performances, and Mechanisms. *ACS Catal.* **2023**, *13*, 1759–1790.

(24) Li, H.; Davis, C. E.; Groy, T. L.; Yaghi, O. M. Coordinatively Unsaturated Metal Centers in the Extended Porous Framework of $Zn_3(BDC)_3$,$6CH_3OH$. *J. Am. Chem. Soc.* **1998**, *120*, 2186–2187.

(25) Li, H.; Eddaoudi, M.; O'Keeffe; Yaghi, O. M. Design and Synthesis of an Exceptionally Stable and Highly. *Nature* **1999**, *402*, 276–279.

(26) S.S.Y. Chui; S.M.F. Lo; J.P.H. Charmant; A.G. Orpen; I.D. Williams. A Chemically Functionalizable Nanoporous Material $[Cu_3(TMA)_2(H_2O)_3]_n$. *Science,* **1999**, *283*, 1148-1150.

(27) Kinoshita, Y.; Matsubara, I.; Higuchi, T.; Saito, Y. The Crystal Structure of Bis(Adiponitrilo)Copper(I) Nitrate. *Bull. Chem. Soc. Jpn.* **1959**, *32*, 1221–1226.

(28) Scott, E. S.; Audrieth, L. F. Inorganic Polymerization Reactions. *J. Chem. Educ.* **1954**, *31*, 168–175.

(29) Tomic, E. A. Thermal Stability of Coordination Polymers. *J. Appl. Polym. Sci.* **1965**, *9*, 3745–3752.

(30) Hoskins, B. F.; Robson, R. Design and Construction of a New Class of Scaffolding-like Materials Comprising Infinite Polymeric Frameworks of 3D-Linked Molecular Rods. A Reappraisal of the $Zn(CN)_2$ and $Cd(CN)_2$ Structures and the Synthesis and Structure of the Diamond-Related Framework. *J. Am. Chem. Soc.* **1990**, *112*, 1546–1554.

(31) Batten, S. R.; Hoskins, B. F.; Robson, R. Two Interpenetrating 3D Networks Which Generate Spacious Sealed-Off Compartments Enclosing of the Order of 20 Solvent Molecules in the Structures of $Zn(CN)(NO_3)(Tpt)_{2/3}$ •solv (Tpt = 2,4,6-Tri(4-Pyridyl)-1,3,5-Triazine, Solv = $\sim^3/_4 C_2H_2Cl_4$•$^3/_4 CH_3OH$ or $\sim^3/_2 CH$. *J. Am. Chem. Soc.* **1995**, *117*, 5385–5386.

(32) Yaghi, O.M.; Li. H. Hydrothermal Synthesis of a Metal-Organic Framework Containing Large Rectangular Channels. *J. Am. Chem. Soc.* **1995**, *117*, 10401–10402.

(33) Li, H.; Li, L.; Lin, R. B.; Zhou, W.; Zhang, Z.; Xiang, S.; Chen, B. Porous Metal-Organic Frameworks for Gas Storage and Separation: Status and Challenges. *EnergyChem* **2019**, *1*, 100006.

(34) Qian, Q.; Asinger, P. A.; Lee, M. J.; Han, G.; Mizrahi Rodriguez, K.; Lin, S.; Benedetti, F. M.; Wu, A. X.; Chi, W. S.; Smith, Z. P. MOF-Based Membranes for Gas Separations. *Chem. Rev.* **2020**, *120*, 8161–8266.

(35) Bavykina, A.; Kolobov, N.; Khan, I. S.; Bau, J. A.; Ramirez, A.; Gascon, J. Metal-Organic Frameworks in Heterogeneous Catalysis : Recent Progress, New Trends, and Future Perspectives. *Chem. Rev* **2019**, *120*, 8468–8535.

(36) Wang, Q.; Gao, Q.; Al-enizi, A. M.; Nafady, A.; Ma, S. Recent Advances in MOF-Based Photocatalysis : Environmental Remediation under Visible Light. *Inorg. Chem. Front.* **2020**, *7*, 300–339.

(37) Yuan, H.; Li, N.; Fan, W.; Cai, H.; Zhao, D. Metal-Organic Framework Based Gas Sensors. *Adv. Sci.* **2022**, *2104374*, 1–27.

(38) Yusuf, V. F.; Malek, N. I.; Kailasa, S. K. Review on Metal-Organic Framework Classification, Synthetic Approaches, and Influencing Factors : Applications in Energy, Drug Delivery, and Wastewater Treatment. *ACS Omega* **2022**, *7*, 44507–44531.

(39) Sohrabi, H.; Ghasemzadeh, S.; Shakib, S.; Majidi, M. R.; Razmjou, A.; Yoon, Y.; Khataee, A. Metal − Organic Framework-Based Biosensing Platforms for the Sensitive Determination of Trace Elements and Heavy Metals : A Comprehensive Review. *Ind. Engineering Chem. Res.* **2023**, *62*, 4611–4627.

(40) Zheng, Y.; Sun, F.; Han, X.; Xu, J.; Bu, X. Recent Progress in 2D Metal-Organic Frameworks for Optical Applications. *Advanced Opt. Mater.* **2020**, *2000110*, 1–17.

(41) Ma, N.; Horike, S. Metal − Organic Network-Forming Glasses. *Chem. Rev.* **2022**, *122*, 4163–4203.

(42) Mageto, T.; Souza, F. M. De; Kaur, J.; Kumar, A.; Gupta, R. K. Chemistry and Potential Candidature of Metal-Organic Frameworks for Electrochemical Energy Storage Devices. *Fuel Process. Technol.* **2023**, *242*, 107659.

(43) Rasheed, T.; Tuoqeer, M. Metal–Organic Frameworks as Self-Sacrificing Modalities for Potential Environmental Catalysis and Energy Applications : Challenges and Perspectives. *Coord. Chem. Rev.* **2023**, *480*, 215011.

(44) Li, S.-L.; Xu, Q. Metal–Organic Frameworks as Platforms for Clean Energy. *Energy Environ. Sci.* **2013**, *6*, 1656–1683.

(45) Steinert, D. M.; Ernst, S.; Henninger, S. K.; Janiak, C. MOFs for Heat Transformation Metal-Organic Frameworks as Sorption Materials for Heat Transformation Processes. *Eur. J. Inorg. Chem.* **2020**, *2020*, 4502–4515.

(46) Sharma, D.; Rasaily, S.; Pradhan, S.; Baruah, K.; Tamang, S.; Pariyar, A. HKUST-1 Metal–Organic Framework as an Efficient Dual-Function Catalyst: Aziridination and One-Pot Ring-Opening Transformation for Formation of β-Aryl Sulfonamides with C–C, C–N, C–S, and C–O Bonds. *Inorg. Chem.* **2021**, *60*, 7794–7802.

(47) Chen, B.; Ockwig, N. W.; Millward, A. R.; Contreras, D. S.; Yaghi, O. M. High H_2 Adsorption in a Microporous Metal–Organic Framework with Open Metal Sites. *Angew. Chemie - Int. Ed.* **2005**, *44*, 4745–4749.

(48) Espín, J.; Luis, G.-T.; Nchez, A. C.-S.́; Imaz, I.; Maspoch, D. Photothermal Activation of Metal–Organic Frameworks Using a UV−Vis Light Source. *ACS Appl. Mater. Interfaces* **2018**, *10*, 9555–9562.

(49) Muldoon, P. F.; Liu, C.; Miller, C. C.; Koby, S. B.; Gamble Jarvi, A.; Luo, T. Y.; Saxena, S.; O'Keeffe, M.; Rosi, N. L. Programmable Topology in New Families of Heterobimetallic Metal-Organic Frameworks. *J. Am. Chem. Soc.* **2018**, *140*, 6194–6198.

(50) Morales-Vidal, J.; García-Muelas, R.; Ortuño, M. A. Defects as Catalytic Sites for the Oxygen Evolution Reaction in Earth-Abundant MOF-74 Revealed by DFT. *Catal. Sci. Technol.* **2021**, *11*, 1443–1450.

(51) Wang, J.; Liu, L.; Chen, C.; Dong, X.; Wang, Q.; Alfilfil, L.; Alalouni, M. R.; Yao, K.; Huang, J.; Zhang, D.; Han, Y. Engineering Effective Structural Defects of Metal-Organic Frameworks to Enhance Their Catalytic Performances. *J. Mater. Chem. A* **2020**, *8*, 4464–4472.

(52) Dissegna, S.; Epp, K.; Heinz, W. R.; Kieslich, G.; Fischer, R. A. Defective Metal-Organic Frameworks. *Adv. Mater.* **2018**, *30*, 1704501.

(53) Fan, Z.; Wang, Z.; Cokoja, M.; Fischer, R. A. Defect Engineering: An Effective Tool for Enhancing the Catalytic Performance of Copper-MOFs for the Click Reaction and the A3 Coupling. *Catal. Sci. Technol.* **2021**, *11*, 2396–2402.

(54) Baek, J.; Rungtaweevoranit, B.; Pei, X.; Park, M.; Fakra, S. C.; Liu, Y. S.; Matheu, R.; Alshmimri, S. A.; Alshehri, S.; Trickett, C. A.; Somorjai, G. A.; Yaghi, O. M. Bioinspired Metal-Organic Framework Catalysts for Selective Methane Oxidation to Methanol. *J. Am. Chem. Soc.* **2018**, *140*, 18208–18216.

(55) Cao, C. C.; Chen, C. X.; Wei, Z. W.; Qiu, Q. F.; Zhu, N. X.; Xiong, Y. Y.; Jiang, J. J.; Wang, D.; Su, C. Y. Catalysis through Dynamic Spacer Installation of Multivariate Functionalities in Metal-Organic Frameworks. *J. Am. Chem. Soc.* **2019**, *141*, 2589–2593.

(56) Zhou, T. Y.; Auer, B.; Lee, S. J.; Telfer, S. G. Catalysts Confined in Programmed Framework Pores Enable New Transformations and Tune Reaction Efficiency and Selectivity. *J. Am. Chem. Soc.* **2019**, *141*, 1577–1582.

(57) Banerjee, A.; Upadhyay, K. K.; Puthusseri, D.; Aravindan, V.; Madhavi, S.; Ogale, S. MOF-Derived Crumpled-Sheet-Assembled Perforated Carbon Cuboids as Highly Effective Cathode Active Materials for Ultra-High Energy Density Li-Ion Hybrid Electrochemical Capacitors (Li-HECs). *Nanoscale* **2014**, *6*, 4387–4394.

(58) Liu, B.; Shioyama, H.; Akita, T.; Xu, Q. Metal-Organic Framework as a Template for Porous Carbon Synthesis. *J. Am. Chem. Soc* **2008**, *130*, 5390–5391.

(59) Salunkhe, R. R.; Kaneti, Y. V.; Yamauchi, Y. Metal-Organic Framework-Derived Nanoporous Metal Oxides toward Supercapacitor Applications: Progress and Prospects. *ACS Nano* **2017**, *11*, 5293–5308.

(60) Xia, W.; Mahmood, A.; Zou, R.; Xu, Q. Metal-Organic Frameworks and Their Derived Nanostructures for Electrochemical Energy Storage and Conversion. *Energy Environ. Sci.* **2015**, *8*, 1837–1866.

(61) Qiu, T.; Liang, Z.; Guo, W.; Tabassum, H.; Gao, S.; Zou, R. Metal–Organic Framework-Based Materials for Energy Conversion and Storage. *ACS Energy Lett.* **2020**, *5*, 520–532.

(62) Li, D.; Liu, T.; Yan, Z.; Zhen, L.; Liu, J.; Wu, J.; Feng, Y. MOF-Derived Cu_2O/Cu Nanospheres Anchored in Nitrogen-Doped Hollow Porous Carbon Framework for Increasing the Selectivity and Activity of Electrochemical CO2-to-Formate Conversion. *ACS Appl. Mater. Interfaces* **2020**, *12*, 7030–7037.

(63) Rashti, A.; Lu, X.; Dobson, A.; Hassani, E.; Feyzbar-Khalkhali-Nejad, F.; He, K.; Oh, T. S. Tuning MOF-Derived Co_3O_4/$NiCo_2O_4$Nanostructures for High-Performance Energy Storage. *ACS Appl. Energy Mater.* **2021**, *4*, 1537–1547.

(64) Luo, S.; Li, X.; Zhang, B.; Luo, Z.; Luo, M. MOF-Derived Co_3O_4@NC with Core-Shell Structures for N_2 Electrochemical Reduction under Ambient Conditions. *ACS Appl. Mater. Interfaces* **2019**, *11*, 26891–26897.

(65) Lu, J. Y.; Yuan, Y. R.; Hu, X.; Liu, W. J.; Li, C. X.; Liu, H. Q.; Li, W. W. MOF-Derived Fe2O3/Nitrogen/Carbon Composite as a Stable Heterogeneous Electro-Fenton Catalyst. *Ind. Eng. Chem. Res.* **2020**, *59*, 1800–1808.

(66) Zhang, Z.; Xiao, Y.; Lei, Y.; Tang, J.; Qiao, X. Catalytic Hydrolysis of β-Lactam Antibiotics *via* MOF-Derived MgO Nanoparticles Embedded on Nanocast Silica. *Sci. Total Environ.* **2020**, *738*, 139742.

(67) Kang, H.; Shin, J.; Kim, T. H.; Lee, Y.; Lee, D.; Lee, J.; Kim, G.; Cho, E. A. Metal-Organic Framework-Derived Magnesium Oxide@Carbon Interlayer for

Stable Lithium-Sulfur Batteries. *ACS Sustain. Chem. Eng.* **2023**, *11*, 1344–1354.

(68) Qiao, Y.; Li, N.; Dong, M.; Jia, P.; Ma, C.; Zhang, T.; Jiao, T. MOF-Derived MnO/C Nanocomposites for High-Performance Supercapacitors. *Nanomaterials* **2022**, *12*, 1–11.

(69) Mao, M.; Wu, X.; Hu, Y.; Yuan, Q.; He, Y. B.; Kang, F. Charge Storage Mechanism of MOF-Derived Mn_2O_3 as High Performance Cathode of Aqueous Zinc-Ion Batteries. *J. Energy Chem.* **2020**, *52*, 277–283.

(70) Meng, X. X.; Li, J. Y.; Yang, B. L.; Li, Z. X. MOF-Derived NiO Nanoparticles Prilled by Controllable Explosion of Perchlorate Ion: Excellent Performances and Practical Applications in Supercapacitors. *Appl. Surf. Sci.* **2020**, *507*, 145077.

(71) Alf, M.; Gargiulo, V.; Amati, M.; Maraloiu, V.; Maddalena, P.; Lettieri, S. Photoluminescence-Based Optical Sensing of Oxygen. *Catalysts* **2021**, *11*, 795.

(72) Shi, L.; Benetti, D.; Li, F.; Wei, Q.; Rosei, F. Phase-Junction Design of MOF-Derived TiO2 Photoanodes Sensitized with Quantum Dots for Efficient Hydrogen Generation. *Appl. Catal. B Environ.* **2020**, *263*, 118317.

(73) Kimitsuka, Y.; Hosono, E.; Ueno, S.; Zhou, H.; Fujihara, S. Fabrication of Porous Cubic Architecture of ZnO Using Zn-Terephthalate MOFs with Characteristic Microstructures. *Inorg. Chem.* **2013**, *52*, 14028–14033.

(74) Hu, C.; Hu, X.; Li, R.; Xing, Y. MOF Derived ZnO/C Nanocomposite with Enhanced Adsorption Capacity and Photocatalytic Performance under Sunlight. *J. Hazard. Mater.* **2020**, *385*, 121599.

(75) Ahmed Malik, W. M.; Afaq, S.; Mahmood, A.; Niu, L.; Yousaf ur Rehman, M.; Ibrahim, M.; Mohyuddin, A.; Qureshi, A. M.; Ashiq, M. N.; Chughtai, A. H. A Facile Synthesis of CeO_2 from the GO@Ce-MOF Precursor and Its Efficient Performance in the Oxygen Evolution Reaction. *Front. Chem.* **2022**, *10*, 1–17.

(76) More, G. S.; Srivastava, R. Efficient Activation of CO_2 over Ce-MOF-Derived CeO_2 for the Synthesis of Cyclic Urea, Urethane, and Carbamate. *Ind. Eng. Chem. Res.* **2021**, *60*, 12492–12504.

(77) Guo, H.; Li, T.; Chen, W.; Liu, L.; Yang, X.; Wang, Y.; Guo, Y. General Design of Hollow Porous $CoFe_2O_4$ Nanocubes from Metal-Organic Frameworks with Extraordinary Lithium Storage. *Nanoscale* **2014**, *6*, 15168–15174.

(78) Zheng, F.; Zhu, D.; Shi, X.; Chen, Q. Metal-Organic Framework-Derived Porous Mn1.8Fe1.2O4 Nanocubes with an Interconnected Channel Structure as High-Performance Anodes for Lithium Ion Batteries. *J. Mater. Chem. A* **2015**, *3*, 2815–2824.

(79) Yang, J.; Ye, H.; Zhang, Z.; Zhao, F.; Zeng, B. Metal–Organic Framework Derived Hollow Polyhedron $CuCo_2O_4$ Functionalized Porous Graphene for Sensitive Glucose Sensing. *Sensors Actuators, B Chem.* **2017**, *242*, 728–735.

(80) Wu, R.; Qian, X.; Zhou, K.; Wei, J.; Lou, J.; Ajayan, P. M. Porous Spinel $Zn_xCo_{3-x}O_4$ Hollow Polyhedra Templated for High-Rate Lithium-Ion Batteries. *ACS Nano* **2014**, *8*, 6297–6303.

(81) Zhao, J.; Wang, F.; Su, P.; Li, M.; Chen, J.; Yang, Q.; Li, C. Spinel $ZnMn_2O_4$ Nanoplate Assemblies Fabricated via "Escape-by-Crafty-Scheme" Strategy. *J. Mater. Chem.* **2012**, *22*, 13328–13333.

(82) Chen, S.; Xue, M.; Li, Y.; Pan, Y.; Zhu, L.; Zhang, D.; Fang, Q.; Qiu, S. Porous ZnCo2O4 Nanoparticles Derived from a New Mixed-Metal Organic Framework for Supercapacitors. *Inorg. Chem. Front.* **2015**, *2*, 177–183.

(83) Ye, Z.; Jiang, Y.; Li, L.; Wu, F.; Chen, R. *Rational Design of MOF-Based Materials for Next-Generation Rechargeable Batteries*; **2021**; Vol. 13.

(84) He, X.; Jin, Y.; Jia, M.; Jia, M.; Wang, H.; Imran, M. MOF-Derived Carbon Coated Cu_3P with Ni Doping as Advanced Supercapacitor Electrode Materials. *Sustain. Energy Fuels* **2022**, *6*, 5360–5370.

(85) Konnerth, H.; Matsagar, B. M.; Chen, S. S.; Prechtl, M. H. G.; Shieh, F. K.; Wu, K. C. W. Metal-Organic Framework (MOF)-Derived Catalysts for Fine Chemical Production. *Coord. Chem. Rev.* **2020**, *416*, 213319.

(86) Tran, V. A.; Do, H. H.; Le, V. T.; Vasseghian, Y.; Vo, V.; Ahn, S. H.; Kim, S. Y.; Lee, S. W. Metal-Organic-Framework-Derived Metals and Metal Compounds as Electrocatalysts for Oxygen Evolution Reaction: A Review. *Int. J. Hydrogen Energy* **2022**, *47*, 19590–19608.

(87) Xia, B. Y.; Yan, Y.; Li, N.; Wu, H. Bin; Lou, X. W. D.; Wang, X. A Metal-Organic Framework-Derived Bifunctional Oxygen Electrocatalyst. *Nat. Energy* **2016**, *1*, 1–8.

(88) Kundu, A.; Kuila, T.; Murmu, N. C.; Samanta, P.; Das, S. Metal-Organic Framework-Derived Advanced Oxygen Electrocatalysts as Air-Cathodes for Zn-Air Batteries: Recent Trends and Future Perspectives. *Mater. Horizons* **2023**, *10*, 745–787.

(89) Wan, K.; Luo, J.; Zhou, C.; Zhang, T.; Arbiol, J.; Lu, X.; Mao, B.; Zhang, X.; Fransaer, J. Hierarchical Porous Ni_3S_4 with Enriched High-Valence Ni Sites as a Robust Electrocatalyst for Efficient Oxygen Evolution Reaction. *Adv. Funct. Mater.* **2019**, *29*, 1900315.

(90) Hu, L.; Li, W.; Wang, L.; Wang, B. Turning Metal-Organic Frameworks into Efficient Single-Atom Catalysts via Pyrolysis with a Focus on Oxygen Reduction Reaction Catalysts. *EnergyChem* **2021**, *3*, 100056.

(91) Dhakshinamoorthy, A.; Alvaro, M.; Garcia, H. Claisen–Schmidt Condensation Catalyzed by Metal-Organic Framework. *Adv. Synth. Catal.* **2010**, *352*, 711–717.

(92) Saha, D.; Maity, T.; Koner, S. Alkaline Earth Metal-Based Metal–Organic Framework: Hydrothermal Synthesis, X-Ray Structure and Heterogeneously Catalyzed Claisen–Schmidt Reaction. *Dalt. Trans*. **2014**, *43*, 13006–13017.

(93) Abednatanzi, S.; Gohari Derakhshandeh, P.; Depauw, H.; Coudert, F. X.; Vrielinck, H.; Van Der Voort, P.; Leus, K. Mixed-Metal Metal-Organic

Frameworks. *Chem. Soc. Rev*. **2019**, *48*, 2535–2565.

(94) Hu, M. L.; Safarifard, V.; Doustkhah, E.; Rostamnia, S.; Morsali, A.; Nouruzi, N.; Beheshti, S.; Akhbari, K. Taking Organic Reactions over Metal-Organic Frameworks as Heterogeneous Catalysis. *Microporous Mesoporous Mater*. **2018**, *256*, 111–127.

(95) Pariyar, A.; Asl, H. Y.; Choudhury, A. Tetragonal versus Hexagonal: Structure-Dependent Catalytic Activity of Co/Zn Bimetallic Metal−Organic Frameworks. *Inorg. Chem*. **2016**, *55*, 9250–9257.

(96) Julião, D.; Barbosa, A. D. S.; Peixoto, A. F.; Freire, C.; Castro, B. De; Balula, S. S.; Cunha-silva, L. Improved Catalytic Performance of Porous Metal–Organic Frameworks for the Ring Opening of Styrene Oxide. *CrystEngComm* **2017**, *19*, 4219–4226.

(97) Wang, Z.; Chen, G.; Ding, K. Self-Supported Catalysts. *Chem. Rev.* **2009**, *109*, 322–359.

(98) Jiang, W.; Yang, J.; Liu, Y. Y.; Song, S. Y.; Ma, J. F. A Porphyrin-Based Porous rtl Metal–Organic Framework as an Efficient Catalyst for the Cycloaddition of CO_2 to Epoxides. Chem.-A Eur. J. **2016,** 22, 16991–16997.

(99) Fujita, M.; Washizu, S.; Ogura, K.; Kwon, Y. J. Preparation, Clathration Ability, and Catalysis of a Two-Dimensional Square Network Material Composed of Cadmium(II) and 4, 4′-Bipyridine. *J. Am. Chem. Soc.* **1994**, *116*, 1151–1152.

(100) Ladrak, T.; Smulders, S.; Roubeau, O., Teat, S. J.; Gamez, P.; Reedijk, J. Manganese-Based Metal – Organic Frameworks as Heterogeneous Catalysts for the Cyanosilylation of Acetaldehyde. *Eur. J. Inorg. Chem*. **2010**, 3804–3812.

(101) Wang, J.; Zhang, J.; Peh, S. B.; Zhai, L.; Ying, Y.; Liu, G.; Cheng, Y.; Zhao, D. Dimensional Impact of Metal-Organic Frameworks in Catalyzing Photoinduced Hydrogen Evolution and Cyanosilylation Reactions. *ACS Appl. Energy Mater*. **2019***, 2*, 298–304.

(102) Zhu, C; Xia, Q; Chen, X; Liu, Y; Du, X; Cui, Y. Chiral Metal−Organic Framework as a Platform for Cooperative Catalysis in Asymmetric Cyanosilylation of Aldehydes. *ACS Catal.* **2016**, *6*, 7590–7596.

(103) Horike, S.; Dinca, M.; Tamaki, K.; Long, J. R. Size-Selective Lewis Acid Catalysis in a Microporous Metal-Organic Framework with Exposed Mn^{2+} Coordination Sites. *J. Am. Chem. Soc*. **2008**, *130*, 18, 5854–5855

(104) Dhakshinamoorthy, A.; Alvaro, M.; Garcia, H. Metal–Organic Framework as Solid Acid Catalysts for Acetalization of Aldehydes with Methanol. *Adv. Synth. Catal*. **2010**, *352*, 3022–3030.

(105) Liu, M.; Wu, J.; Hou, H. Metal–Organic Framework (MOF)-Based Materials as Heterogeneous Catalysts for C−H Bond Activation. *Chem.-A Eur. J*. **2019**, *25*, 2935–2948.

(106) Xu, F.; Kang, W.-F.; Wang, X.-N.; Kou, H.-D.; Jin, Z.; Liu, C.-S. Synergic Effect of Copper-Based Metal–Organic Frameworks for Highly Efficient C–H

Activation of Amidines. *RSC Adv.* **2017**, *7*, 51658–51662.

(107) Phan, A.; Yaghi, O. Metal-Organic Frameworks as Catalysts for the Conversion of Methane to Acetic Acid. *Inorg. Chem.* **2011**, *50,* 16, 7388–7390.

(108) Karmakar, A.; Guedes Da Silva, M. F. C.; Pombeiro, A. J. L. Zinc Metal-Organic Frameworks: Efficient Catalysts for the Diastereoselective Henry Reaction and Transesterification. *Dalt. Trans.* **2014**, *43*, 7795–7810.

(109) Fan, Y.; Yanwei, R.; L. J; Yue, C.; Jiang, H. Enhanced Activity and Enantioselectivity of Henry Reaction by the Postsynthetic Reduction Modification for a Chiral Cu(Salen)-Based Metal-Organic Framework. *Inorg. Chem*. **2018**, *57*, 11986–11994.

(110) Long, W.; Qiu, W.; Guo, C.; Li, C.; Song, L.; Bai, G.; Zhang, G.; He, H.; Kuznetsov, M. L. A Copper-Based Metal-Organic Framework as an Efficient and Reusable Heterogeneous Catalyst for Ullmann and Goldberg Type C-N Coupling Reactions. *Molecules* **2015**, *20*, 21178–21192.

(111) Truong, T.; Nguyen, C. V.; Truong, N. T.; Phan, N. T. S. Ligand-Free N-Arylation of Heterocycles Using Metal-Organic Framework [Cu(INA)$_2$] as an Efficient Heterogeneous Catalyst. *RSC Adv.* **2015**, *5*, 107547–107556.

(112) Li, Z.; Meng, F.; Zhang, J.; Xie, J.; Dai, B. Efficient and Recyclable Copper-Based MOF-Catalyzed N-Arylation of N-Containing Heterocycles with Aryliodides. *Org. Biomol. Chem.* **2016**, *14*, 10861–10865.

(113) Ma, P.; Meng, F.; Wang, N.; Zhang, J.; Xie, J.; Dai, B. Heterogeneous Amorphous Cu–MOF-74 Catalyst for C-N Coupling Reaction. *ChemistrySelect* **2018**, *3*, 10694–10700.

(114) Liu, C.; Cui, J.; Wang, Y.; Zhang, M. A Novel Two-Dimensional Metal-Organic Framework as a Recyclable Heterogeneous Catalyst for the Dehydrogenative Oxidation of Alcohol and TheN-Arylation of Azole Compounds. *RSC Adv.* **2021**, *11*, 11739–11744.

(115) Maity, T.; Saha, D.; Koner, S. Aromatic N-Arylations Catalyzed by Copper-Anchored Porous Zinc-Based Metal–Organic Framework under Heterogeneous Conditions. *ChemCatChem* **2014**, *6*, 2373–2383.

(116) Rouzifar, M.; Sobhani, S.; Farrokhi, A.; Sansano, J. M. Fe-MIL-101 Modified by Isatin-Schiff-Base-Co: A Heterogeneous Catalyst for C-C, C-O, C-N, and C-P Cross-Coupling Reactions. *New J. Chem.* **2021**, *45*, 19963–19976.

(117) Rabiei, K.; Mohammadkhani, Z.; Keypour, H.; Kouhdareh, J. Palladium Schiff Base Complex-Modified Cu(BDC-NH$_2$) Metal–Organic Frameworks for C–N Coupling. *RSC Adv.* **2023**, *13*, 8114–8129.

(118) Veisi, H.; Neyestani, N.; Pirhayati, M.; Ahany Kamangar, S.; Lotfi, S.; Tamoradi, T.; Karmakar, B. Copper Nanoparticle Anchored Biguanidine-Modified Zr-UiO-66 MOFs: A Competent Heterogeneous and Reusable Nanocatalyst in Buchwald-Hartwig and Ullmann Type Coupling Reactions. *RSC Adv.* **2021**, *11*, 22278–22286.

(119) Lee, S. W.; Dao, P. D. Q.; Lim, H. J.; Cho, C. S. Synthesis of Imidazo[1,2-

f]Phenanthridines by Recyclable Magnetic MOF-Catalyzed Coupling and Cyclization of 2-(2-Bromoaryl)Imidazoles with Cyclohexane-1,3-Diones Followed by Aromatization. *ACS Omega* **2022**, *7*, 18486–18497.

(120) Esrafili, L.; Morsali, A.; Dehghani Firuzabadi, F.; Retailleau, P. Development of Porous Cobalt-/Copper-Doped Carbon Nanohybrids Derived from Functionalized MOFs as Efficient Catalysts for the Ullmann Cross-Coupling Reaction: Insights into the Active Centers. *ACS Appl. Mater. Interfaces* **2020**, *12*, 43115–43124.

(121) Kar, A. K.; Srivastava, R. Selective Synthesis of Cu-Cu_2O/C and CuO-Cu_2O/C Catalysts for Pd-Free C-C, C-N Coupling and Oxidation Reactions. *Inorg. Chem. Front.* **2019**, *6*, 576–589.

(122) Lam, P. Y. S.; Clark, C. G.; Saubern, S.; Adams, J.; Winters, M. P.; Chan, D. M. T.; Combs, A. New Aryl/Heteroaryl C-N Bond Cross-Coupling Reactions via Arylboronic Acid/Cupric Acetate Arylation. *Tetrahedron Lett.* **1998**, *39*, 2941–2944.

(123) Evans, D. A.; Katz, J. L.; West, T. R. Synthesis of Diaryl Ethers through the Copper-Promoted Arylation of Phenols with Arylboronic Acids. An Expedient Synthesis of Thyroxine. *Tetrahedron Lett.* **1998**, *39*, 2937–2940.

(124) Chan, D. M. T.; Monaco, K. L.; Wang, R. P.; Winters, M. P. New N- and O-Arylations with Phenylboronic Acids and Cupric Acetate. *Tetrahedron Lett.* **1998**, *39*, 2933–2936.

(125) Chen, J. Q.; Li, J. H.; Dong, Z. B. A Review on the Latest Progress of Chan-Lam Coupling Reaction. *Adv. Synth. Catal.* **2020**, *362*, 3311–3331.

(126) Wang, B.; Yang, P.; Ge, Z. W.; Li, C. P. A Porous Metal-Organic Framework as Active Catalyst for Multiple C-N/C-C Bond Formation Reactions. *Inorg. Chem. Commun.* **2015**, *61*, 13–15.

(127) Li, Z. H.; Xue, L. P.; Wang, L.; Zhang, S. T.; Zhao, B. T. Two-Dimensional Copper-Based Metal-Organic Framework as a Robust Heterogeneous Catalyst for the N-Arylation of Imidazole with Arylboronic Acids. *Inorg. Chem. Commun.* **2013**, *27*, 119–121.

(128) Khosravi, A.; Mokhtari, J.; Naimi-jamal, M. R.; Tahmasebi, S.; Panahi, L. $Cu_2(BDC)_2(BPY)$–MOF: An Efficient and Reusable Heterogeneous Catalyst for the Aerobic Chan–Lam Coupling Prepared via Ball-Milling Strategy. *RSC Adv.* **2017**, *7*, 46022–46027.

(129) Leo, P.; Martínez, F.; Calleja, G.; Briones, D.; Wojtas, L.; Orcajo, G. New URJC-1 Material with Remarkable Stability and Acid-Base Catalytic Properties. *Polymers,* **2016**, *8*, 44.

(130) Zheng, W.; Lee, L. Y. S. Metal-Organic Frameworks for Electrocatalysis: Catalyst or Precatalyst? *ACS Energy Lett.* **2021**, *6*, 2838–2843.

(131) Rani, P.; Srivastava, R. Cu(I) Metal Organic Framework Catalyzed C-C and C-N Coupling Reactions. *Tetrahedron Lett.* **2014**, *55*, 5256–5260.

(132) Devarajan, N.; Suresh, P. Framework-Copper-Catalyzed C−N Cross-Coupling of Arylboronic Acids with Imidazole: Convenient and Ligand-Free Synthesis

of N-Arylimidazoles. *ChemCatChem* **2016**, *8*, 2953–2960.

(133) Jiang, D.; Mallat, T.; Krumeich, F.; Baiker, A. Copper-Based Metal-Organic Framework for the Facile Ring-Opening of Epoxides. *J. Catal.* **2008**, *257*, 390–395.

(134) Tranchemontagne, D. J.; Hunt, J. R.; Yaghi, O. M. Room Temperature Synthesis of Metal-Organic Frameworks: MOF-5, MOF-74, MOF-177, MOF-199, and IRMOF-0. *Tetrahedron* **2008**, *64*, 8553–8557.

(135) Devic, T.; Horcajada, P.; Serre, C.; Salles, F.; Maurin, G.; Moulin, B.; Heurtaux, D.; Clet, G.; Vimont, A.; Grenéche, J. M.; Le Ouay, B.; Moreau, F.; Magnier, E.; Filinchuk, Y.; Marrot, J.; Lavalley, J. C.; Daturi, M.; Férey, G. Functionalization in Flexible Porous Solids: Effects on the Pore Opening and the Host-Guest Interactions. *J. Am. Chem. Soc.* **2010**, *132*, 1127–1136.

(136) Zhu, B. J.; Yu, X. Y.; Jia, Y.; Peng, F. M.; Sun, B.; Zhang, M. Y.; Luo, T.; Liu, J. H.; Huang, X. J. Iron, and 1,3,5-Benzenetricarboxylic Metal-Organic Coordination Polymers Prepared by Solvothermal Method and Their Application in Efficient as(V) Removal from Aqueous Solutions. *J. Phys. Chem. C* **2012**, *116*, 8601–8607.

(137) Xamena, F. X. L. I.; Cirujano, F. G.; Corma, A. An Unexpected Bifunctional Acid-Base Catalysis in IRMOF-3 for Knoevenagel Condensation Reactions. *Microporous Mesoporous Mater.* **2012**, *157*, 112–117.

(138) Anbu, N.; Dhakshinamoorthy, A. $Cu_3(BTC)_2$ Metal-Organic Framework Catalyzed N-Arylation of Benzimidazoles and Imidazoles with Phenylboronic Acid. *J. Ind. Eng. Chem.* **2018**, *65*, 120–126.

(139) Wang, D.; Wang, M.; Li, Z. Fe-Based Metal-Organic Frameworks for Highly Selective Photocatalytic Benzene Hydroxylation to Phenol. *ACS Catal.* **2015**, *5*, 6852–6857.

(140) Zheng, J.; Ye, J.; Ortuño, M. A.; Fulton, J. L.; Gutiérrez, O. Y.; Camaioni, D. M.; Motkuri, R. K.; Li, Z.; Webber, T. E.; Mehdi, B. L.; Browning, N. D.; Penn, R. L.; Farha, O. K.; Hupp, J. T.; Truhlar, D. G.; Cramer, C. J.; Lercher, J. A. Selective Methane Oxidation to Methanol on Cu-Oxo Dimers Stabilized by Zirconia Nodes of an NU-1000 Metal-Organic Framework. *J. Am. Chem. Soc.* **2019**, *141*, 9292–9304.

(141) Korzyński, M. D.; Dinca, M. Oxidative Dehydrogenation of Propane in the Realm of Metal-Organic Frameworks. *ACS Cent. Sci.* **2017**, *3*, 10–12.

(142) Arai, T.; Kawasaki, N.; Kanoh, H. Magnetically Separable Cu-Carboxylate MOF Catalyst for the Henry Reaction. *Synlett* **2012**, *23*, 1549–1553.

(143) Takao, O.; Yasuhiro, U. Aquacatalytic Aerobic Oxidation of Benzylic Alcohols with a Self-Supported Bipyridyl–Palladium Complex. *Chem. Lett.* **2009**, *38*, 902–903.

(144) Tu, T. N.; Nguyen, K. D.; Nguyen, T. N.; Truong, T.; Phan, N. T. S. New Topological $Co_2(BDC)_2(DABCO)$ as a Highly Active Heterogeneous Catalyst for the Amination of Oxazoles via Oxidative C-H/N-H Couplings. *Catal. Sci. Technol.* **2016**, *6*, 1384–1392.

(145) Nguyen, K. D.; Doan, S. H.; Ngo, A. N. V.; Nguyen, T. T.; Phan, N. T. S. Direct C–N Coupling of Azoles with Ethers via Oxidative C–H Activation under Metal–Organic Framework Catalysis. *J. Ind. Eng. Chem.* **2016**, *44*, 136–145.

(146) Truong, T.; Nguyen, K. D.; Doan, S. H.; Phan, N. T. S. Efficient and Recyclable $Cu_2(BPDC)_2(DABCO)$-Catalyzed Direct Amination of Activated sp^3 C-H Bonds by *N-H* Heterocycles. *Appl. Catal. A Gen.* **2016**, *510*, 27–33.

(147) Tran, T. V.; Le, H. T. N.; Ha, H. Q.; Duong, X. N. T.; Nguyen, L. H. T.; Doan, T. L. H.; Nguyen, H. L.; Truong, T. A Five Coordination Cu(II) Cluster-Based MOF and Its Application in the Synthesis of Pharmaceuticals *via* sp^3 C-H/N-H Oxidative Coupling. *Catal. Sci. Technol.* **2017**, *7*, 3453–3458.

(148) Singh, G. S.; Sudheesh, S.; Keroletswe, N. Recent Applications of Aziridine Ring Expansion Reactions in Heterocyclic Synthesis. *Arkivoc* **2017**, *2018*, 50–113.

(149) Feng, J. J.; Zhang, J. Synthesis of Unsaturated N-Heterocycles by Cycloadditions of Aziridines and Alkynes. *ACS Catal.* **2016**, *6*, 6651–6661.

(150) Lugiņina, J.; Turks, M. Non-Activated Aziridines as Building Blocks for the Synthesis of Aza-Heterocycles (Microreview). *Chem. Heterocycl. Compd.* **2016**, *52*, 773–775.

(151) Fanourakis, A.; Docherty, P. J.; Chuentragool, P.; Phipps, R. J. Recent Developments in Enantioselective Transition Metal Catalysis Featuring Attractive Noncovalent Interactions between Ligand and Substrate. *ACS Catal.* **2020**, *10*, 10672–10714.

(152) Coin, G.; Patra, R.; Rana, S.; Biswas, J. P.; Dubourdeaux, P.; Clémancey, M.; De Visser, S. P.; Maiti, D.; Maldivi, P.; Latour, J. M. Fe-Catalyzed Aziridination Is Governed by the Electron Affinity of the Active Imido-Iron Species. *ACS Catal.* **2020**, *10*, 10010–10020.

(153) Evans, D. A.; Paul, M. M.; Bilodeau, M. T. Copper-Catalyzed Aziridination of Olefins by (N-(p-Toluenesulfonyl)Imino)Phenyliodinane. *J. Org. Chem.* **1991**, *56*, 6744–6746.

(154) Evans, D. A.; Paul, M. M.; Bilodeau, M. T. Development of the Copper-Catalyzed Olefin Aziridination Reaction. *J. Am. Chem. Soc.* **1994**, *116*, 2742–2753.

(155) Li, Z.; Conser, K. R.; Jacobsen, E. N. Asymmetric Alkene Aziridination with Readily Available Chiral Diimine-Based Catalysts. *J. Am. Chem. Soc.* **1993**, *115*, 5326–5327.

(156) Llaveria, J.; Beltrán, Á.; Sameera, W. M. C.; Locati, A.; Díaz-Requejo, M. M.; Matheu, M. I.; Castillón, S.; Maseras, F.; Pérez, P. J. Chemo-, Regio-, and Stereoselective Silver-Catalyzed Aziridination of Dienes: Scope, Mechanistic Studies, and Ring-Opening Reactions. *J. Am. Chem. Soc.* **2014**, *136*, 5342–5350.

(157) Borrego, E.; Pérez, P. J.; Caballero, A. Make It Green: Copper-Catalyzed Olefin Aziridination in Water with an Iminoiodonane. *Eur. J. Inorg. Chem.*

2021, *2021* (48), 5091–5095. https://doi.org/10.1002/ejic.202100825.

(158) Avenier, F.; Latour, J. M. Catalytic Aziridination of Olefins and Amidation of Thioanisole by a Non-Heme Iron Complex. *Chem. Commun.* **2004**, *4* (13), 1544–1545. https://doi.org/10.1039/b404561k.

(159) Taylor, S.; Gullick, J.; McMorn, P.; Bethell, D.; Bulman Page, P. C.; Hancock, F. E.; King, F.; Hutchings, G. J. Catalytic Asymmetric Heterogeneous Aziridination of Styrene Using CuHY: Effect of Nitrene Donor on Enantioselectivity. *J. Chem. Soc. Perkin Trans.* **2001**, *9*, 1714–1723.

(160) Liu, Y.; Li, Z.; Yuan, G.; Xia, Q.; Yuan, C.; Cui, Y. Chiral Cu(Salen)-Based Metal-Organic Framework for Heterogeneously Catalyzed Aziridination and Amination of Olefins. *Inorg. Chem.* **2016**, *55*, 12500–12503.

(161) Noorpoor, Z.; Tavangar, S. Preparation and Characterization of Cu Based on 5,5'-Bistetrazole as a Recyclable Metal-Organic Framework and Application in Synthesis of Diaryl Ether by the Ullmann Coupling Reaction. *J. Coord. Chem.* **2021**, *74*, 1651–1662.

(162) Wang, M.; Yuan, B.; Ma, T.; Jiang, H.; Li, Y. Ligand-Free Coupling of Phenols and Alcohols with Aryl Halides by a Recyclable Heterogeneous Copper Catalyst. *RSC Adv.* **2012**, *2*, 5528–5530.

(163) Sadeghi, S.; Jafarzadeh, M.; Reza Abbasi, A.; Daasbjerg, K. Incorporation of CuO NPs into Modified UiO-66-NH_2 Metal-Organic Frameworks (MOFs) with Melamine for Catalytic C-O Coupling in the Ullmann Condensation. *New J. Chem.* **2017**, *41*, 12014–12027.

(164) Yahyazadeh, A.; Ramezani, L.; Sheykhan, M. The First C-Cl Activation in Ullmann C-O Coupling by MOFs Leila. *ChemCatChem* **2018**, *10*, 4636.

(165) Ha, H. Q.; Nguyen, H. T. D.; Pham, T. H. M.; Pham, V. T.; Truong, T. Towards Optical Application of Metal-Organic Frameworks: Cu-MOFs as Sole Heterogeneous Photocatalyst for Arylation of Phenols at Room Temperature. *Catal. Commun.* **2018**, *117*, 79–84.

(166) Zheng, Q.; Chen, J.; Rao, G. Recent Advances in C–O Bond Construction via C–H Activation. **2019**, *55*, 569–586.

(167) Phan, N. T. S.; Vu, P. H. L.; Nguyen, T. T. Expanding Applications of Copper-Based Metal-Organic Frameworks in Catalysis: Oxidative C-O Coupling by Direct C-H Activation of Ethers over $Cu_2(BPDC)_2(BPY)$ as an Efficient Heterogeneous Catalyst. *J. Catal.* **2013**, *306*, 38–46.

(168) Luz, I.; Corma, A.; Llabrés I Xamena, F. X. Cu-MOFs as Active, Selective and Reusable Catalysts for Oxidative C-O Bond Coupling Reactions by Direct C-H Activation of Formamides, Aldehydes, and Ethers. *Catal. Sci. Technol.* **2014**, *4*, 1829–1836.

(169) Sharma, V.; De, D.; Bharadwaj, P. K. A Multifunctional Metal-Organic Framework for Oxidative C-O Coupling Involving Direct C-H Activation and Synthesis of Quinolines. *Inorg. Chem.* **2018**, *57*, 8195–8199.

(170) Tran, C. B.; Duong, X. N. T.; Lu, H. D.; Cao, T. T. V; Truong, T. RSC Advances under Heterogeneous Metal–Organic Framework Catalysis :

Synthesis of Ethenzamide. *RSC Adv.* **2018**, *8*, 2829–2836.

(171) Ahmadzadeh, Z.; Mokhtari, J.; Rouhani, M. Cu-MOF : An efficient Heterogeneous Catalyst for the Synthesis of Symmetric Anhydrides *via* the C– Bond Activation of Aldehydes. *RSC Adv.* **2018**, *8*, 24203–24208.

(172) Dhakshinamoorthy, A.; Alvaro, M.; Concepcion, P.; Garcia, H. Chemical Instability of $Cu_3(BTC)_2$ by Reaction with Thiols. *Catal. Commun.* **2011**, *12*, 1018–1021.

(173) Dhakshinamoorthy, A.; Alvaro, M.; Garcia, H. Aerobic Oxidation of Thiols to Disulfides Using Iron Metal-Organic Frameworks as Solid Redox Catalysts. *Chem. Commun.* **2010**, *46*, 6476–6478.

(174) Tian, A. Q.; Liu, S.; Ren, Z. L.; Wang, L.; Li, D. S. Metal–Organic Frameworks of Cu2(TPTC)-Catalyzed Cascade C–S Coupling/C_{sp2}–H Hydroxylation Reaction. *J. Iran. Chem. Soc.* **2020**, *17*, 1339–1345.

(175) Zhu, Y. Y.; Lan, G.; Fan, Y.; Veroneau, S. S.; Song, Y.; Micheroni, D.; Lin, W. Merging Photoredox and Organometallic Catalysts in a Metal–Organic Framework Significantly Boosts Photocatalytic Activities. *Angew. Chemie - Int. Ed.* **2018**, *57*, 14090–14094.

(176) Alinezhad, H.; Ghasemi, S.; Cheraghian, M. MOF Nano Porous-Supported C-S Cross-Coupling through One-Pot Post-Synthetic Modification. *J. Organomet. Chem.* **2019**, *898*, 120867.

(177) Mohammadinezhad, A.; Akhlaghinia, B. CoII Immobilized on an Aminated Magnetic Metal-Organic Framework Catalyzed C-N and C-S Bond Forming Reactions: A Journey for the Mild and Efficient Synthesis of Arylamines and Arylsulfides. *New J. Chem.* **2019**, *43*, 15525–15538.

(178) Suzuki, A. Synthetic Studies via the Cross-Coupling Reaction of Organoboron Derivatives with Organic Halides. *Pure App Chem.,* **1991**, *63*, 419–422.

(179) Miyaura, N.; Suzuki, A. Palladium-Catalyzed Cross-Coupling Reactions of Organoboron Compounds. *Chem Rev* **1995**, *95*, 2457–2483.

(180) Mora, M.; Jiménez-sanchidrián, C.; Ruiz, J. R. Heterogeneous Suzuki Cross-Coupling Reactions over Palladium / Hydrotalcite Catalysts. *J. Colloid Interface Sci.* **2006**, *302*, 568–575.

(181) Phan, N. T. S.; Van Der Sluys, M.; Jones, C. W. On the Nature of the Active Species in Palladium Catalyzed Mizoroki-Heck and Suzuki-Miyaura Couplings- Homogeneous or Heterogeneous Catalysis, a Critical Review. *Adv. Synth. Catal.* **2006**, *348*, 609–679.

(182) Yin, L.; Liebscher, J. Carbon-Carbon Coupling Reactions Catalyzed by Heterogeneous Palladium Catalysts. *Chem. Rev.* **2007**, *107*, 133–173.

(183) Llabrés i Xamena, F. X.; Abad, A.; Corma, A.; Garcia, H. MOFs as Catalysts: Activity, Reusability and Shape-Selectivity of a Pd-Containing MOF. *J. Catal.* **2007**, *250*, 294–298.

(184) Miguel-Casañ, E.; Darawsheh, M. D.; Fariña-Torres, V.; Vitórica-Yrezábal, I. J.; Andres-Garcia, E.; Fañanás-Mastral, M.; Mínguez Espallargas, G.

Heterometallic Palladium-Iron Metal-Organic Framework as a Highly Active Catalyst for Cross-Coupling Reactions. *Chem. Sci.* **2022**, *14*, 179–185.

(185) Wang, J.; Li, T.; Zhao, Z.; Zhang, X.; Pang, W. Pd Nanoparticles Embedded Into MOF - 808 : Synthesis, Structural Characteristics, and Catalyst Properties for the Suzuki – Miyaura Coupling Reaction. *Catal. Letters* **2022**, *152*, 1545–1554.

(186) Sun, D.; Li, Z. Double-Solvent Method to Pd Nanoclusters Encapsulated inside the Cavity of NH_2-Uio-66(Zr) for Efficient Visible-Light-Promoted Suzuki Coupling Reaction. *J. Phys. Chem. C* **2016**, *120*, 19744–19750.

(187) Gong, X. F.; Zhang, L. Y.; Zhang, H. X.; Cui, Y. M.; Jin, F. C.; Liu, Y.; Zhai, Y. F.; Li, J. H.; Liu, G. Y.; Zeng, Y. F. Highly Active Heterogeneous $PdCl_2$/MOF Catalyst for Suzuki–Miyaura Cross-Coupling Reactions of Aryl Chloride. *Zeitschrift fur Anorg. und Allg. Chemie* **2020**, *646*, 1336–1341.

(188) Sun, Z.-H.; Chen, W.; Wang, L.-Y.; Wang, L.; Tang, Y.-H.; Qian, B.-B.; He, M.-Y.; Chen, Q.; Zhang, Z.-H. Noble-metal free Suzuki–Miyaura reaction catalyzed by magnetically recyclable MOF composites *Appl. Organomet. Chem.* **2022**, *36*, 6842.

(189) Tang, H.; Yang, M.; Li, X.; Zhou, M.; Bao, Y.; Cui, X.; Zhao, K. Synthesis of Biaryl Compounds via Suzuki Homocoupling Reactions Catalyzed by Metal–Organic Frameworks Encapsulated with Palladium Nanoparticles. *Inorg. Chem. Commun.* **2021**, *123*, 108368.

(190) Elumalai, P.; Mamlouk, H.; Yiming, W.; Feng, L.; Yuan, S.; Zhou, H. C.; Madrahimov, S. T. Recyclable, and Reusable Heteroleptic Nickel Catalyst Immobilized on Metal-Organic Framework for Suzuki-Miyaura Coupling. *ACS Appl. Mater. Interfaces* **2018**, *10*, 41431–41438.

(191) Gao, S.; Zhao, N.; Shu, M.; Che, S. Palladium Nanoparticles Supported on MOF-5: A Highly Active Catalyst for a Ligand- and Copper-Free Sonogashira Coupling Reaction. *Appl. Catal. A Gen.* **2010**, *388*, 196–201.

(192) Parshamoni, S.; Sanda, S.; Jena, H. S.; Konar, S. A Copper Based Pillared-Bilayer Metal–Organic Framework: Its Synthesis, Sorption Properties and Catalytic Performance. *Dalt. Trans.* **2014**, *43*, 7191–7199.

(193) Mohammadi, L.; Hosseinifard, M.; Vaezi, M. R. Stabilization of Palladium-Nanoparticle-Decorated Postsynthesis-Modified Zr-UiO-66 MOF as a Reusable Heterogeneous Catalyst in C-C Coupling Reaction. *ACS Omega* **2023**, *8*, 8505–8518.

(194) Huang, Y.; Gao, S.; Liu, T.; Lü, J.; Lin, X.; Li, H.; Cao, R. Palladium Nanoparticles Supported on Mixed-Linker Metal-Organic Frameworks as Highly Active Catalysts for Heck Reactions. *Chempluschem* **2012**, *77*, 106–112.

(195) Parshamoni, S.; Nasani, R.; Paul, A.; Konar, S. Synthesis of a Palladium Based MOF: Via an Effective Post-Synthetic Modification Approach and Its Catalytic Activity towards Heck Type Coupling Reactions. *Inorg. Chem. Front.* **2021**, *8*, 693–699.

(196) Keypour, H.; Kouhdareh, J.; Alavinia, S.; Rabiei, K.; Mohammadi, M.; Maryamabadi, A.; Babaei, S. Post-Synthetic Modification of Dual-Porous UMCM-1-NH_2 with Palladacycle Complex as an Effective Heterogeneous Catalyst in Suzuki and Heck Coupling Reactions. *J. Organomet. Chem.* **2023**, *989*, 122646.

(197) Azad, M.; Rostamizadeh, S.; Estiri, H.; Nouri, F. Ultra-Small and Highly Dispersed Pd Nanoparticles inside the Pores of ZIF-8: Sustainable Approach to Waste-Minimized Mizoroki–Heck Cross-Coupling Reaction Based on Reusable Heterogeneous Catalyst. *Appl. Organomet. Chem.* **2019**, *33*, 1–13.

(198) Radwan, A.; Jin, H.; He, D.; Mu, S. *Design Engineering, Synthesis Protocols, and Energy Applications of MOF-Derived Electrocatalysts*; Springer Singapore, **2021**; Vol. 13.

(199) Yang, B.; Li, B.; Xiang, Z. Advanced MOF-Based Electrode Materials for Supercapacitor and Electrocatalytic Oxygen Reduction. *Nano Res.* **2023**, *16*, 1338–1361.

(200) Sanati, S.; Morsali, A.; García, H. First-Row Transition Metal-Based Materials Derived from Bimetallic Metal-Organic Frameworks as Highly Efficient Electrocatalysts for Electrochemical Water Splitting. *Energy Environ. Sci.* **2022**, *15*, 3119–3151.

(201) Qin, X.; Kim, D.; Piao, Y. Carbon Energy - 2020 - Qin - Metal-organic Frameworks-derived Novel Nanostructured Electrocatalysts for Oxygen Evolution. *Carbon Energy* **2021**, *3*, 66–100.

(202) Yang, C.; Ma, X.; Zhou, J.; Zhao, Y.; Xiang, X.; Shang, H.; Zhang, B. Recent Advances in Metal-Organic Frameworks-Derived Carbon-Based Electrocatalysts for the Oxygen Reduction Reaction. *Int. J. Hydrogen Energy* **2022**, *47*, 21634–21661.

(203) Ma, S.; Goenaga, G. A.; Call, A. V.; Liu, D. J. Cobalt Imidazolate Framework as Precursor for Oxygen Reduction Reaction Electrocatalysts. *Chem.-A Eur. J.* **2011**, *17*, 2063–2067.

(204) Collins, G.; Rupa, P.; Karthik, R.; Shim, J.; Sukanya, R.; Breslin, C. B. Electrochimica Acta Mesoporous Carbon-Based Materials and Their Applications as Non-Precious Metal Electrocatalysts in the Oxygen Reduction Reaction. *Electrochim. Acta* **2023**, *439*, 141678.

(205) Chen, Q.; Zhang, Z.; Zhang, R.; Hu, M.; Shi, L.; Yao, Z. Recent Progress of Non-Pt Catalysts for Oxygen Reduction Reaction in Fuel Cells. *Processes* **2023**, *11*, 361.

(206) Kiani, M.; Qing, X.; Zhang, W. Non-Precious Metal Electrocatalysts Design for Oxygen Reduction Reaction in Polymer Electrolyte Membrane Fuel Cells : Recent Advances, Challenges, and Future Perspectives. *Coord. Chem. Rev.* **2021**, *441*, 213954.

(207) Zhang, P.; Sun, F.; Xiang, Z.; Shen, Z.; Yun, J.; Cao, D. ZIF-Derived in Situ Nitrogen-Doped Porous Carbons as Efficient Metal-Free Electrocatalysts for Oxygen Reduction Reaction. *Energy Environ. Sci.* **2014**, *7*, 442–450.

(208) Zhang, L.; Su, Z.; Jiang, F.; Yang, L.; Qian, J.; Zhou, Y.; Lia, W.; Hong, M. Highly Graphitized Nitrogen-Doped Porous Carbon Nanopolyhedra Derived from ZIF-8 Nanocrystals as Efficient Electrocatalysts for Oxygen Reduction Reactions. *Nanoscale* **2014**, *6*, 6590–6602.

(209) Jiao, L.; Wan, G.; Zhang, R.; Zhou, H.; Yu, S.; Jiang, H. From Metal–Organic Frameworks to Single-Atom Fe Implanted N- Doped Porous Carbons : Efficient Oxygen Reduction in Both Alkaline. *Angew. Chemie - Int. Ed.* **2018**, *57*, 1–6.

(210) Peiqun, Y.; Tao, Y.; Yuen, W.; Lirong, Z.; Yue, L.; Ei, L.; Huanxin, J.; Junfa, Z.; Xun, H.; Zhaoxiang, D.; Gang, Z.; Shiqiang, W.; Li, Y. Single Cobalt Atoms with Precise N-Coordination as Superior Oxygen Reduction Reaction. *Angew. Chemie - Int. Ed.* **2016**, *55*, 10800–10805.

(211) Xia, W.; Tang, J.; Li, J.; Zhang, S.; Wu, K. C. W.; He, J.; Yamauchi, Y. Defect-Rich Graphene Nanomesh Produced by Thermal Exfoliation of Metal–Organic Frameworks for the Oxygen Reduction Reaction. *Angew. Chemie - Int. Ed.* **2019**, *58*, 13354–13359.

(212) Shang, H.; Zhou, X.; Dong, J.; Li, A.; Zhao, X.; Liu, Q.; Lin, Y.; Pei, J.; Li, Z.; Jiang, Z.; Zhou, D.; Zheng, L.; Wang, Y.; Zhou, J.; Yang, Z.; Cao, R.; Sarangi, R.; Sun, T.; Yang, X.; Zheng, X.; Yan, W.; Zhuang, Z.; Li, J.; Chen, W.; Wang, D.; Zhang, J.; Li, Y. Engineering Unsymmetrically Coordinated Cu-S_1N_3 Single Atom Sites with Enhanced Oxygen Reduction Activity. *Nat. Commun.* **2020**, *11*, 1–11.

(213) Zhong, X.; Ye, S.; Tang, J.; Zhu, Y.; Wu, D.; Gu, M.; Pan, H.; Xu, B. Engineering Pt, and Fe Dual-Metal Single Atoms Anchored on Nitrogen-Doped Carbon with High Activity and Durability towards Oxygen Reduction Reaction for Zinc-Air Battery. *Appl. Catal. B Environ.* **2021**, *286*, 119891.

(214) Wen, Y.; Rong, H.; Zhan, T. A 2D MOF Derived Core-Shell Structured Nanocomposite as Effective Electrocatalyst for Oxygen Reduction Reaction. *J. Electroanal. Chem.* **2018**, *833*, 454–461.

(215) Wu, R.; Liu, M.; Peng, Y.; Yao, S.; Guo, X. MOF / CC-Derivatives with Trace Amount of Cobalt Oxides as Ef Fi Cient Electrocatalysts for Oxygen Reduction Reaction. *Chinese Chem. Lett.* **2019**, *30*, 989–994.

(216) Ribeiro, E. L.; Davis, E. M.; Mokhtarnejad, M.; Hu, S.; Mukherjee, D.; Khomami, B. MOF-Derived PtCo/Co3O4 Nanocomposites in Carbonaceous Matrices as High-Performance ORR Electrocatalysts Synthesized via Laser Ablation Techniques. *Catal. Sci. Technol.* **2021**, *11*, 2969–3296.

(217) Song, L.; Tang, J.; Wang, T.; Wu, C.; Ide, Y.; He, J. Self-Supported ZIF-Derived Co_3O_4 Nanoparticles-Decorated Porous *N*-Doped Carbon Fibers as Oxygen Reduction Catalyst. *Chem. Eur. J.* **2019**, *25*, 1–8.

(218) He, Y.; Hwang, S.; Cullen, D. A.; Uddin, M. A.; Langhorst, L.; Li, B.; Karakalos, S.; Kropf, A. J.; Wegener, E. C.; Sokolowski, J.; Chen, M.; Myers, D.; Su, D.; More, K. L.; Wang, G.; Litster, S.; Wu, G. Highly Active Atomically Dispersed CoN4 Fuel Cell Cathode Catalysts Derived from Surfactant-Assisted MOFs: Carbon-Shell Confinement Strategy. *Energy*

Environ. Sci. **2019**, *12*, 250–260.

(219) Li, Z.; Shao, M.; Zhou, L.; Ruikang, Z.; Cong, Z.; Min, W.; David G., E.; Duan, X.; The. Directed Growth of Metal-Organic Frameworks and Their Derived Carbon-Based Network for Effi Cient Electrocatalytic Oxygen Reduction. *Adv. Energy Mater.* **2016**, *28*, 2337–2344.

(220) Xiao, J.; Zhao, C.; Hu, C.; Xi, J.; Wang, S. Pudding-Typed Cobalt Sulfides / Nitrogen and Sulfur Dual-Doped Hollow Carbon Spheres as a Highly Efficient and Stable Oxygen Reduction Electrocatalyst. *J. Power Sources* **2017**, *348*, 183–192.

(221) Tianhua, Z.; Yonghua, D.; Shengming, Y.; Xuezeng, T.; Hongbin, Y.; Xin, W.; Bin, L.; Haimei, Z.; Shizhang, Q.; Xu, R. Nitrogen-Doped Cobalt Phosphate@Nanocarbon Hybrids for Efficient Electrocatalytic Oxygen Reduction. *Energy Environ. Sci.* **2016**, *9*, 2563–2570.

(222) Xia, W.; Zou, R.; An, L.; Xia, D.; Guo, S. Metal-Organic Framework Route to In-Situ Encapsulation of Co@Co_3O_4@C Core@Bishell Nanoparticles into Highly Ordered Porous Carbon Matrix for Oxygen Reduction. *Energy* **2014**, *8*, 568–576.

(223) Guangju, Z.; Chuanxi, L.; Juan, L.; Lei, Z.; Ruihua, L.; Xiao, H.; Hui, H.; Hailiang, H.; Yang, L.; Kang, Z. One-Step Conversion from Metal–Organic Frameworks to Co_3O_4@N-Doped Carbon Nanocomposites towards Highly Efficient Oxygen Reduction Catalysts. *J. Mater. Chem. A* **2014**, *2*, 8184–8189.

(224) Haolin, T.; Shichang, C.; Shilei, X.; Zhengbang, W.; Yexiang, T.; Mu, P.; Lu, X. Metal–Organic-Framework-Derived Dual Metal- and Nitrogen-Doped Carbon as Efficient and Robust Oxygen Reduction Reaction Catalysts for Microbial Fuel Cells *Adv. Sci.* **2016**, *3*, 1500265.

(225) Yu-Zhen, C.; Chengming, W.; Zhen-Yu, W.; Yujie, X.; Qiang, X.; Shu-Hong, Y.; Jiang, H.-L. From Bimetallic Metal-Organic Framework to Porous Carbon: High Surface Area and Multicomponent Active Dopants for Excellent Electrocatalysis. *Adv. Mater.* **2015**, *27*, 5010–5016.

(226) Zou, L.; Hou, C.; Liu, Z.; Pang, H.; Xu, Q. Superlong Single-Crystal Metal–Organic Framework Nanotubes. *J. Am. Chem. Soc.* **2018**, *140*, 15393–15401.

(227) Xue, Y.; Guo, Y.; Zhang, Q.; Xie, Z.; Wei, J. MOF - Derived Co and Fe Species Loaded on N - Doped Carbon Networks as Efficient Oxygen Electrocatalysts for Zn - Air Batteries. *Nano-Micro Lett.* **2022**, *14*, 1–12.

(228) Li, Y.; Zhang, W.; Li, J.; Ma, H.; Du, H.; Li, D.; Wang, S.; Zhao, J.; Dou, J.; Xu, L.; Li, Y.; Zhao, J.; Li, J.; Dou, J.; Xu, L. Fe-MOF-Derived Efficient ORR/OER Bifunctional Electrocatalyst for Rechargeable Zinc–Air Batteries. *ACS Appl. Mater. Interfaces* **2020**, *12*, 44710–44719.

(229) Song, D.; Hu, C.; Gao, Z.; Yang, B.; Li, Q.; Zhan, X.; Tong, X.; Tian, J. Metal–Organic Frameworks (MOFs) Derived Materials Used in Zn–Air Battery. *Materials* **2022**, 15, 5837

(230) Su, P.; Xiao, H.; Zhao, J.; Yao, Y.; Shao, Z.; Li, C.; Yang, Q. Nitrogen-Doped Carbon Nanotubes Derived from Zn–Fe-ZIF Nanospheres and Their

Application as efficient Oxygen Reduction Electrocatalysts with in-situ Generated Iron Species. *Chem. Sci.* **2013**, *4*, 2941–2946.

(231) Zhao, D.; Shui, J.-L.; Chen, C.; Chen, X.; Reprogle, B. M.; Wanga, D.; Liu, D.-J. Iron Imidazolate Framework as Precursor for Electrocatalysts in Polymer Electrolyte Membrane Fuel Cells. *Chem. Sci.* **2012**, *3*, 3200–3205.

(232) Hou, Y.; Huang, T.; Wen, Z.; Mao, S.; Cui, S.; Chen, J. Metal − Organic Framework-Derived Nitrogen-Doped Core-Shell-Structured Porous Fe/Fe_3C@C Nanoboxes Supported on Graphene Sheets for Efficient Oxygen Reduction Reactions. *Adv. Energy Mater.* **2014**, *4*, 1400337.

(233) Gao, S.; Fan, B.; Feng, R.; Ye, C.; Wei, X.; Xu, J.; Bu, X. N-Doped-Carbon-Coated Fe_3O_4 from Metal-Organic Framework as Efficient Electrocatalyst for ORR. *Nano Energy* **2017**, *40*, 462–470.

(234) Huang, Z.; Xie, N.; Zhang, M.; Xu, B. Nonpyrolyzed Fe−N Coordination-Based Iron Triazolate Framework: An Efficient and Stable Electrocatalyst for Oxygen Reduction Reaction. *ChemSusChem* **2019**, *12*, 200–207.

(235) Qingxue, L.; Li Rong, Z.; Yan Yu, L.; Jianping, H.; Jingxiang, Z.; Chen, J. Metal-Organic-Framework-Derived Fe-N/C Electrocatalyst with Five-Coordinated Fe-Nx Sites for Advanced Oxygen Reduction in Acid Media. *ACS Catal.* **2017**, *7*, 1655–1663.

(236) Chen, Y.; Ji, S.; Wang, Y.; Dong, J.; Chen, W.; Li, Z.; Shen, R.; Zheng, L.; Zhongbin Zhuang, D. W.; Li, Y. Isolated Single Iron Atoms Anchored on N-Doped Porous Carbon as an Efficient Electrocatalyst for the Oxygen Reduction Reaction. *Angew. Chemie Int. Ed. English* **2017**, *56*, 6937 –6941.

(237) Jiang, R.; Li, L.; Sheng, T.; Hu, G.; Chen, Y.; Wang, L.; Jiang, R.; Li, L.; Sheng, T.; Hu, G.; Chen, Y.; Wang, L. Edge-Site Engineering of Atomically Dispersed Fe–N_4 by Selective C–N Bond Cleavage for Enhanced Oxygen Reduction Reaction Activities. *J. Am. Chem. Soc* **2018**, *140*, 11594–11598.

(238) Chen, Y.; Ji, S.; Zhao, S.; Chen, W.; Dong, J.; Cheong, W.; Shen, R.; Wen, X.; Zheng, L.; Rykov, A. I.; Cai, S.; Tang, H.; Zhuang, Z.; Chen, C.; Peng, Q.; Wang, D.; Li, Y. Enhanced Oxygen Reduction with Single-Atomic-Site Iron Catalysts for a Zinc-Air Battery and Hydrogen-Air Fuel Cell. *Nat. Commun.* **2018**, *9*, 5422.

(239) Li, J.; Chen, M.; Cullen, D. A.; Hwang, S.; Wang, M.; Li, B.; Liu, K.; Karakalos, S.; Lucero, M.; Zhang, H.; Lei, C.; Xu, H.; Sterbinsky, G. E.; Feng, Z.; Su, D.; More, K. L.; Wang, G.; Wang, Z.; Wu, G. Atomically Dispersed Manganese Catalysts for Oxygen Reduction in Proton-Exchange Membrane Fuel Cells. *Nat. Catal.* **2018**, *1*, 935–945.

(240) Qu, Y.; Li, Z.; Chen, W.; Lin, Y.; Yuan, T.; Yang, Z.; Zhao, C.; Wang, J.; Zhao, C.; Wang, X.; Zhou, F.; Zhuang, Z.; Wu, Y. Direct Transformation of Bulk Copper into Copper Single Sites via Emitting and Trapping of Atoms. *Nat. Catal.* **2018**, *1*, 781–786.

(241) Lai, Q.; Zhu, J.; Zhao, Y.; Liang, Y.; He, J.; Chen, J. MOF-Based Metal-Doping-Induced Synthesis of Hierarchical Porous Cu–N/C Oxygen Reduction Electrocatalysts for Zn–Air Batteries. *Small* **2017**, *4*, 1–11.

(242) Li, J.; Zhou, N.; Song, J.; Fu, L.; Yan, J.; Tang, Y.; Wang, H. Cu−MOF-Derived Cu/Cu_2O Nanoparticles and CuNxCy Species to Boost Oxygen Reduction Activity of Ketjenblack Carbon in Al−Air Battery. *ACS Sustain. Chem. Eng.* **2018**, *6*, 413−421.

(243) Chhetri, K.; Dahal, B.; Mukhiya, T.; Prasad, A.; Muthurasu, A.; Kim, T.; Kim, H.; Yong, H. Integrated Hybrid of Graphitic Carbon-Encapsulated Cu_xO on Multilayered Mesoporous Carbon from Copper MOFs and Polyaniline for Asymmetric Supercapacitor and Oxygen Reduction Reactions. *Carbon,* **2021**, *179*, 89–99.

(244) Yi, X.; He, X.; Yin, F.; Chen, B.; Li, G.; Yin, H. Co-CoO-Co_3O_4/N-Doped Carbon Derived from Metal-Organic Framework: The Addition of Carbon Black for Boosting Oxygen Electrocatalysis and Zn-Air Battery. *Electrochim. Acta* **2019**, *295*, 966–977.

(245) He, X.; Tan, J.; Yin, F.; Chen, B.; Liang, X.; Li, G.; Yin, H. Well-Dispersed Co–Co3O4 Hybrid Nanoparticles on N-Doped Carbon Nanosheets as a Bifunctional Electrocatalyst for Oxygen Evolution and Reduction Reactions. *Int. J. Hydrogen Energy* **2019**, *44*, 24184–24196.

(246) McCrory, C. C. L.; Jung, S.; Peters, J. C.; Jaramillo, T. F. Benchmarking Heterogeneous Electrocatalysts for the Oxygen Evolution Reaction. *J. Am. Chem. Soc.* **2013**, *135*, 16977–16987.

(247) Li, J. *Oxygen Evolution Reaction in Energy Conversion and Storage: Design Strategies Under and Beyond the Energy Scaling Relationship*; Springer Nature Singapore, **2022**; Vol. 14.

(248) Shi, Z.; Wang, X.; Ge, J.; Liu, C.; Xing, W. Fundamental Understanding of the Acidic Oxygen Evolution Reaction: Mechanism Study and State-of-the-Art Catalysts. *Nanoscale* **2020**, *12*, 13249–13275.

(249) Zhang, B.; Zheng, X.; Voznyy, O.; Comin, R.; Bajdich, M.; García-Melchor, M.; Han, L.; Xu, J.; Liu, M.; Zheng, L.; De Arquer, F. P. G.; Dinh, C. T.; Fan, F.; Yuan, M.; Yassitepe, E.; Chen, N.; Regier, T.; Liu, P.; Li, Y.; De Luna, P.; Janmohamed, A.; Xin, H. L.; Yang, H.; Vojvodic, A.; Sargent, E. H. Homogeneously Dispersed Multimetal Oxygen-Evolving Catalysts. *Science* **2016**, *352*, 333–337.

(250) Kim, D.; Kim, D.; Jeon, Y.; Li, Y.; Lee, J.; Kang, J.; Lee, L. Y. S.; Piao, Y. Zeolitic Imidazolate Frameworks Derived Novel Polyhedral Shaped Hollow Co-B-O@Co_3O_4 Electrocatalyst for Oxygen Evolution Reaction. *Electrochim. Acta* **2019**, *299*, 213–221.

(251) Chen, G.; Shan, H.; Li, Y.; Bao, H.; Hu, T.; Zhang, L.; Liu, S.; Ma, F. Hollow PtCu Nanoparticles Encapsulated into a Carbon Shell *via* Mild Annealing of Cu Metal-Organic Frameworks. *J. Mater. Chem. A* **2020**, *8*, 10337–10345.

(252) Chen, M.; Ju, M. G.; Garces, H. F.; Carl, A. D.; Ono, L. K.; Hawash, Z.; Zhang, Y.; Shen, T.; Qi, Y.; Grimm, R. L.; Pacifici, D.; Zeng, X. C.; Zhou, Y.; Padture, N. P. Highly Stable and Efficient All-Inorganic Lead-Free Perovskite Solar Cells with Native-Oxide Passivation. *Nat. Commun.* **2019**, *10*, 1–8.

(253) Lin, Y.; Chen, G.; Wan, H.; Chen, F.; Liu, X.; Ma, R. 2D Free-Standing

Nitrogen-Doped Ni-Ni_3S_2 @Carbon Nanoplates Derived from Metal–Organic Frameworks for Enhanced Oxygen Evolution Reaction. *Small* **2019**, *15*, 1–11.

(254) Yan, L.; Cao, L.; Dai, P.; Gu, X.; Liu, D.; Li, L.; Wang, Y.; Zhao, X. Metal-Organic Frameworks Derived Nanotube of Nickel–Cobalt Bimetal Phosphides as Highly Efficient Electrocatalysts for Overall Water Splitting. *Adv. Funct. Mater.* **2017**, *27*, 1–10.

(255) Yang, X.; Wu, X.; Guo, Z.; Li, Q.; Wang, H.; Ke, C.; Zeng, W.; Qiu, X.; He, Y.; Liang, X.; Kim, Y. Phosphorus/Nitrogen Co-Doped and Bimetallic MOF-Derived Cathode for All-Solid-State Rechargeable Zinc-Air Batteries. *RSC Adv.* **2020**, *10*, 33327–33333.

(256) Zhao, A.; Xu, G.; Li, Y.; Jiang, J.; Wang, C.; Zhang, X.; Zhang, S.; Zhang, L. MOF-Derived Hierarchical CoSe2with Sheetlike Nanoarchitectures as an Efficient Bifunctional Electrocatalyst. *Inorg. Chem.* **2020**, *59*, 12778–12787.

(257) Hu, Z.; Hao, L.; Quan, F.; Guo, R. Recent Developments of Co3O4-Based Materials as Catalysts for the Oxygen Evolution Reaction. *Catal. Sci. Technol.* **2022**, *12*, 436–461.

(258) Liu, H.; Xia, G.; Zhang, R.; Jiang, P.; Chen, J.; Chen, Q. MOF-Derived RuO_2/Co_3O_4 Heterojunctions as Highly Efficient Bifunctional Electrocatalysts for HER and OER in Alkaline Solutions. *RSC Adv.* **2017**, *7*, 3686–3694.

(259) Zhou, J.; Dou, Y.; Zhou, A.; Shu, L.; Chen, Y.; Li, J. R. Layered Metal-Organic Framework-Derived Metal Oxide/Carbon Nanosheet Arrays for Catalyzing the Oxygen Evolution Reaction. *ACS Energy Lett.* **2018**, *3*, 1655–1661.

(260) Gong, Y.; Xu, Z.; Pan, H. Facile Synthesis and Characterization of MOF-Derived Porous Co_3O_4 Composite for Oxygen Evolution Reaction. *ChemistrySelect* **2019**, *4*, 1131–1137.

(261) Zheng, S.; Guo, X.; Xue, H.; Pan, K.; Liu, C.; Pang, H. Facile One-Pot Generation of Metal Oxide Hydroxide@Metal-Organic Framework Composites: Highly Efficient Bifunctional Electrocatalysts for Overall Water Splitting. *Chem. Commun.* **2019**, *55*, 10904–10907.

(262) Huang, Z. Q.; Lu, W. X.; Wang, B.; Chen, W. J.; Xie, J. L.; Pan, D. S.; Zhou, L. L.; Song, J. L. A Mesoporous C, N-Co Doped Co-Based Phosphate Ultrathin Nanosheet Derived from a Phosphonate-Based-MOF as an Efficient Electrocatalyst for Water Oxidation. *Catal. Sci. Technol.* **2019**, *9*, 4718–4724.

(263) Liu, X.; Li, Y.; Cao, Z.; Yin, Z.; Ma, T.; Chen, S. Current Progress of Metal Sulfides Derived from Metal-Organic Frameworks for Advanced Electrocatalysis: Potential Electrocatalysts with Diverse Applications. *J. Mater. Chem. A* **2022**, *10*, 1617–1641.

(264) Wu, L. L.; Wang, Q. S.; Li, J.; Long, Y.; Liu, Y.; Song, S. Y.; Zhang, H. J. Co_9S_8 Nanoparticles-Embedded N/S-Codoped Carbon Nanofibers Derived from Metal–Organic Framework-Wrapped CdS Nanowires for Efficient Oxygen Evolution Reaction. *Small* **2018**, *14*, 1–9.

(265) Du, J.; Wang, R.; Lv, Y. R.; Wei, Y. L.; Zang, S. Q. One-Step MOF-Derived

Co/Co_9S_8 Nanoparticles Embedded in Nitrogen, Sulfur, and Oxygen Ternary-Doped Porous Carbon: An Efficient Electrocatalyst for Overall Water Splitting. *Chem. Commun.* **2019**, *55*, 3203–3206.

(266) Li, Y.; Mao, Z.; Wang, Q.; Li, D.; Wang, R.; He, B.; Gong, Y.; Wang, H. Hollow Nanosheet Array of Phosphorus-Anion-Decorated Cobalt Disulfide as an Efficient Electrocatalyst for Overall Water Splitting. *Chem. Eng. J.* **2020**, *390*, 124556.

(267) Peng, H.; Zhang, W.; Song, Y.; Yin, F.; Zhang, C.; Zhang, L. In Situ Construction of Co/Co_3O_4 with N-Doped Porous Carbon as a Bifunctional Electrocatalyst for Oxygen Reduction and Oxygen Evolution Reactions. *Catal. Today* **2020**, *355* (January), 286–294.

(268) Pan, H.; Huang, X.; Lu, Z.; Zhang, Z.; An, B.; Wu, D.; Wang, T.; Chen, X.; Cheng, F. Dual Oxidation and Sulfurization Enabling Hybrid Co/Co_3O_4@CoS in S/N-Doped Carbon Matrix for Bifunctional Oxygen Electrocatalysis and Rechargeable Zn-Air Batteries. *Chem. Eng. J.* **2021**, *419*, 129619.

(269) Yu, N. F.; Wu, C.; Huang, W.; Chen, Y. H.; Ruan, D. Q.; Bao, K. L.; Chen, H.; Zhang, Y.; Zhu, Y.; Huang, Q. H.; Lai, W. H.; Wang, Y. X.; Liao, H. G.; Sun, S. G.; Wu, Y. P.; Wang, J. Highly Efficient Co_3O_4/Co@NCs Bifunctional Oxygen Electrocatalysts for Long Life Rechargeable Zn-Air Batteries. *Nano Energy* **2020**, *77*, 105200.

(270) Liu, H.; Mai, Z.; Xu, X.; Wang, Y. A Co-MOF-Derived Oxygen-Vacancy-Rich Co_3O_4-Based Composite as a Cathode Material for Hybrid Zn Batteries. *Dalt. Trans.* **2020**, *49*, 2880–2887.

(271) Singh, T.; Das, C.; Bothra, N.; Sikdar, N.; Das, S.; Pati, S. K.; Maji, T. K. MOF Derived Co_3O_4@Co/NCNT Nanocomposite for Electrochemical Hydrogen Evolution, Flexible Zinc-Air Batteries, and Overall Water Splitting. *Inorg. Chem.* **2020**, *59*, 3160–3170.

(272) Wang, Y.; Wang, S.; Liu, D.; Zhou, L.; Du, R.; Li, T. Normal-Pulse-Voltage-Assisted in Situ Fabrication of Graphene-Wrapped MOF-Derived CuO Nanoflowers for Water Oxidation. *Chem. Commun.* **2020**, *56*, 8750–8753.

(273) Wu, J. X.; He, C. T.; Li, G. R.; Zhang, J. P. An Inorganic-MOF-Inorganic Approach to Ultrathin CuO Decorated Cu-C Hybrid Nanorod Arrays for an Efficient Oxygen Evolution Reaction. *J. Mater. Chem. A* **2018**, *6*, 19176–19181.

(274) Jin, H.; Kou, Z.; Cai, W.; Zhou, H.; Ji, P.; Liu, B.; Radwa, A.; He, D.; Mu, S. P-Fe Bond Oxygen Reduction Catalysts toward High-Efficiency Metal-Air Batteries and Fuel Cells. *J. Mater. Chem.* **2020**, *8*, 9121–9127.

(275) Li, T. T.; Qian, J.; Zheng, Y. Q. Facile Synthesis of Porous CuO Polyhedron from Cu-Based Metal–Organic Framework (MOF-199) for Electrocatalytic Water Oxidation. *RSC Adv.* **2016**, *6*, 77358–77365.

(276) Zhao, L.; Kuang, X.; Liu, Z.; Hou, Y.; Wang, Z.; Wei, Q.; Lee, J. Y.; Kang, B. Anchoring CuO Nanoparticles On C, N-Codoped G-C_3N_4 Nanosheets from Melamine-Entrapped MOF Gel for High-Efficiency Oxygen Evolution. *ChemNanoMat* **2019**, *5*, 1170–1175.

(277) Rong, J.; Xu, J.; Qiu, F.; Zhu, Y.; Fang, Y.; Xu, J.; Zhang, T. Sea Urchin-Like MOF-Derived Formation of Porous Cu_3P@C as an Efficient and Stable Electrocatalyst for Oxygen Evolution and Hydrogen Evolution Reactions. *Adv. Mater. Interfaces* **2019**, *6*, 1–11.

(278) Rong, J.; Qiu, F.; Zhang, T.; Fang, Y.; Xu, J.; Zhu, Y. Self-Directed Hierarchical $Cu_3(PO_4)_2$/Cu-BDC Nanosheets Array Based on Copper Foam as an Efficient and Durable Electrocatalyst for Overall Water Splitting. *Electrochim. Acta* **2019**, *313*, 179–188.

(279) Xie, A.; Zhang, J.; Tao, X.; Zhang, J.; Wei, B.; Peng, W.; Tao, Y.; Luo, S. Nickel-Based MOF Derived Ni@NiO/N–C Nanowires with Core-Shell Structure for Oxygen Evolution Reaction. *Electrochim. Acta* **2019**, *324*, 134814.

(280) Guo, Y.; Zhou, Y.; Nan, Y.; Li, B.; Song, X. Ni-Based Nanoparticle-Embedded N-Doped Carbon Nanohorns Derived from Double Core−Shell CNH@PDA@NiMOFs for Oxygen Electrocatalysis. *ACS Appl. Mater. Interfaces* **2020**, *12*, 12743−12754.

(281) Hu, Q.; Huang, X.; Wang, Z.; Li, G.; Han, Z.; Yang, H.; Ren, X.; Zhang, Q.; Liu, J.; He, C. Unconventionally Fabricating Defect-Rich NiO Nanoparticles within Ultrathin Metal-Organic Framework Nanosheets to Enable High-Output Oxygen Evolution. *J. Mater. Chem. A* **2020**, *8*, 2140–2146.

(282) Ma, M.; Yang, G.; Wang, H.; Lu, Y. Science Direct Ordered Distributed Nickel Sulfide Nanoparticles across Graphite Nanosheets for Efficient Oxygen Evolution Reaction Electrocatalyst. *Int. J. Hydrogen Energy* **2019**, *44*, 1544–1554.

Chapter II:

Synthesis & Characterization of Metal-Organic Framework

Part of this chapter has been published in Inorg. Chem. **2022**, *61*, 13685–13699, *(DOI*: 10.1021/acs.inorgchem.2c00270) and *Inorg. Chem.* **2023**, *63, 3026-3025, (DOI: 10.1021/acs.inorgchem.2c03707)*

Abstract

Over the past two decades, a range of diverse synthetic strategies has been employed in the design of metal-organic frameworks (MOFs) due to the vast array of potential synthetic possibilities. This chapter provides a detailed synthetic method used in the production of metal-organic frameworks (MOFs) used in this study. This chapter elaborates on the synthesis of various known and novel MOFs that were utilized for the catalytic analysis presented in the forthcoming chapters of this thesis. Following the standard procedure, the synthesis and characterization of some known MOFs such as HKUST-1, Cu-BDC, ZIF, MIL, MOF-74, Mn-SKU-1, Mn-SKU-2, Cu-SKU-3 **(**SKU=Sikkim University) etc., have been discussed in detail. Furthermore, we report the synthesis of novel MOFs such as Cu-1D, Cu-SKU-4, and Ni-SKU-5. All the MOFs synthesized have been rigorously characterized using SCXRD, PXRD, FTIR, BET surface area analysis, elemental analysis, TGA, and SEM techniques.

II.1 Introduction

Since their discovery in the late 1990s,[1–3] research on metal-organic frameworks (MOFs) has been rapidly increasing, with almost one million MOF structures reported to date,[4] with various synthetic modifications.[5] MOF materials are produced through the repetitive coordination of linkers (ligands) to metal ions.[6] The metal ions in this case are referred to as primary building units (PBU), while the metal ions coordinated with organic ligands forming a repeating unit are called secondary building units (SBU).[7] The development of MOFs with varying dimensions requires a rational design approach that heavily relies on the coordination nature and strength between the PBU and SBU, which are governed by Pearson's soft-hard acid-base (SHAB) principle. In general, organic azolate ligands with carboxylate functional groups, sulphonic acid groups, etc. that have (O, O)-, (N, O)-, and (N, N)-donor atoms are classified as hard base linkers. On the other hand, linkers with (N, S)-, (N, P)-, (S, S)-, and (P, S)-donor atoms are typically considered soft base ligands. Likewise, certain metal ions such as Mn^{2+}, Cu^{2+}, Zn^{2+}, Ag^{+}, Ni^{2+}, Pd^{2+}, etc., are classified as soft acid centers, while others such as Al^{3+}, Fe^{3+}, Zr^{4+}, Cr^{3+},etc etc., are regarded as hard acid centers. Scheme II.1. depict some examples of organic linkers that feature coordination sites of nitrogen and oxygen.[8]

Among many, a crucial challenge for the synthesis of MOFs includes regulation of the formation of well-defined inorganic building blocks while avoiding the decomposition of the organic linker. Additionally, the control of crystallization kinetics is vital to promote the growth of crystalline MOFs phases for easy structural determination.[9] Typically, MOFs are synthesized in a solvent at temperatures ranging from room temperature to approximately 250 °C, with the energy input being provided through conventional electric heating or alternative means such as electric potential,

electromagnetic radiation, and mechanical waves (ultrasound).[10] In the following section, we will outline the trends in the synthetic methodologies of MOFs.

Scheme II.1. Few examples of organic linkers generally used for the synthesis of MOF.

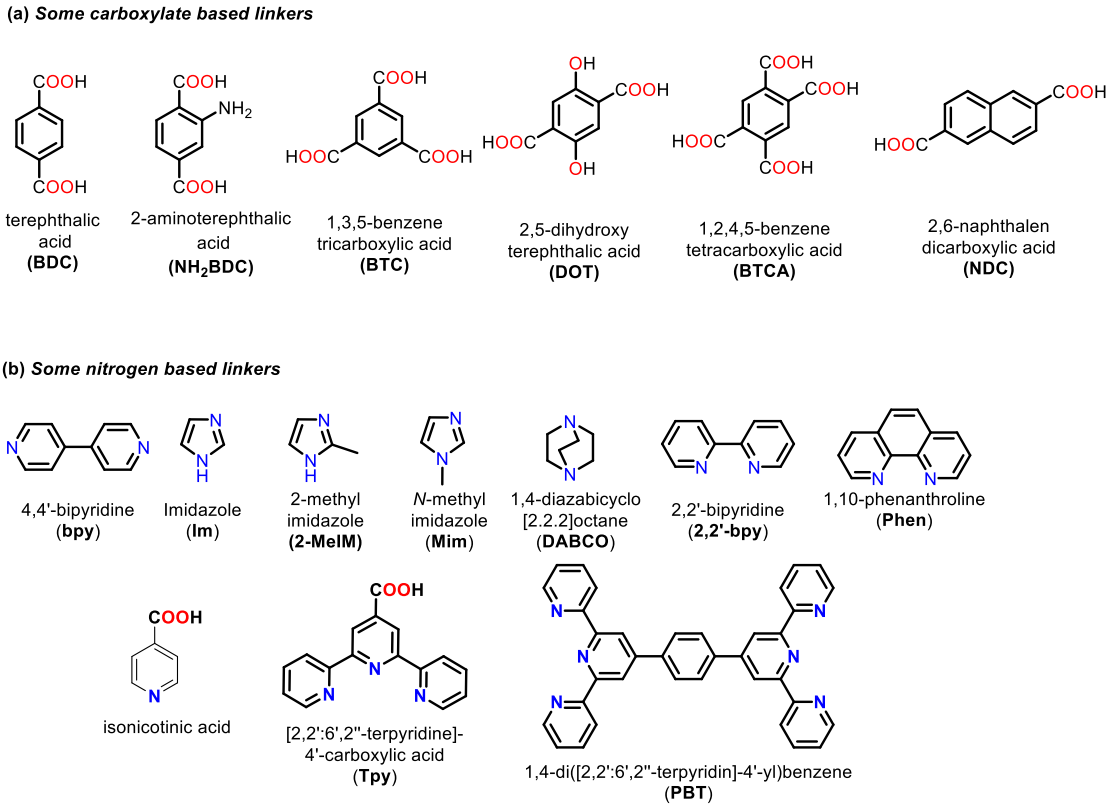

II.2. Synthetic Procedure for MOF

The conventional approach for synthesizing MOFs is through solvothermal (or hydrothermal) methods, which typically involve using an autoclave to perform reactions with organic solvents such as alcohols, formamides, sulfoxide, nitriles, and pyridine at high pressure and temperatures close to the boiling point of the solvent (around 100-250 °C).[11] Other techniques used to synthesize MOFs include room-temperature mixing, diffusion, sonochemical, electrochemical, mechanochemical, microwave-assisted, and continuous flow methods.[12–14] In the following section, we will provide a brief overview of these different synthetic methods for MOF synthesis.

II.2.1. The Solvothermal synthesis of MOF:

Solvothermal synthesis is a widely used method for synthesizing MOFs. This method involves the reaction of metal ions or clusters with organic ligands in a solvent under high-temperature and pressure conditions. A special reaction vessel is required to carry the solvothermal reaction that can withstand high pressure and temperature. For this, polytetrafluoroethylene (PTFE) lined or Teflon-coated containers inside a stainless steel autoclave are generally used. The various part of the PTFE-lined autoclave is shown in figure II.1.

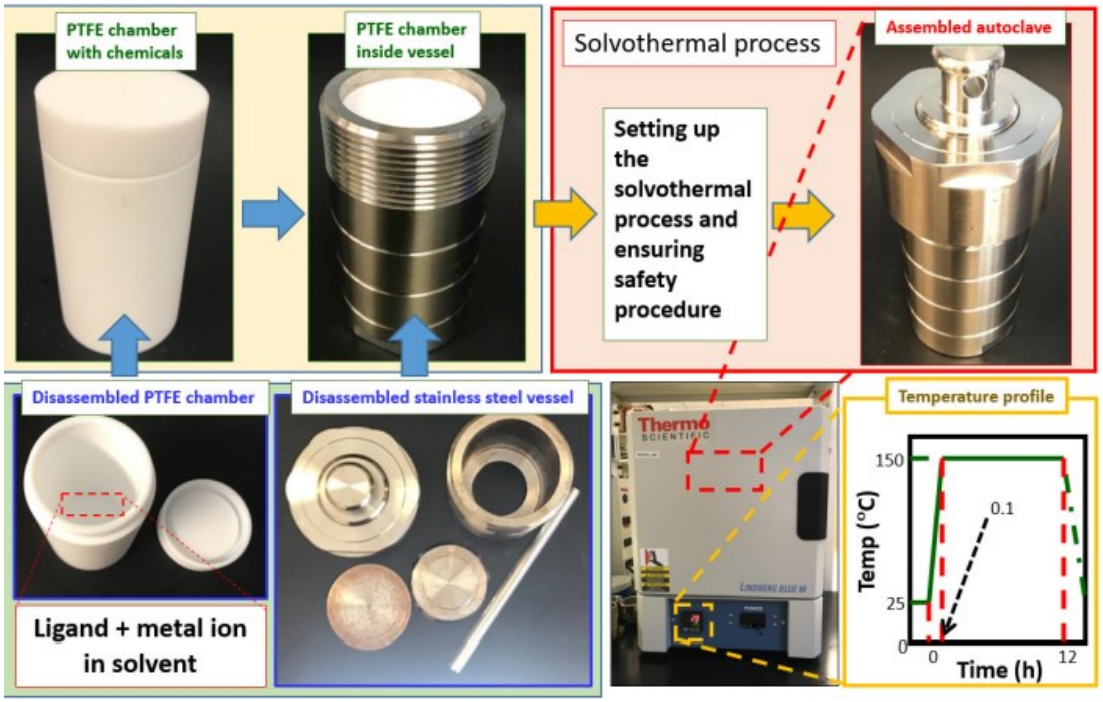

Figure II.1: Different part of PTFE lined autoclave.

In solvothermal synthesis, the solvent serves both as a reaction medium and a template for the formation of the MOFs. Typically, the reactants mixed together in a solvent or solvent mixture are taken in PTFE-lined containers that are sealed inside a stainless steel autoclave. The vessel is then heated in an oven at varied temperatures (typically between 80 to 250 ℃) under autogenous pressure for several hours. Programmable

muffle furnaces are mostly used during synthesis due to their precise temperature control and programmable setting. One can set the desired heating rate, isothermal temperature, duration, and cooling rate in the furnace's programming. Additionally, the ability to program the furnace to ramp up and down the temperature at specific rates is important for controlling the crystallization process. The high pressure and temperature conditions promote the nucleation and growth of MOF crystals by inducing the formation of coordination bonds between the metal ions or clusters and the organic ligands. The solvent also plays a critical role in the synthesis process by controlling the size and shape of the resulting MOF crystals.[15] Furthermore, apart from the solvents, the composition of SBU and thereby the architecture of MOF is also highly dependent on the type of metal ions, and ligand functionality. When metal nitrates are utilized as the metal precursor, the resulting interaction with the organic carboxylate linker can lead to the production of a substantial amount of HNO_3. This, in turn, can hinder the rapid formation of MOFs by causing their dissolution in an acidic solution, thus favoring slow re-crystallization. In contrast, the use of metal acetylacetonate salts in conjunction with carboxylate salts generates acetylacetonate, which has a milder pKa (8.8-9.0) in H_2O at 27 °C.[16] As a result, this combination does not significantly alter the rate of crystallization, and the time required for recrystallization can be reduced.[11,12] Monotopic linkers such as acetic acid, benzoic acid, and hydrogen fluoride are sometimes utilized as a modulator for the process of crystallization in MOFs. This is because they participate in forming bonds with the metal ion, thereby slowing down the formation of structural bonds.[17,18] In MOF synthesis, polar protic solvents are commonly used due to their higher solubility compared to metal salts. Generally, polar protic solvents, such as *N, N*-dimethylformamide (DMF) and *N, N*-diethylformamide (DEF) are used as they can initiate proton abstraction from organic linkers through self-

decomposition, forming amines.[19] To influence the rate of crystallization, co-solvents such as ethanol and water are often used alongside the primary solvent. The effect of solvent on the framework and properties of MOF was reported by Zang *et al.*[15] by synthesizing $Cu_3(BTC)_2$ MOF in an ethanol and water mixture. The formation of the crystalline $Cu_3(BTC)_2$ MOF was observed by the authors only when the ethanol content exceeded 30 vol%. Similarly, Halladj *et al.*[20] did not detect any ZIF-8 formation in water during its synthesis. However, the authors did observe the formation of ZIF-8 MOF only when DMF and methanol solvents were used. Vinu *et al.*[21] where synthesized novel 2D microporous Al-MOF (CYCU-7 and CAU-11) under hydrothermal and solvothermal conditions. The authors observed that MOFs synthesized by an ethanol-based solvothermal method exhibited a considerable level of linker-missing defects compared to those synthesized by the water-based hydrothermal method. Achieving optimal temperature and timing is also crucial in the solvothermal method to obtain high-quality crystals.[22,23] If the crystal is heated below 80 degrees, it may result in the formation of amorphous material. On the other hand, excessively high temperatures can lead to the formation of metal oxide. To date, this method has been used to synthesize various classes of MOFs (such as Fe-, Zr-, Cu-, and Zn-based MOFs), as detailed in the comprehensive review published recently.[10] With the main advantage of being able to produce high-crystalline MOFs single crystal and with high purity and narrow size distribution, suitable for large-scale production, the solvothermal method is one of the most preferred methods for MOF synthesis. The solvothermal method also has some limitations, e.g., it can be challenging to control the size and morphology of the MOF crystals. The high-temperature and pressure conditions used in this method not only limit the choice of solvent but also are time-consuming and energy-intensive.

II.2.2. Room temperature synthesis of MOFs.

A relatively convenient method for the synthesis of MOFs in bulk is the rapid synthesis through the addition of base resulting in rapid deprotonation of carboxylic acid, forming a powdered crystalline MOF at room temperature. Typically, this method involves the gradual introduction of a base such as triethylamine (TEA) into the metal-ligand mixture while constantly stirring to achieve a uniform particle size. This method is particularly suitable for organic linkers that are thermally less stable, such as acetylene dicarboxylic acid. For instance, IRMOF-0, ($Zn_4O(ADC)_4(Et_3N)_6$) a combination of Zn^{2+} ions and acetylene dicarboxylate (ADC) linker, is synthesized at room temperature due to the low stability of ADC.[24] This technique for the synthesis of MOFs is considered a green method as it is easy to carry out with less energy capital.[25] However, while it is rapid and scalable, it is not suitable for generating diffractable single-crystals at room temperature. Alternatively, a sub-group of room-temperature synthesis involves the slow evaporation of the reaction mixture consisting of lower boiling point solvents at a critical concentration, which may result in the formation of diffractable single-crystals over a long time of exposure.

II.2.3. Diffusion method for MOF synthesis.

The diffusion method is an alternative to the solvothermal method for obtaining diffractable crystals at or below room temperature. There are two types of diffusion methods: vapor diffusion and layering method, as shown in figure II.2. The vapor diffusion method of synthesizing MOFs involves using two vials of different sizes. The smaller vial contains the solution of metal salt while the larger vial is equipped with the amine and serves as a shield. Slow deprotonation is initiated by the slow deposition of amine vapor, which slows down the reaction and the crystallization process. Whereas the layering technique relies on the formation of crystals at the interface of two solvents.

One solvent (containing metal) is added to create a distinct layer over another solvent (containing ligand). creating an interface of two organic solvents Crystals are generally formed at the interface due to the slow diffusion at the junction. This technique has been used to prepare MOFs such as ZIF-8 ([$Zn(MeIM)_2$], MeIM= 2-methylimidazole),[26] ($Ni_3Co_1)_3Fe_1$-MOF,[27] and MOF-199 [$Cu_3(BTC)_2$].[28] The diffusion method is an important synthetic technique for obtaining single-crystals of MOFs, particularly when the reaction in an autoclave produces either an amorphous or gel-like substance instead of crystals.

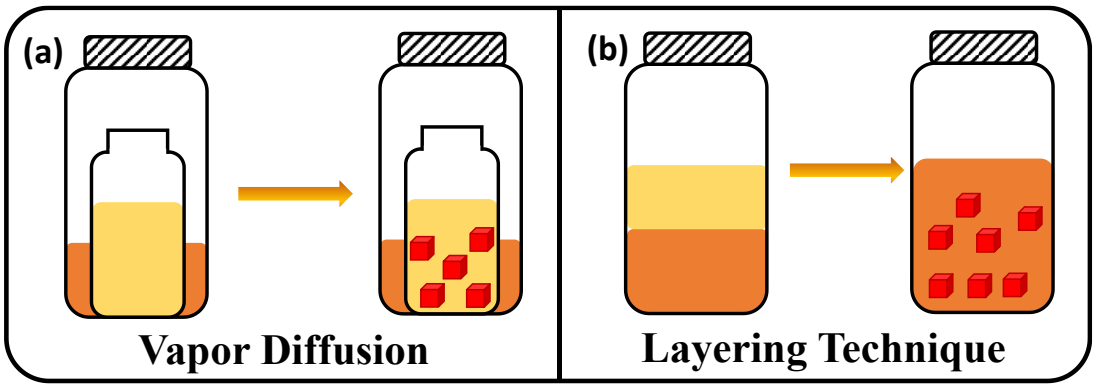

Figure II.2: Illustration of (a) vapor diffusion and (b) layering technique for MOF synthesis.

II.2.4. Sonochemical method for synthesis of MOFs.

The sonochemical method uses high ultrasonic frequencies (20-40 kHz) and is fluently used in MOF synthesis (Figure II.3).[12] Nevertheless, since the wavelength of ultrasound is considerably larger than the size of molecules, the direct interaction of ultrasound radiation with reactants to create or break chemical bonds is not possible. However, during the ultrasonic energy, the formation of tiny bubbles is generated due to the acoustic pressure being lower than the vapor pressure of the solution.[12] These microbubbles then collapse adiabatically, releasing a significant amount of energy, which in turn causes a short-term increase in both temperature and pressure within the

system.[29] Consequently, the accelerated rates of nucleation and crystal growth caused by this process significantly reduce the reaction time required for MOF crystal formation. Also, an increase in solvent vapor pressure leads to a decrease in the sonochemical reaction rate, therefore often high boiling point solvents such as DMF are used for this method.[30]Kim *et al*. utilized the sonochemical method to synthesize MOF-177 ($ZnO_4(BTB)_2$, BTB= 1,3,5-benzenetribenzoate) using *N*-methyl pyrrolidone, which resulted in the production of high-quality micro-crystals of size 5–50 μm in a relatively short amount of time (35 min) compared the solvothermal method that required 48 h.[31]

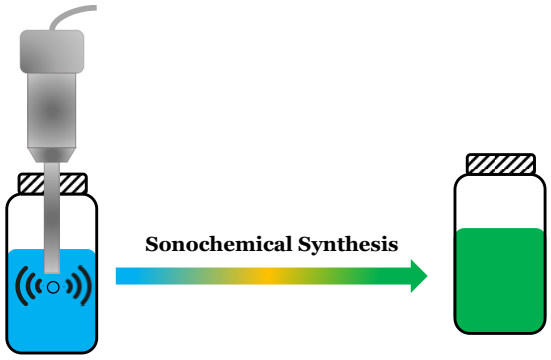

Figure II.3: Sonochemical synthesis of MOF.

II.2.5. Micro-wave assisted method for synthesis of MOFs.

Large-scale production of MOFs can pose a challenge due to the extended preparation time involved and thus microwave-assisted synthesis offers a solution.[32] By utilizing microwave irradiation, the polar molecules rotate and produce thermal energy, which triggers chemical reactions. Among the wide microwave frequencies range the 2.45 GHz (12.2 cm) frequency is used in laboratory-scale reactions due to its optimal penetration depth. The solvothermal synthesis conditions frequently employed in MOF production can be adapted to microwave-assisted synthesis as long as the reaction

mixture absorbs microwave energy. Due to an enhanced nucleation rate resulting from direct heating of the reactants, this approach results in a considerably shorter MOF formation time (less than an hour) than conventional solvothermal methods, However, the high microwave energy (800-1000 W) may lead to the formation of MOFs in the form of fine or poorly crystallized powder, which may not be suitable for practical use. Consequently, it is crucial to optimize the irradiation power and reaction time to regulate the particle size and crystallinity of the MOF materials.[33] Nguyen *et al.*[34] recently reported the synthesis of zirconium-based, MOF Zr-NDC (NDC= 2,6-naphthalene dicarboxylate) by heating 10 mL DMF homogeneous mixture of $ZrCl_2$ NDC and acetic acid at 120 °C, 90 W for 3 min. The Zr-NDC MOF synthesized has a size of 100 nm and a highly defective framework with a missing linker. With high defect content, it was efficiently applied to the adsorption of organic dye. However, because of the intricate distribution of the MW field, hot spots emerge within the MW reactor, which in turn causes localized overheating, ultimately hindering the favorable nucleation and growth of MOF crystals. To overcome this issue, *Zhou et al.*[35] employed numerical simulation to achieve a well-informed design for MW-assisted synthesis that effectively eliminates these hot spots. The experimental set up done by Zhou *et al.* for MW synthesis of MOF was shown in figure II.4 where they reported the synthesis of MIL-88B Fe. In their experimental set up the MW was produced using a continuous variable generator and was then conveyed through a waveguide into the MW cavity. The cavity featured a glass flask that was positioned in the center, comprising a tank with a capacity of 250 mL designed for holding the liquid samples, along with an outer jacket intended for accommodating the coolant, specifically polydimethylsiloxane. To guarantee the stability of the coolant temperature, the volume of the outer jacket was

three times that of the reactant solution. The jacket was linked to a circulating oil bath machine, which was utilized to maintain the oil temperature at the desired level.

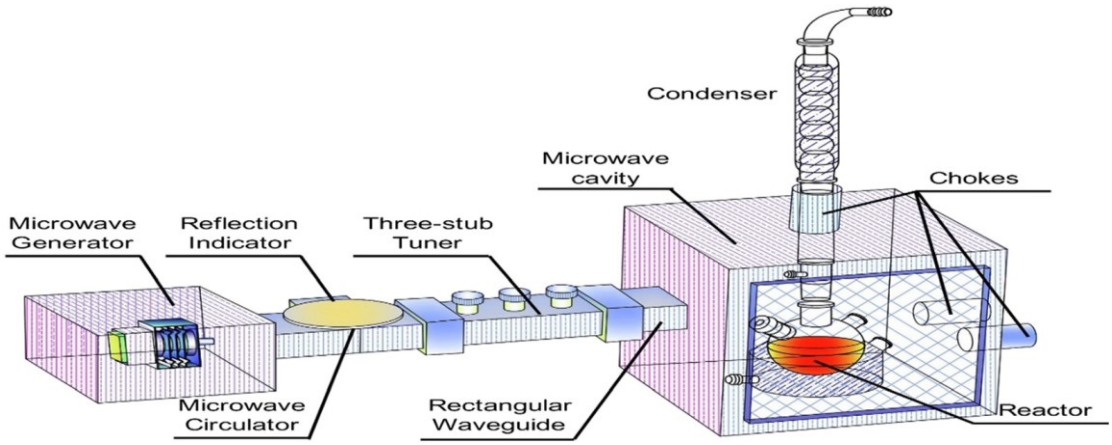

FigureII.4: Experimental set up of microwave synthesis of MIL-88B Fe as reported by Zhou *et.al.* Reprinted with permission from ref. [35] Copyright 2022, Elsevier.

II.2.6. Mechanochemical method for synthesis of MOFs.

The mechanochemical synthetic method uses mechanical force instead of traditional sources of energy such as heat, light, or electricity for activating chemical reactions. In this approach, the energy required to initiate the chemical reaction is provided by mechanical force, often through techniques such as grinding, milling, or shearing.[36] With the use of mechanical force, this method offers several advantages, including the ability to perform reactions at room temperature and the avoidance of solvents. This method is also a non-equilibrium process as it relies on the collision of reactants, leading to rapid mass transfer and swift crystallization. However, the method is unlikely to produce single crystals due to the nature of the reaction. Also, achieving the desired product in a shorter time is heavily dependent on the milling speed, and therefore inadequate milling (insufficient active collisions) may lead to no /partial reaction.

Although raising the milling frequency may promote the formation of the desired product, it can also result in the generation of undesired by-products due to a significant rise in the system's temperature.[37] To prevent the formation of impurities, small amounts of additives such as ethanol or salts are added to enhance the reaction time while maintaining the optimal milling speed.[19]

II.3. Characterization techniques of MOFs:

Designing a MOF with specific functionalities involves three broad stages: ligand synthesis (in case of commercially unavailable ligands) followed by MOF synthesis, and lastly their characterization. Initially, synthesizing organic linkers, whether known or novel and characterizing them properly through various spectroscopic techniques is critical. These linkers are then utilized to optimize the synthesis of MOFs, which are again dependent on various parameters as discussed earlier.

To fully characterize a MOF material, it is necessary to use multiple techniques and protocols. For the crystal structure determination of MOFs, single-crystal X-ray diffraction analysis is considered the most crucial tool. The most reliable way to accurately identify the structure of a MOF is to use single crystal X-ray diffraction (SCXRD). It can provide information about the unit cell dimensions, the orientation of the crystal lattice, and the arrangement of atoms and molecules within the crystal. However, like any other material, the quality and size of the crystal grown is the primary factor limiting the collection of trustworthy data. Typically, crystals should be larger than 5-10 μm, but this can be sometimes difficult to achieve for certain families of MOFs. In addition, the use of powder X-ray diffraction (PXRD) techniques is valuable, as experimental PXRD data can complement the PXRD patterns simulated from SCXRD analysis. This can help to confirm the product formation and phase purity of

the synthesized material in bulk.[38] In cases where it is not possible to grow single crystals of MOFs, the structure can still be determined using PXRD data, although this is generally a more difficult process. To date, there have been several successful methods, either used alone or in combination, to solve the crystal structure of MOFs using powder diffraction.[39] In certain cases, the structure of MOFs has been determined through direct methods applied to powder data. An example of this is UiO-66, as reported by Cavka *et al.*[40] which was solved using direct methods (included in EXPO2013),[41] based on high-quality diffraction data collected with synchrotron radiation. Spectroscopic techniques such as Fourier-transform infrared spectroscopy (FTIR) and solid-state nuclear magnetic resonance (NMR) spectroscopy can be used to determine the chemical composition and bonding environment in MOFs. FTIR is particularly useful in identifying functional groups of organic linkers before and after coordination with meta nodes of MOF. Therefore, a good practice is to compare the FTIR spectra of the free ligand to that of synthesized MOF and observe the shift of the functional group of linkers. For example, the BTC ligand is a commonly used ligand for MOF synthesis and it shows the characteristics peak at 1700 cm^{-1} due to the stretching frequency of C=O. However, in HKUST-1 MOF the C=O frequency arises at 16 cm-1. Generally, after the coordination, there is a decrease in bond length thereby bathochromic shift of coordinated functional groups can be expected. Furthermore, solid-NMR may be useful as it gives information on the coordination and chemical environment of metal ions. Thermal stability is one of the important properties of MOF it can be effectively determined By utilizing thermogravimetric analysis (TGA). Not only the thermal stability but one can also analyze the composition and the exclusion of labile ligands and absorbed solvents. Additionally, differential scanning calorimetry (DSC) can also be employed to investigate the thermal behavior of MOFs, such as their

phase transitions and thermal energy. To confirm the chemical stability of MOFs, one can subject them to various chemicals and then perform PXRD analysis on the treated samples, which can be matched to the simulated PXRD. Further, one can also conduct elemental CHN analysis on the treated samples. The potential of MOFs as porous coordination polymers in the field of gas adsorption, storage, and sensing is enormous. Therefore, it is crucial to utilize gas adsorption measurements, such as nitrogen sorption, to understand the porosity of MOFs, including the surface area, pore size distribution, and pore volume. These measurements are typically carried out at different temperatures (generally at lower temperature with the use of liquid N_2) to evaluate the impact of temperature on gas adsorption. The structural properties of MOF can further characterized using electron microscope images. Scanning electron microscopy (SEM) is a powerful imaging technique that can provide high-resolution images of the surface of MOFs. The technique works by scanning a beam of electrons over the surface of the MOF, and detecting the electrons that are scattered back. The resulting image provides a detailed view of the surface morphology, particle size, and distribution of the MOFs. Transmission electron microscopy (TEM) is another imaging technique that can provide even higher resolution images of the internal structure of MOFs. TEM works by passing a beam of electrons through the MOF, and measuring how the electrons are scattered as they pass through. The resulting image provides a detailed view of the internal structure of the MOF, including its porosity and crystal structure. Both SEM and TEM are commonly used in MOF research to investigate the morphology and structure of MOFs. They can be used to identify the size and shape of MOF particles, and to study the effects of post-synthetic functionalization on the morphology and structure of MOFs. These techniques are particularly valuable for studying the behaviour of MOFs in real-world applications, such as gas adsorption and catalysis,

where the morphology and structure of MOFs can have a significant impact on their performance. Depending on the specific properties of the MOF being studied, other techniques such as X-ray photoelectron spectroscopy (XPS), atomic force microscopy (AFM), or Raman spectroscopy, among others, may also be utilized. It is to be noted that none of the single characterization technique provide the detailed information about the over properties of MOF. However, when different techniques were used in conjunction, a more comprehensive understanding of the chemical and physical properties of MOFs can be understood. The various property and its associated characterization techniques is summarized in table II.1 below.

Table II.1: Summary table for MOF property and characterization to be performed.

Sl No	MOF property	Characterization technique
1.	Crystallinity and structure refinement	Single crystal X-ray diffraction, Powder X-ray diffraction,
2.	Phase purity, Bulk Purity	NMR, FT-IR, PXRD compared to SCXRD
3.	Elemental composition	ICP-OES, Elemental CHN analysis, SEM-EDX
4.	Thermal stability	TGA, variable temperature PXRD
5.	Chemical stability	Treating MOF with chemicals and performing PXRD, EDX, SEM, CHN
6.	Surface area	N_2 BET surface area analyzer
7.	Particle size distribution	DLS, SEM, TEM
8.	Coordination of ligands	FT-IR, Raman
9.	Morphology	SEM, HRTEM

In this chapter, we present various methods such as ultra-sonication, room temperature, and solvothermal synthesis for the synthesis of MOFs. The study focuses on the synthesis and characterization of several important MOFs that are crucial for understanding the catalytic properties of MOFs. The MOFs were thoroughly analyzed

using techniques such as SCXRD, PXRD, elemental analysis, TGA, FTIR, SEM, and BET surface area analysis. The study also includes the synthesis of new 1D and 2D MOFs that explore the concept of growth restriction in MOFs and are compared with existing materials for use as catalysts. All of the synthesized MOFs, including the novel ones, have been studied for their catalytic properties in coupling reactions. Some of the synthesized MOFs were also used as a template to derive metal composites for application in the electrocatalytic oxygen process.

II.4. Results and Discussion:

With discussions made so far in this thesis, it can be understood that MOFs have the potential to be a profitable material for use in maximum organic reactions, making them a promising candidate for heterogeneous catalysis. Further with their intriguing structural properties and large pore volume, MOFs have established themselves as an interesting altruistic template for the synthesis of metal composites. Therefore, the main focus of this thesis work is to design a robust heterogeneous catalytic system using MOFs and MOF-based materials for organic and electrocatalytic reactions. To accomplish this, we began our research by synthesizing known MOFs that have the potential for practical applications. Here after, in this chapter, the discussion is categorized into two sections where in the first part the synthesis of reported MOF and their characterization has been discussed. Similarly in the second section, the design, synthesis, and characterization of novel MOF has been meticulously discussed.

II.4.1 Synthesis of Known Metal-Organic Frameworks.

II.4.1.1 Synthesis of HKUST-1 MOF:

The synthesis of HKUST-1 (HKUST= Hong Kong University of Science and Technology) was conducted following the method reported by Schlichte *et al*., with a

slight modification on the isothermal temperature.[42] The illustrate general synthesis process is illustrated in scheme II.2.

Scheme II.2. Reaction Scheme for the synthesis of HKUST-1.

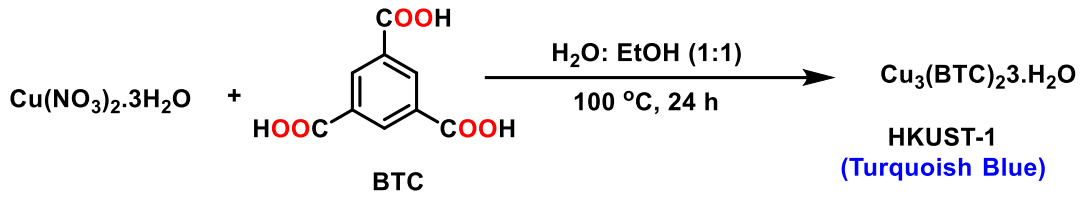

A solvothermal method was performed for the synthesis of HKUST-1 MOF. Typically, 0.42 g of benzene tricarboxylic acid (BTC) or trimesic acid, (2 mmol), was taken in a vial and dissolved in 6 mL of ethanol through sonication. In another vial, 0.875 g of $Cu(NO_3)_2.3H_2O$, (3.62 mmol) was dissolved in 6 mL of H_2O. The two solutions of two vials were mixed together and transferred in PTFE lined autoclave and kept in a preheated hot air oven at 100°C for 22 h. After the reaction was cooled down to room temperature turquoise blue crystalline material was obtained. The material was filtered, washed with ethanol, and subjected to solvent exchange with acetone multiple times for 24 h. The product was dried at 100 °C and PXRD was performed to match the reported data (Figure II.5).

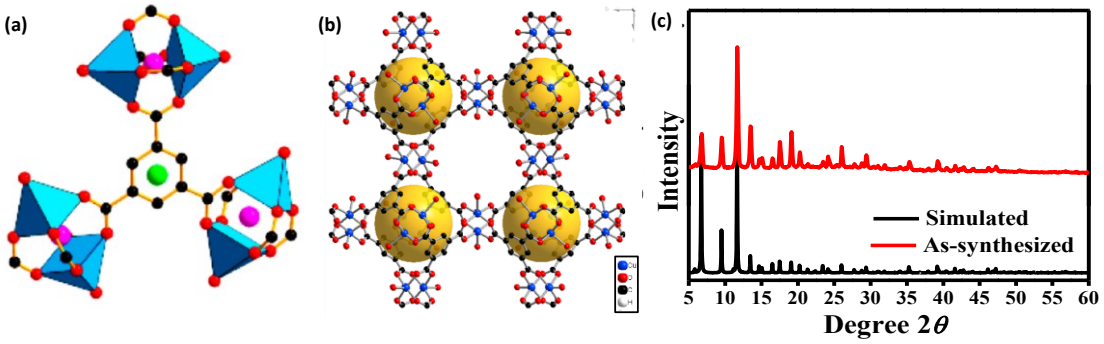

Figure II.5: (a) The three-paddle wheel SBUs linked with organic ligand BTC in HKSUT-1. (b) The polymeric framework of HKUST-1 was drawn using the reported *cif* file from CCDC: 987873 and (c) The PXRD patterns of the simulated and synthesized HKUST-1 MOF.

The analysis of HKUST-1 using PXRD at a temperature of 298 K and a Cu source with a wavelength of 1.54 Å exhibited excellent correspondence with the simulated PXRD patterns. This outcome indicates that the desired material was synthesized successfully with a high degree of purity. Additionally, the FT-IR was also measured using a KBr pallet, and the spectra of the catalyst are in agreement with the reported data, with a maximum absorption of 3433 (b), 1646 (s), 1587 (w), 1448 (m), 1371 (m), 1112 (m), and 727 (m).

II.4.1.2. Synthesis of Cu-BDC MOF

Cu(BDC) MOF or MOF-2 (Cu) is one of the well-known MOFs and it has been synthesized following the reported procedure by Tannenbaum *et al.* with slight changes in procedure modifications.[43]A general reaction scheme has been illustrated in scheme II.3.

Scheme II.3. General reaction for the synthesis of **Cu-BDC MOF**.

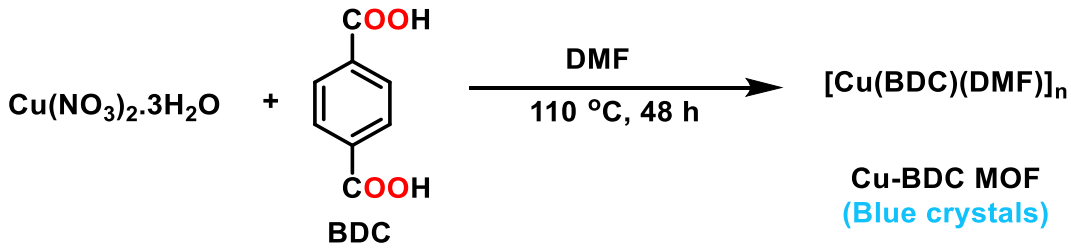

Typically, 80 mg of terephthalic acid (0.5 mmol) was completely dissolved in 6 mL of DMF. In another vial, 121 mg of $Cu(NO_3)_2 \cdot 3H_2O$ (0.5 mmol) was also dissolved in 6 mL of DMF. The resulting salt solution was added to the vial containing the BDC solution, and the mixture was stirred for 2 min. The entire solution was then transferred into a 25 mL PTFE-lined autoclave and kept in a preheated hot air oven at 110°C for 48 h.

After the reaction was cooled down to room temperature blue crystalline material was obtained that was thoroughly washed with DMF to dissolve the unreacted ligand. The washing was also done several times with methanol followed by acetone and the material was dried completely before characterization. The SBU of Cu-BDC MOF containing paddle wheel structure has been shown in figure II.6a. The PXRD analysis of Cu-BDC recorded at a temperature of 298 K using a Cu source with a wavelength of 1.54 Å exhibited perfect resemblance with the simulated PXRD patterns, indicating the successful synthesis of the desired material (Figure II.6b).

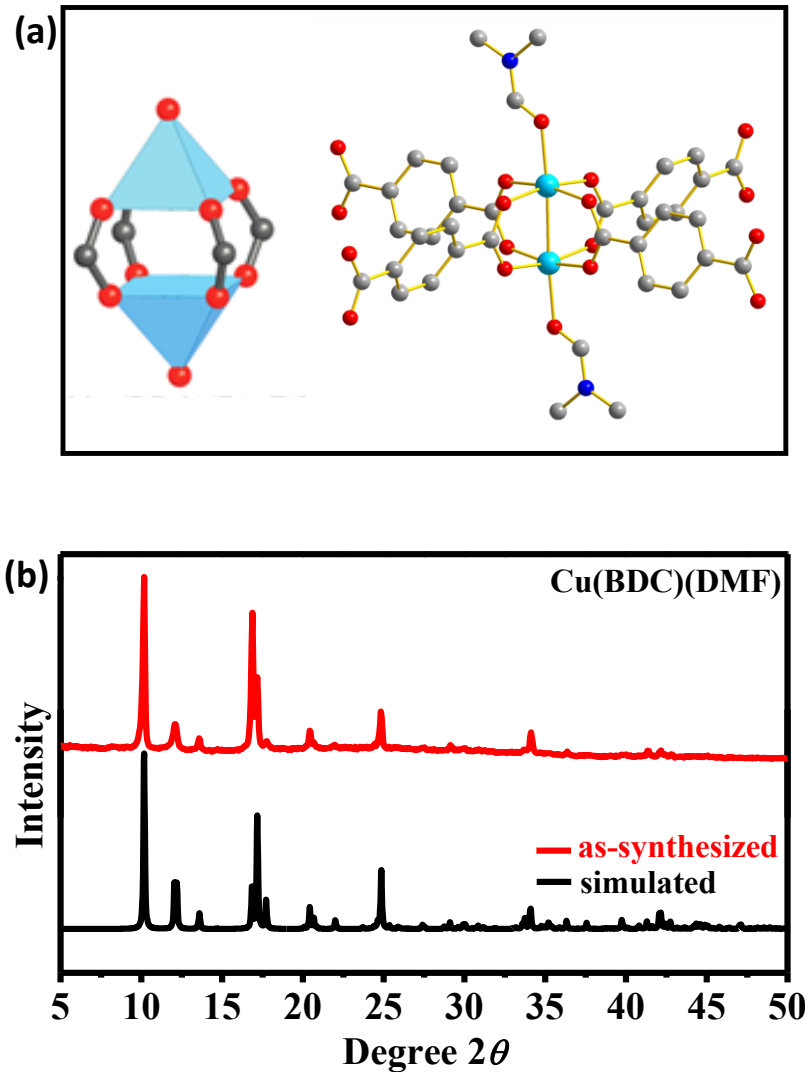

Figure II.6: (a) SBU of Cu-BDC MOF Cu-paddle wheel structure (b) The PXRD of the simulated and synthesized Cu-BDC-MOF. Derived from *cif* file with CCDC: 1444330.

II.4.1.3. Solvothermal synthesis of M-MOF-74

The MOF-74 series of MOF was synthesized solvothermal method following the reported procedure.[44] The general scheme followed for the synthesis of M-MOF-74 has been depicted in scheme II.4.

Scheme II.4: General reaction for the synthesis of **M-MOF-74** (M=Cu, Ni, Co, Mn).

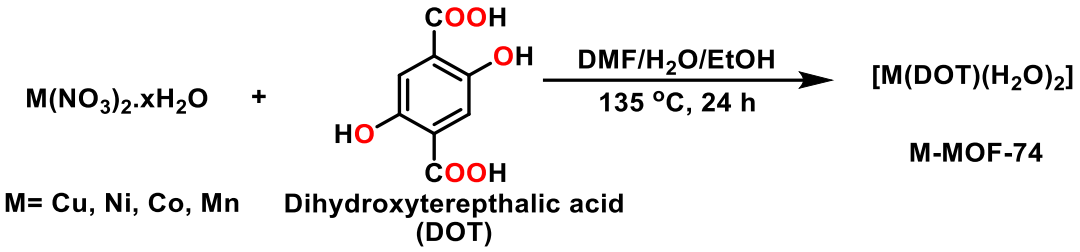

Typically, $M(NO_3)_2 \cdot xH_2O$ (M=Cu, Ni, Co, Mn) (1.11 mmol) and 2,5-dihydroxy terephthalic acid (0.336 mmol) was dissolved in a 30 mL 15:1:1 mixture of DMF/EtOH/H_2O in a glass vial using sonication. The vials were tightly capped, and subjected to 135 ºC in an oven for 24 h. Following the reaction, the mixture was allowed to cool to room temperature and crystalline material was obtained. The blue, green purple, and brown, colored crystalline material was obtained from the vial containing metals such as Cu, Ni, Co, and Mn respectively. The SBU as shown in figure II.7a is connected by a DOT ligand and a polymeric framework with a large pore diameter is formed in M-MOF-74 (Figure II.7b). The resulting crystalline substance was characterized by PXRD analysis using a Cu source (1.54 Å) at 298 K and compared with the reported data (Figure II.7c). The PXRD patterns of the simulated *cif* file (CCDC: 270293) showed a higher resemblance to all isostructural MOF-74 samples, indicating successful synthesis of the desired material. The MOF was washed with methanol a few times and then heated at 120 °C under a dynamic vacuum before being used as a catalyst.

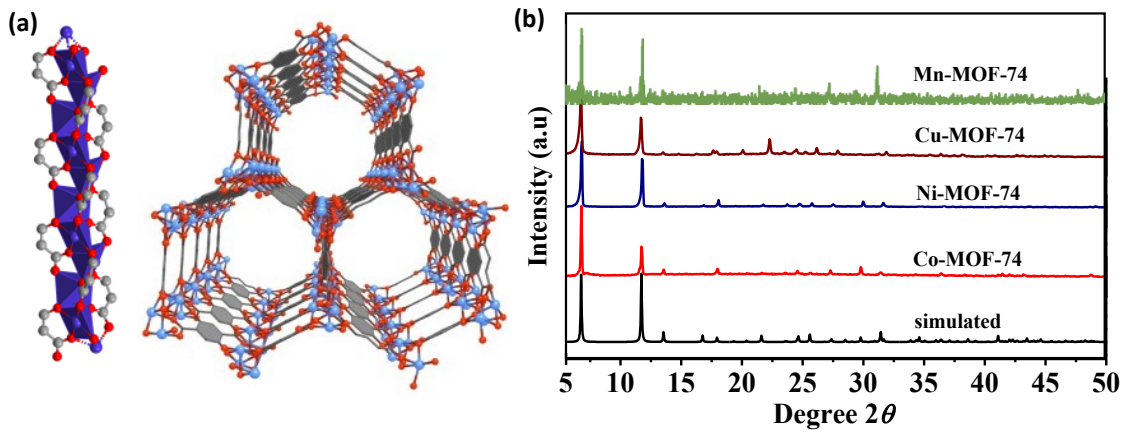

Figure II.7: (a) The porous channels (12 Å) of MOF-74 polymeric framework and (b) M-MOF-74's (M= Co, Ni, Cu, and Mn) simulated and as-synthesized PXRDs comparison.

II.4.1.4. Synthesis of MIL-100 (Fe) – RT:

A MIL-100 (Fe) MOF (MIL= Matériaux de l'Institut Lavoisier) was prepared by the reported room temperature method by Guesh *et al*.[45] A general scheme followed for the synthesis of MIL-100 (Fe) MOF has been illustrated in scheme II.5.

Scheme II.5: General reaction for the synthesis of MIL-100 (Fe)

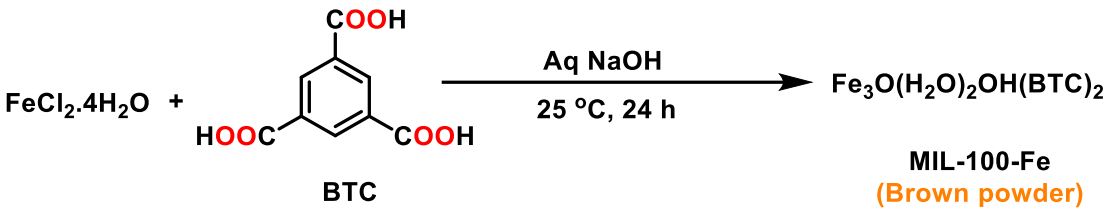

At first, the solution of trimesic acid (1.676 g, 7.6 mmol) was dissolved in 22.8 mL of 1 M aqueous NaOH (0.912 g, 11.3 mmol). Similarly, a second solution was prepared by dissolving $FeCl_2.4H_2O$ (2.26) in 77.2 mL of water, which was then stirred until a clear solution was formed. The BDC solution was slowly added dropwise to the $FeCl_2.4H_2O$ solution, and the resulting reaction mixture was constantly stirred at room

temperature for 24 h. The mixture was then washed with water and ethanol before being dried under vacuum to yield an orange-colored product. The polymeric unit of MIL-100 (Fe) has been represented in figure II.8a. The synthesized compound was analyzed using PXRD analysis, which showed a good match between the diffracted patterns of the as-synthesized material and the simulated patterns (Figure II.8b).

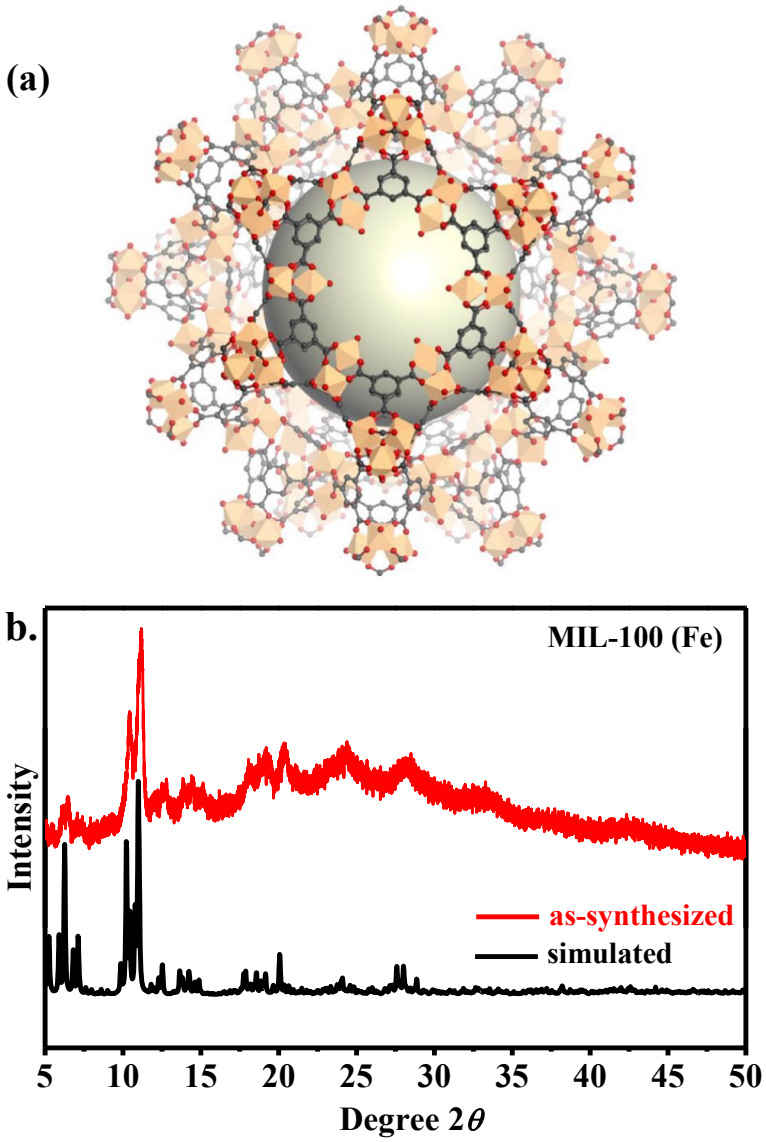

Figure II.8: ((a) The polymeric framework of MIL-100 (Fe), Reproduced from ref. [46] with permission from the Royal Society of Chemistry and (b) A comparative PXRD patterns of MIL-100 (Fe) between experimental and simulated from *cif* file CCDC 640536.

II.4.1.5. Synthesis of ZIF-8 and ZIF-67:

The Zeolitic imidazolate frameworks (ZIFs) are the category of metal-organic frameworks (MOFs) that shares the same topology as zeolites.[47] The two ZIFs containing Zn and Co metal are well known as ZIF-8 and ZIF-67. These two frameworks have been prepared using the reported room temperature synthesis technique as reported by Gross *et al.*[48] A general reaction scheme followed for the synthesis ZIF-MOF has been illustrated in scheme II.6.

Scheme II.6: General reaction for the synthesis of zeolitic imidazolate frameworks.

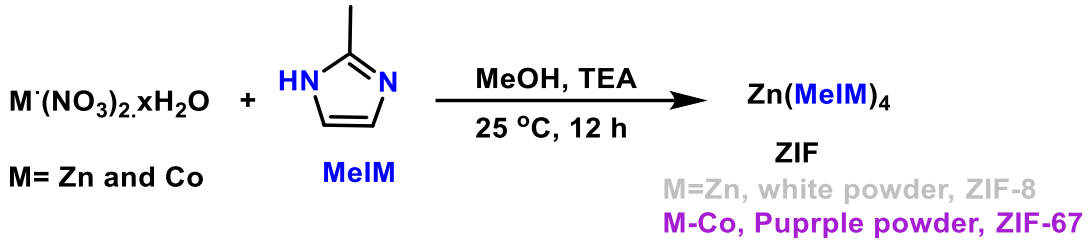

A solution containing 2.46 mmol of $M(NO_3)_2 \cdot 6H_2O$ (M= Zn, Co) was prepared by dissolving it in 50 mL of deionized (DI) water. In a separate container, a mixture of 1.622 g of 2-methyl imidazole (MeIM) (19.75 mmol) and 2.00 g of TEA (triethyl amine) (19.76 mmol) was dissolved in 50 mL of DI water by stirring. The meatal salt solution was then added to the stirred MeIM/TEA solution, resulting in an immediate formation of white or purple suspension. This suspension was then stirred for 10 min and the mixture was separated through centrifugation, the supernatant was decanted, and the solid was re-suspended in DI water. The ZIF remained in the water for 12 h, was separated through centrifugation, and re-suspended in DI water again. After another 12 h, the ZIF suspension was centrifuged, and the solid was collected and dried in the air in a 110 °C oven. Finally, the sample was dried under vacuum at 150 °C for

1 h prior to PXRD characterization. The agreement between the PXRD patterns and the simulated patterns, as shown in Figure II, confirms the formation of ZIF-8 and ZIF-67.

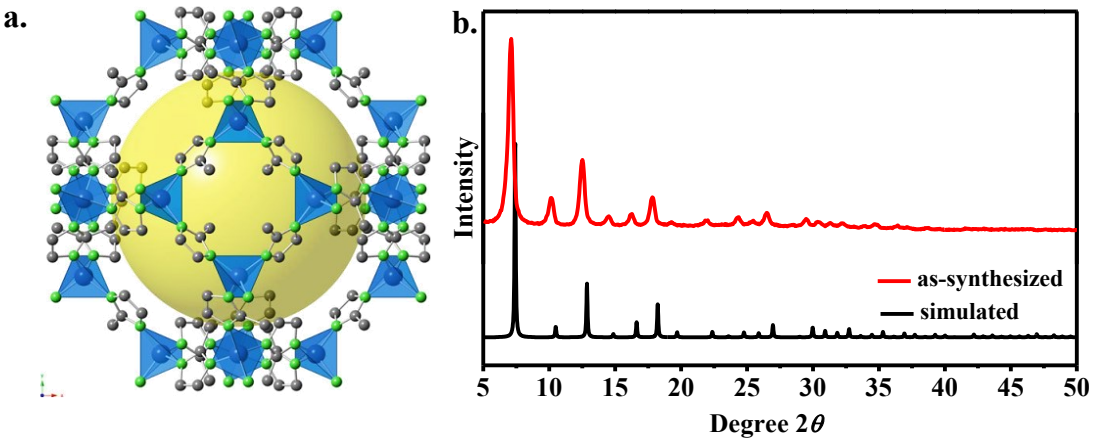

Figure II.9: (a) The polymeric structure of ZIF-8 and (b) A comparative representation of PXRD patterns of as-synthesized (red) and simulated (black) ZIF-8 (CCDC: 864309).

II.4.1.6. Synthesis of Mn-SKU-1 MOF:

The synthesis of both **Mn-SKU-1**(*SKU= Sikkim University*) was carried out using a reported procedure. The general reaction scheme for the synthesis of Mn-SKU-1 has been described in scheme II.7.

Scheme II.7: Reaction scheme for the synthesis of Mn-SKU-1 MOF

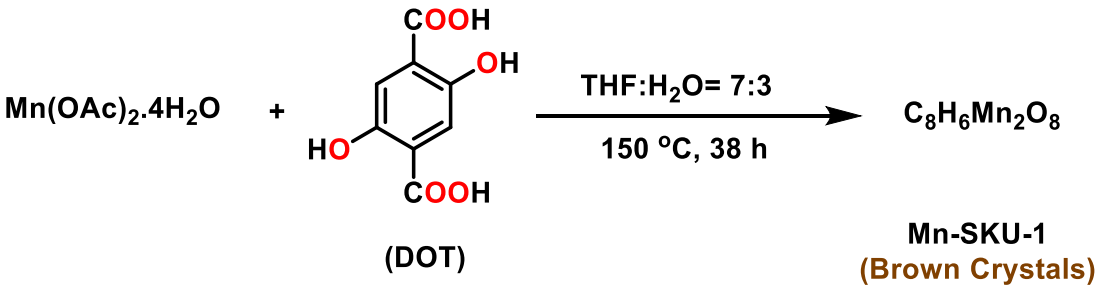

Following the conventional solvothermal method, **Mn-SKU1** MOF was synthesized by preparing two separate solutions of $Mn(OAc)_2 \cdot 4H_2O$ (0.244 g, 1.0 mmol) in 5 mL distilled water and DOT (0.099 g, 0.5 mmol) in 5 mL THF with further sonication for

approximately 5 min. The solutions were mixed together and then transferred to a PTFE-lined autoclave (20 mL) and placed inside a programmable muffle furnace. The furnace was programmed to heat initially at 0.63 °C per min for up to 150 °C and was then kept isothermal at 150 °C for 38 h. After the reaction time, the autoclave was allowed to cool to room temperature which resulted in the formation of fine brown-colored crystals. The product was then washed with THF, water, and ethanol and dried overnight under a vacuum at 120 °C. Yield: 61 mg; FT-IR**:** 3400, 1650, 1386 cm^{-1}; Elem. anal. Calcd: C, 28.26; H, 1.78. Found: C, 28.67; H, 1.88. The polymeric unit and accessible pores in Mn-SKU-2 MOF was shown in figure II.10a-b. The PXRD performed and matched with simulated data shows excellent bulk purity of the synthesized sample (Figure II.10c).

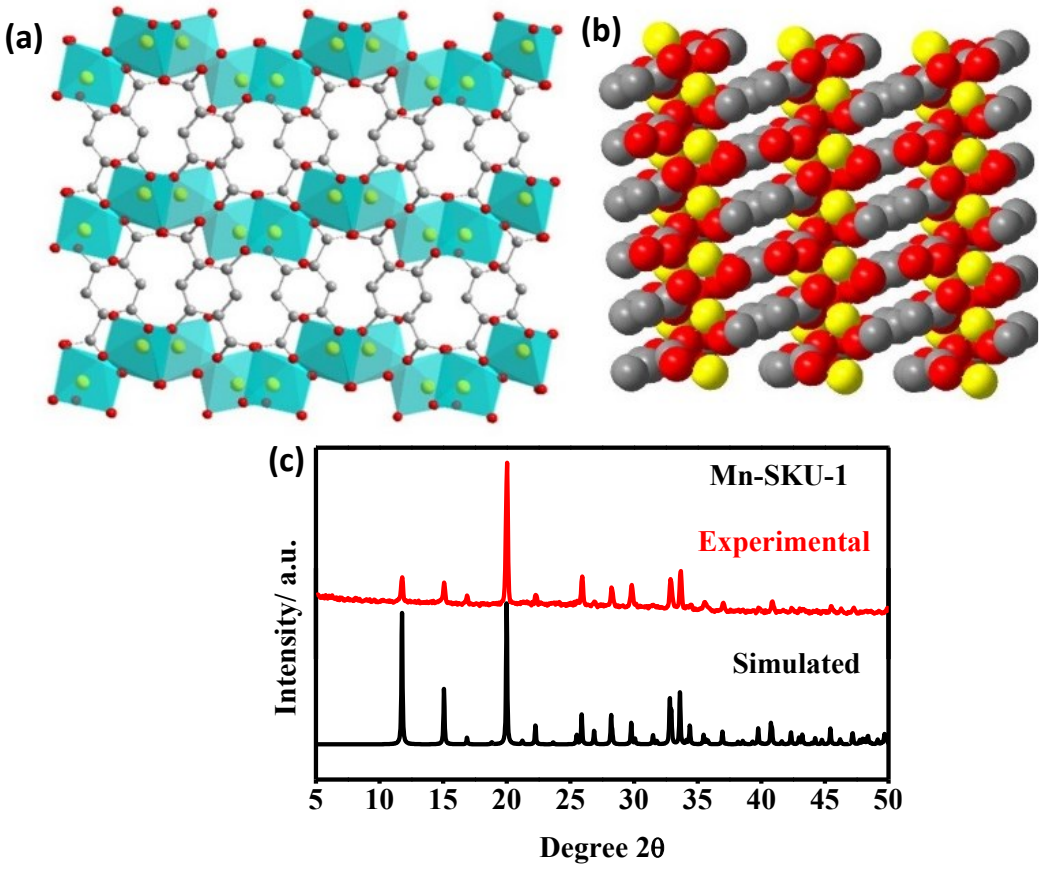

Figure II.10: (a) Illustration of polymeric network of Mn-SKU-1 (b) accessible voids in Mn-SKU-1 (c) Comparative PXRD patterns of Mn-SKU-1 with the simulated patterns (CCDC No: 2165378).

II.4.1.7. Synthesis of Mn-SKU-2 MOF:

Following the similar solvothermal method as that of Mn-SKU-1 and introducing 4,4' bipyridine ligand on the reaction system, Mn-SKU-2 was synthesized as shown in scheme II.8.

Scheme II.8: Reaction scheme for the synthesis of Mn-SKU-2.

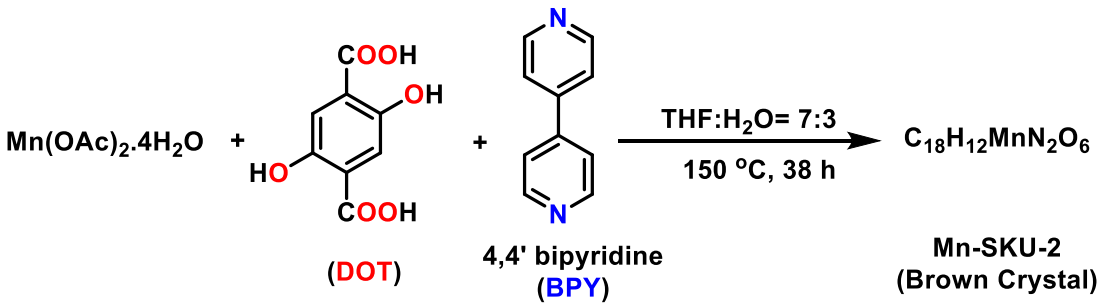

In general, a solution of Mn(OAc)2·4H2O (0.122 g, 0.5 mmol) was typically dissolved in 5 mL of distilled water. Additionally, two distinct solutions of 2,5-dihydroxyterephthalic acid (0.099 g, 0.5 mmol) and 4,4'-bipyridine (0.078 g, 0.5 mmol) were also made in 5 mL of THF each. Following sonication for around 5 minutes, the aforementioned solutions were moved to a 20 mL Teflon-lined stainless-steel autoclave and subjected to heat inside a programmable muffle furnace. The heating rate of the furnace was configured to 0.63 °C per minute until it reached 150 °C, where it was held for a duration of 38 h. After the furnace cooled to room temperature, it produced fine, brown-colored crystals. These crystals underwent washing procedures with THF, distilled water, and ethanol before being dried overnight under a vacuum at 120 °C. The yield was 105 mg and the FT-IR values were 1590, 1486, and 1290 cm-1. The calculated elemental analysis showed C, 53.09; H, 2.97; N, 6.88, while the found values were C, 52.99; H, 3.30; N, 6.29. The SCXRD analysis shows that the Mn-SKU-2 has

large void (Figure II.11a) enough for catenation of another similar framework in it thereby generating 3D→3D interpenetrating framework. The interpenetrating unit of Mn-SKU-2 is illustrated in figure II.11b. The PXRD collected for the synthesized sample shows a similar pattern as that of the simulated data showing the excellent bulk purity of the synthesized sample (Figure II.11c).

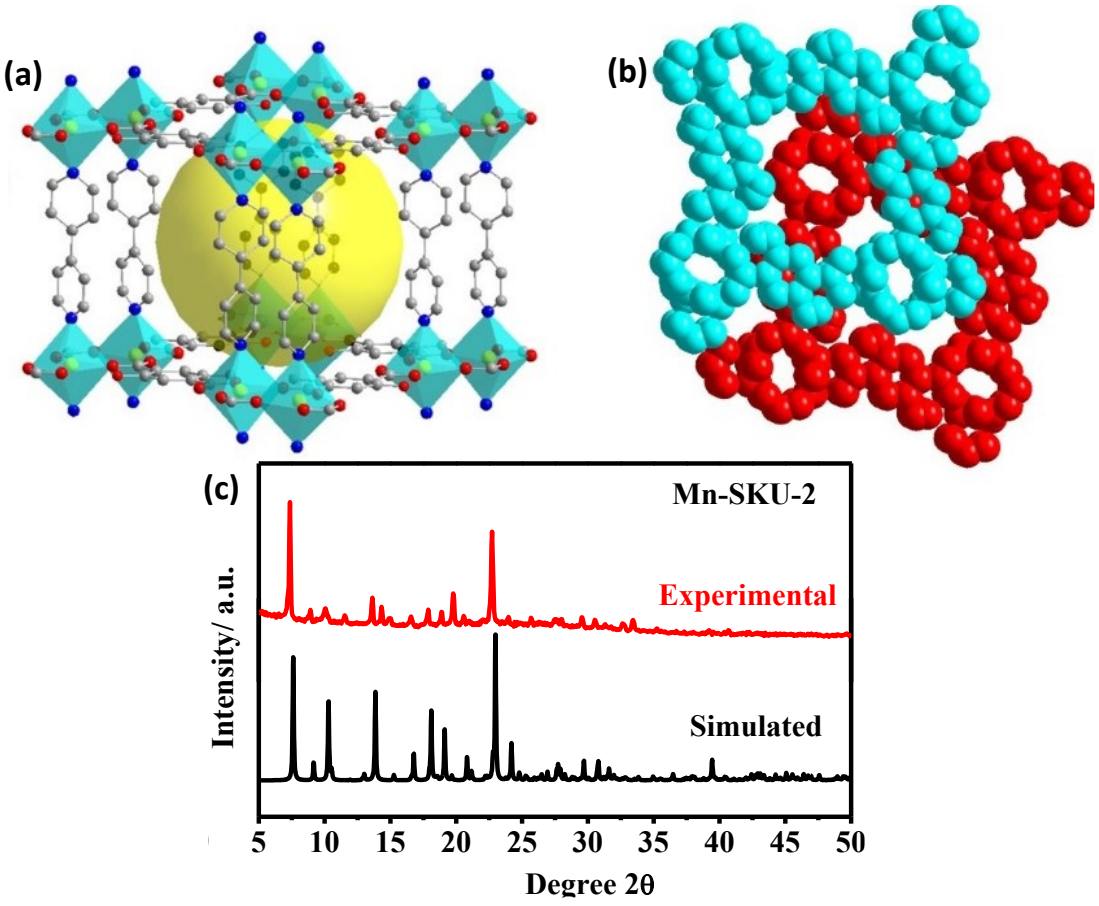

Figure II.11: (a) Illustration of potential void in Mn-SKU-2 without interpenetration (b) 3D→3D interpenetration representation of Mn-SKU-2, and (c) comparative PXRD patterns of Mn-SKU-2 with the simulated patterns (CCDC no: 2165595).

II.4.1.8. Synthesis of Cu-SKU-3 MOFs:

The Cu-SKU-3 MOF was synthesized following the synthetic procedure reported before and the general reaction is depicted in scheme II.9.

Scheme II.9: Reaction scheme for the synthesis of Cu-SKU-3 MOF

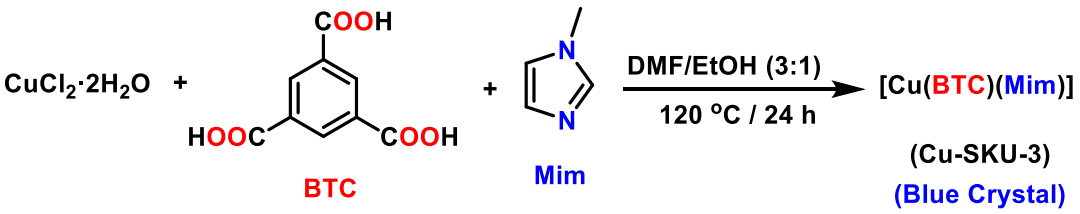

.

The solvothermal technique was employed to carry out the synthesis using a mixture of DMF and ethanol in a 3:1 ratio. Initially, trimesic acid (BTC) weighing around 210 mg and 1 mmol was dissolved in approximately 6 mL of DMF. Next, 256 mg of $CuCl_2.2H_2O$ (1.5 mmol) was dissolved in 2 mL of ethanol using sonication, and the resulting copper solution was added to the vial containing BTC. To this mixture, 270 µL of N-methyl imidazole (3.38 mmol) was added quickly, which caused the solution to change from pale yellow to greenish blue instantly. The reaction mixture was then transferred to a PTFE-lined autoclave and heated at 130 °C for 22 hours. The reaction was allowed to slowly cool down at a rate of 3.5 °C per minute to obtain blue-colored crystals that were washed several times with DMF followed by EtOH and acetone. The resulting catalyst was then subjected to a solvent exchange process with acetone for 24 hours and was used for catalysis directly without activation. The polymeric growth of Cu_SKU-3 is illustrated in figureII.12a and Cu was found to obtain a penta coordination with Mim and BDC ligands. The PXRD performed for the sample shows similar peaks to that of the simulated pattern thereby concluding the excellent purity of the synthesized sample (Figure II.12b).

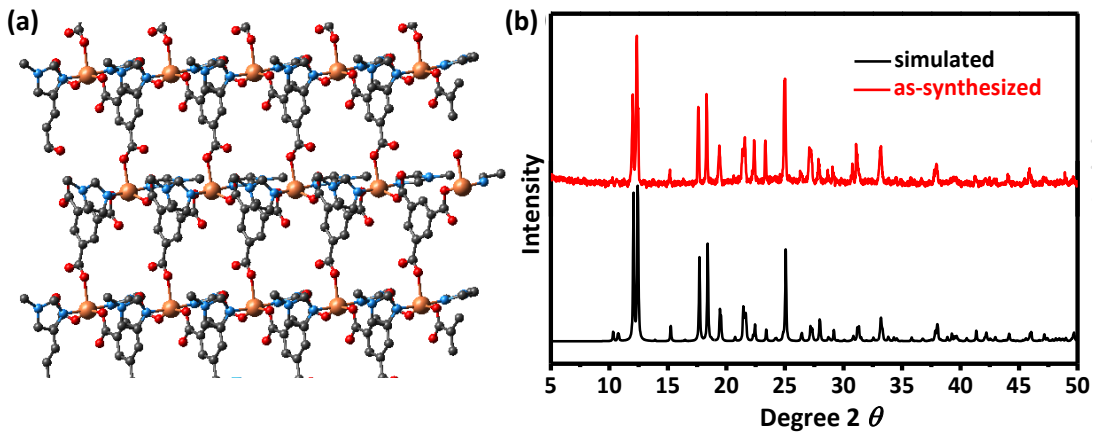

Figure II.12: (a) 2D-sheet-like polymeric network of Cu-SKU-3 and (b) PXRD patterns of the synthesized (red) and simulated (black) Cu-SKU-3 MOF (CCDC: 2209956)

II.4.2. Solvothermal synthesis of novel metal-organic frameworks.

II.4.2.1. Synthesis and characterization of Cu-1D MOF:

The solvothermal technique was employed to conduct the synthesis using a mixture of DMF and ethanol in a 3:1 ratio. In general, $CuCl_2 \cdot 2H_2O$ (0.1705 g, 1 mmol), 1,4-benzene dicarboxylic acid (0.1661 g, 1 mmol), and *N*-methylimidazole (0.16 mL, 2 mmol) were added to 8 ml of a DMF and EtOH solution (3:1 by volume) at room temperature and stirred until all the solutes dissolved (Scheme II.10).

Scheme II.10: Reaction scheme for the synthesis of Cu-1D.

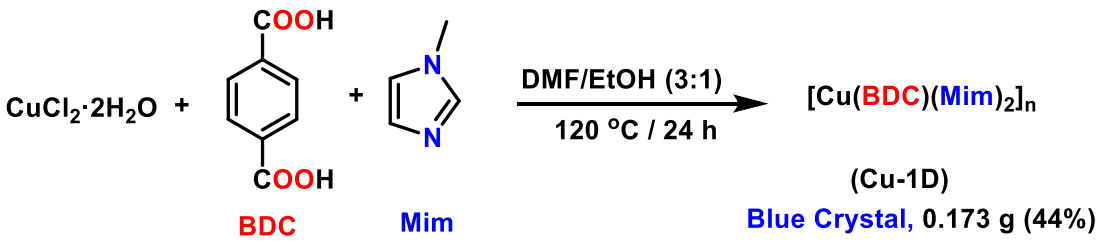

The resulting solution was then transferred to a 20 mL Teflon-lined hydrothermal bomb, sealed, and heated at 100°C for 24 hours to yield blue crystals. The crystals were subsequently washed several times with DMF and EtOH to eliminate any unreacted

ligands and air-dried. Yield = 44%. The synthesized MOF was characterized using elemental analysis FT-IR, SCXRD, PXRD, TGA, BET-surface area analyzer, and SEM. The CHN analysis carried out for the sample with the expected formula $C_{16}H_{16}N_4O_4Cu$ is given in Table II.2.

Table II.2: CHN analysis of Cu-1D sample.

Atom	C	H	N
Calculated	49.04	4.12	14.30
Experimental	49.26	4.29	14.21

The FT-IR was performed to confirm the coordination environment in Cu-1D with organic ligands using KBr pallets. The analysis of spectra showed the major peaks at 654, 742, 820, 940, 1025, 1098, 1358, 1411, 1551, 1601, 2925 and 3130 cm^{-1}. Based on FT-IR analysis, the bathochromic shift for the υ (C=O) bands was observed from 1720 cm^{-1} in BDC to 1601 cm^{-1} in Cu-1D suggesting the possible coordination of C=O bond to Cu-metal (Figure II.13).[49–52]Additionally, the peaks at 3130, 2925, and 1358 cm^{-1} were attributed to the coordination of the Mim unit to the metal center(Figure II.14).[49,53] Next, the structural refinements of Cu-1D were acquired by diffracting a suitable single crystal with a Cu source (1.54 Å) at 298 K. The obtained data was analyzed on the olex-2 platform and solved using the shelXL refinements.[54,55] The crystal structure analysis confirmed that the Cu(II) polymeric complex crystallizes in a monoclinic crystal system with *P2₁/c* space group, and hasthe formula unit $[Cu(BDC)(Mim)_2]_n$. Table II.3 summarizes the crystallographic data and the results of the structure refinement obtained from the new data acquisition. The crystal has been uploaded to the CCDC data base and can be accessed for further details with CCDC no 2118552.

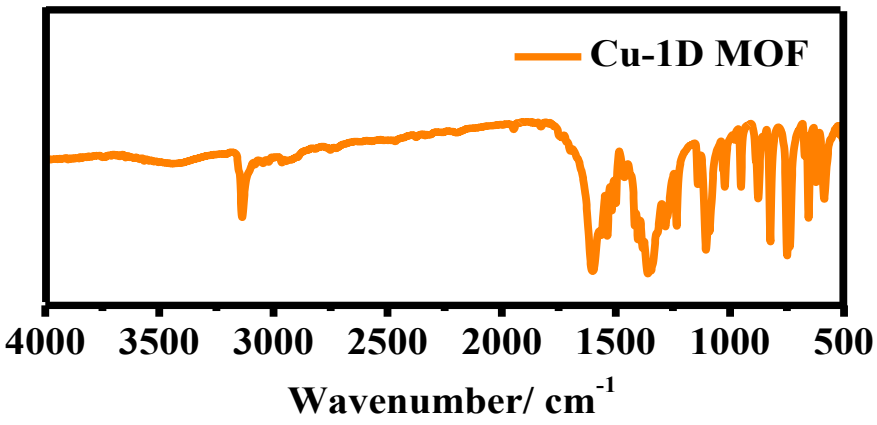

Figure II.13: FT-IR of Cu-1D performed with KBr pallets.

Table II.3: Crystallographic data and structure refinement results for Cu-1D.

	[Cu(BDC)(Mim)$_2$]n
Identification code	**Cu-1D**
Empirical Formula	$C_{16}H_{16}N_4O_4Cu$
Formula Weight (g/mol)	391.87
Wavelength (Å)	0.71073
Crystal System	Monoclinic
Space Group	$P2_1/c$
a (Å)	5.3003 (15)
b (Å)	14.729 (4)
c (Å)	11.049 (3)
α (°)	90.0
β (°)	104.918 (11)
γ (°)	90.0
Volume (Å^3)	833.5 (4)
Z	2
Calculated Density (mg/m^3)	1.561
Goodness of fit on F^2	1.042
Final R indices I>2sigma	R1= 0.0469, wR2= 0.1050
R indices (all data)	R1= 0.0813, wR2= 0.1199
Largest diff. Peak/`Hole (eÅ^{-3})	0.43/-0.24
CCDC number	2118552

Following the structural refinement, a simulation of the PXRD was conducted and then compared to the experimental PXRD data of the synthesized sample. The well-matched alignment of the PXRD peaks between the experimental and simulated data, as illustrated in figure II.14, indicates a high level of bulk purity in the sample, which is also well supported by the elemental CHN analysis.

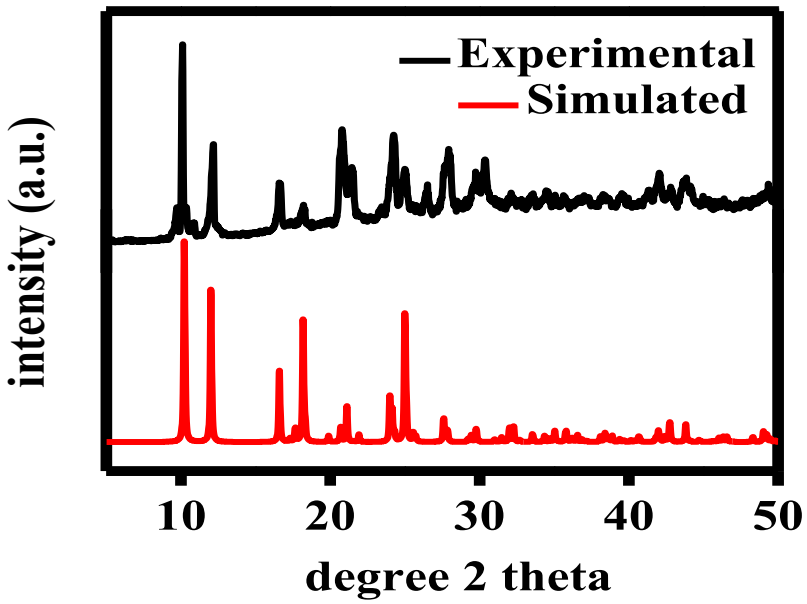

Figure II.14: PXRD comparison of Cu-1D between simulated and experimental data.

The SCRD structural refinement is further extrapolated to draw an ORTEP diagram of the labeled asymmetric unit of Cu-1D (Figure II.15a). As shown in the figure the asymmetric of Cu-1D is composed of one Cu^{2+} ion, two nitrogen atoms (N1 and N2), four carbon atoms (C1, C2, C3, and C4) from the Mim unit, two oxygen atoms (O1 and O2), and four additional carbon atoms (C5, C6, C7, and C8) from the BDC unit. The coordination of the two oxygen atoms from two BDC units and two terminal Mim units in a trans configuration creates a square planar Cu(II) center in the polymeric complex, with each N-Cu-O angle measuring 90°. The two Mim units coordinate the Cu(II) center from the equatorial position and facilitate the growth of the polymeric structure

exclusively along one dimension, resulting in a linear 1D chain in the "c" direction, with two BDC ligands in a plane at the axial position (Figure II.15b).

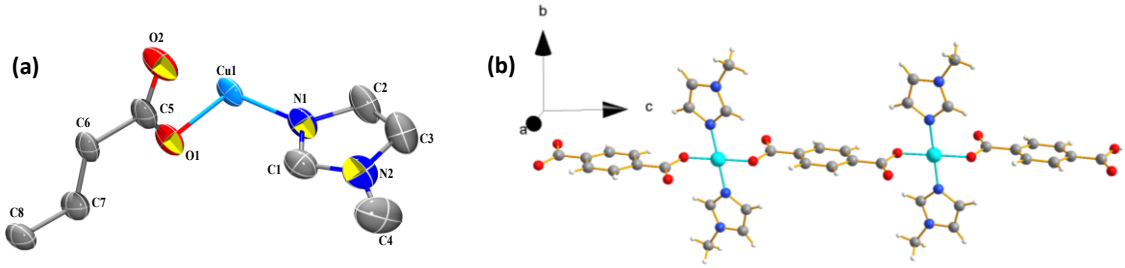

Figure II.15: (a) ORTEP diagram for an asymmetric unit of Cu-1D with labeling. (b) The polymeric growth of Cu-1D along the "c" axis forming a one-dimensional coordination chain.

The bond lengths of Cu-O and Cu-N in Cu-1D were determined to be 1.945(19) Å and 1.992(3) Å, respectively. These values are consistent with those expected for a Cu(II) ion with a linear Cu-Cu-Cu (180°) angle and a Cu-Cu distance of 10.955(3) Å. The polymeric complex in one dimension is arranged as endless rows and columns in the solid-state, through non-covalent interactions. Meanwhile, the 2-D framework is composed of an infinite 1-D polymeric chain that is tightly packed through strong intermolecular H-bonding interaction (Figure II.16a) between 02′-H1A (2.53 Å) and 02′-H4A (2.53 Å), as well as CH….π interactions between C(4)-H(4C) and Cg(3) (the centroid of the Mim unit) (2.94 Å) ring. The presence of hydrogens in the Mim unit leads to the formation of both intermolecular and intramolecular hydrogen bonding interactions. Specifically, the hydrogen atoms (H1A and H2A) from the C1 and C2 carbons in the Mim unit are involved in intramolecular hydrogen bonding with O1 at distances ranging from 2.52-2.53 Å, resulting in the co-planarity of the Mim and O1-O1′ unit. In addition, non-covalent π-π, CH….π, and hydrogen bonding interactions were found to contribute to the stabilization of the 3D solid crystalline structure (Figure II.16b).

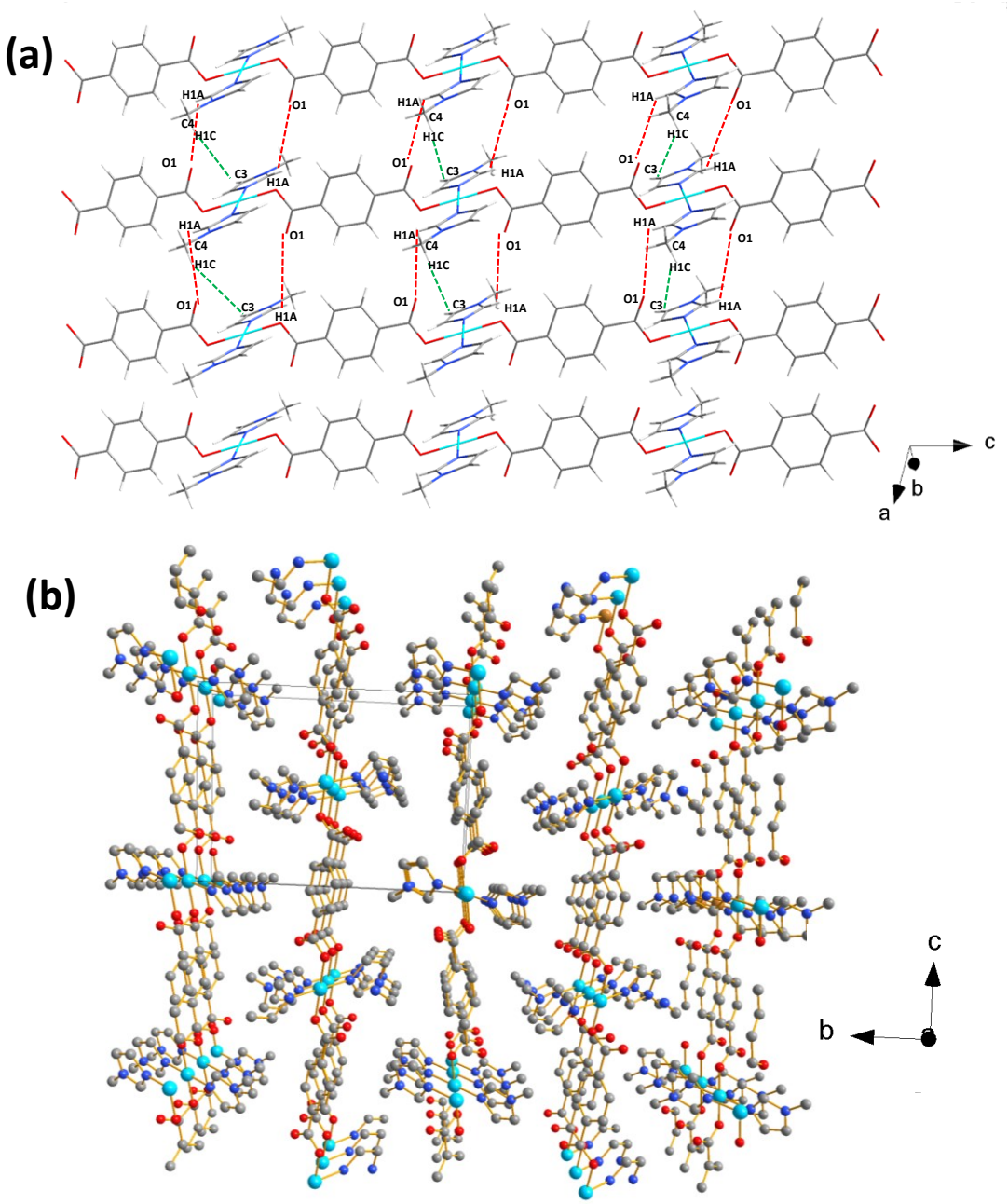

Figure II.16: (a) H-bond stabilized 2D arrangement of the **Cu-1D** showing non-covalent interaction (red dash for O-H hydrogen bonding and green dash for C-H interactions). (b) C-H….π stabilized 3D network of **Cu-1D**.

Overall, the 3D growth of the Cu-1D framework can be thought of as a layered morphology where one layered is stacked above another resulting in a sheet-like layered morphology. To visualize the layered morphology of Cu-1D MOF the synthesized

sample is subjected to SEM imaging and as expected the layered on one sheet above another is seen in SEM images (Figure II.17a-c).

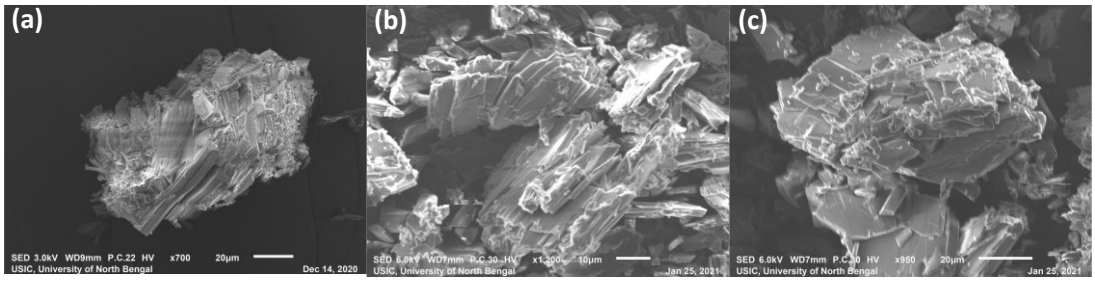

Figure II.17: (a)-(c) SEM images of Cu-1D showing a morphology with stacking of layers one above another.

From the SCXRD and SEM analysis, the role of non-covalent interaction in maintaining the 3D framework of Cu-1D framework was found vital. Therefore, the various non-covalent interaction present in the polymeric framework was thoughtfully quantified through theoretical Hirshfeld surface (HS) analysis using the software *Crystal Explorer 21.5*.[56] The analysis of HS is a widely recognized technique for representing non-covalent intermolecular interactions in a crystal structure.[57] This method involves dividing the crystal space into regions where the ratio of electronic contributions from the promolecule to the procrystal is 0.5. [58,59] The resulting surface is then color-coded using normalized contact distance (d_{norm}) and can be visualized as shown in Figure II.18a. In the visualization of HS, the white region corresponds to close contacts that are equal to the sum of the Van der Waals radii. Meanwhile, the red and blue regions represent contacts that are closer or farther than the sum of Van der Waals radii, respectively. Figure II.18b illustrates red spots that appear over the hydrogen (H) atoms of the oxygen and nitrogen atoms, indicating the presence of strong hydrogen bonding. This bonding can be further visualized using green dashed lines. To obtain quantitative values of intermolecular interactions in terms of individual interatomic contacts' contributions, 2D fingerprints are generated for the asymmetric unit of Cu-1Dand the

terms d_e and d_i correspond to the distances of the nearest atom outside and inside the HS, respectively.[60] The 2D fingerprint plot shown in Figure II.19c depicts the overall interaction within the crystal packing as a function of the distances d_e and d_i ranging from 0.4 to 2.6 Å. The overall fingerprint in Figure II.19c appears as a greyed-out background, with only specific contacts

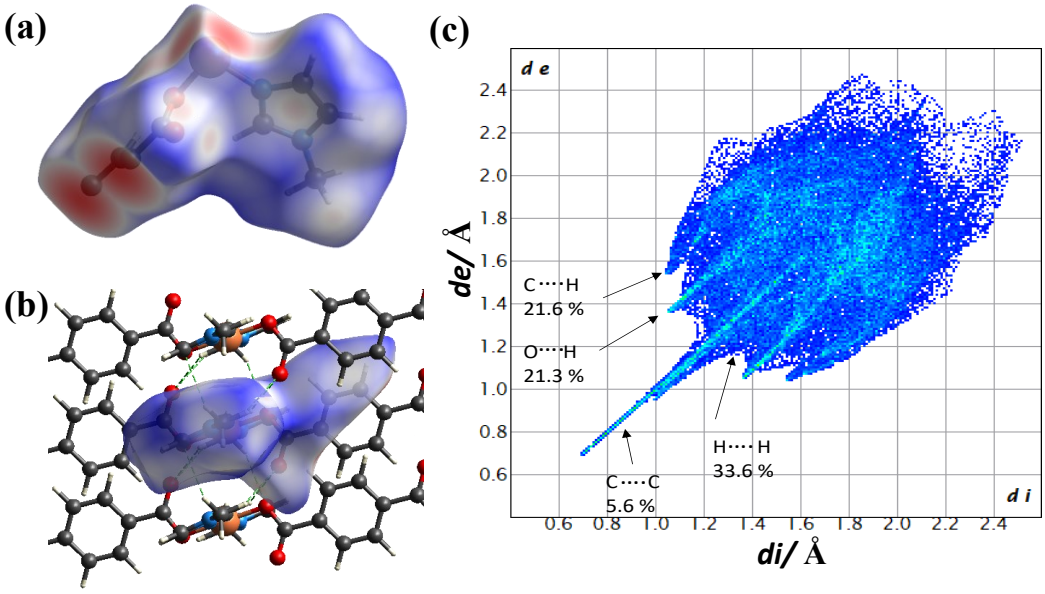

Figure II.18: (a) The HS corresponding to the asymmetric unit of Cu-1D MOF, plotted within the over d_{norm} values from -1.1833 to 1.2607 au. (b) HS indicates H bonding interactions with green dotted lines. (c) The 2D fingerprint plot of Cu-1D MOF highlighting different intermolecular interactions.

highlighted, including reciprocal contacts. The analysis reveals that the H…H interactions have the highest contribution (33.6%) among all the interatomic contacts, as depicted in the corresponding fingerprint plot where d_e and d_i values are equal. In this plot, the blue regions indicate the contacts with distances shorter or longer than the sum of van der Waals radii of atoms, which is approximately 1.4 Å. The analysis of the fingerprint plot also reveals two prominent spikes for C...H/H...C and O...H/H...O contacts, which appear at d_e+d_i distances of approximately 3.2 Å and 2.65 Å,

respectively. These contacts contribute 21.6% and 21.3%, respectively, to the overall intermolecular interactions. In contrast, the C-H...N, C...C, and Cu...O contacts exhibit weaker interactions, with percentage contributions of 4.7%, 5.6%, and 3.3%, respectively. Furthermore, TGA analysis of Cu-1D MOF shows the thermal stability of synthesized polymeric framework up to 200 °C. However, incremental mass loss of 23% and 59% at temperatures between 200-450 °C was found the that can be accounted for the loss of one Mim ligand (23%) first and second for one BDC ligand along with one Mim ligand (59%) (Figure II.19a). Cu-1D was analyzed for its surface area, which was found to be 88.0 m^2g^{-1} according to BET analysis, comparable to the cobalt analog of Cu-1D previously reported by Pariyar *et al.* (Figure II.19b).[53] The average pore diameter of Cu-1D was determined to be 3.1 nm (Figure II.19c), indicating the mesoporous nature of the material. These N_2 adsorption results are consistent with other 1D MOFs, which typically have lower surface areas when compared to 2D or 3D MOFs.[61]

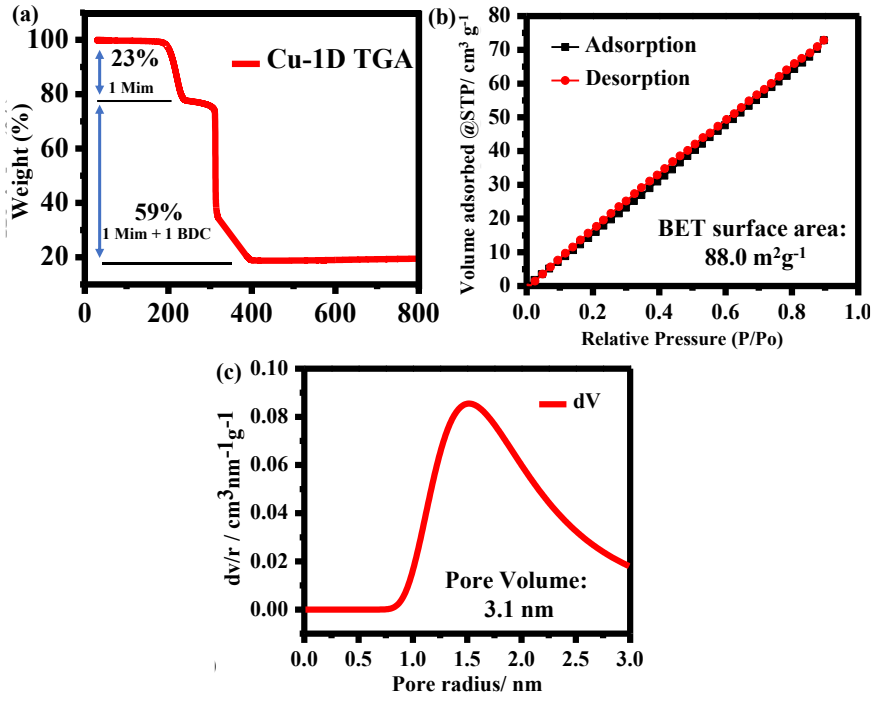

Figure II.19: (a) TGA plot of Cu-1D (b) BET surface area profile and (c) Plot of pore radius for Cu-1D MOF

Interestingly, Cu-1D also shows structural stability in aqueous solutions, as confirmed by the PXRD of the sample that is soaked in aqueous solution after 24 h. Figure II.20 depicts the PXRD pattern of treated and fresh samples and well matched PXRD pattern with-out the presence of any extra peaks conclusively indicates the framework integrity of Cu-1D MOF.

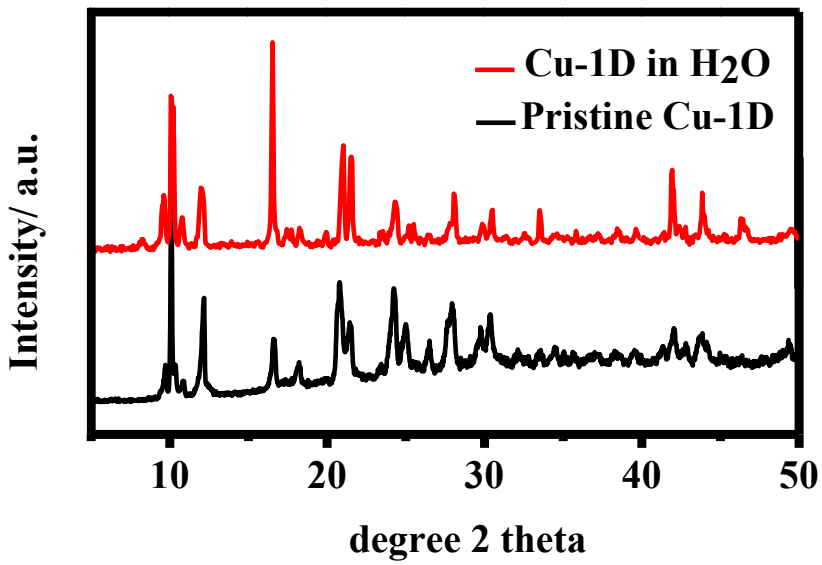

Figure II.20: PXRD of H_2O treated and pristine Cu-1D MOF.

II.4.2.2. Synthesis of Cu-SKU-4 Cu-MOFs:

With the small change in the organic linker, a novel Cu-MOF is prepared which is isologous to Cu-1D MOF prepared and discussed above. All the synthetic procedure is the same as that of Cu-1D MOF except the carboxylate ligand BDC is replaced with the NDC ligand (NDC= naphthalene dicarboxylic acid). Both BDC and NDC have similar coordinating sites however the differences can be seen with the presence of one extra benzene ring in NDC. Being a novel MOF, the name of this material is given as Cu-SKU-4 where SKU is designated to Sikkim University. Cu-SKU-4 was typically synthesized via the solvothermal method using DMF and ethanol (3:1) as solvents.

Firstly, around 1 mmol of naphthalene-2,6-dicarboxylic acid (NDC) weighing 216 mg was dissolved in about 6 mL of DMF. Next, 170 mg of $CuCl_2.2H_2O$ (1.0 mmol) was dissolved in 2 mL of ethanol (Scheme II.11).

Scheme II.11. Reaction scheme for the synthesis of Cu-SKU-4.

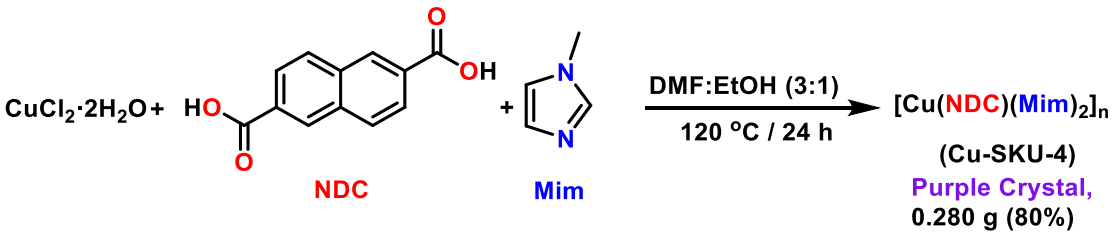

The resulting copper solution was added to the vial containing NDC, and 180 µL of N-methyl imidazole (2 mmol) was swiftly added to the mixture, turning it greenish. The reaction mixture was then transferred to a PTFE-lined autoclave and reacted at 120 °C for 24 h. Purple-coloured crystals, suitable for SCXRD analysis were obtained by slowly cooling the reaction at a rate of 3.5 °C/min. The yield obtained was 280 mg which accounts for about 80% with respect to the limiting reactant. The catalyst was subjected to solvent exchange with methanol and acetone for 24 hours and used directly for catalysis without requiring activation. The yield obtained was 280 mg. The CHN analysis carried out for the sample with the expected formula $C_{20}H_{23}N_5O_7Cu$ is given in Table II.4.

Table II.4: CHN analysis of Cu-SKU-4 sample.

Atom	C	H	N
Calculated	47.20	4.56	13.76
Experimental	49.59	4.16	13.40

The FT-IR was performed using KBr pallets and showed the major peaks at 656, 743, 816, 1007, 1128, 1392, 1506, 1590, 2930, and 3150 cm^{-1}. Similar to Cu-1D, the bathochromic shift for the υ(C=O) bands was observed from 1690 cm^{-1}in NDC to 1590 cm^{-1} in FT-IR of Cu-SKU-4 indicating coordination of C=O bond to Cu-metal (Figure II.21).[49–52]Additionally, the peaks at 3150, 2930, and 1392 cm^{-1} were attributed to the coordination of the Mim unit to the metal center and are in good agreement with the FT-IR spectra of Cu-1D (Figure II.21).[49,53]

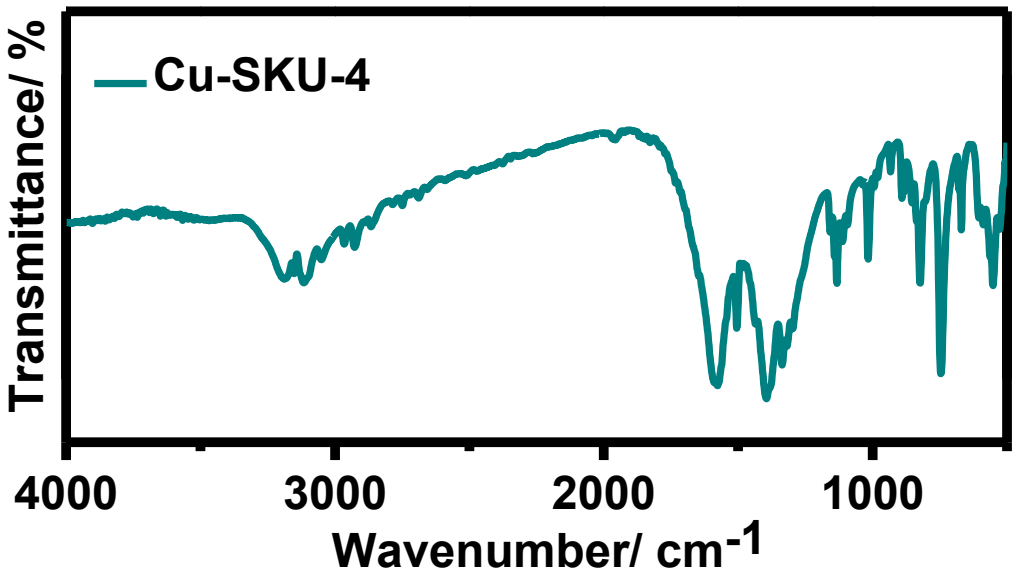

Figure II.21: FT-IR spectra of Cu-SKU-4 performed with KBr pallet.

The crystal structure analysis confirmed that the Cu(II) polymeric complex crystallizes in a monoclinic crystal system with $P2_1/c$ space group, and has the formula unit $[Cu(NDC)(Mim)_2]_n$. Table II.5 summarizes the crystallographic data and the results of the structure refinement obtained from the new data acquisition. The SCXRD revealed a similar structure to that of Cu-1D. The polymeric growth of Cu-SKU-4 shows a similar structure as that of Cu-1D where *N*-methylimidazole restricts the growth towards one axis and allows the growth of MOF only specific axis (Figure II.22a).

Further the infinite chain is stabilized by various non-covalent interaction and also give rise to the three-dimensional structure of Cu-SKU-4 as shown in Figure II.22b.

Table II.5: Crystallographic data and structure refinement results for Cu-SKU-4.

	[Cu(NDC)(Mim)$_2$]n
Identification code	**Cu-SKU-4**
Empirical Formula	$C_{20}H_{18}CuN_4O_4$
Formula Weight (g/mol)	441.92
Wavelength (Å)	1.54
Crystal System	monoclinic
Space Group	$P2_1/C$
a (Å)	9.4413 (9)
b (Å)	10.1536 (4)
c (Å)	14.9471 (15)
α (°)	90.0
β (°)	136.931 (18)
γ (°)	90.0
Volume (Å^3)	978.5 (3)
Z	2
Calculated Density (mg/m^3)	1.500
Goodness of fit on F^2	1.064
Final R indices I>2sigma	R_1=0.0615, wR_2=0.1740
R indices (all data)	R_1=0.0711, wR_2=0.1867
Largest diff. Peak/`Hole (eÅ^{-3})	0.98/-0.52
CCDC number	2264054

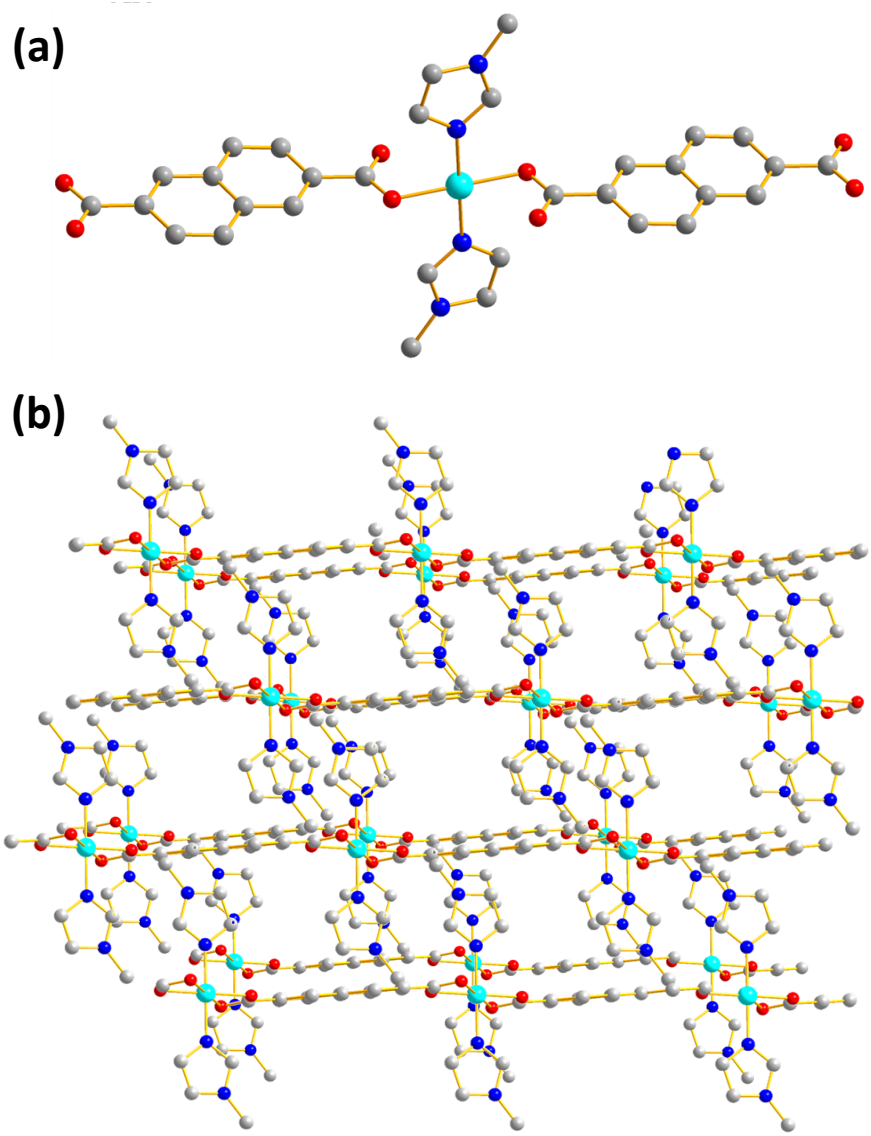

Figure II.22: (a) Asymmetric unit of Cu-SKU-4 showing polymeric growth only to one axis (b) 3D network of Cu-SKU-4 stabilized by non-covalent interactions.

The PXRD for synthesized polymeric material was performed and compared with the PXRD derived from SCXRD analysis. As shown in figure II.23a the comparative PXRD are in good agreement with each other and the absence of any extra peaks indicates the excellent bulk purity of the sample. The TGA analysis shows the thermal stability of the sample upto 390 °C (Figure II.23b). The incremental loss from ~400 °C

could be ascribed to one NDC and one Mim unit that accounts for 70% of the overall molecular weight of the Cu-SKU-4.

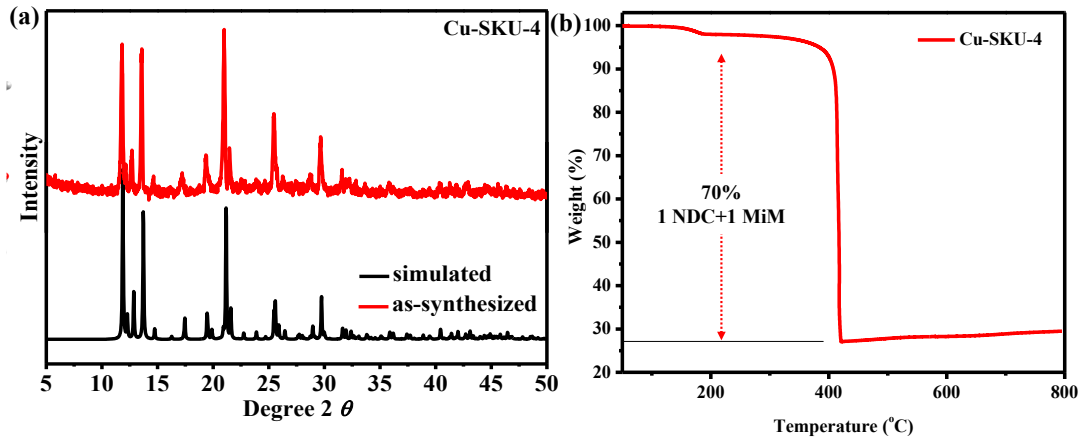

Figure II.23: (a) Comparison of simulated and experimental PXRD of Cu-SKU-4 (b) TGA profile of Cu-SKU-4 in a range of 50-800 ℃.

II.4.2.3. Synthesis of Ni-SKU-5 MOF:

Based on the synthesis of above discussed two Cu-MOFs, the Ni-MOF was synthesized with the use of BDC and 2-methyl imidazole ligand. Precisely, $NiCl_2 \cdot 6H_2O$ (0.2377 g, 1 mmol), 1,4-benzene dicarboxylic acid (0.1661 g, 1 mmol), and N-methylimidazole (0.16 ml, 2 mmol) were stirred into 8 ml of a DMF and EtOH solution (3:1 by volume) at room temperature (Scheme II.12).

Scheme II.12: Reaction scheme for the synthesis of Ni-SKU-5.

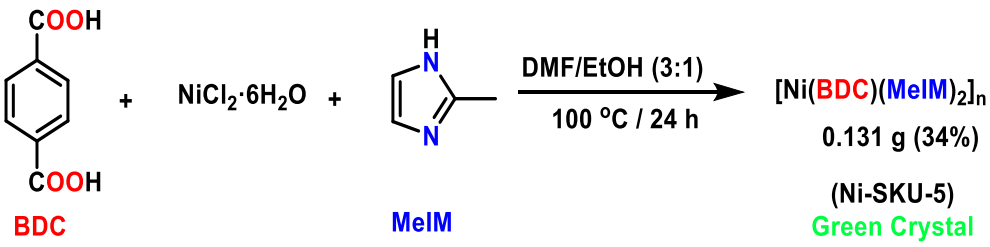

After all the solutes dissolved it was then sealed in a PTFE-lined autoclave and placed in a preheated oven at 100 ℃ for 24 h, giving green crystals. The crystals were washed repeatedly with DMF followed by EtOH, to remove unreacted ligands and dried in air. A yield of 0.131 g was obtained that accounts for the 34%. The CHN analysis carried out for the sample with the expected formula $C_{16}H_{16}N_4O_4Ni$ is given in table II.6.

Table II.6: CHN analysis of Ni-SKU-5 sample.

Atom	C	H	N
Calculated	47.65	4.17	14.38
Experimental	49.61	3.93	14.42

The FT-IR was performed using KBr pallets showed the major peaks at 653, 787, 825, 952, 1101, 1191, 1258, 1355, 1542, 1622, 2946, and 3118 cm^{-1}. The peaks are in well agreement with he previously synthesized Cu-1D and Cu-SKU-4 MOF and similar to them, the bathochromic shift for the υ(C=O) bands was observed from 1720 cm^{-1} in BDC to 1622 cm^{-1} in FT-IR of Ni-SKU-5 (Figure II.24).[49–52]Additionally, the peaks at 3118, 2946, and 1355 cm^{-1} were attributed to the coordination of the MeIM unit to the metal center and are in well agreement with the FT-IR spectra of Ni-SKU-5 (Figure II.25).[49,53]

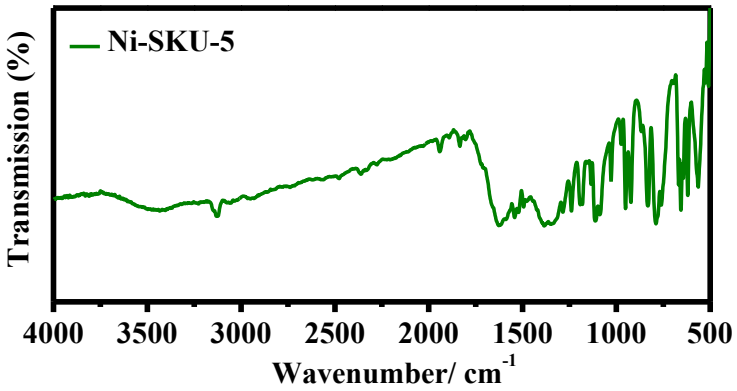

Figure II.24: FT-IR spectra of Ni-SKU-5 recorded using KBr pallet.

The crystal structure analysis confirmed that the Ni(II) polymeric complex crystallizes in a monoclinic crystal system with a *C2/c* space group, and has the formula unit $[Ni(BDC)(MeIM)_2]_n$. Table II.7 summarizes the crystallographic data and the results of the structure refinement obtained from the new data acquisition. The crystal has been uploaded to the CCDC data base and can be accessed for further details with CCDC no 2118552.

Table II.7: Crystallographic data and structure refinement results for **Ni-SKU-5**.

	$[Ni(BDC)(MeIM)_2]n$
Identification code	**Ni-SKU-5**
Empirical Formula	$C_{16}H_{16}N_2O_4Ni$
Formula Weight (g/mol)	387.04
Wavelength (Å)	0.71073
Crystal System	Monoclinic
Space Group	C2/c
a (Å)	13.9342(4)
b (Å)	16.5685(4)
c (Å)	14.5470(3)
α (°)	90.0
β (°)	97.351(2)
γ (°)	90.0
Volume ($Å^3$)	3330.84(14)
Z	8
Calculated Density (mg/m^3)	1.544
Goodness of fit on F^2	1.058
Final R indices I>2sigma	R1= 0.0668, wR2= 0.1823
R indices (all data)	R1= 0.0734, wR2= 0.1925
Largest diff. Peak/`Hole ($eÅ^{-3}$)	1.13/-1.18
CCDC number	2264115

Following the structural refinement, a simulation of the PXRD was conducted and then compared to the experimental PXRD data of the synthesized sample. The well-matched alignment of the PXRD peaks between the experimental and simulated data, as illustrated in Figure II.25, indicates a high level of bulk purity in the sample, which is also well supported by the elemental CHN analysis.

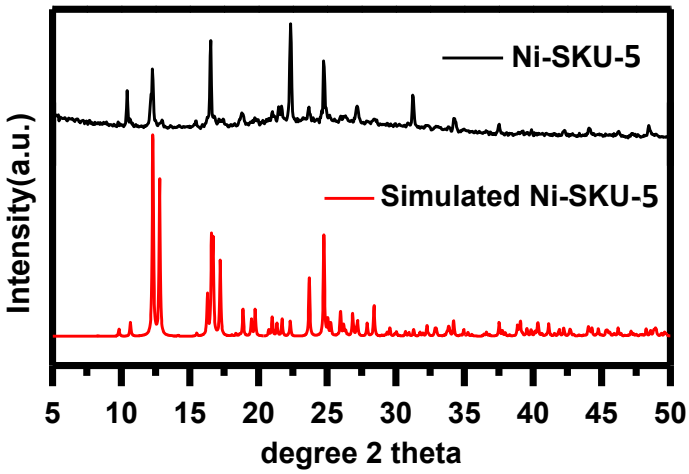

Figure II.25: PXRD comparison of Ni-SKU-5 between simulated and experimental data.

The ORTEP diagram of the labeled asymmetric unit of Ni-SKU-5 is shown in figure II.26a where the Ni(II) center is placed at the center of a distorted octahedral coordinated by four oxygen atoms from *bis*-bidentate coordination of BDC ligand and two nitrogen atom from two MeIM unit. The coordination of two MeIM units from the equatorial position hinders the growth of polymeric units towards the b-axis where the BDC moiety bridges two Ni(II) atom resulting in the formation of a zig-zag 1-D chain (Figure II.26b). The bond distance, Ni-O (2.067(2) Å-2.062(2) Å) and Ni-N (2.043(3))Å are in agreement with Ni(II)-O/N bond distances of earlier known 1-D Ni(II) coordination polymers. The 1-D polymeric structure grows along the c axis giving infinite chains and forms a 2D structure (Figure II.26c).

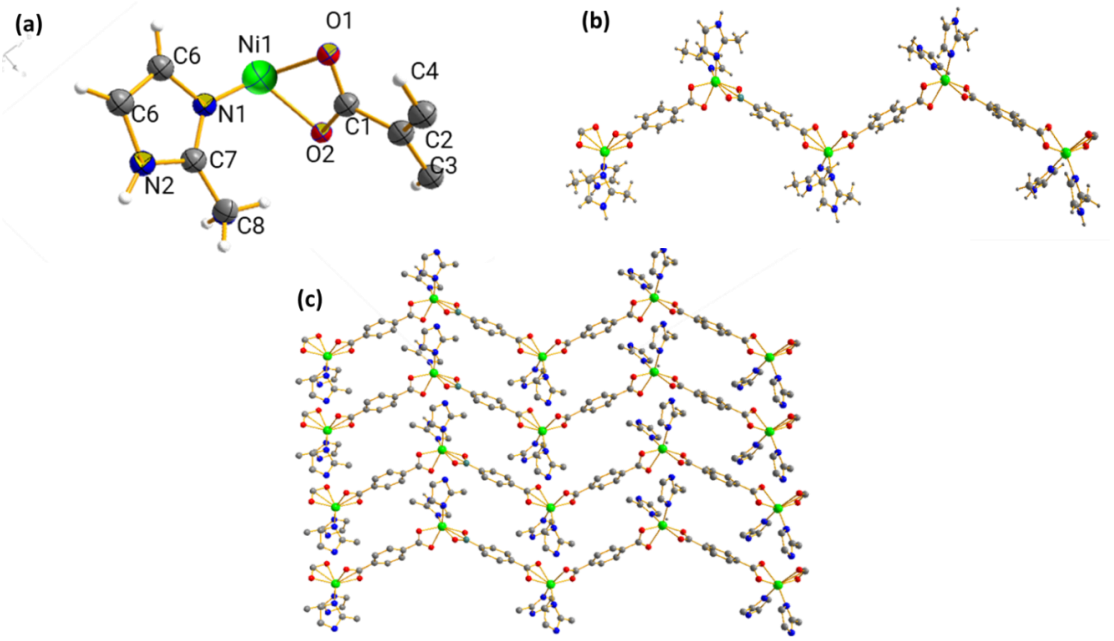

Figure II.26: (a) Crystal structure of Ni-SKU-5 (a) ORTEP diagram of Ni-SKU-5 showing asymmetric unit (H atoms are omitted for clarity). (b) The polymeric one-dimensional coordination chain of Ni-SKU-5 along the "c" axis. (c) H-bond stabilized 2D arrangement of the Ni-SKU-5.

The thermogravimetric analysis (TGA) of Ni-SKU-5 shows the removal of one MeIM unit at a temperature around 380°C which accounts for 22% weight loss. The second and final weight loss (53%) was noted at around 360 °C which may be due to the decomposition of BDC and the remaining MeIM unit (Figure II.27a). The N_2 adsorption experiment performed to evaluate the BET surface area of 36.8 m^2 g^{-1} for Ni-SKU-5 The chemical stability of Ni-SKU-5 in various solvents was validated in a similar way as that of Cu-1D MOF by dispersing the MOF crystals in aqueous solvents for 24 h and collecting the PXRD thereafter. The similar PXRD peaks of the treated samples to that of as-synthesized samples indicate the framework intactness in coordinating, non-coordinating and aqueous solvents. Furthermore, we conducted a study to assess the stability of the MOF in various organic solvents before using it in catalysis. The Ni-SKU-5 crystals were immersed in organic solvents and water for 24 h, and PXRD

analysis was used to confirm their crystallinity. Additionally, we evaluated the water stability of Ni-SKU-5 by immersing it in water for 5 days. The PXRD analysis showed that the material remained crystalline even after extended exposure to water, indicating its high-water stability.

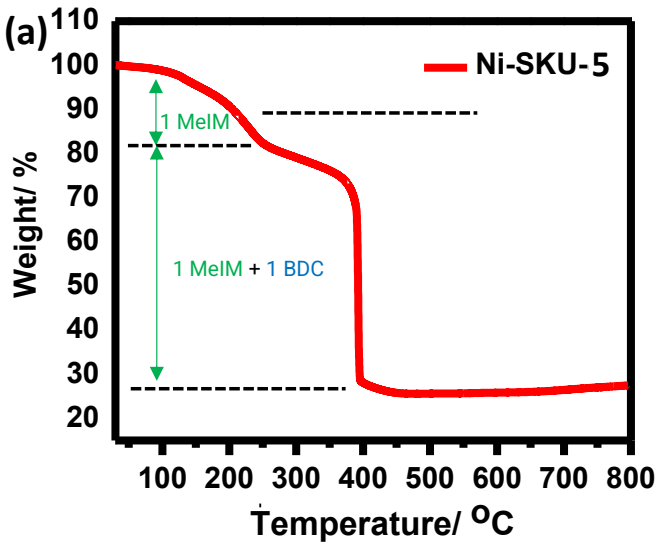

Figure II.27: TGA profile of Ni-SKU-5 MOF.

II.5. Conclusion:

To summarize, this chapter provides an overview of the synthesis and characterization of MOFs, followed by a detailed discussion of the synthesis methods and characterization techniques used for several well-known MOFs, including Mn-SKU-1, Mn-SKU-2, Cu-SKU-3, HKUST-1, ZIF-8/67, and MIL-100. In addition, we explore the synthetic method for novel ligands and MOFs (Cu-SKU-4, Cu-1D, and Ni-SKU-5), investigating the impact of auxiliary blocker ligands such as Mim and MeIM. The stability of these MOFs is theoretically attributed to non-bonding interactions, such as O-H/O, C-C, and C-N, quantified using Hirshfeld surface analysis. Both chemical (solvent stability) and thermal (TGA analysis) assessments highlight the robust nature of these MOFs, making them ideal candidates for use as heterogeneous catalysts in targeted studies.

II.6 Experimental

II.6.1. Materials:

All chemicals and solvents were used without purification unless otherwise mentioned. BDC, BTC, Mim, MeIM, TEA, DOT, and 4,4'-bipyridine, were purchased from Sigma Aldrich and used as obtained. Naphthalene dicarboxylic acid (NDC) was bought from TCI, India. $M(NO_3)_2 \cdot 6H_2O$ (M= Ni, CO, Mn, Zn), $Mn(OAc)_2 \cdot 4H_2O$, NaOH, $NiCl_2.6H_2O$ and DMF was bought from Merck and used as obtained. $Cu(NO_3)_2.3H_2O$ $FeCl_2.4H_2O$ $CuCl_2.2H_2O$, and THF was bought from Thomas Baker.

II.6.2. Physical methods:

Nabertherm B180 muffle furnace was used during solvothermal synthesis. PXRD analysis was performed on PANalytical high-resolution X-ray Diffractometer equipped with a Cu K_α radiation (λ = 1.5418 Å) at a scan rate of 5° min^{-1}. SCXRD intensity data sets were collected on a Super Nova Agilent diffractometer (Model No: 8D-91-45-400) with monochromated Mo Kα radiation (0.7107 Å) and Cu Kα (1.54184 Å). All the FTIR spectra were acquired using Bruker ALPHA E. The BET surface areas were obtained using Quanta chrome Nova Touch LX2. TG analysis was carried out at a heating rate of 10 °C min^{-1} with a N_2 flow rate of 60 mL min^{-1}in a TA Instruments, TGA Q-50 Analyzer. SEM images were taken on JSM-6360 SEM. The crystallographic data for structural analysis of diffracted crystal data were solved by Olex-2 software[54] using ShelXL refinements.[55] The CHN analysis of MOF was performed in a Perkin–Elmer 2400, Series II.

II.7. References:

(1) Li, H.; Davis, C. E.; Groy, T. L.; Yaghi, O. M. Coordinatively Unsaturated Metal Centers in the Extended Porous Framework of $Zn_3(BDC)_3$,$6CH_3OH$. *J. Am. Chem. Soc.* **1998**, *120*, 2186–2187.

(2) Li, H.; Eddaoudi, M.; O'Keeffe; Yaghi, O. M. Design and Synthesis of an Exceptionally Stable and Highly. *Nature* **1999**, *402*, 276–279.

(3) S.S.Y. Chui; S.M.F. Lo; J.P.H. Charmant; A.G. Orpen; I.D. Williams. A Chemically Functionalizable Nanoporous Material $[Cu_3(TMA)_2(H_2O)_3]N$. *Science,* **1999**, *283*, 1148.

(4) Moosavi, S. M.; Nandy, A.; Jablonka, K. M.; Ongari, D.; Janet, J. P.; Boyd, P. G.; Lee, Y.; Smit, B.; Kulik, H. J. Understanding the Diversity of the Metal-Organic Framework Ecosystem. *Nat. Commun.* **2020**, *11*, 4068.

(5) Gascon, J.; Corma, A.; Kapteijn, F.; Xamena, F. X. L. i. Metal Organic Framework Catalysis: Quo Vadis? *ACS Catal.* **2014**, *4*, 361–378.

(6) Furukawa, H.; Cordova, K. E.; O'Keeffe, M.; Yaghi, O. M. The Chemistry and Applications of Metal-Organic Frameworks. *Science,* **2013**, *341*, 1230444–1230444.

(7) Klinowski, J.; Almeida Paz, F. A.; Silva, P.; Rocha, J. Microwave-Assisted Synthesis of Metal-Organic Frameworks. *Dalt. Trans.* **2011**, *40*, 321–330.

(8) Gagnon, K. J.; Perry, H. P.; Clearfield, A. Conventional and Unconventional Metal À Organic Frameworks Based on Phosphonate Ligands : MOFs and UMOFs. *Chem. Rev.* **2012**, *112*, 1034–1054.

(9) An, H. T.; Zhang, X.; Dong, C.; Lu, M. Y.; Li, R.; Xie, Y.; Xie, L. H.; Li, J. R. Seed-Aided Green Synthesis of Metal-Organic Frameworks in Water. *Green Chem. Eng.* **2023**, *4*, 64–72.

(10) Udourioh, G. A.; Solomon, M. M.; Matthews-Amune, C. O.; Epelle, E. I.; Okolie, J. A.; Agbazue, V. E.; Onyenze, U. Current Trends in the Synthesis, Characterization and Application of Metal-Organic Frameworks. *React. Chem. Eng.* **2022**, *8*, 278–310.

(11) Howarth, A. J.; Peters, A. W.; Vermeulen, N. A.; Wang, T. C.; Hupp, J. T.; Farha, O. K. Best Practices for the Synthesis, Activation, and Characterization of Metal − Organic Frameworks. *Chem. Mater.* **2017**, *29*, 26–39.

(12) Furukawa, H. Synthesis and Characterization of Metal–Organic Frameworks. In *Gas Adsorption in Metal–Organic Frameworks*; Glover, T. G., Mu, B., Eds.; 2018; p 65.

(13) Stock, N.; Biswas, S. Synthesis of Metal-Organic Frameworks (MOFs): Routes to Various MOF Topologies, Morphologies, and Composites. *Chem. Rev.* **2012**, *112*, 933–969.

(14) Han, Y.; Yang, H.; Guo, X. *Synthesis Methods and Crystallization of MOFs*; 2020.

(15) Zhang, B.; Zhang, J.; Liu, C.; Sang, X.; Peng, L.; Ma, X.; Wu, T.; Han, B.; Yang,

G. Solvent Determines the Formation and Properties of Metal-Organic Frameworks. *RSC Adv.* **2015**, *5*, 37691–37696.

(16) Stary, J.; Liljenzin, J. O. Critical Evaluation of Equilibrium Constants Involving Acetylacetone and Its Metal Chelates. *Pure Appl.Chem.* **1982**, *54*, 2557–2592.

(17) Zahn, G.; Zerner, P.; Lippke, J.; Kempf, F. L.; Lilienthal, S.; Schröder, C. A.; Schneider, A. M.; Behrens, P. Insight into the Mechanism of Modulated Syntheses: In Situ Synchrotron Diffraction Studies on the Formation of Zr-Fumarate MOF. *CrystEngComm* **2014**, *16*, 9198–9207.

(18) Vermoortele, F.; Bueken, B.; Le Bars, G.; Van De Voorde, B.; Vandichel, M.; Houthoofd, K.; Vimont, A.; Daturi, M.; Waroquier, M.; Van Speybroeck, V.; Kirschhock, C.; De Vos, D. E. Synthesis Modulation as a Tool to Increase the Catalytic Activity of Metal-Organic Frameworks: The Unique Case of UiO-66(Zr). *J. Am. Chem. Soc.* **2013**, *135*, 11465–11468.

(19) Dodson, R. A.; Kalenak, A. P.; Matzger, A. J. Solvent Choice in Metal-Organic Framework Linker Exchange Permits Microstructural Control. *J. Am. Chem. Soc.* **2020**, *142*, 20806–20813.

(20) Akhundzadeh Tezerjani, A.; Halladj, R.; Askari, S. Different View of Solvent Effect on the Synthesis Methods of Zeolitic Imidazolate Framework-8 to Tuning the Crystal Structure and Properties. *RSC Adv.* **2021**, *11*, 19914–19923.

(21) Vinu, M.; Senthil Raja, D.; Jiang, Y. C.; Liu, T. Y.; Xie, Y. Y.; Lin, Y. F.; Yang, C. C.; Lin, C. H.; Alshehri, S. M.; Ahamad, T.; Salunkhe, R. R.; Yamauchi, Y.; Deng, Y. H.; Wu, K. C. W. Effects of Structural Crystallinity and Defects in Microporous Al-MOF Filled Chitosan Mixed Matrix Membranes for Pervaporation of Water/Ethanol Mixtures. *J. Taiwan Inst. Chem. Eng.* **2018**, *83*, 143–151.

(22) Sun, J.; Yu, X.; Zhao, S.; Chen, H.; Tao, K.; Han, L. Solvent-Controlled Morphology of Amino-Functionalized Bimetal Metal-Organic Frameworks for Asymmetric Supercapacitors. *Inorg. Chem.* **2020**, *59*, 11385–11395.

(23) Zhang, N.; Zhang, J. Y.; Jia, Q. X.; Deng, W.; Gao, E. Q. Solvent-Controlled Structural Diversity Observed in Three Cu(II) MOFs with a 2,2′-Dinitro-Biphenyl-4,4′-Dicarboxylate Ligand: Synthesis, Structures and Magnetism. *RSC Adv.* **2015**, *5*, 70772–70780.

(24) Tranchemontagne, D. J.; Hunt, J. R.; Yaghi, O. M. Room Temperature Synthesis of Metal-Organic Frameworks: MOF-5, MOF-74, MOF-177, MOF-199, and IRMOF-0. *Tetrahedron* **2008**, *64*, 8553–8557.

(25) Reinsch, H. "Green" Synthesis of Metal-Organic Frameworks. *Eur. J. Inorg. Chem.* **2016**, 4290–4299.

(26) Huang, X.-C.; Lin, Y.-Y.; Zhang, J.-P.; Chen, X.-M. Ligand-Directed Strategy for Zeolite-Type Metal– Organic Frameworks: Zinc(II) Imidazolates with Unusual Zeolitic Topologies. *Angew. Chemie Int. Ed. English* **2006**, *45*, 1557–1559.

(27) Niu, S.; Li, C.; Huo, J.; Dong, W.; El Hankari, S.; Liang, Y.; Li, Q. Ultrathin Trimetal-Organic Framework Nanosheet Electrocatalysts for the Highly

Efficient Oxygen Evolution Reaction. *ACS Omega* **2021**, *6*, 13946–13952.

(28) Al-Ghoul, M.; Issa, R.; Hmadeh, M. Synthesis, Size and Structural Evolution of Metal-Organic Framework-199 via a Reaction-Diffusion Process at Room Temperature. *CrystEngComm* **2017**, *19*, 608–612.

(29) Mason, T. J. Ultrasound in Synthetic Organic Chemistry. *Chem. Soc. Rev.* **1997**, *26*, 443–451.

(30) Suslick, K. S.; Gawienowski, J. J.; Schubert, P. F.; Wang, H. H. Sonochemistry in Non-Aqueous Liquids. *Ultrasonics* **1984**, *22*, 33–36.

(31) Jung, D.; Yang, D.; Kim, J.; Ahn, W. Facile Synthesis of MOF-177 by a Sonochemical Method Using 1-Methyl-2-Pyrrolidinone as a Solvent. *Dalt. Trans.* **2010**, *39*, 2883–2887.

(32) Ni, Z.; Masel, R. I. Rapid Production of Metal-Organic Frameworks via Microwave-Assisted Solvothermal Synthesis. *J. Am. Chem. Soc.* **2006**, *128*, 12394–12395.

(33) Choi, J.; Son, W.; Kim, J.; Ahn, W. Metal-Organic Framework MOF-5 Prepared by Microwave Heating : Factors to Be Considered. *Microporous Mesoporous Mater.* **2008**, *116*, 727–731.

(34) Nguyen, L. H. T.; Nguyen, H. T. T.; Le, B. Q. G.; Dang, M. H. D.; Nguyen, T. T. T.; Mai, N. X. D.; Doan, T. L. H. Microwave-Assisted Solvothermal Synthesis of Defective Zirconium-Organic Framework as a Recyclable Nano-Adsorbent with Superior Adsorption Capacity for Efficient Removal of Toxic Organic Dyes. *Colloids Interface Sci. Commun.* **2022**, *46*, 100511.

(35) Zhao, Z.; Li, H.; Zhao, K.; Wang, L.; Gao, X. Microwave-Assisted Synthesis of MOFs: Rational Design via Numerical Simulation. *Chem. Eng. J.* **2022**, *428*, 131006.

(36) Klimakow, M.; Klobes, P.; Thünemann, A. F.; Rademann, K.; Emmerling, F. Mechanochemical Synthesis of Metal-Organic Frameworks: A Fast and Facile Approach toward Quantitative Yields and High Specific Surface Areas. *Chem. Mater.* **2010**, *22*, 5216–5221.

(37) Pichon, A.; James, S. L. An Array-Based Study of Reactivity under Solvent-Free Mechanochemical Conditions — Insights and Trends. *CrystEngComm* **2008**, *10*, 1839–1847.

(38) Wilmer, C. E.; Leaf, M.; Lee, C. Y.; Farha, O. K.; Hauser, B. G.; Hupp, J. T.; Snurr, R. Q. Large-Scale Screening of Hypothetical Metal-Organic Frameworks. *Nat. Chem.* **2012**, *4*, 83–89.

(39) Gándara, F.; Bennett, T. D. Crystallography of Metal-Organic Frameworks. *IUCrJ* **2014**, *1*, 563–570.

(40) Cavka, J. H.; Jakobsen, S.; Olsbye, U.; Guillou, N.; Lamberti, C.; Bordiga, S.; Lillerud, K. P. A New Zirconium Inorganic Building Brick Forming Metal Organic Frameworks with Exceptional Stability. *J. Am. Chem. Soc.* **2008**, *130*, 13850–13851.

(41) Altomare, A.; Cuocci, C.; Giacovazzo, C.; Moliterni, A.; Rizzi, R.; Corriero, N.;

Falcicchio, A. EXPO2013: A Kit of Tools for Phasing Crystal Structures from Powder Data. *J. Appl. Crystallogr.* **2013**, *46*, 1231–1235.

(42) Schlichte, K.; Kratzke, T.; Kaskel, S. Improved Synthesis , Thermal Stability and Catalytic Properties of the Metal-Organic Framework Compound $Cu_3(BTC)_2$. *Microporous Mesoporous Mater.* **2004**, *73*, 81–88.

(43) Carson, C. G.; Hardcastle, K.; Schwartz, J.; Liu, X.; Hoffmann, C.; Gerhardt, R. A.; Tannenbaum, R. Synthesis and Structure Characterization of Copper Terephthalate Metal – Organic Frameworks. *Eur. J. Inorg. Chem.* **2009**, 2338–2343.

(44) Zhou, W.; Wu, H.; Yildirim, T. Enhanced H_2 Adsorption in Isostructural Metal−Organic Frameworks with Open Metal Sites: Strong Dependence of the Binding Strength on Metal Ions. *J. Am. Chem. Soc.* **2008**, *130*, 15268–15269.

(45) Guesh, K.; Caiuby, A.D.C.; Mayoral, Á.; Díaz-García, M.; Díaz, I.; Sanchez-Sanchez, M. Sustainable Preparation of MIL-100(Fe) and Its Photocatalytic Behavior in the Degradation of Methyl Orange in Water. *Cryst. Growth Des.* **2017**, *17*, 1806–1813.

(46) Yuan, S.; Feng, L.; Wang, K.; Pang, J.; Bosch, M.; Lollar, C.; Sun, Y.; Qin, J.; Yang, X.; Zhang, P.; Wang, Q.; Zou, L. Stable Metal – Organic Frameworks : Design , Synthesis , and Applications. *Adv. Mater.* **2018**, *30*, 1704303.

(47) Park, K. S.; Ni, Z.; Côté, A. P.; Choi, J. Y.; Huang, R.; Uribe-Romo, F. J.; Chae, H. K.; O'Keeffe, M.; Yaghi, O. M. Exceptional Chemical and Thermal Stability of Zeolitic Imidazolate Frameworks. *Proc. Natl. Acad. Sci. U. S. A.* **2006**, *103*, 10186–10191.

(48) Gross, A. F.; Sherman, E.; Vajo, J. J. Aqueous Room Temperature Synthesis of Cobalt and Zinc Sodalite Zeolitic Imidizolate Frameworks. *Dalt. Trans.* **2012**, *41*, 5458–5460.

(49) Cheng, D.; Khan, M. A.; Houser, R. P. Copper(II) and Cobalt(II) Coordination Polymers with Bridging 1,2,4,5-Benzenetetracarboxylate and N-Methylimidazole: Coordination Number-Determined Sheet Topology. *J. Chem. Soc. Dalt. Trans.* **2002**, 4555–4560.

(50) Zhu, L. N.; Zhang, L. Z.; Wang, W. Z.; Liao, D. Z.; Cheng, P.; Jiang, Z. H.; Yan, S. P. $[Zn(BDC)(H_2O)_2]_n$: A Novel Blue Luminescent Coordination Polymer Constructed from BDC-Bridged 1-D Chains via Interchain Hydrogen Bonds (BDC = 1,4-Benzenedicarboxylate). *Inorg. Chem. Commun.* **2002**, *5*, 1017–1021.

(51) Song, Y. J.; Zhang, P.; Ji, J. W.; Han, Z. B. Influence of the Size of Aromatic Chelate Ligands on the One-Dimensional Chains of Copper(II) Dicarboxylate Coordination Polymers. *Russ. J. Coord. Chem. Khimiya* **2009**, *35*, 698–703.

(52) Go, Y. B.; Wang, X.; Anokhina, E. V.; Jacobson, A. J. A Chain of Changes: Influence of Noncovalent Interactions on the One-Dimensional Structures of Nickel(II) Dicarboxylate Coordination Polymers with Chelating Aromatic Amine Ligands. *Inorg. Chem.* **2004**, *43*, 5360–5367.

(53) Pariyar, A.; Gopalakrishnan, S.; Stansbery, J.; Patel, R. L.; Liang, X.;

Gerasimchuk, N.; Choudhury, A. A 1-D Coordination Polymer Route to Catalytically Active Co@C Nanoparticles. *RSC Adv.* **2016**, *6*, 38533–38540.

(54) Dolomanov, O. V; Bourhis, L. J.; Gildea, R. J.; Howard, J. A. K.; Puschmann, H. OLEX2 : A Complete Structure Solution , Refinement and Analysis Program. *J. Appl. Crystallogr.* **2009**, *42*, 339–341.

(55) Sheldrick, G. M. Crystal Structure Refinement with SHELXL. *Acta Crystallogr. Sect. C Struct. Chem.* **2015**, *C71*, 3–8.

(56) Spackman, P. R.; Turner, M. J.; McKinnon, J. J.; Wolff, S. K.; Grimwood, D. J.; Jayatilaka, D.; Spackman, M. A. CrystalExplorer: A Program for Hirshfeld Surface Analysis, Visualization and Quantitative Analysis of Molecular Crystals. *J. Appl. Crystallogr.* **2021**, *54*, 1006–1011.

(57) Hirshfeld, F. L. Bonded-Atom Fragments for Describing Molecular Charge Densities. *Theor. Chim. Acta* **1977**, *44*, 129–138.

(58) Spackman, M. A.; Jayatilaka, D. Hirshfeld Surface Analysis. *CrystEngComm* **2009**, *11*, 19–32.

(59) Spackman, M. A.; Byrom, P. G. A Novel Definition of a Molecule in a Crystal. *Chem. Phys. Lett.* **1997**, *267*, 215–220.

(60) Spackman, M. A.; McKinnon, J. J. Fingerprinting Intermolecular Interactions in Molecular Crystals. *CrystEngComm* **2002**, *4*, 378–392.

(61) López-Periago, A.; Vallcorba, O.; Frontera, C.; Domingo, C.; Ayllón, J. A. Exploring a Novel Preparation Method of 1D Metal Organic Frameworks Based on Supercritical CO_2. *Dalt. Trans.* **2015**, *44*, 7548–7553.

Chapter III

MOF Catalyzed Intermolecular & Intramolecular Cross-Coupling Reaction

Part of this chapter has been published in Inorg. Chem. **2022***, 61*, 13685–13699,

DOI: 10.1021/acs.inorgchem.2c00270

Abstract

The coordinatively unsaturated sites (CUS) are pivotal in metal-centred catalysis for the substrate to bind and react. Metal-organic frameworks (MOFs) with their robust structure, can possess CUS without disturbing the framework integrity. It can be done typically by the post-synthetic treatment of MOFs under heat and high vacuum that removes the feebly attached ligands or adsorbed solvents from the metal center or frameworks. These post-synthetic treatments of MOFs are referred to as "activation of MOF" and are time-consuming and associated with only thermally stable MOFs that hinder the overall progress of MOF toward catalysis. Herein we report the catalytic activity of Cu-1D MOF with readily available towards coupling reactions. The Cu-1D MOF has CUS as synthesized and does not require any activation to be catalytically active. The role of CUS was extensively studied and compared with other MOFs that require prior activation to be catalytically active. The Intermolecular C-heteroatom cross-coupling of a variety of *N*-heterocycles, aliphatic, aromatic, alicyclic amines & amides (C-N), phenols (C-O), and thiols (C-S) with aryl halides (halide = I, Br) were achieved with 70 to 95% yield, better than the state of art Cu-based homogenous system. The mechanistic pathway was studied with experimental and computational methods. Mechanistically, the C-N coupling catalytic cycle is initiated by the *in-situ* reduction of Cu(II) by KOH/DMSO to Cu(I) species. Subsequently, Cu(I) undergoes oxidative addition followed by reductive elimination to form a cross-coupled product. High stereoselectivity was found for the intramolecular C-N coupling reaction to give tetrahydro quinoxalines with an enantiomeric excess (*ee*) of more than 98.5%.

III.1. Introduction

Transition metal-catalyzed cross-coupling of aryl halide and heteroatom (N, O, S) to form C-X (X= N, O, S) bonds has emerged as an important reaction for synthesizing aromatic amines in various fields of basic and applied research. The presence of abundant heteroatom especially nitrogen in natural products, pharmaceuticals, bioactive molecules, synthetic organic compounds etc, makes the process of formation of C-X (X= N, O, S) bond remarkably significant.[1–4] The pioneer report for the formation of the C-N bond was made in the 19th century by Ullmann[5] and Goldberg[6] independently using a stoichiometric amount of copper salt. However, the formation of adequate waste and harsh reaction conditions are some of the major drawbacks noted for this procedure that led chemists to investigate other methodologies. Subsequently, after many years in 1983, Migita *et al.* reports the formation of a C-N bond between an aryl halide and amino stannate using a palladium catalyst.[7] Later, in the 1990s Buchwald *et al.*[8] and Hartwig *et al*[9] independently report the C-N bond formation using copper and palladium catalyst along with a strong base and suitable diamine or phosphine ligands. The Buchwald and Hartwig method with a palladium catalyst and organic ligands has a relatively large substrate scope with high functional group tolerance.[10] It is also one of the most followed procedures in academic and industrial chemistry, compared to other conventional methods such as nucleophilic aromatic substitution (S_NAr), Ullmann, and Goldberg cross-coupling reactions as these methods have a limited substrate scope. However, most advancement is achieved in cross-coupling reactions using palladium-based complexes, and that involves a homogeneous process. Using a Pd-based catalyst the palladium metal contamination in the reaction mixture is one of the major problems of the homogeneous process and considerable purification of the reaction mixture was required after completion of the reaction with

Pd catalysis.[11,12] The stability of Pd is again a major challenge with this approach. Therefore, despite the utmost development the low abundance, etc.[13] Also, the efficiency of palladium catalyst depends on the nature of the ligand that determines the electronic density of Pd metal and some important ligand system worth mentioning are bi-aryl phosphines (Buchwald ligand),[14,15] phosphine based ligands,[16] nitrogen-containing hetero-cyclic carbenes,[17,18] carbapalladacycles[19] etc. Nevertheless, the use of ligands also hampers the atom economy of catalytic system. Therefore, the formation of C–N bond under ligand free, mild and inexpensive conditions is still a challenging task. Compared to the Pd-analogue, the copper-based catalysts are non-toxic, abundantly available and are one of the first catalyst used for C-N bond formation. In recent days it has remarkably developed mostly due to the accessibility to Cu species upto four stable oxidation state of 0 to +3, cost effective, green catalyst etc.[20] Various copper based heterogeneous catalyst have been reported in due time where the work reported by Punniyamurthy and group is notable as they have used CuO nanoparticles as heterogeneous catalyst for C-N,[21] C-O and C-S[22] bond formation and plethora of substrate scope has been established.

Not surprisingly, MOFs with well exposed catalytic sites have been explored towards various cross coupling reactions. Phan *et. al.* utilized $Cu(INA)_2$ (INA=isonicotinic acid) MOF and demonstrated its higher catalytic activity in *N*-arylation in comparison to common homogeneous copper catalysts and other Cu-MOFs.[23] Xie *et al.* reported the use of Cu containing MOF-199 for the Ullmann type coupling reaction and they were able to obtain target products in moderate to excellent yields.[24] Koner and their research group have successfully designed an efficient heterogeneous catalyst for C-N cross-coupling reactions. They achieved this by anchoring a Cu(II) Schiff-base moiety into the porous isoreticular metal-organic framework (IRMOF-PI-Cu) through a post-

synthetic modification method.[25] There is an increasing number of reports that demonstrate the direct application of MOFs in coupling reactions, indicating the expanding utility of MOFs in this field.[26,27]

Although MOFs with high metal content, ordered crystallinity, high surface area, and well exposed catalytic sites have been widely explored towards many organic transformations. Most of the MOFs requires activation priorto reaction to be catalytically active. As the active metal sites in MOFs are mostly coordinated to organic ligands/linkers/solvents during synthesis and makes them less available for the substrates to bind and interact. The removal of these liable ligands/linkers/solvents (or guest molecules in pores) *via* post-synthetic treatment generates coordinatively unsaturated sites (CUS) in metal centre that is accessible for reactants, making MOF a promising catalyst.[28] Several MOFs such as MIL-101 (Cr),[29] HKUST-1,[30] Zr-UiO MOF,[31] MIL-100 (Fe),[32] etc are well known to act as catalyst towards organic reactions only after generation of CUS *via* activation. However, these post synthetic activation process of MOF is time consuming as some solvents are less volatile (e.g DMF) and removing them from the MOFs pore requires high temperature and long evacuation time. For example, when the active sites are occupied by solvents like DMF, it requires high temperature or long evacuation times. As a result, even for a robust MOF with high thermal and chemical stability, degradation of the MOF are reported on overheating under vacuum.[33] Again, in most of the cases when MOF is to be recycled efficiently, repetitive activation is required. Therefore, to get rid of activation process in MOF, we envisioned the design of MOF that has pre-existing CUS and does not require post synthetic activation to be catalytically active. To do so we have synthesized Cu-based MOF using benzene dicarboxylic acid and *N*-methylimidazole (Mim) as coordinating ligand. Interestingly, the rational use of Mim ligand coordinates to Cu

metal from axial position that allows the growth of polymeric framework strictly towards one dimension. The one-dimensional polymeric framework has a tetra coordinated Cu metal and thereby synthetically available CUS. Over all, in this chapter, we present the application of Cu-1D MOF with pre-existing CUS as multifunctional recyclable catalyst for cross coupling reaction to form C(heteroatom)-X (X=N, S & O) bonds (Figure III.1).

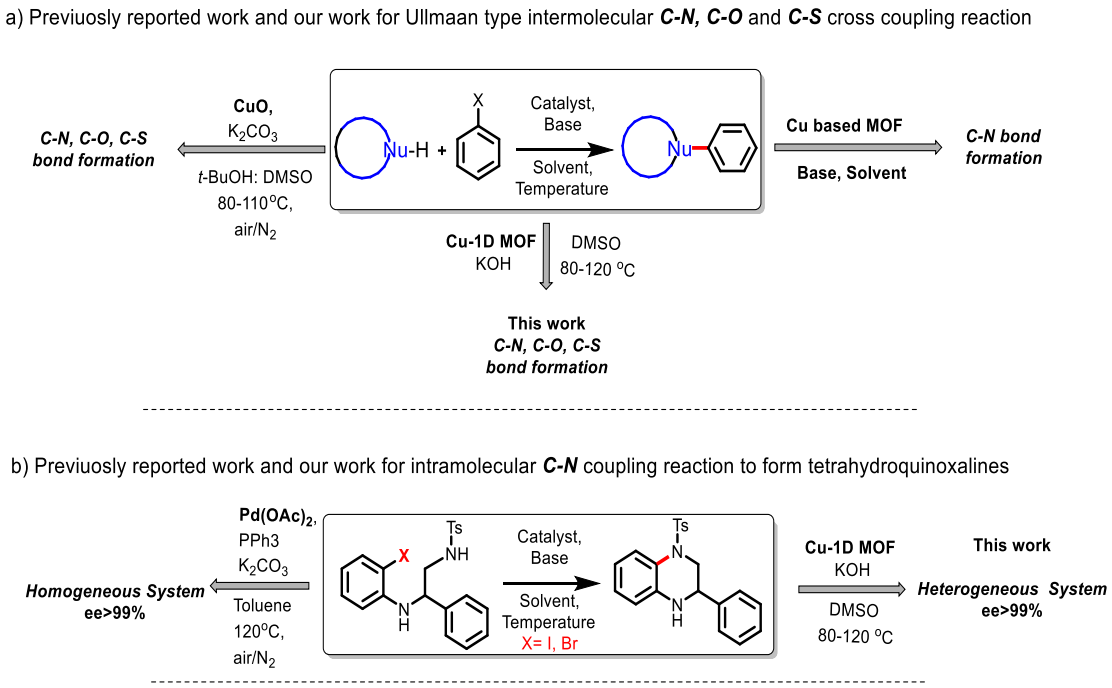

Figure III.I. Comparative catalytic approach of our work with previously reported work of intermolecular C-N, C-O, C-S coupling,[42-47] intramolecular C-N coupling.[37]

III.2. Result and discussion:

III.2.1. Intermolecular C-N coupling reaction:

The square planar geometry of tetra coordinated Cu metal centre in Cu-1D has readily available CUS, where substrate can bind and react and unlike other MOFs it does not require an activation to be catalytically active. The catalytic potential of Cu-1D MOF has been explored towards cross coupling reaction to form C-N, C-S and C-O bonds.

At first the C-N bond formation was explored and reaction between pyrazole (**1a**) and iodobenzene (**2a**) was chosen as a model reaction (Scheme III.1).

Scheme III.1: Model reaction for Cu-1D catalyzed intermolecular C-N coupling reaction.

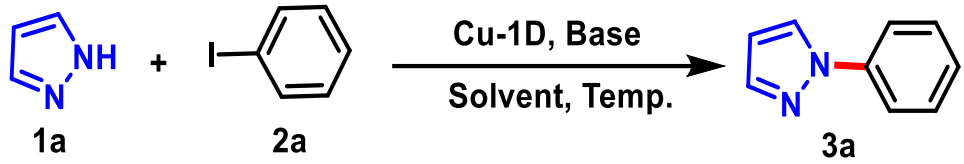

The model reaction was optimized methodically to study the effect of solvents, temperature, bases and catalyst amount. The progress of reaction was timely monitored using TLC giving iodine stain and all the products were purified by column chromatography techniques. To begin with, the reaction was initiated with pyrazole (**1a**, 1.0 equiv.) as a limiting substrate and to facilitate complete consumption of the pyrazole (N-H partner), the Ar-X partner iodobenzene (**2a)** was used in excess **(**1.5 equiv.) along with 2.5 mol% of **Cu-1D** as catalyst and KOH (1.5 equiv.) as base (Table III.1, entry 1). The reaction was processed using DMF as a solvent at 120 °C and in a time span of 5 h, a new product was formed. The product was isolated using column chromatographic techniques using 10% *EtOAc:hexane* as eluent. The formation of desired product 1-phenyl-1*H*-pyrazole (**3a**) was confirmed from the ^{1}H & ^{13}C-NMR (figure III.2) that give downfield doublet (d) peak at 7.87 (*J*=2.52 Hz) and 7.74 (*J*=1.8 Hz) which can be assigned to the protons from pyrazole ring (H4 and H6) receptively (Figure III.1a). The two aromatic proton, H1 and H2 from benzene ring shows a doublet and triplet respectively at δ = 7.69 (*J*=7.4 Hz) and 7.43 (*J*=7.8 Hz) ppm. Similarly, triplet of one proton each for H3 (benzene ring) and H6 (pyrazzole ring) were observed at δ = 7.27 (*J*=7.4 Hz) and 6.44 (*J*=2.0 Hz) ppm respectively. The ^{13}C-NMR of the isolated product shows seven peaks responding to seven different carbon environments

in the product. The respective peaks for C1, C2, C3, C4, C5, C6 and C7 was observed at the chemical shift value of 119.1, 129.4, 126.8, 140.1, 126.4, 107.6 and 141.0 respectively.

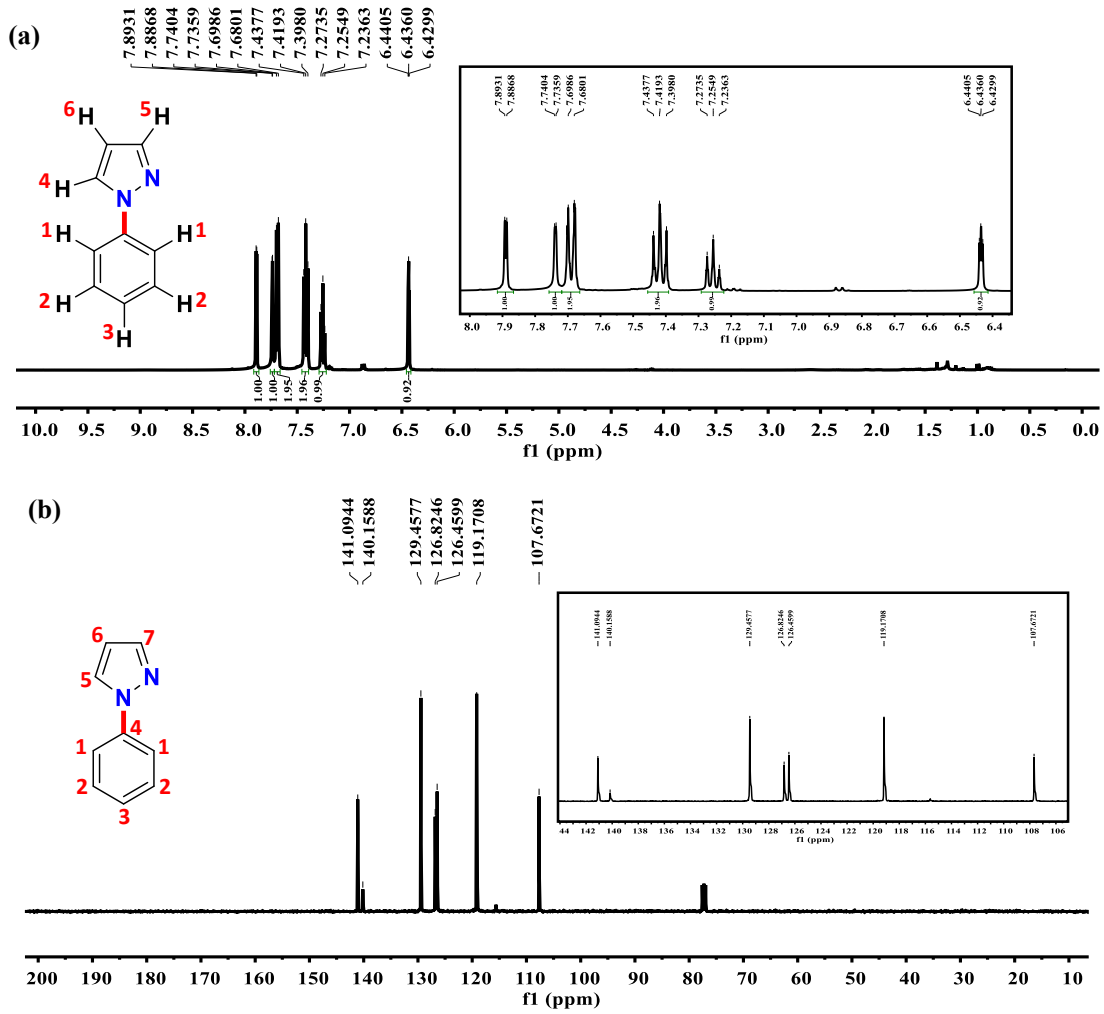

Figure III.2: (a) ^{1}H-NMR (400 MHz) and (b) ^{13}C-NMR (100 MHz) of **3a** in $CDCl_3$.

Furthermore, the optimization of the reaction was performed. The effect of base was scrutinized by performing the model reaction with Na_2CO_3, K_2CO_3, Cs_2CO_3 and NaOH where **3a** was formed with respective yield of <1%, 40%, 87% and 85% (Table III.1, entries 1−5). Higher yield with strong base indicates the breaking of N-H bond to be a key step in this catalytic process. Next when different solvents were used for the

reaction system, the reaction progressed only with polar solvents (CH_3CN, dioxane, DMF etc) (Table III.1, entries 6−9)**.** Nevertheless, substituting DMF with DMSO as the solvent of the catalytic reaction resulted in an increase in higher yield from 90% to 95% (Table III.1, entry 10). The reaction was found efficient only with polar solvents which points to the involvement of ionic intermediates in the reaction. Increasing the catalytic loading to 5 mol% did not improve the efficacy of model reaction and it is worth mentioning that the reaction performed in the absence of catalyst did not produce **3a**, marking the catalytic of Cu-1D MOF. Lastly, the reaction at lower temperature (100 and 80 ℃) did not progress the product yield (Table III.1, entry 14-15). Therefore, the reaction at 120 °C using DMSO as solvent, KOH as base and 2.5 mol% catalytic loading was chosen as the best optimal reaction condition for Cu-1D MOF catalyzed cross coupling reaction.

Table III.1. Optimization studies for C−N cross-coupling reaction between pyrazole (**1a**) and iodobenzene (**2a**).*

Entry	Catalyst (mol %)	Base	Solvent	Temp (°C)	Time (h)	Yield (%)[a]
1.	**Cu-1D** (2.5)	KOH	DMF	120 °C	5	90
2.	**Cu-1D** (2.5)	Na_2CO_3	DMF	120 °C	5	trace
3.	**Cu-1D** (2.5)	K_2CO_3	DMF	120 °C	5	40
4.	**Cu-1D** (2.5)	NaOH	DMF	120 °C	5	85
5.	**Cu-1D** (2.5)	Cs_2CO_3	DMF	120 °C	5	87
6.	**Cu-1D** (2.5)	KOH	toluene	110 °C	6	trace
7.	**Cu-1D** (2.5)	KOH	CH_3CN	80 °C	5	67
8.	**Cu-1D** (2.5)	KOH	dioxane	100 °C	5	72
9.	**Cu-1D** (2.5)	KOH	H_2O	100 °C	5	nr
10.	**Cu-1D** (2.5)	KOH	DMSO	120 °C	1.5	95
11.	-	KOH	DMSO	120 °C	6	nr
12.	**Cu-1D** (5.0)	KOH	DMSO	120 °C	1.5	92
13.	**Cu-1D** (1.0)	KOH	DMSO	120 °C	1.5	90
14	**Cu-1D** (2.5)	KOH	DMSO	100 °C	2.5	40
15	**Cu-1D** (2.5)	KOH	DMSO	80 °C	2.5	20

*Reactions conditions: Pyrazole (1 mmol), iodobenzene (1.5 equiv.), base (1.5 equiv), catalyst (2.5 mol%), solvent (1 mL). [a]The yields are isolated yield.

The optimized reaction condition of Cu-1D catalytic system was applied to establish diverse substrate scope for C-N bond formation between aryl halide and variety of NH containing compounds such as *N*-heterocycles, amides, arylamine, and long-chain aliphatic amines. The reaction of *N*-heterocycle (pyrazole, **1a**) was performed with iodobenzene (**2a-f)** bearing various substituents to understand their electronic effects on *N*-arylation (Figure III.3). In general, *N*-arylated products were obtained in lower yields with the electron-donating substituents (*p*-CH_3: 78%, **3b**), (*p*-OCH_3: 68%, **3c**), however yield of the products are comparatively higher with electron-withdrawing groups (*p*-NO_2: 81%, **3d**) and (*p*-F:80%, **3e**).

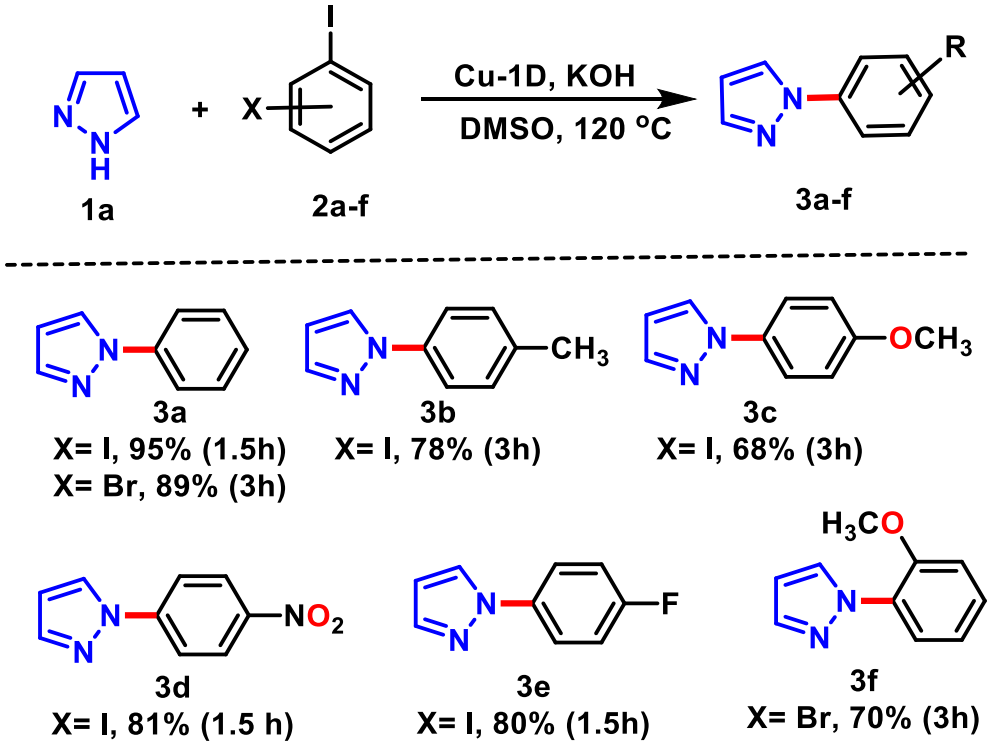

Figure III.3: Substrate scope for intermolecular C-N coupling reactions between pyrazole and derivatives of aryl halide.

The differences in reactivity observed could be explained by the ability of electron-withdrawing groups in enhancing the reactivity of iodobenzene derivatives in C−N cross-coupling reactions, while the opposite effect is observed for electron-donating

groups. Further with bromobenzene as a coupling partner, slightly lower yield was obtained for the products of all the C-N coupling reactions compared to the iodobenzene counterpart. The corresponding coupling product (**3f**) was obtained in 70% yield with the *ortho*-methoxy bromobenzene (**1f**). The reaction system was further validated with various halide groups (Br and Cl) in aryl halide. When bromobenzene was used as halide partner, the desired product **3a** was formed with a yield of 89% in 3 h however with chlorobenzene desired product was not formed. The higher bond dissociation energy of C-Cl bond (78.8 kcal mol^{-1}) which is comparatively higher than C-Br (65.7 kcal mol^{-1}) and C-I (57.3 kcal mol^{-1}) inhibits the reaction with Chloro-halides. Furthermore, when the substrate containing additional functional group like chlorine (4-bromochlorobenzene) was treated with pyrazole, C-N coupling still proceeded through the C-Br bond. The product 1-(4-chlorophenyl)-*1H*-pyrrole (**3g**) was formed (Scheme III.2) in 56% yield showing that the coupling is specific to bromine and highly tolerant to other competing functional group like chlorine.

Scheme III.2: Reaction with 4-bromochlorobenzene to validate chloro-tolerance in the Cu-1D catalyzed C-N coupling reaction system

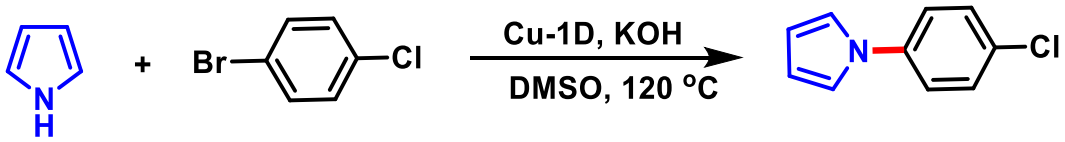

1b **2g** **3g,** 56%, 3 h

The efficacy of the catalytic system was also evaluated with a library of other *N*-heterocycles having free NH group as substrates under the optimized reaction condition. The corresponding *N*-arylated derivatives of imidazole (**3h-j**, 86-95%,), pyrrole (**3k-l**, 89-92%,), indole (**3m-n**, 90-76%,), triazole (**3o**, 89%,) and benzimidazole (**3p,** 78%) were obtained in very good to excellent yields (Figure III.4). It is to be noted

that Xie *et al.* has also reported the formation 93% of **3k** product in 12 h using MOF-199 whereas in our case, **Cu-1D** gives 92% of **3k** in just 2 h.[24]

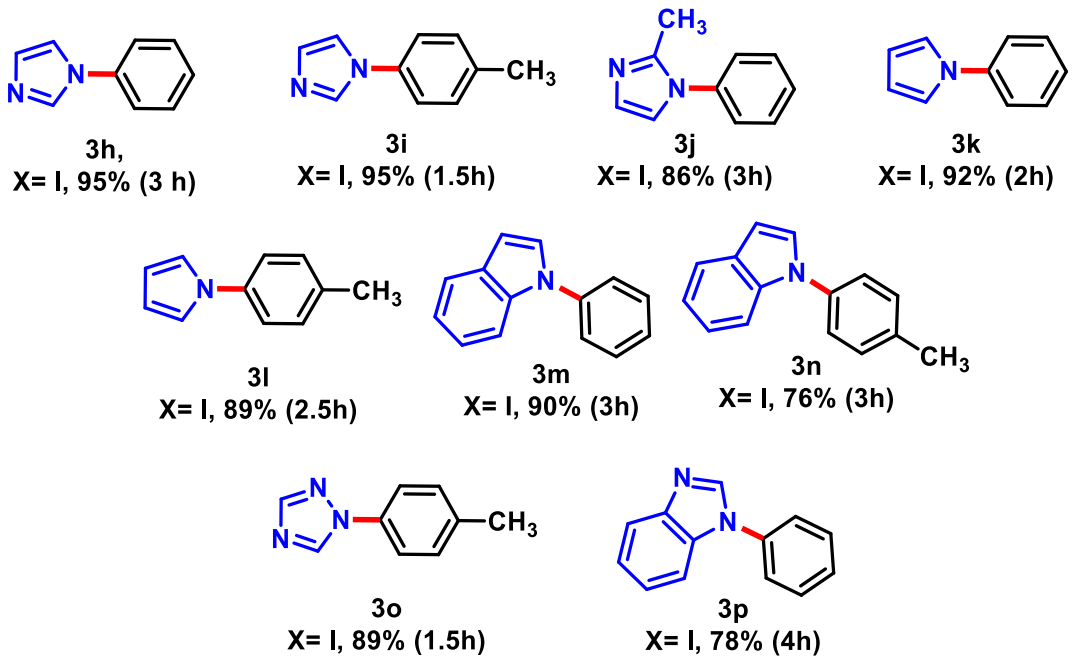

Figure III.4: Substrate scope for Cu-1D catalyzed C-N coupling reaction with various other *N*-heterocycles having free NH group.

The catalytic system was then studied with various alicyclic *N*-heterocycles. The substrates scope was established and desired C-N coupled product was obtained with alicyclic *N*-heterocycles substrate such as indoline, 1,2,3,4-tetrahydroisoquinoline, and morpholine that produced the product **3q** (83%), **3r-s** (85-90%) and **3t** (71%) respectively (Figure III.5). It is to be noted that in order to avoid the aromatization of indoline at 120 °C the reaction was conducted at 80 °C.[34]

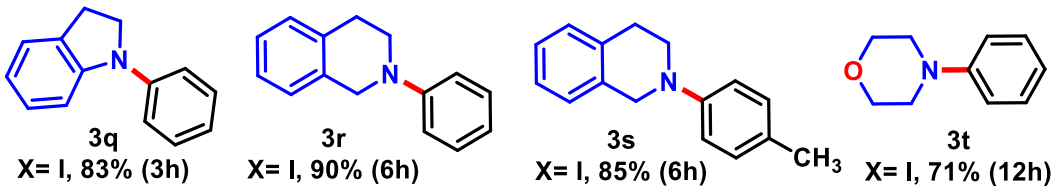

Figure III.5: Substrate scope for Cu-1D catalyzed C-N coupling reaction with various alicyclic N-heterocycles substrate.

The coupling product was also formed for benzamide (**1u**) and aniline (**1v**) as substrate and product yield of 85% (**3u**) and 83% (**3v**) respectively was obtained (Figure III.6). The long-chain aliphatic amines (oleylamine and octylamine) were also employed as a substrate and under the optimal reaction condition 90-91% product yield was obtained for **3w** and **3x**. Previously these C-N coupled product with long chain amines was formed by the reaction between oleyl alcohol and aniline as reported by Mandal *et al.* with a product yield of 80%.[35]

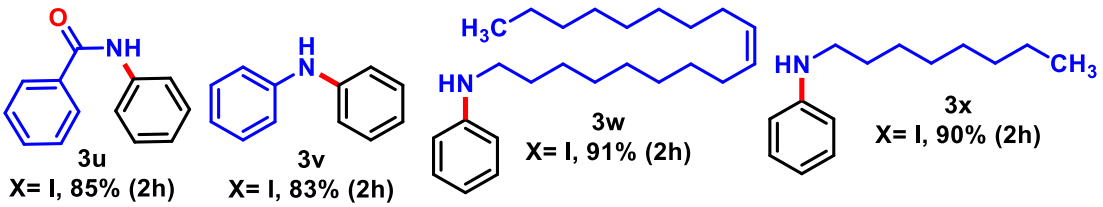

Figure III.6: Substrate scope for Cu-1D catalyzed C-N coupling reaction with primary amine and long chain amine substrate.

III.2.2. Intermolecular C-O and C-S coupling reaction:

After investigating the variety of substrate library for C-N bond formation we shifted our focus to explore the intermolecular cross coupling reaction between phenol/thiol derivatives and iodobenzene derivatives that forms corresponding C-O and C-S bond respectively. Under the optimized reaction the corresponding C-O cross coupled products (**5a-d**) were obtained in excellent yield from 72-83% (Figure III.2) and C-S cross coupled products (**5e-g**) in 85-86% yield. The electron withdrawing group derivatized aryl halide has positive effect to the produced cross coupled product with phenol/thiol. It is to be noted that the C-O and C-S bond formation was previously reported by Punniyamurthy *et al.* using CuO as heterogeneous catalyst. However, when compared to Cu-1D catalyst, more time and temperature is required to produced appreciable yield of desired cross coupled product.[21,22,36]

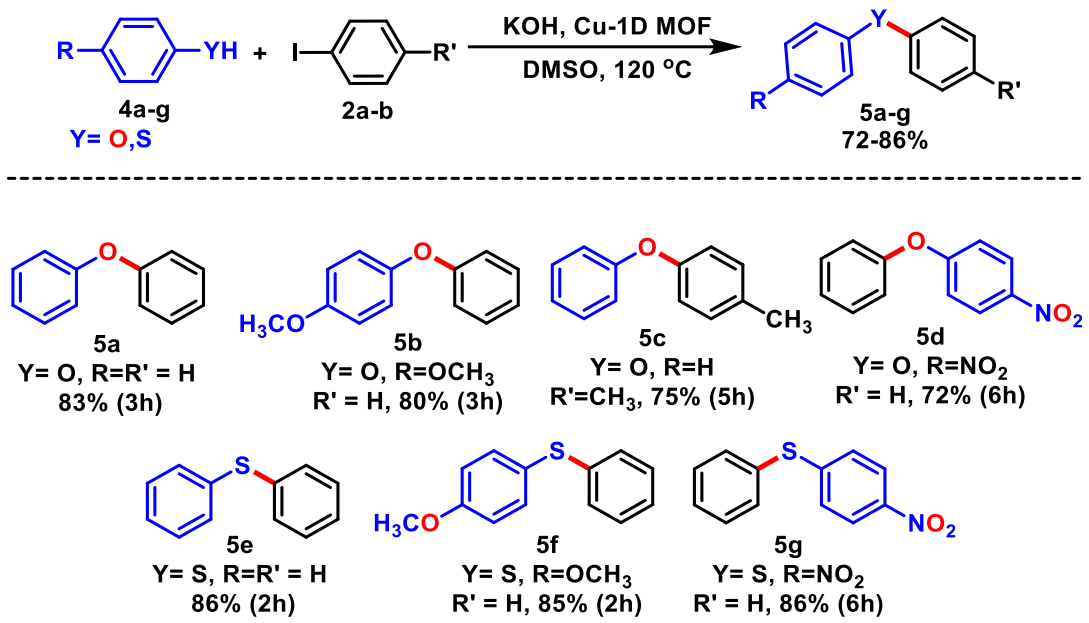

Figure III.7: Substrate scope for intermolecular C-O and C-S coupling reactions. Reaction condition: Phenols/thiols (1 mmol), aryl halide (1.5 equiv.), KOH (1.5 equiv.), Cu-1D (2.5 mol%), DMSO (1 mL). The yields are isolated yields.

With all these results the Cu-1D MOF nestle as a versatile catalyst towards intermolecular C−X (X=N, O, S) coupling reactions with a widespread range of substrate tolerance. Previously, CuO has been reported to form C-heteroatom bond with various coupling partner such as aryl halides, tosylates, and boronic acids. Compared to our catalytic system CuO system is kinetically inferior and desired cross-coupled products is produced at an elevated time and temperature.[21,22,36] The coupling of amides and aryl halides (Cl, Br, and I) through the Buchwald–Hartwig amination reaction has been widely successful in both industrial and research applications using palladium[8,9] and copper[37] catalysts. However, this method is limited to primary and cyclic amides/amines and utilizes a costly Pd-catalytic system. Cu-1D, on the other hand, can form C-heteroatom bonds with aryl halides (I, Br) and a diverse array of N-containing molecules, including azoles (such as imidazole, pyrazole, and triazole), cyclic and alicyclic amines, primary amide, long-chain amine, primary and secondary amines, phenols, and thiols. Additionally, when compared to previously reported MOF-based

catalysts such as [Cu(INA)$_2$],[23] MOF-199,[24] IRMOF-3-PI-Cu,[25] Cu-MOF-74[27] and Cu(tpa)-MOF[38] for C-N bond product formation, Cu-1D catalysts were able to produce a significant amount of the desired product within a shorter time frame (Table III.2). As a result, the utilization of Cu-1D catalysts presents a cost-effective substitute for expensive palladium-based catalysts and other MOF-based systems.

Table III.2. Catalytic comparison for heterogeneous Cu catalytic system towards cross coupling reaction.

Sl. No	Catalyst	Yield (%)	Time (h)	Reference
1.	[Cu(INA)$_2$]	94%,	6 h	23
2.	MOF-199	93%	12 h	24
3.	IRMOF-3-PI-Cu	92%,	20 h	25
4.	Cu-MOF-74	90%	24 h	27
5.	CuO NP	93%	15 h	37
7.	Cu(tpa)-MOF	99%,	12 h	38
8.	Cu-1D	95%	1.5 h	Our work

III 2.3. Intramolecular C-N coupling reaction:

Intramolecular cross coupling reaction, is well known and have been extensively applied in industry to synthesis pharmacologically important and biologically active compounds. These coupling reactions being one of the less explored fields in MOF catalysis, we envisioned the practicability of our Cu-1D MOF catalytic system in synthesis of biologically important tetrahydroquinoxalines moieties *via* intramolecular C−N bond formation. Previously these moieties were reported to be synthesized *via* hydrogenation of quinoxalines, Diels−Alder [4+2] cycloaddition reaction, intramolecular Mitsunobu cyclization, amination reaction etc.[39–42] In 2011 Ghorai *et al.*

reported the Pd-catalyzed intramolecular C-N bond formation for synthesis of chiral tetrahydroquinoxalines *via* S_N2-type ring-opening of activated aziridines with 2-bromoanilines. Capitalizing the similar reaction and using from ring-opening product of activated aziridines and 2-arylanilines as a substrate, we developed a ligand-free heterogeneous method for the synthesis of tetrahydroquinoxalines with our Cu-1D MOF *via* intramolecular C-N bond formation (SchemeIII.3).

Scheme III.3: Model for intramolecular C-N coupling reaction.

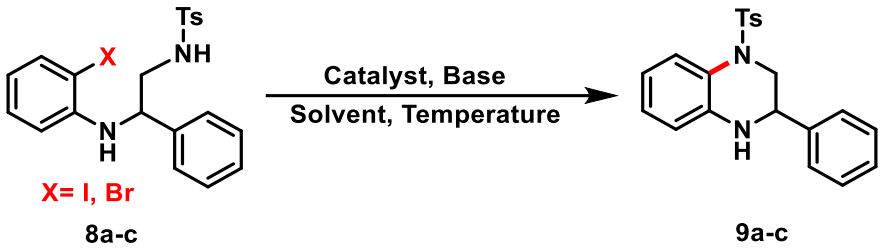

At first the substrates (**8a-c**) was prepared following the reported procedure[43] by reacting 2-aryl-*N*-tosyl aziridines and 2-iodoaniline/2-bromoaniline. The synthesized substrates **8a** was then treated under optimized reaction condition **(**Table III.1, entry 10) that produced 56% of desired product **9a**. However, on increasing the catalytic loading to 10 mol%, the substrate (**8a**, 1 mmol) produced yield upto 78% of desired product (**9a**). Therefore, with slight modification on optimized condition, intramolecular coupling reaction was initiated and various derivative of tetrahydroquinoxalines (**9a-c**) product was formed in 67-78% (Figure III.3). The intramolecular coupling with Cu-1D catalyst was also found to be feasible with bromine and 70% of **9a** was isolated. The electronic effects of the substituents were also studied for catalytic system where electron withdrawing group (-Cl) decreases the catalytic efficiency (**9b**, 67 % in 5 h) and electron donating group ($-CH_3$) has positive effect (**9c**, 76% in 3 h).

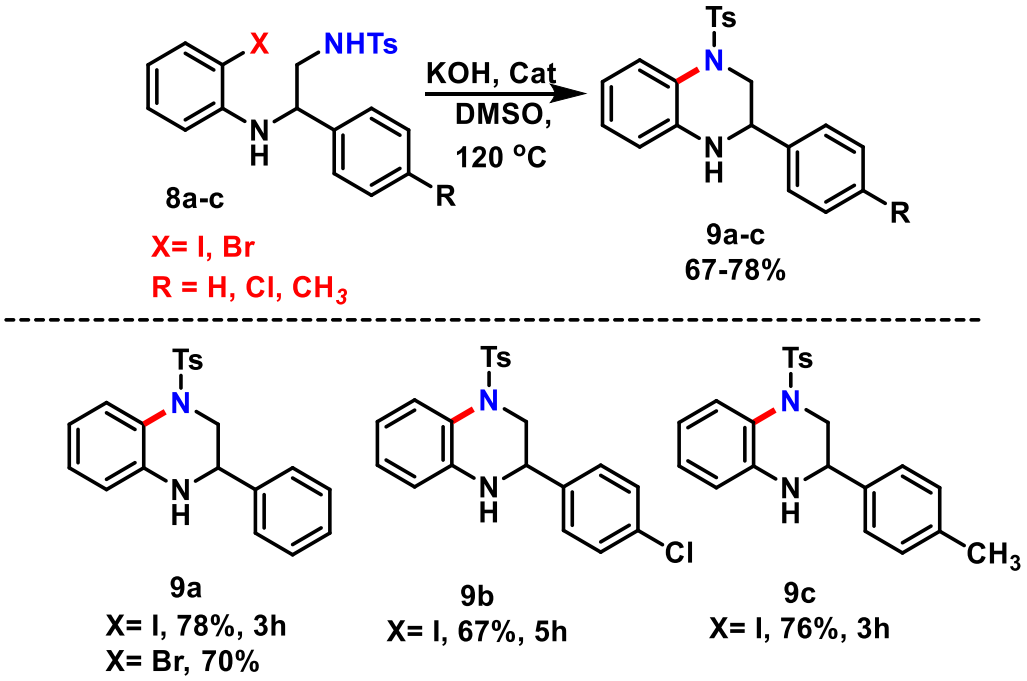

Figure III.8: Substrate scope for intramolecular C-N coupling reactions. Reaction condition: **8a-c** (1 mmol), base (1.5 equiv.), Cu-1D (10 mol%), DMSO (1 mL). The yields given are isolated yields.

To the best of our knowledge, product (3-(p-tolyl)-1-tosyl-1,2,3,4-tetrahydroquinoxaline) **(9c)** has not yet been reported. Therefore, the product **9c** was comprehensively characterized using SCXRD and NMR spectroscopy. The single crystal was grown by evaporating the mixture of **9c** dissolved in $CDCl_3$. The suitable crystal was loaded and diffracted using Cu X-ray source (λ=1.54 Å) at room temperature. The SCXRD analysis reveals that the **9c** crystallized with monoclinic crystal system and has a space group *P21/c*. The visualization of **9c** was presented as a ORTEP diagram in figure III.9. and all the necessary crystallographic data and structure refinement results for **9c** is given in table III.3.

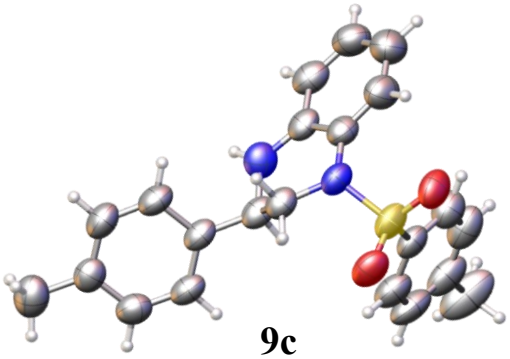

Figure III.9. ORTEP diagram for the crystal structure of **9c** (3-(p-tolyl)-1-tosyl-1,2,3,4-tetrahydroquinoxaline).

Table III.3. Crystallographic data and structure refinement results for **9c**.

Identification code	**9c**
Empirical formula	$C_{22}H_{22}N_2O_2S$
Formula weight	378.47
Crystal system	monoclinic
Space group	$P2_1/c$
a/Å	12.4354(10)
b/Å	9.0272(7)
c/Å	17.5653(12)
α/°	90
β/°	97.986(7)
γ/°	90
Volume/Å^3	1952.7(3)
Z	4
ρ_{calc}g/cm^3	1.287
μ/mm^{-1}	1.622
F(000)	800.0
Independent reflections	3589 [R_{int} = 0.0684, R_{sigma} = 0.0767]
Data/restraints/parameters	3589/0/246
Goodness-of-fit on F^2	1.032
Final R indexes [I>=2σ (I)]	R_1 = 0.0910, wR_2 = 0.2159
Final R indexes [all data]	R_1 = 0.1333, wR_2 = 0.2638
Largest diff. peak/hole / e Å^{-3}	0.54/-0.36
CCDC No.	2130894

Furthermore, to characterize the product **9c** NMR spectroscopy was performed using $CDCl_3$. The ^1H NMR and ^{13}CNMR spectra of **9c** is given in the figure III.10a-b. The doublet at δ=7.77 (*J*=8.2 Hz) ppm was due to the one aromatic hydrogen (H9). The doublet peak at δ=7.57 (*J*=7.9 Hz) ppm and δ=7.28 (*J*=7.4 Hz) ppm is due to two aromatic-hydrogen H17, H13 and H8, H4 respectively. The multiplet from δ=7.18-7.07 ppm accounts for five aromatic hydrogens such as H5, H7, H10, H14 and H16. Further, the triplet at δ=6.79 (*J*=8.0Hz) ppm and a doublet at δ=6.58 (*J*=8.0 Hz) ppm could be assigned to H11 and H12 respectively. The two aliphatic hydrogen H1, H2 can be

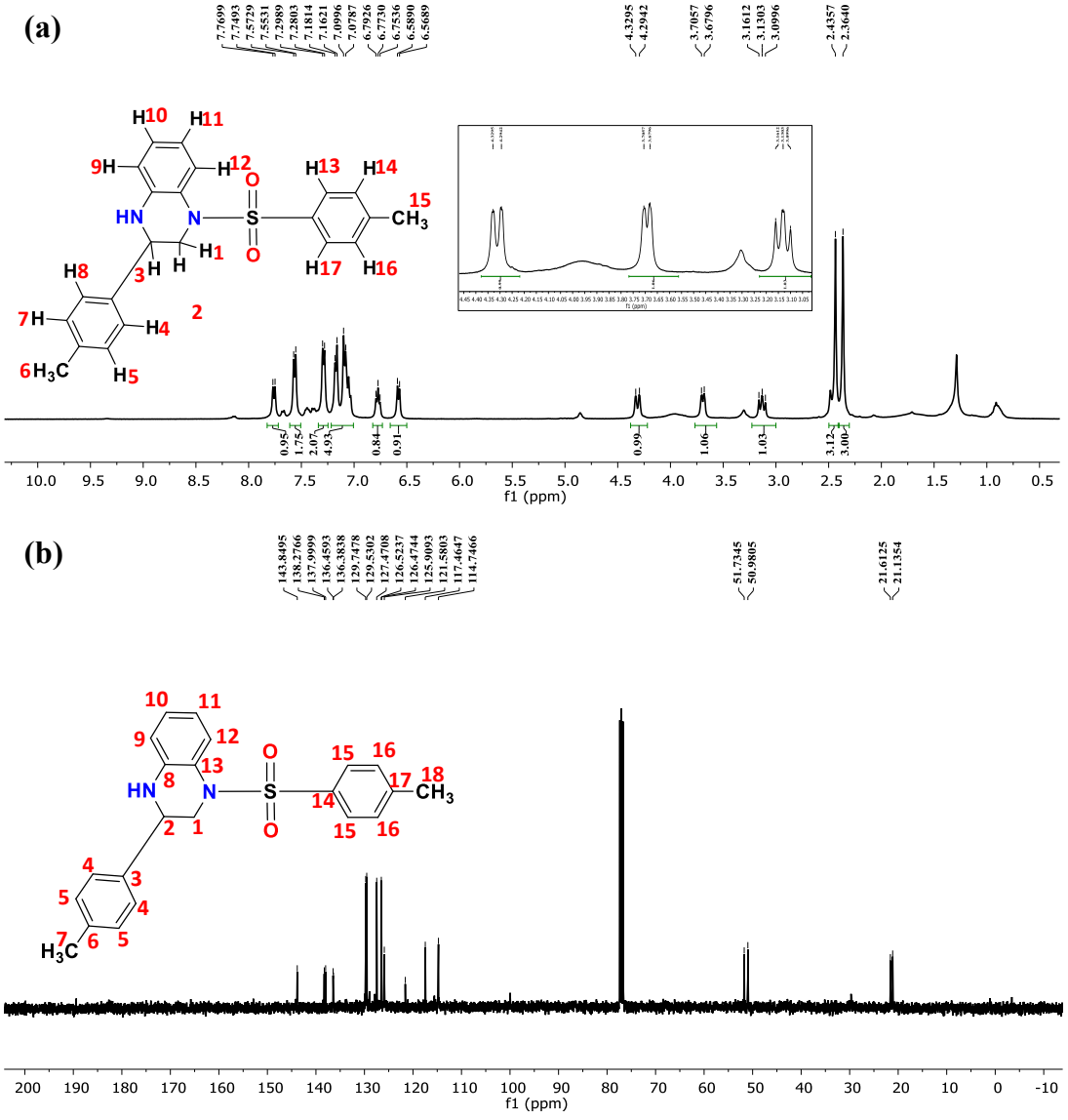

Figure III.10. (a) ^1HNMR (400 MHz) with hydrogen labelled in structure and (b) ^{13}CNMR (100 MHz) with carbon labelled in structure of **9c** in $CDCl_3$.

observed at δ=4.32 and δ=3.13 ppm with coupling constant of 14.1 and 12.3 Hz has a board peak due to the geminal coupling (inset Figure III.10a). A board peak observed at 3.37 ppm can be assigned to H3 proton as it has a coupling constant of 10.4 Hz due to the vicinal coupling with adjacent proton. Lastly the two-methyl hydrogen H6 and H12 has a singlet at 2.43 and 2.36 ppm respectively. The ^{13}C-NMR conducted at 100 MHz, using $CDCl_3$ shows eighteen peaks where fourteen are in aromatic and four are in aliphatic region (Figure III.10b). The ^{13}C peaks at δ143.8, 138.2, 137.9, 136.4, 136.3, 129.7, 129.5, 127.4, 126.5, 126.4, 125.9, 121.5, 117.4, 114.7, ppm that can be ascribed to the aromatic carbon from C3 to C17. Similarly, the peaks at 51.7, 50.9, 21.6 and 21.1 ppm can be assigned to aliphatic carbon C1, C2, C7 and C18.

Next, to explore the efficacy of Cu-1D catalyst in the synthesis of chiral tetrahydroquinoxalines was performed. An optically pure ring-opening product, (*S*)-*N*-(2-((2-iodophenyl) amino)-2-phenylethyl)-4-methylbenzenesulfonamide (**8a**) was synthesized and subjected to intramolecular C-N coupling reaction under optimized condition (Scheme III.4). The cyclized product, (*S*)-3-phenyl-1-tosyl-1,2,3,4-tetrahydroquinoxaline (***S*-9a**) was formed in good yield and the HPLC data shows an excellent enantiomeric excess (*ee* > 98.5%) indicating the preservation of chirality in the final coupling product (Figure III.11). On reaction with the racemic substrate **8a** produced racemic product as shown in figure III.11(a) with two HPLC peak for respective stereo-isomers whereas exclusively one isomer ***S*-9a** was found for ***S*-8a** (figure III.11b)**.**

Scheme III.4: Cu-1D catalyzed synthesis of chiral tetrahydroquinoxalines *via* intramolecular C-N bond formation.

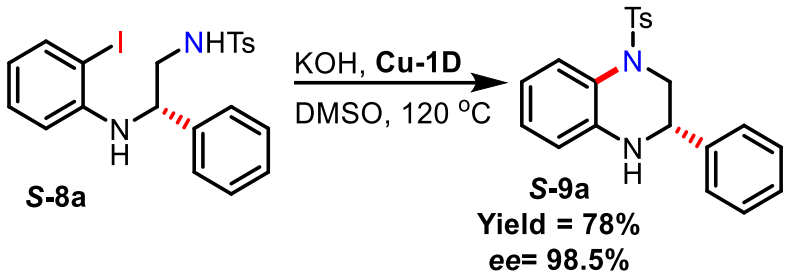

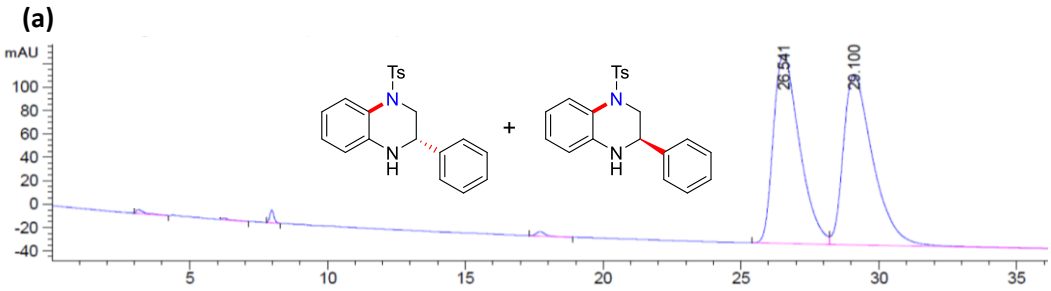

Peak	Ret. Time (min)	Width (min)	Area (mAU*s)	Height (mAU*s)	Area %
1	26.541	1.0067	1.06526 e^4	161.67493	48.8119
2	29.100	1.1168	1.09019 e^4	145.72063	49.9541

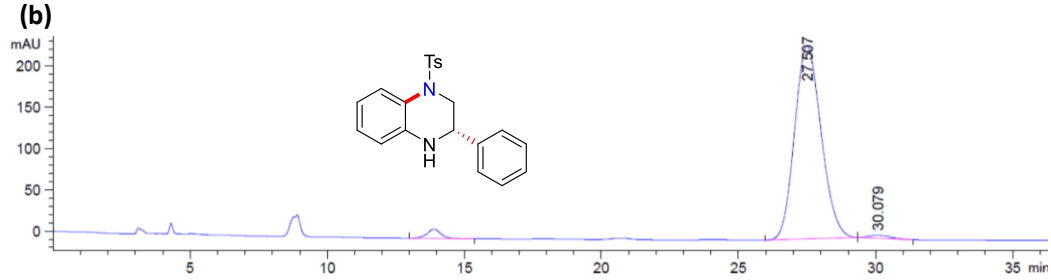

Peak	Ret. Time (min)	Width (min)	Area (mAU*s)	Height (mAU*s)	Area %
1	27.507	1.0511	1.57539 e^4	234.10103	96.2886
2	30.079	0.8377	211.52023	3.82157	1.2928

Figure III.11: (a) HPLC chromatogram of racemic **9a** (Chiralcel OD-H, hexane:isopropyl (90:10). (b) HPLC chromatogram of non-racemic (*S*)-**9a** (Chiralcel OD-H, hexane:isopropyl (90:10), *ee* >98.5%). Method for HPLC: Agilent Technologies 1200 infinity series using Daicel CHIRALCEL OD-H column, 10% IPA in hexanes, 0.8 mL min^{-1}, λ = 254 nm.

III.2.4. Role of CUS in Cu-1D:

The efficiency of Cu-1D catalyst was directly compared with various Cu(II) salts such as $Cu(NO_3)_2$, $CuCl_2$, $Cu(OAc)_2$, etc., and other Cu based MOFs, such as MOF-74(Cu), Cu(BDC) and HKUST-1(Cu). Under identical reaction condition the catalytic system of Cu-1D has better yields than other catalytic system as depicted in table III.4. It is to be noted that various cross coupling reaction has been previously explored by various group with different Cu based MOFs.[24,27,44] Often, higher reaction time is required for these catalytic systems to produce cross coupled products. This can be justified as the Cu sites in these MOFs are occupied with liable solvents and metal sites are not readily available for substrate to bind, thereby hindering the progress of reaction.

Table III.4. Comparison in the catalytic activity of Cu-1D with several homogeneous copper salts and other Cu based MOFs at 120 °C.

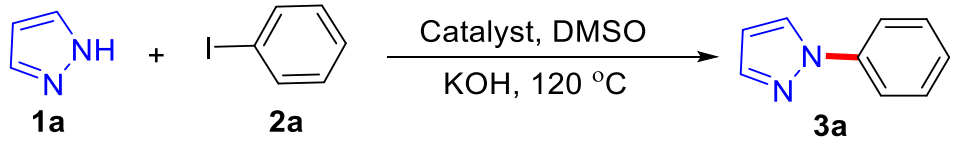

1a 2a 3a

Sl. No	Cu-Catalyst	Time	Yield (%)
1.	$CuCl_2$	3 h	58
2.	$Cu(NO_3)_2$	3 h	49
3.	$Cu(OAc)_2$	3 h	65
4.	Cu (BDC) MOF	3 h	62
5.	Cu-MOF-74	3 h	43
6.	HKUST-1 (Cu) MOF	3 h	75
7.	Cu-1D	1.5 h	95

For example, Cu(BDC) MOF contains a Cu2 dimer, where BDC ligand is coordinated in a bidentate bridging fashion and DMF molecule in axial fashion. Pitchumani et al. had reported the use of Cu-BDC MOF towards aerobic homocoupling of arylboronic acids to form symmetrical biphenyls products.[44] During the reaction, the authors conducted FTIR and noted the lack of a stretching frequency at 1663 cm^{-1} that was previously present in the pristine Cu-BDC MOF. This frequency was attributed to the C=O of the axially coordinated DMF solvent. Additionally, a new peak at around 3442 cm^{-1} was observed, which was attributed to the B-OH stretching frequency of arylboronic acid. These observations suggest that weakly coordinated DMF was substituted by arylboronic acid, leading to the generation of in-situ CUS on the metal nodes during the reaction and also highlights the importance of open metal site for progress of reaction. Similarly, HKUST-1 MOF (with apical H_2O) for C-N coupling of pyrrole and Ph-I requires 12 h and 10 mol% of catalyst to give 93% of desired product (**3l**) whereas Cu-1D delivers 92% **3l** in just 2h.[24]

III.2.5. Mechanistic investigation for Cu-1D catalyzed C-N coupling reaction:

The catalytic pathway for Cu-1D catalytic system towards C-N coupling reaction was meticulously studied from both experimental and computational techniques. At first the model reaction was introduced with radical quencher 2,2,6,6-tetramethylpiperidin-1-yloxyl (TEMPO, 1 *equiv.* to substrate) and progress of reaction was observed. The presence of TEMPO did not hinder the reaction progress (Scheme III.5). Furthermore, reactions under air and inert atmosphere gave almost the same reaction yield indicating the non-involvement of any radical species in catalytic pathway.

Scheme III.5: Reaction with radical quencher TEMPO.

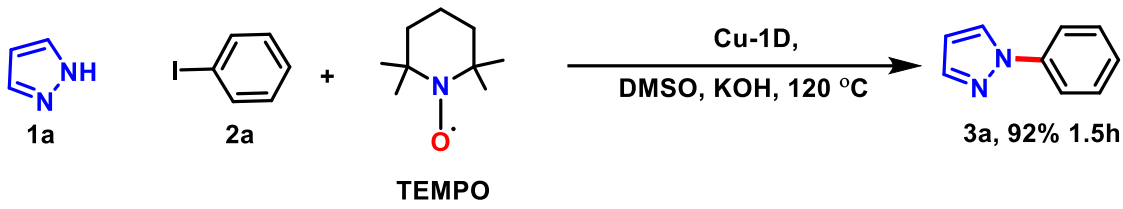

The reaction initially proceeds *via* reduction of the catalytic Cu(II) centres to Cu(I) in presence of DMSO and KOH at 120 °C. The reduction of Cu species was at first confirmed by performing electron paramagnetic resonance (EPR) experiments. The solid EPR measurements was performed at room temperature for Cu-1D MOF that shows the characteristic d^9-Cu(II) signal at g=2.066 with axial symmetry in EPR spectra confirming the presence of paramagnetic d^9-Cu(II) species in Cu-1D MOF (Figure III.12a).[45,46] Next, Cu-1D MOF (100 mg) was treated with KOH (56.1 mg) and DMSO (1 mL) at 120 °C and EPR was performed. The silent EPR spectra recorded for treated Cu-1D MOF indicates the reduction of d^9-Cu(II) to d^{10}-Cu(I) (Figure III.12a). Additionally, it is been known that a Cu(II)-Phen complex is known to absorb at 700 nm region, making Phen a useful indicator for detection of Cu ions. [47] Therefore, with the use of optical spectroscopy, it was revealed that the chelating ligand 1, 10-phenanthroline (Phen) was able to interact with both Cu(II) in situ, as demonstrated in Figure III.12b. In our case, the UV-Vis spectra of the Cu-1D suspension (solvent: DMSO) in the presence of Phen showed an absorbance at 690 nm, indicating *d-d* transition of d^9 Cu(II) species and specifically to Cu(II)-Phen interaction (Figure III.12b). However, the addition of KOH to the reaction mixture followed by heating at 120 °C resulted in the subdued peak at 690 nm. These observations are consistent with previous reports and suggest that the conversion of Cu(II) to Cu(I) species had occurred.[47]

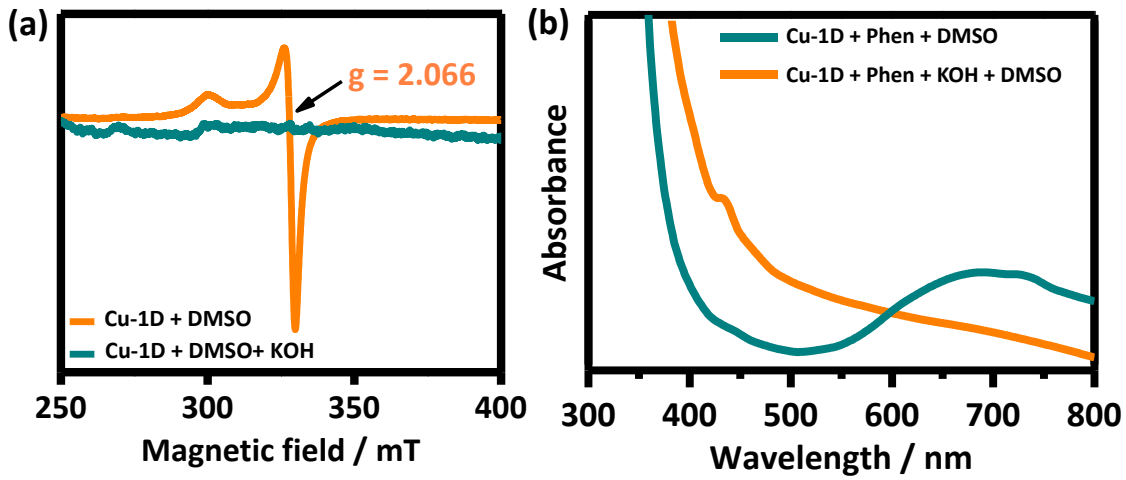

Figure III.12: (a) EPR spectra of paramagnetic **Cu-1D** and silent EPR of diamagnetic **Cu-1D** in a reaction mixture with KOH and DMSO at 120 °C; (b) UV-vis spectra of Cu-1D with Phen in DMSO and Cu-1D with Phen and KOH at 120 °C in DMSO.

The reduction of paramagnetic Cu(II) to diamagnetic Cu(I) was further supported by ^{1}H NMR experiments, performed for Cu-1D MOF under controlled condition. At first, conc. H_2SO_4 digested Cu-1D MOF was subjected to ^{1}H NMR experiments with different deuterated solvents such as D_2O and DMSO-d_6 (Figure III.13a-b). The experimental spectra in both solvents shows the broadening of NMR signals indicating the presence of d^9-Cu(II) species. The FWHM of 0.14 ppm was calculated for characteristic DMSO-d_6 at chemical shift value of 2.542 ppm (Figure III.13b, inset). In our case, ^{1}H NMR performed for Cu-1D treated with KOH and DMSO at 120 °C shows the peak at 1.98 ppm (Figure III.13c) that could be assigned for the presence of dimethyl sulphide (DMS) and is in agreement with the literature[49] whereas no peak for dimethyl sulfone and dimethyl disulphide was observed. The experimentally found DMS in our catalytic system resulted due to the thermal decomposition of DMSO, initially to methanethiol and paraformaldehyde and subsequent oxidation of methanethiol to DMS is responsible for the *in-situ* reduction of Cu(II) to Cu(I).[50,51]

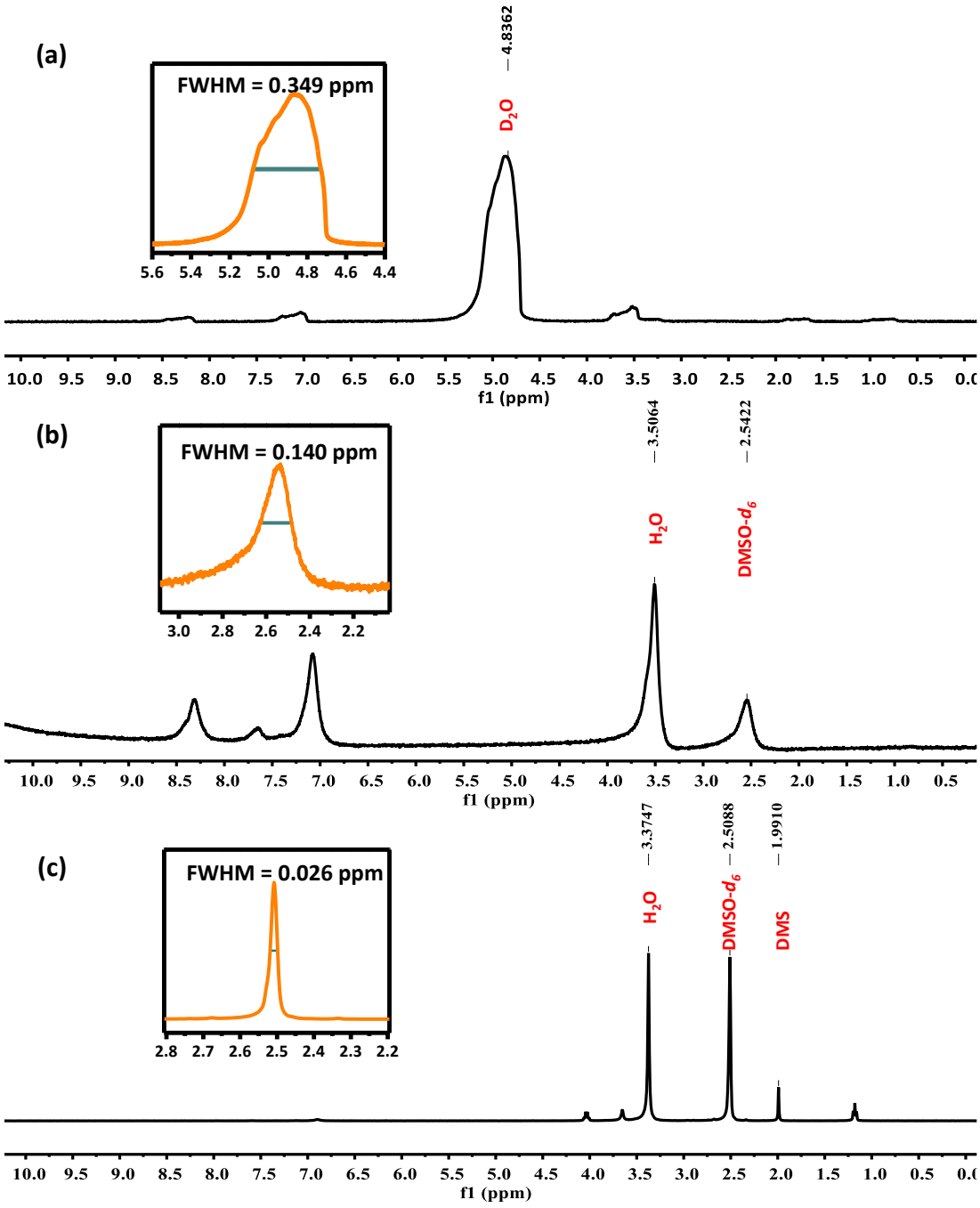

Figure III.13: ^{1}H NMR of Cu-1D performed under different solvent condition for mechanistic study. (a) Cu-1D MOF digested in conc. H_2SO_4 and the ^{1}H NMR was performed using D_2O as a solvent. (b) Cu-1D MOF digested in conc. H_2SO_4 and the ^{1}H NMR was performed using DMSO-d_6 as a solvent. (c) ^{1}H NMR of Cu-1D was performed using DMSO-d_6 as a solvent in presence of KOH.

Mechanistically, Cu-1D catalyzed C-N coupling reaction proceeds *via* oxidative addition and reduction elimination pathway (Figure III.14). The reaction was initiated

with the *in-situ* reduction of Cu(II) to Cu(I) species in presence of KOH and DMSO at 120 °C. The Cu(I) then undergoes oxidative addition with aryl halide (step **A**) to give the oxidized intermediate-1 (**INT-1**). Next, in step **B**, KOH abstracts the proton from the substrate eliminating water and potassium halide. The simultaneous nucleophilic substitution of halide with the substrate further leads to the formation of **INT-2**. Lastly, the reductive elimination of **INT-2** in step **C** gives the desired product (P) along with the regeneration of active Cu sites in Cu-1D.

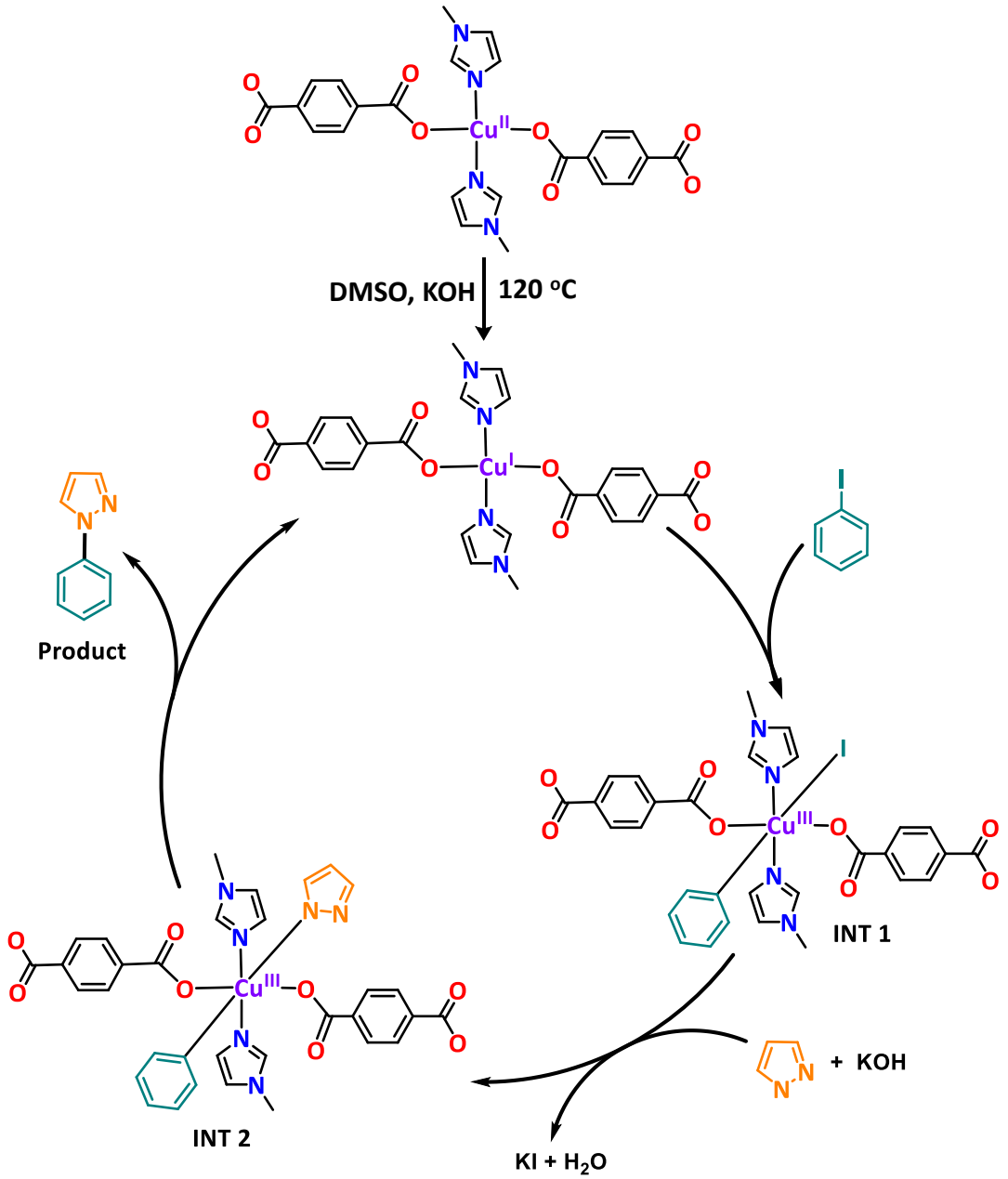

Figure III.14: Plausible catalytic cycle for Cu-1D catalyzed C–N cross coupling reaction.

The proposed plausible catalytic cycle is further established performing DFT calculations using Gaussian 09 program.[1]. Geometries of **TS** and all stationary points were fully optimised by vibrational frequency calculations at B3LYP/ LANL2dz level of theory and their optimized geometry is depicted in figure III.15a.

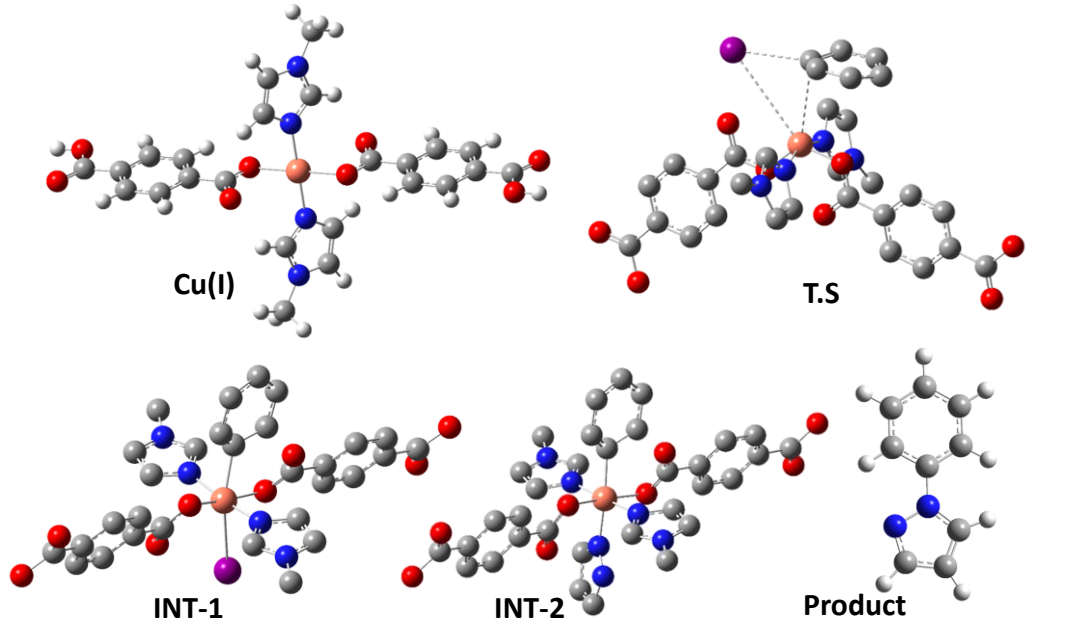

Figure III.15: Optimized structure of different species involved in catalytic cycle.

As per the experimental results the C-N coupling reaction begins with the reduction of Cu(II) to Cu(I) and initial DFT calculation shows Cu+1/singlet being stable than Cu+2/doublet by 23.6 kcal mol^{-1}. The oxidative addition on step **A** between active Cu(I) species and Ph-I progress *via* formation of **TS** as confirmed by an imaginary frequency. An energy barrier of 30.2 kcal mol^{-1} with respect to that of the Cu(I) intermediate (Figure III.16) was noted that is in good agreement with literature values.[52–55] Furthermore, the **INT-1** and **INT-2** formed in step A and B during catalytic pathway is coordinated as Cu (III) Ph-I and Cu (III) Ph-Py has an energy of -22.3 kcal mol^{-1} and -26.0 kcal mol^{-1} respectively relative to Cu(I) singlet. Lastly the reductive elimination of **INT-2** in step C results the stable coupling product P and calculated relative energy was found to be -51.0 kcal mol^{-1}. The calculated free energy profile diagram plot as

depicted in figure III.16 was found to be in good agreement with the proposed reaction pathway (Figure III.14) and the summarized data for different species involved in the proposed mechanism is given in table III.5.

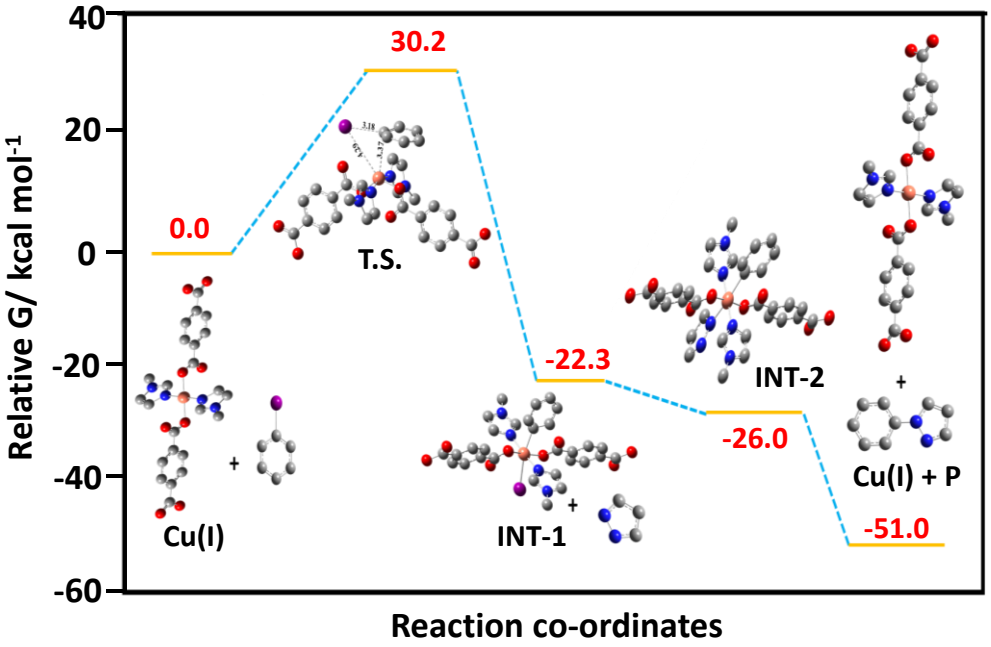

Figure III.116: Relative free energy (kcal/mol) profile diagram for the formation of C-N coupling product P at B3LYP level of theory with the LANL2DZ basis set for all atoms. Hydrogen atoms are omitted for clarity. Interatomic distances are in Å.

Table III.5: Summarised data for different species involved in the proposed mechanism. Electronic energy (EE) + zero-point energy (ZPE), Electronic energy (EE), enthalpy (H), entropy (S) and free energy (G).

Species	EE+ZPE (kcal/mol)	EE (kcal/mol)	H(kcal/mol)	S (Cal/mol.K)	G(kcal/mol)
Cu(I)+reactants	0	0	0	0	0
TS1	5.1	66.2	-0.2	-102.0	30.2
INT-1	-46.9	53.0	-50.5	-94.5	-22.3
INT-2	-53.7	29.5	-59.5	-112.3	-26.0
Cu(I) + product	-44.7	-39.8	-43.5	25.1	-51.0

The given data are calculated in gaseous phase at temperature= 298.150 K and pressure= 1.0 atm.

III.2.6. Recyclability and leaching Test:

The hereogeneous nature of the catalyst was established by performing hot filtration or leaching test during the course of C-N coupling reaction. At first the model reaction was initiated and solid catlyst was removed from reaction mixture after 0.5 h through centrifugation. The yield of the prodcut was calculated performing ^{1}H NMR of supernantant where conversion of 46% was noted (Figure III.17). The supernantant was further stirred in absence of Cu-1D catalyst for 1.5 h and ^{1}H NMR was performed which shows no change in the product yield. As the reaction did not progressed in the supernatant (Table III.1 entry 11), the constant yield of the product after removal of Cu-1D indicates the absence of any active Cu species leached from the solid catalyst.

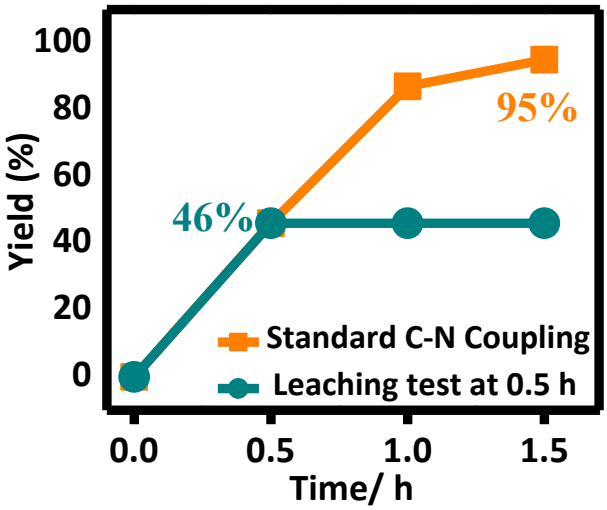

Figure III.17: Line graph of leaching test for Cu-1D MOF in reaction mixture of C-N coupling reaction at different time interval.

Next, the catalyst recyclibility was meticuliously analyzed with model reaction. In a 10 mL round bottom flask pyrazole (1.0 mmol) and iodobenzene (1.5 mmol) was added followed by addition of Cu-1D catalyst (2.5 mol%), KOH (1.0 mmol) and DMSO (1 mL). The reaction mixture was placed in 120 °C preheated oil bath with contant stirring. The product yield was calculated by ^{1}H NMR using acetophenone (175 µL, 1.5 mmol) as an internal standard and characteristic peak of product **3a** at δ 6.44 (t, J = 2.04 Hz,

1H) was identified for yield calculation. The yield of the corresponding C-N coupling product **3a** for the 1st cycle was 95%. For the 2nd cycle, again pyrazole (1.0 mmol) and iodobenzene (1.5 mmol) was added into the same reaction vial followed by KOH (1.0 mmol) and DMSO (1 mL). The reaction mixture was further stirred for another 1.5 h. The overall yield for the 2nd cycle was 89%. The process followed in 2nd cycle was repeated for the 3rd and 4th cycle and an overall yield of **3a** in 82% and 75% respectively was found. The diagrammatic representation of whole process is depicted in figure III.18a. With minimum decrease (<7%) in the yield in every cycle the catalyst performance was found to be adequate upto four cycle (Figure III.18b). The small decrease in yield in each cycle is common phenomenon for MOF catalysed reaction and is accredited to the deactivation of catalytic sites.[56,57]

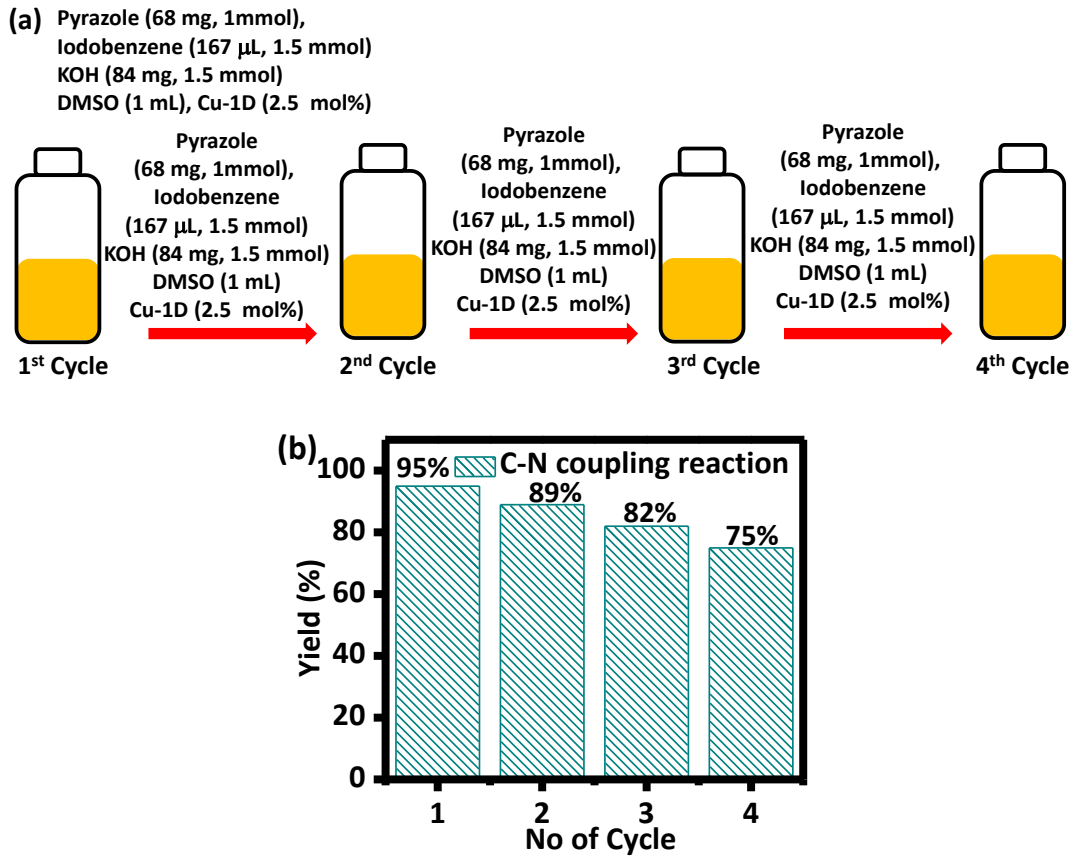

Figure III.18: (a) Representation of the recyclability test of Cu-1D MOF for C-N coupling reaction and aziridination reaction for four cycles. (b) Histogram for reusability of Cu-1D MOF in C-N coupling reaction.

The PXRD and FT-IR was performed after fourth cycle and when compared with the fresh one shows the absence of any extra peaks indicating the structural preservation of Cu-1D catalyst for C-N coupling reaction under optimized condition (Figure 19a-b). The gram scale reaction fro C-N coupling reaction was performed to validate the practical application of Cu-1D catalytic system. At first the 10 mmol (0.680 g) of pyrazole was reacted with 15 mmol (373.0 g) of 4-nitroiodobenzene under optimized reaction condition. After 2 h the reaction was quenched with H_2O and coloumn chromatography was performed that procduced 73% (1.38 g) of desired product **3d** (Scheme III.6). Therefore, the gram scale prodcution of the product 3d shows the practical applicability of Cu-1D catalytic system towards industrial applications.

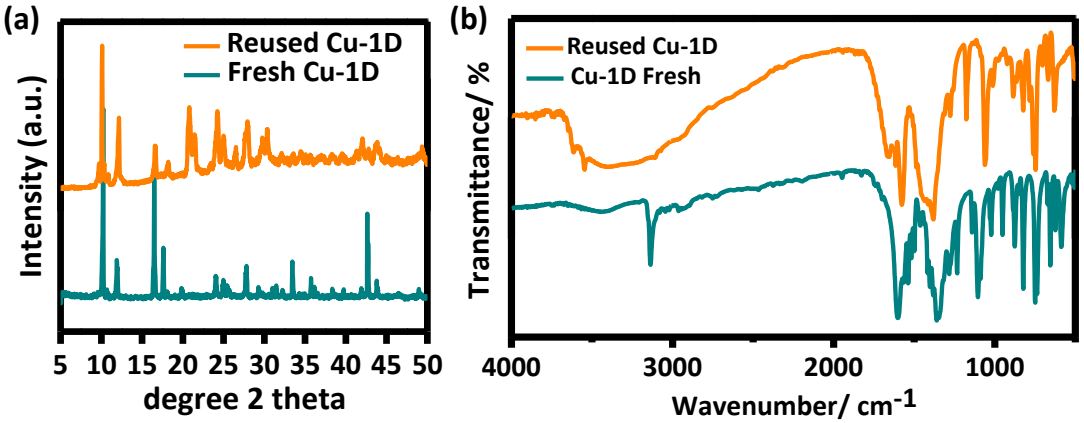

Figure III.19: (a) PXRD and (b) FT-IR comparison of fresh Cu-1D catalyst and for Cu-1D catalyst after four cycles of C-N coupling.

Scheme III.6: Gram scale recaction with Cu-1D catalytic system.

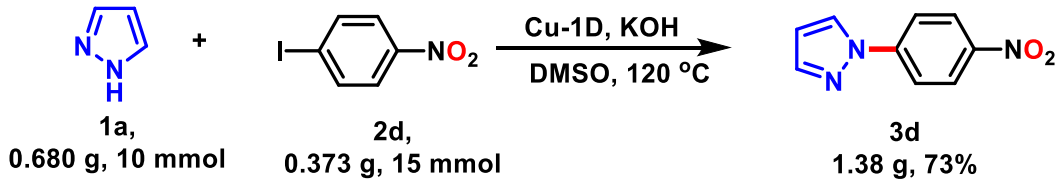

III.3. Conclusion:

In summary, novel Cu-1D MOF with the pre-existing CUS was directly applied in a variety of reactions such as intermolecular/ intramolecular C-N cross-coupling, intermolecular C-X (X=S, O) coupling. Unlike other MOFs, Cu-1D does not require any activation process to be catalytically active. The cross-coupled products were obtained in high yield (up to 95%) and exhibited high substrate scope that includes a range of aliphatic, aromatic & alicyclic amines, amides and *N*-heterocycles (C-N), phenols (C-O), thiols (C-S), etc. with aryl-halide (Ph-X, X=Br/ I) as coupling partner. The intramolecular C-N coupling reactions (yield up to 75%) were found to be stereoselective with ee > 98.5%. EPR, NMR, UV-Vis and DFT studies show the reduction of paramagnetic Cu-1D catalyst to diamagnetic Cu(I) species during initiation of the catalytic cycle and follow the conventional two-electron two-step coupling process. The active metal sites involved in catalysis are solely from solid Cu-1D and no evidence of leaching of active copper species in the reaction mixture was detected. The Cu-1D catalyst can be easily separated and reused again with high retention of activity up to the fourth cycle. The comparative study with different catalytic system shows the importance of CUS in this reaction and Cu-1D fairs better than other copper based catalytic system.

III.4. Experimental Section:

III.4.1. Materials:

All Chemicals and solvents were used without purification unless otherwise mentioned. 1,4-benzene dicarboxylic acid *N*-methyl imidazole, 2-methyl imidazole, imidazole, pyrazole, 2-bromo aniline, 4-nitroiodobenzene, 4-methyliododbenzene, triazole, benzimidazole, 4-chloro bromobenzene, 2-methoxy iodobenzene, 4-methoxy iodobenzene, 4-fluoro iodobenzene, tetrahyroisoquinoline, morpholine, indoline, oleylamine, octylamine, benzamide, phenol, thiol, iodobenzene diacetate, *p*-toluenesulfonamide, chloramine-T, 4-azidotoluene and all deuterated solvents were purchased from Sigma Aldrich and used as obtained. Indole, phenol, thiophenol, acetophenone, aniline, acetonitrile, dichloromethane, and dimethylformamide were purchased from Merck along with molecular sieves (5Å). The chemicals 4-methoxy thiophenol, 4-nitro thiophenol, 4-methoxy phenol, 4-methyl phenol and 4-nitro phenol was bought from TCI, India. 2,2,6,6-Tetramethylpiperidin-1-yl)oxyl (TEMPO) was bought from Avra. Solvents DMSO, petroleum ether and ethyl acetate was bought from Finar and used as obtained.

III.4.2. Physical methods:

^{1}H and ^{13}C-NMR were collected in $CDCl_3$ and DMSO-d_6 using Bruker ASCEND^{TM} 400. Multiplicity was indicated as follows: s (singlet), d (doublet), t (triplet), q (quartet), dd (doublet of doublet) and m (multiplet). All the FTIR spectra were acquired using Bruker ALPHA E. The UV-visible spectra were collected using Perkin Elmer (Model: LS 55). X-band EPR spectra were recorded on a Magnettech GmbH MiniScope MS400 spectrometer (equipped with temperature controller TC H03, Magnettech, Berlin, Germany), where the microwave frequency was measured with an FC400 frequency counter. SEM images were taken on JSM-6360 Scanning Electron Microscope. HPLC

was performed on Agilent Technologies 1200 infinity series using Daicel CHIRALCEL OD-H column, 10% IPA in hexanes, 0.8 mL min^{-1}, λ=254 nm. The thin-layer chromatography (TLC) was used for monitoring the reaction progress using silica gel 60 F_{254} coated plates under a UV lamp. Further I_2 stain was also used to monitor the formation of the product.

III.4.3. General Procedure for C-X (X= N, O, S) coupling reaction:

In a 10 mL round bottom flask, substrate (amine, phenol and thiol) (1.0 mmol) and aryl halide (1.5 mmol) were added followed by addition of **Cu-1D** catalyst (2.5 mol%), KOH (1.5 mmol) and DMSO (1 mL). The reaction vessel was placed in 120 °C preheated oil bath with contant stirring. The progress of reaction was monitored by TLC. For reaction with indoline and morpholine as substrate, the reaction vessel was placed in 80 °C preheated oil bath with contant stirring. After completion of reaction, the reaction was quenched with H_2O and EtOAc was introduced. The organic compound in the reaction mixture was extracted with EtOAc and dehydrated using Na_2SO_4. The resulting EtOAc solution was subsequently dried under vacuum, and the pure product was obtained through column chromatography using an eluent consisting of EtOAc and hexane.

III.4.4. Synthesis of opening product (8a-d):

The synthesis of ring-opening product (**8a-d**) was carried following a reported technique with few modifications.[43] In a two-neck RB, about 150 mg (0.55 mmol) of tosylaziridne (**12a**) was added and the system was kept under nitrogen atmosphere. To this, 2-iodoaniline (157 mg, 0.72 mmol) was added to the RB under constant nitrogen flow followed by addition of 500 µL of CH_3CN as solvent. Further 10 mol % of $Cu(OTf)_2$ was quickly added and the reaction mixture was stirred at room temperature

for 12 h. The progress of the reaction was monitored using TLC. After the completion of the reaction, the mixture was separated using column chromatography technique using ethyl acetate/hexane (1:9) to afford 216.6 mg (0.44 mmol) of the ring opening product *N*-(2-((2-iodophenyl)amino)-2-phenylethyl)-4-methylbenzenesulfonamide.

III.4.5. General procedure for synthesis of tetrahydroquinoxalines (9a-d):

10 mL round bottom flask was charged with 2-aryl-N-tosylaziridines (1 mmol) followed by **Cu-1D** catalyst (10 mol%), KOH (1 mmol) and DMSO (1 mL). The reaction vessel was placed in 120 °C preheated oil bath with contant stirring. The progress of reaction was monitored by TLC. After completion of reaction, work up was initited with 10% EtOAc and the organic part was passed through Na_2SO_4. It was then vaccum dried and pure product was obtained through column chromatography.

III.4.6. DFT calculations:

DFT calculations were performed using Gaussian 09 program.[1] To understand the mechanistic pathway within the catalytic cycle in coupling reactions using **Cu-1D**, analogous DFT calculations for Cu+2(doublet), Cu+1(singlet), transition state *via* oxidative addition of aryl iodide to Cu+1(singlet) and Cu+3 (triplet) states of intermediates were carried out. Geometries of all stationary points were fully optimised and characterised by vibrational frequency calculations at B3LYP/ LANL2dz level of theory. The calculated gas phase Gibbs free energy refers to 298.15 K and 1 atm. Initial DFT calculation indicates Cu+1/singlet being slightly stable than Cu+2/doublet by 23.6 kcal mol^{-1}. Hence, Cu(I) intermediate is expected to be the initial active form of the catalyst which enters the catalytic cycle (also confirmed by ^{1}H-NMR & EPR). Further, Cu(I) intermediate via oxidative addition of phenyl iodide forms the stable transition state (**TS-1)**, after which Cu(III) intermediate (**INT-1**) is formed.

III. 5. Spectral Data of products:

Synthesis of 1-phenyl-1H-pyrazole (3a).

Following the general procedure, the reaction mixture was subjected to stir for 1.5 h at 120 °C to afford the pure product **3a** (137.7 mg, 0.95 mmol) as a thick liquid in 95% yield. The separation of product **3a** was performed using column chromatography in 9:1 (Hexane/EtOAc). ^{1}H NMR (400 MHz, $CDCl_3$) δ 7.87 (d, J = 2.52 Hz, 2H), 7.74-7.68 (m, 3H), 7.43 (t, J = 7.8 Hz, 2H), 7.27 (t, J = 2.0 Hz, 1H), 6.44 (t, J = 2.04 Hz, 1H); ^{13}C NMR (100 MHz, $CDCl_3$) δ 141.0, 140.1, 129.4, 126.8, 126.4, 119.1, 107.6.

Synthesis of 1-(p-tolyl)-1H-pyrazole (3b).

Following the general procedure, the reaction mixture was subjected to stir for 3 h at 120 °C to afford the pure product **3b** (123.39 mg, 0.78 mmol) as a thick liquid in 78% yield. The separation of product **3b** was performed using column chromatography in 9:1 (Hexane/EtOAc) ^{1}H NMR (400 MHz, $CDCl_3$) δ 7.84 (d, J = 2.44 Hz, 1H), 7.72 (d, J = 1.72 Hz, 1H), 7.57 (d, J = 8.4 Hz, 2H), 7.21 (d, J = 8.16 Hz, 2H), 6.42 (t, J = 2.2 Hz, 1H); ^{13}C NMR (100 MHz, $CDCl_3$) δ 140.7, 138.0, 136.1, 129.9, 126.6, 119.1, 107.3, 20.8.

Synthesis of 1-(4-methoxyphenyl)-1H-pyrazole (3c).

Following the general procedure, the reaction mixture was subjected to stir for 3 h at 120 °C to afford the pure product **3c** (118.37 mg, 0.68 mmol) as a thick liquid in 68% yield. The separation of product **3c** was performed using column chromatography in 9:1 (Hexane/EtOAc). ^{1}H NMR (400 MHz, $CDCl_3$) δ 7.78 (d, J = 2.4 Hz, 1H), 7.68 (d, J = 7.76 Hz, 1H), 7.56 (d, J = 9.0 Hz, 2H), 6.92 (d, J = 8.96 Hz, 2H), 6.40 (t, J = 2.2 Hz, 1H), 3.76 (s, 3H); ^{13}C NMR (100 MHz, $CDCl_3$) δ 158.1, 140.5, 133.9, 126.7, 120.7, 114.4, 107.1, 55.4.

Synthesis of 1-(4-nitrophenyl)-1H-pyrazole (3d).

Following the general procedure, the reaction mixture was subjected to stir for 1.5 h at 120 °C to afford the pure product **3d** (153.22 mg, 0.81 mmol) as a yellow solid in 81% yield. The separation of product **3d** was performed using column chromatography in 9:1 (Hexane/EtOAc). ^{1}H NMR (400 MHz, DMSO-d_6) δ 8.69 (d, J = 2.32 Hz, 1H), 8.32 (d, J = 8.56 Hz, 2H), 8.09 (d, J = 8.56 Hz, 2H), 7.85 (s, 1H), 6.63 (s. 1H); ^{13}C NMR (100 MHz, DMSO-d_6) δ 145.1, 144.4, 143.2, 129.3, 125.8, 118.8, 109.8.

Synthesis of 1-(4-fluorophenyl)-1H-pyrazole (3e).

Following the general procedure, the reaction mixture was subjected to stir for 1.5 h at 120 °C to afford the pure product **3e** (129.64 mg, 0.80 mmol) as a thick liquid in 80% yield. The separation of product **3e** was performed using column chromatography in 9:1 (Hexane/EtOAc). ^{1}H NMR (400 MHz, DMSO-d_6) δ 8.49 (d, J = 2.28 Hz, 1H), 7.81 (d, J = 8.2 Hz, 2H), 7.75 (s, 1H), 7.62 (d, J = 8.16 Hz, 2H), 6.54 (s, 1H); ^{13}C NMR (100 MHz, DMSO-d_6) δ 141.7, 139.8, 138.5, 128.1, 120.8, 108.6, 91.25.

Synthesis of 1-(2-methoxyphenyl)-1H-pyrazole (3f).

Following the general procedure, the reaction mixture was subjected to stir for 1.5 h at 120 °C to afford the pure product **3f** (121.94 mg, 0.70 mmol) as a thick liquid in 70% yield. The separation of product **3f** was performed using column chromatography in 9:1

(Hexane/EtOAc). ^{1}H NMR (400 MHz, $CDCl_3$) δ 8.06 (d, J = 2.44 Hz, 1H), 7.77-7.42 (m, 2H), 7.34-7.29 (m, 1H), 7.10-7.05 (m, 2H), 6.46 (t, J = 4.28 Hz, 1H), 3.88 (s, 3H); ^{13}C NMR (100 MHz, $CDCl_3$) δ 151.3, 140.0, 131.5, 130.1, 129.7, 125.2, 121.1, 112.3, 106.1, 55.9.

Synthesis of 1-(4-chlorophenyl)-1H-pyrrole (3g).

Following the general procedure, the reaction mixture was subjected to stir for 3 h at 120 °C to afford the pure product **3g** (99.4 mg, 0.56 mmol) as a white solid in 56% yield. The separation of product **3g** was performed using column chromatography in 9:1 (Hexane/EtOAc). ^{1}H NMR (400 MHz, $CDCl_3$) δ 7.42-7.33 (m, 4H), 7.65 (t, J = 2.2 Hz, 2H), 6.38 (t, J = 2.2 Hz, 2H); ^{13}C NMR (100 MHz, $CDCl_3$) δ 132.5, 131.0, 129.6, 121.6, 119.2, 110.8.

Synthesis of 1-phenyl-1H-imidazole (3h).

Following the general procedure, the reaction mixture was subjected to stir for 2 h at 120 °C to afford the pure product **3h** (143.27 mg, 0.91 mmol) as a thick liquid in 91% yield. The separation of product **3h** was performed using column chromatography in 7:3 (Hexane/EtOAc). ^{1}H NMR (400 MHz, DMSO-d_6) δ 8.29 (s, 1H), 7.76 (s, 1H), 7.65 (d, J = 7.88 Hz, 2H), 7.53 (t, J = 7.68 Hz, 2H), 7.38 (t, J = 7.36 Hz, 1H), 7.13 (s, 1H) ; ^{13}C NMR (100 MHz, DMSO-d_6) δ 137.3, 136.0, 130.3, 127.3, 120.7, 118.4.

Synthesis of 1-(p-tolyl)-1H-imidazole (3i).

Following the general procedure, the reaction mixture was subjected to stir for 3 h at 120 °C to afford the pure product **3i** (112.32 mg, 0.74 mmol) as a thick liquid in 74%. The separation of product **3i** was performed using column chromatography in 7:3 (Hexane/EtOAc). ^{1}H NMR (400 MHz, $CDCl_3$) δ 7.61 (s, 1H), 7.04-6.96 (m, 6H), 2.14 (s, 3H); ^{13}C NMR (100 MHz, $CDCl_3$) δ 137.1, 135.3, 134.6, 130.1, 129.8, 121.0, 118.0, 20.6.

Synthesis of 2-methyl-1-phenyl-1H-imidazole (3j).

Following the general procedure, the reaction mixture was subjected to stir for 3 h at 120 °C to afford the pure product **3j** (136.05 mg, 0.86 mmol) as a thick liquid in 86% yield. The separation of product **3j** was performed using column chromatography in 5:5 (Hexane/EtOAc). ^{1}H NMR (400 MHz, DMSO-d_6) δ 7.56-7.42 (m, 5H), 7.29 (s, 1H), 6.94 (s, 1H), 2.27 (s, 3H); ^{13}C NMR (100 MHz, DMSO-d_6)δ 138.0, 130.0, 128.3, 127.5, 125.6, 121.3, 13.9.

Synthesis of 1-phenyl-1H-pyrrole (3k).

Following the general procedure, the reaction mixture was subjected to stir for 2 h at 120 °C to afford the pure product **3k** (131.62 mg, 0.92 mmol) as white solid in 92% yield. The separation of product **3k** was performed using column chromatography in 9:1 (Hexane/EtOAc). ^{1}H NMR (400 MHz, DMSO-d_6) δ 7.57 (d, J = 7.88 Hz, 2H), 7.47 (t, J = 7.60 Hz, 2H), 7.37-7.36 (m, 2H), 7.25(d, J = 7.32 Hz, 1H), 6.27 (s, 2H); ^{13}C NMR (100 MHz, DMSO-d_6) δ 140.3, 130.1, 125.7, 119.7, 119.3, 110.9.

Synthesis of 1-(p-tolyl)-1H-pyrrole (3l).

Following the general procedure, the reaction mixture was subjected to stir for 2 h at 120 °C to afford the pure product **3l** (139.81 mg, 0.89 mmol) as white solid in 89%

yield. The separation of product **3l** was performed using column chromatography in 9:1 (Hexane/EtOAc). ^{1}H NMR (400 MHz, DMSO-*d*$_6$) δ 7.44 (d, *J* = 7.92 Hz, 2H), 7.31 (s, 2H), 7.24 (d, *J* = 7.88 Hz 2H), 6.24-6.23 (m, 2H), 2.31 (s, 3H); ^{13}C NMR (100 MHz, DMSO-*d*$_6$) δ 138.1, 134.8, 130.4, 119.6, 119.2, 110.6, 20.79.

Synthesis of 1-phenyl-1H-indole (3m).

Following the general procedure, the reaction mixture was subjected to stir for 2 h at 120 °C to afford the pure product **3m** (173.08 mg, 0.90 mmol) as thick liquid in 90% yield. The separation of product **3m** was performed using column chromatography in 9:1 (Hexane/EtOAc). ^{1}H NMR (400 MHz, $CDCl_3$) δ 8.14-8.11 (m, 1H), 7.98-7.96 (m, 1H), 7.80-7.74 (m, 4H), 7.63-7.60 (m, 4H), 7.07 (d, *J* = 3.24 Hz, 1H); ^{13}C NMR (100 MHz, $CDCl_3$) δ 140.1, 136.2, 130.0, 129.8, 128.3, 126.7, 124.6, 122.8, 121.6, 120.8, 111.0, 104.1.

Synthesis of 1-(p-tolyl)-1H-indole (3n).

Following the general procedure, the reaction mixture was subjected to stir for 2 h at 120 °C to afford the pure product **3n** (157.39 mg, 0.76 mmol) as thick liquid in 76% yield. The separation of product **3n** was performed using column chromatography in 9:1 (Hexane/EtOAc). ^{1}H NMR (400 MHz, $CDCl_3$) δ 7.97 (d, *J* = 7.52 Hz, 1H), 7.81 (d, J = 7.72 Hz, 1H), 7.60 (d, *J* = 8.08 Hz, 2H), 7.53-7.46 (m, 5H), 6.94-6.93 (m, 1H), 2.64 (s, 3H); ^{13}C NMR (100 MHz, $CDCl_3$) δ 137.5, 136.4, 130.3, 129.5, 128.2, 124.5, 122.5, 121.3, 120.5, 110.8, 103.5, 21.2.

Synthesis of 1-phenyl-1H-1,2,4-triazole (3o).

Following the general procedure, the reaction mixture was subjected to stir for 3 h at 120 °C to afford the pure product **3o** (129.10 mg, 0.89 mmol) as thick liquid in 89% yield. The separation of product **3o** was performed using column chromatography in 9:1 (Hexane/EtOAc). ^{1}H NMR (400 MHz, DMSO-*d*$_6$) δ 9.32 (s, 1 H), 8.25 (s, 1H), 7.86 (d, *J* = 7.80 Hz, 2H), 7.57 (t, *J* = 7.64 Hz, 2H), 7.43 (t, *J* = 7.40 Hz, 1H); ^{13}C NMR (100 MHz, DMSO-*d*$_6$) δ 152.9, 142.8, 137.2, 130.2, 128.2, 119.8.

Synthesis of 1-phenyl-1H-benzo[d]imidazole (3p).

Following the general procedure, the reaction mixture was subjected to stir for 4 h at 120 °C to afford the pure product **3p** (151.38 mg, 0.78 mmol) as thick liquid in 78% yield. The separation of product **3p** was performed using column chromatography in 8:2 (Hexane/EtOAc). ^{1}H NMR (400 MHz, $CDCl_3$) δ 8.06 (s, 1 H), 7.86 (d, *J* = 8.92 Hz, 1H), 7.50-7.45 (m, 3H), 7.41-7.38 (m, 3H), 7.30-7.25 (m, 2H); ^{13}C NMR (100 MHz, $CDCl_3$) δ 143.9, 142.3, 136.2, 133.6, 130.0, 128.0, 123.9, 123.7, 122.8, 120.5, 110.5.

Synthesis of 1-phenylindoline (3q).

Following the general procedure, the reaction mixture was subjected to stir for 5 h at 80 °C to afford the pure product **3q** (161.93 mg, 0.83 mmol) as thick liquid in 83% yield. The separation of product **3q** was performed using column chromatography in 97:3 (Hexane/EtOAc). ^{1}H NMR (400 MHz, $CDCl_3$) δ 7.44 (t, *J* = 8.56 Hz, 2H), 7.32 (d, *J* = 8.60 Hz, 2H), 7.26 (t, *J* = 7.16 Hz,2H), 7.17 (t, *J* = 7.6 Hz, 1H), 7.06 (t, *J* = 6.12 Hz, 1H), 6.85 (t, *J* = 7.36 Hz, 1H) 4.04 (t, *J* = 8.44 Hz, 2H), 3.21 (t, *J* = 8.44 Hz, 2H).

^{13}C NMR (100 MHz, $CDCl_3$) δ 147.1, 144.2, 131.2, 129.1, 127.1, 125.0, 120.9, 118.8, 117.7, 108.1, 52.1, 28.2.

Synthesis of 2-phenyl-1,2,3,4-tetrahydroisoquinoline (3r).

Following the general procedure, the reaction mixture was subjected to stir for 6 h at 80 °C to afford the pure product **3r** (188.20 mg, 0.90 mmol) as thick liquid in 90% yield. The separation of product **3r** was performed using column chromatography in 97:3 (Hexane/EtOAc). ^{1}H NMR (400 MHz, $CDCl_3$) δ 7.37 (t, J = 8.28 Hz, 2H), 7.28-7.20 (m, 4H), 7.04 (d, J = 8.24 Hz, 2H), 6.91 (d, J = 7.32 Hz, 1H), 4.47 (s, 2H), 3.63 (t, J = 5.84 Hz, 2H), 3.06 (t, J = 5.80 Hz, 2H). ^{13}C NMR (100 MHz, $CDCl_3$) δ 150.5, 134.9, 134.4, 129.2, 128.5, 126.5, 126.3, 126.0, 118.7, 115.1, 50.7, 46.5, 29.

Synthesis of 2-(p-tolyl)-1,2,3,4-tetrahydroisoquinoline (3s).

Following the general procedure, the reaction mixture was subjected to stir for 6 h at 80 °C to afford the pure product **3s** (189.66 mg, 0.85 mmol) as thick liquid in 85% yield. The separation of product **3s** was performed using column chromatography in 9:1 (Hexane/EtOAc). ^{1}H NMR (400 MHz, $CDCl_3$) δ 7.39-7.32 (m, 6H), 7.13 (t, J = 8.4 Hz, 2H), 4.56 (s, 2H), 3.71 (t, J = 5.84 Hz, 2H), 3.19 (t, J = 5.88 Hz, 2H), 2.52 (s, 3H); ^{13}C NMR (100 MHz, $CDCl_3$) δ 148.8, 134.9, 134.7, 129.9, 128.8, 128.5, 126.7, 126.4, 126.1, 116.0, 51.6, 47.4, 29.3, 20.7.

Synthesis of 4-phenylmorpholine (3t).

Following the general procedure, the reaction mixture was stirred for 12 h at 80 °C to afford the pure product **3t** (115.8 mg, 0.71 mmol) as thick liquid in 71% yield. The separation of product **3t** was performed using column chromatography in 85:15 (Hexane/EtOAc). ^{1}H NMR (400 MHz, $CDCl_3$) δ 7.35 (t, J = 8.64 Hz, 2H), 6.98-6.92 (m, 3H), 3.92 (t, J = 4.8 Hz, 4H), 3.21 (t, J = 4.88 Hz, 4H); ^{13}C NMR (100 MHz, $CDCl_3$) δ 151.2, 129.2, 120.1,

Synthesis of N-phenylbenzamide (3u).

Following the general procedure, the reaction mixture was subjected to stir for 2 h at 120 °C to afford the pure product **3u** (167.51 mg, 0.85 mmol) as thick liquid in 85% yield. The separation of product **3u** was performed using column chromatography in 9:1 (Hexane/EtOAc). ^{1}H NMR (400 MHz, DMSO-d_6) δ 10.27 (s, 1H), 7.95 (d, J = 7.36 Hz, 2H), 7.77 (d, J = 7.8 Hz, 2H), 7.61-7.51 (m, 3H) 7.36 (t, J = 7.76 Hz, 2H), 7.11 (t, J = 7.52 Hz, 1H). ^{13}C NMR (100 MHz, DMSO-d_6) δ 166.0, 139.5, 135.3, 132.0, 129.0, 128.8, 128.0, 124.1, 120.8.

Synthesis of diphenylamine (3v).

Following the general procedure, the reaction mixture was subjected to stir for 2 h at 120 °C. The separation of product **3v** was performed using column chromatography in 9:1 (Hexane/EtOAc) to afford the pure product **3v** (140.34 mg, 0.83 mmol) as thick liquid in 83% yield. ^{1}H NMR (400 MHz, $CDCl_3$) δ 7.36 (t, J = 7.88 Hz, 4H), 7.14 (d, J = 7.96 Hz, 4H), 7.02 (t, J = 7.36 Hz, 2H), 5.78 (s, 1H); ^{13}C NMR (100 MHz, $CDCl_3$) δ 143.1, 129.4, 121.0, 117.8.

Synthesis of (*Z*)-*N*-(octadec-9-en-1-yl)aniline (3w).

Following the general procedure, the reaction mixture was subjected to stir for 2 h at 120 °C. The separation of product **3w** was performed using column chromatography in 9:1 (Hexane/EtOAc) to afford the pure product **3w** (309.34 mg, 0.90 mmol) as colourless liquid in 90% yield. ^{1}H NMR (400 MHz, $CDCl_3$) δ 7.21 (t, J = 7.24 Hz, 2H), 6.73 (t, J = 7.32 Hz, 1H), 6.62 (d, J = 7.92 Hz, 2H), 5.42-5.34 (m, 2H), 3.13 (t, J = 7.12 Hz, 2H), 2.07-1.97 (m, 3H), 1.67-1.60 (m, 2H), 1.43-1.29 (m, 23H), 0.93-0.88 (m, 3H); ^{13}C NMR (100 MHz, $CDCl_3$) δ 148.5, 130.0, 129.8, 129.2, 117.0, 112.6, 44.0, 31.9, 29.8, 29.6, 29.4, 29.3, 29.2, 27.2, 22.7, 14.1, 1.08.

Synthesis of *N*-octylaniline (3x).

Following the general procedure, the reaction mixture was subjected to stir for 2 h at 120 °C. The separation of product **3x** was performed using column chromatography in 9:1 (Hexane/EtOAc) to afford the pure product **3x** (186.86 mg, 0.91 mmol) as colourless liquid in 91% yield. ^{1}H NMR (400 MHz, $CDCl_3$) δ 7.24 (t, J = 8.21 Hz, 2H), 6.75 (t, J = 7.28 Hz, 1H), 6.64 (d, J = 8.28 Hz, 2H), 3.15 (t, J = 7.2 Hz, 2H), 1.69-1.31 (m, 10H), 0.95-0.92 (m, 3H); ^{13}C NMR (100 MHz, $CDCl_3$) δ 148.5, 129.2, 117.0, 112.6, 44.0, 31.8, 29.6, 29.4, 29.3, 27.2, 22.7, 14.1, 1.09.

Synthesis of oxydibenzene (5a).

Following the general procedure, the reaction mixture was subjected to stir for 3 h at 120 °C. The separation of product **5a** was performed using column chromatography in 9:1 (Hexane/EtOAc) to afford the pure product **5a** (141.15 mg, 0.83 mmol) as thick liquid in 83% yield. ^{1}H NMR (400 MHz, $CDCl_3$) δ 7.38 (t, J = 8.16 Hz, 4H), 7.14 (t, J = 7.32 Hz, 2H), 7.04 (d, J = 7.72 Hz, 4H). ^{13}C NMR (100 MHz, $CDCl_3$) δ 157.2, 129.7, 123.2, 118.9.

Synthesis of 1-methoxy-4-phenoxybenzene (5b).

Following the general procedure, the reaction mixture was subjected to stir for 3 h at 120 °C. The separation of product **5b** was performed using column chromatography in 9:1 (Hexane/EtOAc) to afford the pure product **5b** (160.06 mg, 0.80 mmol) as thick liquid in 80% yield. ^{1}H NMR (400 MHz, $CDCl_3$) δ 7.38 (t, J = 7.92 Hz, 2H), 7.13-7.01 (m, 5H), 6.96-6.94 (m, 2H), 3.85 (s, 3H); ^{13}C NMR (100 MHz, $CDCl_3$) δ 152.7, 150.1, 139.5, 135.4, 134.9, 131.8, 129.3, 44.7.

Synthesis of 1-methyl-4-phenoxybenzene (5c).

Following the general procedure, the reaction mixture was subjected to stir for 5 h at 120 °C to afford the pure product **5c** (138.06 mg, 0.75 mmol) as thick liquid in 75% yield. The separation of product **5c** was performed using column chromatography in 9:1 (Hexane/EtOAc). ^{1}H NMR (400 MHz, $CDCl_3$) δ 7.40 (t, J = 7.68 Hz, 2H), 7.20 (d, J = 8.28 Hz, 2H), 7.15 (t, J = 6.6 Hz, 1H), 7.06 (d, J = 7.56 Hz, 2H), 7.00 (d, J = 8.48 Hz, 2H), 2.40 (s, 3H); ^{13}C NMR (100 MHz, $CDCl_3$) δ 157.8, 154.8, 132.9, 130.2, 129.6, 122.8, 119.1, 118.4, 20.7.

Synthesis of 1-nitro-4-phenoxybenzene (5d).

Following the general procedure, the reaction mixture was subjected to stir for 5 h at 120 °C to afford the pure product **5d** (154.84 mg, 0.72 mmol) as yellow thick liquid in 72% yield. The separation of product **5d** was performed using column chromatography in 8:2 (Hexane/EtOAc). ^{1}H NMR (400 MHz, $CDCl_3$) δ 8.05 (d, J = 8.84 Hz, 2H), 7.56-7.54 (m, 2H), 7.47-7.46 (m, 3H), 7.18 (d, J = 8.84 Hz, 2H); ^{13}C NMR (100 MHz, $CDCl_3$) δ 148.4, 145.3, 134.7, 130.2, 130.4, 130.0, 129.6, 126.7, 124.0.

Synthesis of diphenylsulfane (5e).

Following the general procedure, the reaction mixture was subjected to stir for 2 h at 120 °C to afford the pure product **5e** (160.0 mg, 0.86 mmol) as thick liquid in 86% yield. The separation of product **5e** was performed using column chromatography in 9:1 (Hexane/EtOAc). ^{1}H NMR (400 MHz, $CDCl_3$) δ 7.47 (d, J = 8.52 Hz, 4H), 7.42 (t, J = 8.08 Hz, 4H), 7.34 (d, J = 6.8 Hz, 2H); ^{13}C NMR (100 MHz, $CDCl_3$) δ 135.9, 131.1, 129.3, 127.1.

Synthesis of (4-methoxyphenyl)(phenyl)sulfane (5f).

Following the general procedure, the reaction mixture was subjected to stir for 2 h at 120 °C to afford the pure product **5f** (183.65 mg, 0.85 mmol) as thick liquid in 85% yield. The separation of product **5f** was performed using column chromatography in 9:1 (Hexane/EtOAc). ^{1}H NMR (400 MHz, $CDCl_3$) δ 7.45 (d, J = 8.64 Hz, 2H), 7.128-7.14 (m, 5H), 6.64 (d, J = 8.56 Hz, 2H), 3.83 (s, 3H); ^{113}C NMR (100 MHz, $CDCl_3$) δ 159.8, 138.6, 135.4, 128.9, 128.1, 125.7, 124.2, 114.9, 55.38.

Synthesis of (4-nitrophenyl)(phenyl)sulfane (5g).

Following the general procedure, the reaction mixture was subjected to stir for 3 h at 120 °C to afford the pure product **5g** (189.45 mg, 0.82 mmol) as yellow liquid in 82% yield. The separation of product **5g** was performed using column chromatography in 9:1 (Hexane/EtOAc). ^{1}H NMR (400 MHz, $CDCl_3$) δ 8.04 (d, J = 8.88 Hz, 2H), 7.56-7.53 (m, 2H), 7.47-7.45 (m, 3H), 7.17 (d, J = 8.92 Hz, 2H) ^{13}C NMR (100 MHz, $CDCl_3$) δ 148.6, 145.4, 134.9, 130.5, 130.2, 129.8, 126.8, 124.1.

Synthesis of 3-phenyl-1-tosyl-1,2,3,4-tetrahydroquinoxaline (9a).

Following the general procedure, the reaction mixture was subjected to stir for 5 h at 120 °C. The separation of product **9a** was performed using column chromatography in 9:1 (Hexane/EtOAc) to afford the pure product **9a** (284.01 mg, 0.78 mmol) as white solid in 78% yield. **HPLC:** Daicel CHIRALCEL OD-H column, 10% IPA in hexanes, 0.8 mL/min, λ= 254 nm, R_t(major) = 26.5 min, R_t(minor) = 29.1 min; ee = 99%. ^{1}H NMR (400 MHz, $CDCl_3$) δ 7.69 (d, J = 8.5 Hz, 1H), 7.49 (d, J = 8.2 Hz 2H), 7.29-7.21 (m, 5H), 7.13 (d, J = 7.8 Hz, 2H), 6.99 (t, J = 7.1 Hz, 1H), 6.70 (t, J = 7.3 Hz, 1H), 6.52 (d, J = 8.0 Hz, 1H), 4.24 (dd, J = 14.2 Hz, 1.9 Hz, 1H), 3.93 (s, 1H), 3.62 (dd, J = 10.6 Hz, 3.32 Hz, 1H), 3.10-3.04 (m, 1H), δ 2.36 (s, 3H), ^{13}C NMR (100 MHz, $CDCl_3$) δ 143.9, 139.4, 137.9, 136.2, 129.8, 128.8, 128.4, 127.4, 126.6, 125.9, 121.5, 117.5, 114.8, 51.8, 50.9, 21.6.

Synthesis of 3-(4-chlorophenyl)-1-tosyl-1,2,3,4-tetrahydroquinoxaline (9b).

Following the general procedure, the reaction mixture was subjected to stir for 5 h at 120 °C to afford the pure product **9b** (266.7 mg, 0.67 mmol) as white solid in 67% yield. The separation of product **9b** was performed using column chromatography in 9:1 (Hexane/EtOAc). ^{1}H NMR (400 MHz, $CDCl_3$) δ 7.71 (d, *J* = 8.2 Hz, 1H), 7.51 (d, *J* = 8.0 Hz 2H), 7.31-7.25 (m, 4H), 7.12 (d, *J* = 8.2 Hz, 2H), 7.03 (t, *J* = 8.0 Hz, 1H), 6.76 (t, *J* = 8.2 Hz, 1H), 6.58 (d, *J* = 7.88 Hz, 1H), 4.25 (dd, *J* = 14.1 Hz, 3.4 Hz, 1H), 3.98 (s, 1H), 3.68 (dd, *J* = 10.2 Hz, 3.4 Hz, 1H), 3.13-3.07 (m, 1H), 2.41 (s, 3H); ^{13}C NMR (100 MHz, $CDCl_3$) δ 144.0, 137.9, 137.6, 136.2, 134.1, 129.8, 129.0, 128.0, 127.4, 126.5, 121.6, 117.8, 114.9, 51.3, 50.8, 21.6

Synthesis of 3-(p-tolyl)-1-tosyl-1,2,3,4-tetrahydroquinoxaline (9c).

Following the general procedure, the reaction mixture was subjected to stir for 5 h at 120 °C to afford the pure product **9c** (287.65 mg, 0.76 mmol) as thick liquid in 76% yield. The separation of product **9c** was performed using column chromatography in 9:1 (Hexane/EtOAc). ^{1}H NMR (400 MHz, $CDCl_3$) δ 77.75 (d, *J* = 8.2 Hz, 1H), 7.56 (d, *J* = 7.9 Hz 2H), 7.28 (d, *J* = 7.4 Hz 2H), 7.18-7.07 (m, 5H), 6.67 (t, *J* = 8.0 Hz, 1H), 6.77 (t, *J* = 7.8 Hz, 1H), 6.58 (d, *J* = 8.0 Hz, 1H), 4.31 (d, *J* = 14.1 Hz, 3.4 Hz, 1H), 3.69 (s, 1H), 3.69 (d, *J* = 10.4 Hz, 3.4 Hz, 1H), 3.13 (t, *J* = 12.3 Hz, 1H), 2.43 (s, 3H), 2.36 (s, 3H); ^{13}C NMR (100 MHz, $CDCl_3$) δ 143.8, 138.2, 137.9, 136.4, 136.3, 129.7, 129.5, 127.4, 126.5, 126.4, 125.9, 121.5, 117.4, 114.7, 51.7, 50.9, 21.6, 21.1

III. 6. NMR Spectra of some noted products:

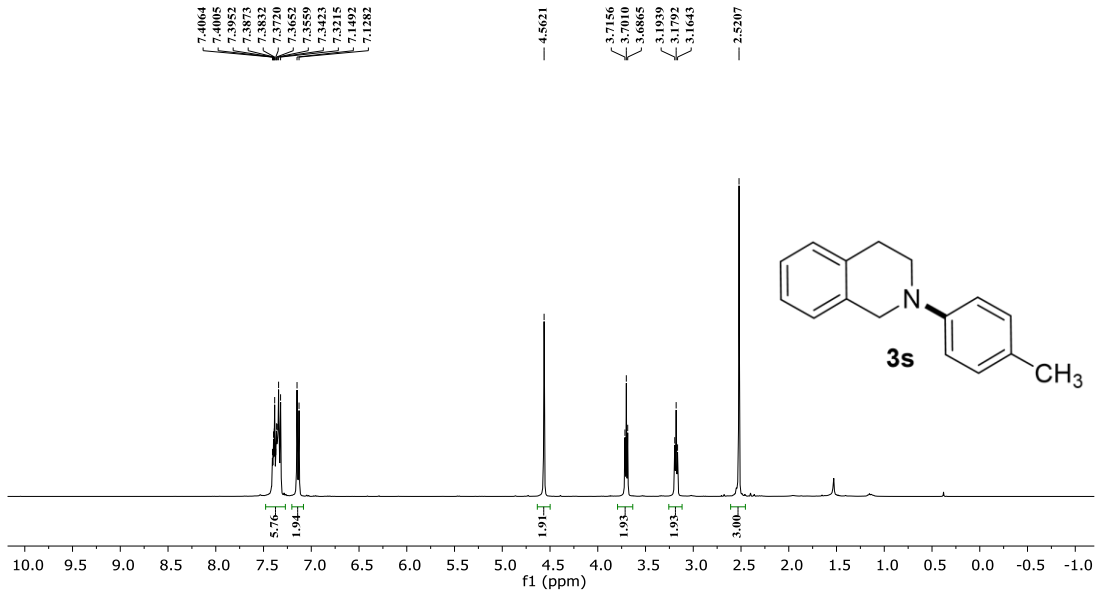

Figure III.20: ^{1}H-NMR of **3s** in $CDCl_3$

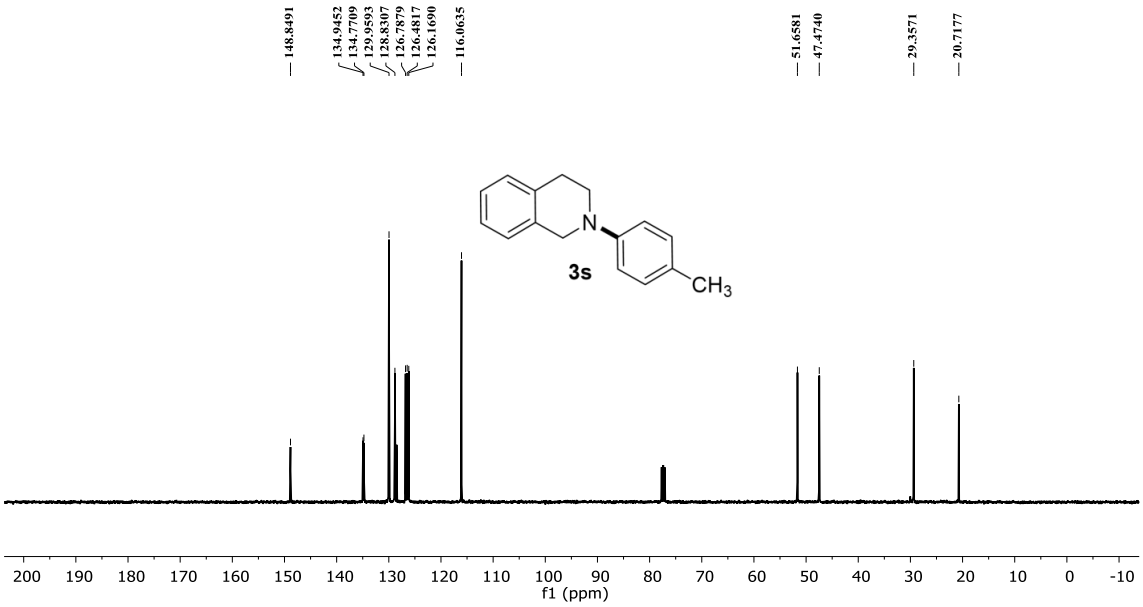

Figure III.21: ^{13}C-NMR of **3s** in $CDCl_3$

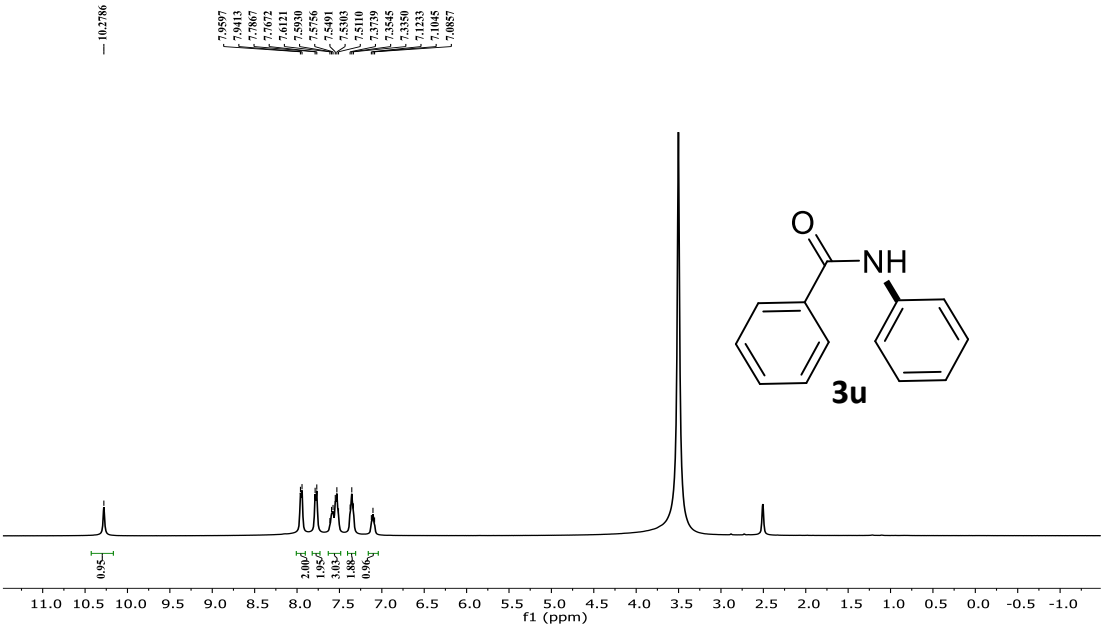

Figure III.22: ^{1}H-NMR of **3u** in DMSO-*d*$_6$

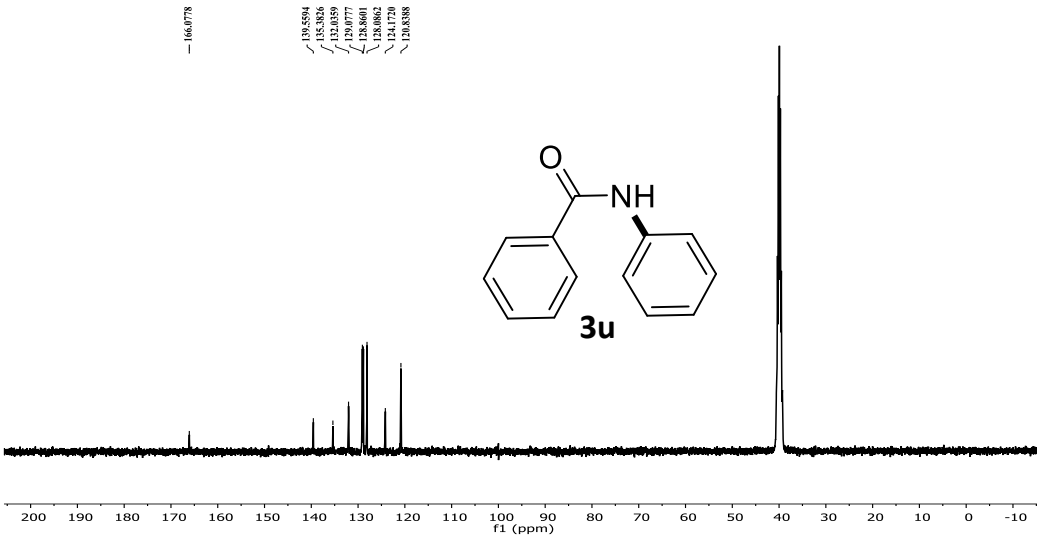

Figure III.23: ^{13}C-NMR of **3u** in DMSO-*d*$_6$

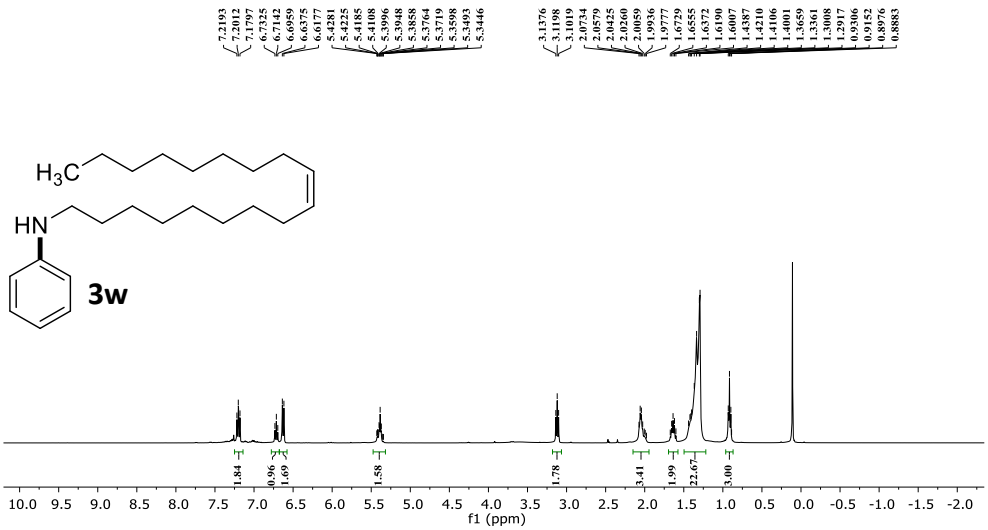

Figure III.24: ^{1}H-NMR of **3w** in $CDCl_3$

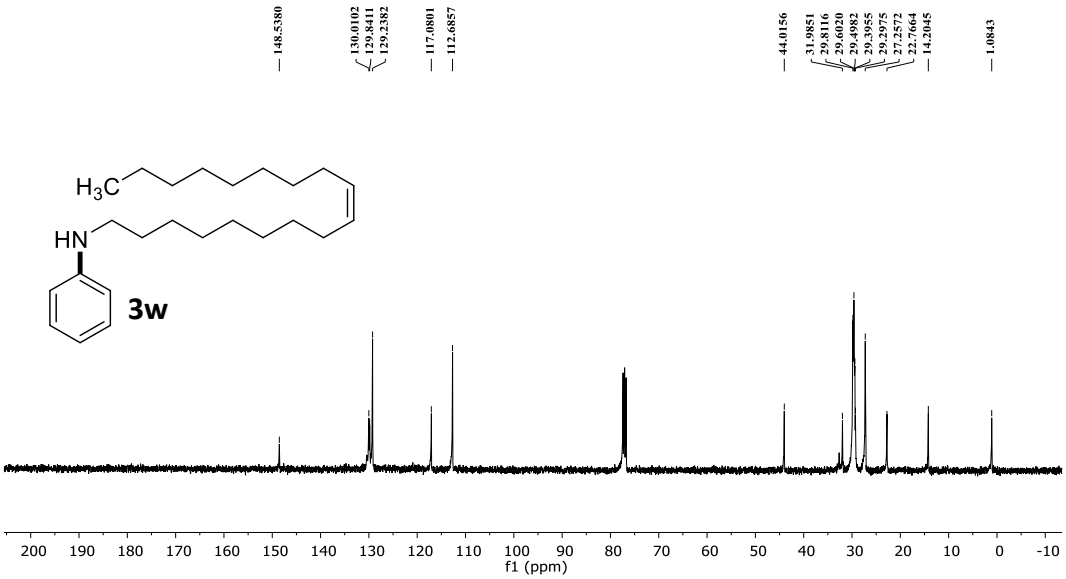

Figure III.25: ^{13}C-NMR of **3w** in $CDCl_3$

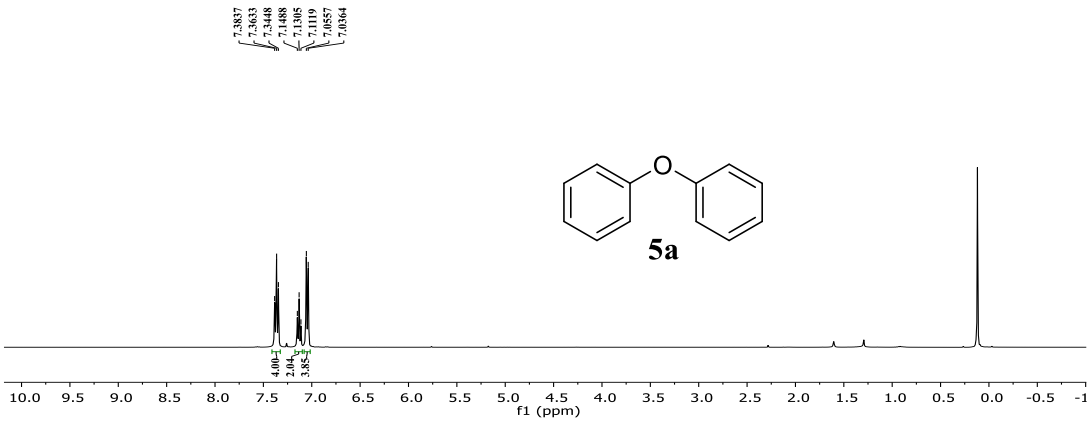

Figure III.26: ^{1}H-NMR of **5a** in $CDCl_3$

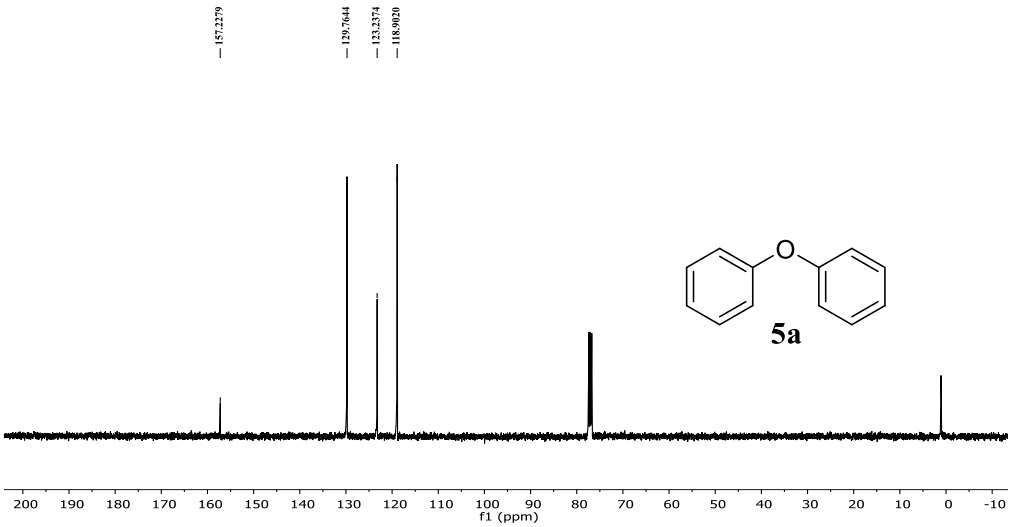

Figure III.27: ^{13}C-NMR of **5a** in $CDCl_3$

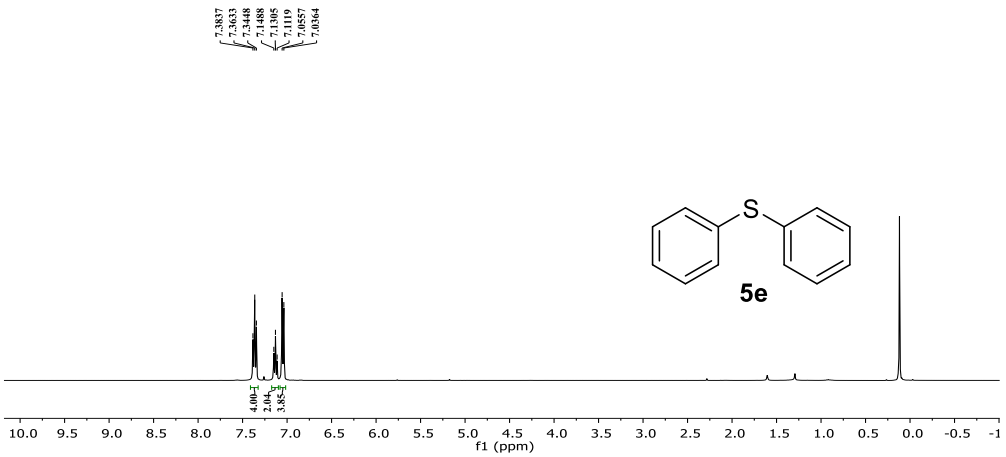

Figure III.28: ^{1}H-NMR of **5e** in $CDCl_3$

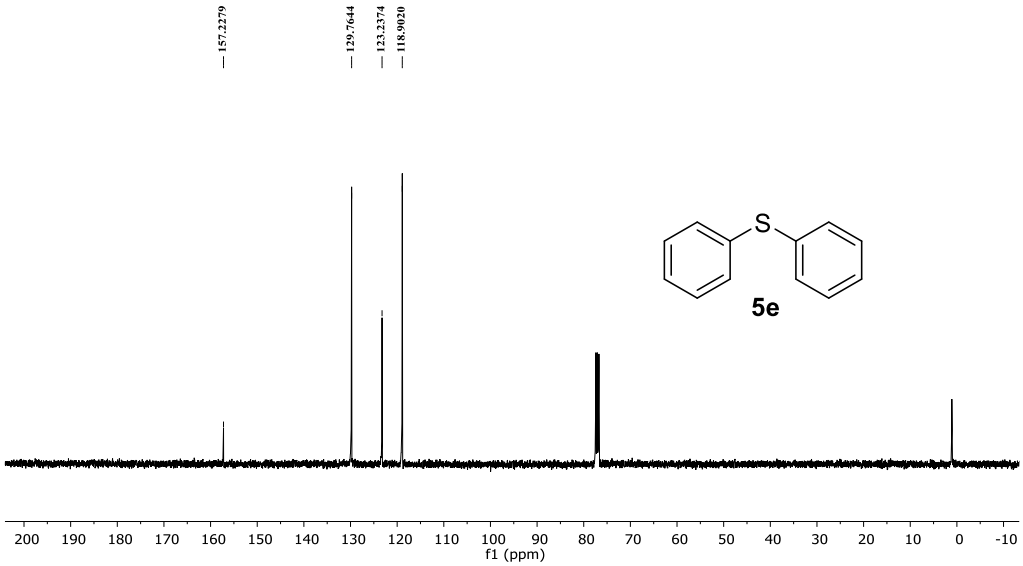

Figure III.29: ^{13}C-NMR of **5e** in $CDCl_3$

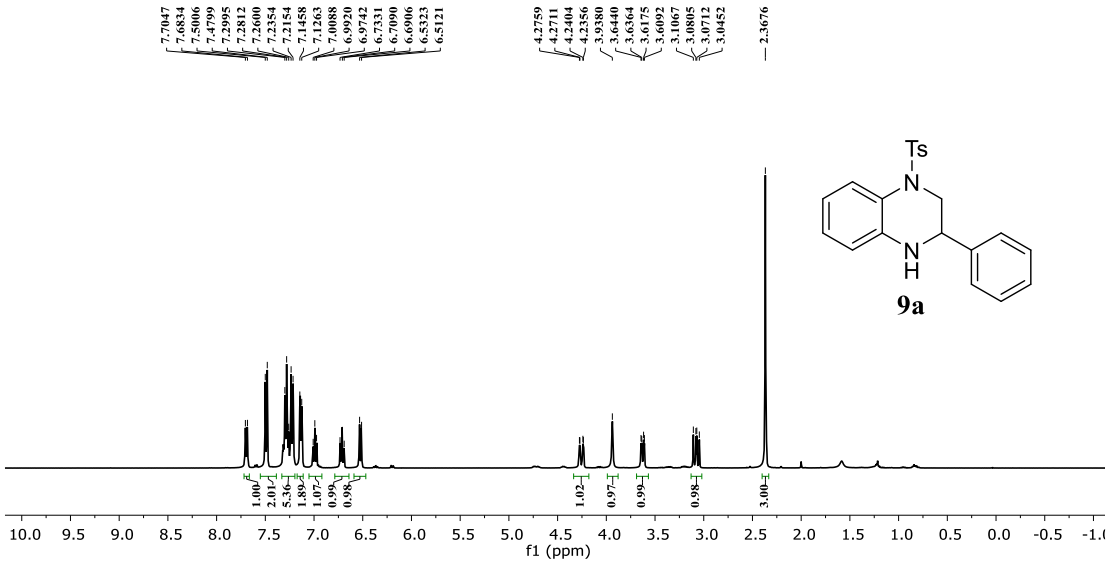

Figure III.30: ^{1}H-NMR of **9a** in $CDCl_3$

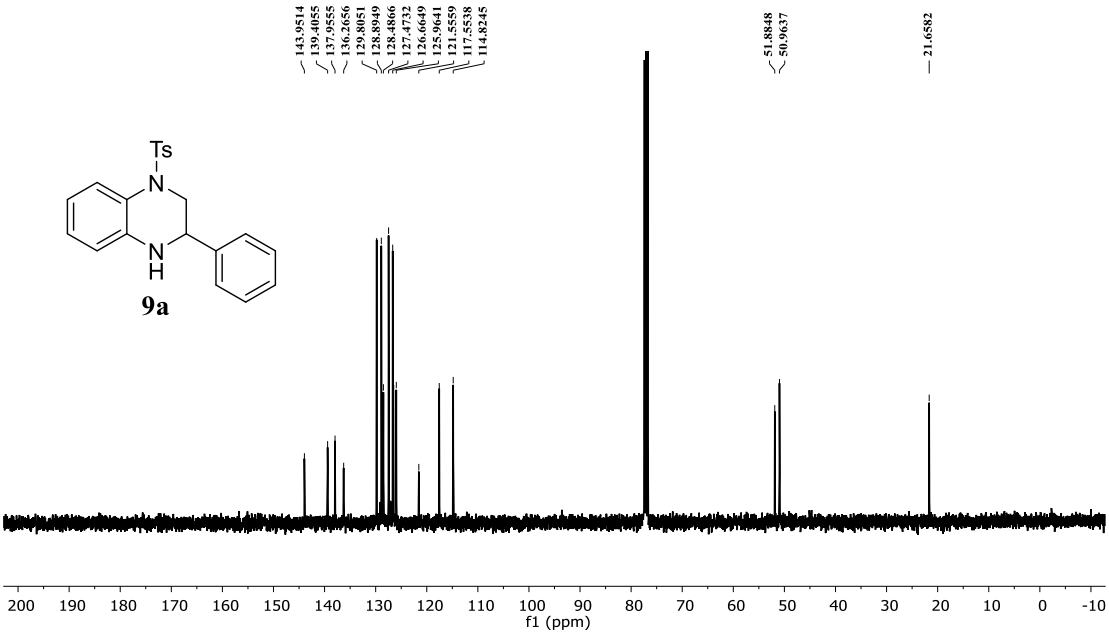

Figure III.31: ^{13}C-NMR of **9a** in $CDCl_3$

III.7. References:

(1) Devendar, P.; Qu, R. Y.; Kang, W. M.; He, B.; Yang, G. F. Palladium-Catalyzed Cross-Coupling Reactions: A Powerful Tool for the Synthesis of Agrochemicals. *J. Agric. Food Chem.* **2018**, *66*, 8914–8934.

(2) Ruiz-Castillo, P.; Buchwald, S. L. Applications of Palladium-Catalyzed C-N Cross-Coupling Reactions. *Chem. Rev.* **2016**, *116*, 12564–12649.

(3) Corbet, J. P.; Mignani, G. Selected Patented Cross-Coupling Reaction Technologies. *Chem. Rev.* **2006**, *106*, 2651–2710.

(4) Roughley, S. D.; Jordan, A. M. The Medicinal Chemist's Toolbox: An Analysis of Reactions Used in the Pursuit of Drug Candidates. *J. Med. Chem.* **2011**, *54*, 3451–3479.

(5) Ullmann, F. Ueber Eine Neue Bildungsweise von Diphenylaminderivaten. *Berichte der Dtsch. Chem. Gesellschaft* **1903**, *36*, 2382–2384.

(6) Goldberg, I. Ueber Phenylirungen Bei Gegenwart von Kupfer Als Katalysator. *Berichte der Dtsch. Chem. Gesellerschaft* **1906**, *39*, 108–109.

(7) Masanori, K.; Masayuki, K.; Toshihiko, M. Palladium-Catalyzed Aromatic Amination of Aryl Bromides with N, N-Diethylamino-Tributyltin. *Chem. Lett.* **1983**, *12*, 927–928.

(8) Guram, A. S.; Rennels, R. A.; Buchwald, S. L. A Simple Catalytic Method for the Conversion of Aryl Bromides to Arylamines. *Angew. Chemie Int. Ed. English* **1995**, *34*, 1348–1350.

(9) Louie, J.; Hartwig, J. F. Palladium-Catalyzed Synthesis of Arylamines from Aryl Halides. Mechanistic Studies Lead to Coupling in the Absence of Tin Reagents. *Tetrahedron Lett.* **1995**, *36*, 3609–3612.

(10) Forero-Cortés, P. A.; Haydl, A. M. The 25th Anniversary of the Buchwald-Hartwig Amination: Development, Applications, and Outlook. *Org. Process Res. Dev.* **2019**, *23*, 1478–1483.

(11) Corma, A.; Garcia, H. Silica-Bound Homogenous Catalysts as Recoverable and Reusable Catalysts in Organic Synthesis. *Adv. Synth. Catal.* **2006**, *348*, 1391–1412.

(12) Yin, L.; Liebscher, J. Carbon-Carbon Coupling Reactions Catalyzed by Heterogeneous Palladium Catalysts. *Chem. Rev.* **2007**, *107*, 133–173.

(13) Hassan, J.; Sévignon, M.; Gozzi, C.; Schulz, E.; Lemaire, M. Aryl-Aryl Bond Formation One Century after the Discovery of the Ullmann Reaction. *Chem. Rev.* **2002**, *102*, 1359–1469.

(14) Martin, R.; Buchwald, S. L. Palladium-Catalyzed Suzuki-Miyaura Cross-Coupling Reactions Employing Dialkylbiaryl Phosphine Ligands. *Acc. Chem. Res.* **2008**, *41*, 1461–1473.

(15) Schlummer, B.; Scholz, U. Palladium-Catalyzed C-N and C-O Coupling - A Practical Guide from an Industrial Vantage Point. *Adv. Synth. Catal.* **2004**, *346*, 1599–1626.

(16) Beletskaya, I. P.; Cheprakov, A. V. Heck Reaction as a Sharpening Stone of

Palladium Catalysis. *Chem. Rev.* **2000**, *100*, 3009–3066.

(17) Kantchev, E. A. B.; O'Brien, C. J.; Organ, M. G. *Palladium Complexes of N-Heterocyclic Carbenes as Catalysts for Cross-Coupling Reactions - A Synthetic Chemist's Perspective*; 2007; Vol. 46.

(18) Fortman, G. C.; Nolan, S. P. *N*-Heterocyclic Carbene (NHC) Ligands and Palladium in Homogeneous Cross-Coupling Catalysis: A Perfect Union. *Chem. Soc. Rev.* **2011**, *40*, 5151–5169.

(19) Herrmann, W. A.; Brossmer, C.; Reisinger, C. P.; Riermeier, T. H.; Öfele, K.; Beller, M. Palladacycles: Efficient New Catalysts for the Heck Vinylation of Aryl Halides. *Chem. - A Eur. J.* **1997**, *3*, 1357–1364.

(20) Beletskaya, I. P.; Cheprakov, A. V. Copper in Cross-Coupling Reactions: The Post-Ullmann Chemistry. *Coord. Chem. Rev.* **2004**, *248*, 2337–2364.

(21) Rout, L.; Jammi, S.; Punniyamurthy, T. Novel CuO Nanoparticle Catalyzed C-N Cross Coupling of Amines with Lodobenzene. *Org. Lett.* **2007**, *9* , 3397–3399.

(22) Rout, L.; Sen, T. K.; Punniyamurthy, T. Efficient CuO-Nanoparticle-Catalyzed C-S Cross-Coupling of Thiols with Iodobenzene. *Angew. Chemie - Int. Ed.* **2007**, *46*, 5583–5586.

(23) Truong, T.; Nguyen, C. V.; Truong, N. T.; Phan, N. T. S. Ligand-Free N-Arylation of Heterocycles Using Metal–Organic Framework [Cu(INA)$_2$] as an Efficient Heterogeneous Catalyst. *RSC Adv.* **2015**, *5*, 107547–107556.

(24) Li, Z.; Meng, F.; Zhang, J.; Xie, J.; Dai, B. Efficient and Recyclable Copper-Based MOF-Catalyzed *N*-Arylation of N-Containing Heterocycles with Aryliodide. *Org. Biomol. Chem.* **2016**, *14*, 10861–10865.

(25) Maity, T.; Saha, D.; Koner, S. Aromatic N-Arylations Catalyzed by Copper-Anchored Porous Zinc-Based Metal – Organic Framework under Heterogeneous Conditions. *ChemCatChem* **2014**, *6*, 2373–2383.

(26) Kousik, S.; Velmathi, S. Engineering Metal–Organic Framework Catalysts for C−C and C−X Coupling Reactions: Advances in Reticular Approaches from 2014–2018. *Chem. - A Eur. J.* **2019**, *25*, 16451–16505.

(27) Ma, P.; Meng, F.; Wang, N.; Zhang, J.; Xie, J.; Dai, B. Heterogeneous Amorphous Cu–MOF-74 Catalyst for C-N Coupling Reaction. *ChemistrySelect* **2018**, *3*, 10694–10700.

(28) Mondloch, J. E.; Karagiaridi, O.; Farha, O. K.; Hupp, J. T. Activation of Metal-Organic Framework Materials. *CrystEngComm* **2013**, *15*, 9258–9264.

(29) Hupp, J. T.; Poeppelmeler, K. R. Chemistry: Better Living through Nanopore Chemistry. *Science* **2005**, *309*, 2008–2009.

(30) Bae, J.; Jung, J. W.; Park, H. Y.; Cho, C. H.; Park, J. Oxygen Plasma Treatment of HKUST-1 for Porosity Retention upon Exposure to Moisture. *Chem. Commun.* **2017**, *53*, 12100–12103.

(31) Liu, Y.; Klet, R. C.; Hupp, J. T.; Farha, O. Probing the Correlations between the Defects in Metal-Organic Frameworks and Their Catalytic Activity by an Epoxide Ring-Opening Reaction. *Chem. Commun.* **2016**, *52*, 7806–7809.

(32) Hall, J. N.; Bollini, P. Metal-Organic Framework MIL-100 Catalyzed

Acetalization of Benzaldehyde with Methanol: Lewis or Brønsted Acid Catalysis? *ACS Catal.* **2020**, *10*, 3750–3763.

(33) Woodliffe, J. L.; Ferrari, R. S.; Ahmed, I.; Laybourn, A. Evaluating the Purification and Activation of Metal-Organic Frameworks from a Technical and Circular Economy Perspective. *Coord. Chem. Rev.* **2021**, *428*, 213578.

(34) Balogh-Hergovich, É.; Speier, G. Kinetics and Mechanism of the Dehydrogenation of Indolines to Indoles with Dioxygen Catalyzed by Chloro(Pyridine)Copper(I) in Dichloromethane Solution. *J. Mol. Catal.* **1986**, *37*, 309–316.

(35) Banik, A.; Ahmed, J.; Sil, S.; Mandal, S. K. Mimicking Transition Metals in Borrowing Hydrogen from Alcohols. *Chem. Sci.* **2021**, *12*, 8353–8361.

(36) Jammi, S.; Sakthivel, S.; Rout, L.; Mukherjee, T.; Mandai, S.; Mitra, R.; Saha, P.; Punniyamurthy, T. CuO Nanoparticles Catalyzed C-N, C-O, and C-S Cross-Coupling Reactions: Scope and Mechanism. *J. Org. Chem.* **2009**, *74*, 1971–1976.

(37) Altman, R. A.; Buchwald, S. L. 4,7-Dimethoxy-1,10-Phenanthroline: An Excellent Ligand for the Cu-Catalyzed N-Arylation of Imidazoles. *Org. Lett.* **2006**, *8*, 2779–2782.

(38) Devarajan, N.; Suresh, P. Framework-Copper-Catalyzed C−N Cross-Coupling of Arylboronic Acids with Imidazole: Convenient and Ligand-Free Synthesis of N-Arylimidazoles. *ChemCatChem* **2016**, *8*, 2953–2960.

(39) Tang, W.; Xu, L.; Fan, Q. H.; Wang, J.; Fan, B.; Zhou, Z.; Lam, K. H.; Chan, A. S. C. Asymmetric Hydrogenation of Quinoxalines with Diphosphinite Ligands: A Practical Synthesis of Enantioenriched, Substituted Tetrahydroquinoxalines. *Angew. Chemie - Int. Ed.* **2009**, *48*, 9135–9138.

(40) Abraham, C. J.; Paull, D. H.; Scerba, M. T.; Grebinski, J. W.; Lectka, T. Catalytic, Enantioselective Bifunctional Inverse Electron Demand Hetero-Diels-Alder Reactions of Ketene Enolates and o-Benzoquinone Diimides. *J. Am. Chem. Soc.* **2006**, *128*, 13370–13371.

(41) Samanta, K.; Panda, G. A New Synthesis of Amino Acid-Based Enantiomerically Pure Substituted 2,3,4,4^{a},5,6-Hexahydro-1H-Pyrazino[1,2-a]Quinoxalines. *Org. Biomol. Chem.* **2010**, *8*, 2823–2828.

(42) Li, B.; Ju, Z.; Zhou, M.; Su, K.; Yuan, D. A Reusable MOF-Supported Single-Site Zinc(II) Catalyst for Efficient Intramolecular Hydroamination of o-Alkynylanilines. *Angew. Chemie - Int. Ed.* **2019**, *58*, 7687–7691.

(43) Pradhan, S.; Shahi, C. K.; Bhattacharyya, A.; Chauhan, N.; Ghorai, M. K. Divergent and Stereospecific Routes to Five to Eight-Membered 1,3- and 1,4-Di-Aza-Heterocycles *via* Ring-Opening Cyclization of Activated Aziridines with Aryl Amines. *ChemistrySelect* **2017**, *2*, 550–556.

(44) Puthiaraj, P.; Suresh, P.; Pitchumani, K. Aerobic Homocoupling of Arylboronic Acids Catalysed by Copper Terephthalate Metal-Organic Frameworks. *Green Chem.* **2014**, *16*, 2865–2875.

(45) Šimėnas, M.; Kobalz, M.; Mendt, M.; Eckold, P.; Krautscheid, H.; Banys, J.; Pöppl, A. Synthesis, Structure, and Electron Paramagnetic Resonance Study of

a Mixed Valent Metal − Organic Framework Containing Cu2 Paddle- Wheel Units. *J. Phys. Chem. C* **2015**, *119*, 4898−4907.

(46) Mkami, H. E. L.; Mohideen, M. I. H.; Pal, C.; Mckinlay, A.; Scheimann, O.; Morris, R. E. EPR and Magnetic Studies of a Novel Copper Metal Organic Framework (STAM-I). *Chem. Phys. Lett.* **2012**, *544*, 17–21.

(47) Lefèvre, G.; Franc, G.; Tlili, A.; Adamo, C.; Taillefer, M.; Ciofini, I.; Jutand, A. Contribution to the Mechanism of Copper-Catalyzed C-N and C-O Bond Formation. *Organometallics* **2012**, *31*, 7694–7707.

(48) Yang, Q.; Sheng, M.; Li, X.; Tucker, C.; Vásquez Céspedes, S.; Webb, N. J.; Whiteker, G. T.; Yu, J. Potential Explosion Hazards Associated with the Autocatalytic Thermal Decomposition of Dimethyl Sulfoxide and Its Mixtures. *Org. Process Res. Dev.* **2020**, *24*, 916–939.

(49) Kazemnejadi, M.; Shakeri, A.; Nikookar, M.; Shademani, R.; Mohammadi, M. Selective and Metal-Free Epoxidation of Terminal Alkenes by Heterogeneous Polydioxirane in Mild Conditions. *R. Soc. Open Sci.* **2018**, *5*, 171541.

(50) Sharma, P.; Rohilla, S.; Jain, N. Copper Acetate-DMSO Promoted Methylthiolation of Arenes and Heteroarenes. *J. Org. Chem.* **2015**, *80*, 4116–4122.

(51) Wu, Q.; Wang, L. Immobilization of Copper(II) in Organic-Inorganic Hybrid Materials: A Highly Efficient and Reusable Catalyst for the Classic Ullmann Reaction. *Synthesis (Stuttg).* **2008**, *13*, 2007–2012.

(52) Capdevila, L.; Andris, E.; Briš, A.; Tarrés, M.; Roldán-Gómez, S.; Roithová, J.; Ribas, X. Silver(I)-Catalyzed C-X, C-C, C-N, and C-O Cross-Couplings Using Aminoquinoline Directing Group via Elusive Aryl-Ag(III) Species. *ACS Catal.* **2018**, *8*, 10430–10436.

(53) Chen, T.; Yan, M.; Zheng, C.; Yuan, J.; Xu, S.; Chen, R.; Huang, W. A Theoretical Insight into the Mechanism of Cu(I)-Catalyzed C-N Coupling between Aryl Halides and Aqueous Ammonia. *Chinese J. Chem.* **2015**, *33*, 961–966.

(54) Giri, R.; Brusoe, A.; Troshin, K.; Wang, J. Y.; Font, M.; Hartwig, J. F. Mechanism of the Ullmann Biaryl Ether Synthesis Catalyzed by Complexes of Anionic Ligands: Evidence for the Reaction of Iodoarenes with Ligated Anionic CuI Intermediates. *J. Am. Chem. Soc.* **2018**, *140*, 793–806.

(55) Li, L. C.; Zhang, L.; Wang, W.; Pan, R.; Mao, S.; Tian, A. M. Investigation on the Mechanism for C–N Coupling of 3-Iodopyridine and Pyrazole Catalyzed by Cu(I). *Int. J. Chem. Kinet.* **2016**, *48*, 11–22.

(56) Dhakshinamoorthy, A.; Alvaro, M.; Garcia, H. Aerobic Oxidation of Benzylic Alcohols Catalyzed by Metal-Organic Frameworks Assisted by TEMPO. *ACS Catal.* **2011**, *1*, 48–53.

(57) Sharma, D.; Rasaily, S.; Pradhan, S.; Baruah, K.; Tamang, S.; Pariyar, A. HKUST-1 Metal Organic Framework as an Efficient Dual-Function Catalyst: Aziridination and One-Pot Ring-Opening Transformation for Formation of β-Aryl Sulfonamides with C–C, C–N, C–S, and C–O Bonds. *Inorg. Chem.* **2021**, *60*, 7794–7802.

Chapter IV

MOF towards Cross Dehydrogenative Coupling and Knoevenagel Condensation Reaction

Abstract

In this chapter, Cu-1D MOF with pre-existing CUS is applied towards cross dehydrogenative coupling (CDC) reaction to form C-O bond between 2-hydroxybenzaldehyde derivative and dioxane that involves direct C-H bond activation. Under the optimized reaction condition, the Cu-1D catalyst produce the desired product 2-{(1,4 dioxan-2-yl)oxy}benzaldehyde with a yield of 95% in 0.5 h. The catalytic system was also applied to form various carbamates by reacting 2-hydroxybenzaldehyde derivative and DMF, where a yield upto 92% was noted for carbamates product. In order to understand the role of CUS in Cu-1D MOF, the CDC reaction was conducted with other well-known Cu-based MOFs such as HKUST-1, CU-BDC(DMF), Cu-SKU-5 and Cu-SKU-4. Profound effect of available coordinating sites was found as MOF with available CUS could efficiently catalyse CDC reaction under optimized condition. MOFs such as as-synthesized HKUST-1 and Cu-BDC(DMF) being devoid of CUS required more than 12 h to deliver considerable amount of product yield. Further with the availability of Lewis acid and Bronsted basic site on Cu-1D MOF, its catalytic potential was further explored towards Knoevenagel condensation reaction. The reaction between benzaldehyde and malononitrile forms >99% of desired product within 0.5 h with Cu-1D as catalyst. In addition, a novel malononitrile product has also been reported with a yield of 98%. The heterogeneous nature of the catalyst for both CDC and Knoevenagel reactions were established by performing leaching tests where the recycled catalyst produced upto 82% and 98% of respective product in the 4th cycle.

IV.1. Introduction:

The transition metal-catalyzed introduction of C-heteroatom and C-C bond, to form the carbon skeleton of a value-added complex scaffold is enthralling. Typically, the requirement of prefunctionalized reactant, stoichiometric amount of catalyst, and adequate amount of hazardous waste production are a major concern from atom-economic and environmental aspects.[1,2] Among many, cross dehydrogenative coupling (CDC) reactions *via* C-H activation and Knoevenagel condensation reaction could offer an environmentally benign route to overcome such drawbacks. In the CDC reaction, the formation of C-X (X= N, O, C, etc) bond takes place with the loss of two hydrogens, one from the C-H bond and another from either the N-H or O-H bonds of the second coupling partner (Scheme IV.1). Therefore, the formation of C-X bond does not require any pre-functionalization. However, the cleavage of hydrogen from the C-H bond is challenging and thermodynamically uphill, so a metal catalyst and an oxidant are required for these reactions.

Scheme IV.1: General scheme for cross-dehydrogenative coupling reaction.

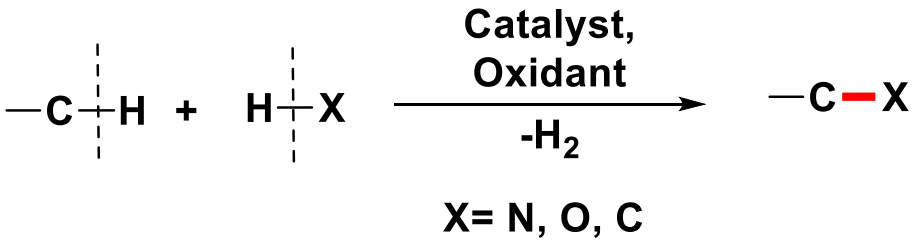

Transition metal catalysts, such as Cu, Fe, Co, Ni, Pd, Rh, etc have been employed towards successful CDC reactions.[3] Recently, various fruitful developments have been shown towards CDC reactions and potentially applied in pharmaceuticals, agrochemicals, and organic materials.[4,5] In most of the reaction schemes, the participation of homogenous catalyst is evident. The development of the heterogenous catalytic system for CDC reaction was also seen in recent years where the use of

nanoparticles, zeolites, MOFs, etc are reported. Among several MOFs, a few Cu-based MOFs have been reported towards CDC reactions of 2-carbonyl-substituted phenols with ether or formamides. Phan *et al.*[6] reported the use of $Cu_2(BPDC)_2(BPY)$ MOF as a solid catalyst towards CDC and later Corma *et al.*[7] also reported the similar CDC reaction using $[Cu(im)_2]$ (im= imidazolate) MOF followed by Bhardwaj *et al.*[8] with $\{[Cu_6(L)_3(H_2O)_6]\cdot(14DMF)(9H_2O)\}_n$ (L=5′-amino-1,1′:4′,1″-terphenyl-3,3″,5,5″-tetracarboxylic acid) MOF.

Like the CDC reaction, the Knoevenagel condensation (named after German chemist Emil Knoevenagel) is a classic organic reaction that forms a C-C bond between an aldehyde or a ketone and a compound containing active methylene group (e.g., malonate or an ester) (Scheme IV.2). The reaction is typically catalyzed by acidic or basic site and involves the removal of a proton from the methylene group, followed by an attack of the resulting enolate on the carbonyl compound. The reaction can be used to synthesize a wide range of products, including *α,β*-unsaturated carbonyl compounds, which are important intermediates in the synthesis of pharmaceuticals, agrochemicals, and other organic compounds. Patai *et al.* in 1960 reported the non-catalyzed Knoevenagel reaction by use of an appropriate solvent (EtOH or H_2O) where 99% of desired product was reported for a reaction between 4-nitrobenzaldehyde and malononitrile within a period of 5 min at 25 ℃.

However, when benzaldehyde was used as a substrate, more than 2 h and an elevated temperature (60 ℃) was required to obtain a yield of 99%. These results indicate that the rate of reaction depends on the reactivity of the substrate and highlights the necessity of a catalyst. Furthermore, the use of a strong base such as pyridine, piperidine, etc was found to have a positive impact on the reaction yield whereas strong acids were found to inhibit the overall reaction.[9] In recent times, the use of acid-base-

Scheme IV.2: General scheme for Knoevenagel condensation reaction.

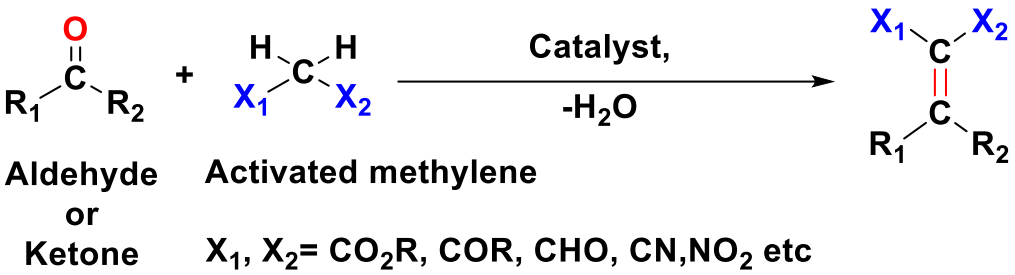

supported catalysts has gained popularity as they possess both acidic and basic properties and can facilitate multistep reactions within a single catalytic system, leading to enhanced catalytic efficiency and higher yields of products.[10] The acidic and basic sites can work in synergy to activate electrophiles and nucleophiles simultaneously, making the catalytic process more efficient and effective.[11] In that regard, a metal node within a MOF that possesses unoccupied *d*-orbitals can function as a Lewis acid, while the ligand, which contains elements with lone pairs, can act as a Bronsted base. Nevertheless, MOFs with dual functional catalytic activity have shown active participation in recent years toward the heterogenous catalytic system for Knoevenagel reaction.[12,13] Apart from MOFs, heterogeneous catalysts such as carbon nanotubes,[14] mesoporous titanosilicates,[15] Cu_3TATAT,[16] zeolites[17], etc have also been enormously developed towards the Knoevenagel reaction. The catalytic sites in MOF can be generated by activating and generating CUS in metal nodes. The CUS in MOF is directly related to the Lewis acid character of metal nodes. Although the generation of CUS is required for group transfer reactions such as aziridination, the reactions like ring opening of different heterocycles do not necessarily require CUS.[18] From Chapter III too we understood the importance of CUS in organic transformation for the generation of cross-coupled bonds. On careful observation of the previous reports, various MOFs are reported to be efficient towards

CDC and Knoevenagel condensation reactions where the role of CUS was not discussed appropriately. Mechanistically these two reactions proceed through a different pathway, as CDC requires the formation of a chelated complex with substrate and metal node highlighting the requirement of an open metal site for substrate to bind. On the other hand, the Knoevenagel condensation reaction generally proceeds through various catalytic cycles. The mechanism involves deprotonation of the acidic hydrogen to form an enolate anion, which then reacts with the aldehyde or ketone to form a β-keto ester or α-β, unsaturated ester. The resulting compound undergoes a dehydration reaction to form an α-β unsaturated carbonyl compound, which is then protonated to form the final product. The rate of reaction directly depends in the available basic sites of catalyst to abstract a proton from an active methylene group. Therefore, Knoevenagel condensation reaction being a base catalyzed reaction, CUS of MOF with Lewis acid sites may or may not be required. Motivated to find the detailed study in these problems, in this chapter we have emphasize to understand the role of CUS in CDC and Knoevenagel reaction. The reaction was performed with several Cu-MOF such as HKUST-1 (Cu), Cu-BDC, Cu-SKU-3 and Cu-1D MOF. These MOFs were reasonably chosen for study considering the availability of CUS as HKUST-1(Cu) and Cu-BDC are hexa-coordinated, activated HKUST-1(Cu) and Cu-SKU-3 are penta-coordinated MOF and lastly, Cu-1D and Cu-SKU-4 MOFs are tetra-coordinated MOF. The study towards understanding the importance of open metal sites in MOF catalyst towards CDC reaction and Knoevenagel reaction has not been made before to the best of our knowledge. Therefore, our findings may serve towards rational design and development of environmentally friendly, economically inexpensive and reusable heterogeneous catalytic system for above-mentioned reactions.

IV.2. Results and Discussions:

IV.2.1. Cross-Dehydrogenative Coupling Reaction:

To demonstrate the viability of copper-based MOF as a catalyst, the CDC reactions involving the C−H bond activation were optimized using Cu-1D MOF by reacting 1,4-dioxane (**1a**) and 2-hydroxybenzaldehyde as model reaction (Scheme IV.3). To begin with, the reaction was initiated with 2-hydroxybenzaldehyde (**1a**, 1.0 mmol.) as a limiting substrate and 70%TBHP as an oxidant was used in 1.5 equiv. along with 20 mol% of Cu-1D catalyst (2.5 mol%) and 20 mmol dioxane as a C-H coupling partner (Scheme IV.3). The high stoichiometric ratio of dioxane was utilized as it serves as a solvent and substrate within the reaction system.

Scheme IV.3: Model reaction for the cross-dehydrogenative coupling (CDC) reaction.

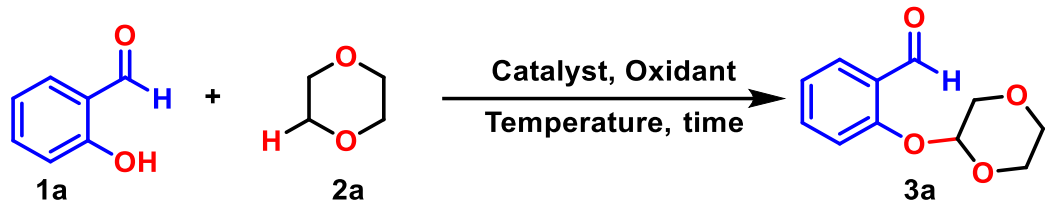

The progress of the reaction was observed through TLC and the final yield was calculated after isolating the desired product via purification through silica gel chromatography. All isolated products were confirmed with ^{1}H nuclear magnetic resonance (NMR), and ^{13}C NMR. To obtain an optimal reaction condition, the model reaction was precisely studied with the effect of temperature, catalyst loading, and oxidant. At first, the model reaction was performed with different oxidants (air, O_2, 30% H_2O_2, and 70% TBHP) at 80 °C with 10 mol% catalytic loadings (Table IV.1 entry 1-4). Employing air and O_2 gas as an oxidant, the formation of desired product **3a** was not observed. However, the reaction efficiently produced **3a** in the presence of 30% H_2O_2 with a product yield of 25%. Next,70% TBHP remarkably increased the yield of desired product up to 86% in 1.5 h. The effect of temperature over the reaction was

meticulously monitored with TBHP and 10% catalyst loading from 60 °C to 110 °C (entry 5-9). The reaction progressed significantly with an increase in temperature, however, the yield of the reaction did not improve above 100 °C. Next, the reaction was screened with different catalyst loading using TBHP as an oxidant (Table IV.1 entry 10-14) at 80 °C. The increase in catalyst loading to 15 and 20 mol% did not improve the progress of the and 10 mol% loading of the catalyst was found optimal for the reaction process Therefore, with the optimal condition the reaction was carried out with 2-hydroxybenzaldehyde (**1a**, 1.0 mmol.), dioxane (**2a**, 20 mmol.), 70% TBHP (1.5 equiv.) as an oxidant and 10 mol% of Cu-1D catalyst at 100 ℃ to deliver 95% of 2-((1,4-dioxan-2-yl)oxy)benzaldehyde as the desired product **3a** (entry 12). When the reaction was conducted in the absence of the catalyst, no substantial progress in product formation was observed indicating the catalytic behaviour of the Cu-1D catalyst.

Table IV.1. Optimization studies for CDC reaction between 2-hydroxybenzaldehyde (**1a**) and dioxane (**2a**).

Entry	Cu-1D Catalyst (mol %)	Oxidant	Temp (°C)	Time (h)	Yield (%)[a]
1.	20	70% TBHP	80 °C	1.5	75
2.	20	30% H_2O_2	80 °C	2	25
3.	20	O_2	80 °C	3	trace
4.	20	Air	80 °C	3	nr
5.	20	70% TBHP	50 ℃	3	42
6.	20	70% TBHP	80 ℃	1.5	75
7.	20	70% TBHP	90 ℃	1.5	78
8.	20	70% TBHP	100 ℃	0.5	95
9.	20	70% TBHP	110 ℃	2.5	95
10.	2.5	70% TBHP	100 ℃	1	72
11.	5	70% TBHP	100 ℃	0.5	88
12.	10	70% TBHP	100 ℃	0.5	95
13.	15	70% TBHP	100 ℃	0.5	95
14	Blank	70% TBHP	100 ℃	12	trace

a = yields are isolated yields

With the Further, the electronic effects of the substituent on the reaction system were studied by using various electron-withdrawing and donating substituent (**1a-f)** under the optimized geometry and a variety of substrate libraries was established (Figure IV.1). In general, 4 substituted 2-{(1,4-dioxan-2-yl)oxy}benzaldehyde products with new C-O bonds were obtained in appreciable yields with the electron-donating substituents (*p*-CH_3:92%, 0.5 h, **3b**), (*p*-OCH_3: 89%,0.5 h, **3c**). Previously, a yield of 85% and 89% was reported by Phan *et al.*[6] and Bhardwaj *et al.*[8] for product **3b** respectively. However, yields of the products are comparatively lower with electron-withdrawing groups (*p*-NO_2: 60%, 3 h, **3d**). For product **3d** a yield of 33% is reported by CuCl[19], 48%, by $Cu_2(BPDC)_2(BPY)$[6] and 76% using $\{[Cu_6(L)_3(H_2O)_6]$ (14DMF) $(9H_2O)\}_n$[8] MOF respectively. The halogen-substituted 2-hydroxybenzaldehyde produced notable yields of the corresponding products [(*p*-Cl:73%, 1.5 h, **3e**) and (*p*-Br:80%, 1 h, **3f**)] and it is worth noting that the optimized reaction conditions were also suitable for halogen-substituted derivatives indicating the catalytic system to be halogen tolerant.

The reactivity of the Cu-1D catalyst towards CDC reaction between 2-hydroxybenzaldehyde and 1-4 dioxane was further compared with various hydrated Cu(II) salts. (Table IV.2 entries 1-3). The desired product **3a** was formed with a yield of 68%, 65%, and 70% for $CuCl_2.2H_2O$, $Cu(NO_3)_2.3H_2O$, and $Cu(OAc)_2.H_2O$ respectively in a time span of 1 h under our optimized reaction condition. The use of $Cu(OAc)_2$ and CuCl salts have been meticulously explored previously for CDC reaction by various groups (Table IV.2 entry 4-5).[19,20] The formation of 95% of **3a** in 0.5 h by Cu-1D MOF catalyst indicates that the Cu-1D catalytic system is kinetically more efficient than the homogeneous copper salt system. Furthermore, the CDC reaction previously reported by various Cu-based MOFs has been depicted in Table IV.2 entry

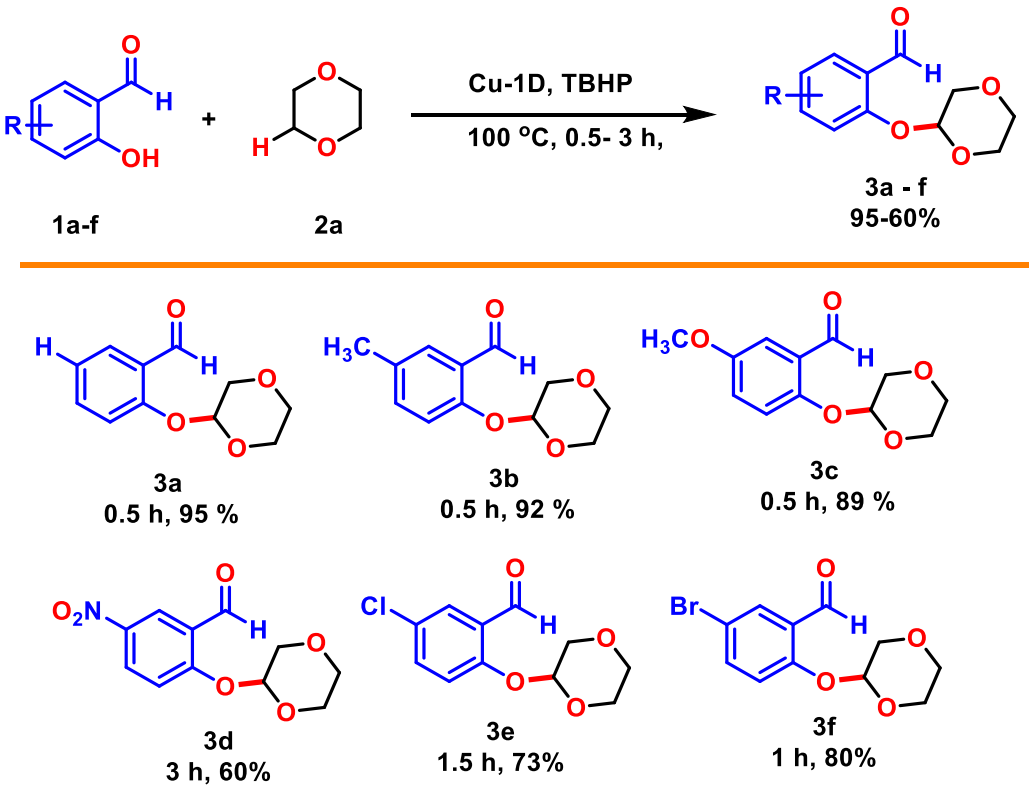

Figure IV.1: Substrate scope for Cu-1D catalyzed CDC reaction for dioxane and substituted 2-hydroxybenzaldehyde.

6-9. The $Cu_2(BPDC)_2(BPY)$ MOF reported by Phan *et al.*[6] forms 99% of desired product **3a** in 2 h. Similarly, Corma *et al.*[7] have reported the formation of **3a** with a yield of 82% and 83% within 0.5 h and 1.5 h by $[Cu(im)_2]$ and $[Cu(2\text{-pymo})_2]$ MOFs respectively. Lastly, the formation of **3a** was also found by Bhardwaj *et al.*[8] with carboxylate-based Cu-MOF and a yield of 95% in 1 h was reported. Although, very few MOFs have been employed for CDC reaction and when compared, the Cu-1D system was found to have a higher catalytic performance showing the stronger catalytic efficiency of the Cu-1D catalyst. Furthermore, known MOFs such as ZIF-8 (Zn), ZIF-67 (Co) and MIL-100 (Fe) gave inferior results under the optimized condition confirming the Cu-based MOF to be optimum catalyst for CDC reaction.

Table IV.2. Comparative table of the CDC reactions with different Cu-MOF and homogeneous salts

Entry	Catalyst	Time (h)	Yield (%)	Reference
1.	$Cu(OAc)_2.H_2O$	1	70	Our work
2.	$Cu(NO_3)_2.3H_2O$	1	65	Our work
3.	$CuCl_2.2H_2O$	1	68	Our work
4.	CuCl	15 min	92	19
5.	$Cu(OAc)_2$	3	79	20
6.	$Cu_2(BPDC)_2(BPY)$ MOF	2	99	6
7.	$\{[Cu_6(L)_3(H_2O)_6]$ (14DMF) $(9H_2O)\}_n$ MOF	1	95	8
8.	$[Cu(im)_2]$ MOF	0.5	83	7
9.	$[Cu(2\text{-pymo})_2]$ MOF	1.5	82	7
10.	Cu-1D MOF	0.5	95	Our work
11.	ZIF-8 (Zn)	3	trace	Our work
12.	ZIF-67 (Co)	3	20	Our work
13.	MIL-100 (Fe)	3	trace	Our work

The productive C−H activation of ether for CDC reaction of substituted 2-hydroxybenzaldehyde with dioxane undoubtedly demonstrates the efficiency of Cu-1D catalyst. The substrate scope of the CDC reaction was further extended to form carbamates analogues as a desired product *via* aldehydic C-H activation of dimethyl formamide. The presence of organic carbamates is a significant structural feature found in a variety of biologically active natural compounds, agrochemicals, and pharmaceuticals. Organic carbamates also have a significant impact on organic chemistry as they serve as protective groups and important intermediates.[21,22] Carbamates exhibit outstanding pharmacological properties, including their effectiveness as antibacterial, neuroprotective, antineoplastic, and anti-filarial agents, as well as inhibitors of endocannabinoid hydrolase and acetylcholinesterase.[23–26]

Typically, carbamates are synthesized using chloroformates or isocyanates, with phosgene or similar substitutes being used as starting materials.[27,28]. To avoid the use of toxic phosgene, metal-catalyzed reactions, and carbon dioxide have been employed as alternatives in the synthesis of carbamates.[29] Despite the availability of various reported protocols, including Hofmann and Curtius rearrangements,[30] there is still a lack of an efficient, environmentally friendly, and safe method for synthesizing carbamates. In a recent study by Barve *et al.,* it was demonstrated that several copper salts can serve as catalysts for the oxidative C-O coupling reaction between dialkyl formamides and 2-hydroxybenzaldehyde utilizing TBHP as the oxidant.[31] Following a similar reaction procedure, Corma *et al.* has reported the use of Cu-based MOF for the formation of carbamates.[7] The efficiency of Cu-1D MOF has also been explored for this reaction with some changes in the optimized reaction condition. In brief, 2-hydroxybenzaldehyde (**1a**, 1.0 equiv), DMF (**4a**, 50 equiv), 70% TBHP (1.5 equiv) as an oxidant and 10 mol% of Cu-1D catalyst at 120 °C to deliver 2-formylphenyl dimethyl carbamate (**5a**) as the desired product (Scheme IV.4). The reaction system of Cu-1D efficiently formed **5a** in good yield of 92% within a span of 1 h. For the product **5a,** the yield of 92% and 97% was reported in a time span of 3 h and 1.5 h with the use of [Cu(2-pymo)$_2$] and [Cu(im)$_2$] MOF respectively.[7] Apart from MOF, the Co@C-N nanoparticles derived from Co-MOF has also been reported to produce the desired carbamates **5a** with 90% yield in 24 h.[32]

Scheme IV.4: Model reaction for CDC reaction forming carbamates

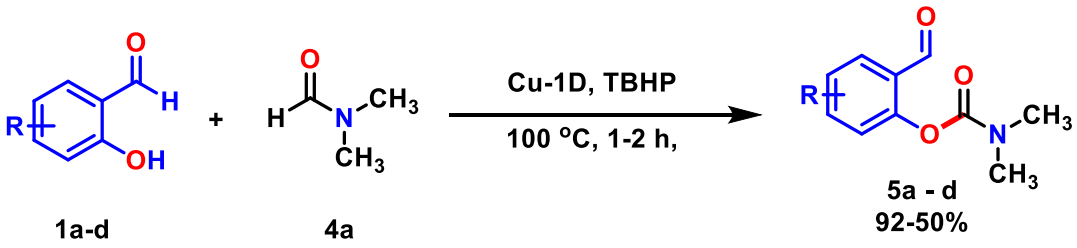

Furthermore, when substituted 2-hydroxybenzaldehydes were used as substrates in the reaction system, the process effectively converted these substrates to their respective carbamates (Figure IV.2). The electron-donating substituent on 2-hydroxybenzaldehydes produced an appreciable yield of respective products (*p*-CH_3:90%, 1 h, **5b**). However, with electron-withdrawing groups of the products were comparatively lower in yield (*p*-Cl: 87%, 1 h, **5c**), and (*p*-Br:89%, 1 h, **5d**).

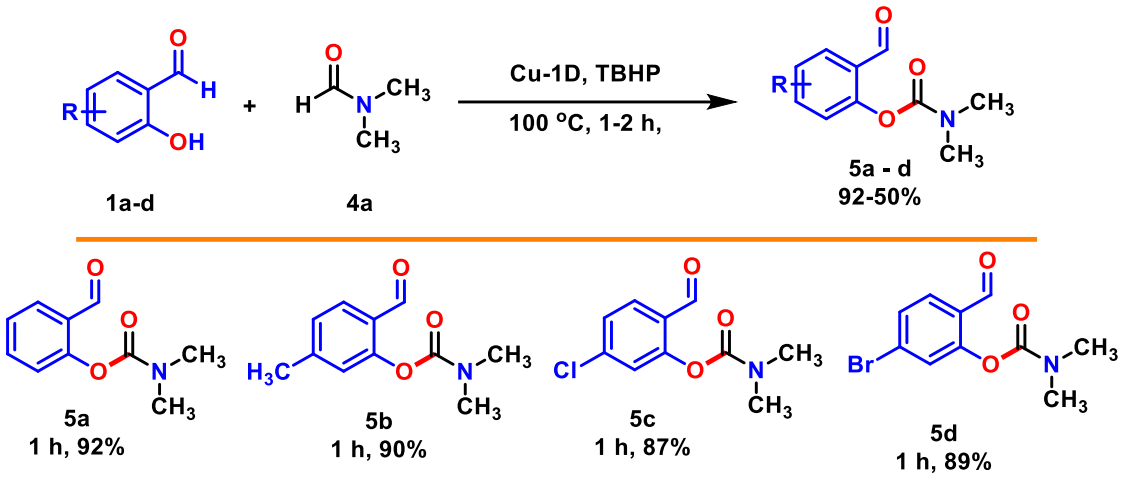

Figure IV.2: Substrate scope of Cu-1D catalyzed CDC reaction for DMF and substituted 2-hydroxybenzaldehyde.

IV.2.2. Mechanistic Insights of CDC

The catalytic cycle for the CDC reaction was investigated by performing some control experiments. At first, the radical inhibitor TEMPO was introduced to investigate the involvement of radicals in the catalytic cycle. The presence of TEMPO marginally decreased the yield of product **3a** indicating the participation of radical species in the catalytic cycle. Previously, Yang *et al.* utilized a porphyrin-based CuTECP catalyst for CDC reaction, and the mechanism was established meticulously.[33] The authors have detected the presence of 1,4-dioxane radical in ESI-MS for TEMPO treated reaction mixture where a peak at $[M+H]^+$= 244.1909 was ascribed to the TEMPO-1,4-dioxane

adduct. Also, the electron paramagnetic resonance (EPR) spectra of the reaction mixture have a free radical EPR signal centered at g=2.0, which aided the authors in confirming the formation of a carbon radical in this CDC reaction. In our case, when phenol was used instead of 2-hydroxybenzaldehyde, no desired product was obtained indicating the role of formyl moiety in directing the group toward the progress of the reaction (Scheme IV.5). The results obtained are consistent with an earlier study which proposed that the presence of the ortho-carbonyl (formyl) group is crucial for the creation of a complex with transition metals that functions as a bidentate ligand.[34,35]

Scheme IV.5: Reaction of phenol with dioxane under optimized condition.

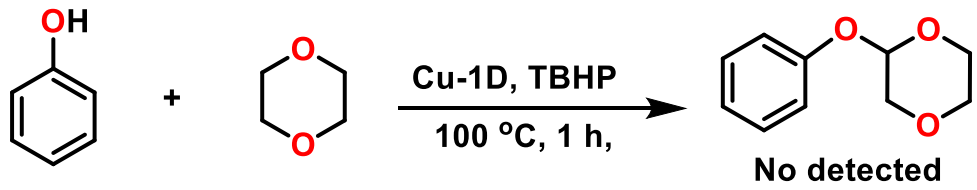

A plausible reaction pathway is proposed in figure IV.3 based on these observations and previous literature.[36] Mechanistically, the open metal sites in Cu-1D at first bind with the 2-hydroxybenzaldehyde to form a chelating copper complex (Complex A, step-1). Simultaneously, TBHP produces hydroxyl and tert-butoxyl radicals. The formation of radicals in the reaction system is crucial as it abstracts hydrogen from the chelating copper complex to form complex B (step-2) and 1,4 dioxane to form a radical dioxane species (Radical B). Also, it accounts for the lack of product formation when no oxidant is present (Table IV.1 entry 4). Lastly, in step-3 a radical A and complex B react to form a desired product **3a** regenerating the Cu-1D catalyst.

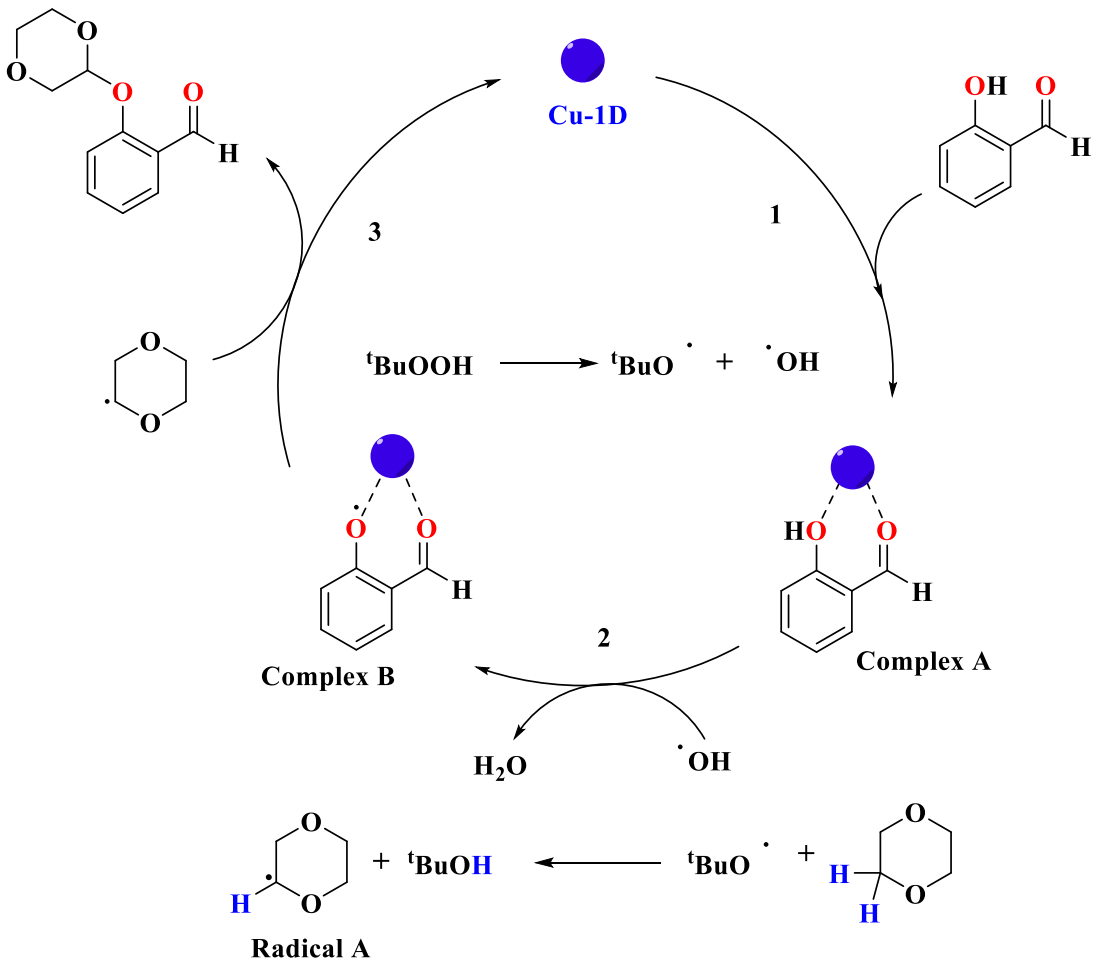

Figure IV.3: Proposed catalytic cycle for Cu-1D catalyzed CDC reaction.

IV.2.3. Knoevenagel condensation reaction:

Next, after the detailed study of the CDC reaction, the catalytic activity of the Cu-MOF catalyst was also studied towards the Knoevenagel condensation reaction. To obtain an optimal reaction condition benzaldehyde (**6a,** 1 mmol) and malononitrile (**7a,** 1.1 mmol) was chosen as a model substrate to produce 2-benzylidenemalononitrile (**8a**) as a desired product (Scheme IV.6). Initially, the reaction was performed under room temperature using 10% catalytic loading using various solvent such as methanol. ethanol, DMF, toluene, acetonitrile, and 1,4-dioxane (Table IV.3 entry 1-4).

Scheme IV.6: Model reaction for Knoevenagel condensation reaction

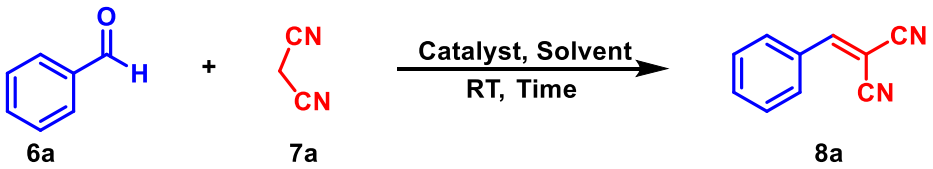

6a 7a 8a

The reaction took 1 h with DMF and acetonitrile to produce an appreciable yield of desired product **8a**. The solvents like toluene and 1,4 dioxane gave poor results as the reaction could not form an appreciable product even after 3 h (Table IV.3 entry 4 and 5). Furthermore, when MeOH and EtOH were used the reaction was completed within 0.5 h. Interestingly, the reaction took only 20 min for the reaction to complete under solvent-free conditions (Table IV.3 entry 7). However, since many aldehydes are solids, and limits the feasibility of solvent-free reaction conditions. Therefore, for such a solid substrate, MeOH/EtOH which is green in nature, was optimized as a solvent.[37,38] Next, the amount of catalyst was optimized under solvent-free conditions, where 5 mol% of was found to be optimum with 20 min and the further increase of catalyst did not improve the yield of the reaction (Table IV.3, entry 8-11). The reaction conducted in the absence of a catalyst (Table IV.3 entry 12) produced only 70% of desired product **8a** in 12h thereby confirming the role of Cu-1D catalyst in the reaction cycle. Therefore, the optimized reaction condition for Cu-1D catalyzed Knoevenagel condensation reaction was found with 3 mol% catalyst loading at room temperature with and without MeOH as a solvent considering the nature of the substrate used.

Table IV.3: Optimization studies for Knoevenagel condensation reaction between benzaldehyde (**6a**) and malononitrile (**7a**).

Entry	Cu-1D Catalyst (mol %)	Solvent	Temp (°C)	Time (h)	Yield (%)[a]
1.	10	DMF	25	1	91
2.	10	ACN	25	2	90
3.	10	1,4-dioxane	25	>3	42
4.	10	Toluene	25	>3	50
5.	10	MeOH	25	0.5	>99
6.	10	EtOH	25	0.5	>99
7.	10	-	25	0.3	>99
8.	10	-	25	0.3	>99
9.	5	-	25	0.3	>99
10.	3	-	25	1	>99
11.	1	-	25	1.5	93
12.	blank	MeOH	25	12	70

a=yields are isolated yields

The Knoevenagel reaction is one of the most explored reactions by MOFs. Not only copper-based MOF but MOFs such as NUC-65Br (In-based MOF),[12] NUC-53 (Y-based MOF),[39] NUC-45 (Pb-based MOF),[40] NUC-28 (Tm-based MOF),[41] DUT-52-$(NH_2)_2$-1 (Zr-based MOF),[42] NUC-58 (Tb-based MOF),[43] etc have been found efficient towards Knoevenagel condensation reaction. Further, a detailed comparison between the reactivity of Cu-1D MOF with previously reported copper and other MOFs for the Knoevenagel reaction was highlighted in table IV.4.

Table IV.4: Comparative table of the Knoevenagel condensation reactions with different MOF catalytic system.

Entry	Catalyst	Time (h)	Temp (°C)	Yield (%)	Ref.
1.	$\{[(CH_3)_2NH_2]_2[CaZn(TDP)(H_2O)]\cdot 3DMF\cdot 3H_2O\}_n$	1	60	97	44
2.	$\{[Zn(HL)_2]\}n$	2	25	100	45
3.	$Tb_6(\mu_3\text{-}OH)_8\cdot(2\text{-}FBA)_2\cdot(H_2O)_6\cdot(DCBA)_2]\cdot 10DMF\cdot 4H_2O$	6	25	>99	46
4.	Mg-ABDC	8	80	95	47
5.	$Pt/CN\text{-}ZrO_2$	2	80	100	48
6.	$\{[Co_2(tdc)_2(tpxn)]\cdot solvent\}_n$	1	25	96	49
7.	$[Cu_2Cu_4I_4(ANA)_4(DMF)_4]_n$	10	100	>99	50
8.	NUC-38Yb	24	45	96	51
9.	$[Zn(bix)]\{V_2O_6\}$	1	60	>99	52
10.	$Ni_3(BTC)_2(4\text{-}TPT)_2(H_2O)_6\cdot(H_2O)_{1.5}$	6	RT	97	53
11.	JLU-MOF116 (In) JLU-MOF117 (In)	2 1.5	40 40	95 99	54
12.	CSMCRI-19 (Ni)	6	60	99	13
13.	$[Cu_2(L)(H_2O)_3]\cdot 4DMF\cdot 6H_2O$	6.5	RT	98	55
14.	$\{[Cu_2(\mu_3\text{-}pdba)_2(2,2'\text{-}bipy)]\cdot 2H_2O\}_n$	1	25	>99	56
15.	JNU-402-NH2 (Zn)	1	80	>99	57
16.	JLU-MOF112 (Y)	2	120	99	58
17.	UiO-66@Schiff-Base-Cu(II)	0.16	80	91	59
18.	NUC-56a (In, Tm)	8	65	99	60
19.	SPUZ-1 (Zr)	0.5	60	99	61
20.	ZIF-90/TETA (Zn)	2	40	98.7	62
21.	Cu-1D	0.5	RT	>99	Our work

Now applying the optimized reaction condition, the substrate scope study for the Knoevenagel condensation reaction was investigated with a library of aromatic aldehydes. At first, the electron-withdrawing substituted benzaldehyde was employed in the reaction mixture and a positive effect on reaction kinetics was observed (Figure IV.4). The presence of NO_2 and CF_3 group in the para position of benzaldehyde gave appreciable yield of desired products **8b** and **8c** within the time interval of 25 min. However, with *p*-chlorobenzaldehyde as substrate, it required 1 h to deliver 95% of **8d**. The di-NO_2 substitution at para and ortho position did not change the progress of the reaction and gave quantitative (>99%) product **8e,** whereas the meta-substituted NO_2 substrate produced 97% of **8f** in 30 min respectively. With the appreciable yield of halogen derivatives, the reaction system can be considered to be tolerable with halogens.

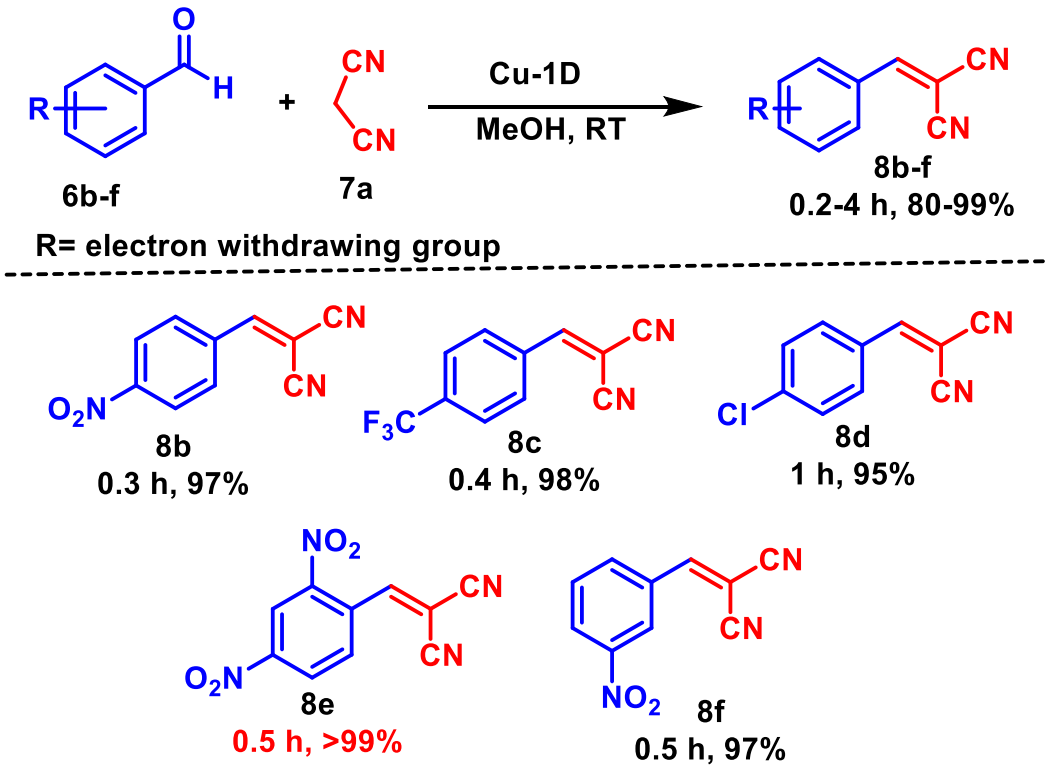

Figure IV.4: Substrate scope for Knoevenagel condensation reaction established with a derivative of benzaldehyde containing electron-withdrawing group.

The effect of electron-donating substituents was also explored (Figure IV.5) and a relatively higher time was required to deliver an appreciable yield of the desired product (**8g-j**) which may be due to lowering of electrophilicity in the carbonyl group of benzaldehyde by electron donating group.[63,64] The yield for *p*-CH_3 substituted product (**8g**) was found to be 85% in 3 h and 90% for *p*-OCH_3 (**8h**) in 4 h. However, disubstituted -OCH_3 on the meta position produced 98% of desired product **8i** in 1.5 h. This may be due to less pronounced inductive effect in the meta position than the para position. Similarly, the presence of the -OCH_3 group in the ortho position produced 80% of desired product **8j** within 2 h.

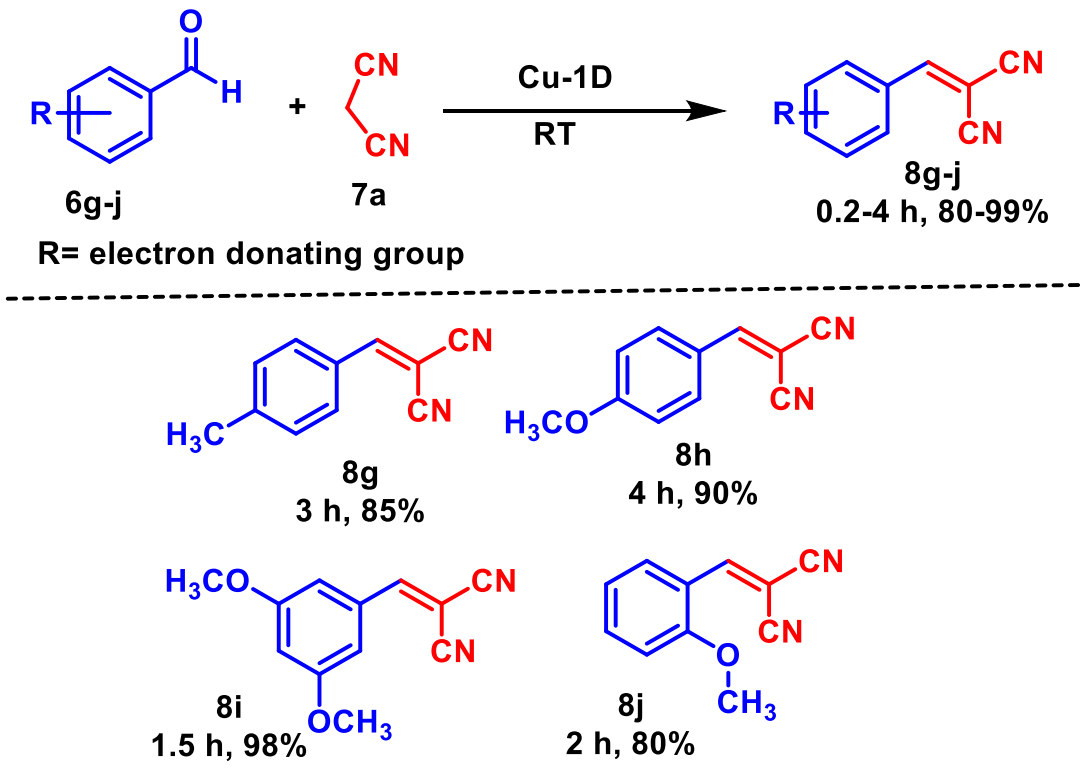

Figure IV.5: Substrate scope for Knoevenagel condensation reaction established with a derivative of benzaldehyde containing electron-donating group.

IV.2.4. Synthesis of novel malononitrile molecules

Our initial attempts for sequential tandem reaction *via the* introduction of malononitrile in the CDC reaction could not afford the desired product. However, when pure 2-{(1,4-dioxan-2-yl)oxy}benzaldehyde (**3a**) was reacted with malononitrile under optimized conditions, the reaction was completed in 1.2 h forming an off-white solid product (Scheme IV.7).

Scheme IV.7: Reaction scheme to obtain novel malononitrile derivatives.

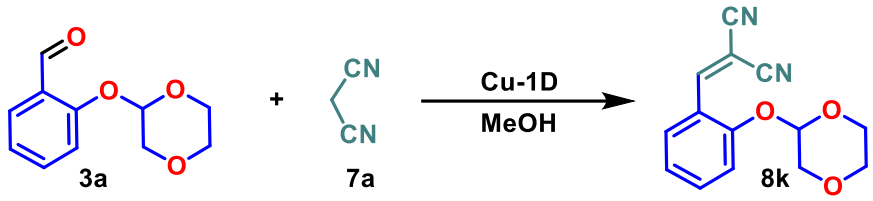

The product formed was recrystallized in MeOH and dried before NMR characterization. The ^{1}H and ^{13}CNMR as shown in figure IV.6 confirms the formation of 2-[2-{(1,4-dioxan-2-yl)oxy}benzylidene]malononitrile **(8k)** as desired product with a yield of 98%. The singlet at δ=8.36 ppm can be assigned to the β–hydrogen from malononitrile after the reaction. Two doublets at δ=8.20 ppm with coupling constant *J*= 8.0 Hz and δ=7.25 ppm with *J*= 8.5 Hz can be assigned to aromatic phenyl protons H2 & H5. The other aromatic phenyl protons H3 and H4 gives triplet and resonates at δ= 7.13 &7.56 ppm with *J* values of 7.7 & 8.1 Hz respectively. A multiplet at δ 4.06–4.00 was assigned to H6 protons from dioxane moiety whereas the multiplet for H7 can be observed at δ 3.64 ppm. Similarly, a doublet for two protons H8 at δ 3.92 (*J*=9.5 Hz) and a broad singlet (unresolved multiplet) for two protons H9 at δ 3.81 can be observed. Lastly, the singlet at δ 5.39 ppm for H10 is also observed which is the most acidic hydrogen of the dioxan fragment. The ^{13}C NMR conducted at 100 MHz, using $CDCl_3$ shows 14 peaks (Figure IV.6b). The ^{13}C peaks at *δ* 156.13, 154.47, 136.39,

128.66, 122.45, 120.79, 115.17, 114.29, 93.82, 81.95, 68.20, 65.92, 61.28 ppm can be well ascribed to the carbon present in the product **8k**.

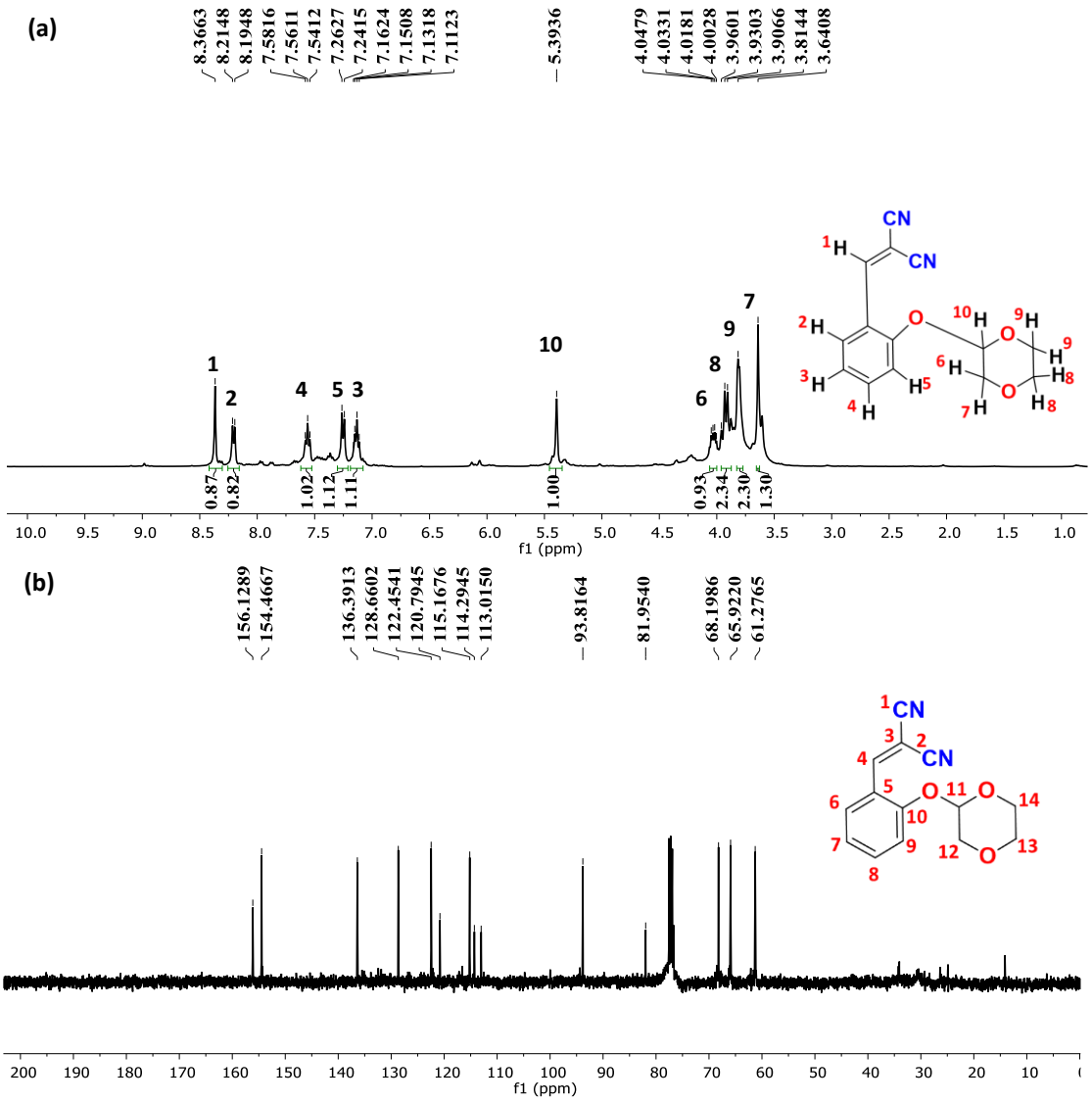

Figure IV.6: (a) ^{1}H and (b) ^{13}C-NMR recorded with $CDCl_3$ for novel malononitrile product **8k**.

IV.2.5. Mechanistic insights of Knoevenagel reaction:

The unsaturated Cu(II) metal centers in the Cu-MOF catalyst (tetracoordinate copper centers) act as Lewis acid sites that interact with the H−C=O functionality of benzaldehyde (figure IV.7). This interaction polarizes the functionality and enhances the electrophilicity of the corresponding carbon atom, thereby facilitating nucleophilic

attack by malononitrile, which acts as a nucleophile precursor. Additionally, the Lewis acid site interacts with the −CN moiety of malononitrile, increasing the acidity of the methylene functionality and enhancing its deprotonation. The basic sites in Cu-catalyst (O-carboxylate sites and *N*-methylimidazole in Cu-1D, Cu-SKU-3, Cu-SKU-4, and DMF in Cu-BDC) abstract H^+ from the $-CH_2-$ group, producing a nucleophile that attacks the H−C=O moiety of benzaldehyde, resulting in the formation of a C-C bond. The reaction then undergoes dehydration, resulting in the formation of the 2-benzylidenemalononitrile (**8a**) as a product.

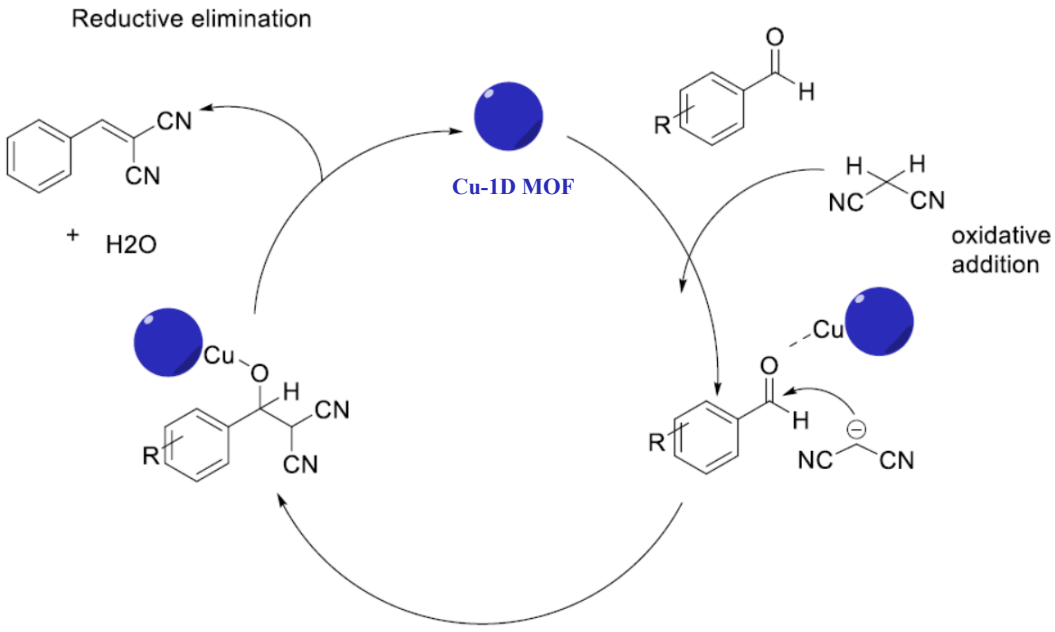

FigureIV.7: Proposed catalytic cycle for Cu-1D catalyzed Knoevenagel Reaction.

IV.2.6. Understanding the Role of CUS in CDC and Knoevenagel Reaction:

IV.2.6.1. Structural analysis of Cu-MOF catalyst:

The various Cu-based MOF such as HKUST-1 (Cu), Cu-BDC, Cu-MOF-74, Cu-SKU-3, and Cu-1D MOF catalysts were synthesized using the solvothermal techniques as

discussed in Chapter II (Section II.4.1-2). The synthesized Cu-MOFs were characterized using PXRD, FT-IR, TGA analysis, and BET-surface area techniques. To have a better understanding of the role of CUS towards coupling reaction, C-H activation, and Knoevenagel reaction these MOFs were chosen rationally. The chosen MOFs has copper as a central metal atom and similar kind of organic ligands. All the Cu-MOFs have the central metal atom Cu in +2 oxidation state, however, there is a notable difference in coordination number. The detailed structural analysis shows that HKUST-1 (Cu) has a Cu_2 dimer that forms paddle wheel type of secondary building units (SBU) with the coordination of 4-BTC^{3-} unit from six vertices and 2-H_2O molecules from an axial position. The coordination of BTC unit and H_2O molecules further directs the central metal atom to form a pseudo-octahedral geometry that has overall a hexa-coordination and as a result, accessible open metal sites or CUS are absent in as-synthesized HKUST-1 MOF (Figure IV.8a). However, the CUS in HKSUT-1 can be simply generated by removing the apical H_2O molecule from the as-synthesized HKUST-1 MOF at 120 °C under dynamic vacuum for 12 h (Figure IV.8b). This method of generating CUS is also referred as activation of MOF. The activation of HKUST-1 can be confirmed with bare eyes as the blue colour of as-synthesized HKUST-1 changes to turquoise blue after the removal of apical H_2O and the MOF now may be referred to as activated HKUST-1 (act. HKUST-1) Similarly, the Cu-BDC MOF is synthesized using BDC (BDC= benzene dicarboxylic acid) ligand and alike HKUST-1, it also possesses the Cu_2 dimer paddle wheel. The difference is in the coordination at the axial position where DMF molecule is coordinated to the Cu centre in Cu-BDC-MOF instead of H_2O. The Cu-BDC also has a hexa-coordination on central metal ion with an absence of accessible open metal sites (Figure IV.8c).

The Cu-SKU-3 MOF was synthesized using BTC and Mim (Mim= *N*-methylimidazole) ligand in 3:2 DMF: EtOH solvent at 120 ℃ for 24 h. The structural analysis of Cu-SKU-3 from SCXRD shows the coordination of the 3-BTC unit from an equatorial position and the 2-MeIM unit from an axial position forming a six-edged SBU. Further, the capping of central Cu-metal by two Mim from the axial position restricts the perpendicular growth of the polymeric framework thereby generating a 2D sheet-like structure where Cu-obtains a penta-coordinated environment and has one accessible open meta site (Figure IV.8d).

Lastly, by changing BTC with BDC ligand, Cu-1D MOF was synthesized using similar technique as that of Cu-SKU-3. The 2-BDC unit coordinates from an equatorial position and two methylimidazole units from an axial position thereby the growth of the polymeric framework towards the perpendicular axis is restricted and the MOF extends only in one dimension. The central copper metal has a tetra coordination (Figure IV.8e) and attains a square planar geometry. As a result, sufficient open metal sites or CUS are available in Cu-1D MOF in as-synthesized condition and thereby doesn't warrants prior activation. Furthermore, Cu-SKU-4 is isoreticular to Cu-1D MOF where the BDC unit is replaced by naphthalene dicarboxylic acid (NDC). Cu-SKU-4 also has a similar geometry (Figure IV.8f) as that of Cu-1D and has the availability of open metal sites for a substrate to bind and react during catalytic reactions. A detailed study of CDC and Knoevenagel reaction was done with six Cu-based MOFs among which each two has *hexa, penta,* and *tetra* coordination with zero, one, and two available CUS/open metal sites respectively. The detailed representation of all SBU of MOFs under study is showcased in figure IV.8a-f.

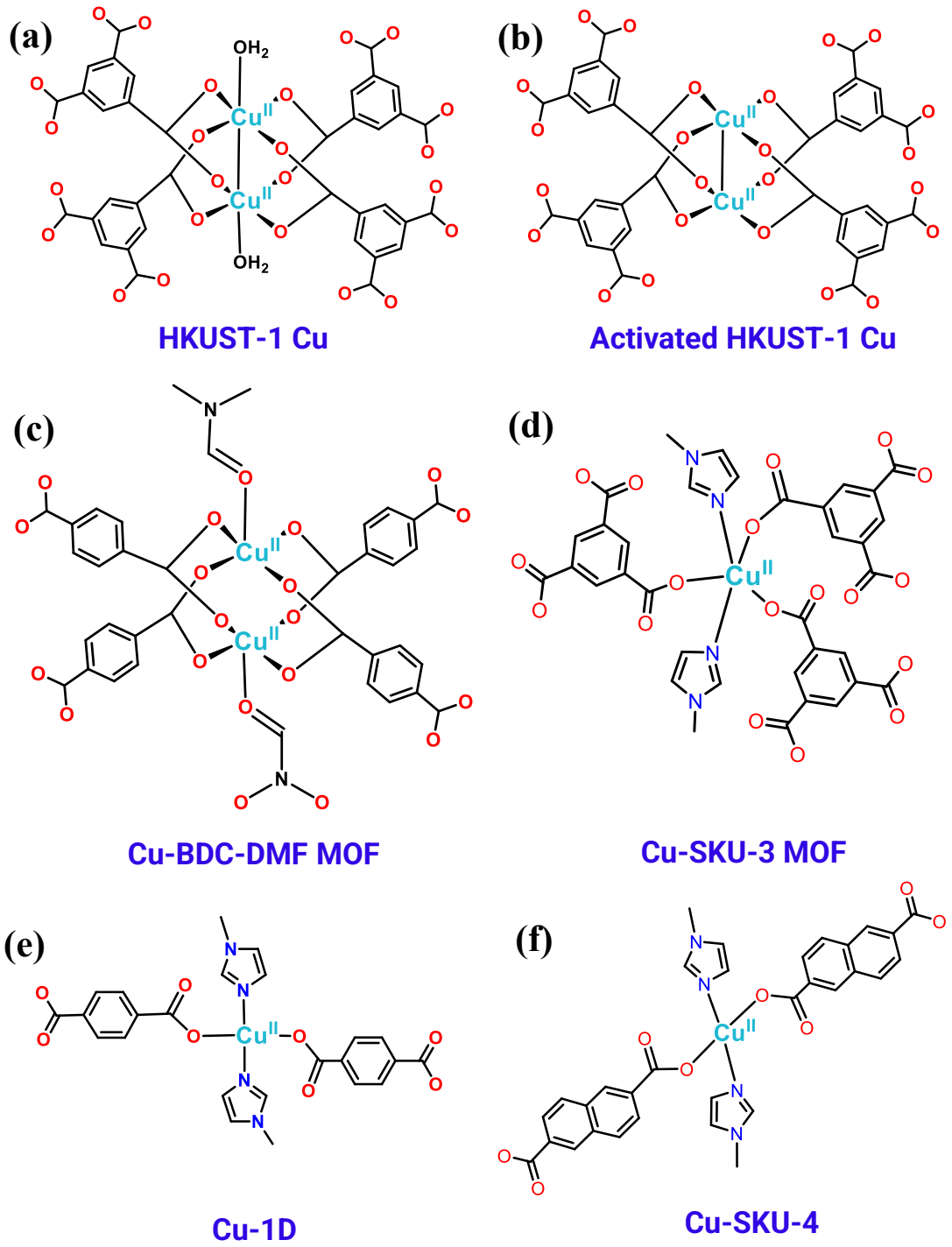

Figure IV.8: Structural representation of (a) HKUST-1 with hexa-coordination (b) activated HKUST-1 with penta-coordination (c) Cu-BDC with hexa-coordination (d) Cu-SKU-1 with penta-coordination and (d) Cu-1D with tetra-coordination. (f) Cu-SKU-4 with tetra coordination.

IV.2.6.2. Reaction analysis of various Cu-MOF catalysts:

The catalytic study of MOFs with structurally different Cu-MOFs were employed towards the CDC reaction and Knoevenagel reaction. For CDC reaction 2-hydroxybenzaldehyde (**1a**) was reacted with 1,4-dioxane (**2a**) to afford 2-((1,4-dioxan-2-yl)oxy)benzaldehyde (**3a**) as desired product. Similarly, for Knoevenagel reaction benzaldehyde (**6a**) was reacted with malononitrile (**7a**) to afford 2-benzylidenemalononitrile (**8a**). The HKUST-1(Cu) MOF when employed without any activation produced only 45% of desired product **3a** after 6 h (Table IV.5). On the other hand, Cu-BDC MOF produced 36% of **3a** within 6 h. The penta coordinated Cu-MOF such as activated HKUST-1 (Cu) and Cu-SKU-3 produced a good amount of **3a** with a yield of 75% and 98% in 6 and 1 h respectively. However, compared to these MOFs, Cu-1D with tetra coordination and sufficient open metal sites was found to form the desired product with good yield (95% of **3a**) within 0.5 h. To further confirm the efficiency of tetra coordinated Cu center the reaction was conducted with Cu-SKU-4 which is also isoreticular to Cu-1D MOF. The desired product was again found to form up to 95% in 0.75 h. These results therefore clearly indicate the importance of open metal sites on a catalyst to be an efficient towards CDC reaction. The higher time required for HKUST-1 (Cu) and Cu-BDC MOFs could be due to the unavailability of open meta sites. This was further understood from the observation made by Pitchumani *et al.* for Cu-BDC MOF during a homocoupling reaction. As Cu(BDC) MOF contains a Cu2 dimer with the BDC ligand coordinated in a bidentate bridging fashion and the DMF molecule in an axial fashion. The optimal time span for the homocoupling reaction using Cu(BDC)-MOF-62 as a catalyst was found to be 16 h with a 100 mg catalyst loading. During the reaction, the FT-IR spectrum of Cu(BDC) MOF showed the absence of DMF carbonyl stretching frequency at 1663 cm^{-1} and the presence of a

new peak around 3442 cm^{-1} that can be attributed to the B−OH stretching frequency of the substrate (phenylboronic acid). This confirms the substitution of weakly coordinated DMF to generate in situ CUS. Unlike previously reported MOFs system, Cu(II) centers in our synthesized MOFs such as Cu-1D, Cu-SKU-3, and Cu-SKU-4 forms a stable tetra and penta-coordinated frameworks and with readily available active sites makes the system free from in situ activation or deactivation processes and thereby efficiently catalyse CDC and Knoevenagel reaction.

Table IV.5: Comparison in the catalytic activity of Cu-1D with Cu-based MOFs under optimized reaction conditions.

(a) Cross-dehydrogenative Coupling Reaction

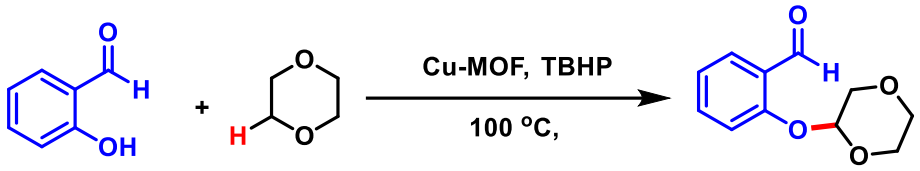

(b) Knoevenagel Condensation Reaction

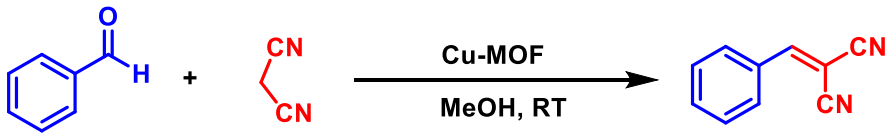

Sl. No	Cu-MOF Catalyst	(a) CDC Reaction		(b) Knoevenagel	
		Time (h)	Yield (%)	Time (h)	Yield (%)
1.	HKUST-1 (Cu) MOF	**6**	45	>12	55
2.	Cu-BDC MOF	6	36	0.83	95
3.	Activated HKUST-1 Cu MOF	6	75	1.5	90
4.	Cu-SKU-3	1	98	1.25	>99
5.	Cu-1D MOF	0.5	95	0.5	>99
6.	Cu-SKU-4 MOF	0.75	95	0.5	>99

IV.2.7. Recyclability and heterogeneous test of the catalyst after CDC and Knoevenagel reaction:

The catalytic activity of Cu-1D towards CDC reaction and Knoevenagel reaction was found to be superior to other prior reported Cu-based MOF such as Cu-BDC, HKUST-1, Cu(BPDC), $Cu_2(BPDC)_2(BPY)$ and homogeneous Cu (II) salts such as $CuCl_2$, $Cu(OAc)_2$ and $Cu(NO_3)$. Although the homogeneous Cu (II) salt has considerable conversion in both the CDC reaction and Knoevenagel reaction, but it could not be recovered and reused. In that context, the Cu-1D MOF has the advantage of both recyclability and reusability. The recyclability of Cu-1D MOF was therefore inspected for CDC reaction over four consecutive reaction cycles. The catalyst can still produce 80% and 98% of desired product **3a** and **8a** respectively in the 4^{th} run which indicates the recyclability and reusability of Cu-1D (Figure IV.9a). The catalyst after completion of the fourth cycle was recovered by simple centrifugation and washed with DCM followed by ethanol and dried at room temperature. The PXRD was performed for recycled catalyst where a comparative PXRD pattern of recovered catalyst matches with fresh Cu-1D confirming the crystallinity of Cu-1D even after the 4^{th} cycle (Figure IV.9b). However, it was observed that after 4^{th} run the PXRD peak intensity of Cu-1D is broadened compared to the sharp peak intensity of fresh Cu-1D which may be due to the reduction of catalyst size after several reaction runs.

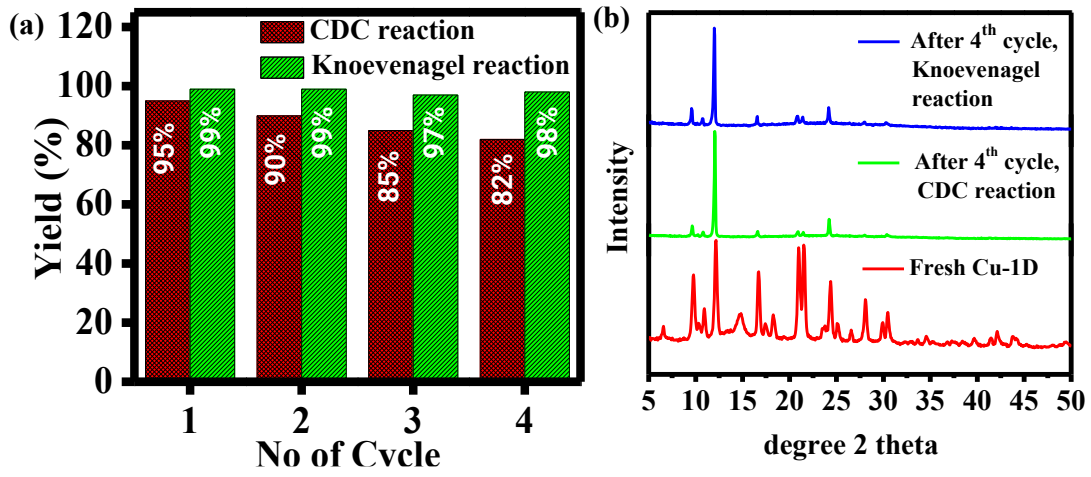

Figure IV.9: (a) Histogram for reusability of **Cu-1D** MOF in CDC and Knoevenagel reaction (b) PXRD comparison of simulated data with catalyst collected after four cycles of CDC and Knoevenagel reaction.

After the recyclability and reusability investigation, the heterogeneity test of the catalyst was performed using a simple hot filtration test. Two reaction vessel (vessel 1 and vessel 2) was set for the CDC reaction and Knoevenagel reaction that was allowed to run simultaneously under similar condition. After 5 min an aliquot was taken out from both vessels and the catalyst was removed by simple filtration from reaction vessel 1 and the supernatant was allowed to stir further. A yield of 43% was found for 10 minutes for the CDC reaction and 35% for the Knoevenagel reaction. (Figure IV.10a-b). The catalyst was removed by simple filtration and the supernatant was further stirred in the absence of **Cu-1D** catalyst for 0.5 h the yield of the reaction did not improve after the removal of the catalyst indicating the absence of any active Cu species which could leach from the solid catalyst.

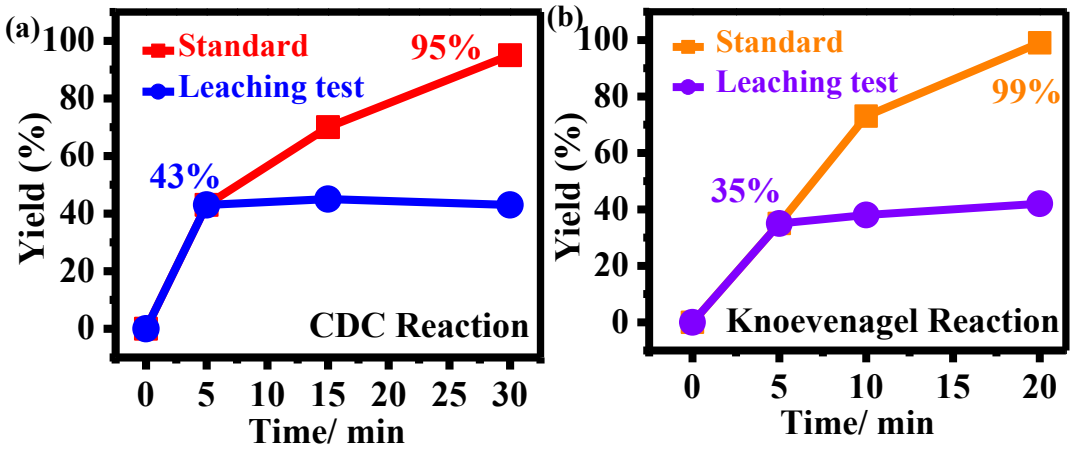

Figure IV.10: Line graph of leaching test for **Cu-1D** MOF in the reaction mixture of (a) CDC reaction and (b) Knoevenagel condensation reaction.

IV.3. Conclusion:

In summary, Cu-based MOF with various coordinating sites was directly applied in a variety of reactions such as CDC reaction forming C-O cross-coupling products via C-H activation and Knoevenagel reaction forming C=C bond. The MOFs such as HKUST-1 and Cu-BDC-DMF, were found less effective towards CDC reaction. Interestingly, Cu-BDC-DMF MOF with no CUS performed well in the Knoevenagel reaction showing the role of DMF as Bronsted base sites. However, the MOFs with pre-existing CUS are found efficient in both reactions under study and a good amount of product was obtained in a short span of time. Further with the use of aldehyde obtained from the CDC reaction, a seminal report for the formation of novel malonitrile derivatives was also reported. The leaching test performed for both reactions using Cu-1D MOF shows no evidence of the leaching of active copper species in the reaction mixture. Furthermore, the Cu-1D catalyst can be easily separated and reused again with high retention of activity up to the fourth cycle. The comparative study with different catalytic systems shows the importance of CUS in this reaction and Cu-MOF with pre-existing CUS fairs better than other copper-based catalytic systems.

IV.4. Experimental Section:

IV.4.1. Materials:

All Chemicals and solvents were used without purification unless otherwise mentioned. 2-hydroxybenzaldehyde, 4-methylsalicyldehyde, 4-methoxysalicyldehyde, 4-nitrosalicyldehyde, 4-chlorosalicyldehyde, 4-bromosalicyldehyde, and all deuterated solvents were purchased from Sigma Aldrich and used as obtained. Benzaldehyde, 4-nitrobenzaldehyde, 4-trifluoromethyl benzaldehyde, 4-chlorobenzaldehyde, 2,4-dinitrobenzaldehyde, nicotinaldehyde, 3-nitrobenzaldehyde, 2-bromobenzaldehyde, 4-methylbenzaldehyde, 4-methoxybenzaldehyde, 3,5-dimoethoxybenzaldehyde, 2-methoxybenzaldehyde, dioxane, acetonitrile, methanol, toluene, DCM, and DMF were bought from Merck. Malononitrile was brought from Spectra Chem. 2,2,6,6-Tetramethylpiperidin-1-yl)oxyl (TEMPO) was purchased from Avra and petroleum ether and ethyl acetate from Finar and was used as obtained.

IV.4.2. Physical methods:

^{1}H and ^{13}C-NMR were collected in $CDCl_3$ using Bruker ASCEND^{TM} 400. All the FTIR spectra were acquired using Bruker ALPHA E. The thin-layer chromatography (TLC) was used for monitoring the reaction progress using silica gel 60 F_{254} coated plates under a UV lamp. Further I_2 stain was also used to monitor the formation of the product.

IV.4.3. General Procedure for C-O coupling reaction (3a-f &5a-f):

In a 10 mL round bottom flask 2 hydroxybenzaldehyde (1.0 mmol) and 1,4-dioxane/DMF (2 mL, 20 mmol) were added followed by the addition of **Cu-MOF** catalyst (10 mol%), and 220 μL 70% TBHP was added (1.5 mmol). The reaction vessel was placed in a 100 °C preheated oil bath with constant stirring. The progress of the

reaction was monitored in TLC. For reaction with DMF, the reaction vessel was placed in a 120 °C preheated oil bath with constant stirring. After completion of the reaction, workup was initiated with EtOAc, and the organic part was dried over Na_2SO_4. It was then vacuum dried and pure product was obtained through column chromatography using 9:1 hexane/EtOAc eluent.

IV.4.4. General Procedure for Knoevenagel reaction forming C=C bond (8a-o):

In a 10 mL round bottom flask benzaldehyde (1.0 mmol) and malononitrile (1.1 mmol) were added followed by the addition of **Cu-MOF** catalyst (10 mol%) and 2 mL μL of MeOH/EtOH. The reaction vessel was stirred at room temperature and the progress was constantly monitored using TLC. After completion of the reaction, the solid products formed are recrystallized using MeOH and for liquid products, workup was initiated with EtOAc, and the organic part was dried over Na_2SO_4. It was then vacuum dried to obtain a pure product.

IV. 5. Spectral Data of products:

Synthesis of 2-((1,4-dioxan-2-yl)oxy)benzaldehyde (3a).

The separation of product **3a** was performed using column chromatography in 9:1 (Hexane/EtOAc). ^{1}H NMR (400 MHz, $CDCl_3$) δ 10.45 (s, 1H), 7.73 (d, *J* = 8.0 Hz, 1H), 7.43 (t, *J* = 6.9 Hz, 1H), 7.14 (d, *J* = 8.1 Hz, 1H), 7.06 – 6.89 (m, 1H), 5.32 (s, 1H), 4.11 – 3.93 (m, 1H), 3.92 – 3.74 (m, 2H), 3.75 – 3.61 (m, 2H), 3.53 (dd, *J* = 11.4, 3.7 Hz, 1H). ^{13}C NMR (100 MHz, $CDCl_3$) δ 189.45 , 158.99 , 135.77 , 127.93 , 125.43 , 121.98 , 115.41 , 93.59 , 68.24 , 65.90, 61.21.

Synthesis of 2-((1,4-dioxan-2-yl)oxy)-5-methylbenzaldehyde (3b).

The separation of product **3b** was performed using column chromatography in 9:1 (Hexane/EtOAc). ^{1}H NMR (400 MHz, $CDCl_3$) δ 10.51 (s, 1H), 7.63 (d, *J* = 1.9 Hz, 1H), 7.33 (dd, *J* = 8.5, 2.2 Hz, 1H), 7.12 (d, *J* = 8.5 Hz, 1H), 5.35 (t, *J* = 2.2 Hz, 1H), 4.10 (dt, *J* = 11.9, 5.8 Hz, 1H), 3.90 (t, *J* = 2.2 Hz, 2H), 3.82 – 3.75 (m, 2H), 3.62 (dt, *J* = 11.8, 3.0 Hz, 1H), 2.30 (s, 3H). ^{13}C NMR (100 MHz, $CDCl_3$) δ 189.78, 157.08 , 136.51 , 131.71 , 128.10 , 125.34 , 115.57 , 93.93 , 68.40 , 66.00 , 61.39 , 20.35

Synthesis of 2-((1,4-dioxan-2-yl)oxy)-5-methoxybenzaldehyde (3c)

The separation of product **3c** was performed using column chromatography in 9:1 (Hexane/EtOAc). ^{1}H NMR (400 MHz, $CDCl_3$) δ 10.41 (s, 1H), 7.87 (d, J=8.4 Hz, 1H), 6.75 (s, 1H), 6.65 (d, J=8.6 Hz, 1H), 5.39 (t, J=2.4 Hz, 1H), 4.19-4.13 (m, 1H), 3.96-3.93 (m, 2H), 3.89 (s, 3H), 3.96-3.83 (m, 2H), 3.69-3.63 (m, 1H) ppm. ^{13}C NMR (100 MHz, $CDCl_3$) δ 188.2, 161.0, 160.5, 130.1, 119.7, 107.6, 101.2, 94.0, 68.4, 66.0, 61.3, 55.7 ppm.

Synthesis of 2-((1,4-dioxan-2-yl)oxy)-5-nitrobenzaldehyde (3d)

The separation of product **3d** was performed using column chromatography in 8:2 (Hexane/EtOAc). 10.56 (s, 1H), 8.73 (d, J=2.8, 1H), 8.42 (dd, J=2.8, 9.2 Hz, 1H), 7.39 (d, J=9.2 Hz, 1H), 5.55 (t, J=2.0 Hz, 1H), 4.13-4.05 (m, 1H), 3.97-3.94 (m, 2H), 3.88-3.85 (m, 2H), 3.69-3.66 (m, 1H) ppm. ^{13}C NMR (100 MHz, $CDCl_3$) δ187.4, 162.8, 142.4, 130.3, 125.3, 124.3, 115.8, 94.0, 68.0, 65.9, 61.2 ppm.

Synthesis of 2-((1,4-dioxan-2-yl)oxy)-5-chlorobenzaldehyde (3e)

The separation of product **3e** was performed using column chromatography in 9:1 (Hexane/EtOAc). ^{1}H NMR (400 MHz, $CDCl_3$) δ 10.45 (s, 1H), 7.75 (d, J = 2.7 Hz, 1H), 7.44 (dd, J = 8.9, 2.8 Hz, 1H), 7.18 (d, J = 8.9 Hz, 1H), 5.35 (s, 1H), 4.07 (ddd, J = 12.1, 7.0, 5.4 Hz, 1H), 3.96 – 3.83 (m, 2H), 3.79 (dd, J = 7.3, 2.7 Hz, 2H), 3.61 (dt, J = 11.8, 2.9 Hz, 1H) ppm. ^{13}C NMR (101 MHz, $CDCl_3$) δ 188.22, 157.44, 135.27, 127.78, 127.68, 126.52, 117.19, 94.00, 68.23, 65.95, 61.29 ppm.

Synthesis of 2-((1,4-dioxan-2-yl)oxy)-5-bromobenzaldehyde (3f)

The separation of product **3f** was performed using column chromatography in 9:1 (Hexane/EtOAc).^{1}H NMR (400 MHz, $CDCl_3$) δ 10.48 (s, 1H), 7.96 (d, J = 2.7 Hz, 1H), 7.63 (dd, J = 8.9, 2.6 Hz, 1H), 7.16 (d, J = 8.9 Hz, 1H), 5.39 (t, J = 2.2 Hz, 1H), 4.11 (ddd, J = 12.1, 6.9, 5.7 Hz, 1H), 4.01 – 3.88 (m, 2H), 3.87 – 3.79 (m, 2H), 3.64 (dt, J = 11.8, 2.8 Hz, 1H) ppm. ^{13}C NMR (101 MHz, $CDCl_3$) δ 188.23, 157.91, 138.22, 130.82, 126.84, 117.48, 115.04, 93.88, 68.25, 65.98, 61.27 ppm.

Synthesis of 2-formylphenyl dimethylcarbamate (5a)

The separation of product **5a** was performed using column chromatography in 9:1 (Hexane/EtOAc). ^{1}H NMR (400 MHz, $CDCl_3$) δ 10.20 (s, 1H), 7.87 (d, J = 7.6 Hz, 1H), 7.61 (t, J = 7.7 Hz, 1H), 7.34 (t, J = 7.5 Hz, 1H), 7.24 (d, J = 8.2 Hz, 1H), 3.16 (s, 3H), 3.04 (s, 3H). ^{13}C NMR (101 MHz, Chloroform-*d*) δ 188.91, 154.21, 152.97, 135.21, 129.85, 128.42, 125.79, 123.6, 36.90, 36.61 ppm.

Synthesis of 2-formyl-4-methylphenyl dimethylcarbamate (5b)

The separation of product **5b** was performed using column chromatography in 9:1 (Hexane/EtOAc). ^{1}H NMR (400 MHz, $CDCl_3$) δ 10.13 (s, 1H), 7.63 (d, J = 2.2 Hz, 1H),

7.37 (dd, *J* = 8.3, 2.3 Hz, 1H), 7.09 (d, *J* = 8.3 Hz, 1H), 3.12 (s, 3H), 3.00 (s, 3H), 2.34 (s, 3H) ppm. ^{13}C NMR (101 MHz, Chloroform-*d*) δ 189.06, 154.47, 150.88, 135.91, 135.60, 129.87, 128.01, 123.43, 36.83, 36.54, 20.63 ppm.

Synthesis 4-chloro-2-formylphenyl dimethylcarbamate (5c)

The separation of product **5c** was performed using column chromatography in 9:1 (Hexane/EtOAc). ^{1}H NMR (400 MHz, $CDCl_3$) δ 10.13 (s, 1H), 7.82 (d, *J* = 2.7 Hz, 1H), 7.54 (dd, *J* = 8.8, 2.7 Hz, 1H), 7.21 (d, *J* = 8.7 Hz, 1H), 3.15 (s, 3H), 3.03 (s, 3H) ppm. ^{13}C NMR (101 MHz, Chloroform-*d*) δ 187.26, 153.70, 152.05, 137.76, 131.99, 129.68, 125.56, 118.97, 36.96, 36.62 ppm.

Synthesis of 4-bromo-2-formylphenyl dimethylcarbamate (5d)

The separation of product **5f** was performed using column chromatography in 9:1 (Hexane/EtOAc). ^{1}H NMR (400 MHz $CDCl_3$) δ 10.10 (s, 1H), 7.95 (d, *J* = 2.5 Hz, 1H), 7.67 (dd, *J* = 8.7, 2.6 Hz, 1H), 7.13 (d, *J* = 8.7 Hz, 1H), 3.14 (s, 3H), 3.02 (s, 3H) ppm. ^{13}C NMR (101 MHz, $CDCl_3$) δ 187.35, 153.79, 151.54, 134.84, 131.51, 129.37, 128.93, 125.24, 36.96, 36.61 ppm.

Synthesis of 2-benzylidenemalononitrile (8a)

After completion of the reaction, the product **8a** was recrystallized on MeOH. The crystals formed were washed with cold MeOH and dried before NMR characterization. ^{1}H NMR (400 MHz, $CDCl_3$) δ 7.85 (d, J = 8.0 Hz, 2H), 7.74 (s, 1H), 7.59 (t, J = 7.5 Hz, 1H), 7.50 (t, J = 7.8 Hz, 2H).; ^{13}C NMR (100 MHz, CDCl3); δ = 160.00, 134.73, 130.98, 130.80, 129.65, 113.80, 112.64, 82.90.

Synthesis of 2-(4-nitrobenzylidene)malononitrile (8b)

After completion of the reaction, the product **8b** was recrystallized on MeOH. The crystals formed were washed with cold MeOH and dried before NMR characterization. ^{1}H NMR (400 MHz, $CDCl_3$) 8.26 (d, J = 7.6 Hz, 2H), 7.91 (s, 1H), 7.47 (d, J = 7.4 Hz, 2H). ^{13}C NMR (100 MHz, CDCl3)δ 157.60 , 145.81 , 137.00 , 131.70 , 124.40 , 114.16, 113.33 , 80.93.

Synthesis of 2-(4-(trifluoromethyl)benzylidene)malononitrile (8c)

After completion of the reaction, the product **8c** was recrystallized on MeOH. The crystals formed were washed with cold MeOH and dried before NMR characterization. ^{1}H NMR (400 MHz, $CDCl_3$) δ 8.04 (d, J = 8.1 Hz, 2H), 7.87 (s, 1H), 7.83 (d, J = 8.3 Hz, 2H). ^{13}C NMR (100 MHz, $CDCl_3$) δ 158.06, 130.72, 126.60, 126.56.

Synthesis of 2-(4-chlorobenzylidene)malononitrile (8d)

After completion of the reaction, the product **8d** was recrystallized on MeOH. The crystals formed were washed with cold MeOH and dried before NMR characterization. ^{1}H NMR (400 MHz, $CDCl_3$) δ 7.88 (d, J = 8.4 Hz, 2H), 7.76 (s, 1H), 7.54 (d, J = 8.6 Hz, 2H). ^{13}C NMR (100 MHz, $CDCl_3$) δ 158.27, 141.17, 131.83, 130.08, 129.27, 113.42, 83.38.

Synthesis of 2-(2,4-dinitrobenzylidene)malononitrile (8e)

After completion of the reaction, the product **8e** was recrystallized on MeOH. The crystals formed were washed with cold MeOH and dried before NMR characterization. ^{1}H NMR (400 MHz, $CDCl_3$) δ 9.16 (d, *J* = 2.2 Hz, 1H), 8.70 (dd, *J* = 8.5, 2.3 Hz, 1H), 8.46 (s, 1H), 8.02 (d, *J* = 8.5 Hz, 1H). ^{13}C NMR (100 MHz, $CDCl_3$) 156.11, 149.92, 132.12, 131.83, 129.05, 121.24, 111.41, 110.25, 91.11.

Synthesis of 2-(3-nitrobenzylidene) malononitrile (8f)

After completion of the reaction, the product **8f** was recrystallized on MeOH. The crystals formed were washed with cold MeOH and dried before NMR characterization.^{1}H NMR (400 MHz, $CDCl_3$) δ 8.69 (s, 1H), 8.49 (d, J = 8.2 Hz, 1H), 8.34 (s, 1H), 7.94 (s, 1H), 7.82 (d, J = 8.1 Hz, 1H). ^{13}C NMR (100 MHz, $CDCl_3$) δ 157.07, 148.68, 134.89, 132.03, 131.00, 128.22, 125.52, 112.68, 111.66, 86.75.

Synthesis of 2-(4-methylbenzylidene)malononitrile (8g)

After completion of the reaction, the product **8g** was recrystallized on MeOH. The crystals formed were washed with cold MeOH and dried before NMR characterization. ^{1}H NMR (400 MHz, $CDCl_3$) δ 7.83 (d, J = 8.2 Hz, 2H), 7.74 (s, 1H), 7.36 (d, J = 8.0 Hz, 2H), 2.48 (s, 3H). ^{13}C NMR (100 MHz, $CDCl_3$) δ 159.74, 146.36, 130.91, 130.37, 128.48, 114.00, 112.8, 81.26, 22.01.

Synthesis of 2-(4-methoxybenzylidene)malononitrile (8h)

After completion of the reaction, the product **8h** was recrystallized on MeOH. The crystals formed were washed with cold MeOH and dried before NMR characterization. ^{1}H NMR (400 MHz, $CDCl_3$) δ 7.94 (d, *J* = 8.9 Hz, 2H), 7.68 (s, 1H), 7.04 (d, *J* = 8.9 Hz, 2H), 3.94 (s, 3H). ^{13}C NMR (100 MHz, $CDCl_3$) δ 158.85, 133.45, 124.04, 115.15, 114.42, 113.34, 78.58, 55.81.

Synthesis of 2-(3,5-dimethoxybenzylidene)malononitrile (8i)

After completion of the reaction, product **8j** was recrystallized on MeOH. The crystals formed were washed with cold MeOH and dried before NMR characterization. ^{1}H NMR (400 MHz, $CDCl_3$) δ 7.70 (s, 1H), 7.04 (s, 2H), 3.85 (s, 6H), ppm. ^{13}C NMR (101 MHz, $CDCl_3$) δ 161.26, 160.09, 132.37, 113.66, 112.64, 108.26, 107.19, 83.07, 55.68 ppm.

Synthesis of 2-(2-methoxybenzylidene) malononitrile (8j)

After completion of the reaction, the product **8k** was recrystallized on MeOH. The crystals formed were washed with cold MeOH and dried before NMR characterization.^{1}H NMR (400 MHz, $CDCl_3$) δ 8.31 (s, 1H), 8.19 (d, J = 7.8 Hz, 1H), 7.61 (t, J = 1.3 Hz, 1H), 7.09 (t, J = 7.7 Hz, 1H), 7.01 (d, J = 8.4 Hz, 1H), 3.95 (s, 3H). ^{13}C NMR (100 MHz, $CDCl_3$) δ 158.98, 154.48, 136.54, 128.86, 121.21, 120.21, 114.34, 113.02, 111.57, 55.98.

IV.6. Spectral data of some noted compounds:

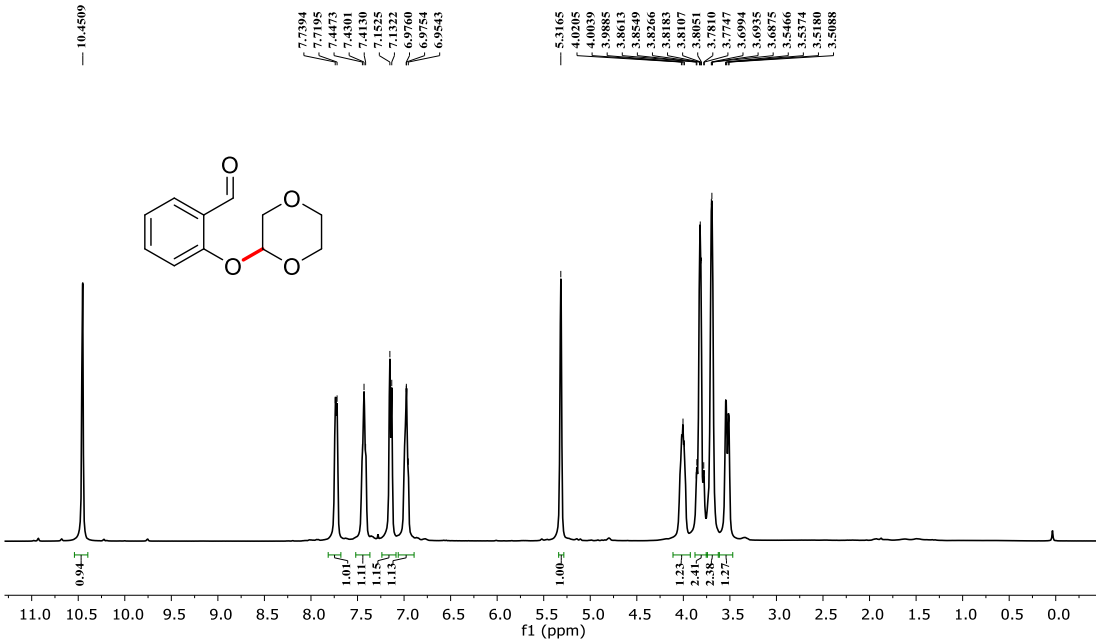

Figure IV.11: ^{1}H-NMR of **3a** in $CDCl_3$

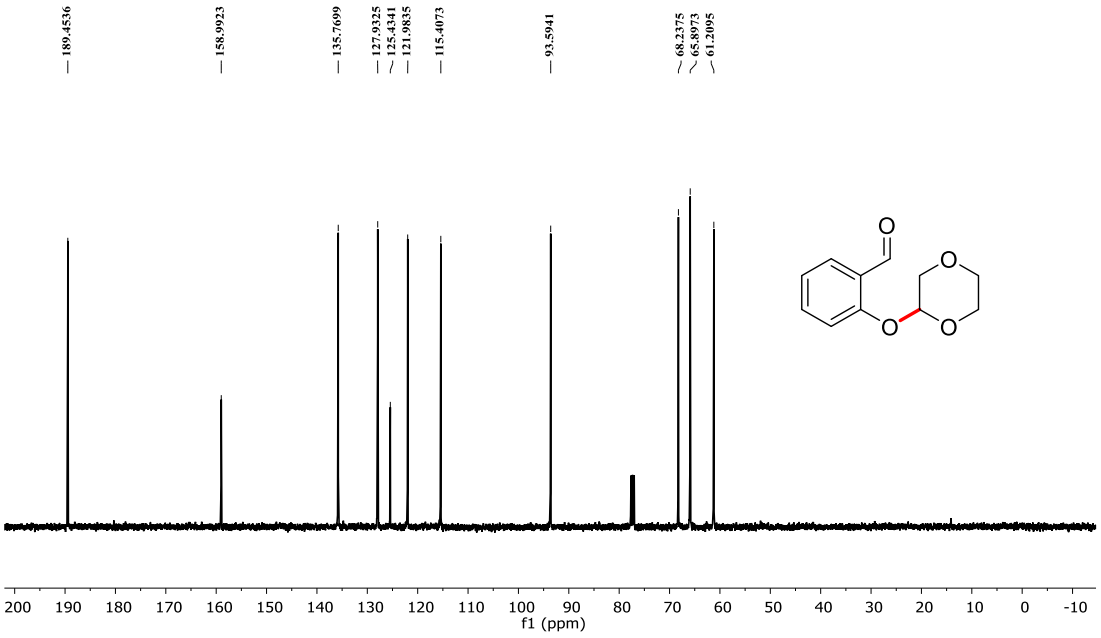

Figure IV.12: ^{13}C-NMR of **3a** in $CDCl_3$

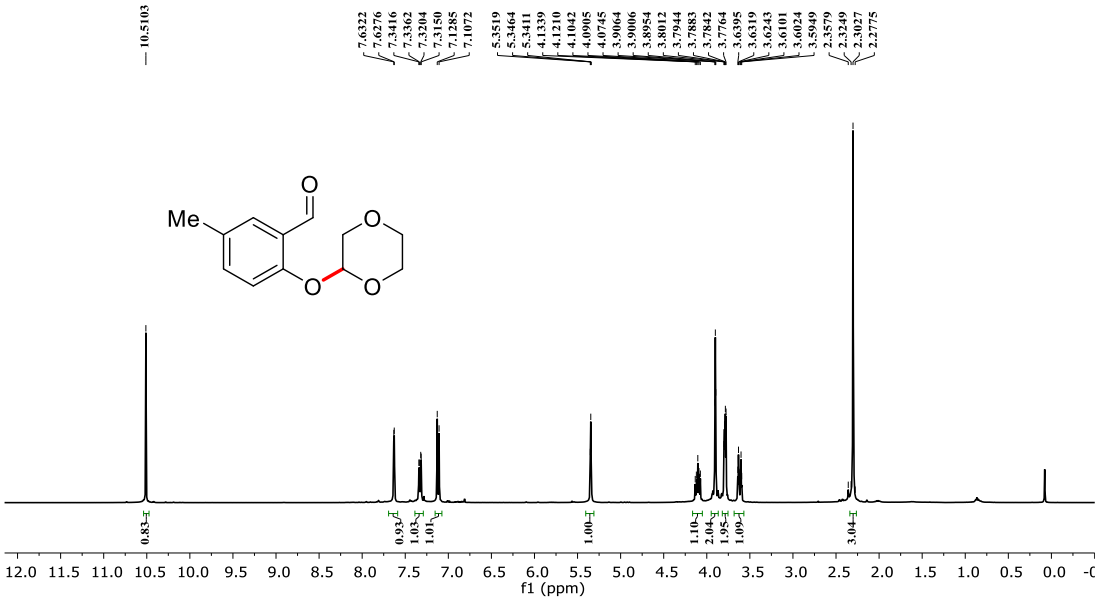

Figure IV.13: ^{1}H-NMR of **3b** in $CDCl_3$

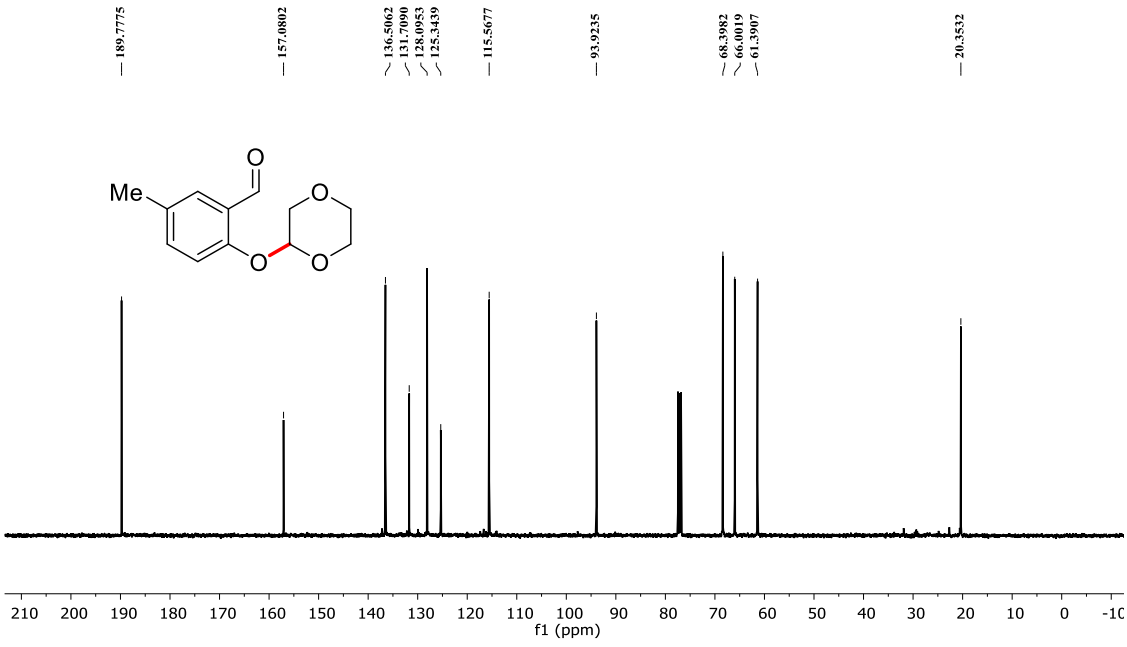

Figure IV.14: ^{13}C-NMR of **3b** in $CDCl_3$

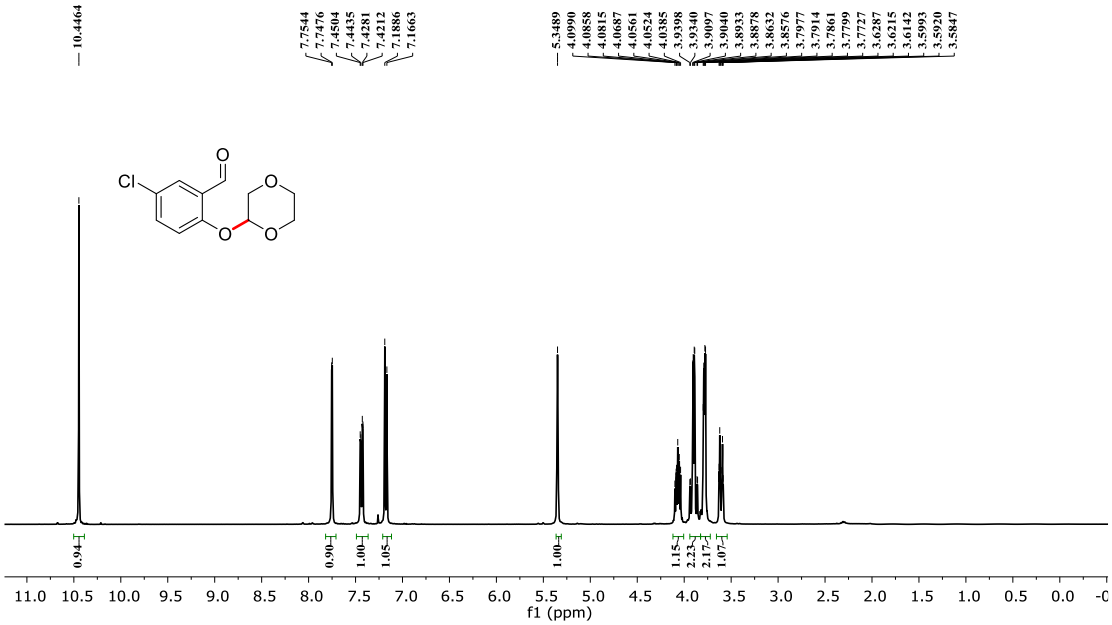

Figure IV.15: ^{1}H-NMR of **3e** in $CDCl_3$

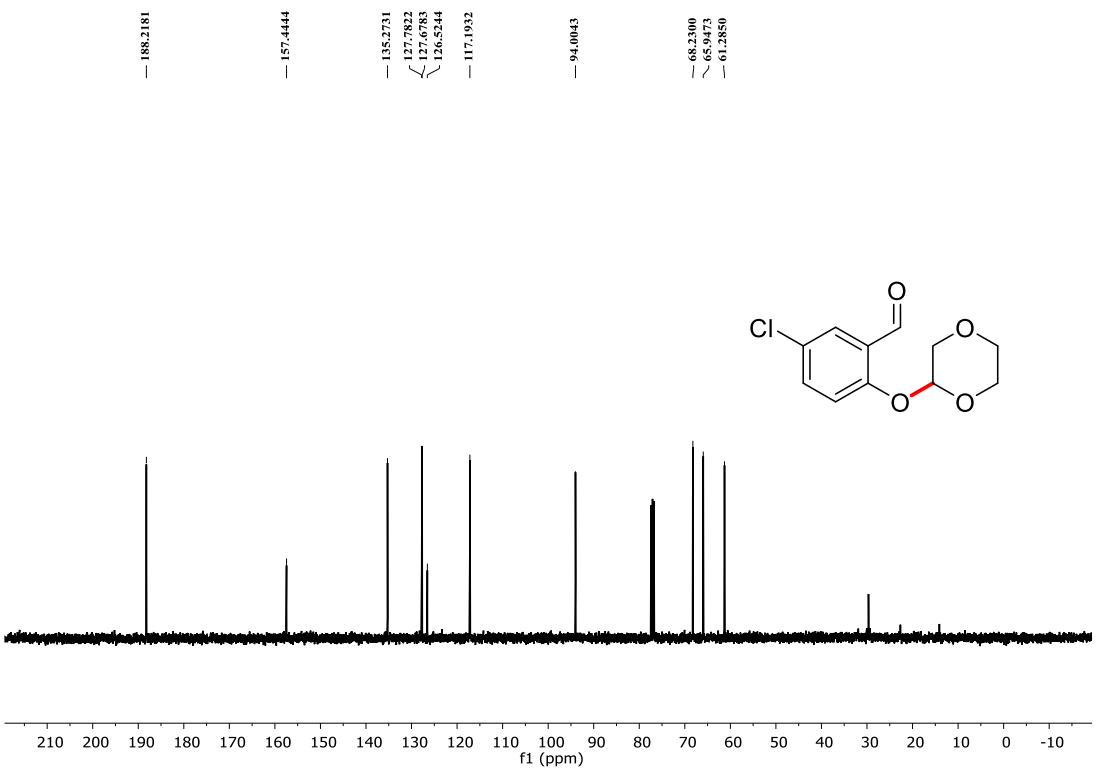

Figure IV.16: ^{13}C-NMR of **3e** in $CDCl_3$

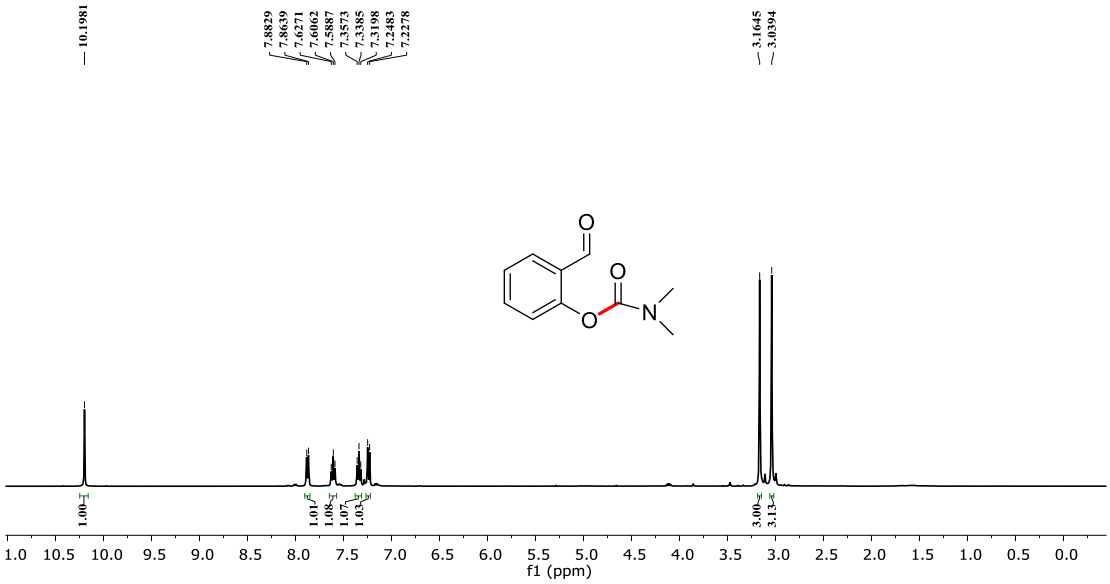

Figure IV.17: ^{1}H-NMR of **5a** in $CDCl_3$

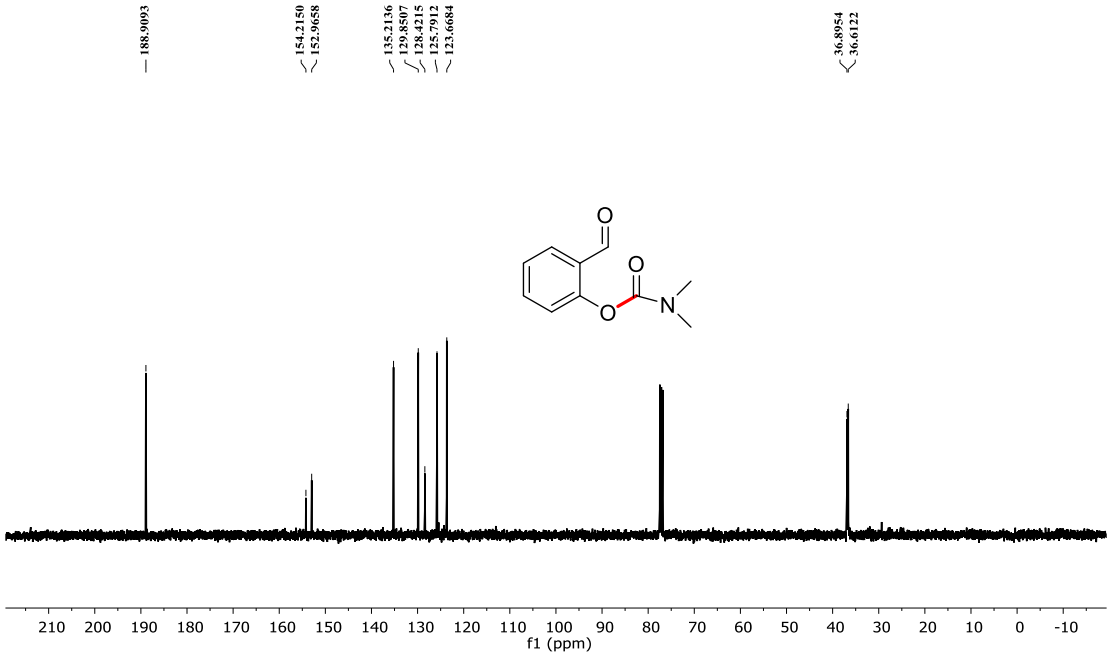

Figure IV.18: ^{13}C-NMR of **5a** in $CDCl_3$

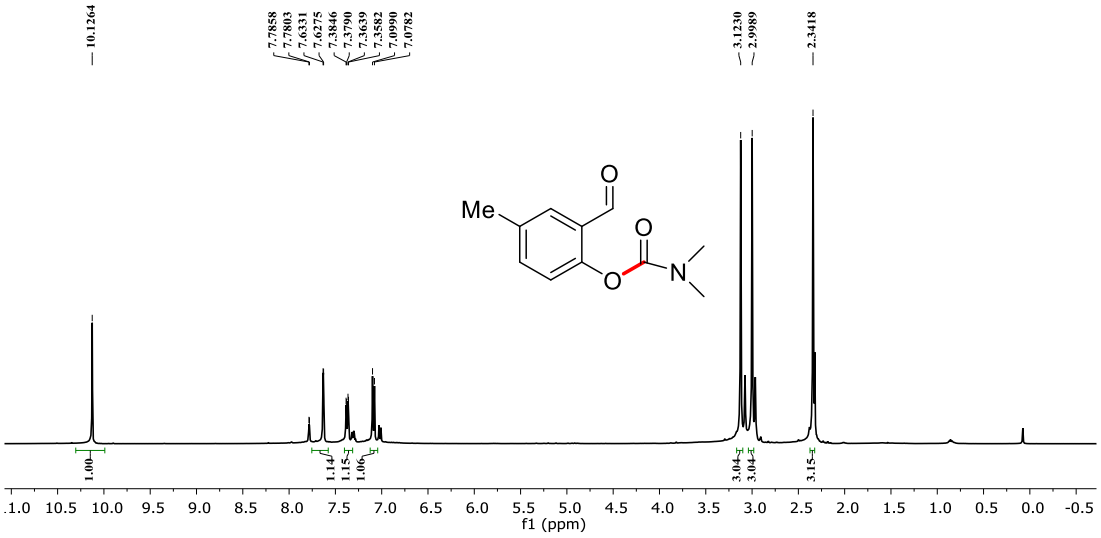

Figure IV.19: ^{1}H-NMR of **5b** in $CDCl_3$

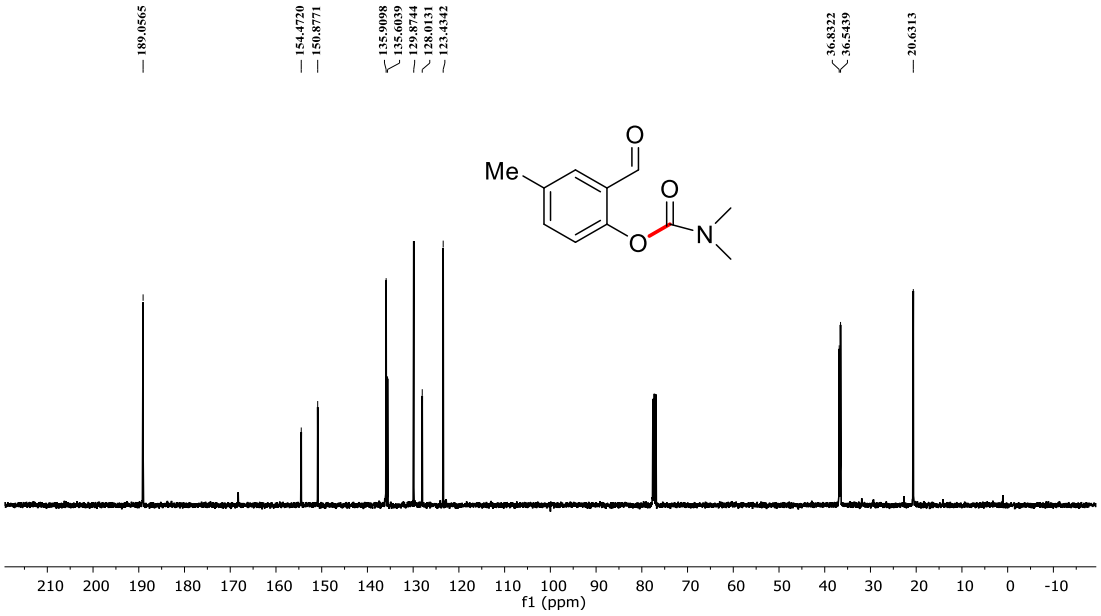

Figure IV.20: ^{13}C-NMR of **5b** in $CDCl_3$

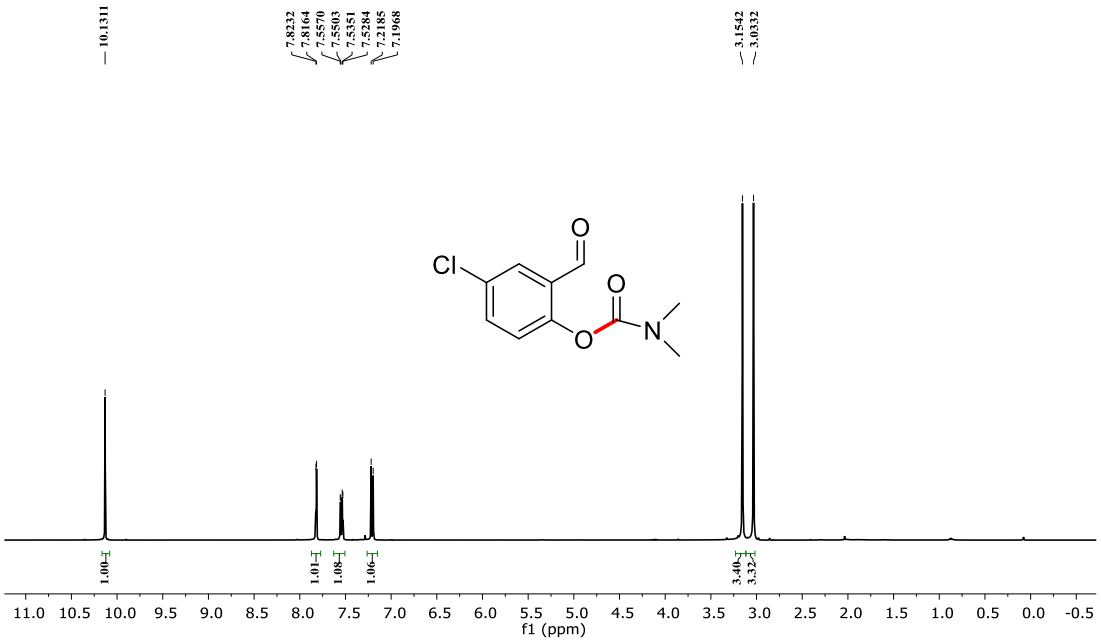

Figure IV.21: ^{1}H-NMR of **5c** in $CDCl_3$

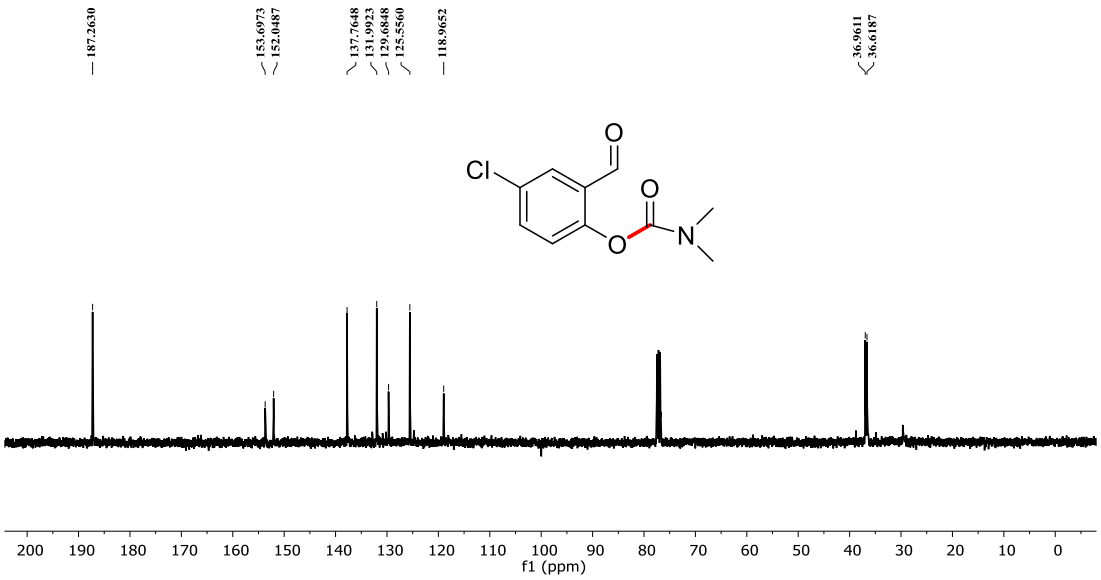

Figure IV.22: ^{13}C-NMR of **5c** in $CDCl_3$

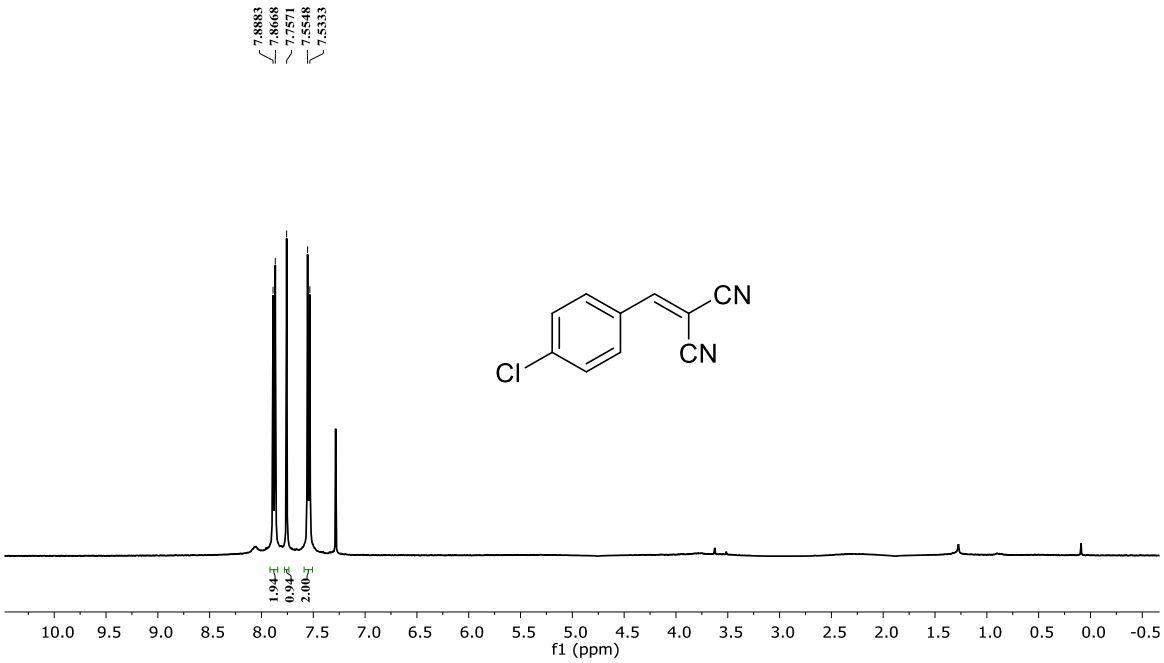

Figure IV.23: ^{1}H-NMR of **8d** in $CDCl_3$

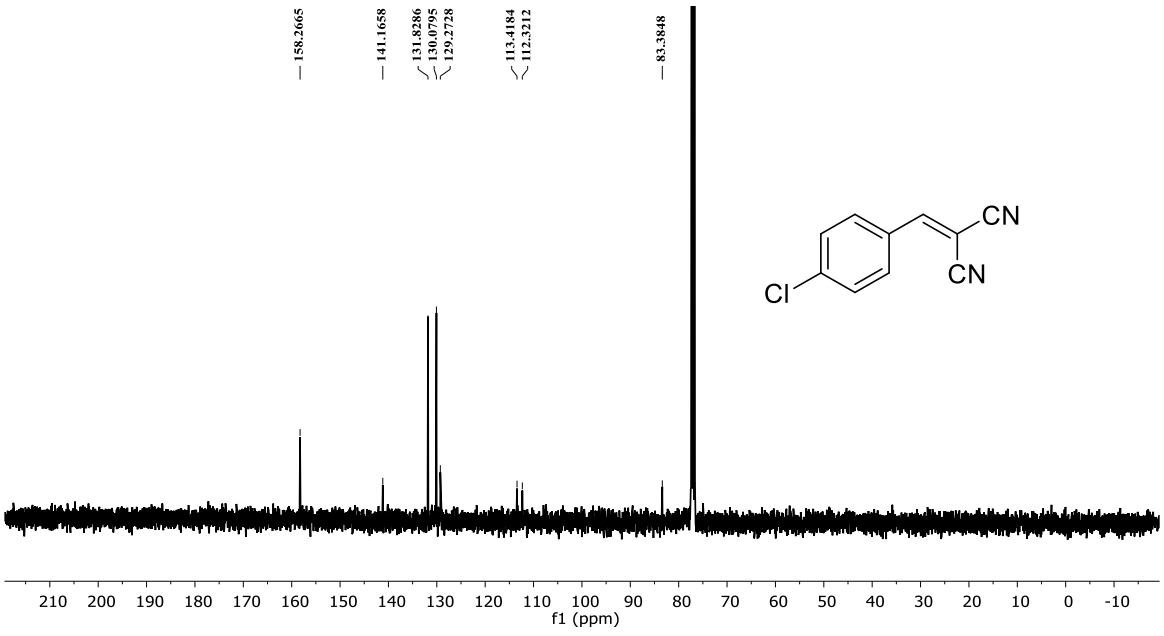

Figure IV.24: ^{13}C-NMR of **8d** in $CDCl_3$

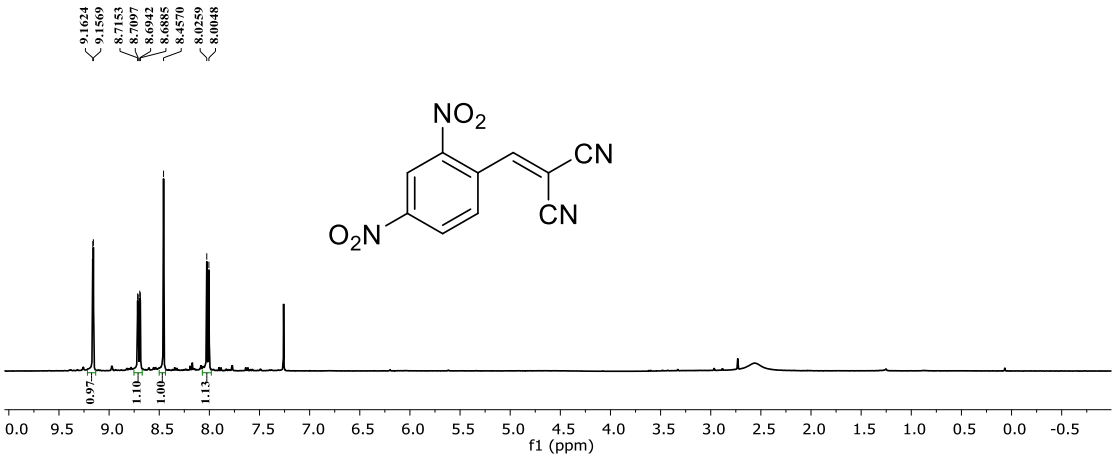

Figure IV.25: ^{1}H-NMR of **8e** in $CDCl_3$

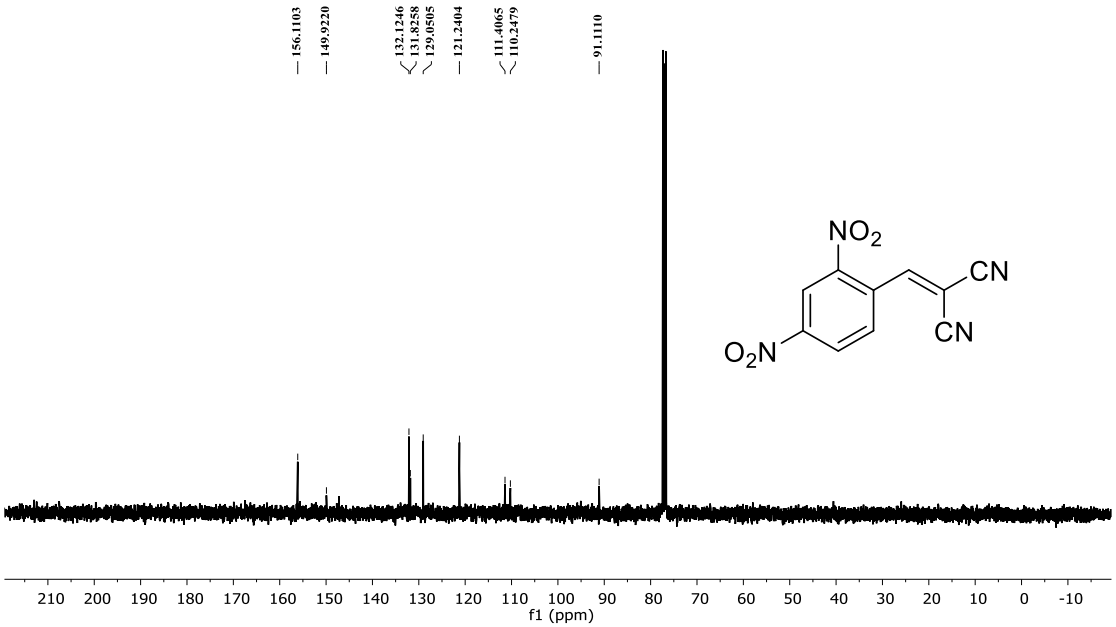

Figure IV.26: ^{1}H-NMR of **8e** in $CDCl_3$

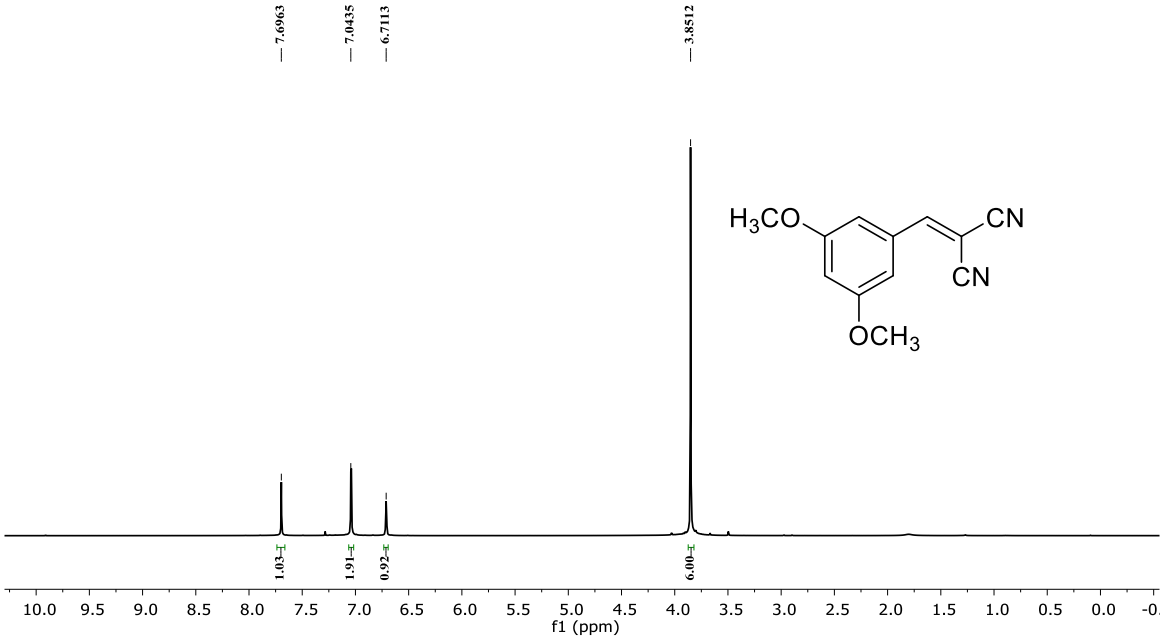

Figure IV.27: ^{1}H-NMR of **8j** in $CDCl_3$

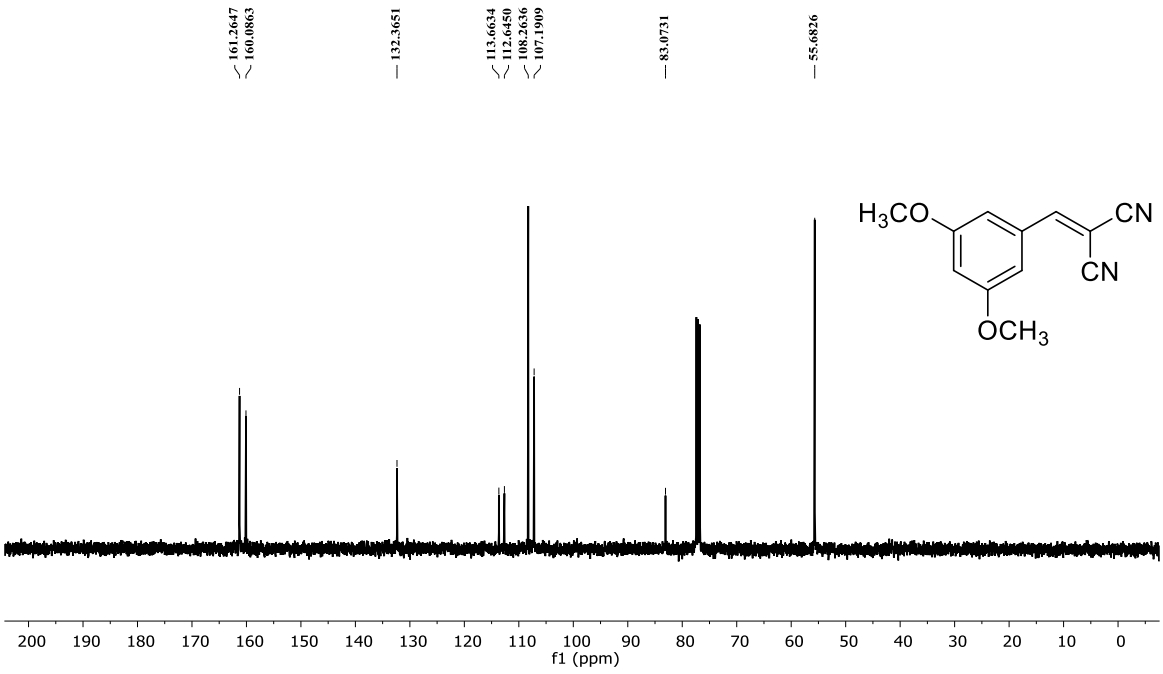

Figure IV.28: ^{13}C-NMR of **8j** in $CDCl_3$

IV.7. Reference:

Formation One Century After the Discovery of the Ullmann Reaction. *Chem. Rev.* **2002**, *102*, 1359–1469.

(2) Li, Z.; Li, C. J. Highly Efficient Copper-Catalyzed Nitro-Mannich Type Reaction: Cross-Dehydrogenative-Coupling between sp^3 C-H Bond and sp^3 C-H Bond. *J. Am. Chem. Soc.* **2005**, *127*, 3672–3673.

(3) Faisca Phillips, A. M.; Pombeiro, A. J. L. Recent Developments in Transition Metal-Catalyzed Cross-Dehydrogenative Coupling Reactions of Ethers and Thioethers. *ChemCatChem* **2018**, *10*, 3354–3383.

(4) Gong, H.; Zeng, H.; Zhou, F.; Li, C.-J. Rhodium(I)-Catalyzed Regiospecific Dimerization of Aromatic Acids: TwoDirect C-H Bond Activations in Water. *Angew. Chemie Int. Ed.* **2015**, *54*, 5718–5721.

(5) Huang, C. Y.; Kang, H.; Li, J.; Li, C. J. En Route to Intermolecular Cross-Dehydrogenative Coupling Reactions. *J. Org. Chem.* **2019**, *84*, 12705–12721.

(6) Phan, N. T. S.; Vu, P. H. L.; Nguyen, T. T. Expanding Applications of Copper-Based Metal-Organic Frameworks in Catalysis: Oxidative C-O Coupling by Direct C-H Activation of Ethers over $Cu_2(BPDC)_2(BPY)$ as an Efficient Heterogeneous Catalyst. *J. Catal.* **2013**, *306*, 38–46.

(7) Luz, I.; Corma, A.; Llabrés I Xamena, F. X. Cu-MOFs as Active, Selective and Reusable Catalysts for Oxidative C-O Bond Coupling Reactions by Direct C-H Activation of Formamides, Aldehydes, and Ethers. *Catal. Sci. Technol.* **2014**, *4*, 1829–1836.

(8) Sharma, V.; De, D.; Bharadwaj, P. K. A Multifunctional Metal-Organic Framework for Oxidative C-O Coupling Involving Direct C-H Activation and Synthesis of Quinolines. *Inorg. Chem.* **2018**, *57*, 8195–8199.

(9) Appaturi, J. N.; Ratti, R.; Phoon, B. L.; Batagarawa, S. M.; Din, I. U.; Selvaraj, M.; Ramalingam, R. J. A Review of the Recent Progress on Heterogeneous Catalysts for Knoevenagel Condensation. *Dalt. Trans.* **2021**, *50*, 4445–4469.

(10) Wang, D.; Wang, B.; Ding, Y.; Wu, H.; Wu, P. A Novel Acid-Base Bifunctional Catalyst (ZSM-5@$Mg_3Si_4O_9(OH)_4$) with Core/Shell Hierarchical Structure and Superior Activities in Tandem Reactions. *Chem. Commun.* **2016**, *52*, 12817–12820.

(11) Margelefsky, E. L.; Zeidan, R. K.; Davis, M. E. Cooperative Catalysis by Silica-Supported Organic Functional Groups. *Chem. Soc. Rev.* **2008**, *37*, 1118–1126.

(12) Liu, S.; Chen, H.; Fan, L.; Zhang, X. Highly Robust {In_2}-Organic Framework for Efficiently Catalyzing CO_2 Cycloaddition and Knoevenagel Condensation. *Inorg. Chem.* **2023**, *62*, 3562–3572.

(13) Seal, N.; Karmakar, A.; Kundu, S.; Neogi, S. Undulated Ni(II)-Framework with In Situ-Grafted Open-Metal and Basic Sites for High-Performance Electrochemical Water Oxidation and Flexible Composite-Driven Size-Exclusive Autotandem Catalysis. *ACS Sustain. Chem. Eng.* **2023**, *11*, 979–993.

(14) Tuci, G.; Luconi, L.; Rossin, A.; Berretti, E.; Ba, H.; Innocenti, M.; Yakhvarov, D.; Caporali, S.; Pham-Huu, C.; Giambastiani, G. Aziridine-Functionalized Multiwalled Carbon Nanotubes: Robust and Versatile Catalysts for the Oxygen Reduction Reaction and Knoevenagel Condensation. *ACS Appl. Mater.*

Interfaces **2016**, *8*, 30099–30106.

(15) Karmakar, B.; Chowdhury, B.; Banerji, J. Mesoporous Titanosilicate Ti-TUD-1 Catalyzed Knoevenagel Reaction: An Efficient Green Synthesis of Trisubstituted Electrophilic Olefins. *Catal. Commun.* **2010**, *11*, 601–605.

(16) Miao, Z.; Luan, Y.; Qi, C.; Ramella, D. The Synthesis of a Bifunctional Copper Metal-Organic Framework and Its Application in the Aerobic Oxidation/Knoevenagel Condensation Sequential Reaction. *Dalt. Trans.* **2016**, *45*, 13917–13924.

(17) García-Martínez, J.; Johnson, M.; Valla, J.; Li, K.; Ying, J. Y. Mesostructured Zeolite y - High Hydrothermal Stability and Superior FCC Catalytic Performance. *Catal. Sci. Technol.* **2012**, *2*, 987–994.

(18) Sharma, D.; Rasaily, S.; Pradhan, S.; Baruah, K.; Tamang, S.; Pariyar, A. HKUST-1 Metal-Organic Framework as an Efficient Dual-Function Catalyst: Aziridination and One-Pot Ring-Opening Transformation for Formation of β-Aryl Sulfonamides with C-C, C-N, C-S, and C-O Bonds. *Inorg. Chem.* **2021**, *60*, 7794–7802.

(19) Barve, B. D.; Wu, Y. C.; El-Shazly, M.; Korinek, M.; Cheng, Y. Bin; Wang, J. J.; Chang, F. R. Copper-Catalyzed Selective C-O Bond Formation by Oxidative α-C(Sp3)-H/O-H Coupling between Ethers and Salicylaldehydes. *Tetrahedron* **2015**, *71*, 2290–2297.

(20) Kumar, G. S.; Pieber, B.; Reddy, K. R.; Kappe, C. O. Copper-Catalyzed C-O Bond Formation by Direct a-C H Bond Activation of Ethers in Batch and Continuous Flow Formats. *Chem. - A Eur. J.* **2012**, *18*, 6124–6128.

(21) Bou Chedid, R.; Brümmer, M.; Wibbeling, B.; Fröhlich, R.; Hoppe, D. Stereo- and Regiochemical Divergence in the Substitution of a Lithiated Alk-1-En-3-Yn-2-Yl Carbamate: Synthesis of Highly Enantioenriched Vinylallenes or Alk-3-En-5-Yn-1-Ols. *Angew. Chemie - Int. Ed.* **2007**, *46*, 3131–3134.

(22) Dangerfield, E. M.; Timmer, M. S. M.; Stocker, B. L. Total Synthesis without Protecting Groups: Pyrrolidines and Cyclic Carbamates. *Org. Lett.* **2009**, *11*, 535–538.

(23) Fu, L.; Liu, X.; Ling, C.; Cheng, J.; Guo, X.; He, H.; Ding, S.; Yang, Y. Design, Synthesis, and Structure-Activity Relationship Studies of Conformationally Restricted Mutilin 14-Carbamates. *Bioorganic Med. Chem. Lett.* **2012**, *22*, 814–819.

(24) Ram, S.; Wise, D. S.; Wotring, L. L.; McCall, J. W.; Townsend, L. B. Synthesis and Biological Activity of Certain Alkyl 5-(Alkoxycarbonyl)-1H-Benzimidazole-2-Carbamates and Related Derivatives: A New Class of Potential Antineoplastic and Antifilarial Agents. *J. Med. Chem.* **1992**, *35*, 539–547.

(25) Pomeranz, Y.; Robbins, G. S. Amino Acid Composition of Buckwheat. *J. Agric. Food Chem.* **1972**, *20*, 270–274.

(26) Niphakis, M. J.; Johnson, D. S.; Ballard, T. E.; Sti, C.; Cravatt, B. F. O-Hydroxyacetamide Carbamates as a Highly Potent and Selective Class of Endocannabinoid Hydrolase Inhibitors. *ACS Chem. Neurosci.* **2012**, *3*, 418–426.

(27) Majer, P.; Randad, S. R. A Safe and Efficient Method for Preparation of *N, N'*-Unsymmetrically Disubstituted Ureas Utilizing Triphosgene. *J. Org. Chem.* **1994**, *59*, 1937–1938.

(28) Pasquato, L.; Modena, G.; Cotarca, L.; Delogu, P.; Mantovani, S. Conversion of Bis(Trichloromethyl), Carbonate to Phosgene and Reactivity of Triphosgene, Diphosgene, and Phosgene with Methanol. *J. Org. Chem.* **2000**, *65*, 8224–8228.

(29) Shang, J.; Liu, S.; Ma, X.; Lu, L.; Deng, Y. A New Route of CO_2 Catalytic Activation: Syntheses of N-Substituted Carbamates from Dialkyl Carbonates and Polyureas. *Green Chem.* **2012**, *14*, 2899–2906.

(30) Yoshimura, A.; Luedtke, M. W.; Zhdankin, V. V. (Tosylimino)Phenyl-λ 3-Iodane as a Reagent for the Synthesis of Methyl Carbamates via Hofmann Rearrangement of Aromatic and Aliphatic Carboxamides. *J. Org. Chem.* **2012**, *77*, 2087–2091.

(31) Barve, B. D.; Wu, Y. C.; El-Shazly, M.; Chuang, D. W.; Chung, Y. M.; Tsai, Y. H.; Wu, S. F.; Korinek, M.; Du, Y. C.; Hsieh, C. T.; Wang, J. J.; Chang, F. R. Synthesis of Carbamates by Direct C-H Bond Activation of Formamides. *European J. Org. Chem.* **2012**, No. 34, 6760–6766.

(32) Bai, C.; Yao, X.; Li, Y. Easy Access to Amides through Aldehydic C-H Bond Functionalization Catalyzed by Heterogeneous Co-Based Catalysts. *ACS Catal.* **2015**, *5*, 884–891.

(33) Yang, S.; Xiong, M. F.; Tian, W. Q.; Zhang, H.; Xiao, X. Y.; Liu, H. Y.; Chang, C. K. Construction of C–O Bond via Cross-Dehydrogenative Coupling of sp^3 C–H Bond with Phenols Catalyzed by Copper Porphyrin. *Tetrahedron* **2020**, *76*, 131569.

(34) Rout, S. K.; Guin, S.; Banerjee, A.; Khatun, N.; Gogoi, A.; Patel, B. K. Directing Group Assisted Copper-Catalyzed Chemoselective O-Aroylation of Phenols and Enols Using Alkylbenzenes. *Org. Lett.* **2013**, *15*, 4106–4109.

(35) Barve, B. D.; Wu, Y. C.; El-Shazly, M.; Chuang, D. W.; Cheng, Y. Bin; Wang, J. J.; Chang, F. R. Copper-Catalyzed Oxidative Coupling of Formamides with Salicylaldehydes: Synthesis of Carbamates in the Presence of a Sensitive Aldehyde Group. *J. Org. Chem.* **2014**, *79*, 3206–3214.

(36) Yi, H.; Zhang, G.; Wang, H.; Huang, Z.; Wang, J.; Singh, A. K.; Lei, A. Recent Advances in Radical C-H Activation/Radical Cross-Coupling. *Chem. Rev.* **2017**, *117*, 9016–9085.

(37) Tekin, K.; Hao, N.; Karagoz, S.; Ragauskas, A. J. Ethanol: A Promising Green Solvent for the Deconstruction of Lignocellulose. *ChemSusChem* **2018**, *11*, 3559–3575.

(38) Capello, C.; Fischer, U.; Hungerbühler, K. What Is a Green Solvent? A Comprehensive Framework for the Environmental Assessment of Solvents. *Green Chem.* **2007**, *9*, 927–993.

(39) Chen, H.; Liu, S.; Lv, H.; Qin, Q. P.; Zhang, X. Nanoporous {Y2}-Organic Frameworks for Excellent Catalytic Performance on the Cycloaddition Reaction of Epoxides with CO2 and Deacetalization-Knoevenagel Condensation. *ACS Appl. Mater. Interfaces* **2022**, *14*, 18589–18599.

(40) Liu, S.; Chen, H.; Zhang, X. Bifunctional $\{Pb_{10}K_2\}$-Organic Framework for High Catalytic Activity in Cycloaddition of CO_2 with Epoxides and Knoevenagel Condensation. *ACS Catal.* **2022**, *12*, 10373–10383.

(41) Zhang, T.; Zhang, Z.; Chen, H.; Zhang, X.; Li, Q. Catalytic Investigation of CO2 Chemical Fixation and the Knoevenagel Condensation Reaction for a TmIII–

Organic Framework. *Cryst. Growth Des.* **2022**, *22*, 304–312.

(42) Gogoi, C.; Nagarjun, N.; Rana, A.; Dhakshinamoorthy, A.; Biswas, S. Diamino Group-Functionalized Zr-Based Metal-Organic Framework for Fluorescence Sensing of Free Chlorine in the Aqueous Phase and Knoevenagel Condensation. *Dalt. Trans.* **2022**, *51*, 6964–6975.

(43) Lv, H.; Chen, H.; Fan, L.; Zhang, X. Nanocage-Based Tb3+-Organic Framework for Efficiently Catalyzing the Cycloaddition Reaction of CO2with Epoxides and Knoevenagel Condensation. *Inorg. Chem.* **2022**, *61*, 15558–15568.

(44) Chen, H.; Fan, L.; Zhang, X. Highly Robust 3s-3d {CaZn}-Organic Framework for Excellent Catalytic Performance on Chemical Fixation of CO_2 and Knoevenagel Condensation Reaction. *ACS Appl. Mater. Interfaces* **2020**, *12*, 54884–54892.

(45) Liu, F.; Kumar, S.; Li, S.; You, H.; Ren, P.; Zhao, L. Bifunctional Design of Stable Metal-Organic Framework Bearing Triazole–Carboxylate Mixed Ligand: Highly Efficient Heterogeneous Catalyst for Knoevenagel Condensation Reaction under Mild Conditions. *Catal. Commun.* **2020**, *142*, 106032.

(46) Cai, K.; Tan, W.; Zhao, N.; He, H. Design and Assembly of a Hierarchically Micro-and Mesoporous MOF as a Highly Efficient Heterogeneous Catalyst for Knoevenagel Condensation Reaction. *Cryst. Growth Des.* **2020**, *20*, 4845–4851.

(47) Song, X.; He, Y.; Cai, Z.; Li, X.; Sun, Y.; Liu, H.; Lu, Y.; Hou, J.; Han, E. Three Amino-Functionalized Alkaline Earth Metal-Organic Frameworks as Catalysts for Knoevenagel Condensation. *ChemistrySelect* **2020**, *5*, 11510–11516.

(48) Huang, A.; Nie, R.; Zhang, B.; Pei, Y.; Chen, M.; Behera, R.; Yu, J.; Luan, X.; Hunter, N. T.; Ke, M.; Huang, W. Tandem Condensation-Hydrogenation to Produce Alkylated Nitriles Using Bifunctional Catalysts: Platinum Nanoparticles Supported on MOF-Derived Carbon. *ChemCatChem* **2020**, *12*, 602–608.

(49) Laha, B.; Khullar, S.; Gogia, A.; Mandal, S. K. Effecting Structural Diversity in a Series of Co(II)-Organic Frameworks by the Interplay between Rigidity of a Dicarboxylate and Flexibility of Bis(Tridentate) Spanning Ligands. *Dalt. Trans.* **2020**, *49*, 12298–12310.

(50) Jin, F. An Excellently Stable Heterovalent Copper–Organic Framework Based on Cu_4I_4 and $Cu(COO)_2N_2$ SBUs: The Catalytic Performance for CO_2 Cycloaddition Reaction and Knoevenagel Condensation Reaction. *Inorg. Chem. Commun.* **2020**, *116*, 107940.

(51) Zhang, T.; Chen, H.; Liu, S.; Lv, H.; Zhang, X.; Li, Q. Highly Robust {Ln_4}-Organic Frameworks (Ln=Ho, Yb) for Excellent Catalytic Performance on Cycloaddition Reaction of Epoxides with CO2 and Knoevenagel Condensation. *ACS Catal.* **2021**, *11*, 14916–14925.

(52) Tian, H.; Liu, S.; Zhang, Z.; Dang, T.; Lu, Y.; Liu, S. Highly Stable Polyoxovanadate-Based Zn-MOF with Dual Active Sites as a Solvent-Free Catalyst for C-C Bond Formation. *ACS Sustain. Chem. Eng.* **2021**, *9*, 4660–4667.

(53) Zhang, Y. Y.; Liu, Q.; Zhang, L. Y.; Bao, Y. M.; Tan, J. Y.; Zhang, N.; Zhang, J. Y.; Liu, Z. J. MOFs Assembled from C3 symmetric Ligands: Structure, Iodine Capture and Role as Bifunctional Catalysts towards the Oxidation-Knoevenagel Cascade Reaction. *Dalt. Trans.* **2021**, *50*, 647–659.

(54) Qiao, J.; Zhang, B.; Zhang, L.; Liu, Y. Practice of Function-Oriented Synthesis: High-Efficiency CO_2 Conversion and Knoevenagel Condensation by Two Novel In3-Based MOFs with High-Density Active Sites under Mild Conditions. *J. Mater. Chem. A* **2022**, *10*, 17773–17781.

(55) Afaq, S.; Akram, M. U.; Malik, W. M. A.; Ismail, M.; Ghafoor, A.; Ibrahim, M.; Nisa, M. un; Ashiq, M. N.; Verpoort, F.; Chughtai, A. H. Amide Functionalized Mesoporous MOF LOCOM-1 as a Stable Highly Active Basic Catalyst for Knoevenagel Condensation Reaction. *ACS Omega* **2023**, *8*, 6638–6649.

(56) Cheng, X.; Guo, L.; Wang, H.; Gu, J.; Yang, Y.; Kirillova, M. V.; Kirillov, A. M. Coordination Polymers Constructed from an Adaptable Pyridine-Dicarboxylic Acid Linker: Assembly, Diversity of Structures, and Catalysis. *Inorg. Chem.* **2022**, *61*, 17951–17962.

(57) Huang, G. Q.; Chen, J.; Huang, Y. L.; Wu, K.; Luo, D.; Jin, J. K.; Zheng, J.; Xu, S. H.; Lu, W. Mixed-Linker Isoreticular Zn(II) Metal-Organic Frameworks as Brønsted Acid-Base Bifunctional Catalysts for Knoevenagel Condensation Reactions. *Inorg. Chem.* **2022**, *61*, 8339–8348.

(58) Qiao, J.; Zhang, B.; Yu, X.; Zou, X.; Liu, X.; Zhang, L.; Liu, Y. A Stable Y(III)-Based Amide-Functionalized Metal-Organic Framework for Propane/Methane Separation and Knoevenagel Condensation. *Inorg. Chem.* **2022**, *61*, 3708–3715.

(59) Ghobakhloo, F.; Azarifar, D.; Mohammadi, M.; Keypour, H.; Zeynali, H. Copper(II) Schiff-Base Complex Modified UiO-66-NH_2(Zr) Metal-Organic Framework Catalysts for Knoevenagel Condensation-Michael Addition-Cyclization Reactions. *Inorg. Chem.* **2022**, *61*, 4825–4841.

(60) Lv, H.; Chen, H.; Hu, T.; Zhang, X. Nanocage-Based {In_2Tm_2}-Organic Framework for Efficiently Catalyzing the Cycloaddition Reaction of CO_2 with Epoxides and Knoevenagel Condensation. *Inorg. Chem. Front.* **2022**, *9*, 5788–5798.

(61) Zuo, W.; Yang, S.; Xing, Y.; Xiao, X.; Fan, D.; Li, H.; Wang, G.; Qin, B.; You, S.; Jia, X. Amorphous Zirconium Metal-Organic Frameworks Assembled from Mixed Porphyrins as Solvent-Free Catalysts for Knoevenagel Condensation. *Dalt. Trans.* **2022**, *51*, 6631–6637.

(62) Shi, Y.; Xiong, D.; Li, Z.; Wang, H.; Qiu, J.; Zhang, H.; Wang, J. Ambient CO_2/N_2 Switchable Pickering Emulsion Emulsified by TETA-Functionalized Metal-Organic Frameworks. *ACS Appl. Mater. Interfaces* **2020**, *12*, 53385–53393.

(63) Wang, X. S.; Liang, J.; Li, L.; Lin, Z. J.; Bag, P. P.; Gao, S. Y.; Huang, Y. B.; Cao, R. An Anion Metal-Organic Framework with Lewis Basic Sites-Rich toward Charge-Exclusive Cationic Dyes Separation and Size-Selective Catalytic Reaction. *Inorg. Chem.* **2016**, *55*, 2641–2649.

(64) Ugale, B.; Dhankhar, S. S.; Nagaraja, C. M. Construction of 3D Homochiral Metal-Organic Frameworks (MOFs) of Cd(II): Selective CO_2 Adsorption and Catalytic Properties for the Knoevenagel and Henry Reaction. *Inorg. Chem. Front.* **2017**, *4*, 348–359.

Chapter V

MOF Derived Composites for Electrocatalytic Oxygen Process

Part of this chapter has been published in Inorg. Chem. **2023***, 62, 7,* 3026–3035;

DOI: *10.1021/acs.inorgchem.2c03707*

Abstract

The oxygen reduction reaction (ORR) at cathode and oxygen evolution reaction (OER) at anode are one of the most challenging processes that affects the efficiency of many alternative energy systems such as fuel cell, metal batteries, water electrolysis, etc. Currently, noble metal-based catalysts such as Pt, Ru, and Ir are the most effective catalysts for these oxygen process in terms of kinetic values. However, their limited availability, high cost, and corrosive nature necessitate the development of low-cost alternatives. In this chapter, we have studied the application of Mn & Ni based MOFs as an altruistic template to derive metal/metal oxide composites for electrocatalytic process. Two novel Mn-MOFs (Mn-SKU-1 and Mn-SKU-2) were pyrolyzed under N_2 at 600°C, and porous α-Mn_2O_3 composites (PSKU-1 and PSKU-2) are produced, with a BET surface area of 90.8 (for PSKU-1) and 179.3 $m^2\ g^{-1}$ (for PSKU-2). These mesoporous MOF-derived α-Mn_2O_3 when applied towards electrocatalytic reduction of oxygen in 0.1 M KOH solution, shows onset potential of 0.90 V for PSKU-1 and 0.93 V for PSKU-2 *vs* RHE, with the current density of 4.8 and 6.0 mA cm^{-2}, respectively at 1600 rpm. The ORR process was found to undergo four electron pathways as confirmed from the RDE/RRDE experiments. The electrocatalyst PSKU-2 is cost-effective, user-friendly, retains 90% of its activity after ten hours of continuous use, and is more recyclable than Pt/C. The onset potential, maximum current density and kinetic values (J_k = 11.68 mA^{-2} and Tafel slope = 85.0 mV dec^{-1}) obtained in this study are higher than the values reported for pure Mn_2O_3. Furthermore, we have also derived Ni/NiO-composites by pyrolyzing novel Ni-SKU-5 MOF at 450 °C for 4 h. The derived nickel composites were applied as a bifunctional electrocatalyst for both ORR and OER with an overpotential of 290 mV and 350 mV *vs* RHE respectively.

V.1. Introduction:

The global energy demand is widely fulfilled by non-renewable fossil fuels (coals, natural gas, oils, etc) that yields high greenhouse gas emission and its depleting stock indicates a clear future of global energy crises.[1] It is estimated that the fossil fuel will run out of stock by 2090 if its consumption is continued at the current rate. Therefore, a practice to use sustainable and renewable feedstocks as an energy source can benignly deliver future energy demands. Today the research is oriented to develop alternative energy sources using solar,[2] hydro,[3] wind,[4] tidal,[5] geothermal[6] and biomass energy as renewal resources.[7,8] Among many alternative, hydrogen based fuel cell technology have gained enormous attention with the uses of earth abundant hydrogen as a clean fuel delivering environment-friendly by-product.[9] A fuel cell electrochemically converts the chemical energy of a fuel to electrical energy by without mechanical/thermal processes. It is estimated that one kilogram of hydrogen can produce an energy equivalent to a gallon of gasoline which is equal to 33.7 kWh.[10] In a typical proton exchange membrane fuel cell (PEMFCs) as shown in Figure V.1., the elementary reaction that take place are the oxidation of H_2 at the anode (hydrogen oxidation reaction, HOR) followed by reduction of O_2 at the cathode (oxygen reduction reaction, ORR) [11] .

The HOR reaction at the anode (eq V.1) gives a theoretical redox potential of 0.0V whereas the reduction of oxygen at the cathode (ORR) is 1.23 V (eq. V.2) vs RHE at 298 K and 1 atm P_{H2} and P_{O2} giving rise to overall cell voltage of 1.23V for the overall system.

Reactions at the electrodes:

Anode: $2H_2 \rightarrow 4H^+ + 4e^- E^o = 0.00\ V$ V.1

Cathode: $O_2 + 4H + + 4e^- \leftrightarrow 2H_2O E^o = 1.23\ V$ V.2

The electrolytic environment of the fuel cell determines the half reactions of the PEMFC.

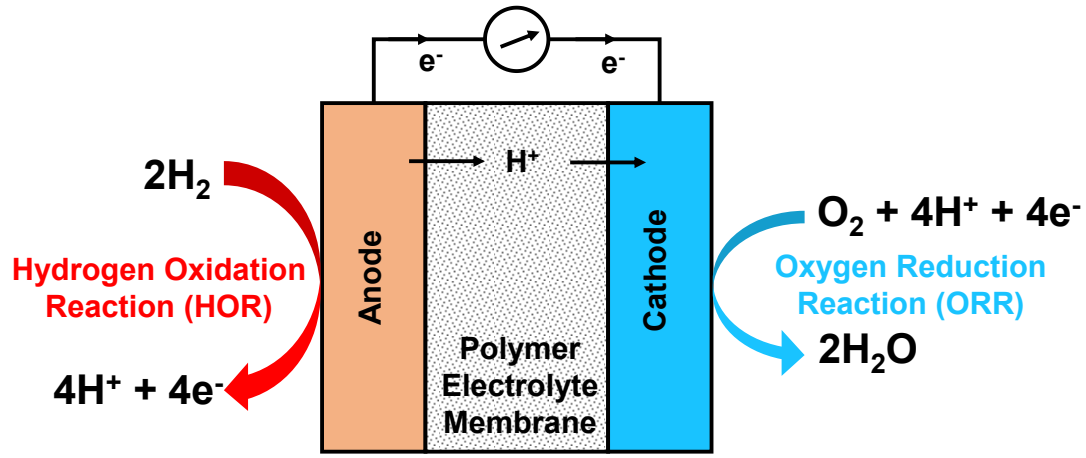

Figure V.1. Schematic of proton exchange membrane fuel cell (PEMFC).

Hydrogen as a fuel is generally generated through two methods such as water electrolysis and steam reforming of fossil fuels. However, the latter is considered to be less environmentally friendly due to the production of CO_2 alongside hydrogen. This further result in a lower purity of hydrogen, and affects the fuel cell's life cycle and efficiency. On the other hand the electrochemical water splitting process comprises of two half-cell reactions (Figure V.2).[12] The reduction process at cathode is known as the hydrogen evolution reaction (HER) i.e. $4H^+ + 4e^- \rightarrow 2H_2$ and the oxidation process at anode is better known and oxygen evolution reaction (OER) i.e. $2H_2O \rightarrow O_2 + 4H + + 4e^-$.

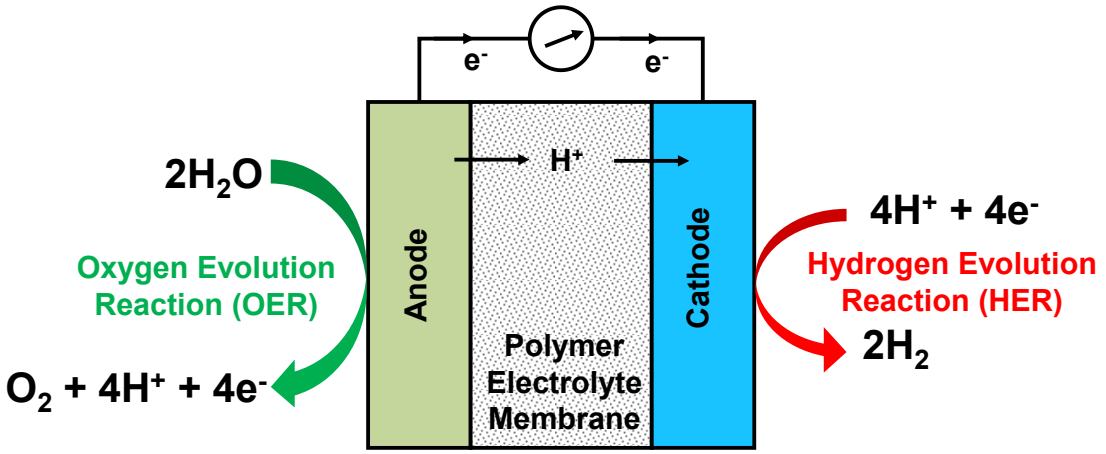

Figure V.2. Schematic of electrochemically driven water splitting reactions.

Additionally, energy storage devices such as batteries also form a major components of energy solution which can offset the unpredictable fluctuations in energy demand, owing to their relatively low production costs and high theoretical energy density for storage. Today, the batteries are applied widely from tiny button cells for hearing aids to large-scale batteries for electric vehicles and energy are stored on a massive scale. As of now, lithium-ion batteries (LIBs) maintain an unparalleled dominance in the energy storage market.[13–15] The reason behind this is their well-understood chemistry, as well as significant improvements in their performance and associated manufacturing processes over the past two decades. However, rise in its price due to increased demand and its scarcity presents a critical challenge to long-term applicability of LIBs. Consequently, it is crucial to explore post-lithium batteries that do not rely on lithium as a resource and in that case one promising alternative to LIBs is metal-air batteries.[16] In a metal air batteries, the two-oxygen process (OER and ORR) are the key reactions (Figure V.3). During discharge, the oxygen reduction reaction (ORR) converts O_2 to OH^-, while during charging, the oxygen evolution reaction (OER) takes place.[17]

It is worth noting that metal-air batteries exhibit significantly higher theoretical energy densities compared to LIBs. However, their full potential has not been realized yet, largely due to the oxygen electrocatalysis at the cathode of metal-air batteries and their development is greatly hindered by the various challenges related to the oxygen process.

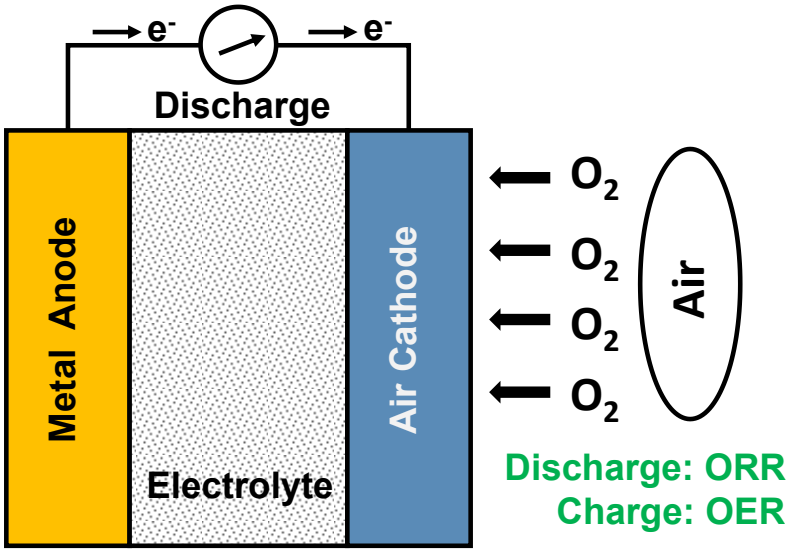

Figure VI.3. Schematic of metal-air batteries.

V.1.2. Challenges of oxygen process:

Nevertheless, the progress and efficiency of the alternative source of energy like fuel cell, metal air batteries or electrochemical water splitting reactions, is greatly dependent on the kinetics of the oxygen process. At a glance oxygen process may appear to be a simple method, but this is not the case. The process of ORR and OER is an area that requires advancement in both science and technology to address the challenges that come with it. One of the major challenges is its positive ΔG value that makes the oxygen process thermodynamically uphill. The redox potential of oxygen is at higher (E^0=1.23

V *vs* RHE) and the rate is about six orders slower than the rate of hydrogen process (E^0=0.00 V *vs* RHE). Often catalyst is required to lower the overall activation energy of oxygen process and novel metals such as platinum-based catalysts are currently the benchmark for the ORR process. Similarly, IrO_2 and RuO_2 are state-of-the-art catalyst for OER process.[18] Regardless of enhanced kinetics with noble metal catalyst, their less abundancy, high cost, and corrosive nature limits the development of low-cost fuel cells.[19] Therefore, developing an affordable catalyst with high performance, high stability for oxygen process (ORR and OER) is an urgent task despite the tremendous progress made with a noble metal catalyst.[20]

V.1.3. Noble-metal free catalyst towards electrocatalytic oxygen process:

Transition metal oxide (TMOs) with their abundant availability, simple synthetic procedure, variable oxidation states, and varied morphology has gained enormous attention as a low-cost ORR/OERcatalyst.[20–23] Extensive research has been carried out for TMOs as an ORR/OER catalyst and their electrocatalytic activity was reported to be dependent on morphology, surface area, exposed facets, synthetic procedure. Also, as TMOs are semiconductors in nature, improving its electrical conductivity enhances their electrocatalytic activity.[24,25]

Metal organic frameworks (MOFs) with their intriguing properties such as, robust framework, high porosity, high surface area, unique morphology have found versatile application in different field. The MOFs as an altruistic template or precursor to derive various metal composites is one of the prominent application of MOFs and is rapidly expanding research area in recent years.[26] The post synthetic pyrolysis of MOFs at desired temperature and atmosphere are reported to deliver metal composites that has structural features similar to that of its parent MOF. Therefore, the MOF derived

composites also may have a high surface area, high porosity, morphology similar to that of parent MOF, high metal sites, etc as that of its parent MOF.

Furthermore, during the post synthetic pyrolysis of MOF at high temperature, the charring of coordinated organic ligand takes place forming porous carbon material along with the metal composites. Yamauchi *et al.* reports the synthesis of nitrogen-doped porous carbon (NPC) material using Zn based ZIF-8 MOF as an altruistic template.[27] The NPCs forms morphology similar to that of its parent MOF ZIF-8. The derived NPC also possess high surface area (~1100 m^2g^{-1}) with pore diameter of 1.06 nm, which is close to its parent MOF ZIF-8.[27] However, the retention of structural characteristics in MOF derived metal composites astoundingly depends on the pyrolysis conditions such as ramping temperature, isothermal time, inert atmosphere and MOF template. Harsh conditions like abrupt ramping, longer isolation time at high temperatures, non-inert atmosphere during pyrolysis are some typical challenges that hinder yield of desired structural and chemical composition of final derived composites.[28,29] The treatment of ZIF-67, a Co-based MOF at 600-800 °C under N_2 atmosphere has formed Co-NPC as reported by Yamauchi *et al*.[30] However, when same ZIF-67 MOF was treated at high temperature under air, porous Co_3O_4 was formed as a final product.[31] It was also found that at high temperature under N_2 atmosphere crystallization of derive Co-NPs increase along with the enhanced graphitization of porous carbon matrix which results in increased conductivity of overall derived composites. The derived composites with catalytic active sites, conductive and porous N-doped nanocarbon matrix, can considered as a potential material for electrocatalysis. Furthermore, there are reports where MOF derived metal oxides have abundant porosity and oxygen vacancies that can exhibit efficient catalytic activity towards electrocatalytic oxygen processes.

V.2. Result and discussion:

V.2.1. Synthesis of Mn_2O_3 (PSKU-1 and PSKU-2) from Mn-SKU-1 and Mn-SKU-2.

The manganese-based MOFs Mn-SKU-1 and Mn-SKU-2 were rationally synthesized for the derivation of metal composites that can exhibit efficient electrocatalytic activity towards ORR. In Mn-SKU-1, the coordination of Mn and DOT ligands forms a sheet-like structure giving rise to non-interpenetrating MOF. However, Mn-SKU-2 contains the coordination of metal with two ligands DOT and BPY. The use of BPY ligand with strut length of ~7.07 Å opens possibility for creating a large cuboidal void where catenation of another 3D framework results in the formation of interpenetrating MOF. Therefore, the Mn-SKU-1 represents a typical traditional MOF while Mn-SKU-2 is an interpenetrating MOF. These Mn-based MOFs were used as a template to derive manganese oxide under controlled environment. In details, the samples were finely grinded and then transferred into a quartz boat. The boat containing the MOF was placed in a tube furnace and ramped at a heating rate of 10 °C min^{-1} up to 600 °C maintaining a continuous N_2 flow of 60 mL min^{-1}. The furnace temperature at 600 °C was maintained till 3 h and allowed to cool naturally to room temperature following which a black coloured product was collected from both analogue of MOFs. These pyrolyzed samples derived from Mn-SKU-1 and Mn-SKU-2 were designated as PSKU-1 and PSKU-2. Both the product showed characteristic peak for α-Mn_2O_3. Although MOF-derived α-Mn_2O_3 composites have shown diverse applications as sensors,[32] supercapacitors,[33–39] zinc ion batteries,[40–42] lithium-ion batteries,[43–47] heterogeneous catalysis,[48,49], etc., this is the first work on their practical use as ORR catalyst (Figure V.4).

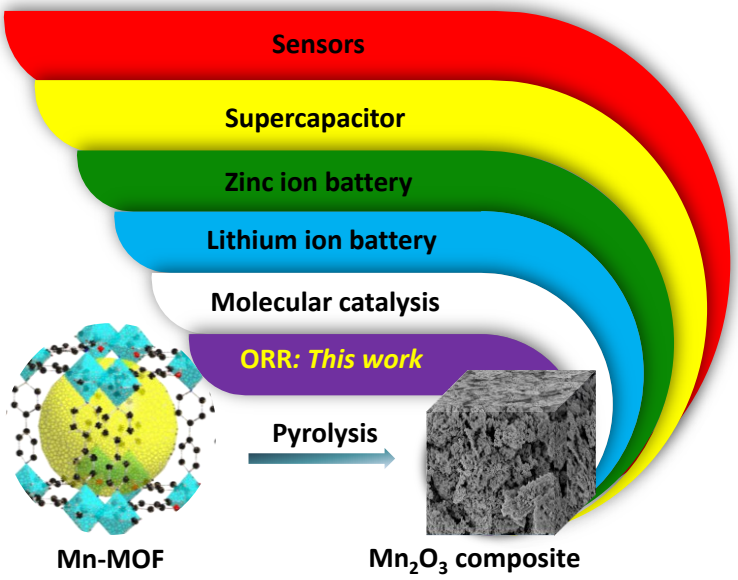

Figure V.4: Application of Mn-MOF derived α-Mn_2O_3 for sensors, supercapacitors, zinc-ion battery, lithium-ion battery, molecular catalysis and ORR (our work)

V.2.2. Characterization of PSKU-1 and PSKU-2.

At first, the PXRD of the derived composites PSKU-1 and PSKU-2 was conducted and the PXRD pattern found was in good agreement with α-Mn_2O_3 (JCPDS No 96–810-3498) having cubic crystal system and I_{a3} space group (Figure V.5). Further, the PXRD data shows an excellent bulk purity of derived PSKU-1 and PSKU-2, as no extra peaks were observed apart from the peaks of α-Mn_2O_3.

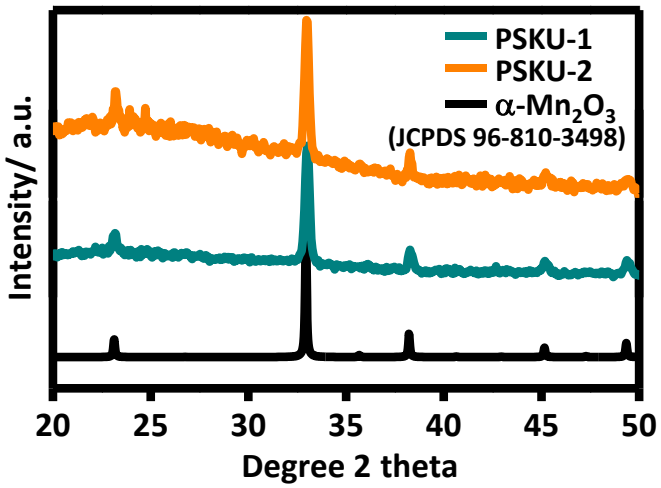

Figure V.5: PXRD of PSKU-1 and PSKU-2 compared with JCPDS 96-810-3498.

The FT-IR conducted for the derived samples shows the stretching peak at a range of 674 cm^{-1} and 578 cm^{-1} which can be accredited to the stretching frequencies of Mn-O bond (figure V.6a).[50] This is further confirmed through Raman spectra (Figure V.6b), where the bands around 685 and 310 cm^{-1} are due to the symmetric and asymmetric stretch of bridge oxygen species (Mn-O-Mn) respectively.[51,52] In the Raman spectra, the peak around 1356 cm^{-1} can be attributed to the high defect containing carbon, formed by the charring of organic ligand moiety present in MOF at high temperature.[53]

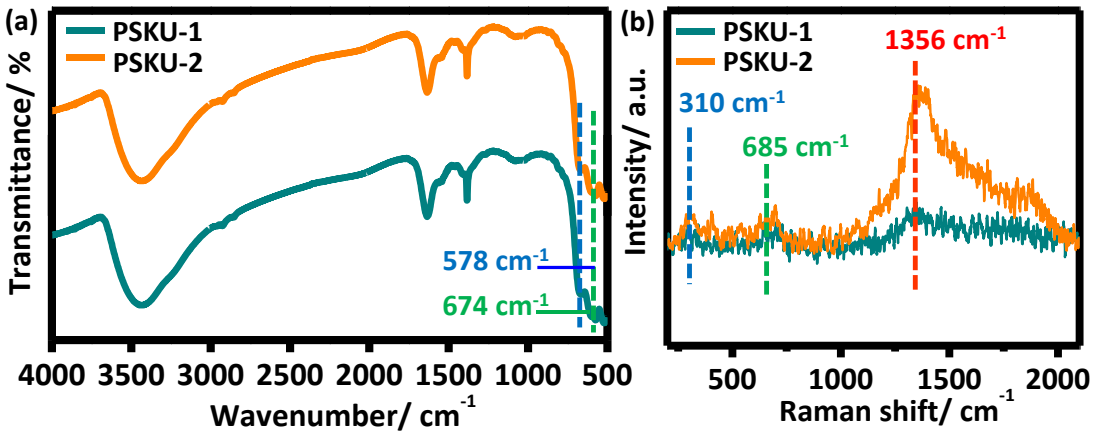

Figure V.6: (a) FT-IR spectra and (b) Raman spectra of PSKU-1 and PSKU-2.

Next, to evaluate the permanent porosity of the derived composites BET SA was evaluated by studying the nitrogen adsorption isotherm at 77 K. Compared to the BET, SA for Mn-SKU-1 and Mn-SKU-2 were found to be 76.8 $m^2 g^{-1}$ and 34.9 $m^2 g^{-1}$ whereas after pyrolysis, the SA of the derived composites PSKU-1 and PSKU-2 was increased to a value of 90.8 and 179.3 $m^2 g^{-1}$ respectively (Figure V.7a-b).

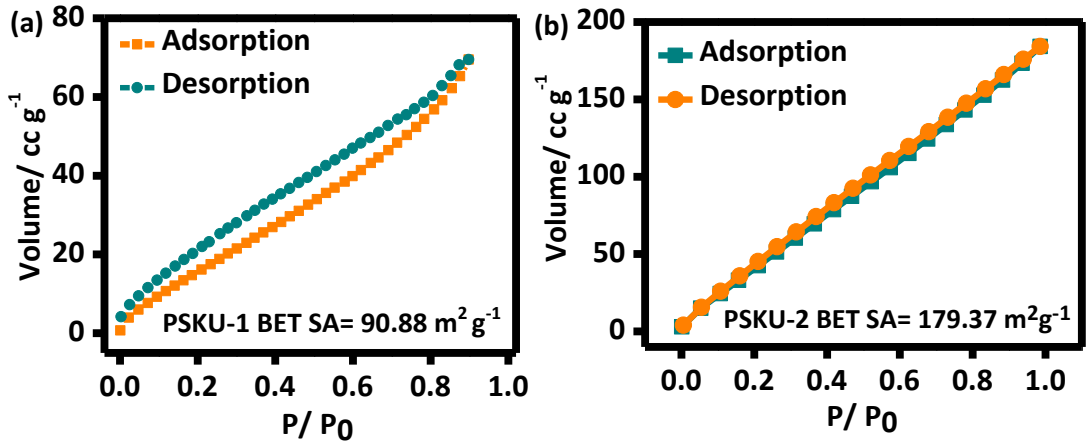

Figure V.7: BET surface area comparison of (a) PSKU-1 and (b) PSKU-2.

The pore volume calculated for PSKU-1 and PSKU-2 was found to be 0.15 and 0.25 $cm^3\ g^{-1}$ respectively (Figure V.8a-b). It should be noted that Mn_2O_3 obtained from Mn-BTC MOF (BTC=benzene tricarboxylic acid) has been reported independently by Huang *et al.*[33] Kang *et al.*[41] and Mahanty *et al.,*[43] with SA values of 24.0, 38.5, and 44.0 $m^2\ g^{-1}$ respectively. Similarly, Wang *et al.* reported the formation of Mn_2O_3 by calcination of Mn-MIL-100 MOF at 400 °C and found the SA to be 62.5 $m^2\ g^{-1}$.[37] The SA of Mn_2O_3 was found to be 127 $m^2\ g^{-1}$ when obtained through the calcination of acid-digested $CaMnO_3$ using a soft template citrate-gel method.[54,55] Meanwhile, Liu *et al*[47] achieved a high SA of 129.0 $m^2\ g^{-1}$ through the pyrolysis of interpenetrating Mn-MOF. In comparison, the SA obtained in our study for PSKU-2 is comparatively higher than that of other reported pristine α-Mn_2O_3 (FigureV.8c) derived from Mn-MOFs.[42,46,56–60] An increase in the SA in case of PSKU-2 may be due to the elimination of 3D→3D homo interpenetration from Mn-SKU-2 after pyrolysis, which leads to the creation of large voids that are easily accessible.[61]

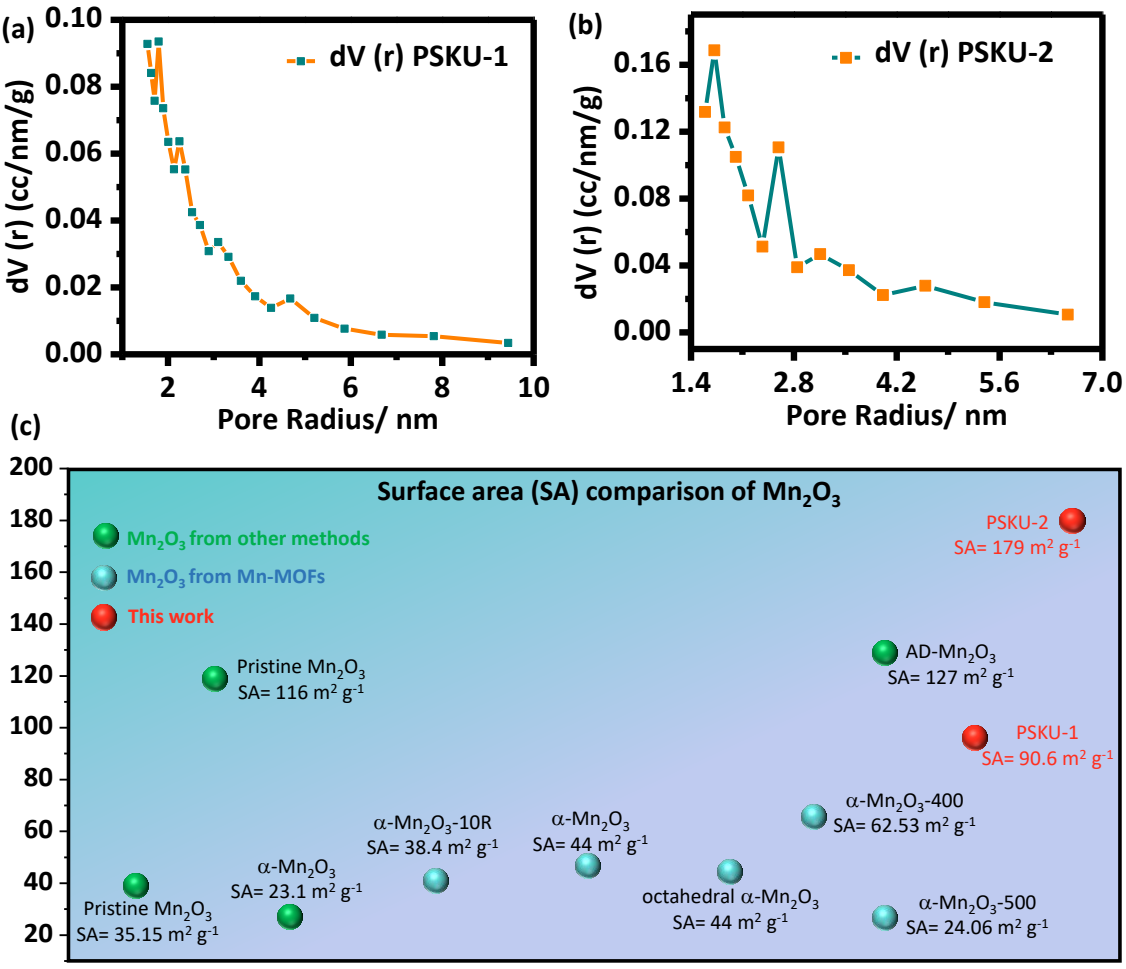

Figure V.8: BJH pore distribution plot of (a) PSKU-1 (b) PSKU-2 and (c) BET surface area comparison of PSKU-1 and PSKU-2 with other reported Mn_2O_3.

The morphological characterization was performed using scanning electron microscope (SEM). The SEM images shows that the morphology of PSKU-1 and PSKU-2 are similar to its parent Mn-SKU-MOFs (Figure V.9a-f) indicating an altruistic nature of synthesized Mn-MOF under optimized pyrolysis condition. The formation of porous surfaces resulted from the decomposition of the organic linker in the MOF framework after pyrolysis was also seen in the SEM images.[62,63] However, on closer look the surface texture and porosity of two derived composites were not same. The texture in the surface of PSKU-2 is more compared to other and in the case of **PSKU-1**, layered compact facets were also identified in addition to porous facets (Figure V.9e-f).

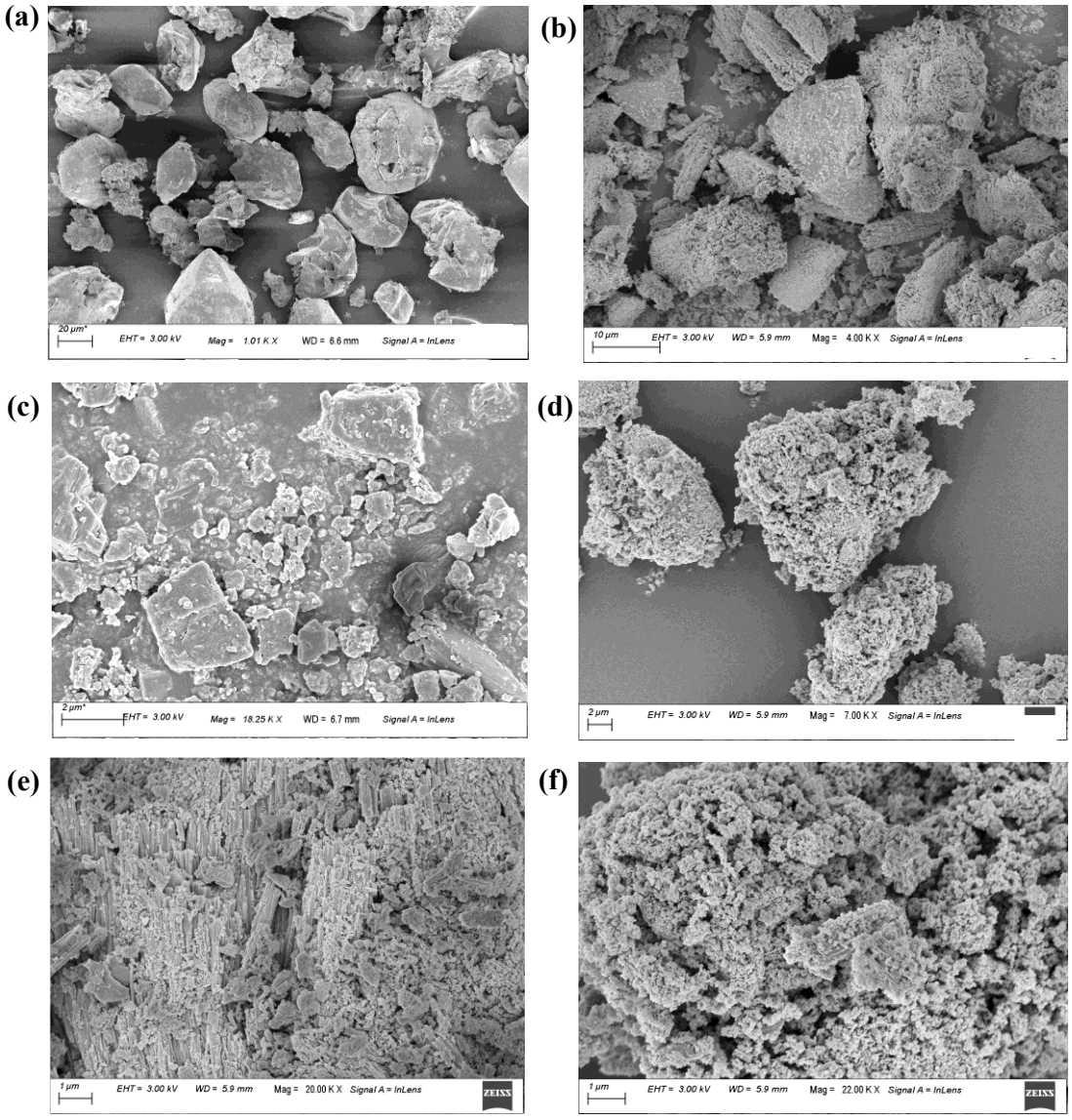

Figure V.9: SEM images of. (a) Mn-SKU-1 (b) PSKU-1. (c) Mn-SKU-2 (d) PSKU-2; high resolution SEM images of (e) PSKU-1 and (f) PSKU-2.

High-resolution transmission electron microscopy (HRTEM) shows a conformal coating of carbon around the metal oxide for both PSKU-1 (Figure V.10a) and PSKU-2 (Figure V.10c). The lattice spacing of 0.561 nm and 0.317 nm was observed for PSKU-1 and PSKU-2, respectively which could be indexed to (111) and (122) planes of α-Mn_2O_3 (Figure V.10b and d). Additionally, the selected area electron diffraction (SAED) images in the inset of figure V.10b and d revealed the high crystallinity of the composites obtained.

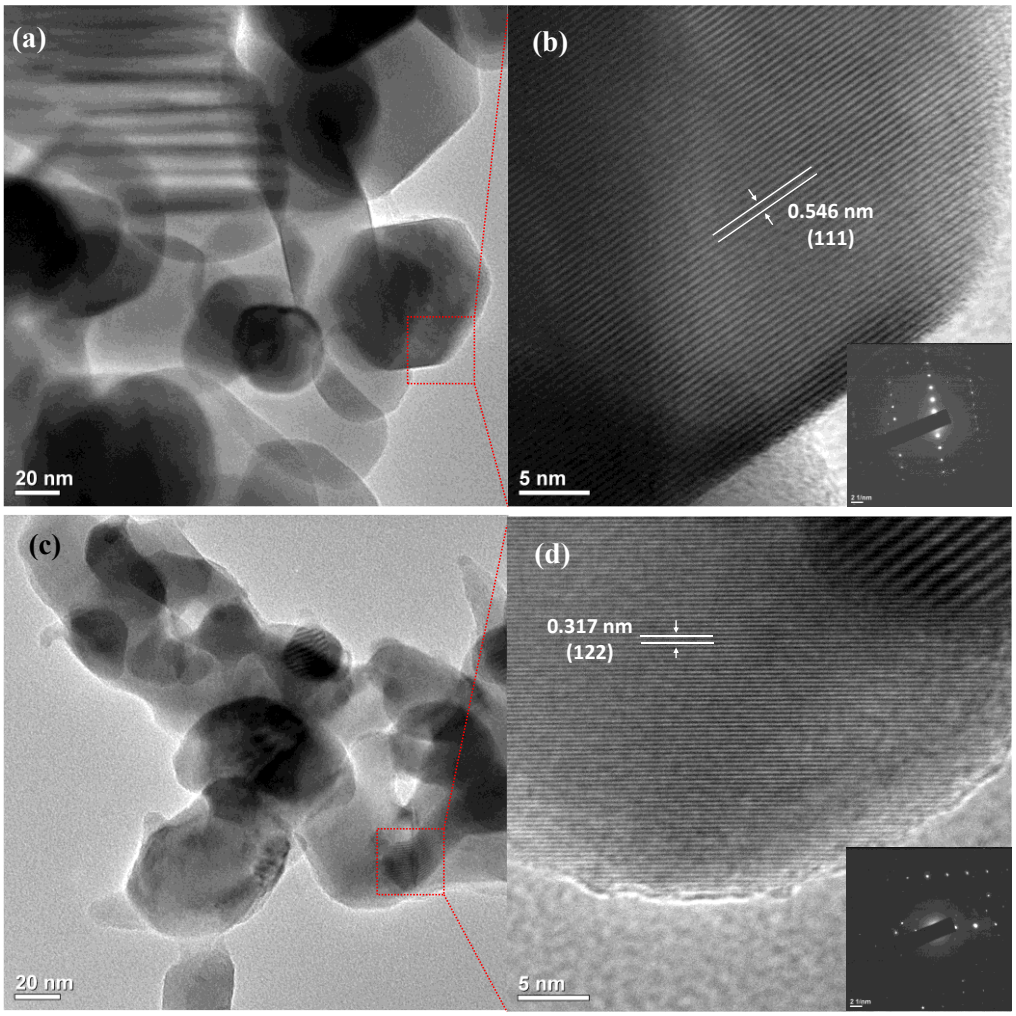

Figure V.10: (a) HRTEM images of PSKU-1 (b) HRTEM images of PSKU-1 interpreted as per *d*- spacing values of α-Mn_2O_3 with SAED pattern in inset (c) HRTEM images of PSKU-2 (d) HRTEM images of PSKU-2 interpreted as per *d*-spacing values of α-Mn_2O_3 with SAED pattern in the inset.

The composition of both PSKU-1 and PSKU-2 was verified performing energy dispersive X-Ray (EDX). The peaks of Mn, O and C were found in the EDX spectra (Figure V.11). The conductive carbon, as confirmed form the EDX data have been formed due to the charring of the organic linker of MOF at high temperatures. However, no signature for crystalline carbon is observed in the PXRD of PSKU-1 and PSKU-2 (Figure V.5a). Therefore, the products are robust composites of crystalline α-Mn_2O_3 and amorphous carbon.[64] Despite the coordination of the BPY ligand in Mn-SKU-2,

the absence of nitrogen peak in EDX spectra also confirms the purity of derived composites.

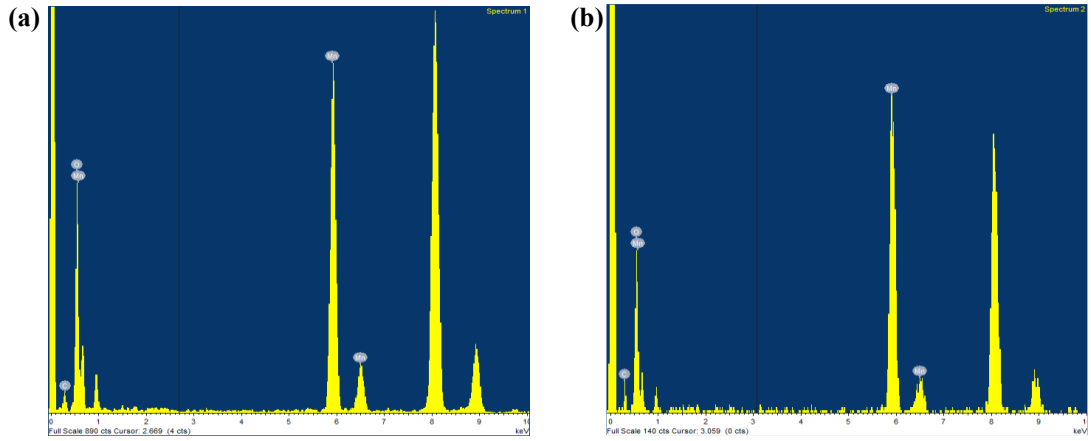

Figure V.11: EDX spectra of (a) PSKU-1 and (b) PSKU-2.

Table V.1: Summarized weight% and atomic% of Mn, O and C obtained after EDX analysis of PSKU-1 and PSKU-2.

	PSKU-1		PSKU-2	
Element	**Weight%**	**Atomic%**	**Weight%**	**Atomic%**
Mn	84.60	60.80	86.99	65.13
O	13.92	34.36	11.36	29.21
C	1.47	4.85	1.65	5.65
Total	100		100	

V.2.3. Electrocatalytic oxygen reduction reaction with PSKU-1 and PSKU-2:

The electrochemical activity of PSKU-1 and PSKU-2 was thoroughly studied by modifying the glassy carbon electrode with drop casting method to be used as a cathode material. Typically, 2 mg PSKU-1/PSKU-2 and 1 mg of Vulcan carbon X-72 were

dispersed in 1 mL of ethanol respectively followed by the addition of 10 μL Nafion solution (5 wt% in water). The mixture was sonicated for 30 min to prepare a homogeneous catalyst ink. The working electrode was then modified by drop casting the ink suspension on bare GCE. All the experiments were conducted in 0.1 M KOH (electrolyte) and was bubbled with N_2 or O_2 for 30 min to ensure the saturation before performing ORR measurements. The BASi epsilon setup was used for all electrochemical experiments at room temperature in a standard three-electrode cell with a glassy carbon electrode (GCE, radius: 0.07 mm) as working electrode, platinum wire as counter electrode, and 0.3 M KCl saturated *Ag/AgCl as* reference electrode. The current density was normalized to the geometrical area and the measured potential *vs* Ag/AgCl (E^o=0.199 V) was converted to a reversible hydrogen electrode (RHE) scale according to the Nernst equation (equation V.3).

$$E_{RHE} = E_{Ag/AgCl} + 0.059pH + 0.199 \qquad \text{.....V.3}$$

At first, the cyclic voltammetry (CV) was performed at a scan rate of 10 mV s^{-1} using modified electrodes in N_2 saturated 0.1 KOH solution. No noticeable reduction peaks were observed within the potential between 1.0-0.5 V *vs* RHE. However, when the electrolyte was saturated with O_2 gas under similar condition, the cathodic (O_2) reduction peak at 0.66 V *vs* RHE for PSKU-1 (Figure V.12a) and 0.73 V *vs* RHE for PSKU-2 (Figure V.12b) was observed. These reduction peaks confirmed the electrochemical reduction of dissolved O_2 by the modified composites electrode.

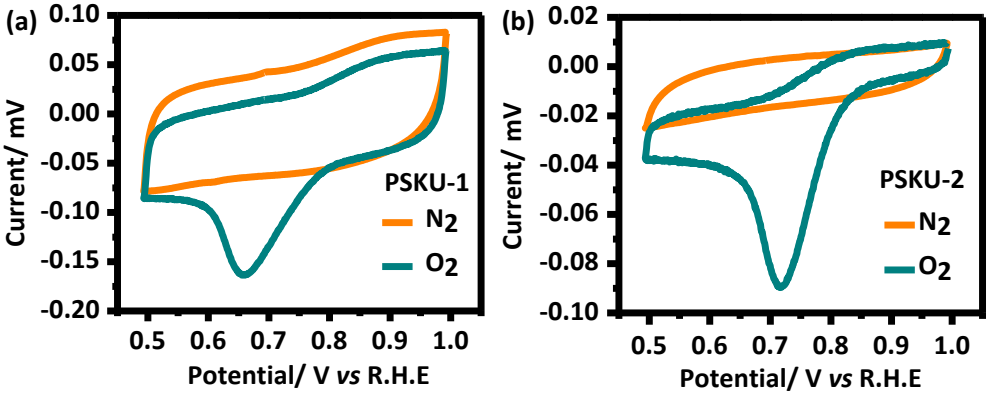

Figure V.12: CV response of (a) **PSKU-1** and (b) **PSKU-2** modified GC electrode in N_2 and O_2 saturated 0.1 M KOH solution at a scan rate of 10 mV s^{-1}.

Linear sweep voltammetry (LSV) was performed for GC coated PSKU-1/PSKU-2 in O_2 saturated 0.1 M KOH at different rotation speed ranging from 400-2500 rpm using rotating disc electrode (RDE) and show linear increase in current density with the increase in rotation speed. As shown in figure V.13a. PSKU-1 modified electrode has an onset potential of 0.90 V *vs* RHE with current density value*s* between 3.22 to 6.35 mA cm^{-2} at 0.2 V. Similarly, on the other hand PSKU-2 has an onset potential of 0.93 V *vs* RHE with current density ranging from 2.43 to 9.92 mA cm^{-2} (Figure V.13b) at 0.2 V. The CV and LSV experiments show that PSKU-2 is comparatively efficient than PSKU-1 with respect to current density and onset potential.

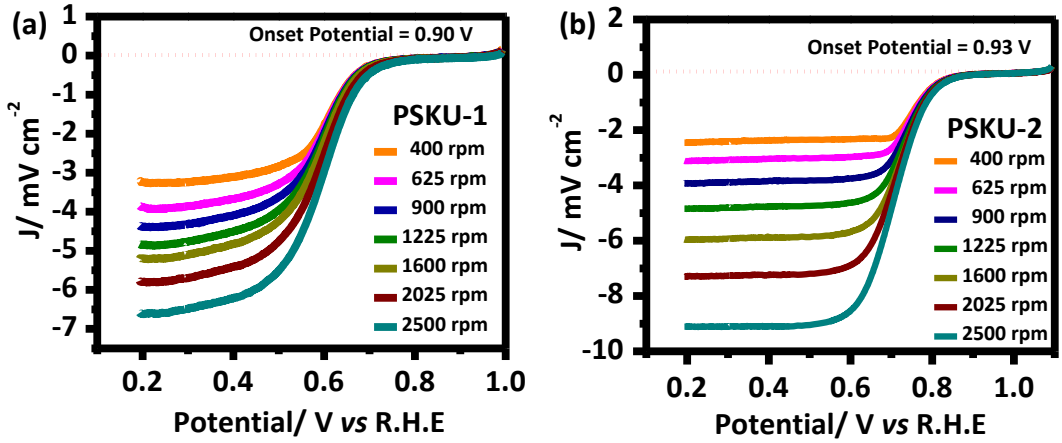

Figure V.13: LSV plot of (a)PSKU-1 and (b) PSKU-2 generated from RDE measurement at different rotation.

Figure V.14a shows that under the same conditions and with the same catalytic loading, the electrochemical output is better for PKSU-2. The improved activity of PSKU-2 compared to PSKU-1 can be ascribed to (i) greater density of Mn active sites in PSKU-2 (86.9 wt.%) as compared to PSKU-1 (84.6 wt.%) and (ii) the higher specific surface area of PSKU-2 compared to PSKU-1 that allows oxygen to more easily access the metal sites.

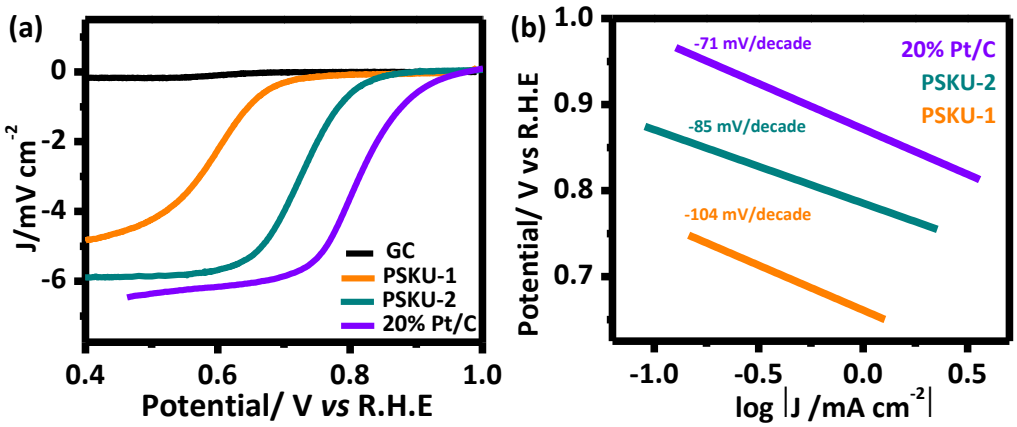

Figure V.14: (a) Comparative LSV plot of GC, PSKU-1, PSKU-2 and 20% Pt/C performed in O_2 saturated 0.1 M KOH solution at a scan rate of 10 mV s^{-1} and 1600 rpm. (b) Tafel plot for PSKU-1, PSKU-2, and 20% Pt/C.

Interestingly, the onset potential of PSKU-1 and PSKU-2 were found comparable to 20% Pt/C (0.97 V) and relatively higher than that of GC (0.70 V). The half-wave potential ($E_{1/2}$) of the various catalytic systems at 1600 rpm were found as follows: 0.62 V for PSKU-1, 0.72 V for PSKU-2, 0.81 V for 20% Pt/C, and 0.59 V for GC. Further at 1600 rpm, the maximum I_d measured for PSKU-2 at a potential of 0.46 V was found to be 5.82 $mAcm^{-2}$. This value is close to that of 20% Pt/C, with 6.52 mA cm^{-2}, and is significantly higher than that of PSKU-1 (4.80 mA cm^{-2}) and GC electrode (0.19 mA cm^{-2}). Under the given condition, the Tafel slope calculated from the LSV plots were found to be -85 mV dec^{-1}, -104 mV dec^{-1} and -71 mV dec^{-1} for PSKU-2, PSKU-1 and 20% Pt/C respectively (Figure V.14b). It is to be noted that the ORR activity of Mn-

MOFs derived composites is similar to some of Pt-based catalyst reported earlier. The PtCo@CoNC/NTG catalyst has $E_{1/2}$ of 0.94 V *vs* RHE and Tafel slope of 71 mV dec^{-1} as reported by Xia *et al.*[47] Similarly, Wu *et al.* reported Pt/FeN4–C catalyst to obtain $E_{1/2}$ of 0.9 V *vs* RHE towards ORR.[46]

The onset values found with PSKU-1 and PSKU-2 are found better than commercially available Mn_2O_3 (0.59 V) and comparable to the state-of-the-art system such as Mn_2O_3 synthesized from aerosol-spray-assisted approach (1.01 V),[60] Mn_2O_3/NC-500-20% (0.80 V),[67] Mn_2O_3/C (0.88 V),[68] α-Mn_2O_3 prism (0.75 V),[69] NiO-Mn_2O_3/C (0.67 V),[70] 30% Pd-Mn_2O_3(0.97 V),[71] Ni-doped Mn_2O_3 (0.935 V)[72] (Table V.2).

Table V.2: Comparison of ORR electro-catalytic system of as-synthesized Mn_2O_3 with Mn_2O_3 synthesized via different methodologies.

Entry	Onset (V *vs* R.H.E)	Electrolyte	Methodology	Ref
Mn_2O_3	1.01 V	0.1 M KOH	facile aerosol-spray-assisted approach (ASAA)	60
Mn_2O_3/NC-500-20%	0.80 V	0.1 M KOH	two-step strategy involving a hydrothermal method and a solid-state method	67
Mn_2O_3/C	0.88 V	0.1 M KOH	hydrothermal method with Vulcan XC-72 as a supporting material	68
α-Mn_2O_3 Prism	0.747 V	0.1 M KOH	low-temperature hydrothermal method	69
α-Mn_2O_3 commercial	0.590 V	0.1 M KOH	Commercially available	70
NiO-Mn_2O_3/C	0.67 V	1 M NaOH	NiO and MnO_2 pyrolyzed at 500 °C at N_2 and chitosan	71
30% Pd-Mn_2O_3	0.97 V	0.1 M KOH	the facile solvothermal method with Pd support	72
PSKU-1	0.90 V	0.1 M KOH	Pyrolysis of pristine Mn-SKU-1 MOF	This Work
PSKU-2	0.93 V	0.1 M KOH	Pyrolysis of pristine Mn-SKU-2 MOF	This Work

The RDE results were further evaluated to acquire Koutecky-Levich (K-L) plots for the estimation of number of electrons involved during the reduction of oxygen and kinetic current density (J_k) at different rotation speed. K-L plot is between the reciprocal current densities (1/J) against the reciprocal root of the angular rotation rate ($\omega^{-1/2}$). The number of electrons transferred (n) was calculated from the slopes (B) of the K-L equation[73] (equation V.4 and V.5) in which J, J_K, and J_L are the measured current density, the kinetic current density, and the diffusion-limiting current density, respectively, F is the Faraday constant (96485 C mol^{-1}), D_0 is the diffusion coefficient (1.9 X 10^{-5} cm^2 s^{-1}) C_0 is the bulk concentration (1.2 x 10^{-6} mol cm^{-3}) of O_2 and ν is the kinetic viscosity (0.01 cm^2 s^{-1}) of an electrolyte 0.1 M KOH. Similarly, the D_0, C_0 and ν of O_2 at 1.0 M KOH is 7.8 x10^{-4} cm^2 s^{-1} 1.8 x 10^{-5} mol cm^{-3} and 0.01 cm^2 s^{-1} respectively.

$$\frac{1}{J} = \frac{1}{J_K} + \frac{1}{J_L} = \frac{1}{J_K} + \frac{1}{B\omega^{1/2}} \qquad \text{..... V.4}$$

$$\boldsymbol{B = 0.62nFC_0(D_0)^{2/3}(\nu)^{-1/6}} \qquad \text{..... V.5}$$

The K-L plot derived from the RDE experiment were shown in figure V.15a-b where excellent linear relationship was exhibited in both PSKU-1 and PSKU-2. The slopes are approximately constant over the range of potential that indicates the first-order reaction kinetics.[74] Furthermore, the kinetic current J_k calculated from the intercept and the values of 4.65 and 11.68 mA cm^{-2} at 0.6 V *vs* RHE was obtained for PSKU-1 and PSKU-2 respectively. The electron transfer number (n) calculated from the slope of the fitted linear line using equation V.5 was found to be 3.7 and 3.9 for PSKU-1 and PSKU-2 respectively indicating 4-electron process towards oxygen reduction.

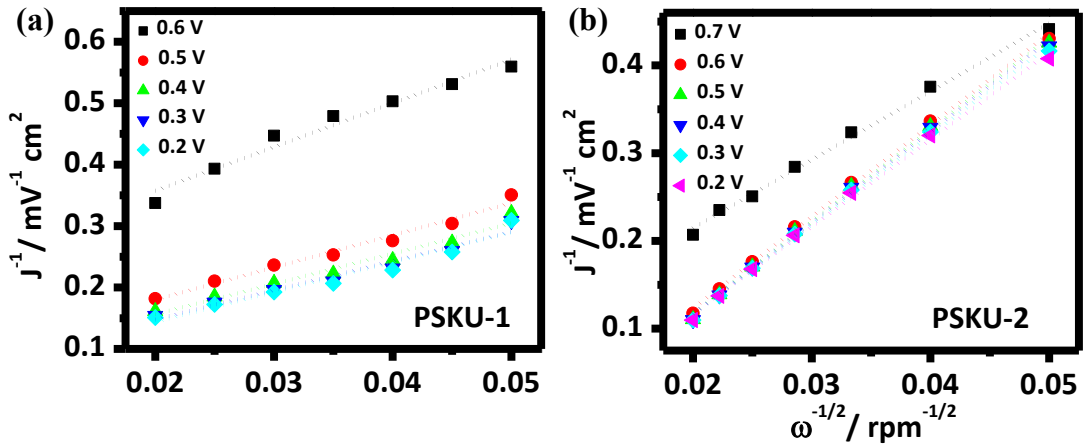

Figure V.15: K-L plot of (a) PSKU-1 and (b) PSKU-2 derived from respective LSV plot.

To further confirm the 4-electron process and to estimate the percentage of H_2O_2 formed, rotating ring disk electrode (RRDE) experiments were performed. RRDE measurements were recorded by scanning the disk electrode cathodically at a scan rate of 10 mV s^{-1} at 1600 rpm. The electron transfer number (*n*) was determined by the following equation:

$$n = \frac{4I_D}{I_D + \frac{I_R}{N}} \qquad \text{..... V.6}$$

where I_D is the disk current, I_R is the ring current and N = 0.37, the current collection efficiency of the Pt ring. The peroxide percentage (% HO^{2-}) was calculated based on the equation:

$$\% HO_2^- = 200 \times \frac{\frac{I_R}{N}}{I_D + \frac{I_R}{N}} \qquad \text{.....V.7}$$

Negligible anodic ring current (I_r) was observed during RRDE experiments for the ORR and an estimation (equation V.7) for H_2O_2% was accounted to be 5.14% and 4.12% for PSKU-1 and PSKU-2 respectively. From the RRDE data, the obtained graphs for both PSKU-1 and PSKU-2 is shown in figure V.16a-b. The value of I_R and I_D was taken at a potential at 0.35 V *vs* RHE and on calculation the number of electrons

(equation V.8) was found to 3.89 and 3.82 for PSKU-1 and PSKU-2 respectively. The number of electrons calculated through RRDE experiments are also in good agreement with the values from the K-L plot (Figure V.15a-b). The experimental results are further in good agreement with the previous reports of α-Mn_2O_3 towards ORR.[25,60,75]

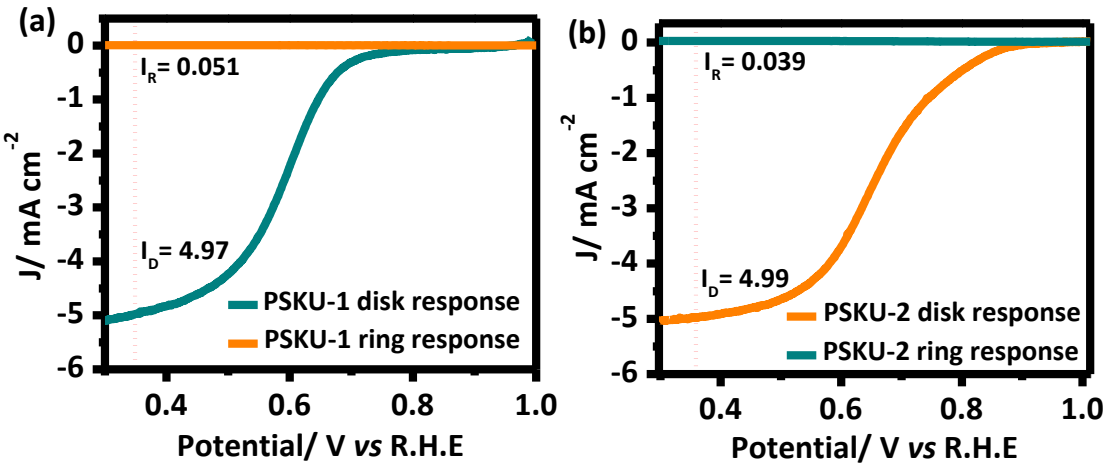

Figure V.16: RRDE response from risk and disk electrode for ORR at 1600 rpm and a scan rate of 10 mV s^{-1} catalyzed by (a) PSKU-1 and (b) PSKU-2.

The electrocatalytic stability of **PSKU-1** and **PSKU-2** was investigated with control potential electrolysis (CPE) measurements in O_2 saturated 0.1 M KOH solution (Figure V.17a). The *I-T* plot shows that **PSKU-2** retains 90% of its current after 10 h of continuous reduction process and fairs better than **PSKU-1** and 20% Pt/C. The PXRD performed for **PSKU-2** after the electrochemical ORR shows no extra peaks other than the peak for α–Mn_2O_3 peaks confirming the structural integrity of derived composites after electrocatalysis (Figure V.17b). The residual carbon that forms a conformal coating around α-Mn_2O_3 particles prevents the dissolution of the manganese ions in alkaline electrolyte, contributing the ion adsorption/desorption at the electrode interface and increasing catalytic stability.[36]

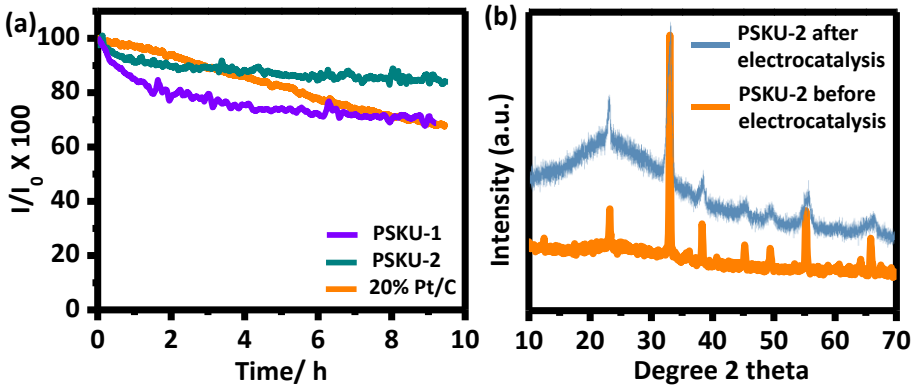

Figure V.17: (a) CPE measurement of PSKU-1, PSKU-2, and 20% Pt/C for stability validation. (b) PXRD of PSKU-2 before and after electrocatalysis.

Furthermore, to rule out the possible deposition of Pt cluster onto the non-precious **PSKU-2** working electrode, measurements were also performed using GC as an auxiliary electrode. A relative comparison of LSV using Pt wire and GC as an auxiliary electrode (Figure V.18) shows that the onset potential and the current densities are the same in both cases. The electrocatalytic activity of **PSKU-2** using GC as auxiliary electrode was efficient even after the 100th cycle, confirming that the ORR activity is purely from the **PSKU-2** working electrode (Figure V.18) and not from Pt-cluster deposition.

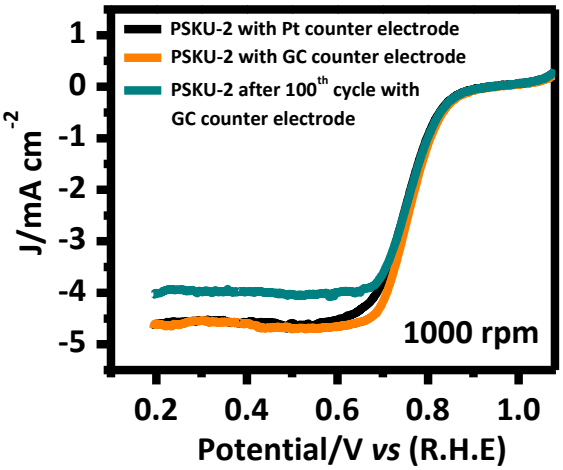

Figure V.18: Comparative LSV plot of PSKU-2 working electrode performed with different counter electrodes. The black plot was obtained with Pt counter electrode, the orange plot with the GC counter electrode, and the dark cyan plot was generated after the 100th cycle using GC as a counter electrode.

After the comprehensive study of Mn-MOFs derived Mn_2O_3 composites towards ORR we applied the catalyst towards anodic OER (oxygen evolution reaction). The efficiency of derived composites towards OER was carried using standard procedure, with 0.1 M and 1 M KOH solution as an electrolyte. However, both PSKU-1 and PSKU-2 could not produce an appreciable result towards OER. Therefore, to validate the efficiency of MOF derived composites towards OER, we begin to develop other metal containing MOF derived composites that can have an activity towards both ORR and OER. The oxygen evolution reaction is highly efficient when using electrocatalysts such as RuO_2 and IrO_2.[76] Despite their high productivity, the limited availability and high expense have hindered their widespread use as electrocatalysts. As a result, there has been significant effort in exploring alternative, cost-effective substitutes based on transition metals such as Fe, Ni, Co, and Mo to replace these precious catalysts.[77] The field of developing electrocatalysts for the OER has extensively researched with transition metal-based alternatives, including phosphides, oxides, and sulphides.[78] Oxides, in particular, have gained significant interest due to their malleable structure and high valence state. To enhance their activity, a new generation of catalysts more focused on a synergistic approach among specific solid materials, exploiting their mutual co-action. By combining different phases, these strategies based on synergistic effects further may uncover the potential of transition metal oxide-based electrocatalysts. Transition metals, including MnO_2, Co_3O_4, and NiO have gained attention as substitutes for noble metal-based electrocatalysts as oxygen electrocatalysts for both the OER and ORR. Research by Zhuang *et al.* has shown that transition metal oxides exhibit varying OER activity, with NiOx demonstrating the highest activity, followed by NiO_x>CoO_x>FeO_x>MnO_x, making NiOx an excellent candidate for electrocatalysis.[79] Despite the promising potential of individual metallic oxides for

ORR/OER, most of them only meet a few performance parameters and fail to satisfy the overall performance criteria. Furthermore, the electronic conductivity of these oxides is generally inadequate, presenting a significant challenge in achieving high electrocatalytic activity. MOF derived metal oxide were reported to possess improved conductivity due to presence of embedded graphitized carbon. Therefore, with an effort to develop efficient bifunctional catalyst for ORR & OER, Ni/NiO composites was derived from Ni-MOF and its activity as bifunctional catalyst was evaluated thoroughly.

V.2.4. Ni-MOF (Ni-SKU-3) derived Ni/NiO towards Bifunctional oxygen process:

The focus on current fuel cell research is on the quest for new alternative materials for highly-efficient, cost effective and durable fuel cells to replace the costly platinum based catalysts.[76,78,80,81]Current trends highlights the use of polymeric crystalline materials including metal organic framework (MOF) acquired through carbonization to decomposed 'left over' residues as easily accessed source for precursor metal nanoparticles, metal oxides and carbonthat are emerging as functional materials for catalysis/energy applications. the use of 2D/1D supramolecular frameworks would allow thermolysis at relatively lower temperatures than the 3D analogue and in turn can gives access to low temperature products.[82] Furthermore, for electrocatalytic oxygen processes, it is known that heteroatom (N, B and P) doped carbon materials show superior electrocatalytic activity.[79] Infact, the presence of carbon-nitrogen structures are also invoked as reaction sites for ORR which outperforms benchmark platinum based catalyst.[84] Due to large charge delocalization as inferred in N-doped graphene (NG), it is also considered as one of the most promising structures for ORR in alkaline solution.[85] Underlying the principle of heteroatom doping into composite metal

nanostructures and their use for electroactive materials, weintitated the work by synthesizing supramolecular Ni based nitrogen rich 1-D coordination polymer. This was used as a precursor to design new Ni based structured nanoporous composites *via* carbonization with hetero atom doping that can be further applied as electrocatalyst towards ORR and OER.

VI.2.5. Synthesis and characterization of Ni-MOF derived Ni/NiO composites:

The reaction of $NiCl_2.6H_2O$, 1,4-benzenedicarboxylic acid (BDC) and 2-methylimidazole (MeIM) in DMF/EtOH at 100ºC for 24 h produces air stable green crystalline 1-D polymeric complex with emperical formula $[Ni(BDC)(MeIM)_2]_n$ and it was designated as Ni-SKU-5 where SKU is abbreviated to *Sikkim University*. The Ni-SKU-5 is isologus to Cu-1D and Cu-SKU-4 MOF where the MOF grows strictly in one dimension. The PXRD of Ni-SKU-5 at increasing temperature reveals that at temperature above 250ºC the evolution of highly crystalline phase takes place. Therefore, carbonization of Ni-SKU-5 at 450ºC for 3h under N_2 was undertaken that yielded a black coloured composite. The PXRD performed for the derived composites shows peaks that can be assigned *fcc* Ni (JCPDS 04-0850) and NiO(JCPDS 78-0423). Figure V.19). No additional peaks were observed apart from the peaks of *fcc* Ni and NiO. Rietveld refinement of derived Ni/NiO composites reveals that the composite is composed of 52% each of *fcc* Ni (JCPDS 04-0850) and 48% NiO (JCPDS 78-0423).

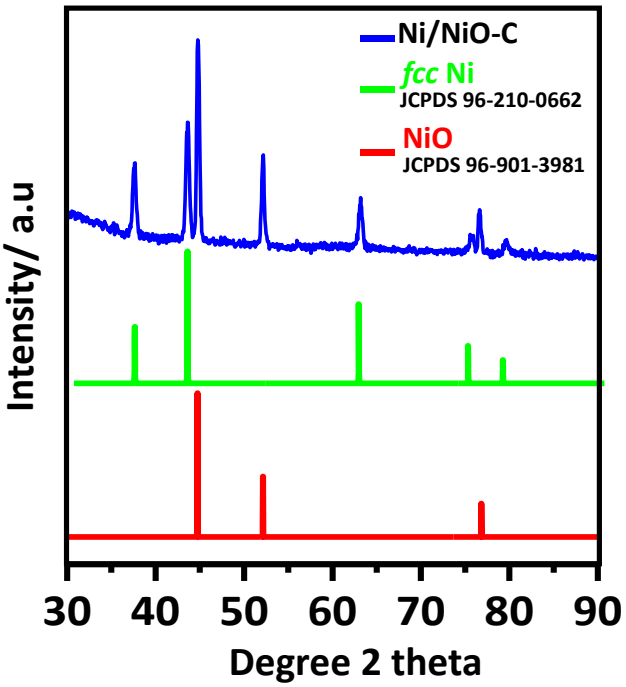

Figure V.19. PXRD of Ni-SKU-5 derived composites(top, blue line) is shown against literature reported for *fcc* Ni and NiO (green & red line).

The (FT-IR) analysis conducted on the derived samples revealed stretching peaks at 610 cm^{-1}, which can be attributed to the stretching frequencies of the Ni-O bond (Figure V.20a). This is further confirmed through Raman spectra, where the Raman bands around 517 cm^{-1} is ascribed due to the one-phonon (1-LO mode) excitations with a vibrational origin (Figure V.20b). Further as reported by Crouéet[86] *et. al.* the presence of lattice and surface defects in nanosized NiO causes one-phonon excitations to be more prominent as compared to a single crystal.[87] The presence of a peak at approximately 1339 cm^{-1} in the Raman spectra may be linked to carbon with a high defect density, which forms due to the charring of organic ligands present in MOF under high temperature.[53] Futhermore, the gas adsorption analysis show that the Ni/NiO composites is porous with BET surface area of 103 $m^2\ g^{-1}$, relatively much higher than Ni-SKU-5 (36.6 $m^2\ g^{-1}$) MOF. Therefore, the composites formed can be illustrated as Ni/NiO embedded on porous carbon.

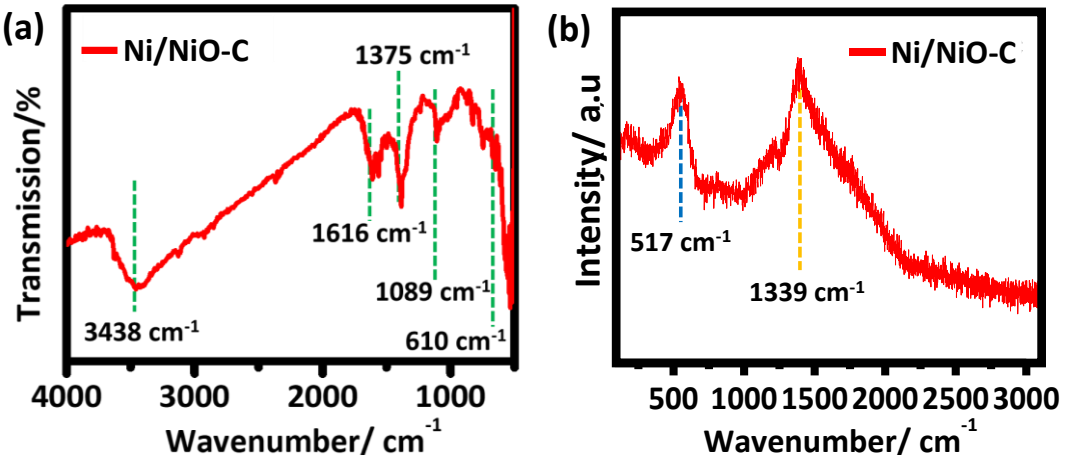

Figure V.20: (a) FT-IR spectra of Ni/NiO-C performed using KBr pellet. (b) Raman spectra of Ni/NiO-C.

The morphology of derived Ni/NiO-C composites was visualized with scaning electron microscopic (SEM) technique. The SEM images shows that the Ni/NiO-composites have the hexagonal shaped morphology (Figure V.21a-b). Furthermore, high-resolution TEM (HRTEM) images (figure V.21c-d) confirmed the existence of two crystalline phases ofNi and NiO. Lattice fringes with interplanar distances of approximately 1.91 and 1.78 Å were observed for the NiO (132) and *fcc* Ni (020) facets, respectively, providing additional evidence of the emergence of the Ni/NiO-C phase of the derived composites (Figure V.21e). The SAED pattern was found to be brightly dotted ring indicating the Ni/NiO-C to be crystalline in nature (Figure V.21f) which is in agreement with the PXRD pattern (Figure V.19a). Furthermore, the calculated *d*-spacing from SAED is indexed with (222), (333), (264) planes of NiO and (222), (040) planes of *fcc* Ni.

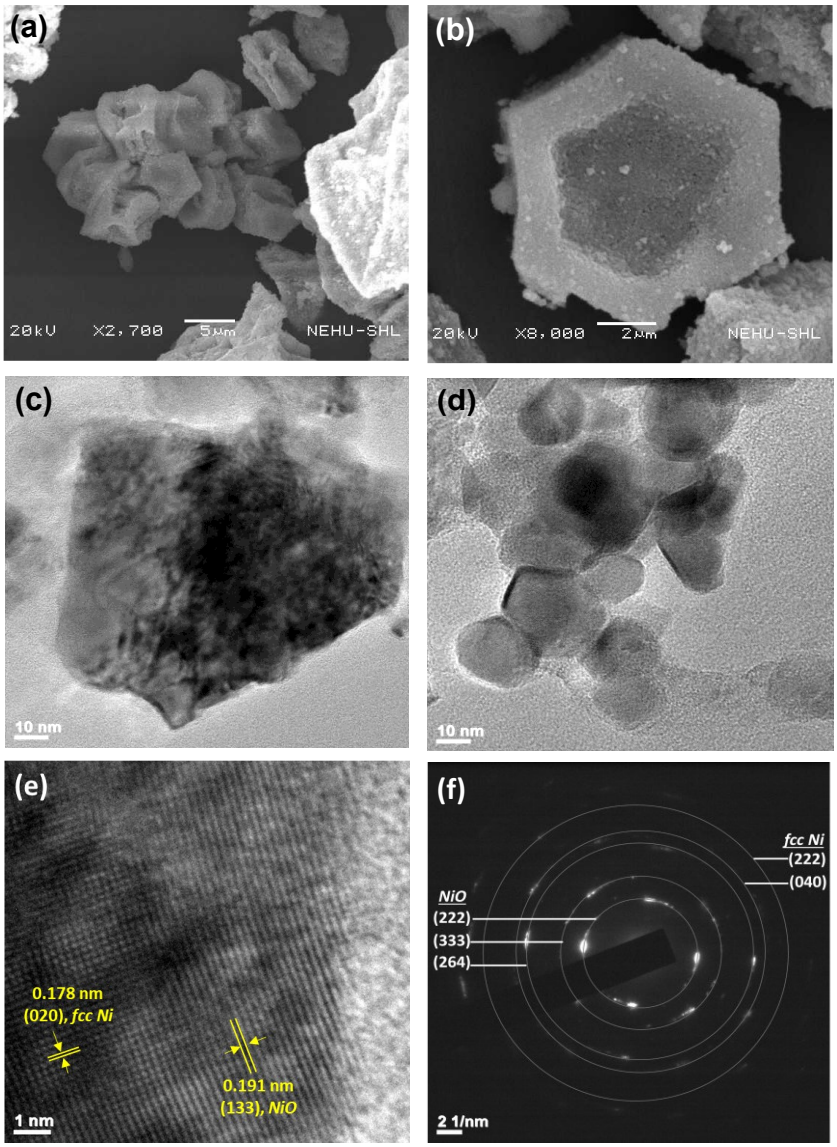

Figure V.21: (a)-(b) SEM images of Ni/NiO-C (c)-(d) TEM images of Ni/NiO-C. (e) HRTEM images and (f) SAED images of Ni/NiO-C interpreted as per *d*-spacing values of *fcc*-Ni and NiO.

The composition of derived composites was further carried out with EDX analysis. The EDX plot of derived Ni/NiO by shows a peaks of Ni, O, and C (Figure V.22) and the respective atom% and weight% is provided in table V.3. No crystalline carbon signature was observed in the PXRD of Ni/NiO (Figure V.19a), indicating that the products are composites of crystalline Ni/NiO and amorphous carbon. Therefore, the derived Ni-composites from Ni-SKU-5 MOF has been abbreviated as Ni/NiO-C hereafter.

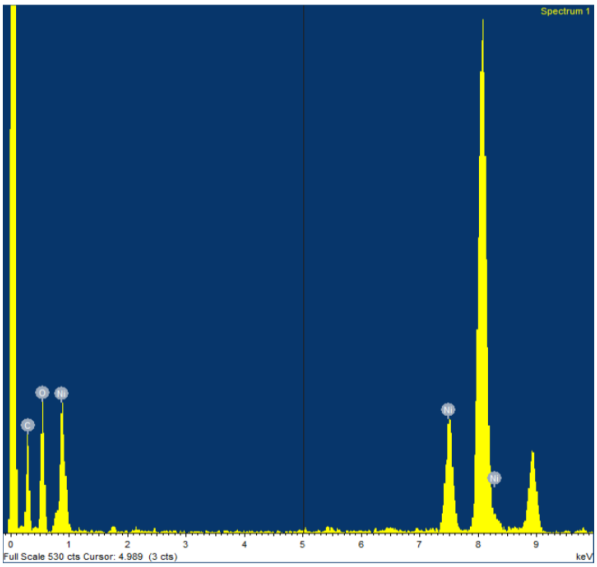

Figure V.22: EDX spectra of Ni/NiO-C.

Table V.3: Summarized weight% and atomic% of Ni, O and C obtained after EDX analysis of Ni/NiO-C.

	Ni/NiO-C	
Element	**Weight%**	**Atomic%**
Ni	63.63	29.17
O	19.12	32.16
C	17.25	38.66
Total	100	

V.2.6. Bifunctional electro-catalyst for oxygen catalysis with Ni/NiO-C:

The electro-catalytic activity of Ni/NiO-C composite was investigated for oxygen reduction reaction (ORR) by drop casting Ni/NiO-C on the surface of freshly polished glassy carbon (GC) electrode following similar procedure as that followed for PSKU-1 and PSKU-2. Typically 20 µL of 5 mg of Ni/NiO-C suspended in 1 mL EtOH along with 10 µL 20 Nafion solution was sonicated for 1 hr to form a homogeneous ink that was drop casted on GC electrode (surface area = 0.196 cm^2). All the experiments were

conducted with 0.1 M KOH as an electrolyte and it was bubbled with N_2 or O_2 for 30 min to ensure N_2/ O_2 saturation before performing ORR measurements. The cyclic voltammetry (CV) of GC coated Ni/NiO in oxygen saturated 1.0 M KOH solution recorded with scan rate of 10 mV s^{-1} show ORR at 0.68V *vs* RHE (Figure V.23). Corresponding CV under N_2 saturated condition shows no reduction peak at negative potential, clearly showing the redox event at 0.68 V to oxygen reduction.

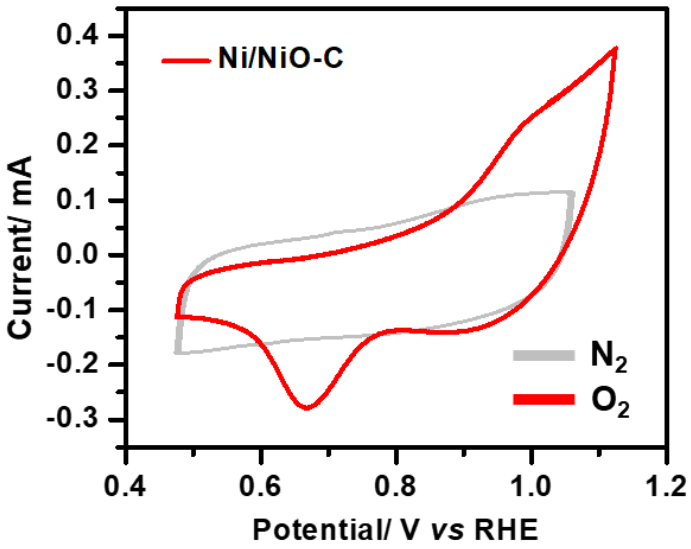

Figure V.23: CV of Ni/NiO-C performed in O_2 and N_2 saturated 1.0 M KOH at scan rate of 10 mV s^{-1}.

The LSV using rotating disc electrode (RDE) for GC coated Ni/NiO in O_2 saturated 1.0 M KOH solution shows linear increase in current density with the increase in rotation speed (Figure V.24b) and the onset potential was measured to be 0.93 V *vs* RHE. The K-L plots (J^{-1} *vs* $\omega^{-1/2}$) (Figure V.24) show linear parallel fitted lines with identical slopes at potentials between 0.7 to 0.3 V indicating first order reaction kinetics with respect to O_2 concentration and a singular electron transfer event in all the potential range.[88] The electron transfer number (n) derived using K-Lplot (equation V.7) was found to be n = 3.6 at 0.6 V suggesting a dominant $4e^-$ pathway for the ORR electrocatalyzed by Ni/NiO-C similar to that of PSKU-1 and PSKU-2.

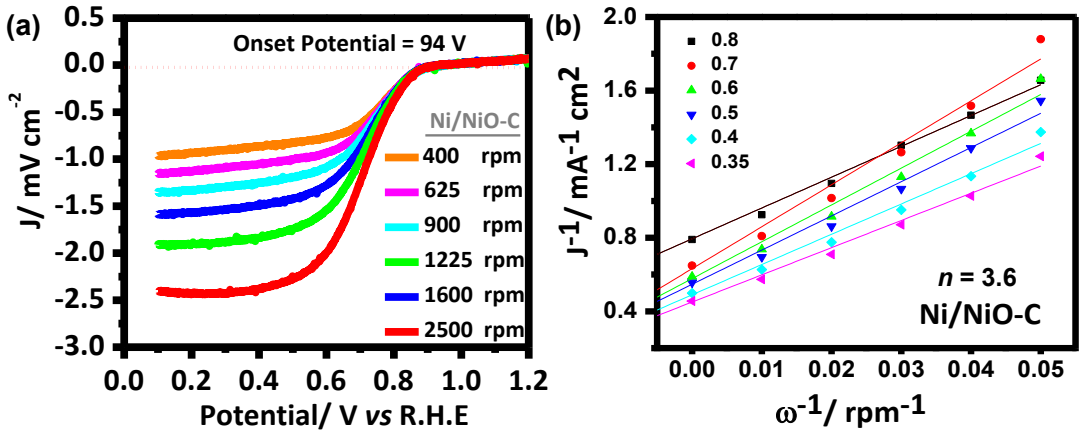

Figure V.24: (a) LSV plot of Ni/NiO-C performed at different rotaion speed in O_2 saturated 1.0 M KOH with scan rate of 10 mV s^{-1}. (b) K-L plot of Ni/NiO-C derived from RDE, LSV plot.

For comparison, ORR activity for GC coated Ni/NiO-C, 20% Pt/C and bare GC were measured under identical condition (Figure V.25). The current density at 0.5 V (with rotating speed of 1600 rpm) for GC coated Ni/NiO-C, bare GC and 20% Pt/C was 2.4, 1.0 and 4.21 mA cm^{-2} respectively. The $E_{1/2}$ calculated for Ni/NiO-C and 20% Pt/C was found to be 0.75 and 0.80 V vs RHE that accounts for the overpotential of 0.48 and 0.43 V respectively.

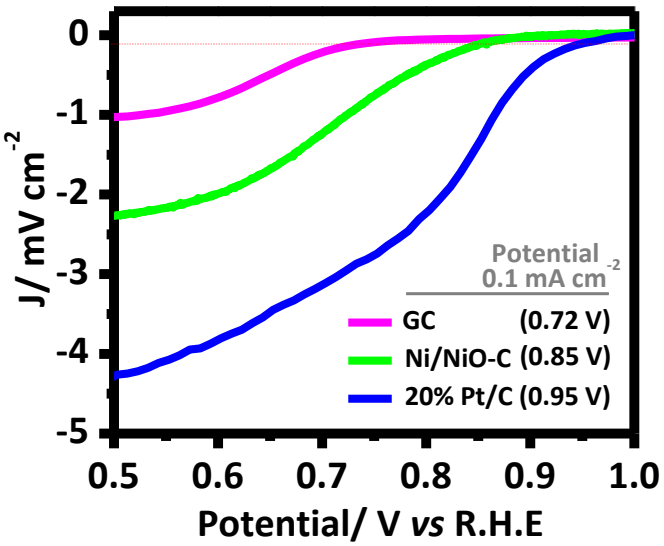

Figure V.25: (a) Comparative LSV plot of GC, Ni/NiO-C and 20% Pt/C in O_2 saturated 1.0 M KOH solution at a scan rate of 10 mV s^{-1} and 1600 rpm.

The electroactive nature of composites with imrpoved condutivity, can be attributed to the presence of *in-situ* carbon produced during pyrolysis of MOF. The kinetic parameter for Ni/NiO-C catalyst measured using K-L plot are found to be better than Pt/C with calculated J_K value of 5.8 mA cm^{-2} at 0.6 V much higher than that of commercially available Pt/C-GC (4.4 mA cm^{-2} at 0.6 V) modified electrode.[88] However, the Tafel slope (FigureV.26a) measured at low overpotential for Ni/NiO-C was found to be -84.4 mV decade-1 slightly higher than Pt/C catalyzed ORR (-60 mV $decade^{-1}$). The stability of Ni/NiO-C catalysts was studied using CPE measurements in an oxygen-saturated 1 M KOH solution (Figure V.26b). The current-time plot indicates that after 10 hours of continuous reduction process, Ni/NiO-C retained 90% of its current and exhibited better stability 20% Pt/C.

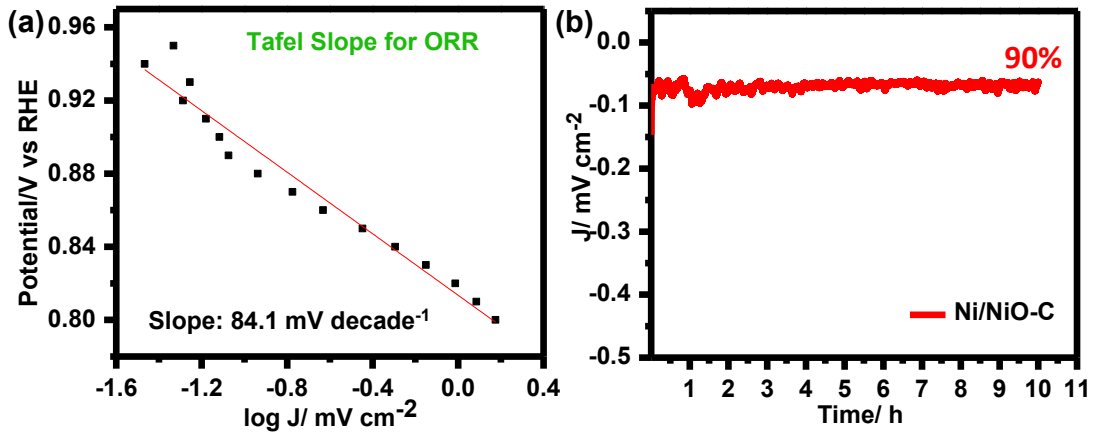

Figure V.26: (a) Tafel plot for **Ni/NiO-C**, at a rotation speed of 1600 rpm. (b) CPE measurement of **Ni/NiO-C** for stability validation.

Next, the bifunctional characteristics of derived Ni/NiO-C composite was studied by performing OER. The ability of Ni/NiO-C towards the OER was assessed in an alkaline environment (1.0 M KOH), with a Pt wire as a counter electrode, Ag/AgCl (saturated KCl filled) as the reference electrode and Ni/NiO-C modified GC electrode as a working electrode with the mass loading of 1.43 mg cm^{-2}. All the measurements were

conducted at 25 °C in 1 M KOH saturated with N_2, and scan rate was set to 10 mV s^{-1}. The LSV performed under above mentioned condition shows the characteristic Ni^0/Ni^{II} redox event at more positive potential of 1.4 V (Figure V.27a). Interestingly, the generation of large anodic current was noticed at potential above 1.45V, indicating oxygen evolution process and thereby demonstrating the bifunctional nature of the derived Ni/NiO-C composites. The potential $E_{j=10\ mA\ cm^2}$ (potential required to achieve a current density of 10 $mAcm^{-2}$) is indicative of a solar water-splitting device with 10% efficiency and is often used as a standard to measure OER activity of catalyst.[89,90] For the derived Ni/NiO-C composites, the potential required to achieve a $E_{j=10\ mA\ cm^2}$ is close to 1.60 V which is similar to that of IrO_2 (1.58 V) and better than RuO_2 (1.64 V) and 20% Pt/C (1.66 V) (Figure V.27). These values further acoount an overpotential of 370 mV for Ni/NiO-C composites and 430 mV for Pt/C, indicating superior electrocatalytic activity of Ni/NiO-C composites for OER.

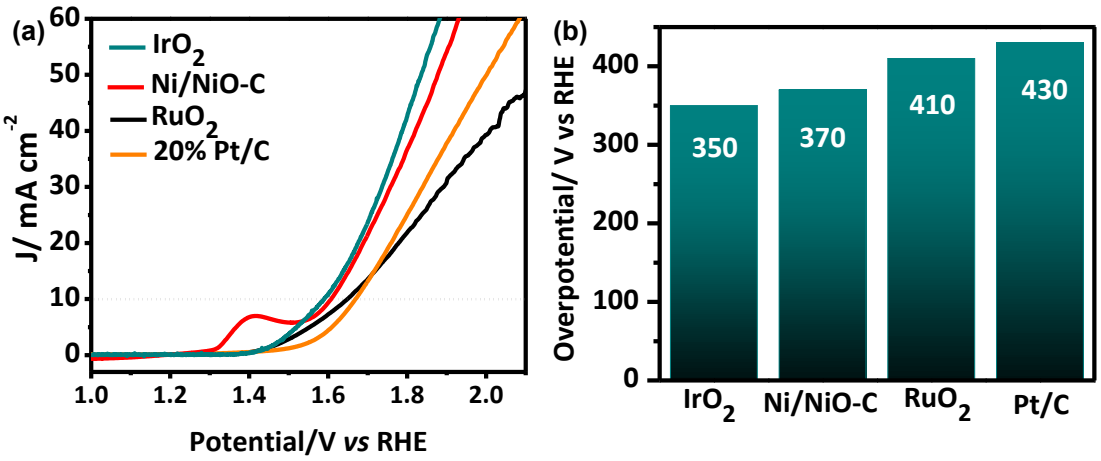

Figure V.27: (a) OER activity of Ni/NiO-C, IrO_2, RuO_2 & 20% Pt/C. (b) Relative comparison of overpotential for Ni/NiO-C, IrO2, RuO2 & 20% Pt/C.

While platinum (Pt) displays a superior ORR activity compared to **Ni/NiO-C** (Figure V.14a), as evidenced by its more positive $E_{1/2}$ value, its OER activity is relatively inferior, as indicated by its higher overpotential of about 430 mV. It is to be noted that

to assess the bifunctional catalytic activity of materials, researchers often evaluate the potential difference between $E_{j=10\ mA\ cm^2}$ from OER and $E_{1/2\ overpotential}$ from ORR activity.[81] A smaller potential difference typically indicates a superior bifunctional performance of material. The potential difference of ~850 mV was accounted for **Ni/NiO-C** whereas for 20% Pt/C the value is 860 mV. Furthermore, the Tafel plot for Ni/NiO-C towards OER was calucated to be 93.08 mV dec^{-1} (Figure V.28). Likewise Liu *et al.* reported the tafel slope of 178, 71 and 62 mV dec^{-1} with NiO, Ni/NiO and porous Ni/NiO electrocatalyst respectively synthesized by encapsulating Ni nanoparticles into mesoporous NiO nanosheets.[77] Similarly Ni@NiO/NeC NW,[91] and NieNiO@3DHPG[92] has a Tafel slope of 100 and 55 mV dec^{-1} respectively. Hence, it can be noted that the Tafel value of Ni-SKU-5 MOF derived Ni/NiO-C is similar to that of the aforementioned composites.

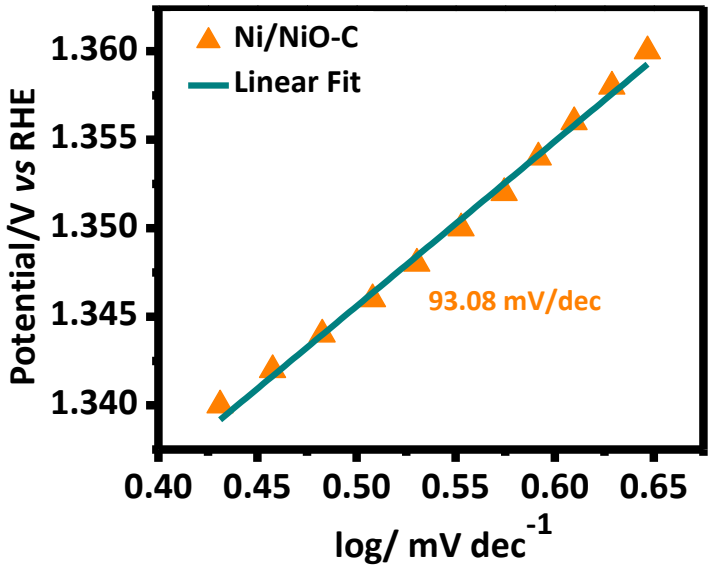

Figure V.28: Tafel slope for Ni-SKU-5 derived Ni/NiO-C catalyzed OER.

The performance of Ni/NiO-C catalyst was compared with the previously reported Ni-based composites towards oxygen process and given in table V.4. The overall performance of Ni-SKU-5 derived Ni/NiO-C electrocatalyst towards oxygen process

was found comparable to previously reported NiO-based electrocatalyst and some state-of art catalyst.

Table V.4: Comparison of Ni-SKU-5 derived Ni/NiO-C electrocatalyst towards ORR and OER with various previously reported Ni-composites electrocatalyst.

Entry	ORR ($E_{1/2}$/V *vs* R.H.E)	OER (E@10mA cm^{-2})	$E_{overall} = E_{OER}-E_{ORR}$	Ref
NiO	0.72	1.69	0.97	77
Ni/NiO	0.74	1.53	0.79	
Porous Ni/NiO	0.75	1.49	0.74	
Pt/C	0.82	1.86	1.04	93
20% Ir/C	0.69	1.61	0.92	94
20%Ru/C	0.61	1.62	1.01	
NiO/CoN	0.68	1.53	0.85	95
$NiCo_2O_4$/C	0.54	1.67	1.13	96
Ni/NiO-C	0.75	1.60	0.85	Our work

The exceptional electrocatalytic capabilities of the porous Ni/NiO-C composite can be attributed to a combination of factors, including the synergistic effects between the metallic Ni core, the interface between Ni and NiO, O-defects in NiO, the *in-situ* carbon and the mesoporous structure. The metallic Ni nanoparticles and O-deficiencies in NiO work together to enhance charge transport in the OER/ORR processes, while the conductive electrons can easily move between the two phases due to electron accumulation at the interface, which in turn enhances the OER/ORR activity of the catalyst.[81] Additionally, the presence of *in-situ* carbon enhanches the conductivity of almost insulator natured metal oxide and the mesoporous structure of the derive composite increases the number of exposed active sites, thereby boosting their electrochemical activity. Overall, the Ni-SKU-5 MOF derived Ni/NiO-C composites demonstrate superior bifunctional activity towards oxygen process (Figure V.29).

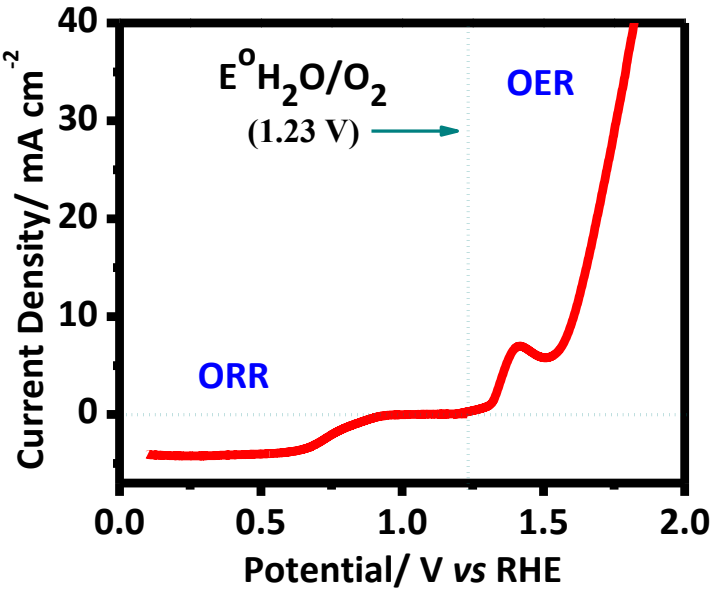

Figure V.29: Bifunctional activity of MOF-derved Ni/NiO-C catalyst towards ORR and OER.

V.3. Conclusion:

In summary two Mn-based MOFs *viz*. Mn-SKU-1 & 3D→3D interpenetrated Mn-SKU-2 were synthesized and thereby post-synthetically modified *via* pyrolysis at 600 °C under N_2 atmosphere. The derived composites were characterized using PXRD, FT-IR, Raman, SEM, TEM, EDX, BET surface area analysis etc and formation of porous α-Mn_2O_3/C composites (PSKU-1 and PSKU-2) was confirmed. The PSKU-2 exhibited a BET surface area of PSKU-1 and PSKU-2 was found to be 90.8 and 179.3 m^2g^{-1}, respectively. The observed increase in porosity of PSKU-2 can be attributed to the presence of a unique interpenetrating network in the MOF precursor. The study investigated the efficacy of the derived composites as an electrocatalyst for ORR and compared it with the standard 20%Pt/C. The study compared the reactivity of the α-Mn_2O_3 composite derived from Mn-SKU-1, which lacks interpenetrating networks. The results showed that the interpenetrating network plays a decisive role in catalytic activity of PSKU-2 compared to PSKU-1 in terms of onset potential (0.93 V

for PSKU-2 and 0.90 V for PSKU-1) and current density (6.0 mA cm^{-2} for PSKU-2 and 4.8 mA cm^{-2} for PSKU-1). Also, PSKU-2 was found to have comparable ORR performance to the state-of-the-art 20% Pt/C under identical conditions. Its onset potential was measured at 0.96 V with a current density of 6.52 mA cm^{-2}. RDE/RRDE measurements also showed that PSKU-2 primarily underwent a four-electron process with negligible formation of H_2O_2. After 10 h of continuous oxygen reduction, PSKU-2 was found to retain the 90% of current which is higher than that of PSKU-1 and Pt/C. The high porosity, abundance of Mn active sites, and the presence of conformal conducting carbon in PSKU-2 makes it a highly desirable electrocatalyst for ORR. This is evident from the stability results, overpotential value, and kinetic parameters, all of which demonstrate the excellent performance of PSKU-2.

In addition, Ni/NiO-C composite has also been synthesized using Ni-SKU-5 under N_2 atmosphere at 450 ºC. The Ni/NiO-C composite was comprehensively characterized by elemental analysis, XRD, XPS, TEM, Raman and surface area analysis.The composites show excellent electrocatalytic ORR as well as OER activity in 1M KOH solution showing bifunctional attributes strongly augmented by conformal hybrid structure and porous framework. With the $E_{1/2}$ overpotential of 480 mV towards ORR and $E_{j=10\ mA\ cm^2}$ overpotential of 370 mV followed by a Tafel slope of 93.03 mV dec^{-1} towards OER, the bifuntional overpotential of Ni/NiO-C compoiste was found to be 850 mv which is similar to the state-of-art-the-catalyst Pt/C with 860 mV.

V.4. Experimental Section:

V.4.1. Materials:

20% Pt/C, IrO_2, RuO_2, Vulcan carbon 72X and 5% Nafion solution, were purchased from Sigma Aldrich. KOH and Ethanol were purchased from Merck. Double distilled water was used during all electrochemical experiments. All the chemicals and reagents were used without any further purification.

V.4.2. Physical Methods:

Powder X-ray diffraction (PXRD) was performed using PANalytical X'Pert Pro diffractometer with Cu Kα radiation (1.56 Å). Elemental analysis was conducted using Eurovector EA 3000 elemental analyzer. FT-IR spectra were collected using Bruker Alpha spectrometer over 400-4000 cm^{-1}. N_2 adsorption isotherm experiments were performed on Quantachrome NOVA Touch LX^2 instrument at 77 K. Pyrolysis of MOF was carried out using Noberterm B180 tube furnace fitted with a customized quartz tube and the samples were placed on an alumina boat. SEM images and EDX were recorded on JSM-6360 Scanning Electron Microscope. Ultrasonication machine from LABMAN was used to prepare the homogenous ink for dropcasting. Micropipette of 10 µL, 200 µL and 1000 µL was used from Tarson. For solvent drying purpose, a rota-evaporator from Heildolph was used. For heating and stiring purpose, magnetic stirrer from IKA was used. Cyclic Voltammograms were recorded using BASi epsilon. The GC, Ag/AgCl and Pt-wire electrode was used as received from Basi epsilon. RDE and RRDE measurement was performed with RRDE-3A Version 2.0 apparatus. TEM images were obtained on FEI Tecnai F20 and Tecnai Osiris TEM operating at 200 kV. Raman spectroscopy was performed in Lab RAM Aramis Horiba Jobin Yvom spectrometer using HeNe laser with 30 sec exposure time.

V.5. Reference:

(1) Hubbert, M. K. Energy from Fossil Fuels. *Science* **1949**, *109*, 103–109.

(2) Khalate, S. A.; Kate, R. S.; Deokate, R. J. A Review on Energy Economics and the Recent Research and Development in Energy and the Cu_2ZnSnS_4 (CZTS) Solar Cells: A Focus towards Efficiency. *Sol. Energy* **2018**, *169*, 616–633.

(3) Blakers, A.; Stocks, M.; Lu, B.; Cheng, C. A Review of Pumped Hydro Energy Storage. *Prog. Energy* **2021**, *3*, 022003.

(4) Bosch, J.; Staffell, I.; Hawkes, A. D. Temporally Explicit and Spatially Resolved Global Offshore Wind Energy Potentials. *Energy* **2018**, *163*, 766–781.

(5) Neill, S. P.; Angeloudis, A.; Robins, P. E.; Walkington, I.; Ward, S. L.; Masters, I.; Lewis, M. J.; Piano, M.; Avdis, A.; Piggott, M. D.; Aggidis, G.; Evans, P.; Adcock, T. A. A.; Židonis, A.; Ahmadian, R.; Falconer, R. Tidal Range Energy Resource and Optimization – Past Perspectives and Future Challenges. *Renew. Energy* **2018**, *127*, 763–778.

(6) Pandey, S. N.; Vishal, V.; Chaudhuri, A. Geothermal Reservoir Modeling in a Coupled Thermo-Hydro-Mechanical-Chemical Approach: A Review. *Earth-Science Rev.* **2018**, *185*, 1157–1169.

(7) Gong, J.; Li, C.; Wasielewski, M. R. Advances in Solar Energy Conversion. *Chem. Soc. Rev.* **2019**, *48*, 1862–1864.

(8) Carrillo, A. J.; González-Aguilar, J.; Romero, M.; Coronado, J. M. Solar Energy on Demand: A Review on High Temperature Thermochemical Heat Storage Systems and Materials. *Chem. Rev.* **2019**, *119*, 4777–4816.

(9) Pourrahmani, H.; Yavarinasab, A.; Siavashi, M.; Matian, M.; Van herle, J. Progress in the Proton Exchange Membrane Fuel Cells (PEMFCs) Water/Thermal Management: From Theory to the Current Challenges and Real-Time Fault Diagnosis Methods. *Energy Rev.* **2022**, *1*, 100002.

(10) Fan, L.; Tu, Z.; Chan, S. H. Recent Development of Hydrogen and Fuel Cell Technologies: A Review. *Energy Reports* **2021**, *7*, 8421–8446.

(11) Rozelle, G. J. Young, R. B. R. Fuel Cell. *J. Chem. Educ* **1959**, *36*, 68–73.

(12) Song, J.; Wei, C.; Huang, Z. F.; Liu, C.; Zeng, L.; Wang, X.; Xu, Z. J. A Review on Fundamentals for Designing Oxygen Evolution Electrocatalysts. *Chem. Soc. Rev.* **2020**, *49*, 2196–2214.

(13) Janek, J.; Zeier, W. G. A Solid Future for Battery Development. *Nat. Energy* **2016**, *1*, 1–4.

(14) Head, J. Relative To the Crater Diameter Is Verv Tvoical. *Science* **1994**, *264*, 1–4.

(15) Yoshino, A. The Birth of the Lithium-Ion Battery. *Angew. Chemie - Int. Ed.* **2012**, *51*, 5798–5800.

(16) Li, Y.; Lu, J. Metal-Air Batteries: Will They Be the Future Electrochemical Energy Storage Device of Choice? *ACS Energy Lett.* **2017**, *2*, 1370–1377.

(17) Wang, C.; Yu, Y.; Niu, J.; Liu, Y.; Bridges, D.; Liu, X.; Pooran, J.; Zhang, Y.; Hu, A. Recent Progress of Metal-Air Batteries-A Mini Review. *Appl. Sci.* **2019**,

9, 1–22.

(18) Wei, C.; Rao, R. R.; Peng, J.; Huang, B.; Stephens, I. E. L.; Risch, M.; Xu, Z. J.; Shao-Horn, Y. Recommended Practices and Benchmark Activity for Hydrogen and Oxygen Electrocatalysis in Water Splitting and Fuel Cells. *Adv. Mater.* **2019**, *31*, 1–24.

(19) Chen, Z.; Higgins, D.; Yu, A.; Zhang, L.; Zhang, J. A Review on Non-Precious Metal Electrocatalysts for PEM Fuel Cells. *Energy Environ. Sci.* **2011**, *4*, 3167–3192.

(20) Osgood, H.; Devaguptapu, S. V.; Xu, H.; Cho, J.; Wu, G. Transition Metal (Fe, Co, Ni, and Mn) Oxides for Oxygen Reduction and Evolution Bifunctional Catalysts in Alkaline Media. *Nano Today* **2016**, *11*, 601–625.

(21) Peera, S. G.; Lee, T. G.; Sahu, A. K. Pt-Rare Earth Metal Alloy/Metal Oxide Catalysts for Oxygen Reduction and Alcohol Oxidation Reactions: An Overview. *Sustain. Energy Fuels* **2019**, *3*, 1866–1891.

(22) Rasool, S. I.; De Bergh, C. © 1970 Nature Publishing Group. *Nat. Publ. Gr.* **1970**, *228*, 726–734.

(23) Wang, Y.; Li, J.; Wei, Z. Transition-Metal-Oxide-Based Catalysts for the Oxygen Reduction Reaction. *J. Mater. Chem. A* **2018**, *6*, 8194–8209.

(24) Li, Q.; Yin, L.; Li, Z.; Wang, X.; Qi, Y.; Ma, J. Copper Doped Hollow Structured Manganese Oxide Mesocrystals with Controlled Phase Structure and Morphology as Anode Materials for Lithium Ion Battery with Improved Electrochemical Performance. *ACS Appl. Mater. Interfaces* **2013**, *5*, 10975–10984.

(25) Fang, Y.; Wang, Y.; Wang, F.; Zhu, J. 3D Structured Mn 2 O 3 Synthesized Using Tween Surfactant: Influence on the Morphology and Oxygen Reduction Catalytic Performance. *CrystEngComm* **2019**, *21*, 420–429.

(26) Guan, B. Y.; Yu, X. Y.; Wu, H. Bin; Lou, X. W. D. Complex Nanostructures from Materials Based on Metal–Organic Frameworks for Electrochemical Energy Storage and Conversion. *Adv. Mater.* **2017**, *29*, 1–20.

(27) Chaikittisilp, W.; Hu, M.; Wang, H.; Huang, H. S.; Fujita, T.; Wu, K. C. W.; Chen, L. C.; Yamauchi, Y.; Ariga, K. Nanoporous Carbons through Direct Carbonization of a Zeolitic Imidazolate Framework for Supercapacitor Electrodes. *Chem. Commun.* **2012**, *48*, 7259–7261.

(28) Liu, B.; Shioyama, H.; Akita, T.; Xu, Q. Metal-Organic Framework as a Template for Porous Carbon Synthesis. *J. Am. Chem. Soc* **2008**, *130*, 5390–5391.

(29) You, S.; Gong, X.; Wang, W.; Qi, D.; Wang, X.; Chen, X.; Ren, N. Enhanced Cathodic Oxygen Reduction and Power Production of Microbial Fuel Cell Based on Noble-Metal-Free Electrocatalyst Derived from Metal-Organic Frameworks. *Adv. Energy Mater.* **2016**, *6*, 1–9.

(30) Torad, N. L.; Hu, M.; Ishihara, S.; Sukegawa, H.; Belik, A. A.; Imura, M.; Ariga, K.; Sakka, Y.; Yamauchi, Y. Direct Synthesis of MOF-Derived Nanoporous Carbon with Magnetic Co Nanoparticles toward Efficient Water Treatment. *Small* **2014**, *10*, 2096–2107.

(31) Li, L.; Tian, T.; Jiang, J.; Ai, L. Hierarchically Porous Co_3O_4 Architectures with Honeycomb-like Structures for Efficient Oxygen Generation from

Electrochemical Water Splitting. *J. Power Sources* **2015**, *294*, 103–111.

(32) Hong, Y.; Wu, M.; Chan, G.; Dai, Z.; Zhang, Y.; Chen, G.; Dong, X. 3D Printed Microfluidic Device with Microporous Mn2O3-Modified Screen Printed Electrode for Real-Time Determination of Heavy Metal Ions. *ACS Appl. Mater. Interfaces* **2016**, *8*, 32940–32947.

(33) Pang, H.; Li, X.; Li, B.; Zhang, Y.; Zhao, Q.; Lai, W. Y.; Huang, W. Porous Dimanganese Trioxide Microflowers Derived from Microcoordinations for Flexible Solid-State Asymmetric Supercapacitors. *Nanoscale* **2016**, *8*, 11689–11697.

(34) Ji, D.; Zhou, H.; Zhang, J.; Dan, Y.; Yang, H.; Yuan, A. Facile Synthesis of a Metal-Organic Framework-Derived Mn2O3 Nanowire Coated Three-Dimensional Graphene Network for High-Performance Free-Standing Supercapacitor Electrodes. *J. Mater. Chem. A* **2016**, *4*, 8283–8290.

(35) Li, S.; Duan, Y.; Teng, Y.; Fan, N.; Huo, Y. MOF-Derived Tremelliform Co_3O_4 /NiO/Mn_2O_3 with Excellent Capacitive Performance. *Appl. Surf. Sci.* **2019**, *478*, 247–254.

(36) Nagamuthu, S.; Ryu, K. S. MOF-Derived Microstructural Interconnected Network Porous Mn_2O_3/C as Negative Electrode Material for Asymmetric Supercapacitor Device. *CrystEngComm* **2019**, *21*, 1442–1451.

(37) Wang, B. R.; Hu, Y.; Pan, Z.; Wang, J. MOF-Derived Manganese Oxide/Carbon Nanocomposites with Raised Capacitance for Stable Asymmetric Supercapacitor. *RSC Adv.* **2020**, *10*, 34403–34412.

(38) Chen, Y.; Yang, R.; Chen, C.; Li, Y.; Wei, M. Construction of Hierarchical Mn_2O_3 Hollow Microspheres Derived from Metal–Organic Frameworks for High Performance Supercapacitors. *J. Power Sources* **2021**, *505*, 230077.

(39) Xie, Z.; Lyu, Z.; Wang, J.; Li, A.; François-Xavier Corvini, P. Ultrafine-Mn_2O_3@N-Doped Porous Carbon Hybrids Derived from Mn-MOFs: Dual-Reaction Centre Catalyst with Singlet Oxygen-Dominant Oxidation Process. *Chem. Eng. J.* **2022**, *429*, 132299.

(40) Gou, L.; Mou, K. L.; Fan, X. Y.; Zhao, M. J.; Wang, Y.; Xue, D.; Li, D. L. Mn_2O_3/ Al_2O_3 Cathode Material Derived from a Metal-Organic Framework with Enhanced Cycling Performance for Aqueous Zinc-Ion Batteries. *Dalt. Trans.* **2020**, *49*, 711–718.

(41) Mao, M.; Wu, X.; Hu, Y.; Yuan, Q.; He, Y. B.; Kang, F. Charge Storage Mechanism of MOF-Derived Mn_2O_3 as High Performance Cathode of Aqueous Zinc-Ion Batteries. *J. Energy Chem.* **2020**, *52*, 277–283.

(42) Liu, C.; Li, Q.; Sun, H.; Wang, Z.; Gong, W.; Cong, S.; Yao, Y.; Zhao, Z. MOF-Derived Vertically Stacked Mn_2O_3@C Flakes for Fiber-Shaped Zinc-Ion Batteries. *J. Mater. Chem. A* **2020**, *8*, 24031–24039.

(43) Maiti, S.; Pramanik, A.; Manju, U.; Mahanty, S. Reversible Lithium Storage in Manganese 1,3,5-Benzenetricarboxylate Metal-Organic Framework with High Capacity and Rate Performance. *ACS Appl. Mater. Interfaces* **2015**, *7*, 16357–16363.

(44) Paquin, F.; Rivnay, J.; Salleo, A.; Stingelin, N.; Silva, C. Multi-Phase Semicrystalline Microstructures Drive Exciton Dissociation in Neat Plastic Semiconductors. *J. Mater. Chem. C* **2015**, *3*, 10715–10722.

(45) Cao, K. Z.; Jiao, L. F.; Xu, H.; Liu, H. Q.; Kang, H. Y.; Zhao, Y.; Liu, Y. C.; Wang, Y. J.; Yuan, H. T. Reconstruction of Mini-Hollow Polyhedron Mn2O3 Derived from Mofs as a High-Performance Lithium Anode Material. *Adv. Sci.* **2015**, *3*, 1–7.

(46) Zheng, F.; Xu, S.; Yin, Z.; Zhang, Y.; Lu, L. Facile Synthesis of MOF-Derived Mn_2O_3 Hollow Microspheres as Anode Materials for Lithium-Ion Batteries. *RSC Adv.* **2016**, *6*, 93532–93538.

(47) Lin, X.; Lin, J.; Deng, H.; Reddy, R. C. K.; Liu, J. Structural Diversity of Zinc(II), Manganese(II), and Gadolinium(III) Coordination Polymers Based on Two Isomeric N-Heteroaromatic Polycarboxylate Ligands: Structures and Their Derived Mn_2O_3 for Lithium Storage Applications. *Inorg. Chem.* **2020**, *59*, 460–471.

(48) Zhang, X.; Li, H.; Hou, F.; Yang, Y.; Dong, H.; Liu, N.; Wang, Y.; Cui, L. Synthesis of Highly Efficient Mn_2O_3 Catalysts for CO Oxidation Derived from Mn-MIL-100. *Appl. Surf. Sci.* **2017**, *411*, 27–33.

(49) Zhang, X.; Lv, X.; Bi, F.; Lu, G.; Wang, Y. Highly Efficient Mn_2O_3 Catalysts Derived from Mn-MOFs for Toluene Oxidation: The Influence of MOFs Precursors. *Mol. Catal.* **2020**, *482*, 110701.

(50) Manigandan, R.; Giribabu, K.; Munusamy, S.; Praveen Kumar, S.; Muthamizh, S.; Dhanasekaran, T.; Padmanaban, A.; Suresh, R.; Stephen, A.; Narayanan, V. Manganese Sesquioxide to Trimanganese Tetroxide Hierarchical Hollow Nanostructures: Effect of Gadolinium on Structural, Thermal, Optical and Magnetic Properties. *CrystEngComm* **2015**, *17*, 2886–2895.

(51) Naeem, R.; Ali Ehsan, M.; Yahya, R.; Sohail, M.; Khaledi, H.; Mazhar, M. Fabrication of Pristine Mn2O3 and Ag- Mn_2O_3 Composite Thin Films by AACVD for Photoelectrochemical Water Splitting. *Dalt. Trans.* **2016**, *45*, 14928–14939.

(52) Ramesh, K.; Chen, L.; Chen, F.; Liu, Y.; Wang, Z.; Han, Y. F. Re-Investigating the CO Oxidation Mechanism over Unsupported MnO, Mn_2O_3 and MnO_2 Catalysts. *Catal. Today* **2008**, *131*, 477–482.

(53) Yang, S. J.; Nam, S.; Kim, T.; Im, J. H.; Jung, H.; Kang, J. H.; Wi, S.; Park, B.; Park, C. R. Preparation and Exceptional Lithium Anodic Performance of Porous Carbon-Coated ZnO Quantum Dots Derived from a Metal-Organic Framework. *J. Am. Chem. Soc.* **2013**, *135*, 7394–7397.

(54) Kuo, C. H.; Mosa, I. M.; Poyraz, A. S.; Biswas, S.; El-Sawy, A. M.; Song, W.; Luo, Z.; Chen, S. Y.; Rusling, J. F.; He, J.; Suib, S. L. Robust Mesoporous Manganese Oxide Catalysts for Water Oxidation. *ACS Catal.* **2015**, *5*, 1693–1699.

(55) Kunchala, R. K.; Pushpendra; Kalia, R.; Naidu, B. S. Irregularly Shaped Mn_2O_3 Nanostructures with High Surface Area for Water Oxidation. *ACS Appl. Nano Mater.* **2021**, *4*, 396–405.

(56) Ryabova, A. S.; Istomin, S. Y.; Dosaev, K. A.; Bonnefont, A.; Hadermann, J.; Arkharova, N. A.; Orekhov, A. S.; Sena, R. P.; Saveleva, V. A.; Kéranguéven, G.; Antipov, E. V; Savinova, E. R.; Tsirlina, G. A. Mn_2O_3 Oxide with Bixbyite Structure for the Electrochemical Oxygen Reduction Reaction in Alkaline Media: Highly Active If Properly Manipulated. *Electrochim. Acta* **2021**, *367*,

137378.

(57) Kuwahara, Y.; Fujibayashi, A.; Uehara, H.; Mori, K.; Yamashita, H. Catalytic Combustion of Diesel Soot over Fe and Ag-Doped Manganese Oxides: Role of Heteroatoms in the Catalytic Performances. *Catal. Sci. Technol.* **2018**, *8*, 1905–1914.

(58) Maiti, S.; Pramanik, A.; Mahanty, S. Electrochemical Energy Storage in Mn_2O_3 Porous Nanobars Derived from Morphology-Conserved Transformation of Benzenetricarboxylate-Bridged Metal-Organic Framework. *CrystEngComm* **2016**, *18*, 450–461.

(59) Zhang, B.; Hao, S.; Xiao, D.; Wu, J.; Huang, Y. Templated Formation of Porous Mn_2O_3 Octahedra from Mn-MIL-100 for Lithium-Ion Battery Anode Materials. *Mater. Des.* **2016**, *98*, 319–323.

(60) Wang, W.; Geng, J.; Kuai, L.; Li, M.; Geng, B. Porous Mn_2O_3 : A Low-Cost Electrocatalyst for Oxygen Reduction Reaction in Alkaline Media with Comparable Activity to Pt/C. *Chem. - A Eur. J.* **2016**, *22*, 9909–9913.

(61) Gong, Y. N.; Xie, Y. R.; Zhong, D. C.; Du, Z. Y.; Lu, T. B. A Two-Fold Interpenetrating Porous Metal-Organic Framework with a Large Solvent-Accessible Volume: Gas Sorption and Luminescent Properties. *Cryst. Growth Des.* **2015**, *15*, 3119–3122.

(62) Oar-Arteta, L.; Wezendonk, T.; Sun, X.; Kapteijn, F.; Gascon, J. Metal Organic Frameworks as Precursors for the Manufacture of Advanced Catalytic Materials. *Mater. Chem. Front.* **2017**, *1*, 1709–1745.

(63) Wang, C.; Kim, J.; Tang, J.; Kim, M.; Lim, H.; Malgras, V.; You, J.; Xu, Q.; Li, J.; Yamauchi, Y. New Strategies for Novel MOF-Derived Carbon Materials Based on Nanoarchitectures. *Chem* **2020**, *6*, 19–40.

(64) Li, Q.; Xu, Y.; Zheng, S.; Guo, X.; Xue, H.; Pang, H. Recent Progress in Some Amorphous Materials for Supercapacitors. *Small* **2018**, *14*, 1–19.

(65) Qiao, Z.; Wang, C.; Li, C.; Zeng, Y.; Hwang, S.; Li, B.; Karakalos, S.; Park, J.; Kropf, A. J.; Wegener, E. C.; Gong, Q.; Xu, H.; Wang, G.; Myers, D. J.; Xie, J.; Spendelow, J. S.; Wu, G. Atomically Dispersed Single Iron Sites for Promoting Pt and Pt_3Co Fuel Cell Catalysts: Performance and Durability Improvements. *Energy Environ. Sci.* **2021**, *14*, 4948–4960.

(66) Huang, L.; Wei, M.; Qi, R.; Dong, C. L.; Dang, D.; Yang, C. C.; Xia, C.; Chen, C.; Zaman, S.; Li, F. M.; You, B.; Xia, B. Y. An Integrated Platinum-Nanocarbon Electrocatalyst for Efficient Oxygen Reduction. *Nat. Commun.* **2022**, *13*, 6703.

(67) Qasim, M.; Hou, J.; Qadeer, M. A.; Butt, S.; Farooq, M. H.; Farooq, M. Q.; Idrees, F.; Tanveer, M.; Zou, J.; Tahir, M. Nitrogen-Doped Carbon Nanosheets Decorated With Mn2O3 Nanoparticles for Excellent Oxygen Reduction Reaction. *Front. Chem.* **2019**, *7*, 3–8.

(68) Hazarika, K. K.; Goswami, C.; Saikia, H.; Borah, B. J.; Bharali, P. Cubic Mn_2O_3 Nanoparticles on Carbon as Bifunctional Electrocatalyst for Oxygen Reduction and Oxygen Evolution Reactions. *Mol. Catal.* **2018**, *451*, 153–160.

(69) Jahan, M.; Tominaka, S.; Henzie, J. Phase Pure α- Mn_2O_3 Prisms and Their Bifunctional Electrocatalytic Activity in Oxygen Evolution and Reduction Reactions. *Dalt. Trans.* **2016**, *45*, 18494–18501.

(70) Chhetri, B. P.; Parnell, C. M.; Wayland, H.; RanguMagar, A. B.; Kannarpady, G.; Watanabe, F.; Albkuri, Y. M.; Biris, A. S.; Ghosh, A. Chitosan-Derived NiO-Mn_2O_3/C Nanocomposites as Non-Precious Catalysts for Enhanced Oxygen Reduction Reaction. *ChemistrySelect* **2018**, *3*, 922–932.

(71) Hong, K. L.; Qie, L.; Zeng, R.; Yi, Z. Q.; Zhang, W.; Wang, D.; Yin, W.; Wu, C.; Fan, Q. J.; Zhang, W. X.; Huang, Y. H. Biomass Derived Hard Carbon Used as a High Performance Anode Material for Sodium Ion Batteries. *J. Mater. Chem. A* **2014**, *2*, 12733–12738.

(72) Kim, H.; Min, K.; Shim, S. E.; Lim, D.; Baeck, S. H. Ni-Doped Mn2O3 Microspheres as Highly Efficient Electrocatalyst for Oxygen Reduction Reaction and Zn-Air Battery. *Int. J. Hydrogen Energy* **2022**, *47*, 2378–2388.

(73) Bard, A. J.; Faulkner, L. R. *Electrochemical Methods: Fundamentals and Applications*, second.; Wiley: New York, 2000.

(74) Liu, R.; Wu, D.; Feng, X.; Müllen, K. Nitrogen-Doped Ordered Mesoporous Graphitic Arrays with High Electrocatalytic Activity for Oxygen Reduction. *Angew. Chemie - Int. Ed.* **2010**, *49*, 2565–2569.

(75) Cao, S.; Han, N.; Han, J.; Hu, Y.; Fan, L.; Zhou, C.; Guo, R. Mesoporous Hybrid Shells of Carbonized Polyaniline/Mn_2O_3 as Non-Precious Efficient Oxygen Reduction Reaction Catalyst. *ACS Appl. Mater. Interfaces* **2016**, *8*, 6040–6050.

(76) Zhang, B.; Zheng, X.; Voznyy, O.; Comin, R.; Bajdich, M.; García-Melchor, M.; Han, L.; Xu, J.; Liu, M.; Zheng, L.; De Arquer, F. P. G.; Dinh, C. T.; Fan, F.; Yuan, M.; Yassitepe, E.; Chen, N.; Regier, T.; Liu, P.; Li, Y.; De Luna, P.; Janmohamed, A.; Xin, H. L.; Yang, H.; Vojvodic, A.; Sargent, E. H. Homogeneously Dispersed Multimetal Oxygen-Evolving Catalysts. *Science* **2016**, *352*, 333–337.

(77) Li, J. *Oxygen Evolution Reaction in Energy Conversion and Storage: Design Strategies Under and Beyond the Energy Scaling Relationship*; Springer Nature Singapore, 2022; Vol. 14.

(78) Chen, Q.; Zhang, Z.; Zhang, R.; Hu, M.; Shi, L.; Yao, Z. Recent Progress of Non-Pt Catalysts for Oxygen Reduction Reaction in Fuel Cells. *Processes* **2023**, *11*, 361.

(79) Zhuang, L.; Ge, L.; Yang, Y.; Li, M.; Jia, Y.; Yao, X.; Zhu, Z. Ultrathin Iron-Cobalt Oxide Nanosheets with Abundant Oxygen Vacancies for the Oxygen Evolution Reaction. *Adv. Mater.* **2017**, *29*, 1606793.

(80) Kiani, M.; Qing, X.; Zhang, W. Non-Precious Metal Electrocatalysts Design for Oxygen Reduction Reaction in Polymer Electrolyte Membrane Fuel Cells : Recent Advances , Challenges and Future Perspectives. *Coord. Chem. Rev.* **2021**, *441*, 213954.

(81) Xia, B. Y.; Yan, Y.; Li, N.; Wu, H. Bin; Lou, X. W. D.; Wang, X. A Metal-Organic Framework-Derived Bifunctional Oxygen Electrocatalyst. *Nat. Energy* **2016**, *1*, 1–8.

(82) Arbulu, R. C.; Jiang, Y. B.; Peterson, E. J.; Qin, Y. Metal–Organic Framework (MOF) Nanorods, Nanotubes, and Nanowires. *Angew. Chemie - Int. Ed.* **2018**, *57*, 5813–5817.

(83) Guo, D.; Shibuya, R.; Akiba, C.; Saji, S.; Kondo, T.; Nakamura, J. Active Sites of Nitrogen-Doped Carbon Materials for Oxygen Reduction Reaction Clarified

Using Model Catalysts. *Science* **2016**, *351*, 361–365.

(84) Strickland, K.; Miner, E.; Jia, Q.; Tylus, U.; Ramaswamy, N.; Liang, W.; Sougrati, M. T.; Jaouen, F.; Mukerjee, S. Highly Active Oxygen Reduction Non-Platinum Group Metal Electrocatalyst without Direct Metal-Nitrogen Coordination. *Nat. Commun.* **2015**, *6*, 1–8.

(85) Sarapuu, A.; Kibena-Põldsepp, E.; Borghei, M.; Tammeveski, K. Electrocatalysis of Oxygen Reduction on Heteroatom-Doped Nanocarbons and Transition Metal-Nitrogen-Carbon Catalysts for Alkaline Membrane Fuel Cells. *J. Mater. Chem. A* **2018**, *6*, 776–804.

(86) Larcher, D.; Croué, K.; Courty, M. Chemical, Textural and Structural Evolution of Ni1-XO Nanoparticles upon Isothermal Air Heating. *Mater. Chem. Phys.* **2016**, *174*, 1–5.

(87) Gandhi, A. C.; Pant, J.; Pandit, S. D.; Dalimbkar, S. K.; Chan, T. S.; Cheng, C. L.; Ma, Y. R.; Wu, S. Y. Short-Range Magnon Excitation in NiO Nanoparticles. *J. Phys. Chem. C* **2013**, *117*, 18666–18674.

(88) Zhou, R.; Zheng, Y.; Jaroniec, M.; Qiao, S. Z. Determination of the Electron Transfer Number for the Oxygen Reduction Reaction: From Theory to Experiment. *ACS Catal.* **2016**, *6*, 4720–4728.

(89) McCrory, C. C. L.; Jung, S.; Peters, J. C.; Jaramillo, T. F. Benchmarking Heterogeneous Electrocatalysts for the Oxygen Evolution Reaction. *J. Am. Chem. Soc.* **2013**, *135*, 16977–16987.

(90) Chen, M.; Ju, M. G.; Garces, H. F.; Carl, A. D.; Ono, L. K.; Hawash, Z.; Zhang, Y.; Shen, T.; Qi, Y.; Grimm, R. L.; Pacifici, D.; Zeng, X. C.; Zhou, Y.; Padture, N. P. Highly Stable and Efficient All-Inorganic Lead-Free Perovskite Solar Cells with Native-Oxide Passivation. *Nat. Commun.* **2019**, *10*, 1–8.

(91) Xie, A.; Zhang, J.; Tao, X.; Zhang, J.; Wei, B.; Peng, W.; Tao, Y.; Luo, S. Nickel-Based MOF Derived Ni @ NiO/N–C Nanowires with Core-Shell Structure for Oxygen Evolution Reaction. *Electrochim. Acta* **2019**, *324*, 134814.

(92) Ullah, N.; Zhao, W.; Lu, X.; Oluigbo, C. J.; Shah, S. A.; Zhang, M.; Xie, J.; Xu, Y. In Situ Growth of M-MO (M = Ni, Co) in 3D Graphene as a Competent Bifunctional Electrocatalyst for OER and HER. *Electrochim. Acta* **2019**, *298*, 163–171.

(93) Liu, Y.; Jiang, H.; Zhu, Y.; Yang, X.; Li, C. Transition Metals (Fe, Co, and Ni) Encapsulated in Nitrogen-Doped Carbon Nanotubes as Bi-Functional Catalysts for Oxygen Electrode Reactions. *J. Mater. Chem. A* **2016**, *4*, 1694–1701.

(94) Gorlin, Y.; Jaramillo, T. F. A Bifunctional Nonprecious Metal Catalyst for Oxygen Reduction and Water Oxidation. *J. Am. Chem. Soc.* **2010**, *132*, 13612–13614.

(95) Yin, J.; Li, Y.; Lv, F.; Fan, Q.; Zhao, Y. Q.; Zhang, Q.; Wang, W.; Cheng, F.; Xi, P.; Guo, S. NiO/CoN Porous Nanowires as Efficient Bifunctional Catalysts for Zn-Air Batteries. *ACS Nano* **2017**, *11*, 2275–2283.

(96) Prabu, M.; Ketpang, K.; Shanmugam, S. Hierarchical Nanostructured $NiCo_2O_4$ as an Efficient Bifunctional Non-Precious Metal Catalyst for Rechargeable Zinc-Air Batteries. *Nanoscale* **2014**, *6*, 3173–3181.

Chapter VI

Conclusion and Future Perspective

VI.1. Summary of thesis:

In this chapter, we present a comprehensive overview of the primary outcome of this thesis, along with an exploration of potential avenues for future research. This thesis was aimed to study various aspects of metal-organic frameworks (MOFs) synthesis and its use in the development of efficient heterogeneous catalytic system. We synthesized 1-D, 2-D, and 3-D MOFs using first-row transition metals and polytopic ligands. Some well-known MOFs such as HKSUT-1, Cu-BDC(DMF), M-MOF-74 (M= Cu, No, Co, Mn), ZIF-8 (Zn), ZIF-67 (Co), Mn-SKU-1, Mn-SKU-2, Cu-1D and Cu-SKU-3 MOFs were reproduced using reported methods. We have also designed and synthesized two novel 1D MOFs such as, Cu-SKU-4, and Ni-SKU-5. During the synthesis of these MOFs, we found the two methylimidazole unit coordinates the metal center from the equatorial position that allows the growth of polymeric structure strictly towards one dimension, and a linear 1D chain is formed that is further extended by the BDC ligands. The synthesized Cu-SKU-4 has a tetracoordinate Cu center with square planar geometry and readily available coordinating unsaturated sites on metal node however Ni-SKU-5 has a hexacoordinated Ni(II) center.

Next, the catalytic activity of synthesized Cu-MOFs was explored towards challenging coupling reactions such as intermolecular/ intramolecular C-N cross-coupling, and intermolecular C-X (X=S, O) coupling. These reactions carry much industrial value and palladium-based compounds are still the best-known catalyst for them. In the thrust of developing a cost-effective catalytic system, Cu-1D MOF was found to be efficient towards this reaction delivering 95% of the desired product within a short span of time. The Cu-1D catalyst shows no leaching of Cu-catalyst and it can be easily separated and reused with high retention of activity up to the fourth cycle. We have also established the mechanism of Cu-1D catalyzed C-N coupling reaction and supported by

experimental and computational evidences. The efficient catalytic activity of Cu-1D MOF towards coupling reaction can be attributed to the readily available open metal sites or coordinatively unsaturated sites (CUS) within the framework. To verify this, we conducted the coupling reaction under optimized conditions with some well-known Cu-MOF such as HKUST-1, Cu-BDC, and Cu-MOF-74 where the open metal sites are not readily available. We found that the coupling reaction with these Cu-MOFs are kinetically slow and inefficient compared to Cu-1D MOF highlighting the role of CUS in the reaction. Further to understand the role of CUS in various coupling reactions we extended our work towards cross-dehydrogenative coupling (CDC) reactions involving C-H activation. A selection of six Cu-based MOFs with distinct coordinating environments was studied in a rational manner, and the CDC reaction was performed. Out of the six MOFs, HKUST-1 and Cu-BDC(DMF) exhibit six-coordinated structures, Cu-SKU-5 and activated HKUST-1 possess penta-coordinated structures, while Cu-1D and Cu-SKU-4 have tetra-coordinated structures. The reactivity of these applied MOF towards CDC reaction was found in the order of tetracoordinated-MOF> pentacoordinated MOF>hexacoordinated MOF. Within the framework, the metal centres with CUS are considered to act as a Lewis acid sites and ligands with available lone pair as Bronsted basic site. Therefore, MOFs with Lewis acid site and Bronsted basic site are usually more efficient due to its multi-catalytic sites. To verify the working mode of multi-catalytic sites of synthesized MOFs, these six Cu-based MOF were further explored towards Knoevenagel condensation reaction. The MOFs with readily available CUS and *N*-containing ligands such as Cu-1D, Cu-SKU-4, Cu-SKU-3, were found to be efficient catalyst and HKUST-1 MOF was found inefficient highlighting multi-catalytic sites in Cu-1D and Cu-SKU-4 MOF.

Next, we proceeded with the post-synthetic modification of MOFs through the process of pyrolysis to produce porous composites. This involved subjecting the MOF to high temperatures in a N_2 atmosphere, carefully selecting the optimal temperature. The MOFs after pyrolysis inherited the structural properties in its derived composites as characterized by SEM and TEM techniques. Further, the surface area of derived composites was found to be increased after pyrolysis. The surface area and the total metal content of the composites derived from 3D→3D interpenetrating MOF was found to be more compared to the one derived from non-interpenetrating MOFs. The observed increase in porosity and total metal content can be attributed to the removal of interpenetrating networks after pyrolysis. Also, the elemental analysis confirmed the formation of metal oxide along with carbon in the derived composites. With the presence of carbon embedded in derived composites, their electrocatalytic behaviour towards oxygen process has been studied. All the derived composites such as PSKU-1, PSKU-2 and Ni/NiO-C were found efficient towards electrocatalytic oxygen reduction reaction (ORR). Their efficiency is also comparable to the state-of-art-the-catalyst as evident from the stability results, overpotential value, and kinetic parameters. Nevertheless, Ni/NiO-C was also found to be efficient towards oxygen evolution reaction and therefore shows a bifunctional electrocatalytic activity.

Overall, in this thesis, MOF and its derived composites have demonstrated superior performance compared to the conventional alternatives towards various molecular and electrocatalytic reactions. The remarkable characteristics exhibited by MOF-based materials can be taken as motivation and can be employed towards studying other catalytic process.

VI.2. Future perspective:

1. The results of our study have demonstrated the benefits of utilizing MOFs with pre-existing CUS in catalytic processes. In this thesis, we successfully synthesized MOFs with such CUS, although limited to 1D structures and lower surface area. Consequently, it would be advantageous to develop 3D MOFs based catalysts that not only possess pre-existing CUS, but also exhibit high porosity and a large surface area.
2. While MOFs have been reported as easily recyclable and reusable materials, the utilization of MOFs in industrial applications for recycling remains limited. Therefore, focus should be given on improving the thermal and chemical stability of MOF for it to be efficient heterogeneous catalyst.
3. The potential of MOFs as a catalyst for designing a one-pot catalytic system in heterogeneous conditions, leading to the production of value-added products needs to be explored more. This approach maintains the atom economy ensuring that the catalytic system to be economically viable and accessible.
4. Gaining a mechanistic understanding of MOF catalysts is crucial for comprehending their operational mechanisms and facilitating the rational design of highly efficient catalysts. The mechanistic study of MOF-catalysed reactions can emerge as a distinct research area in future, contributing significantly to our comprehension of the working mechanism of MOFs in various catalytic reactions.
5. The porous composites derived from MOF was found to have various unique properties comparted to the one synthesized from convectional method. Despite the existence of over 20,000 reported MOFs, the majority of them are derived from well-known MOFs such as ZIF-8 (Zn), ZIF-67(Co), Cu-BTC, Co-BDC, MIL-100. However, it is imperative to also address the exploration of other types of MOFs as

precursors. This broader investigation will contribute to expanding understanding and utilization of MOFs in various applications.

6. The scaling up methods for the synthesis of MOF and its derived composites to facilitate mass production of these promising structures needs to be developed. Given the exceptional characteristics of these MOF material and their derived composites, we firmly believe that they will continue to garner significant attention in the near future. The catalysis community is expected to address all these issues, ensuring advancements in MOF research and development.

Appendix I

List of Publication(s), Patent and Seminar Attended

A.I.1: Thesis Related Publication:

1. Rationally Designed Manganese-Based Metal-Organic Frameworks as an Altruistic Metal Oxide Precursor for Noble Metal-Free Oxygen Reduction Reaction. **Rasaily, S**.; Baruah K.; Sharma, D.; Lepcha P.; Biswas S.; Biswas. A. N.; Tamang, S. and Pariyar, A.*
   Inorg. Chem. **2023**, 62, *7*, 3026–3035 (DOI: 10.1021/acs.inorgchem.2c03707) **IF=5.436**

2. Multifunctional Catalysis by One Dimensional Copper (II) Metal Organic Framework Containing Pre-existing Coordinatively Unsaturated Sites: Intermolecular C-N, C-O, and C-S Cross-Coupling, Stereoselective Intramolecular C-N Coupling and Aziridination Reactions. **Rasaily, S**.; Sharma, D.; Pradhan, S.; Diyali N.; Chettri S.; Gurung B.; Tamang, S.; and Pariyar, A.*
   Inorg. Chem. **2022**, *61*, 35, 13685–13699. (DOI: 10.1021/acs.inorgchem.2c03707) **IF=5.436**

3. Metal–Organic Framework: An Emergent Catalyst in C–N Cross-Coupling Reactions. Diyali N.; **Rasaily S**.; Biswas B.*
   Coordination Chemistry Reviews, **2022**, *469*, 214667.
   (DOI: 10.1016/j.ccr.2022.214667) **IF= 24.833.**

4. Cu (II) Metal Organic Framework as Heterogeneous Catalyst Towards Cross Dehydrogenative Coupling Reaction via C-H Activation and Knoevenagel Condensation Reaction. *Manuscript under construction.*

5. 1D Metal-Organic Framework Route to Bifunctional Electro-Catalyst for Novel Metal-Free Oxygen Process. *Manuscript under construction.*

6. Recent trend and developments on MOF derived composites and their application towards electrocatalytic oxygen reduction reaction. *Manuscript under construction.*

A.I.2: Publication in other areas:

1. A Stereospecific Single-pot Route to Chiral Imidazolidines from Aziridines using 2D Cu Metal-Organic Framework. Sharma, D.; **Rasaily, S**.; Chettri S.; Surekha D.; Tamang, S.; and Pariyar, A.*

   Inorg. Chem. **2023**, *62*, 11, 4540–4549 (DOI: 10.1021/acs.inorgchem.04443r) **IF=5.436**

2. $CsPbBr_3$ Perovskite Quantum Dots as Visible Light Photocatalyst for cyclisation of diamines and amino alcohols: An efficient approach to synthesize Imidazolidines, fused-imidazolines and Oxazolidines. Gurung, B.; Pradhan, S.; Sharma, D.; Bhujel, D.; Basel, S.; Chettri, S.; **Rasaily, S**.; Pariyar, A and Tamang, S.

   Catal. Sci. Technol., **2022,** *12*, 5891-5898 (DOI:10.1039/D2CY00799A)

   IF= 6.177

3. HKUST-1 Metal Organic Framework as an Efficient Dual-Function Catalyst: Aziridination and One- Pot Ring-Opening Transformation for Formation of β-Aryl Sulfonamides with C–C, C–N, C–S, and C–O Bonds. Sharma, D.; **Rasaily, S**.; Pradhan, S.; Baruah, K.; Tamang, S.; and Pariyar, A.*

   Inorg. Chem., **2021**, *60*, 7794−780. (DOI: 10.1021/acs.inorgchem.1c00201)

   IF= 5.436

4. Stable lead-halide perovskite quantum dots as efficient visible light photocatalysts for organic transformations. Pradhan, S.; Bhujel, D.; Gurung, B.; Sharma, D.; Basel, S.; **Rasaily, S**.; Thapa, S.; Borthakur, S.; Ling, W-L.; Saikia, L.; Reiss, P.; Pariyar, A. and Tamang, S.*
   Nanoscale Adv., **2021***, 3*, 1464-1472. (DOI: 10.1039/d0na00992j) **IF=5.598**

5. Synthesis, structures and catalase activities of bis(μ-oxo)di MnIII, III and bis(μ-acetato) di MnII, II complexes bearing a quinolyl donor tripod ligand. Biswas, S.; Das, P.; **Rasaily, S**.; Pariyar, A.; Biswas. A. N.
   Inorganica Chimica Acta, **2019** *492*, 76–8278. (DOI:10.1016/j.ica.2019.04.015)
   IF=3.118

A.I.3: Patent:

1. Process for the Synthesis of Aziridines using Metal-Organic Framework and its Uses thereof. Sharma D.; **Rasaily S**.; Tamang S.; Pariyar A. *Indian Patent, Ref No:202131015781 Application No: TEMP/E-1/17130/2021-KOL, dated 02-04-2021.*

A.I.4: Work presented on seminar(s):

1. One-day International Symposium on, "Recent advances on Self assembled materials and Supramolecular Chemistry", organized by Department of Chemistry, Guru Nanak Dev University, Amritsar, India (2022) (***Oral presentation***)

2. International Conference on Recent Trends in Catalysis 2020, organized by Department of Chemistry, National Institute of Technology, Raipur India. (***Poster presented***)

3. 22nd CRSI National Symposium in Chemistry, organized by Pt. Ravishankar Shukla University, Raipur, Chhattisgarh, India (2018) (***Poster presented and best poster awarded***)

A.I.5: Workshop and training attended:

1. One Day workshop on Instrumentation & Analytical techniques for Chemical Analysis, organized by Department of Chemistry, Sikkim University, India.

2. Web of Science certification programme-2022, organized by Sikkim University, India.

3. Science-2020 (IC-RAPMS- 2020) organized by Kurseong College and St. Joseph's College, Darjeeling, West Bengal, India.

4. DST Inspire Science Camp-2018.

Inorganic Chemistry

pubs.acs.org/IC Article

Multifunctional Catalysis by a One-Dimensional Copper(II) Metal Organic Framework Containing Pre-existing Coordinatively Unsaturated Sites: Intermolecular C–N, C–O, and C–S Cross-Coupling; Stereoselective Intramolecular C–N Coupling; and Aziridination Reactions

Sagarmani Rasaily, Debesh Sharma, Sajan Pradhan, Nilankar Diyali, Shivanand Chettri, Bikram Gurung, Sudarsan Tamang, and Anand Pariyar*

Cite This: *Inorg. Chem.* 2022, 61, 13685–13699 Read Online

ACCESS | Metrics & More | Article Recommendations | Supporting Information

ABSTRACT: The coordinatively unsaturated sites (**CUS**) are vital in metal-centered catalysis. Metal–organic frameworks (MOFs) provide a unique opportunity to generate and stabilize **CUS** due to their robust structure. Generally, the generation of **CUS** in MOFs needs prior activation under heat and high vacuum to remove labile molecules occupying the catalytic sites. Herein, we report a solvothermal synthesis of a ready-to-use copper MOF containing accessible pre-existing **CUS** that does not need activation. The single crystal X-ray diffraction structure reveals a square planar Cu(II) center with two *N*-methylimidazoles (Mim) and one benzenedicarboxylic acid (BDC) with the formula unit $[Cu^{II}(BDC)\text{-}(Mim)_2]_n$ (**Cu-1D**) forming an infinite one-dimensional (1D) chain along the *c* axis. The 1D chains are stabilized by noncovalent $\pi-\pi$, CH$\cdots\pi$, and H-bonding interaction to give 2D (sheet-like) and 3D networks in the solid state. The quantification of non-covalent interaction is studied by Hirshfeld surface analysis, and the formation of a higher architecture in the solid state is confirmed by SEM analysis. The reported **Cu-1D** MOF acts as a solid heterogeneous catalyst and exhibits efficient catalytic activity in intermolecular and intramolecular cross-coupling reactions. Intermolecular C-heteroatom cross-coupling of a variety of *N*-heterocycles, aliphatic, aromatic, alicyclic amines and amides (C–N), phenols (C–O), and thiols (C–S) with aryl halides (halide = I, Br) was achieved with 70 to 95% yield, better than the state-of-the-art Cu-based homogenous system. The C–N coupling catalytic cycle is initiated by the *in situ* reduction of Cu(II) by KOH/DMSO to Cu(I) species. Subsequently, Cu(I) undergoes oxidative addition followed by reductive elimination to form a cross-coupled product. High stereoselectivity was found for the intramolecular C–N coupling reaction to give tetrahydroquinoxalines with an enantiomeric excess (*ee*) of more than 99%. For a broader application, **Cu-1D** was applied as the catalyst for the synthesis of a library of aziridines that gives yields of up to 99% with more than 93% recyclability for each cycle.

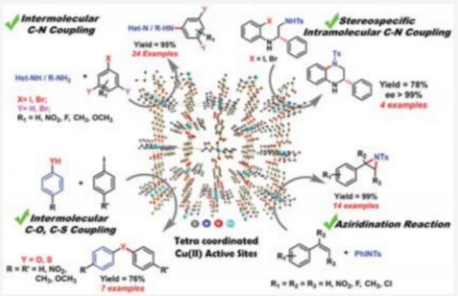

1. INTRODUCTION

The metal–organic frameworks (MOFs), a new class of porous coordination polymer composed of both the inorganic unit (metal ion or cluster) and organic unit (binding struts), has been efficiently used in the field of gas storage,[1] separation,[2] drug delivery,[3] luminescence,[4] and chemical sensors[5] for the past two decades. The presence of high metal content, ordered crystallinity, high surface area, and tunable pore size in MOFs makes them appealing to be used as a solid catalyst for catalytic transformations.[6−9] With catalysis being at the forefront of research in material chemistry,[10,11] most of the reports are oriented towards the synthesis of novel MOFs and their application as a potential multifunctional heterogeneous catalyst towards numerous organic transformations.[12] Although MOF has been employed as a solid catalyst in many organic reactions,[13−15] exploitation of MOFs with pre-existing coordinatively unsaturated sites (**CUS**) as a heterogeneous catalyst focusing on a specific transformation is very limited. One of the limiting factors for the application of MOF as a heterogeneous catalyst is the saturation of its active metal sites by coordinating organic ligands/linkers (or guest

Received: January 25, 2022
Published: August 24, 2022

https://doi.org/10.1021/acs.inorgchem.2c00270
Inorg. Chem. 2022, 61, 13685–13699

Inorganic Chemistry

pubs.acs.org/IC Article

Rationally Designed Manganese-Based Metal–Organic Frameworks as Altruistic Metal Oxide Precursors for Noble Metal-Free Oxygen Reduction Reaction

Sagarmani Rasaily, Khanindram Baruah, Debesh Sharma, Panjo Lepcha, Sachidulal Biswas, Achintesh Narayan Biswas, Sudarsan Tamang, and Anand Pariyar*

Cite This: *Inorg. Chem.* 2023, 62, 3026–3035 Read Online

ACCESS | Metrics & More | Article Recommendations | Supporting Information

ABSTRACT: The sluggish oxygen reduction reaction (ORR) at the cathode is challenging and hinders the growth of hydrogen fuel cells. Concerning kinetic values, platinum is the best known catalyst for ORR; however, its less abundance, high cost, and corrosive nature warrant the development of low-cost catalysts. We report the hydrothermal synthesis of two novel Mn-based metal–organic frameworks (MOFs), $[Mn_2(DOT)(H_2O)_2]_n$ (**Mn-SKU-1**) and $[Mn_2(DOT)_2(BPY)_2(THF)]_n$ (**Mn-SKU-2**) (DOT = 2,5-dihydroxyterephthalate; BPY = 4,4′-bipyridine). **Mn-SKU-1** contains dimeric Mn(II) centers where the two corner-shared MnO_6 octahedra fuse to give rise to an infinite Mn_2O_{10} cluster, whereas the two Mn(II) ions coordinate to DOT and BPY moieties to give rise to a pillared structure in **Mn-SKU-2** and form a 3D → 3D homo-interpenetration MOF with a twofold interpenetrated net. The pyrolysis of as-synthesized Mn-MOFs at 600 °C under N_2 produced exclusively porous α-Mn_2O_3 composites (**PSKU-1** and **PSKU-2**), with the BET surface area of 90.8 (for **PSKU-1**) and 179.3 $m^2\ g^{-1}$ (for **PSKU-2**). These mesoporous MOF-derived α-Mn_2O_3 composites were modified as cathode materials for the electrocatalytic reduction of oxygen. The onset potential for the oxygen reduction reaction was found to be 0.90 V for **PSKU-1** and 0.93 V for **PSKU-2** versus RHE in 0.1 M KOH solution, with the current density of 4.8 and 6.0 mA cm^{-2}, respectively, at 1600 rpm. Based on the RDE/RRDE results, the electrocatalytic oxygen reduction occurs majorly via the four-electron process. The electrocatalyst **PSKU-2** is cheap, easy to use, retains 90% of its activity after 10 h of continuous use, and offers higher recyclability than Pt/C. The onset potential maximum current density and kinetic values (J_k = 11.68 mA cm^{-2} and Tafel slope = 85.0 mV dec^{-1}) obtained in this work are higher than the values reported for pure Mn_2O_3.

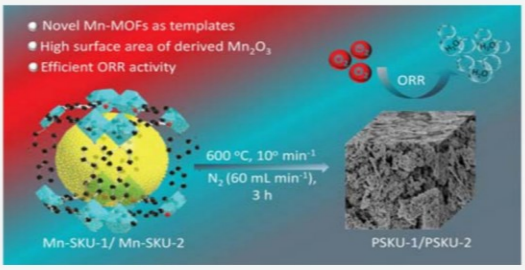

■ INTRODUCTION

Among various sustainable energy sources,[1−6] hydrogen fuel cell or proton exchange membrane fuel cell (PEMFC) is an attractive proposition due to its high calorific value and environment-friendly byproducts.[7,8] Oxidation of H_2 in an anode (hydrogen oxidation reaction, HOR), followed by the reduction of O_2 in the cathode (oxygen reduction reaction, ORR) is the elementary process of PEMFCs. The reduction of oxygen at the cathode takes place at a higher redox potential (E^0 = 1.23 V vs RHE), and the rate is about 6 orders slower than the rate of hydrogen oxidation at the anode. The sluggish ORR at the cathode is one of the major challenges in PEMFCs.[9] Platinum-based materials are still the state-of-the-art catalysts to enhance the kinetics of fuel cells at the cathode, but their less abundancy, high cost, and corrosive nature limit the development of low-cost fuel cells.[10] Therefore, developing an affordable cathode catalyst is an urgent task despite the tremendous progress made with the platinum catalyst.[11] Recently, non-noble metal group electrocatalysts have gained enormous attention in ORR catalysis due to reduced cost.[9,12−14] Manganese-based oxides are naturally abundant, cheap, and relatively nontoxic. α-Mn_2O_3 with abundant defects/oxygen vacancy is a captivating cathodic material for ORR and metal–air batteries.[15,16] The activity of manganese oxide greatly depends on the crystal structure and morphology. A study by Fang *et al.* showed that the globe-like morphology of α-Mn_2O_3 can enhance the activity of ORR as it has more oxygen vacancies compared to the flower-like and rhombohedral shaped α-Mn_2O_3.[17] Heterogeneous catalysis is a surface phenomenon,[18] and materials with higher surface area, higher

Received: October 20, 2022
Published: February 9, 2023

https://doi.org/10.1021/acs.inorgchem.2c03707
Inorg. Chem. 2023, 62, 3026−3035

Coordination Chemistry Reviews 469 (2022) 214667

Contents lists available at ScienceDirect

Coordination Chemistry Reviews

journal homepage: www.elsevier.com/locate/ccr

Review

Metal–Organic Framework: An Emergent Catalyst in C–N Cross-Coupling Reactions

Nilankar Diyali [a], Sagarmani Rasaily [b], Bhaskar Biswas [a,*]

[a] Department of Chemistry, University of North Bengal, Darjeeling 734013, India
[b] Department of Chemistry, Sikkim University, Gangtok 737102, India

ARTICLE INFO

Article history:
Received 23 December 2021
Accepted 7 June 2022

Keywords:
Metal–organic framework
Heterogeneous catalysis
C–N Cross-coupling reaction
Amination reaction
Aziridination reaction
Synthetic approaches

ABSTRACT

Scientific and industrial concern on the rational design of metal–organic frameworks (MOFs) has marked an escalating trend in recent years and rejuvenated. The emergence of C–N cross-coupling reactions gains huge attention for the production of nitrogen-functionalized molecules in value-added pharmaceuticals, tailor-made therapeutics, smart optoelectronic devices, energy harvesting functional materials, etc. Recently, MOF-mediated C–N cross-coupling reactions hold a great promise to replace homogenous and heterogeneous catalysts owing to promising structural features like intriguing porous framework, large catalytic sites and surface area, adequate framework stability, flexible organic linkers, minimal leaching, and easy recyclability. At first, the importance of MOFs and MOFs catalyzed C–N cross-coupling reactions and their beneficial roles over homogeneous and a limited number of other heterogeneous catalysts are fundamentally introduced. Then, the state-of-the-art synthetic approaches for pristine and decorated MOFs are comprehensively reviewed and discussed. The emergence of MOFs as heterogeneous catalysts has been critically analyzed and illuminated with an overview of the mechanistic aspects in various C–N cross-coupling reactions namely Ullmann coupling, Chan-Lam coupling, Buchwald-Hartwig amination, C–H activation and aziridination reactions. Thereafter, different structural parameters conferring the stability and recyclability of the MOFs in the cross-coupling reactions are enumerated. Finally, we forecast the future perspectives on MOFs catalyzed C–N cross-coupling reactions and associated challenges to establish the practical applicability of the catalyst at the industrial level.

Contents

* Corresponding author.
E-mail addresses: bhaskarbiswas@nbu.ac.in, icbbiswas@nbu.ac.in (B. Biswas).

https://doi.org/10.1016/j.ccr.2022.214667
0010-8545/

Appendix II

Details of Diffracted Crystals and DFT Calculations

A.II.1. Crystal data details for Cu-1D

Table A.II.1: Fractional atomic coordinates and equivalent isotropic displacement parameters/$Å^2$ for Cu-1D

Atom	x	y	z	U (eq)
Cu(1)	0	5000	5000	40 (2)
O(1)	2491(5)	5164.7 (15)	6618.7 (18)	48 (6)
O(2)	29 (5)	4151.2 (16)	7271.3 (19)	57 (7)
C(5)	1854 (6)	4694 (2)	7457 (3)	41.5 (8)
C(6)	3525 (6)	4845.2 (18)	8781 (2)	36 (7)
C(7)	7266 (6)	5498 (2)	10208 (3)	41.3 (7)
C(8)	5809 (6)	5344 (2)	8994 (2)	41.2 (7)
N(1)	2179 (5)	4003.2 (18)	4587 (2)	45.1 (7)
N(2)	5221(5)	2972 (2)	4782 (3)	53 (8)
C(1)	4426 (7)	3699 (2)	5282 (3)	47.1(8)
C(2)	3378 (8)	2789 (2)	3698 (3)	64.1(11)
C(3)	1528 (8)	3428 (2)	3578 (3)	59.7 (10)
C(4)	7556 (7)	2433 (3)	5326 (4)	74.4 (12)

Table A.II.2: Anisotropic Displacement Parameters ($Å^2$ x 10^3) for 1D. The Anisotropic displacement factor exponent takes the form: $2\pi^2[h^2a^{*2}U_{11}+2hka^*b^*Uu+..]$

Atom	U_u	U_{22}	U_{33}	U_{23}	U_{13}	U_u
Cu01	48.7(4)	46.1(3)	15.9(2)	0.1(2)	-7.40(19)	-4.7(3)
O002	54.2(14)	61.6(15)	18.1(9)	-1.9(9)	-8.2(9)	-4.1(11)
O003	60.4(15)	63.0(15)	33.6(11)	-3.6(10)	-12.9(10)	-11.9(12)
N004	55.7(17)	47.0(16)	25.8(12)	-1.4(11)	-1.6(11)	-4.3(13)
N005	60(2)	42.2(16)	53.7(18)	2.9(12)	9.5(15)	0.8(14)
C006	42.4(18)	46.6(17)	25.3(15)	-7.9(12)	-10.1(12)	8.0(14)
C007	41.2(17)	39.6(17)	19.1(12)	-5.2(10)	-5.8(11)	8.2(12)
C008	36.5(17)	54(2)	27.1(14)	-1.6(13)	-4.1(12)	-3.4(14)
C009	43.6(18)	54.9(18)	21.1(13)	1.1(12)	1.3(12)	-2.8(14)
C00A	50(2)	49(2)	36.8(16)	2.0(14)	0.9(14)	-5.5(15)
C00B	93(3)	47(2)	44.1(19)	-6.8(16)	4.1(19)	0(2)
C00C	82(3)	52(2)	33.4(17)	-6.6(15)	-6.8(16)	-2(2)
C00D	65(3)	53(2)	98(3)	5(2)	8(2)	5(2)

Table A.II.3: Bond lengths (Å) for Cu-1D

Atom-Atom	Length/ Å	Atom-Atom	Length/ Å
Cu01-O002	1.9456(19)	N005-C00A	1.323(5)
Cu01-O002[1]	1.9456(19)	N005-C00B	1.363(4)
Cu01-N004[1]	1.992(3)	N005-C00D	1.463(4)
Cu01-N004	1.992(3)	C006-C007	1.519(3)
O002-C006	1.271(4)	C007-C008[2]	1.385(4)
O003-C006	1.230(4)	C007-C009	1.383(4)
N004-C00A	1.318(4)	C008-C009	1.384(4)
N004-C00C	1.372(4)	C00B-C00C	1.341(5)

Table A.II.4: Bond angles (°) for Cu-1D

Atom Atom Atom	Angle/°	Atom Atom Atom	Angle/°
O002-Cu01-O002[1]	180.0	C00B-N005-C00D	126.3(3)
O002-Cu01-N004	90.35(10)	O002-C006-C007	115.0(3)
O002-Cu01-N004[1]	89.65(10)	O003-C006-O002	125.3(3)
O002[1]-Cu01-N004[1]	90.35(10)	O003-C006-C007	119.6(3)
O002[1]-Cu01-N004	89.65(10)	C008[2]-C007-C006	120.0(3)
N004[1]-Cu01-N004	180.00(10)	C009-C007-C006	120.7(3)
C006-O002-Cu01	110.93(19)	C009- C007-C008[2]	119.3(2)
C00A-N004-Cu01	127.4(2)	C009- C008-C007[2]	120.9(3)
C00A-N004-C00C	105.3(3)	C007- C009-C008	119.8(3)
C00C-N004-Cu01	127.0(2)	N004- C00A-N005	111.6(3)
C00A-N005-C00B	107.1(3)	C00C-C00B-N005	106.8(3)
C00A-N005-C00D	126.5(3)	C00B-C00C-N004	109.2(3)

Table A.II.5: Torsion Angles for Cu-1D.

A-B-C-D	Angle/ °	A-B-C-D	Angle/ °
Cu01-O002-C006-O003	5.1(4)	C006-C007-C009-C008	-178.7(3)
Cu01-O002-C006-C007	-174.24(19)	C0071-C008-C009-C007	0.3(5)
Cu01-N004-C00A-N005	173.7(2)	C0081-C007-C009-C008	-0.3(5)
Cu01-N004-C00C-C00B	173.4(2)	C00A-N004-C00C-C00B	0.7(4)
O002-C006-C007-C0081	168.0(3)	C00A-N005-C00B-C00C	0.6(4)
O002-C006-C007-C009	-10.3(4)	C00B-N005-C00A-N004	-0.2(4)
O003-C006-C007-C0081	-11.4(4)	C00C-N004-C00A-N005	-0.3(4)
O003-C006-C007-C009	170.3(3)	C00D-N005-C00A-N004	-176.9(3)
N005-C00B-C00C-N004	-0.8(4)	C00D-N005-C00B-C00C	177.3(4)

Table A.II.6: Hydrogen Atom Coordinates ($Å^2 \times 10^3$) and Isotropic Displacement Parameters (A^2x10^3) for $Å^2 \times 10^3$) for Cu-1D.

Atom	x	y	z	U(eq)
H008	8796	5835.55	10347.78	50
H009	6363.7	5575.26	8322.82	49
H00A	5339.14	3963.26	6031.63	57
H00B	3400.23	2312.4	3148.3	77
H00C	39.85	3473.8	2915.22	72
H00D	8698.2	2770.78	5989.12	112
H00E	8442.87	2298.61	4691.55	112
H00F	7060.49	1877.05	5655.14	112
H008	8796	5835.55	10347.78	50

A.II.2. Crystal data details of Cu-SKU-4

Table A.II.7: Fractional Atomic Coordinates ($x10^4$) and Equivalent Isotropic Displacement Parameters ($Å^2 \times 10^3$) for Cu-SKU-4. U_{eq} is defined as 1/3 of the trace of the orthogonalized U_{IJ} tensor.

Atom	x	y	z	U(eq)
CuOl	10000	5000	10000	33.4(3)
O1	7021(4)	5350 (3)	8598 (3)	41.3 (6)
O2	7146 (4)	3847(3)	7587(3)	50.7(8)
N2	10478 (5)	6369 (3)	9292 (3)	42.1(7)
Nl	9891(6)	7945(4)	8052 (4)	50.8(9)
C2	519(5)	5479(4)	5501(4)	34.0(8)
C6	6160 (5)	4586 (4)	7637 (4)	37.0(8)
C3	661(6)	3613(4)	4538 (4)	41.4 (9)
C4	2710 (5)	5491(4)	6523(3)	34.9(8)
Cl	3836 (5)	4592(4)	6538 (3)	34.9(8)
C7	9076 (6)	7146 (4)	8290 (4)	47.2 (9)
C5	2770 (6)	3651(4)	5526(4)	41.5 (9)
C8	12313(7)	6705 (5)	9716 (4)	54.1(11)
C9	11957 (7)	7676 (5)	8959 (5)	58.9(12)
C10	8785(9)	8943 (5)	7022(5)	66.4 (14)

Table A.II.8: Hydrogen Atom Coordinates ($Å^2 \times 10^3$) and Isotropic Displacement Parameters (A^2x10^3) for $Å^2 \times 10^3$) for Cu-SKU-4.

Atom	x	y	z	U(eq)
H3	-11.39	2982.47	3882.22	50
H4	3404.94	6108.05	7192.71	42
H7	7681.06	7140.8	7804.38	57
H5	3520.07	3047.06	5534.77	50
H8	13596.5	6319.02	10417.98	65
H9	12928.09	8082.71	9038.31	71
HlOA	7438.01	9085.52	6656.31	100
HlOB	8635.65	8645.91	6346.41	100
HlOC	9555.11	9751.83	7385.77	100

Table A.II.9: Anisotropic Displacement Parameters ($Å^2$ x 10^3) for Cu-SKU-4. The Anisotropic displacement factor exponent takes the form: $2\pi^2[h^2a^{*2}U_{11}+2hka^*b^*Uu+..]$

Atom	U_u	U_{22}	U_{33}	U_{23}	U_{13}	U_u
CuOl	16.3 (4)	39.9(5)	31.9(5)	-0.7(3)	13.7(4)	-1.3 (3)
01	19.1 (12)	49.9(15)	37.6(14)	-1.1(13)	15.2 (11)	-0.3 (11)
02	26.9(13)	61.9(19)	50.3(16)	-2.7(14)	24.0(13)	6.8 (12)
N2	32.0(15)	46.1(18)	41.8(17)	-3.3(14)	24.9(14)	-5.4 (14)
Nl	61(2)	4 7 (2)	58 (2)	2.7(17)	48(2)	0.7(17)
C2	22.5 (16)	35.5(18)	34.0(17)	0.4 (16)	17.4(15)	0.4 (15)
C6	23.1(17)	38.7(18)	37.9(19)	7.0(16)	18.7(16)	1.9(15)
C3	27.8(17)	42 (2)	39.1(19)	-10.1(16)	19.4(16)	-0.2 (15)
C4	22.9(16)	36.2 (18)	32.5(17)	-2.5(15)	16.0(15)	-2.0(14)
Cl	20.1(17)	41.1(19)	34.9(18)	3.0(15)	17.3(16)	0.4 (15)
C7	43(2)	4 7 (2)	52 (2)	3.0 (19)	35(2)	1.0(18)
cs	27.3(17)	44 (2)	44 (2)	-2.4 (16)	23.0(17)	4.6(15)
C8	34 (2)	71 (3)	50 (2)	0 (2)	28.6(19)	-8(2)
C9	50(2)	65(3)	63 (3)	2 (2)	42(2)	-10(2)
ClO	90 (4)	53(3)	81 (3)	13 (3)	70(3)	11 (3)

Table A.II.10: Bond Lengths for Cu-SKU-4.

Atom-Atom	Length/ Å	Atom-Atom	Length/ Å
Cu01-01	1.954(3)	N1-C10	1.463(6)
Cu01-01'	1.954(3)	C2-C22	1.416(8)
Cu01-N21	1.988(3)	C2-C32	1.415(5)
Cu01-N2	1.988(3)	C2-C4	1.412(5)
01-C6	1.272(5)	C6-C1	1.499(5)
02-C6	1.240 (5)	C3-C5	1.360(5)
N2-C7	1.312(5)	C4-C1	1.390(5)
N2-C8	1.384(5)	C1-C5	1. 410 (6)
N1-C7	1.332(5)	C8-C9	1.346(7)
N1-C9	1.362(6)		

[1]2-X,l-Y,2-Z; [2]-X,l-Y,l-Z

Table A.II.11: Bond Angles for Cu-SKU-4.

Atom-Atom-Atom	Angle/ °	Atom-Atom-Atom	Angle/ °
O1-Cu01-O11	180.0	C4-C2-C22	119.1(4)
O1-Cu01-N2	90.59(13)	C4-C2-C32	121.7(3)
O1-Cu01-N2[1]	89.41(13)	O1-C6-C1	116.8(3)
01[1]-Cu01-N2	89.41(13)	O2-C6-01	123.3(3)
01[1]-Cu01-N2[1]	90.59(13)	O2-C6-C1	119.9(4)
N2[1]-Cu1[1]-N2	180.0	C5-C3-C22	120.7(4)
C6-01-Cu01	109.4(2)	C1-C4-C2	120.7(3)
C7-N2-Cu01	126.6(3)	C4-C1-C6	120.7(3)
C7-N2-C8	104.8(4)	C4-C1-C5	119.3(3)
C8-N2-Cu01	128.6(3)	C5-C1-C6	120.0(3)
C7-N1-C9	107.4(4)	N2-C7-N1	111.9(4)
C7-N1-C10	126.6(4)	C3-C5-C1	121.0(3)
C9-N1-C10	126.0(4)	C9-C8-N2	109.6(4)
C3[2]-C2-C2[2]	119.2(4)	C8-C9-N1	106.2(4)

[1]2-X,l-Y,2-Z; [2]-X,l-Y,l-Z

Table A.II.12: Torsion Angles for Cu-SKU-4.

A-B-C-D	Angle/ °	A-B-C-D	Angle/ °
Cu01-O1-C6-O2	-6.8(5)	C2 -C4-C1-C6	-178.7(3)
Cu01-O1-C6-C1	172.3(2)	C2-C4-C1-C5	-0.7(6)
Cu01-N2-C7-Nl	-179.2 (3)	C6-Cl-C5-C3	178.1(4)
Cu01-N2-C8-C9	179.4 (3)	C31-C2C4C1	-179.7(4)
O1- C6-C1-C4	6.4 (5)	C4-C1-C5-C3	0.1 (6)
O1-C6-C1-C5	-171.6(4)	C7 -N2-C8-C9	0.2 (5)
O2-C6-C1-C4	-174.5(4)	C7 -N1-C9-C8	0.3 (5)
O2-C6-C1-C5	7.5(5)	C8 -N2-C7-Nl	0.0 (5)
N2-C8-C9-N1	-0.3(6)	C9-N1-C7-N2	-0.2(5)
C21-C2-C4-C1	1.0 (6)	C10-N1-C7-N2	-179.4(4)
C21-C3-C5-C1	0.2(6)	C10-N1-C9-C8	179.5(4)

A.II.3. Crystal data table for Ni-SKU-5.

Table A.II.13: Fractional Atomic Coordinates ($x10^4$) and Equivalent Isotropic Displacement Parameters ($Å^2 \times 10^3$) for Ni-SKU-5. U_{eq} is defined as 1/3 of the trace of the orthogonalized U_{IJ} tensor.

Atom	x	y	z	U(eq)
NiOl	2492.1(3)	5997.6(3)	2610.5(4)	13.4 (3)
O002	6102 (2)	8705(2)	7045(2)	22.6(7)
O003	3897 (2)	6287 (2)	3121(2)	22.7(7)
O004	7305(2)	8258(2)	6358(2)	21_1(7)
O005	2752(2)	7070.9(19)	3529(2)	2L 4 (7)
N006	2150(3)	5326(2)	3697 (3)	2L1(8)
N007	2841(3)	4990(2)	1924 (3)	2L8(8)
C008	2153(3)	4424 (3)	4805 (3)	24.0 (9)
C009	6409(3)	8298(3)	6410 (3)	15.6(8)
C00A	2946(3)	3710 (3)	1564(4)	25.8 (10)
C00B	3628(3)	6853(2)	3609(3)	16.3 (8)
C00c	4365(3)	7234 (2)	4323 (3)	15.4 (8)
C00D	5693(3)	7888(2)	5699 (3)	16.5 (8)
C00E	2691(4)	4821(3)	4244 (3)	26.4 (10)
C00F	4722 (3)	7903(3)	5802 (3)	17.9(8)
C00G	4045(3)	7589(3)	5102 (3)	19.0 (9)
C00H	5336 (3)	7197 (3)	4233 (3)	2L 8 (9)
C00I	2347(4)	4298(3)	1800 (3)	25.7(10)
C00J	6015(3)	7543(3)	4918 (3)	23.3 (9)
C00K	3768 (4)	4840(3)	1757(4)	3L8(11)
C00L	1212(4)	5240(3)	3919 (4)	30.9(11)
C00M	1203(4)	4689(4)	4594(4)	40.0 (13)
C00N	3844 (4)	4039(3)	1532 (5)	45.4(17)
C00O	3757(4)	4658(4)	4251(5)	49.3(17)
C00P	1322 (4)	4164(4)	1896(6)	49.4(17)

Table A.II.14: Anisotropic Displacement Parameters ($Å^2$ x 10^3) for Ni-SKU-5. The Anisotropic displacement factor exponent takes the form: $2\pi^2[h^2a^{*2}U_{11}+2hka^*b^*Uu+..]$

Atom	**U_u**	**U_{22}**	**U_{33}**	**U_{23}**	**U_{13}**	**U_u**
NiOl	16.2 (4)	10.7(3)	12.1(4)	-0.24(17)	-3.1(2)	0.05(16)
0002	24.4(17)	23.9(16)	18.5(15)	-7.6(13)	-0.5(12)	-1.0(14)
0003	23.1(16)	19.0(15)	24.9(17)	-9.9(14)	-1.1(13)	-0.7(13)
0004	16.8(15)	26.0 (16)	19.4(15)	-3.5(12)	-2.4 (12)	-2.6(12)
0005	18.6(15)	18.8(15)	24.8(16)	-4.1(12)	-4.0(12)	0.0 (12)
N006	25.8(19)	17.5(17)	19.5(18)	1.2(14)	0.9(15)	2.1 (15)
N007	27.1(19)	18.0(18)	18.7(18)	-3.9(15)	-3.6(15)	0.4 (15)
C008	31(2)	25 (2)	17 (2)	13.2(18)	4.0(17)	5.5 (18)
C009	20(2)	14.0(17)	11.8(18)	1.4(15)	-2.2 (15)	-2.0 (15)
COOA	27 (2)	11.4(19)	39(3)	-14.7(19)	4 (2)	-2.1(17)
COOB	19 (2)	13.2 (18)	15.8(19)	-1.1(15)	-1.2(15)	-4.2 (15)
cooc	20.0(19)	8.8(16)	15.9(19)	-0.5(15)	-3.1(15)	-3.7(15)
COOD	18.9(19)	14.4 (18)	14.7(19)	-1.2(15)	-3.9(15)	-3.3(15)
COOE	33(2)	27 (2)	19(2)	7.4(18)	0.1(18)	1.7(19)
COOF	20(2)	20 (2)	13.1(19)	-2.4 (16)	1.0(15)	-2.4 (16)
COOG	19 (2)	17.8(19)	20 (2)	-1.1(16)	1.7(16)	-2.8 (16)
COOH	22 (2)	24 (2)	18 (2)	-9.6(17)	-1.0(17)	1.5(17)
COOl	35(3)	16 (2)	25 (2)	-7.2(18)	0.1(19)	-1.6(18)
COOJ	18(2)	24 (2)	27 (2)	-8.0(19)	-1.6(17)	-0.3(17)
COOK	34 (3)	2 6 (2)	36(3)	-11(2)	8 (2)	-3(2)
COOL	30(2)	2 6 (2)	38 (3)	9 (2)	8 (2)	1.6(19)
COOM	41(3)	37 (3)	46(3)	13 (3)	20 (3)	4 (2)
COON	37 (3)	33 (3)	68 (5)	-23(3)	14 (3)	1(2)
cooo	32 (3)	61 (4)	53 (4)	32 (3)	-1(3)	14(3)
COOP	30(3)	44 (3)	76(5)	-28 (3)	10 (3)	-15(3)

Table A.II.15: Bond Lengths for Ni-SKU-5.

Atom-Atom	Length/ Å	Atom-Atom	Length/ Å
Ni0l-0002[1]	2.065(3)	C00S-C00E	1.349 (7)
Ni01-0003	2.060 (3)	C00S-C00M	1.390(7)
Ni0l-0004[1]	2.188 (3)	C009-C00D	1.504 (5)
Ni0l-0005	2.226(3)	C00A-C00I	1.356 (6)
Ni01-N006	2.039(4)	C00A-C00N	1.372(8)
Ni01-N007	2.036(4)	C00B-C00C	1.504 (5)
Ni01-C009 1	2.453(4)	C00C-C00G	1.401(6)
Ni01-C00B	2.456(4)	C00C-C00H	1.377(6)
O002-C009	1.261(5)	C00D-C00F	1.380(6)
O003- C00B	1.262(5)	C00D-C00J	1.396 (6)
O004-C009	1.263(5)	C00E-C00O	1.510(7)
O005-C00B	1.264(5)	C00F-C00G	1.396(6)
N006-C00E	1.322(6)	C00H-C00J	1.405 (6)
N006-C00L	1.393(6)	C00l-C00P	1.470 (8)
N007-C00l	1.336(6)	C00K-C00N	1.374 (7)
N007-C00K	1.367(6)	C00L-C00M	1.341(7)

[1]2-X,l-Y,2-Z; [2]-X,l-Y,l-Z

Table A.II.16: Bond Angles for Ni-SKU-5.

Atom-Atom-Atom	Angle/ °	Atom-Atom-Atom	Angle/ °
O0021-Ni0l-O0041	61.83(12)	C00l-N007-C00K	107.6(4)
O0021-Ni0l-0005	96.93(13)	C00K-N007-Ni0l	121.8(3)
O0021-Ni0l-C0091	30.92(14)	C00E-C00S-C00M	107_4(4)
O0021-Ni0l- C00B	126.75(14)	O002-C009-Ni012	57_3(2)
O003-Ni0l-O0021	152.59(16)	O002- C009-O004	120_2 (4)
O003-NiOl-O0041	100.08(13)	O002-C009-C00D	119_2 (4)
O003-Ni0l- C0091	61.54(12)	O00D- C009- Ni012	62_9(2)

O003-Ni0l- C0091	128' 00 (14)	O004-C0099-C00D	120-6(4)
O003-Ni0l- C00B	30.88(14)	O004- C009- Ni012	176-5(3)
00041-NiOl-0005	92.44(12)	C00l-C00A-C00N	108_4 (4)
00041-NiOl-C009 1	30.91(13)	O003-C00B Ni0l	56.9(2)
00041-Ni01-C00B	99.57 (13)	0003-C00B-O005	120.9(4)
0005-NiOl- C0091	94.89(13)	0003-C00B-C00C	118.3 (4)
0005-Ni0l- C00B	30.82(12)	O005-C00B-Ni0l	64.5 (2)
N006-Ni0l-O0021	97.96(14)	O005-C00B-C00C	120.7(4)
N006-Ni0l-O003	98.86(15)	C00C-COOB-NiOl	169.3(3)
N006-Ni0l-O0041	159' 78 (14)	C00G-C00C-C00B	118.4 (4)
N006-Ni0l-O005	90.39(14)	C00H-C00C-C00B	120-6(4)
N006-Ni0lC0091	128.88(15)	C00H-C00C-C00G	120_9(4)
N006-Ni0l-C00B	93.06(14)	C00F-C00D-C009	119_4 (4)
N007-Ni0l-O0021	105.73(14)	C00F-C00D-C00J	121.1(4)
N007-Ni0l-O003	95.30 (14)	C00J-C00D-C009	119.4 (4)
N007-NiOl-O0041	93.70(14)	N006-C00E-C00S	110.8 (4)
N007-Ni0l-O005	156.76(13)	N006-C00E-C00O	127.1(5)
N007-Ni0l-N006	91.53(15)	C00S-C00E-C00O	122.1 (5)
N007-Ni0l-C0091	101.83(14)	C00D-C00F-C00G	119.6(4)
N007-Ni0l-C00B	125.94(15)	C00F-C00G-C00C	119.4 (4)
C0091-Ni0l-C00B	115' 96 (15)	C00C-C00H-C00J	119.7(4)
C009-O002-Ni012	91.8 (3)	N007-C00l-C00A	109.1 (4)
C00B-O003-Ni01	92.2 (3)	N007-C00l-C00P	127.4(5)
C009-0004-Ni012	86.2 (2)	C00A-C00l-C00P	123.5(5)
C00B-0005-Ni0l	84.7(2)	C00D-C00J-C00H	119.1 (4)
C00E- N006-Ni0l	129.8(3)	N007-C00K-C00N	108.8 (5)
C00E- N006-C00L	106.0(4)	C00M-C00L-N006	109.6(5)
C00L- N006-Ni0l	123.7(3)	C00L-C00M-C00S	106.2 (5)
C00l- N007-Ni0l	128.2(3)	C00A-C00N-C00K	106.1 (5)

Table A.II.17: Torsion Angles for Ni-SKU-5.

A-B-C-D	Angle/ °	Atom-Atom-Atom	Angle/ °
Ni011-O002-C009-O004	-1.9 (4)	N006-C00L-C00M-C00S	0.2(7)
Ni011-O002-C009-C00D	-17 9 .7 (3)	N007-C00K-C00N-C00A	0.1(8)
Ni01-O003-C00B-O005	-8.2 (4)	C009-C00D-C00F-C00G	174.1(4)
Ni01-O003-C00B -C00C	16 8.8 (3)	C009-C00D-C00J-C00H	-17 6.8 (4)
Ni011-O004-C009-O002	1.8 (4)	C00B-C00C-C00G-C00F	17 6 .1 (4)
NiO11-O004-C009-C00D	17 9.6 (3)	COOB COOC COOH COOJ	-17 8.7 (4)
Ni01-O005-C00B-O003	7. 6 (4)	C00C-C00H -C00J-C00D	2.7(7)
Ni01-O005-C00B-C00C	-169.3 (4)	C00D-C00F-C00G-C00C	2.7(6)
Ni01-N006-C00E-C008	-17 2 .3 (3)	C00E-N006-C00L-C00M	0.2(6)
Ni01-N006-C00E-C00O	5.4 (8)	C00E-C00S-C00M-C00L	-0.4(7)
Ni01-N006-C00L-C00M	172.7 (4)	C00F-C00D -C00J-C00H	-0.8(7)
NiO1-N007-C00l-C00A	-161.6 (4)	C00G-C00C-C00H-C00J	-2.0(7)
NiO1-N007-C00l-C00P	18.3(8)	C00H-C00C-C00G-C00F	-0.7 (7)
Ni01-N007-C00K-C00N	163.1(5)	C00l-N007-C00K-C00N	-0.4(7)
Ni01-C00B-C00C-C00G	-92.2(17)	C00l-C00A-C00N-C00K	0.2(8)
Ni01-C00B-C00C-C00H	84.6(17)	C00J-C00D-C00F-C00G	-1.9(7)
O002-C009-C00D-C00F	-5.9(6)	C00K-N007-C00l-C00A	0.5(6)
O002-C009-C00D-C00J	170.2 (4)	C00K-N007-C00l-C00P	-17 9 .6(6)
O003-C00B-C00C-C00G	-153.2 (4)	C00L-N006-C00E-C00S	-0.5 (6)
O003-C00B-C00C -C00H	2 3. 6 (6)	C00L-N006-C00E-C00O	177.3 (6)
O004-C009-C00D-C00F	176.3 (4)	C00M -C00S-C00E-N006	0 .6 (6)
O004 -C009-C00D-C00J	-7.6 (6)	C00M-C008-C00E-C00O	-177.3 (6)
O005-C00B-C00C-C00G	2 3 .8 (6)	C00N-C00A-C00l-N007	o .4 (7)
O005-C00B-C00C-C00H	-159.4 (4)	C00N-C00A-C00l-C00P	17 9.7 (6)

A.II.4 DFT Calculation of :

Table A.II.18: Coordinates of atoms in optimised geometry of **Cu(I)**.

Coordinates for Cu (I)			
Atom	Coordinates (Å)		
	X	Y	Z
Cu	-0.0001	0.0007	-0.0004
O	-2.0406	0.0354	-0.4919
C	-2.7265	-0.1841	0.586
O	-2.2715	-0.5327	1.7311
O	2.0402	-0.034	0.4916
C	2.7267	0.1845	-0.5861
O	2.2725	0.533	-1.7316
C	-4.2115	-0.0812	0.3491
C	-5.1029	-0.3414	1.4134
C	-4.7146	0.2733	-0.9213
C	-6.486	-0.2485	1.21
H	-4.6886	-0.6091	2.3805
C	-6.0985	0.3661	-1.1297
H	-4.0084	0.4695	-1.7216
C	-6.9888	0.1055	-0.0634
H	-7.1886	-0.4427	2.0152
H	-6.4989	0.6366	-2.1009
C	4.2115	0.0809	-0.3485
C	4.7138	-0.2734	0.9222
C	5.1035	0.3403	-1.4125
C	6.0976	-0.3669	1.1314
H	4.0071	-0.4688	1.7223
C	6.4864	0.2466	-1.2084
H	4.6898	0.6077	-2.3799
C	6.9885	-0.1072	0.0654
H	6.4974	-0.6372	2.1028
H	7.1895	0.4402	-2.0135
C	8.4585	-0.1956	0.2399
O	9.3132	0.0172	-0.6404
O	8.8358	-0.5543	1.5324

Coordinates for Cu (I)			
Atom	Coordinates (Å)		
	X	Y	Z
H	9.8164	-0.5992	1.5959
C	-8.4589	0.1933	-0.2373
O	-9.3131	-0.0203	0.6434
O	-8.837	0.5519	-1.5296
H	-9.8176	0.5963	-1.5925
C	-0.7635	2.6662	1.2562
C	0.6793	2.8699	-0.401
C	-0.5078	4.0178	1.1085
H	-1.4102	2.1586	1.9538
N	0.4052	4.1352	0.0531
H	1.3494	2.6261	-1.2115
H	-0.8849	4.8736	1.6445
C	0.7627	-2.6641	-1.2588
C	-0.6785	-2.8688	0.3996
C	0.5076	-4.0158	-1.1114
H	1.4087	-2.156	-1.9567
N	-0.4044	-4.1339	-0.0553
H	-1.3479	-2.6257	1.2108
H	0.8844	-4.8713	-1.6482
C	-0.9684	-5.3833	0.4705
H	-1.5396	-5.9026	-0.3066
H	-0.1705	-6.0406	0.8324
H	-1.6382	-5.1532	1.3031
C	0.9699	5.3842	-0.4728
H	0.1725	6.0413	-0.8363
H	1.54	5.9041	0.3047
H	1.6409	5.1536	-1.3042
N	-0.0184	1.9753	0.306
N	0.0182	-1.9737	-0.3076

Cu (I):

Sum of Electronic energy and zero-point energy= -1944.672116 Hartree

Sum of Electronic energy and thermal enthalpy correction= -1944.664229 Hartree

Sum of Electronic energy and thermal free energy correction= -1944.71101 Hartree

Table A.II.19: Coordinates of atoms in optimised geometry of **Cu(II)**.

Coordinates for Cu (II)			
Atom	Coordinates (Å)		
	X	Y	Z
Cu	-0.0001	0.0007	-0.0004
O	-1.9485	0.0978	-0.4399
C	-2.7267	-0.1852	0.5849
O	-2.272	-0.534	1.7301
O	1.9481	-0.0964	0.4396
C	2.7269	0.1856	-0.585
O	2.273	0.5343	-1.7306
C	-4.2116	-0.0827	0.3475
C	-5.1033	-0.3435	1.4114
C	-4.7143	0.272	-0.923
C	-6.4864	-0.251	1.2075
H	-4.6893	-0.6114	2.3786
C	-6.0982	0.3644	-1.1319
H	-4.0079	0.4687	-1.7229
C	-6.9888	0.1032	-0.066
H	-7.1892	-0.4457	2.0124
H	-6.4983	0.6351	-2.1031
C	4.2116	0.0824	-0.3469
C	4.7135	-0.2721	0.9239
C	5.1039	0.3424	-1.4105
C	6.0973	-0.3652	1.1335
H	4.0066	-0.468	1.7236
C	6.4868	0.2491	-1.2059
N	-0.403	-4.134	-0.0567
H	-1.3475	-2.6265	1.2095
H	0.8866	-4.8705	-1.6494
C	-0.9668	-5.3838	0.4685
H	-1.5375	-5.903	-0.309
H	-0.1688	-6.0409	0.8305
H	-1.637	-5.1542	1.3009

Coordinates for Cu (II)			
Atom	Coordinates (Å)		
	X	Y	Z
H	4.6905	0.61	-2.378
C	6.9885	-0.1049	0.0679
H	6.4968	-0.6357	2.105
H	7.1901	0.4432	-2.0107
C	8.4585	-0.1929	0.243
O	9.3134	0.0205	-0.637
O	8.8354	-0.5518	1.5355
H	9.816	-0.5964	1.5993
C	-8.4589	0.1905	-0.2404
O	-9.3133	-0.0236	0.6399
O	-8.8366	0.5494	-1.5327
H	-9.8172	0.5935	-1.596
C	-0.7649	2.6656	1.2567
C	0.6785	2.8702	-0.3999
C	-0.5096	4.0173	1.1095
H	-1.4116	2.1575	1.9539
N	0.4038	4.1353	0.0545
H	1.349	2.6269	-1.2102
H	-0.8871	4.8728	1.6457
C	0.7641	-2.6635	-1.2593
C	-0.6777	-2.8692	0.3985
C	0.5094	-4.0153	-1.1124
H	1.4101	-2.1549	-1.9568
C	0.9683	5.3847	-0.4708
H	0.1708	6.0416	-0.8344
H	1.5379	5.9045	0.3071
H	1.6397	5.1545	-1.302
N	-0.0135	1.9678	0.3111
N	0.0134	-1.9663	-0.3127

Cu (II):

Sum of Electronic energy and zero-point energy= -1944.633528 Hartree

Sum of Electronic energy and thermal enthalpy correction= -1944.626178 Hartree

Sum of Electronic energy and thermal free energy correction= -1944.672212 Hartree

Table A.II.20: Coordinates of atoms in optimised geometry of **TS-1**.

Atom	Coordinates (Å)		
	X	Y	Z
Cu	0.0487	0.6292	-0.0755
O	-1.2221	-0.6088	0.0016
C	-2.4924	-0.3275	-0.0326
O	-2.8694	0.8697	-0.1218
O	1.7748	0.2376	-0.0256
C	2.093	-1.0206	0.0685
O	1.1905	-1.896	0.1226
C	-3.5345	-1.4594	0.0361
C	-4.9021	-1.1554	-0.0007
C	-3.1157	-2.7931	0.1355
C	-5.8508	-2.185	0.0619
H	-5.2219	-0.1372	-0.0765
C	-4.0645	-3.8227	0.198
H	-2.0716	-3.0252	0.1635
C	-5.432	-3.5187	0.1612
H	-6.8949	-1.9527	0.0338
H	-3.7446	-4.8411	0.2738
C	3.5748	-1.4377	0.1135
C	4.579	-0.4621	0.0529
C	3.9193	-2.7924	0.2151
C	5.9276	-0.8409	0.0938
H	4.316	0.5722	-0.0246
C	5.268	-3.1712	0.256
H	3.1527	-3.5374	0.2615
C	6.2721	-2.1954	0.1954
H	6.6942	-0.0959	0.0475
H	5.5311	-4.2055	0.3336
C	7.7541	-2.6116	0.2403
O	8.0637	-3.8279	0.3316
O	8.7785	-1.6157	0.1782
H	9.5501	-1.9197	0.6616
C	-6.4748	-4.65	0.23
O	-7.7027	-4.3766	0.1971
O	-6.0478	-6.011	0.3312
H	-6.6954	-6.5817	-0.089
C	-0.0845	0.8369	-3.0527
C	0.7755	-1.0842	-2.1671
C	0.2461	0.0387	-4.0837
H	-0.5147	1.8146	-3.1158
N	0.7977	-1.193	-3.5084
H	1.1161	-1.8304	-1.4801
H	0.1291	0.2597	-5.1241
C	0.7541	-0.8765	2.309
C	-0.1419	1.1761	2.7541
C	0.7125	-0.744	3.6471
H	1.1185	-1.7215	1.7631
N	0.1361	0.576	3.9262
H	-0.5708	2.1502	2.6443
H	1.0374	-1.4634	4.3694
C	-0.0982	1.1467	5.2605
H	-1.0786	0.8794	5.5955
H	0.6295	0.7636	5.9451
H	-0.016	2.2124	5.212
C	1.2914	-2.3503	-4.2686
H	0.7557	-2.4254	-5.1918
H	2.3347	-2.2255	-4.4707
H	1.1431	-3.2423	-3.6966
N	0.2577	0.1101	-1.825
N	0.204	0.3596	1.7417
C	2.424	4.0431	-1.4416
C	1.0239	4.0965	-1.4042
C	0.2747	3.9827	-0.2888
C	0.9744	4.246	0.8337
C	2.3712	4.202	0.9397
C	3.1134	3.9763	-0.2253
H	2.9518	4.0705	-2.3719
H	0.4681	4.4814	-2.2336
H	0.3836	4.7362	1.5791
H	2.8575	4.3542	1.8806
H	4.1671	3.794	-0.1897
I	-2.8562	3.7783	-0.3017

TS-1:

Sum of Electronic energy and zero-point energy= -2187.030037 Hartree

Sum of Electronic energy and thermal enthalpy correction= -2187.022890 Hartree

Sum of Electronic energy and thermal free energy correction= -2187.073318 Hartree

Table A.II.21: Coordinates of atoms in optimised geometry of **INT-1**.

Atoms	Coordinates (Å)		
	X	Y	Z
N	-0.2101	-3.5006	-1.6955
H	1.8319	-4.1398	-1.9144
H	-0.4043	-5.5255	-2.1601
C	-0.7514	-2.3907	-1.1666
C	1.1189	-3.4127	-1.5858
C	-0.9542	-4.6179	-2.2938
H	-1.7987	-2.1762	-1.1085
N	0.2157	-1.5687	-0.7677
C	1.4031	-2.1958	-0.9637
O	1.9364	0.3938	-0.0329
O	-1.8713	-0.2711	0.1452
O	2.0845	-1.5042	1.3064
O	-2.266	1.5969	-1.1444
C	2.5852	-0.5637	0.5582
C	-2.6563	0.5833	-0.4292
N	-0.1317	1.8032	0.7933
H	2.3752	-1.8154	-0.7238
C	4.1087	-0.4612	0.3494
C	-4.1511	0.264	-0.2534
C	0.8585	2.5324	1.3052
C	-1.2993	2.4096	1.1208
C	4.6252	0.5499	-0.4724
C	4.9774	-1.3707	0.971
C	-4.5112	-0.826	0.5484
C	-5.1437	1.0362	-0.8729
N	0.3623	3.6717	1.815
H	1.8959	2.2776	1.251
H	-2.2848	2.0628	0.8943
C	-0.9695	3.6196	1.7277
H	3.964	1.2517	-0.9365
C	6.0053	0.64	-0.6895
C	6.3611	-1.2795	0.752
H	4.5866	-2.1349	1.6097
H	-3.7497	-1.4143	1.0167
C	-5.8568	-1.1477	0.7397
C	-6.4974	0.7114	-0.6838

Atoms	Coordinates (Å)		
	X	Y	Z
H	-4.8707	1.8692	-1.4878
C	1.143	4.743	2.4513
H	-1.6562	4.3684	2.0635
C	6.8729	-0.2787	-0.0865
H	6.3987	1.4097	-1.3187
H	7.0248	-1.9744	1.2224
C	-6.8503	-0.3795	0.1246
H	-6.1249	-1.9808	1.3554
H	-7.2579	1.2961	-1.157
H	2.1836	4.4997	2.4069
H	0.8438	4.8462	3.4736
H	0.9695	5.664	1.9347
C	8.3883	-0.1838	-0.3507
C	-8.3295	-0.7427	0.3439
O	8.8405	0.7185	-1.1035
O	-8.6312	-1.7202	1.0774
H	-1.9099	-4.7068	-1.8201
H	-1.0903	-4.4332	-3.3389
O	-9.3617	0.024	-0.2811
H	-10.1207	-0.5394	-0.4468
O	9.2812	-1.1199	0.2567
H	10.1338	-0.7028	0.3976
C	-0.0285	-0.7025	1.9706
C	0.0336	0.1991	2.9739
C	0.0003	-2.052	2.0688
C	0.0138	-0.319	4.2731
H	0.0585	1.2578	2.8228
C	-0.0186	-2.5743	3.3705
H	0.0005	-2.7114	1.2279
C	-0.0168	-1.7042	4.4719
H	0.0202	0.3427	5.114
H	-0.039	-3.6335	3.5244
H	-0.037	-2.0986	5.4654
Cu	0.0197	0.1499	-0.0621
I	-0.1138	1.4377	-2.6794

INT-1:

Sum of Electronic energy and zero-point energy= -2187.112951 Hartree

Sum of Electronic energy and thermal enthalpy correction= -2187.102966 Hartree

Sum of Electronic energy and thermal free energy correction= -2187.156980 Hartree

Table A.II.22: Coordinates of atoms in optimised geometry of **INT-2**.

Atom	Coordinates (Å)		
	X	Y	Z
N	-0.2207	-3.782	-0.8885
H	1.8232	-4.4467	-0.9508
H	-0.3998	-5.8594	-0.7853
C	-0.7645	-2.5718	-0.6699
C	1.1079	-3.6616	-0.8226
C	-0.9592	-5.0256	-1.1553
H	-1.8122	-2.3542	-0.6575
N	0.202	-1.6794	-0.4645
C	1.3896	-2.3224	-0.5554
O	1.9531	0.4505	-0.2839
O	-1.921	-0.1912	0.0871
O	2.1283	-1.1005	1.4242
O	-2.304	1.3604	-1.6042
C	2.6145	-0.3651	0.4675
C	-2.6793	0.5368	-0.6693
N	-0.1833	1.9817	0.1984
H	2.3613	-1.8891	-0.4396
C	4.137	-0.3075	0.2386
C	-4.1745	0.2626	-0.414
C	0.7934	2.8496	0.4205
C	-1.3635	2.6299	0.3102
C	4.6604	0.4711	-0.8028
C	5.0001	-1.036	1.069
C	-4.5379	-0.6147	0.6152
C	-5.166	0.875	-1.1945
N	0.27	4.0685	0.6337
H	1.8372	2.6144	0.4154
H	-2.3413	2.2117	0.1968
C	-1.0607	3.9635	0.5851
H	4.0034	1.0334	-1.4325
C	6.0446	0.5125	-1.0211
C	6.3852	-0.9947	0.8508
H	4.6026	-1.6244	1.8688
H	-3.7806	-1.0806	1.2099
C	-5.8873	-0.8832	0.8683
C	-6.5208	0.6034	-0.9427
H	-4.8911	1.5477	-1.9804
C	1.027	5.2845	0.967
H	-1.7641	4.7564	0.7315

Atom	Coordinates (Å)		
	X	Y	Z
C	6.9065	-0.2242	-0.1977
H	6.4429	1.1061	-1.8175
H	7.0432	-1.552	1.4842
C	-6.8802	-0.276	0.0907
H	-6.1598	-1.5533	1.6572
H	-7.28	1.0669	-1.5388
H	2.0736	5.0633	0.9724
H	0.7312	5.6341	1.9345
H	0.8256	6.041	0.2378
C	8.4262	-0.1858	-0.4475
C	-8.3637	-0.5793	0.3764
O	8.8909	0.5074	-1.3889
O	-8.6746	-1.3663	1.3085
H	-1.9099	-4.9888	-0.6656
H	-1.1055	-5.1342	-2.2098
O	-9.3874	0.0303	-0.4134
H	-10.1474	-0.5557	-0.4579
O	9.3093	-0.938	0.3889
H	10.1587	-0.4938	0.4384
C	0.0353	-0.1335	1.866
C	0.1233	0.9704	2.6622
C	0.1066	-1.4326	2.3176
C	0.1639	0.7705	4.0512
H	0.1173	1.9651	2.2668
C	0.1476	-1.6304	3.7063
H	0.0873	-2.2751	1.6589
C	0.1733	-0.5291	4.5728
H	0.1874	1.6118	4.713
H	0.1594	-2.6231	4.1054
H	0.1997	-0.6813	5.6321
Cu	0.0088	0.1576	-0.0881
N	-0.1039	0.4809	-1.9572
C	-0.6592	-0.39	-2.8718
C	0.0673	1.4123	-3.8976
H	-0.5548	0.1973	-4.1154
C	-1.0915	-1.3444	-2.6595
H	0.309	2.1335	-4.6515
H	-0.8859	-0.2014	-5.052
N	0.317	1.5336	-2.5733

INT-2:

Sum of Electronic energy and zero-point energy= -2401.185335 Hartree
Sum of Electronic energy and thermal enthalpy correction= -2401.177619 Hartree
Sum of Electronic energy and thermal free energy correction= -2401.224798 Hartree

able A.II.23: Coordinates of atoms in optimised geometry of product.

Atom	Coordinates (Å)		
	X	Y	Z
C	-1.1482	1.2356	0.0001
C	-2.5531	1.1926	0.0001
C	-3.2309	-0.0409	0
C	-2.4862	-1.2368	-0.0001
C	-1.0823	-1.2083	-0.0001
C	-0.412	0.0326	0
H	-0.6469	2.1988	0.0001
H	-3.1145	2.1237	0.0001
H	-4.3173	-0.0696	0
H	-2.9982	-2.196	-0.0001
H	-0.4963	-2.1196	-0.0001
N	1.0182	0.0541	0
C	1.8746	1.1407	-0.0001
C	3.0246	-0.779	0.0001
C	3.1736	0.6417	0
H	1.5231	2.1596	-0.0002
H	3.7916	-1.5398	0.0001
H	4.0897	1.2121	-0.0001
N	1.7258	-1.1452	0.0001

Product :

Sum of Electronic energy and zero-point energy= -456.498998 Hartree

Sum of Electronic energy and thermal enthalpy correction= -456.487951 Hartree

Sum of Electronic energy and thermal free energy correction= -456.553596 Hartree